



Cristina Maria Vieira Frazão

Recycled Steel Fiber Reinforced Concrete  
for Structural elements subjected to chloride  
attack: Mechanical and Durability  
performance

Universidade do Minho  
Escola de Engenharia



Cofinanciado por:



CIÊNCIA, TECNOLOGIA  
E ENSINO SUPERIOR

**FCT**

Fundação  
para a Ciência  
e a Tecnologia



PORTUGAL  
**2020**



UNIÃO EUROPEIA  
Fundo Social Europeu



Universidade do Minho  
Escola de Engenharia

Cristina Maria Vieira Frazão

Recycled Steel Fiber Reinforced Concrete  
for Structural elements subjected to chloride  
attack: Mechanical and Durability  
performance

Doctoral thesis  
Civil Engineering

Work performed under the supervision of:  
Professor Doutor Joaquim António Oliveira de Barros  
Professor Doutor José Alexandre de Brito Aleixo Bogas

October, 2019

## **DIREITOS DE AUTOR E CONDIÇÕES DE UTILIZAÇÃO DO TRABALHO POR TERCEIROS**

Este é um trabalho académico que pode ser utilizado por terceiros desde que respeitadas as regras e boas práticas internacionalmente aceites, no que concerne aos direitos de autor e direitos conexos.

Assim, o presente trabalho pode ser utilizado nos termos previstos na licença abaixo indicada.

Caso o utilizador necessite de permissão para poder fazer um uso do trabalho em condições não previstas no licenciamento indicado, deverá contactar o autor, através do RepositóriUM da Universidade do Minho.

### ***Licença concedida aos utilizadores deste trabalho***



**Atribuição  
CC BY**

<https://creativecommons.org/licenses/by/4.0/>

## ACKNOWLEDGEMENTS

The research reported in this thesis was carried out at the Department of Civil Engineering of the University of Minho, under the supervision of Prof. Joaquim Barros and Prof. José Alexandre Bogas, to whom I express my deepest gratitude for their support, encouragement, knowledge and valuable suggestions.

I would like to express my sincere gratitude to all institutions and individuals who made this research work possible, namely:

- The financial support provided by the Portuguese Foundation of Science and Technology (FCT) through the Doctoral Program in Eco Construction and Rehabilitation (EcoCoRe) under the PhD grant PD/BD/113638/2015.
- University of Minho, through the Institute for Sustainability and Innovation in Structural Engineering (ISISE) and the Department of Civil Engineering (DEC), for providing the facilities and resources to develop this research work.
- The support provided by CiviTest company in the production of concrete specimens and execution of some experimental tests.
- My special gratitude to Belén Díaz from ENCOMAT, University of Vigo (Spain) for her collaboration in the work related to the investigation on the corrosion susceptibility of Recycled Steel Fiber Reinforced Concrete.
- I would also to thank the collaboration of Fatih Toptan and Alexandra Alves from CMEMS–UMinho in the experimental program of electrochemical tests.
- The support provided by MFPA Company during my stay at the Institute of Mineralogy, Crystallography and Materials Science (IMCM) of the University of Leipzig, Germany. My gratitude goes to Annemarie Herrmann, Andreas König and Florian Fuchs.
- The collaboration of Verónica García Cortés from TECNALIA, Derio (Spain) in the Life Cycle Impact Assessment of fiber reinforced concrete.
- I also would like to acknowledge the help of Delfina Gonçalves, Inês Costa and Christoph de Sousa in the experimental research.
- To the laboratory technicians of the Laboratory of Civil Engineering (LMC and LEST) of University of Minho, I would like to express my gratitude for technical support, especially to Mr. Matos.
- To all my family, colleagues and friends for their support and contribution to this work.
- *Last but not least*, to my life mate Rui for his love, support, help, motivation and patience, especially in the most difficult moments.

## **STATEMENT OF INTEGRITY**

I hereby declare having conducted this academic work with integrity. I confirm that I have not use plagiarism or any form of undue use of information or falsification of results along the process leading to its elaboration.

I further declare that I have fully acknowledged the Code of Ethical Conduct of the University of Minho.

University of Minho, October 2019

Full name: Cristina Maria Vieira Frazão

Signature:

## RESUMO

As fibras de aço recicladas (FAR) provenientes da indústria de reciclagem de pneus tem sido usadas com sucesso no betão para melhorar o seu comportamento pós-fendilhação e a sua capacidade de absorção de energia. Para elementos estruturais expostos em ambientes com cloretos, um dos aspetos mais importantes da durabilidade do Betão Reforçado com Fibras de Aço Recicladas (BRFAR) é a resistência à corrosão. No entanto, a durabilidade do BRFAR é quase inexistente, nomeadamente no que respeita aos efeitos do ataque de cloretos, o que limita a mobilização de todo o potencial do BRFAR.

A presente tese tem como objetivo avaliar o comportamento mecânico e o desempenho de durabilidade do BRFAR sob ataque de cloretos, englobando investigação experimental e analítica/numérica, cujo conhecimento pode futuramente contribuir para regras de projeto e ferramentas de dimensionamento de estruturas em BRFAR. As atividades de investigação realizadas abrangeram duas principais áreas, a tecnologia de produção do BRFAR e a investigação da suscetibilidade à corrosão do BRFAR.

Na primeira área, foi realizado um programa experimental para caracterizar as FAR, em termos de geometria, composição química, propriedades mecânicas e microestrutura. A influência dos detritos de borracha aderidos à superfície das FAR foi avaliada no desempenho das FAR como reforço do betão e na sua resistência à corrosão. Uma composição sustentável de BRFAR foi desenvolvida e avaliadas as suas propriedades mecânicas através de ensaios de flexão e de compressão.

A segunda área incluiu um programa experimental para caracterizar a corrosão das FAR e investigar os seus efeitos nos mecanismos de reforço das fibras desenvolvidos durante o arrancamento da fibra do betão fendilhado previamente exposto a ambiente corrosivo. Adicionalmente, o comportamento pós-fendilhação do BRFAR sob ataque de cloretos foi caracterizado através de ensaios de tração indireta e ensaios com placas redondas. Nestes ensaios, foi considerada a influência da abertura de fenda, do período de exposição em cloretos e do perfil de distribuição/orientação das fibras. Os resultados experimentais foram utilizados para realizar simulações numéricas por análise inversa de modo a derivar as leis constitutivas pós-fendilhação do BRFAR. Foi ainda estimada uma previsão simplificada do teor crítico de cloretos correspondente ao início da corrosão das fibras e do desempenho a longo prazo de um elemento estrutural de BRFAR exposto a um ambiente marítimo agressivo.

Além disso, foram avaliados os benefícios técnicos, ambientais e económicos do uso do BRFAR desenvolvido para aplicação em elementos estruturais, ao nível do material e em comparação com Betão Reforçado com Fibras de Aço Industriais.

**Palavras-chave:** Betão Reforçado com Fibras de Aço Recicladas (BRFAR); Ataque de cloretos; Desempenho mecânico e de durabilidade; Investigação experimental; Simulações numéricas.

## **ABSTRACT**

Recycled Steel Fibers (RSF) derived from the tire recycling industry have been successfully used in concrete to improve its post-cracking load bearing capacity and energy absorption performance. For structural elements exposed to chloride environments, an important aspect of Recycled Steel Fiber Reinforced Concrete (RSFRC) durability is the corrosion resistance. However, research on the durability of RSFRC is almost inexistent, namely concerning the effects of chloride attack, which may limit the mobilization of the full potential of RSFRC.

The present thesis aims to assess the mechanical behavior and durability performance of RSFRC under chloride attack involving both experimental and analytical/numerical research, which knowledge may contribute for future design guidelines and design tools for RSFRC structures. The research activities carried out covered two main fields, the technology of RSFRC manufacturing and the investigation on the corrosion susceptibility of RSFRC.

In the first field, an experimental program was carried out to characterize the RSF in terms of geometry, chemical composition, mechanical properties and microstructure. The influence of rubber particles attached to RSF surface was assessed in the performance of RSF as concrete reinforcement and in its corrosion resistance. A sustainable mix composition of RSFRC was attained and their mechanical properties were evaluated by three-point notched beam bending tests and compressive tests.

The second research field involved an experimental program to characterize the RSF corrosion and to investigate the corrosion effects of RSF on the fiber reinforcement mechanisms developed during the fiber pull-out from cracked concrete previously exposed to corrosive environment. Additionally, the post-cracking behavior of RSFRC under chloride attack was characterized from double edge wedge splitting tests and round panel tests. In these tests, the influence of the crack width, chloride exposure period and fiber distribution/orientation profile was considered. The experimental results were used to perform numerical simulations by inverse analysis, aiming to derive the post-cracking constitutive laws of RSFRC. A simplified prediction of the critical chloride content corresponding to the beginning of fiber corrosion and of the long-term performance of a RSFRC structural element exposed to a specific dry-wet aggressive maritime environment was performed.

In addition, the technical, environmental and economic benefits of using the developed RSFRC for application to structural elements were assessed at material level and compared to Industrial Steel Fiber Reinforced Concrete.

**Keywords:** Recycled Steel Fiber Reinforced Concrete (RSFRC); Chloride attack; Mechanical and durability performance; Experimental research; Numerical simulations.



## TABLE OF CONTENTS

ACKNOWLEDGEMENTS.....	iii
STATEMENT OF INTEGRITY .....	iv
RESUMO .....	v
ABSTRACT .....	vi
TABLE OF CONTENTS .....	vii
LIST OF ABBREVIATIONS.....	xii
LIST OF FIGURES .....	xv
LIST OF SYMBOLS.....	xxii
LIST OF TABLES.....	xxv
1 Introduction .....	1
1.1 Motivation .....	1
1.2 Objectives and Research methodology.....	5
1.3 Structure of the thesis .....	7
2 Literature Overview .....	9
2.1 Recycling of post-consumer tires.....	9
2.1.1 Environmental issues .....	9
2.1.2 Pneumatic tires composition .....	11
2.1.3 Tires recycling.....	12
2.1.4 Recycling Processes to obtain RSF from post-consumer tires .....	14
2.2 Recycled Steel Fiber Reinforced Concrete (RSFRC).....	20
2.2.1 Geometric characterization of RSF.....	20
2.2.2 Chemical composition of RSF.....	23
2.2.3 Tensile strength of RSF .....	23
2.2.4 Pull-out behavior of RSF .....	25
2.2.5 Technology of RSFRC manufacturing.....	30
2.2.6 Compressive behavior of RSFRC .....	32
2.2.7 Post-cracking tensile behavior of RSFRC and testing procedures .....	33
2.2.8 Durability of SFRC exposed to chloride attack .....	45
2.3 Structural elements for coastal breakwaters.....	58
3 Technology of RSFRC manufacturing.....	63
3.1 Introduction.....	63
3.2 Materials.....	64
3.2.1 Cement .....	64
3.2.2 Fly Ash .....	65
3.2.3 Limestone filler .....	66

3.2.4	Aggregates.....	67
3.2.5	Water .....	68
3.2.6	Superplasticizers.....	68
3.2.7	Viscosity modifying admixture.....	69
3.3	Characterization of Recycled Steel Fibers .....	69
3.3.1	Geometric properties.....	69
3.3.2	Chemical composition.....	75
3.3.3	Mechanical properties.....	77
3.3.3.1	Tensile strength .....	77
3.3.3.2	Pre-treatment of RSF to remove rubber debris attached to fiber surface .....	79
3.3.3.3	Young's modulus and Hardness .....	82
3.3.3.4	Fiber pull-out behavior.....	87
3.4	Mix Design Methodologies for RSFRC production.....	92
3.4.1	Mix Compositions .....	92
3.4.2	Mixing procedure and fresh concrete properties.....	95
3.5	Mechanical characterization of RSFRC .....	97
3.5.1	Flexural behavior.....	97
3.5.1.1	Test procedures .....	97
3.5.1.2	Experimental results.....	97
3.5.1.3	Numerical study: determination of the $\sigma - \omega$ law by inverse analysis.....	107
3.5.2	Compressive behavior .....	109
3.5.2.1	Test procedures .....	109
3.5.2.2	Experimental results.....	111
3.5.2.3	Analytical expressions .....	114
3.6	Conclusions .....	119
4	Characterization of RSF corrosion.....	122
4.1	Introduction.....	122
4.2	RSF preparation and electrochemical cell.....	122
4.3	Experimental procedures of electrochemical tests .....	124
4.4	Electrochemical measurements.....	128
4.4.1	Open Circuit Potential .....	128
4.4.2	Potentiodynamic Polarization Resistance .....	129
4.4.3	Linear Polarization Resistance .....	132
4.4.4	SEM Fiber Analysis .....	135
4.5	Corrosion rate and its effect on the mechanical properties of rsf.....	138
4.5.1	Evaluation of RSF mass loss by corrosion .....	138
4.5.2	Tensile strength of corroded RSF .....	143
4.6	Conclusions .....	146

5	RSF pull-out behavior under corrosive action .....	148
5.1	Introduction.....	148
5.2	Experimental program .....	149
5.2.1	Specimens manufacture .....	149
5.2.2	Experimental setup and procedures .....	152
5.2.2.1	Implementation of the crack width.....	152
5.2.2.2	Chloride immersion and electrochemical monitoring.....	152
5.2.2.3	Fiber pull-out bending test.....	154
5.3	Results and discussion .....	155
5.3.1	Characterization of fiber corrosion by electrochemical tests.....	155
5.3.2	Pull-out behavior of corroded steel fibers .....	156
5.4	RSF pull-out tests under corrosive action using X-Ray Micro-computer Tomography.....	161
5.4.1	Specimens manufacture .....	162
5.4.2	Experimental setup and methodology .....	163
5.4.3	Results and discussion.....	166
5.5	Conclusions .....	172
6	Post-cracking behavior of RSFRC under chloride attack .....	174
6.1	Introduction.....	174
6.2	Experimental program .....	175
6.2.1	Specimens manufacture and environmental exposure .....	175
6.2.2	Experimental setup and procedures .....	177
6.3	Experimental results and discussion .....	179
6.3.1	Effect of the rubber content in the corrosion resistance of RSFRC .....	179
6.3.1.1	Assessment of the number of effective fibers .....	185
6.3.2	Long-term corrosion effects on the post-cracking behavior of RSFRC .....	188
6.3.2.1	RSFRC subjected to 10 days of chloride immersion .....	188
6.3.2.2	RSFRC subjected to 3 months of chloride immersion.....	190
6.3.2.3	RSFRC subjected to 6 months of chloride immersion.....	193
6.3.2.4	Assessment of the number of effective fibers.....	196
6.3.2.5	Fiber distribution/orientation profile .....	199
6.4	Numerical simulations.....	205
6.5	Conclusions .....	210
7	Post-cracking behavior of RSFRC under chloride attack .....	213
7.1	Introduction.....	213
7.2	Experimental program .....	214
7.2.1	Specimens manufacture .....	214
7.2.2	Experimental setup .....	215
7.2.3	Parameters in study.....	216

7.2.3.1	Crack width .....	216
7.2.3.2	Environmental exposure .....	218
7.2.3.3	Fiber distribution/orientation profile .....	221
7.2.4	Chloride diffusion in RSFRC.....	222
7.2.4.1	Non-steady state chloride migration tests.....	222
7.2.4.2	Chloride penetration by immersion .....	223
7.2.4.2.1	Chloride penetration and aging coefficient by colorimetric method.....	225
7.3	Results and discussion .....	226
7.3.1	Preliminary RPT-3ps.....	226
7.3.2	Results of RPT-3ps under chloride attack.....	229
7.3.2.1	Modes of failure .....	229
7.3.2.2	Chloride penetration into RSFRC panels .....	230
7.3.2.3	Force-Central deflection relationships .....	233
7.3.2.4	Energy absorption-Central deflection relationships .....	239
7.3.2.5	Stiffness-Central deflection relationships.....	243
7.3.2.6	Force-Crack width relationships.....	245
7.3.2.7	Evaluation of crack width measurements.....	246
7.3.3	Fiber distribution and orientation parameters.....	251
7.3.4	Numerical simulation of the performed RPT-3ps .....	258
7.3.4.1	Numerical model .....	258
7.3.4.2	Numerical results.....	261
7.3.5	Chloride diffusion in RSFRC.....	268
7.3.5.1	Chlorides migration under non-steady state .....	268
7.3.5.2	Resistance to chloride penetration by immersion .....	270
7.3.5.3	Chloride diffusion and aging coefficient by colorimetric method.....	271
7.3.5.4	Resistance to chloride penetration by dry-wet cycles .....	273
7.3.5.4.1	Determination of the chloride diffusion coefficient by colorimetric method.....	273
7.3.5.4.2	Determination of the chloride diffusion coefficient by Fick's 2nd law .....	274
7.3.5.4.3	Determination of surface chloride content by Fick's 2nd law.....	274
7.3.5.4.4	Determination of the critical chloride concentration .....	275
7.3.5.5	Chloride penetration prediction into a RSFRC structural element.....	275
7.4	Conclusions .....	276
8	RSFRC as alternative to ISFRC for reinforcement of the structural elements.....	280
8.1	Introduction.....	280
8.2	Technical benefits of RSFRC: Experimental investigation on the post-cracking behavior ...	281
8.2.1	Splitting tensile tests .....	281
8.2.2	Round Panel tests.....	284
8.3	Environmental impact of RSFRC: Life Cycle Assessment .....	285

8.3.1	Materials .....	286
8.3.2	Goal and Scope definition.....	286
8.3.3	Life Cycle Inventory.....	287
8.3.4	Life Cycle Impact Assessment.....	289
8.4	Economic benefits of RSFRC .....	297
8.5	Conclusions .....	297
9	Conclusions and Future perspectives.....	300
9.1	Main conclusions .....	300
9.2	Recommendations for future research .....	305
10	References.....	306
App_A	Methodology to measure the hardness and elastic modulus by nano-indentation test .....	323
App_B	RSF exposed to chloride immersion .....	326
App_C	Design of the test setup for RPT-3ps .....	330
App_D	Modes of failure of round panels.....	335

## LIST OF ABBREVIATIONS

ACI	American Concrete Institute
ADP	Abiotic Depletion Potential
AP	Acidification potential
ASTM	American Society for Testing and Materials
Avg	Average
CEM	Cement
CEN	European Committee for Standardization
Cf	Fiber content
CG	Crushed granite
Cl	Chloride attacked
CML	Institute of Environmental Sciences – University of Leiden
CMOD	Crack mouth opening displacement
CoV	Coefficient of variation
CS	Coarse river sand
CSM	Continuous stiffness measurement
DEWST	Double edge wedge splitting test
EDS	Energy dispersive X-Ray spectroscopy
EFCA	European Federation of Concrete Admixtures Associations Ltd.
EFNARC	European Federation for Specialist Construction Chemicals and Concrete Systems
ELTs	End-of-life tires
EP	Eutrophication potential
EPA	Environmental Protection Agency
EPD	Environmental product declarations
ETRA	European Tyre Recycling Association
ETRMA	European Tyre & Rubber Manufacturers' Association
EN	European Norm
ENV	Envelope
EU	European Union
FA	Fly Ash
FEG-SEM	Field Emission Gun Scanning Electron Microscope
FhG-IKTS-MD	Fraunhofer-Gesellschaft-System
FRC	Fiber reinforced concrete
FRCC	Fiber reinforced cementitious composites
FS	Fine river sand
GWP	Global warming potential

IEA	International Energy Agency
ISF	Industrial steel fiber
ISFRC	Industrial steel fiber reinforced concrete
ITZ	Interfacial transition zone
LCA	Life Cycle Assessment
LF	Limestone Filler
LVDT	Linear variable differential transformer
MC2010	CEB <i>fib</i> Model Code 2010
MSF	Manufactured undulated steel fiber
MSTT	Modified splitting tensile test
ODP	Ozone depletion potential
PC	Plain concrete
PE-NRe	Non-renewable primary energy consumption
POPC	Photochemical ozone creation potencial
PRSF	Pyrolysed recycled steel fiber
RCT	Rapid chloride test
REF	Reference
RMA	Rubber Manufacturers Association
RPT	Round panel test
RPT-3ps	Round panel supported on three symmetrically arranged pivots
RSF	Recycled steel fiber
RSFRC	Recycled steel fiber reinforced concrete
RTSC	Recycled tire steel cord
RTSF	Recycled tire steel fiber
SCC	Self-compacting concrete
SCE	Saturated calomel electrode
SEM	Scanning electron microscopy
SFRC	Steel fiber reinforced concrete
SFRSC	Steel fiber reinforced sprayed concrete
SFRSCC	Steel fiber reinforced self-compacting concrete
SLS	Serviceability Limit States
SP	Superplasticizer
SPLT	Splitting tensile test
SRSF	Shredded recycled steel fiber
StD	Standard deviation
TGA	Thermogravimetric analysis
ULS	Ultimate Limit State

UPFRC	High performance fiber reinforced concrete
USTMA	United States Tire Manufacturers Association
VMA	Viscosity modifying admixture
VSF	Steel fiber obtained from virgin tire
W	Water
W/B	Water/Binder ratio
W/C	Water/Cement ratio
WBCSD	World Business Council for Sustainable Development
XRF	X-ray fluorescence spectrometry
3D- $\mu$ XCT	X-ray micro-computer tomography
3PNBBT	Three-point notched beam bending test



## LIST OF FIGURES

Figure 2.1 – World’s biggest tire graveyard in Sulaibiya and Tire fire in West Odessa .....	10
Figure 2.2 – Typical tire section and components .....	12
Figure 2.3 – Overview of an ambient shredding process to reduce tires to rubber granulate and steel fibers.....	15
Figure 2.4 – Recycled fibers obtained from shredding process .....	15
Figure 2.5 – Overview of a cryogenic process to reduce tires to rubber granulate and steel fibers .....	17
Figure 2.6 – RSF obtained from cryogenic process.....	17
Figure 2.7 – Tire Pyrolysis Steel Wire Scrap .....	18
Figure 2.8 – RSF obtained by microwave pyrolysis .....	20
Figure 2.9 – Appearance of RSF obtained from the shredded process of ELTs.....	21
Figure 2.10 – Relative frequency of Diameter measurements and Length measurements .....	22
Figure 2.11 – RTSC tensile test setup and failure mode of RSF in direct tensile test.....	24
Figure 2.12 – $\sigma$ - $\epsilon$ diagram for an irregular RSF .....	24
Figure 2.13 – Test setup for single-sided pull-out test and Testing apparatus of double-sided pull-out tests.....	26
Figure 2.14 – Typical applied load-slip curve with a fiber embedded length of 40 mm .....	27
Figure 2.15 – Pull-out load-slip responses for RTSC with different embedment lengths .....	27
Figure 2.16 – An inclined fiber crossing a crack section and components of pull-out force in an inclined fiber ...	29
Figure 2.17 – Three-point notched beam bending test setup and Typical load-CMOD curve of FRC .....	34
Figure 2.18 – Comparison of the flexural behavior of RSFRC and ISFRC.....	35
Figure 2.19 – Load-deflection curves for SFRC mixes at 30, 35 and 45 kg/m <sup>3</sup> from 3PNBBT.....	36
Figure 2.20 – Splitting tensile test setup and Stress distribution in the loading plane .....	38
Figure 2.21 – Splitting tension load-deflection curves and Splitting tensile strength vs. volume of fibers.....	38
Figure 2.22 – Force diagram in DEWST and Details of the DEWST .....	39
Figure 2.23 – BCN test setup in cylindrical specimen and Mechanism of failure of BCN test .....	41
Figure 2.24 – Cracking mechanism and distribution of stresses in BCN test .....	41
Figure 2.25 – Residual strength vs. CMOD obtained from 3PNBBT and BCNT.....	42
Figure 2.26 – RPT setup with three point support and normal failure mode .....	43
Figure 2.27 – Load-deflection curves for SFRC mixes at 30, 35 and 45 kg/m <sup>3</sup> from RPT-3ps.....	43
Figure 2.28 – Schematic representation of chloride induced localized corrosion .....	46
Figure 2.29 – Tuutti’s service life model for corrosion of steel in concrete .....	49
Figure 2.30 – Predicted corrosion initiation of SFRC and plain concrete, with and without applied load .....	50
Figure 2.31 – Results obtained with PC, ISFRC and RSFRC, in terms of Flexural and Compressive strength .....	53
Figure 2.32 – Corrosion spots versus exposure time as a function of W/C.....	55
Figure 2.33 – Chloride penetration depth in the fractured zone versus crack width .....	56

Figure 2.34 – Structure and corrosion mechanisms for SFRC exposed to chlorides .....	57
Figure 2.35 – General view of a tetrapod unit and Tetrapod armor layers for breakwaters.....	59
Figure 2.36 – Rupture of tetrapod legs and Cracking of tetrapods .....	60
Figure 3.1 – Granulometric curves of used aggregates.....	68
Figure 3.2 – Recycled steel fibers.....	70
Figure 3.3 – Micrometer to measure the fiber diameter.....	71
Figure 3.4 – Frequency distribution of fiber diameter measurements.....	71
Figure 3.5 – Frequency distribution of fiber length measurements.....	72
Figure 3.6 – Frequency distribution of fiber length and developed fiber length measurements.....	72
Figure 3.7 – Frequency distribution of curvature index .....	73
Figure 3.8 – Frequency distribution of the aspect ratio .....	73
Figure 3.9 – Localization of the zones for chemical analysis by SEM-EDS in a single reference RSF .....	76
Figure 3.10 – RSF preparation for tensile tests and General view of the test setup for RSF tensile tests .....	78
Figure 3.11 – Tensile stress <i>versus</i> displacement for the RSF submitted to direct tensile test .....	78
Figure 3.12 – TGA analysis of RSF up to 700°C .....	79
Figure 3.13 – Images of the RSF after firing for 1 hour at the selected temperatures .....	80
Figure 3.14 – SEM micrographs of the surface of a single RSF submitted to 350°C.....	80
Figure 3.15 – SEM micrographs of the surface of a single polished RSF .....	81
Figure 3.16 – ISF type 1: general view of multi fibers and single ISF.....	83
Figure 3.17 – Load-Displacement curves obtained in nano-indentation tests of RSF .....	84
Figure 3.18 – Load-displacement curves obtained in nano-indentation tests of ISF.....	85
Figure 3.19 – Test setup for fiber pull-out tests: Preparation of fiber pull-out concrete specimens.....	89
Figure 3.20 – Observation of the debonding process of RSF from concrete with an USB microscope .....	90
Figure 3.21 – Envelope and average Pull-out load-End slip relationship obtained in RSF pull-out tests .....	90
Figure 3.22 – Average Pull-out load-End slip curves obtained from five different types of class 1 RSF .....	92
Figure 3.23 – ISF type 2: general view of multi fibers and single ISF.....	94
Figure 3.24 – Introduction of RSF into the concrete mixer .....	95
Figure 3.25 – Slump tests for a concrete reinforced with 76 kg/m <sup>3</sup> of RSF .....	96
Figure 3.26 – Test setup for 3PNBBT .....	97
Figure 3.27 – Envelope and avg load/flexural stress-deflection curves for RSFRC1%_1 .....	98
Figure 3.28 – Envelope and avg load/flexural stress-deflection curves for RSFRC1%_2&3&4&5 .....	99
Figure 3.29 – Envelope and avg load/flexural stress-deflection curves for RSFRC1%_6 and ISFRC1% .....	100
Figure 3.30 – Load-deflection diagrams for the determination of the equivalent and residual flexural tensile strengths .....	101
Figure 3.31 – Envelope and average load/flexural stress-CMOD curves for beams of RSFRC1%_1 to 5 .....	102

Figure 3.32 – Envelope and avg load/flexural stress-CMOD curves for PC, RSFRC1%_6 and ISFRC1% .....	103
Figure 3.33 – Deflection-CMOD relationship for all the performed 3PNBBT.....	103
Figure 3.34 – Relationship between $f_{eq,2}$ and $f_{eq,3}$ .....	105
Figure 3.35 – Relationships between $f_{eq,2}$ and $f_{R,1}$ ; and $f_{eq,3}$ and $f_{R,4}$ .....	105
Figure 3.36 – Schematic representation of the regions in the fractured zone of specimens for the fiber distribution assessment and Fiber distribution at the fracture section of RSFRC.....	106
Figure 3.37 – Finite element mesh used in the simulation of the 3PNBBTs .....	107
Figure 3.38 – Numerical simulation of the 3PNBBT .....	108
Figure 3.39 – $\sigma - \omega$ relationships obtained by inverse analysis from 3PNBBTs .....	109
Figure 3.40 – Determination of the Compressive strength and Modulus of elasticity .....	111
Figure 3.41 – Average Compressive stress-Longitudinal strain curves obtained in compression tests .....	112
Figure 3.42 – Time dependance of Compressive strength and Modulus of elasticity .....	114
Figure 3.43 – Stress-strain diagram for uniaxial compression.....	115
Figure 3.44 – Experimental and analytical (MC2010 & Cunha <i>et al.</i> , 2008) relationships .....	117
Figure 3.45 – Experimental and analytical (Barros, 1995) relationships.....	119
Figure 4.1 – Electrochemical cell prepared on a particular RSF/3.5 wt% NaCl solution system .....	123
Figure 4.2 – Tafel slope calculation of the polarization curve .....	125
Figure 4.3 – Determination of polarization resistance .....	125
Figure 4.4 – Evolution of $E_{ocp}$ in RSF over the immersion period .....	128
Figure 4.5 – Cyclic polarization curves in three RSF of class 1 – Series I (forward & reverse scan).....	129
Figure 4.6 – Potentiodynamic polarization curves after the immersion period .....	130
Figure 4.7 – Tafel fitting of the polarization curve using the software VoltaMaster.....	131
Figure 4.8 – Linear polarization curves after the immersion period .....	133
Figure 4.9 – SEM micrographs of corroded polished RSF after potentiodynamic polarization (Mag. 100x) .....	135
Figure 4.10 – SEM micrographs of corroded polished RSF after potentiodynamic polarization (Mag. 1000x) ...	136
Figure 4.11 – SEM micrographs of corroded polished RSF after chloride immersion.....	136
Figure 4.12 – SEM micrographs of corroded polished RSF after linear polarization .....	137
Figure 4.13 – Evolution of RSF mass loss under chloride exposure of its total length .....	139
Figure 4.14 – Evolution of mass loss of RSF under chloride exposure of 1 mm of its length.....	139
Figure 4.15 – Evolution of mass loss of RSF under chloride exposure of 0.5 mm of its length.....	140
Figure 5.1 – Appearance of the SCC specimen in the 1 <sup>st</sup> Phase and 2 <sup>nd</sup> Phase .....	151
Figure 5.2 – Supporting system and Load application system for cracked SCC specimens.....	152
Figure 5.3 – Chloride immersion and electrochemical monitoring of RSF into cracked SCC specimen.....	153
Figure 5.4 – Configuration of the steel fiber pull-out bending test.....	155

Figure 5.5 – Variation of the $E_{ocp}$ in RSF during the immersion period of the specimens .....	156
Figure 5.6 – Pull-out load-End slip relationship obtained in RSF pull-out tests of cracked SCC specimens.....	157
Figure 5.7 – Specimen of Series IV after four-point load bending test.....	158
Figure 5.8 – Applied load/Pull-out load-End slip relationship obtained in uncracked SCC specimens.....	158
Figure 5.9 – Aspect of RSF after fiber pull-out test.....	159
Figure 5.10 – Pull-out load-End slip obtained from 4-point bending tests and from direct fiber pull-out tests ....	160
Figure 5.11 – Configuration of measurement setup of 3D- $\mu$ XCT.....	161
Figure 5.12 – Appearance of the mortar specimen in the 1 <sup>st</sup> Phase and 2 <sup>nd</sup> Phase.....	163
Figure 5.13 – Supporting and load application systems for cracked mortar specimens .....	164
Figure 5.14 – Chloride immersion of cracked mortar specimen under tension.....	164
Figure 5.15 – Fiber pull-out test setup defined to employ 3D- $\mu$ XCT.....	165
Figure 5.16 – Identification of x- and y- direction defined for 2D-projection of the specimens.....	166
Figure 5.17 – 2D-projection for determination of initial crack width.....	167
Figure 5.18 – Plot profile of grayvalue obtained for zone A in y-direction .....	167
Figure 5.19 – Plot profile of grayvalue obtained at zone A in y-direction .....	168
Figure 5.20 – 2D-projection obtained for fiber diameter determination at the five states of craked specimen ...	169
Figure 5.21 – Plot profiles of grayvalue obtained in x-direction for the five states of cracked specimen .....	169
Figure 5.22 – 2D-projection of RSF for cracked specimen under successive increments of applied load .....	171
Figure 5.23 – Pore distribution in the cracked mortar specimen.....	172
Figure 6.1 – Schematic representation of the preparation process of DEWST specimens .....	176
Figure 6.2 – Test setup for DEWST .....	178
Figure 6.3 – Assessment of the fiber density in the fractured zone of specimens .....	179
Figure 6.4 – Specimens subjected to 10 days of chloride immersion.....	180
Figure 6.5 – Envelope and average splitting tensile stress-CMOD curves for specimens of Series I, II and III....	181
Figure 6.6 – Average splitting tensile stress-CMOD curves for specimens of Series I, II and III.....	182
Figure 6.7 – Relationship between the crack width and energy absorption during the fracture propagation.....	185
Figure 6.8 – Relationships between the effective fiber density and $G_{F0.3}$ of Series I, II and III .....	186
Figure 6.9 – Relationships between the effective fiber density and $G_{F0.5,1.0,3.0}$ of Series I, II and III .....	187
Figure 6.10 – Specimens after 10 days of chloride immersion .....	188
Figure 6.11 – Cracked surface of specimens after 10 days of chloride immersion .....	189
Figure 6.12 – Envelope and average splitting tensile stress-CMOD curves for specimens of Series IV .....	189
Figure 6.13 – Average splitting tensile stress-CMOD curves for specimens of Series II and IV.....	190
Figure 6.14 – Specimens after 3 months of chloride immersion.....	190
Figure 6.15 – Crack surface of specimens after 3 months of chloride immersion .....	191

Figure 6.16 – SEM micrographs of Class 2 RSF from the fracture surface of RSFRC specimens .....	191
Figure 6.17 – Envelope and average splitting tensile stress-CMOD curves for specimens of Series V .....	193
Figure 6.18 – Specimens after 6 months of chloride immersion.....	193
Figure 6.19 – Crack surface of specimens after 6 months of chloride immersion .....	194
Figure 6.20 – Envelope and average splitting tensile stress-CMOD curves for specimens of Series VI .....	194
Figure 6.21 – Average splitting tensile stress-CMOD curves for specimens of Series IV, V and VI.....	195
Figure 6.22 – Relationship between the crack width and $G_{F\omega}$ of specimens of Series IV, V and VI .....	196
Figure 6.23 – Relationships between the effective fiber density and $G_{F0.3}$ of specimens of Series IV, V and VI	197
Figure 6.24 – Relationships between the effective fiber density and $G_{F0.5,1.0,3.0}$ in Series IV, V, V.....	198
Figure 6.25 – Image processing steps .....	200
Figure 6.26 – Procedure to determine the fiber segregation degree in DEWST specimens.....	202
Figure 6.27 – Splitting tensile stress-CMOD curves for specimens of Series IV, V and VI .....	203
Figure 6.28 – Fiber density in each layer of cutting surface, perpendicular to casting direction.....	205
Figure 6.29 – Fiber density in each layer of cutting surface, parallel to casting direction .....	205
Figure 6.30 – Finite element mesh, support and loading conditions used in the simulation of the DEWST.....	206
Figure 6.31 – Numerical simulation of the DEWST .....	207
Figure 6.32 – $\sigma - \omega$ relationships obtained by inverse analysis for splitting specimens of Series I, II and III ....	208
Figure 6.33 – $\sigma - \omega$ relationships obtained by inverse analysis for splitting specimens of Series IV, V and VI .	209
Figure 6.34 – $\sigma - \omega$ relationships obtained by inverse analysis for splitting specimens of: .....	209
Figure 7.1 – The three pivots support system and Connection between the panel and each pivot.....	215
Figure 7.2 – RPT-3ps test setup.....	216
Figure 7.3 – Position of the crack width measurement with a USB Microscope.....	218
Figure 7.4 – General view of the tanks.....	220
Figure 7.5 – Temperature monitoring of tank solution/water over the 3-month exposure period.....	221
Figure 7.6 – Schematic representation of the preparation process of specimens for chloride migration tests...	222
Figure 7.7 – Rapid chloride migration test.....	223
Figure 7.8 – Chloride penetration test by immersion .....	224
Figure 7.9 – Split section of PC cylindrical specimens.....	225
Figure 7.10 – Force-central deflection curve obtained in Panel 1 of preliminary RPT-3ps.....	227
Figure 7.11 – Avg crack width (1,2,3) - central deflection relationship obtained in preliminary RPT-3ps .....	227
Figure 7.12 – Avg Crack width - central deflection relationship obtained in preliminary RPT-3ps.....	228
Figure 7.13 – Avg crack width (A,B,C) - central deflection relationship obtained in preliminary RPT-3ps.....	229
Figure 7.14 – Crack patterns of the panels .....	230
Figure 7.15 – Corrosion spots at exposed surfaces of RSFRC Panels.....	230

Figure 7.16 – Inspection of RSF at crack surfaces.....	231
Figure 7.17 – Chloride penetration depth at cracked surfaces .....	231
Figure 7.18 – Inspection of RSF on an orthogonal cut plane to a crack surface .....	232
Figure 7.19 – Force-Central deflection relationships of Series I and IV .....	233
Figure 7.20 – Force-Central deflection relationships of Series II and V .....	234
Figure 7.21 – Stiffness parameters determined for each pre-cracked panel .....	234
Figure 7.22 – Normalized stiffness- pre-crack width relationship obtained in the pre-cracked panels .....	236
Figure 7.23 – Force-Central deflection relationships of Series III and VI .....	237
Figure 7.24 – Average Force-Central deflection relationships of Series I to VI.....	238
Figure 7.25 – Average Energy absorption-Central deflection relationships of Series I to VI .....	239
Figure 7.26 – Corrected energy absorption-Central deflection relationships of Series I to VI.....	242
Figure 7.27 – Average Stiffness-Central deflection relationships of Series I to VI.....	244
Figure 7.28 – Average Force-CMOD relationships of Series I to VI.....	246
Figure 7.29 – Crack width measurements with the LVDTs and the microscope in pre-cracked panels .....	247
Figure 7.30 – Measurement of non-linear tensile deformations of a beam under 3-point bending test .....	248
Figure 7.31 – Crack width measurements performed with the microscope at each crack C1,C2 and C3 .....	248
Figure 7.32 – Crack width measurement performed with the microscope at position 1C in the Panel P4 .....	249
Figure 7.33 – Crack width measurements performed with the microscope at each position A, B and C: .....	250
Figure 7.34 – Procedure to determine the fiber segregation degree in round panels .....	251
Figure 7.35 – Crack width-Central deflection relationships of Series I, II and III.....	253
Figure 7.36 – Crack width-Central deflection relationships of Series IV, V and VI.....	256
Figure 7.37 – Crack rotation analysis in RPT-3ps (symmetric crack propagation) .....	259
Figure 7.38 – Crack rotation analysis in RPT-3ps (asymmetric crack propagation) .....	260
Figure 7.39 – Numerical simulation of RPT-3ps from Series I&IV_CI&REF .....	262
Figure 7.40 – Numerical simulation of RPT-3ps from Series II&V_CI&REF .....	263
Figure 7.41 – $\sigma - \omega$ relationships obtained by inverse analysis for RPT-3ps of Series I, II, IV and V.....	264
Figure 7.42 – Numerical simulation of RPT-3ps for non-cracked panels.....	266
Figure 7.43 – $\sigma - \omega$ relationships obtained by inverse analysis for RPT-3ps of Series III and VI.....	267
Figure 7.44 – $\sigma - \omega$ relationships obtained by inverse analysis from RPT-3ps and 3PNBBTs.....	268
Figure 7.45 – Chloride migration tests.....	269
Figure 7.46 – Chloride profiles along specimen depth from exposed surface of RSFRC and PC.....	270
Figure 7.47 – Chloride penetration depth in RSFRC and PC cubes after 3 months of immersion.....	272
Figure 7.48 – Prediction of chloride penetration depth into a RSFRC structural element.....	276
Figure 8.1 – Envelope and average splitting tensile stress-CMOD curves for specimens of RSFRC and ISFRC..	282
Figure 8.2 – Avg force/energy absorption versus central deflection of RSFRC and ISFRC.....	284

Figure 8.3 – Stages of an LCA according to ISO 14040:2006 .....	285
Figure 8.4 – Global warming potential impact .....	291
Figure 8.5 – Ozone depletion potential impact .....	292
Figure 8.6 – Photochemical ozone creation potential impact .....	292
Figure 8.7 – Acidification potential impact .....	293
Figure 8.8 – Eutrophication potential impact .....	294
Figure 8.9 – ADP - Elements.....	294
Figure 8.10 – ADP-Fossil fuels impact .....	295
Figure 8.11 – Non-renewable primary energy (PE-NRe) resources impact .....	296
Figure 8.12 – Renewable primary energy resources impact .....	296
Figure A.1 – Load-displacement data obtained in nano-indentation test .....	331
Figure C.1 – Drawing 1: Front view of the RPT-3ps test setup (units in mm) .....	331
Figure C.2 – Drawing 2: Top views and details of the RPT-3ps test setup by the cutting planes A-A' and B-B' ..	332
Figure C.3 – Drawing 3: Details of the three-pivot support for RPT-3ps .....	333
Figure C.4 – Drawing 4: RPT-3ps test setup for round panels with 800 mm diameter .....	334

## LIST OF SYMBOLS

$A_f$	Cross sectional area of a single RSF
$\beta_a$	Tafel slope for the anodic reactions
$\beta_c$	Tafel slope for the cathodic reactions
$C_c$	Concentration of free chlorides in the pore solution corresponding to the color change boundary
$CI$	Curvature index
$C_0$	Initial chloride content
$C_r$	Reference chloride concentration
$C_s$	Chloride concentration at the exposed surface
$C_x$	Chloride concentration at depth $x$ and immersion time $t$
$\delta$	Displacement; deflection
$\delta_{cr}$	Central deflection corresponding to the pre-crack width $w_{cr}$
$\delta_{K_{ci}}$	Central deflection corresponding to the initial stiffness value $K_{ci}$
$D_c$	Chloride diffusion coefficient obtained from colorimetric method
$D_d$	Apparent chloride diffusion coefficient obtained from Fick's 2 <sup>nd</sup> law
$d_e$	Effective crack depth
$d_f$	Fiber diameter
$D_m$	Chloride migration coefficient
$D_{max}$	Maximum size of the aggregate
$D_{ref}$	Diffusion coefficient at reference time $t_{ref}$
$\epsilon_{c,1}$	Strain at peak load
$E_{cm}$	Young's modulus
$E_{corr}$	Corrosion potential
$E_{(i=0)}$	Corrosion potential obtained from potentiodynamic polarization
$E_{OCP}$	Open circuit potential
$erf$	Error-function
$f_{cm}$	Compressive strength
$f_{ct}$	Tensile strength
$f_{ct,fl}$	Flexural tensile stress
$f_{ct,L}$	Limit of proportionality
$f_{eq}$	Equivalent flexural tensile strength parameters
$F_j$	Load values corresponding to the $CMOD_j$



$f_{R,i}$	Residual flexural strength parameters
$F_{sp}$	Splitting tensile force
$f_u$	Tensile stress
$G_c$	Energy dissipated under compression
$G_f$	Energy dissipated under tension
$G_{F\omega}$	Energy due to fracture propagation up to a given crack width $\omega$
$\lambda$	Aspect ratio
$h_{fs}$	Ligament depth of the fracture surface
$h_{sp}$	Distance between the tip of the notch and the top of the cross section
$i$	Applied current density
$i_{corr}$	Corrosion current density
$K_{ci}$	Initial stiffness
$K_{csecr}$	Reloading secant stiffness
$K_{csecu}$	Unloading secant stiffness
$K_{C_r}$	Chloride penetration parameter
$K_{fu}$	Initial unloading tangent stiffness
$K_{Or}$	Initial reloading tangent stiffness
$L_{ad}$	Fiber embedded length
$l_d$	Developed length of the fiber
$l_f$	Fiber length
$l_{fs}$	Thickness of the fracture surface
$n_{cl}$	Aging coefficient
$\eta_{exp}$	Fiber orientation factor obtained from Eq. proposed by Soroushian and Lee (1990)
$\eta_{img}$	Fiber orientation factor obtained by image analysis
$N^f$	Number of fibers per unit area
$\xi_{seg}$	Fiber segregation parameter
$R_p$	Polarization resistance
$\theta_i$	Angle between the fiber's longitudinal axis and the orthogonal to the cut section
$\sigma$	Stress
$\sigma_{t,split}$	Splitting tensile stress
$\sigma_N$	Nominal tensile stress
$\sigma_\omega$	Residual strength at a given crack width $\omega$
$\tau_{max}$	Bond stress at maximum pull-out load
$V_f$	Fiber volume fraction added to concrete

$\omega$	Crack width
$\omega_{cr}$	Pre-crack width
$W$	Energy absorbed up to a central deflection
$W'$	Corrected energy absorbed up to a central deflection
$W_{cri}$	Critical crack width
$\omega_u$	Ultimate crack opening
$x$	Penetration depth
$x_c$	Colorimetric penetration depth

## LIST OF TABLES

Table 2.1 - Composition by mass of EU car and truck tires.....	12
Table 2.2 - Recycled tire materials by mass <sup>a</sup> produced in EU during 2016-17 .....	13
Table 2.3 - Chemical composition for RSF .....	23
Table 2.4 - Summary of RSF and ISF tensile strength.....	25
Table 2.5 – Results of chloride diffusion coefficient $D_o$ ( $\times 10^{-12} \text{ m}^2.\text{s}^{-1}$ ) .....	49
Table 2.6 – Scale of superficial deterioration of SFRC due to rust.....	54
Table 3.1 – Main characteristics of CEM I 42.5R .....	65
Table 3.2 – Main characteristics of fly ash .....	66
Table 3.3 – Main physical properties of limestone filler .....	66
Table 3.4 – Main chemical properties of limestone filler.....	67
Table 3.5 – Granulometric analysis of aggregates .....	67
Table 3.6 – Main characteristics of the superplasticizers.....	69
Table 3.7 – Main characteristics of the VMA .....	69
Table 3.8 – Average geometric properties of RSF obtained by the supplier.....	70
Table 3.9 – Geometric characterization of used RSF .....	74
Table 3.10 - Chemical composition for reference RSF determined by XRF analysis .....	75
Table 3.11 – Chemical elements identified in the surface of reference RSF .....	76
Table 3.12 – Geometric properties and tensile strength of tested RSF .....	79
Table 3.13 – Chemical elements identified in the surface of RSF submitted to 350°C.....	81
Table 3.14 - Chemical composition for polished RSF determined by XRF analysis.....	82
Table 3.15 – Chemical composition of ISF according to Italian standard UNI 11037:2003.....	83
Table 3.16 – Avg values ( <i>and StD</i> ) of Young's modulus and hardness obtained by nano-indentation tests..	85
Table 3.17 – Mix design for 1 m <sup>3</sup> of concrete .....	87
Table 3.18 – Average values of bond stress obtained in RSF pull-out tests.....	91
Table 3.19 – Mix proportions for 1 m <sup>3</sup> of concrete .....	94
Table 3.20 – Slump and flow of fresh RSFRC .....	96
Table 3.21 – Average results ( <i>and CoV</i> ) of 3PNBBTs.....	104
Table 3.22 –Toughness class obtained for tested FRC beams .....	106
Table 3.23 – RSFRC properties used in the numerical simulation of the 3PNBBTs.....	107
Table 3.24 – Parameters of the $\sigma - \omega$ relationship obtained by inverse analysis.....	109
Table 3.25 – Average results ( <i>and CoV</i> ) of compression tests.....	112
Table 4.1 – Experimental program of electrochemical tests.....	127
Table 4.2 – Results obtained in the potentiodynamic polarization tests.....	131
Table 4.3 – Results obtained in the linear polarization tests .....	134

Table 4.4 – Chemical elements identified in the surface of polished RSF tested.....	138
Table 4.5 – Experimental program to evaluate the RSF mass loss by corrosion .....	139
Table 4.6 – Relevant results of tests to evaluate RSF mass loss by corrosion .....	140
Table 4.7 – Visual observation of RSF surface before and after chloride exposure .....	141
Table 4.8 – Corrosion rate values obtained in RSF submitted to chloride attack .....	142
Table 4.9 – Experimental program to evaluate the tensile strength of corroded RSF .....	143
Table 4.10 – Relevant results to evaluate the mass loss of corroded RSF before tensile tests .....	144
Table 4.11 – Relevant results of direct tensile tests of corroded RSF.....	146
Table 5.1 – Mix design for 1 m <sup>3</sup> of SCC .....	150
Table 5.2 – Experimental program of fiber pull-out bending tests .....	153
Table 5.3 – Relevant results of RSF pull-out tests .....	160
Table 5.4 – Average crack width values obtained with 3D- $\mu$ XCT .....	168
Table 5.5 – Average fiber diameter values obtained with 3D- $\mu$ XCT .....	170
Table 6.1 – Experimental program of DEWSTs .....	177
Table 6.2 – Maximum and residual splitting tensile strength (Series I, II and III).....	184
Table 6.3 – Energy due to fracture propagation (Series I, II and III).....	184
Table 6.4 – Effective fiber counting at fracture surface of splitting specimens of Series I, II and III .....	186
Table 6.5 – Chemical elements identified in the surface of RSF (T=350°C) from the fracture surface of the splitting specimens previously submitted to 3 months of chloride immersion .....	192
Table 6.6 – Maximum and residual splitting tensile strength (Series IV, V and VI).....	195
Table 6.7 – Energy due to fracture propagation (Series IV, V and VI).....	195
Table 6.8 – Effective fiber counting at fracture surface of splitting specimens of Series IV, V and VI .....	197
Table 6.9 – Fiber distribution and orientation parameters of Series IV, V and VI .....	202
Table 6.10 – RSFRC properties used in the numerical simulation of the DEWSTs.....	206
Table 6.11 – Parameters of the $\sigma - \omega$ relationship obtained by inverse analysis (DEWSTs).....	208
Table 7.1 – Experimental program of RPT-3ps .....	219
Table 7.2 – Stiffness parameters for Series I&IV (target $\omega_{cr}$ of 1.0 mm).....	235
Table 7.3 – Stiffness parameters for Series II&V (target $\omega_{cr}$ of 0.5 mm).....	235
Table 7.4 – Pre-crack width, maximum load and energy absorption obtained in RPT-3ps .....	240
Table 7.5 – Corrected energy absorption obtained in RPT-3ps.....	241
Table 7.6 – Parameters $t$ , $K_{ci}$ , $\delta_{K_G}$ , $\omega_{cr}$ and $\delta_{cr}$ of the RSFRC panels .....	244
Table 7.7 – Fiber distribution and orientation parameters in Series I, II and III.....	252
Table 7.8 – Corrected energy absorption obtained in Series I, II and III .....	252
Table 7.9 – Fiber distribution and orientation parameters in Series IV, V and VI.....	255

Table 7.10 – Corrected energy absorption obtained in Series IV, V and VI.....	255
Table 7.11 – Parameters of the $\sigma$ - $\omega$ relationship obtained by inverse analysis in Series I&IV.....	263
Table 7.12 – Parameters of the $\sigma$ - $\omega$ relationship obtained by inverse analysis in Series II&V .....	264
Table 7.13 – Parameters of the $\sigma$ - $\omega$ relationship obtained by inverse analysis in Series III&VI .....	266
Table 7.14 – Chloride migration coefficients in RSFRC and PC specimens.....	269
Table 7.15 – Results of chloride penetration test by immersion.....	270
Table 7.16 – Results of chloride diffusion and aging coefficients .....	271
Table 7.17 – Results of chloride diffusion coefficients .....	272
Table 7.18 – Chloride diffusion coefficient determined by colorimetric method.....	273
Table 7.19 – Surface chloride content determined by Fick’s 2 <sup>nd</sup> law.....	274
Table 7.20 – Critical chloride content determined by Fick’s 2 <sup>nd</sup> law.....	275
Table 8.1 – Maximum and residual splitting tensile strength.....	283
Table 8.2 – Effective fiber counting at fracture surface .....	284
Table 8.3 – Mix proportions for 1 m <sup>3</sup> of fiber reinforced concrete (FRC) .....	286
Table 8.4 – Baseline CML method results for raw materials (for 1 ton).....	289
Table 8.5 – Cumulative Energy Demand (CED) results for raw materials (for 1 ton) .....	289
Table 8.6 – Baseline CML method results for 1 m <sup>3</sup> of concrete .....	289
Table 8.7 – Cumulative Energy Demand (CED) results for 1 m <sup>3</sup> of concrete .....	290
Table 8.8 – Baseline CML method results for 1 MPa of indirect tensile strength .....	297
Table 8.9 – Cumulative Energy Demand (CED) results for 1 MPa of indirect tensile strength.....	297

---

# Chapter 1

---

## INTRODUCTION

### 1.1 MOTIVATION

The evolution of climate change caused by the increased concentrations of greenhouse gas emissions and atmospheric pollution is considered one of the major challenges faced by humanity in the current century, with serious and global consequences for the environment, human health and the economy (de Wilde and Coley, 2012). The buildings and construction sector is one of the main contributors to the above-mentioned phenomena, with a significant impact on global warming, accounting for 36% of global final energy use, and 39% of energy-related CO<sub>2</sub> emissions in 2017 (Source: IEA, 2018). In the recent years, the international scientific community has made efforts to reduce these CO<sub>2</sub> emissions and mitigate their negative environmental footprints by promoting several actions focused on material and environmental sustainability, based on concepts of minimization and reuse of waste (Onuaguluchi and Banthia, 2018). In particular, the use of recycled materials and industrial by-products as sustainable constituents of cement-based materials has become an environmentally and technically promising solution, as it avoids landfill disposal, reduces the depletion of raw materials (due to partial to total replacement by recycled materials) and leads to the reduction of environmental charges by minimizing CO<sub>2</sub> emissions (Paris *et al.*, 2016; Letelier *et al.*, 2017; Onuaguluchi and Banthia, 2018; Leone *et al.*, 2018).

In the recent years, several research studies have explored the potential of end-of-life tires (ELTs) by-products in the construction industry, such as the use of steel fibers obtained from the recycling of ELTs,

herein designated as Recycled Steel Fibers (RSF), in the reinforcement of cement-based materials (Aiello *et al.*, 2009; Centonze *et al.*, 2012; Graeff *et al.*, 2012; Micelli *et al.*, 2014; Caggiano *et al.*, 2015, 2017; Martinelli *et al.*, 2015; Zamanzadeh *et al.*, 2015; Barros *et al.*, 2017; Smrkić *et al.*, 2017; Leone *et al.*, 2018; Lourenço *et al.*, 2018; Onuaguluchi and Banthia, 2018). It is estimated that a total of one billion ELTs is generated every year (Source: WBCSD, 2010) and this amount is expected to increase over the next years, according to the projected global transport growth (Source: OECD/ITF, 2012). The disposal of ELTs in an environmental and productive manner is a high priority goal of the tire business, since the increasing amount of this type of waste is a serious environmental and public health threat (Sienkiewicz *et al.*, 2012). To manage this problem, different countries and states have enacted Codes and Instructions in accordance with the EU Landfill Directive (1999/31/EC) that forbid landfills to accept whole or partial tires, promoting sustainable solutions for the disposal, recovery and reuse of tires. The use of material recovered from waste tires has become the most sustainable strategy to enable investments in recycling ELTs. Most of the efforts concerning the recycling of tires are focused on the extraction and use of rubber (Aiello and Leuzzi, 2010; Azevedo *et al.*, 2012; Boudaoud and Beddar, 2012; Bravo and Brito, 2012; Quadrini *et al.*, 2013; Herrera-Sosa *et al.*, 2015; ETRMA, 2015; Thomas *et al.*, 2016; USTMA, 2018; Sofi, 2018). However, approximately 15 to 25% by weight of a tire is composed of metal (Shulman, 2019). The RSF are currently derived from the tire recycling industry, using mechanical and thermal degradation processes, such as tire shredding, cryogenic reduction and pyrolysis (Pilakoutas *et al.*, 2004; Abraham *et al.*, 2011; Barros *et al.*, 2017). The use of RSF may reduce the emission of CO<sub>2</sub> since recycling saves impressive amounts of energy, contributing to the reduction of the ecological footprint and promoting environmental sustainability (Tchobanoglous and Kreith, 2002). For these reasons, there is a strong motivation for tire recycling and development of new markets for the above waste.

The use of discrete steel fibers as a reinforcement system for cement-based materials is now a current practice for several applications, such as industrial floors, tunnel linings, prefabricated elements, and hydraulic structures. Steel Fiber Reinforced Concrete (SFRC) is increasingly adopted to produce in-situ and prefabricated concrete structures, as partial or total replacement of conventional reinforcement, reducing their construction time and labor costs necessary for the placement of the conventional rebars present in reinforced concrete structural elements. SFRC can also be an auxiliary reinforcement for shrinkage reduction and crack control that contribute for the enhancement of the durability of concrete structures. The potential of using Industrial Steel Fiber (ISF) in reinforced concrete to improve the mechanical and durability performance of concrete structures has been investigated over the past three decades (Ding and Kusterle, 1999; Barros and Figueiras, 1999; Singh and Kaushik, 2003; Granju and

Balouch, 2005; Bentur and Mindess, 2007; Xu and Shi, 2009; Cunha *et al.*, 2010; Caggiano *et al.*, 2012; Barros *et al.*, 2013, 2015a,b; Frazão *et al.*, 2015; Mudadu *et al.*, 2018; Marcos-Meson *et al.*, 2018). The crack opening restraint provided by the reinforcement mechanisms of ISF bridging the cracks (Cunha, 2010) leads to a significant increase of post-cracking load bearing capacity and energy absorption performance, since the stress redistribution provided by fiber reinforcement allows an ultimate load much higher than the cracking load (Barros *et al.*, 2009, 2012; Taheri *et al.*, 2012; Salehian *et al.*, 2014). Recent research is showing that RSF and ISF may exhibit similar mechanical behavior in terms of tensile strength and fiber/matrix bond (Caggiano *et al.*, 2017). However, further research is still needed for addressing the relative behavior between RSF and ISF used for concrete production, in terms of mechanical and durability performance.

According to the available bibliography, RSF derived from the tire recycling industry can be an effective concrete reinforcement for structural and non-structural applications with great economic and environmental beneficial impact (Pilakoutas *et al.*, 2004; Tlemat *et al.*, 2006a; Aiello *et al.*, 2009; Centonze *et al.*, 2012; Graeff *et al.*, 2012; Micelli *et al.*, 2014; Zamanzadeh *et al.*, 2015; Caggiano *et al.*, 2015, 2017; Leone *et al.*, 2016, 2018; Lourenço *et al.*, 2018; Onuaguluchi and Banthia, 2018). The heterogeneity of this fiber system (regarding the geometry, material and microstructure of each fiber) provides a plurality of strengthening mechanisms that can be optimized in a complementary frame, promoting efficiency and durability of the entire reinforcement system, as long as the Recycled Steel Fiber Reinforced Concrete (RSFRC) composition is carefully adjusted to the presence of RSF. RSF reinforcement can significantly reduce the brittle behavior of concrete by improving its toughness and post-cracking resistance (Aiello *et al.*, 2009; Centonze *et al.*, 2012; Micelli *et al.*, 2014; Zamanzadeh *et al.*, 2015). RSF are also used in concrete to restrain the crack opening by bridging the crack surfaces, which leads to improved post-cracking load bearing and energy absorption capacity, with beneficial consequences in terms of concrete durability (Tlemat *et al.*, 2006a; Neocleous *et al.*, 2006; Graeff *et al.*, 2012). However, this ability of the RSF to transfer stresses through a cracked section depends on the effectiveness of the fiber reinforcement, i.e. fiber properties and fiber orientation and distribution (Vandewalle and Dupont, 2003). In this sense, these effects should be considered for structural design, since variations of fiber dispersion in a section may affect the mechanical properties (Abrishambaf, 2015).

According to the results available in the literature, RSF seems to have high potential as an effective concrete reinforcement for application in structural elements, such as the prefabricated plain concrete (PC) blocks, commonly used in the construction of breakwaters to increase the dissipation and absorption of wave energy and to mitigate the adverse effects of coastal erosion, promoting coastal population



security and the socio-economic assets of housing and commercial activities implemented in coastal areas. The production of these PC structural elements has a relative low efficiency in terms of impact resistance and durability for the respective unit cost. During their relatively short service lifetime, these structural elements subjected to severe degradation have different types of pathologies (cracking, considerable relative displacements and deterioration of the concrete by chemical and biological attacks caused by marine microorganisms) that cause a significant (or complete) loss of their effectiveness. The action of microorganisms affects the concrete mainly by contributing to the erosion of the exposed concrete surface, increasing concrete porosity and the transport of degrading materials into the concrete that can accelerate cracking process (Wei *et al.*, 2013). This leads to the need for maintenance interventions with significant costs that undermine the competitiveness of the solution, or even the need for complete reconstruction of the implemented coastal protection system. This is one of the most societal challenges faced by countries with large coastal zones, like Portugal.

Discrete fibers are one suitable reinforcement for this massive type of concrete elements, since the randomly nature of their distribution provides an almost isotropic reinforcement. For structural elements subjected to chloride attack, an important aspect of SFRC durability is the corrosion resistance (Granju and Balouch, 2005; Balouch *et al.*, 2010; ACI 544.5R-10; Frazão *et al.*, 2015, 2016; Marcos-Meson *et al.*, 2018). Corrosive agents may penetrate the concrete through transport mechanisms, whose action are highly dependent on the concrete cracking stage. An increase in the crack width promotes the concrete permeability, favoring the occurrence of corrosion of steel reinforcements (Granju and Balouch, 2005; Nordström, 2005; ACI 544.5R-10). However, the concrete permeability decreases significantly by increasing the fiber content, due to the restraint of crack propagation (Singh and Singhal, 2011). In fact, by limiting the crack width of SFRC to 0.3 mm, it seems that the corrosion is limited to the fibers located at the surface, which has only an aesthetic detrimental impact (Balouch *et al.*, 2010; Frazão *et al.*, 2015, 2016). Therefore, SFRC appears to be a suitable composite material for corrosive environments, such as deicing salt and sea water containing chloride ions.

It is widely reported that steel fiber corrosion is much less severe in SFRC than in steel rebar reinforced concrete structures (Balouch *et al.*, 2010; Sadeghi-Pouya *et al.*, 2013; Berrocal *et al.*, 2013, 2016). Due to their large surface area to volume ratio, steel fibers are more effectively protected by the lime rich layer than the large diameter bars used in conventional reinforced concrete (Chen *et al.*, 2015). However, the insufficient knowledge on the deterioration mechanisms caused by steel fiber corrosion contributes for a conservative design philosophy, which limits the mobilization of the full potential of SFRC (Solgaard *et al.*, 2010). In fact, some design guidelines recommend do not take into account the contribution of fiber

reinforcement of a certain layer thickness for the evaluation of the flexural resistance of SFRC members (RILEM TC 162-TDF, 2003). Knowledge on RSFRC is only some few years old and further research is needed. In particular, research on the durability of RSFRC is still scarce, namely concerning the corrosion resistance. Consequently, understanding the mechanical and durability performance of RSFRC exposed to chloride attack will help towards a more rational design and accurate prediction of the long-term performance of the composite under aggressive chloride exposure conditions.

## **1.2 OBJECTIVES AND RESEARCH METHODOLOGY**

The main purpose of the present work is to assess the potentialities of using RSF from the tire recycling industry as an effective reinforcement of concrete for application in structural elements subjected to chloride environment, with focus on its mechanical and durability performance. To achieve such goal, this study encompasses the following detailed objectives:

- Production of RSFRC with adequate rheological properties and proper mechanical and durability behavior for application in structural elements subjected to chloride attack, such as breakwaters elements;
- Acquisition of new competences on corrosion susceptibility of RSF and evaluation of its effect on the fiber reinforcement mechanisms developed during the fiber pull-out from the matrix in cracked RSFRC;
- Assessment of the influence of the small rubber content attached to the RSF surface in the post-cracking behavior and the corrosion resistance of RSFRC, by using distinct pre-treatment methods for rubber removal from RSF;
- Assessment of the influence of the parameters “crack width” and “fiber distribution and orientation” on the post-cracking performance of pre-cracked and uncracked RSFRC under long-term exposure to chloride environment;
- Prediction of long-term chloride penetration and corrosion initiation in RSFRC elements exposed to chloride environment;
- Development of numerical simulations to obtain the post-cracking constitutive laws of the developed RSFRC, derived from the inverse analysis by fitting the experimental results;
- Assessment of the technical, environmental and economic impact of using RSF as an alternative to ISF for concrete reinforcement;

According to the above-mentioned objectives, the present thesis intends to increase the current knowledge on the durability and long-term behavior of RSFRC under corrosive environments, which may contribute for future guidelines and design tools for RSFRC, whose lack currently limits the use of RSF in concrete construction. To accomplish the objectives listed above, the research methodology that was followed is schematically depicted in Figure 1.1.

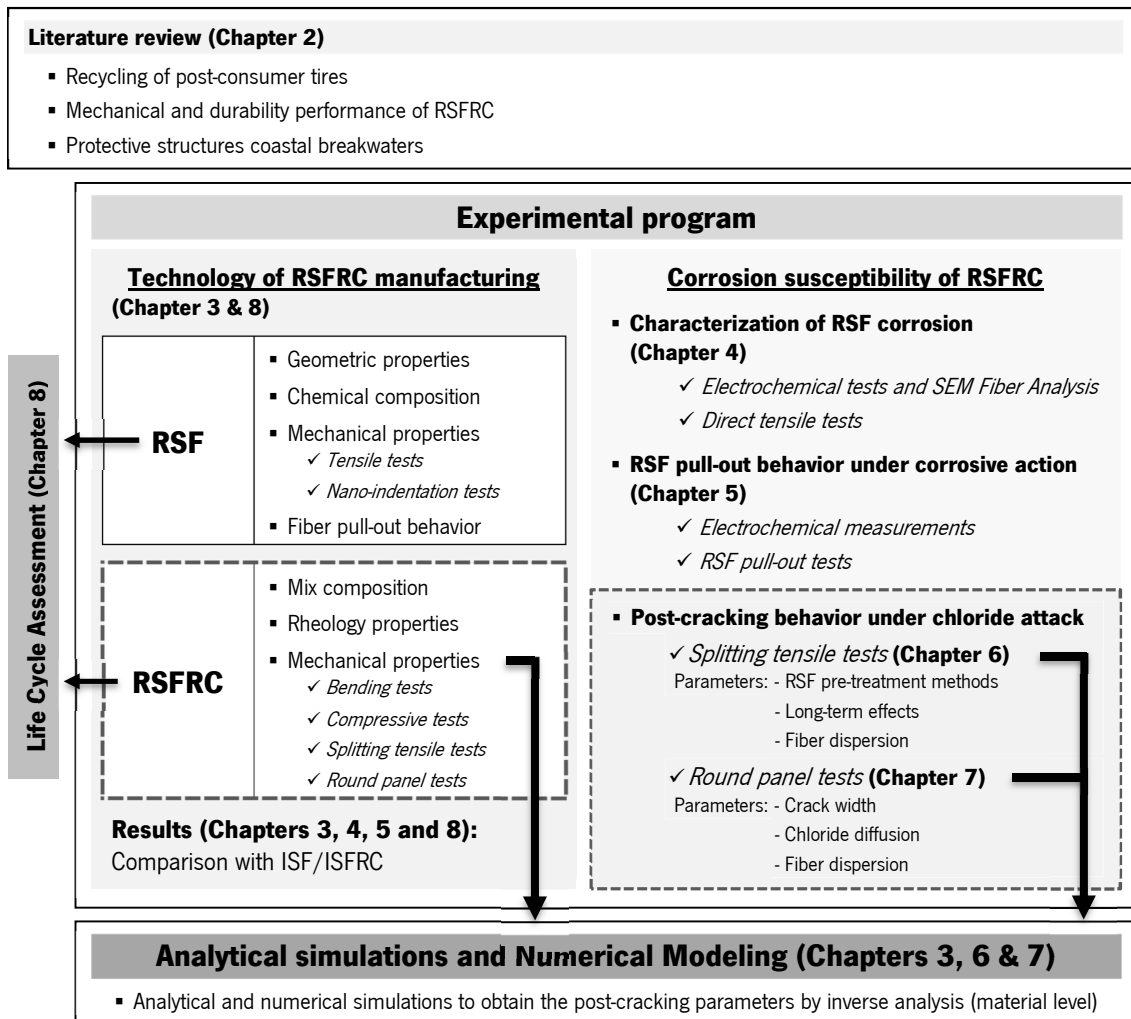


Figure 1.1 – Research methodology

The research methods used in this work include: (i) state-of-the-art review; (ii) Laboratory experiments at material level with small test specimens; (iii) Numerical research at a material level; and, (iv) Life Cycle Analysis. The experimental program is divided into two main group tasks: the first one dedicated to the characterization of RSF, production of RSFRC and assessment of its mechanical properties; the second one dedicated to the investigation on the corrosion susceptibility of RSFRC. The experimental results were used to perform numerical simulations by inverse analysis, aiming to derive the post-cracking constitutive laws of RSFRC.

### 1.3 STRUCTURE OF THE THESIS

The present thesis comprises ten chapters as follows:

Chapter 1 is the introductory chapter and provides the motivation, objectives, research methodology and the outline of the thesis.

Chapter 2 presents a general literature review regarding a set of relevant concepts for the conducted work. This state-of-the-art is focused on three parts: 1<sup>st</sup>) Devoted to the recycling of post-consumer tires, addressing environmental aspects of ELTs disposal and the current recycling processes utilized to obtain RSF from ELTs; 2<sup>nd</sup>) Intended to collect data from recent research on the mechanical performance and corrosion durability of RSFRC and also ISFRC for comparison purposes; 3<sup>rd</sup>) Focused on the structural integrity and durability of PC elements placed in breakwaters for coastal protection.

Chapter 3 describes the experimental work performed to define the RSFRC composition and to evaluate its mechanical behavior. A first part includes the RSF characterization in terms of geometric properties, chemical composition and tensile strength. The influence of two distinct pre-treatment methods, used for rubber removal from RSF surface, on the performance of RSF as concrete reinforcement is also evaluated by using nano-indentation technique and monotonic fiber pull-out tests. The results of the mechanical performance of RSF are compared with those obtained with ISF (Cunha, 2010; Abrishambaf, 2015). A second part addresses the technological aspects for the RSFRC production, namely, the mix design methodology, mixing procedure and rheology properties, as well as the mechanical characterization of RSFRC in terms of flexural and compressive behavior. The laboratory experiments are detailed, and the relevant results are presented and discussed.

In the Chapter 4, the corrosion susceptibility of RSF caused by chloride attack is investigated by electrochemical tests and scanning electron microscopy (SEM) analysis. The results are compared with those obtained with ISF taking into account identical experimental conditions (Frazão *et al.*, 2016). In addition, the corrosion effects on the cross-sectional area of RSF and on the corresponding tensile strength were also evaluated by conducting direct tensile tests on corroded RSF.

The corrosion effects of RSF on the fiber reinforcement mechanisms developed during the fiber pull-out in a self-compacting concrete (SCC) are studied. Non-standard experimental fiber pull-out tests with RSF embedded in cracked specimens of SCC, previously exposed to aggressive environment containing chlorides, are conducted. The influence of crack width is investigated and the corrosion potential of RSF is assessed by electrochemical measurements. The performance of the adopted fiber pull-out methodology is analyzed, including the possibility of using X-Ray Computer Tomography. The specimen's configuration, the experimental setup and the obtained results are described in Chapter 5.

In Chapter 6, the post-cracking behavior of RSFRC under chloride immersion is assessed by splitting tensile tests (SPLT). The influence of three parameters is investigated: 1) Pre-treatment methods used for rubber removal from RSF surface; 2) Long-term effects of chloride immersion; 3) Fiber distribution and orientation. Then, the constitutive laws of RSFRC are derived from the inverse analysis of the experimental results and through the comprehensive nonlinear 2D finite element modeling of SPLT. The experimental and numerical results are presented and discussed.

Chapter 7 details the experimental program conducted to characterize the post-cracking behavior of RSFRC under chloride attack from round panel tests (RPT). The influence of the crack width and the fiber distribution/orientation profile on the force-deflection and the energy dissipation responses obtained in the RPT is investigated. Furthermore, an inverse analysis strategy combining a moment-rotation approach with a model that considers the kinematics conditions of RPT at failure stage and the equilibrium equations is performed to derive the stress-crack width ( $\sigma - \omega$ ) relationship of the RSFRC representative of the RPT. In addition, it is estimated the long-term chloride ingress into RSFRC elements and its corrosion susceptibility, based on a simplified prediction of the critical chloride content. The experimental and numerical results are presented and discussed.

The Chapter 8 addresses the investigation performed to assess the technical, environmental and economic benefits of the developed RSFRC at a material level, with comparison with ISFRC. Regarding the technical benefits, an experimental program is carried out on the post-cracking behavior of RSFRC and ISFRC, by performing SPLT and RPT. Life cycle analysis is performed to assess the environmental benefits of RSF&ISF and RSFRC&ISFRC at a material level. A simplified analysis of the economic benefits of using RSF as a concrete reinforcement, in alternative to ISF, is also considered. The relevant results are presented and discussed.

Chapter 9 summarizes the main conclusions of the developed work and the recommendations for future research. Chapter 10 provides the bibliographic references of all citations used in this thesis.

---

# Chapter 2

---

## LITERATURE OVERVIEW

This chapter provides a literature review about the recycling of post-consumer tires, the mechanical behavior and durability performance of Recycled Steel Fiber Reinforced Concrete (RSFRC) and the structural indicators of plain concrete (PC) elements used for construction of coastal breakwaters. Important emphasis is given to the post-cracking behavior of RSFRC and to the durability of SFRC exposed to chloride environments.

### **2.1 RECYCLING OF POST-CONSUMER TIRES**

#### **2.1.1 Environmental issues**

In 2016, about 318 million units of tires were produced in EU, of which 303 million units were sold for cars and trucks, accounting for 21% of world tire production (ETRMA, 2017a, 2017b). This represents a progressive increase in tire sales compared to previous years (4.2%, 10.5% and 14.9% compared to 2015, 2014 and 2013, respectively) (ETRMA, 2015, 2016, 2017a).

When tires are taken off vehicles, they may become “part-worn tires”, which are reusable for their original purpose as a second-hand purchase or retreated tires after reprocessing, or become “end-of-life tires” (ELTs), which are non-reusable tires in their original form, being classified as non-hazardous waste in themselves (Directive 75/442/EEC amended by Directive 91/156/EC). Until 2003, ELTs were discarded in landfills, however, the indiscriminate disposal of large amounts of post-consumer tires into landfills

proved to be a major environmental concern, especially in developing countries, because of their well-known non-biodegradable nature (Figure 2.1a).

Scrap tires are prone to accumulation of water, where mosquitoes and other insects may find it fertile for breeding, increasing further the risk of spreading human and animal diseases, such as the Dengue Fever and the Encephalitis (Fiksel *et al.*, 2011).

The dark color of tires absorbs heat and their volatile nature at elevated temperatures make scrap tires piles fire hazards (Fiksel *et al.*, 2011). The long-lasting smoke generated by burning tires is hazardous due to the release of toxins (benzene derivatives, dioxins, oxides of nitrogen and sulphur, carbon monoxide, heavy metals, polycyclic aromatic hydrocarbons and particulate matter), that may contaminate soils, air and water, causing pollution, environmental attack and human health problems (Figure 2.1b) (Graeff, 2011).



Figure 2.1 - (a) World's biggest tire graveyard in Sulaibiya, Kuwait, 2013

(Source: <http://www.amusingplanet.com> )

(b) Tire fire in West Odessa, Texas (USA) in 9<sup>th</sup> April 2017 (Source: <https://inhabitat.com> )

The use of scrap tire chips for landscaping has also become controversial due to the leaching of metals as zinc, concentrated at high level in the tires (up to 2% by weight), which is enough to be highly toxic to aquatic life and plants (Elnour and Laz, 2014).

In 2006, the disposal of whole or shredded ELTs into landfills was definitely banned in EU by the Landfill Directive (Council Directive 1999/31/EC), with a few exceptions (tires used as engineering material and bicycle tires and tires with an outside diameter above 1400 mm). This has forced EU member states to focus on responsible and environmental-friendly recovery methods for ELTs. Consequently, many countries transposed this directive into national laws and codes, promoting the development of sustainable options for the disposal, recovery and reuse of tires. With the implementation of the EU waste

framework directive (2008/98/EC), ELT-derived products may no longer be considered as a waste in the future, being studied according to certain criteria to potentially be recognized as a second raw material or an alternative energy source (WBCSD, 2010).

There are no specific European regulations for ELTs recovery. Each EU member state is free to choose its own ELT management model. There are currently 3 different models for managing ELTs: the producer responsibility model; the tax model defining a disposal duty for producers/importers; the free market model that assumes the profitability of ELTs recovery (EPA, 1999; WBCSD, 2010; ETRMA, 2015).

In 2016, the used tires in EU were estimated at 3.5 million tons, of which after sorting out the data of those tires going for reuse or retreading, an estimated 3.0 million tons of ELTs were treated, which represents a rate of 95% (ETRMA, 2018). In the United States, about 4.2 million tons of scrap tires are generated per year, of which 81% is managed to recovery or recycling (USTMA, 2018). The most common markets to manage ELTs currently include energy/raw material recovery (49%) or product/material recycling (46%) (ETRMA, 2015; USTMA, 2018).

The three major applications of ELTs are tire-derived fuel, civil engineering applications and ground rubber for production of artificial turf, asphalt and molded products (Hylands and Shulman, 2003; Fiksel *et al.*, 2011; USTMA, 2018). All these options for ELTs recovery and recycling bring significant environmental and economic benefits, both in terms of reducing greenhouse gas emissions and in terms of energy saving (Ecopneus, 2014; ETRMA, 2015). Since 2005, a total reduction of up to 20% in CO<sub>2</sub> emissions per ton of tires produced was estimated in Europe from ELTs sent to material and energy recovery, which is a reduction of 61% of solvent consumption and a decrease of 46% of water consumption (ETRMA, 2017b).

### **2.1.2 Pneumatic tires composition**

Tires are a complex mixture of very different materials, which include natural and synthetic rubbers, carbon blacks/silicas, reinforcing materials (metals and textiles) and other organic and inorganic minor components. The material composition varies by tire category (passenger tires, truck tires and off-the-road tires). Table 2.1 details the composition by mass of car and truck tires in the EU market. Figure 2.2 illustrates the typical elements of a tire section.



Table 2.1 - Composition by mass of EU car and truck tires (Shulman, 2019)

Material	Car/Utility (%)	Truck/Bus (%)
Rubber/elastomers <sup>a</sup>	48	45
Carbon black/silica	22	22
Metals	15	25
Textiles	+5	-
Zinc oxide	1	2
Sulphur	1	1
Additives	8	5

<sup>a</sup>Natural/synthetic rubber weight ratio: truck tires ± 1-2, car tires ± 3-4

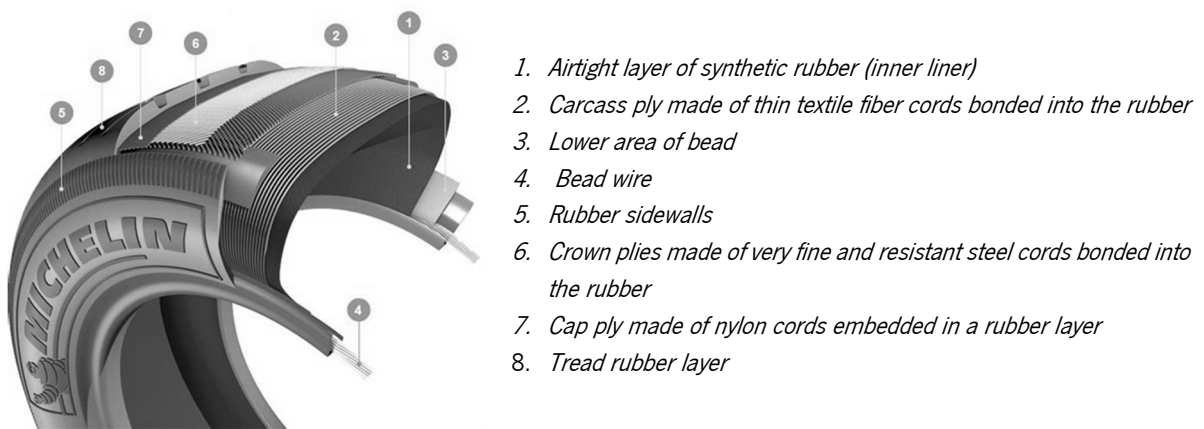


Figure 2.2 - Typical tire section and components (Source: Michelin USA, 2019)

### 2.1.3 Tires recycling

Tire recycling is unique in comparison with other recycling sectors due to the following reasons: it is among the smallest waste streams; tires are essentially homogeneous varying in size; recycling outputs have become strategic materials in different market sectors; under EU legislation, whole and shredded tires and recycling residues cannot be placed in landfills, promoting the development of new options for valorization (Shulman, 2019).

Under the European Commission's waste legislation, tire recycling is a recovery operation that encompasses two functions (Shulman, 2019): 1) Transformation of ELTs with the use of diverse treatments, based on either mechanical or thermo-chemical processes, in order to produce a broad range of materials that will be integrated into the market as a resource to replace the use of raw materials; 2) use of the materials in myriad consumer and industrial products, as well as in construction and civil engineering applications (Shulman, 2019).

There are four basic levels of ELTs treatment described below in terms of its functions (Shulman, 2004):

Level 1 – *Physical destruction of the tire structure*, namely, shape, weight bearing capacity, rigidity, etc. by using mechanical methods, such as bead, sidewall or tread removal, compression, baling or cutting;

Level 2 – *Separation of the tire elements* by using treatments based on mechanical (shredding and chipping, and ambient grinding) and cryogenic size reduction technologies that process the tire to segregate the rubber, metals and textiles;

Level 3 – *Multiphase treatments and technologies* for modifying one or more characteristics of the material liberated during Level 2 by means of mechanical, thermal, chemical, mechanochemical or multi-treatment procedures, such as devulcanization, rubber reclaim, surface modification/activation and pyrolysis;

Level 4 – *Material upgrading treatments* to enhance selected properties or characteristics of the material provided from Level 3, such as production of thermoplastic elastomers, upgraded carbon products and improved rubber reclaim.

The materials outputs from the four levels of ELTs treatments are classified into categories according to their size (CEN/TS 14243:2010). Table 2.2 summarizes the quantities by mass of each output of recycled tire materials produced in EU during 2016-17. The granulate corresponds to the highest amount obtained from the recycling of tires. However, in the recent years, the quantities of specialty powders and steel and textile fibers have increased since they have shown potential for certain applications (Pilakoutas *et al.*, 2004; Shulman, 2019).

Table 2.2 - Recycled tire materials by mass<sup>a</sup> produced in EU during 2016-17  
(adapted from Shulman, 2019)

<b>Material/Product</b>	<b>Fraction (%)</b>	<b>Mass (t)</b>	<b>Principal Uses/Applications</b>
<i>Whole tires</i>	10	121600	<i>Whole, cut or in bales for Civil Engineering and/or construction</i>
<i>Chips 10-50 mm Shreds 50-300 mm</i>	18	218880	<i>Civil Engineering, drainage, landfill engineering, horse tracks</i>
<i>Granulate 1-10 mm</i>	52	632320	<i>Moulded products, sport/play surfaces</i>
<i>Powders &lt; 1 mm</i>	11	133760	<i>Road surfaces, moulded products, rubber sheeting</i>
<i>Specialty powders &lt; 500 µm</i>	8	97280	<i>Pigments, paints, carbon black, tires, thermoplastic elastomers</i>
<i>Steel and textile fibers</i>	1	12160	<i>Concrete, vibration/sound panels, construction</i>

<sup>a</sup> These volumes do not include >30,000t of off-the-road tires (OTRs) that were processed in 2016-17

### **2.1.4 Recycling Processes to obtain RSF from post-consumer tires**

Most recycling methods of ELTs are focused on reusing the rubber constituents (Aiello and Leuzzi, 2010; Azevedo *et al.*, 2012; Boudaoud and Beddar, 2012; Bravo and Brito, 2012; Quadrini *et al.*, 2013; Herrera-Sosa *et al.*, 2015; ETRMA, 2015; Thomas *et al.*, 2016; USTMA, 2018; Sofi, 2018), but few deals with the other tire components, such as steel (Barros *et al.*, 2017; Onuaguluchi and Banthia, 2018).

The steel cord is a high quality and high strength wire, which, if appropriately treated, can be used as reinforcement for concrete (Pilakoutas *et al.*, 2004). The main processes to extract steel wire from tires are *mechanical treatment*, as ambient shredding and cryogenic process, and *thermal degradation*, as conventional and microwave-induced pyrolysis (Abraham *et al.*, 2011; Barros *et al.*, 2017). The amount of extracted steel fibers depends on the type of tire. Car tires contain up to 15% steel, whereas truck tires contain up to 25% steel (Table 2.1).

Comparative life cycle assessment (LCA) studies have shown that RSF production consumes only up to 5% of the energy required to produce ISF (Neocleous *et al.*, 2014; Angelakopoulos and Waldron, 2015).

#### **2.1.4.1 Ambient Shredding Process**

The mechanical shredding treatment is considered as a commercially mature and technologically reliable process and it seems to be the most environmentally friendly alternative, due to the low energy spent for breaking down the tires (Pilakoutas *et al.*, 2004; Graeff, 2011). However, it can be quite costly, as the cutting blades require constant maintenance due to the high rate of deterioration caused by the high strength steel of the tires, which is usually of large diameter in the bead. Tire shredding has increased over the years, since it is more economic to transport shredded tires rather than whole tires (Sonti *et al.*, 2003).

The first step of the shredding process is normally dedicated to removing the bead wires from tires. The bead wire is usually removed through mechanical action by pulling the wire and detaching it from the rubber by a hydraulic pulling system (Graeff, 2011; Micelli *et al.*, 2014).

Tires (both from cars and trucks without bead wire) first pass through various rotating discs on parallel axes that resemble a gear-shaped cutter with teeth, as shown in Figure 2.3. Then, the tires are chopped or shredded until they are reduced to pieces ranging in size from approximately 50 to 300 mm, depending on the efficiency of the shredder and on the distance between the cutters. The subsequent stage normally involves passing the shredded tires through the rotating disc for a second time. The distance between discs is now reduced to provide smaller tire chips of about 10 to 50 mm. Both first and second shredding processes are enough for either energy recovery or material recovery, where the rubber chips or shreds

are used as fuel (Graeff, 2011). Rubber chips are further granulated to produce rubber particles of approximately 1 to 10 mm, which can be used in several applications (Pilakoutas *et al.*, 2004). During this stage, magnets are used to separate the steel fibers from the rubber (Micelli *et al.*, 2014). Textile residues are removed from the steel fibers by blowing the residues away or by a vacuum system (Graeff, 2011). In Figure 2.3, an example of a tire shredding process is shown schematically.

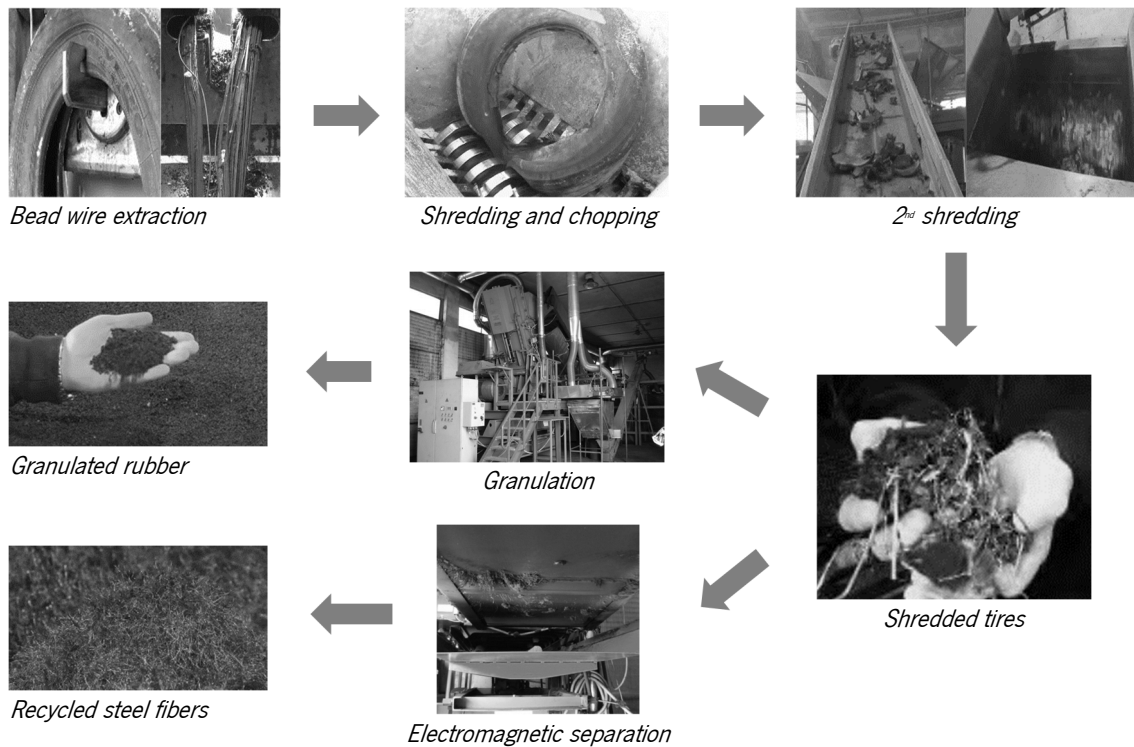


Figure 2.3 - Overview of an ambient shredding process to reduce tires to rubber granulate and steel fibers (Sources: <http://www.recycle.by>, Tlemat *et al.*, 2004a; Micelli *et al.*, 2014)

The resulting steel fibers have pieces of rubber, textile and other residues attached to them. They also present different geometric shapes, as shown in Figure 2.4 (Tlemat *et al.*, 2004a).

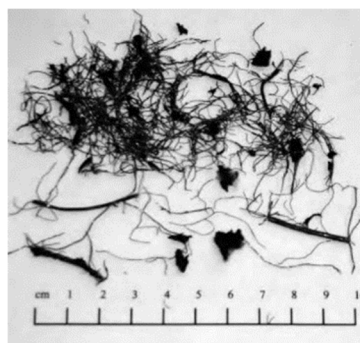


Figure 2.4 - Recycled fibers obtained from shredding process (Tlemat *et al.*, 2004a)

### 2.1.4.2 Cryogenic Process

The mechanical treatment by cryogenic process involves the cooling of tires and their subsequent brittle fracturing and reduction to rubber, steel and textile (Pilakoutas *et al.*, 2004).

The cryogenic process is an efficient alternative to produce rubber granules. However, the method requires high energy input to cool the tires and may also lead to steel embrittlement (Graeff, 2011).

In a typical cryogenic process (Figure 2.5), the used tires are initially shredded at ambient temperature, and then transferred to a deep-freezing tunnel system (Pilakoutas *et al.*, 2004). Inside the first tunnel section, the fragmented tires are pre-cooled by a counter-current of gaseous nitrogen or commercial refrigerants at approximately -120°C (Liang and Hao, 2000; Pilakoutas *et al.*, 2004). The tire pieces are then transferred into the main cooling tunnel, where they are cooled down below their embrittling temperature and, as a result, they become almost as brittle as glass, and size reduction can be more easily performed through crushing and breaking (Pilakoutas *et al.*, 2004; Barros *et al.*, 2017). At the next stage, the fragmented tires are granulated through a series of mills and are reduced to rubber, steel fibers and textile (Pilakoutas *et al.*, 2004). The steel and textile are separated from the rubber granules passing through a steel extraction unit (Pilakoutas *et al.*, 2004).

Due to the embrittlement, the cryogenic grinding process is more effective for producing finer rubber particles, with very sharp edges and less surface area than those obtained by ambient mechanical process (Liang and Hao, 2000).

The physical characteristics of the rubber granulate depend on the grinding process used and determine the mechanical performance of its final application (Presti, 2013).

The extracted steel and fiber liberation are much easier, leading to a clean end product, but it may lose its ductility if it is cooled down below its embrittling temperature (Morris *et al.*, 1989; Reschner, 2008).

The cryogenic process is energy efficient because it requires less energy and fewer pieces of machinery to separate the rubber from the steel rather than ambient-temperature processes (Barros *et al.*, 2017). However, the high cost of liquid nitrogen is the main drawback of this process (Pilakoutas *et al.*, 2004).

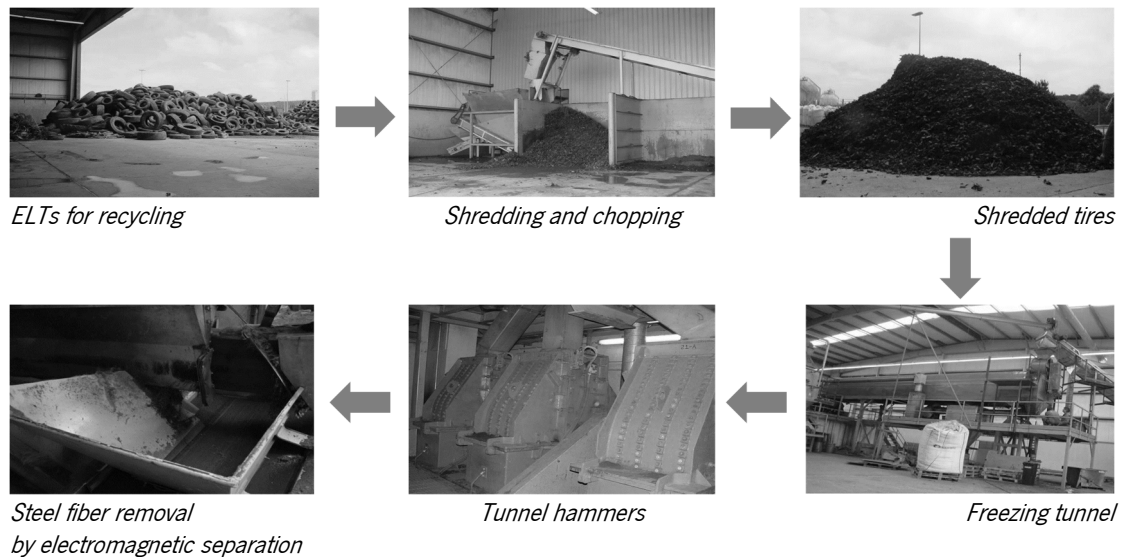


Figure 2.5 - Overview of a cryogenic process to reduce tires to rubber granulate and steel fibers (Zamanzadeh *et al.*, 2015)

The resulting steel fibers obtained from this process are characterized by different diameters, lengths and shapes, and present irregular wrinkles (Figure 2.6).



Figure 2.6 - RSF obtained from cryogenic process (Zamanzadeh *et al.*, 2015)

### 2.1.4.3 Conventional Pyrolysis Process

Pyrolysis involves decomposing of the tires to their organic and inorganic components by applying heat in the absence of oxygen (anaerobic thermal degradation). Tire pyrolysis leads to the release of gases (hydrogen, methane and other hydrocarbons), oils, solid carbon residues of steel and char, and steel (Martinez *et al.*, 2013; Williams, 2013). The process is typically carried out either in a flow of inert gas or under vacuum conditions (Barros *et al.*, 2017).

In a typical pyrolysis plant, tire crumbs are fed into a pyrolysis reactor, where they are heated to the desired temperature. The gases and the liquids are separated from the extracted vapors through a system

of gas-liquid separators, the steel is separated from the char and the char is ground (Pilakoutas *et al.*, 2004).

Yields of a vacuum pyrolysis plant at 500°C and 20 kPa with a capacity of 36,000 metric tons are estimated as follows (Pehlken and Essadiqi, 2005): 34 wt% (in weight) pyrolytic oil 9; 32 wt% pyrolytic carbon black; 17% gas; 15% steel and 2% non-steel fibers.

The main advantage of this process is the minor environmental impact in comparison with other thermochemical processes as gasification and combustion, as well as the possibility of using tire by-products as raw materials (Turer, 2012; Antoniou and Zabaniotou, 2013).

The properties of these three end-products (solid, liquid and gas) depend not only on the source and grade of the tires, but also on the reactor configuration and experimental conditions, such as temperature, duration, pressure and heating rate, among others (Turer, 2012, Antoniou and Zabaniotou, 2013; Williams, 2013). The solid carbon residue left after pyrolysis has potential as a solid fuel or as a low-grade carbon black or may be upgraded to activated carbon. The derived oil may be used as a fuel or upgraded to chemical feedstock. The pyrolysis gases have enough energy value to provide the energy requirements of the pyrolysis process and the recovered steel may also be recycled (Williams, 2013).

There are several studies in the literature focused on the pyrolysis process, such as kinetics, reactor design, products characterization, economics, etc. (Turer, 2012; Martínez *et al.*, 2013; Antoniou and Zabaniotou, 2013; Williams, 2013). Very different experimental procedures, ranging from laboratory to commercial scale plants have been used, including thermogravimetric analyzers, fixed bed reactors, fluidized bed pyrolysis units, vacuum pyrolysis units, spouted bed reactors, etc. (Laresgoiti *et al.*, 2004). The steel comes out of the process still containing some char on its surface. Figure 2.7 shows an example of steel wire scraps derived from tire pyrolysis that can be cut to any length for fibers. In most pyrolysis plants, the tires are shredded before being fed to the reactor and, hence, the RSF are already cut to a certain degree (Pilakoutas *et al.*, 2004).

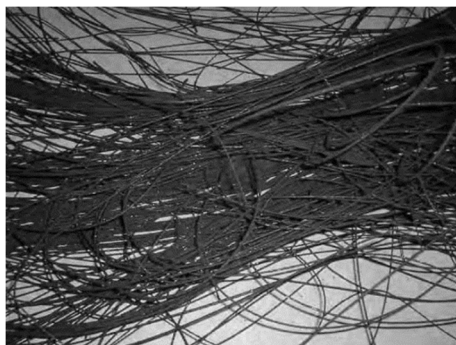


Figure 2.7 - Tire Pyrolysis Steel Wire Scrap (Tlemat *et al.*, 2003a)

Pyrolysis is energy efficient because the derived gases and oil have high gross calorific values and can be used for power generation (Rodriguez *et al.*, 2001; Pilakoutas *et al.*, 2004). It may be difficult to market some of the pyrolysis end-products due to their low quality (especially the char), and consequently, many pyrolysis plants are not economically viable (Pilakoutas *et al.*, 2004).

#### **2.1.4.4 Microwave Induced Pyrolysis Process**

The microwave-induced pyrolysis process optimizes microwave power at the molecular level to thermally decompose tires to their constituents (Pilakoutas *et al.*, 2004; Athanassiades, 2013). According to the developers of this process (Advance Molecular Agitation Technology - AMAT Ltd.), the microwaves can sufficiently excite the molecular bonds of the long-chain rubber hydrocarbons to break them into shorter hydrocarbons, which are released as volatile gases at a temperature around 350°C. The process operates at relatively low temperatures and hence, the derived steel cord and textile wire remain intact, while the rubber is converted to oil, gases and char.

Recent studies have highlighted the promising character of microwave for pyrolysis due to its ability of heating in a short time comparing with traditional heating techniques (Undri *et al.*, 2013; Song *et al.*, 2017). Three products of high calorific value are collected, namely, a solid residue (char) containing up to 92% of carbon and appreciable quantities of mineral matter, a low viscosity oil with a large amount of single ring aromatic hydrocarbons and a gas containing light hydrocarbons, hydrogen and only traces of nitrogen (Undri *et al.*, 2013, 2014).

An example of a microwave pyrolysis system consists of a microwave oven, condenser, oil-gas separator, oil chamber, gas collecting bag and air inlet (Zhang *et al.*, 2018). Before being delivered to the microwave pyrolysis system, waste tires are shredded to a fine particle size. Nitrogen is added into the system via the air inlet, so that the air can be removed from the system. Using the microwave oven control system, the temperature in the oven is increased and kept constant. The high temperature gases produced are led into the condenser via the gas pipeline. The combustible gases not condensable are mixed with the oil that flows into the oil-gas separator via pipeline. The oil flow into the oil chamber and the gas move to the reservoir bag. The only solid product is carbon black, which can be removed from the microwave oven after the pyrolysis (Zhang *et al.*, 2018). Figure 2.8 shows an example of pyrolysed RSF obtained by the microwave process, whose diameters depend on the type of cord used in the tire. In this case, the fibers were obtained from super-single tires and comprised 12 wires of 0.23 mm diameter, twisted together into a core strand of 0.85 mm diameter, surrounded with another 15 twisted wires. On the cord surface there is a single twisted wire with a twist pitch of 5.33 mm. The fiber overall external diameter is



1.55 mm with effective diameter 1.16 mm and a tensile strength in excess of 1250 MPa (Tlemat *et al.*, 2003a).

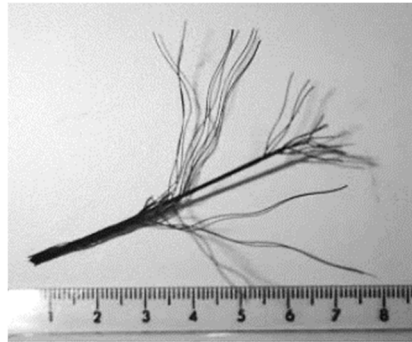


Figure 2.8 - RSF obtained by microwave pyrolysis (Tlemat *et al.*, 2003a)

## 2.2 RECYCLED STEEL FIBER REINFORCED CONCRETE (RSFRC)

Recent research is evidencing that steel fibers derived from the tire recycling industry can be an effective reinforcement system to decrease significantly the brittle behavior of cement based materials, by improving their toughness and post-cracking resistance (Barros *et al.*, 2017; Caggiano *et al.*, 2017; Smrkić *et al.*, 2017; Leone *et al.*, 2018; Lourenço *et al.*, 2018; Onuaguluchi and Banthia, 2018).

In the following sections, focus will be made on the geometric and mechanical properties of RSF, as well as on their use in Fiber Reinforced Concrete (FRC).

### 2.2.1 Geometric characterization of RSF

The RSF are characterized by different diameters and lengths, as well as irregular shapes with curls and twists. Small amounts of rubber particles (up to 20% by mass) and textile residues can also be found in RSF (Hu *et al.*, 2018a; Onuaguluchi and Banthia, 2018). The aspect of the RSF depends on the type of tire used and on the recycling process adopted for recovering the fibers. Figure 2.9 shows the RSF appearance after the shredded process. The fibers need to pass through a post mechanical treatment to clean and sort by specific geometric features, such as the range of length and diameter (Hu *et al.*, 2018a). Sieving treatment is normally required to get the appropriate range of fiber length for use in concrete, i.e. to improve the pos-cracking behavior and also to avoid balling during concrete mixing (Graeff, 2011). Previous studies at the University of Sheffield have shown that the most appropriate length of fibers is in the range of 15 to 25 mm, with an average diameter of around 0.2 mm (Graeff, 2011), leading to these fibers an aspect ratio of 75-125.

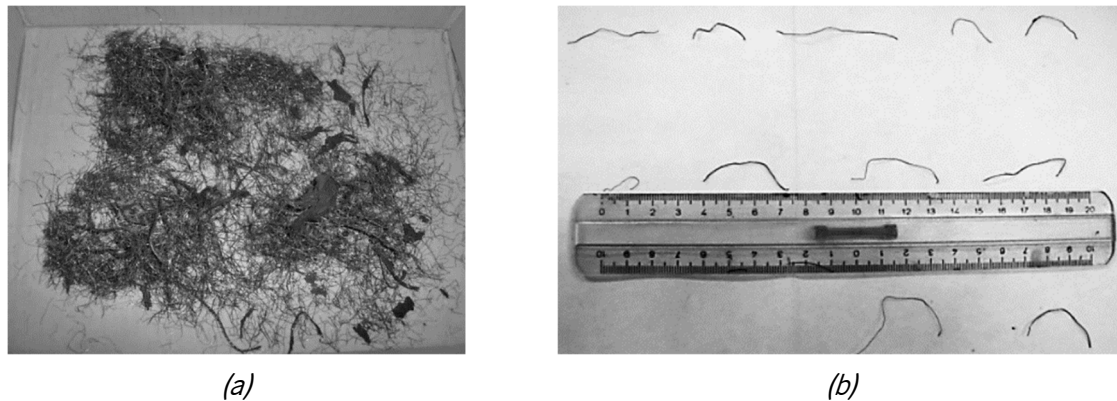


Figure 2.9 - Appearance of RSF obtained from the shredded process of ELTs  
 (a) RSF with rubber particles (b) Individual RSF (Micelli *et al.*, 2014)

For the geometric characterization, the diameter and length should be measured in a representative sample of RSF, which according to the literature consists of more than 1000 fibers (Aiello *et al.*, 2009; Centonze *et al.*, 2012; Martinelli *et al.*, 2015; Caggiano *et al.*, 2017; Hu *et al.*, 2018b; Leone *et al.*, 2018).

The diameter of each fiber could be manually measured by means of a micrometer considering the average of three measures, namely at the two extremities of the fiber and at the mid-point (Aiello *et al.*, 2009; Caggiano *et al.*, 2017).

In accordance with the CNR-DT 204/2006 specifications, the fiber length is defined as the distance between the outer ends of a fiber (Aiello *et al.*, 2009) and the developed length is the total length along the fiber axis (Caggiano *et al.*, 2017).

The measurement of these geometric properties aims to determine the fiber aspect ratio (length-to-diameter), which is a key parameter for controlling the mechanical performance of RSF in FRC.

The RSF length and aspect ratio distributions can also be automatically determined using a specially developed optical system (Hu *et al.*, 2018b).

In order to give details on the geometric properties of RSF, some authors performed statistical analysis by sorting the recorded diameter, length and aspect ratio measurements in different ranges. Figure 2.10 shows an example of the resulting frequency distribution of one RSF sample for different diameter, length and aspect ratio ranges, which was reported by Caggiano *et al.* (2017).

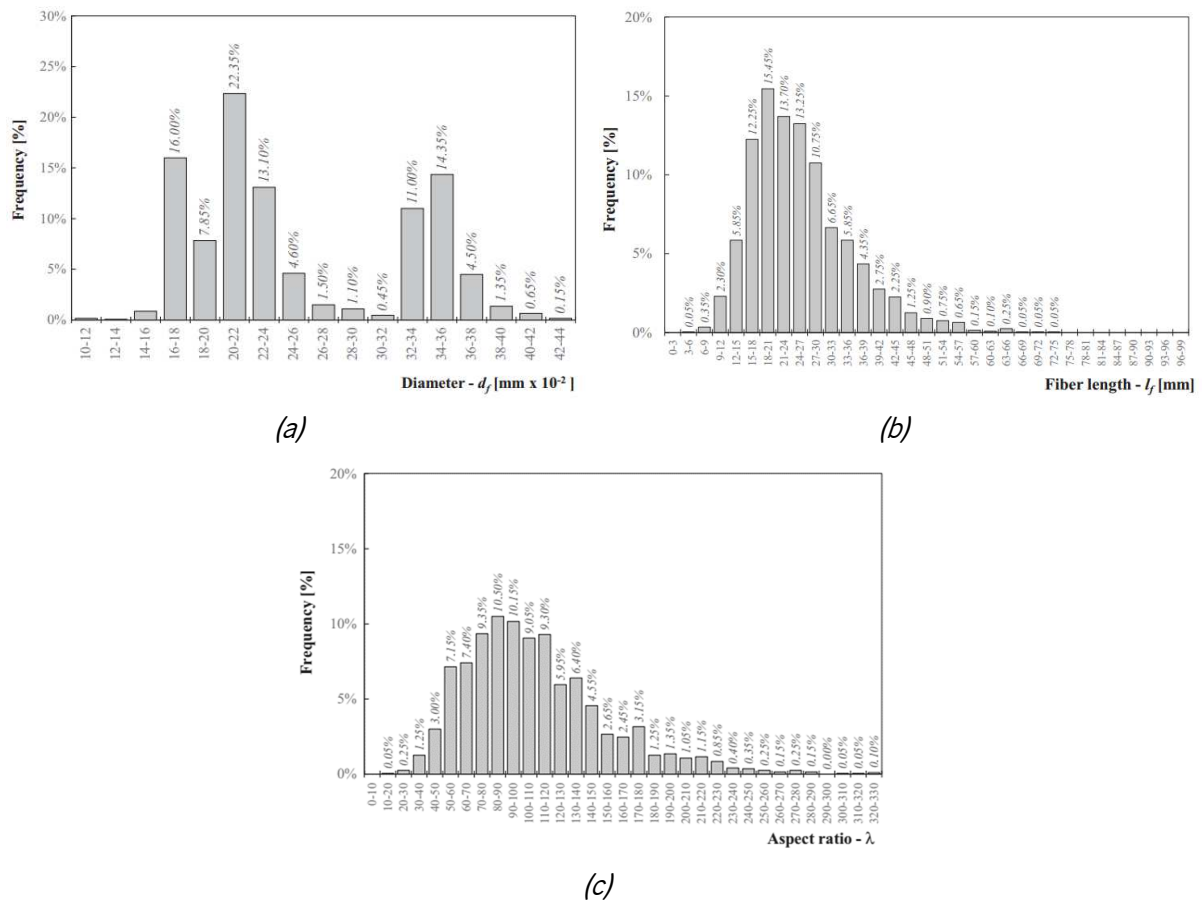


Figure 2.10 – Relative frequency of (a) Diameter measurements (b) Length measurements (c) Aspect ratio determinations (Caggiano *et al.*, 2017)

According to the consulted literature, the RSF diameter measurements highlight a multimodal distribution, probably due to the mixing of different types of tires in the recycling process. However, in general, more than one third of the sampled fibers exhibits a diameter within the same range (Figure 2.10a).

Regarding the RSF length measurements, a unimodal distribution is observed, with more than one half of the sampled fibers exhibiting a value within the range 10-30 mm (Figure 2.10b). This probably resulting from the unified cutting underwent during the recycling process (Caggiano *et al.*, 2017).

Figure 2.10c highlights a unimodal distribution of the aspect ratio, however, the results obtained are quite different between the consulted studies in the literature. Martinelli *et al.* (2015) found that more than one half of RSF exhibited a value within the range 30-60 (57%). The aspect ratio determined by Caggiano *et al.* (2007) was highly variable between 17 and 322 (Figure 2.10c). Leone *et al.* (2018) reported that the largest percentage of RSF (18.25%) is within the range 50-60. More than one half of RSF analyzed by Hu *et al.* (2018b) had an aspect ratio in the range of 60-160.

### 2.2.2 Chemical composition of RSF

Chemical characterization tests were carried out by Micelli *et al.* (2014) to estimate the chemical composition of RSF. The obtained experimental results are presented in Table 2.3.

Table 2.3 - Chemical composition (in %) for RSF (Micelli *et al.*, 2014)

Chemical elements	Fe	Mn	Cu	Zn	Cr	Co
Rectangular cross section	97.89	0.87	0.84	0.32	0.08	-
	98.26	0.85	0.16	0.70	0.04	-
	96.29	0.66	1.86	0.93	0.26	-
	98.87	0.87	0.12	0.10	0.04	-
	98.30	0.77	0.04	0.64	0.24	-
Circular cross section	97.26	0.95	0.68	0.14	0.07	0.29
	97.24	0.95	0.75	0.10	0.06	0.30
	97.38	0.97	0.57	0.11	0.06	0.26
	97.04	0.98	0.84	0.12	0.06	0.24
	96.97	1.00	0.85	0.15	0.05	0.27

The values of Fe, Mn and Cr are consistent with the compositional indications available in the literature for steels used in tires (RMA, 2019).

The composition of steel fibers generally includes carbon steel with variability in composition between 0.60 and 0.77% (or low carbon steel, sometimes with alloying constituents) or stainless steel.

The high value of Cu and Zn is due to the fact that these steels are coated with such materials. In Table 2.3, the presence of Co is also observed for circular cross sections, which is typically added to improve the corrosion resistance and hardening (Micelli *et al.*, 2014).

### 2.2.3 Tensile strength of RSF

The mechanical behavior of RSF can be experimentally evaluated by means of direct tensile tests (Micelli *et al.*, 2014; Hu *et al.*, 2018b). A typical test setup for direct tensile tests is shown in Figure 2.11. In this test configuration, the ends of RTSC (Recycled Tire Steel Cord) were wrapped on small high-strength aluminum cylinders that were fixed within the screwed jaws. This arrangement ensure that the tensile force is applied axially, minimizing any bending and preventing failure at the ends (Hu *et al.*, 2018b). Figure 2.11b shows a typical fiber failure mode occurred during the tensile test.

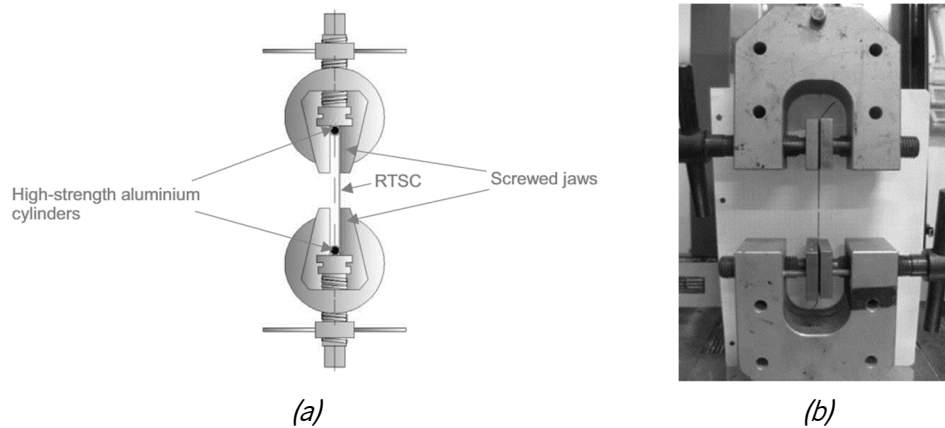


Figure 2.11 – (a) RTSC tensile test setup (Hu *et al.*, 2018b);  
(b) failure mode of RSF in direct tensile test (Micelli *et al.*, 2014)

The effect of the curved shape of the RSF on the mechanical tests, especially referring to fibers with higher curvature, can be analyzed by the  $\sigma$  -  $\epsilon$  diagram shown in Figure 2.12, in which two zones can be distinguished: An initial branch (1), upwardly concave, characterized by high deformations with a relative low level of stress - the applied load is used to “straighten out” the fiber; a second branch (2) with a sharp stiffness variation - “pure tension” stage.

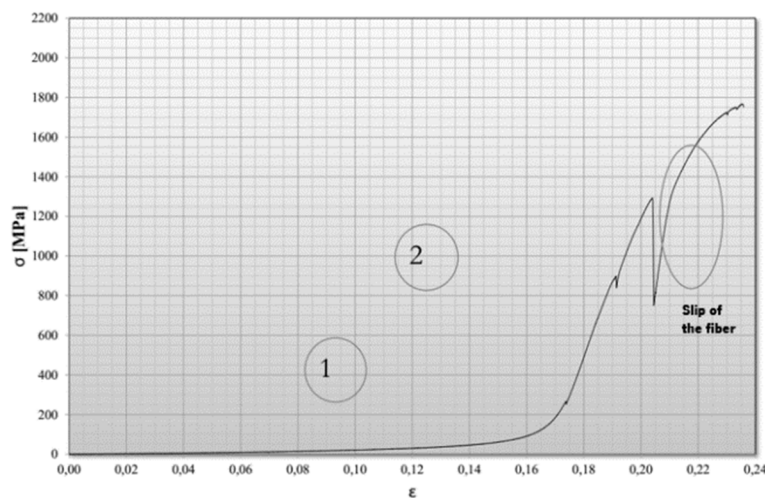


Figure 2.12 –  $\sigma$  -  $\epsilon$  diagram for an irregular RSF (Micelli *et al.*, 2014)

Due to the irregular shape of each fiber, a wide variation of deformations is observed in the tensile tests (Micelli *et al.*, 2014). Moreover, some load drops are recorded during the tests, probably due to fibers slip (Micelli *et al.*, 2014).

Table 2.4 summarizes the average values of RSF tensile strength reported by some studies in the literature. In some cases, values of ISF are provided for comparison purposes.

Table 2.4 - Summary of RSF and ISF tensile strength

First author Year	Fiber type	Number of fibers	Diameter (mm)	Tensile strength (MPa)	CoV (%)
Tlemat 2006a	PRSF	-	0.23	≈2000	-
	SRSF	-	0.80-1.55	>1250	-
	VSF	-	1.55	>1250	-
	ISF-1	-	1.00*	1050	-
	ISF-2	-	1.05	1000	-
Aiello 2009	SRSF	15	0.36	2239	16.02
		15	0.30	2578	8.05
		15	0.25	2314	11.07
Micelli 2014	RSF	16	0.97	1672	13.55
Caggiano 2015	RSF	7	0.19	2235	4.86
Smrkić 2017	RSF	-	0.15	2850	-
	ISF	-	0.55	1100	-
Hu 2018a	RSF	-	0.22	2570	-
	RTSC	-	0.75	2612	-
	ISF1	-	1.00	1450	-
	ISF2	-	0.80	1050	-

Abbreviations: (PRSF) Pyrolysed RSF; (SRSF) Shredded RSF; (VSF) Steel fibers obtained from virgin tire; (RTSC) Recycled tire steel cord  
\* nominal values.

From the results reported in Table 2.4, it seems that the tensile strength is highly dependent of the type of fibers. However, all fibers obtained from recycling processes of tires (PRSF, SRSF, VSF and RTSC) showed higher tensile strength than ISF.

For determining local mechanical properties of RSF, nano-indentation testing is an appropriate method that accurately characterizes the elastic modulus and the hardness of small steel fibers (Broitman, 2017). This technique has shown its efficiency in providing valuable information on the mechanical properties of the microstructure of steel (Pham and Kim, 2015).

#### 2.2.4 Pull-out behavior of RSF

Material properties of fiber-reinforced concrete depend on the bond between the fibers and the matrix. According to Alwan *et al.* (1991), the energy absorption capability of SFRC is attributed to two mechanisms; the material deformation and the initiation and propagation of cracks. Fibers contribute to these mechanisms, as they can improve the energy absorption by either deforming or pulling-out,

depending on their bonding characteristics (Alwan *et al.*, 1991). Pull-out tests are normally used to analyze the bonding characteristics of fibers and to determine the critical fiber length (Tlemat *et al.*, 2003a). However, although extensive research studies have been conducted in this topic, there is still no standard method to determine the bond-slip behavior of fibers in reinforced cement-based materials (Barros *et al.*, 2017).

In general, the pull-out test can be performed with a single or a multi-fiber, and to obtain an accurate pull-out response a suitable testing method must be developed. RSF pull-out tests have been carried out by different researchers, using a single-sided or a double-sided pull-out test method (Tlemat *et al.*, 2003a; Aiello *et al.*, 2009; Caggiano *et al.*, 2015; Hu *et al.*, 2018b). Figures 2.13 show two alternative test configurations for performing RSF pull-out tests.

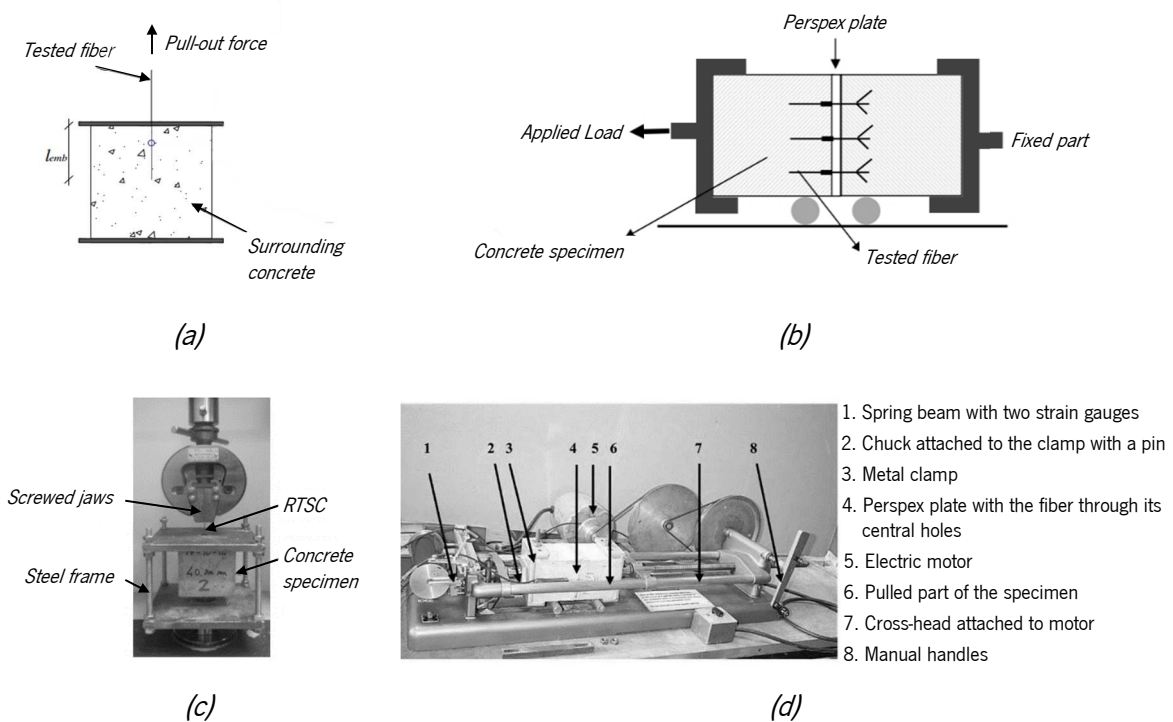


Figure 2.13 – (a) (c) Test setup for single-sided pull-out test (Caggiano *et al.*, 2015; Hu *et al.*, 2018b); (b) (d) Testing apparatus of double-sided pull-out tests (Tlemat *et al.*, 2003a)

Tlemat *et al.* (2003a) concluded that the initial behavior of the pull-out load-slip response is more stable in the multi-fiber fiber test than in single fiber test, especially for fibers with low embedded length, which leads to the conclusion that the multi-fiber test is a more suitable test for determining the pull-out characteristics than the single fiber pull-out test.

Figure 2.14 shows typical applied load-displacement curves, related to a concrete specimen with a fiber embedded length of 40 mm, representing two failure modes of RTSC: cord pull-out; tensile rupture (Hu *et al.*, 2018b).

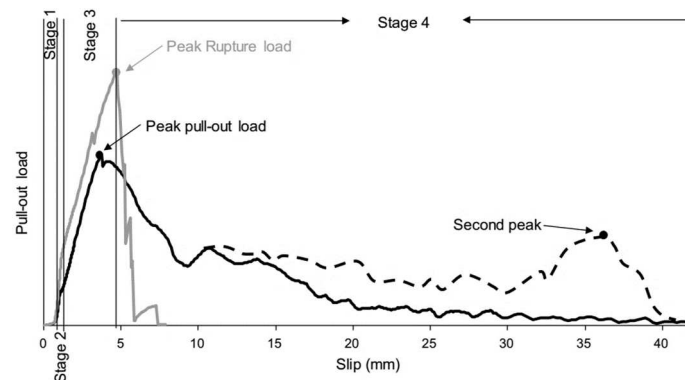


Figure 2.14 – Typical applied load-slip curve with a fiber embedded length of 40 mm (Hu *et al.*, 2018b)

From Figure 2.14, four individual regions can be identified: 1° - Softer initial part that corresponds to the stretching of the wrinkled fiber not embedded in concrete matrix at very low stresses; 2° - Almost linear behavior up to the peak load value, corresponding to the elastic or adhesive bond between the cord and the matrix; 3° - The nonlinearity of the curve starts with damage (micro-cracking) at the interfacial transition zone (ITZ) between RTSC and concrete, resulting in the gradual loss of cord adhesion and mechanical bond; 4° - Softening zone with a decrease of the pull-out load with the increase of fiber slipping; progressive loss of frictional stress between fiber and surrounding matrix – residual bond stress. At long embedment lengths, a second peak can be observed in the curve due to wedging of RTSC. The cord rupture occurs when the bond strength is enough to develop the fiber tensile rupture (Hu *et al.*, 2018b).

Figures 2.15a,b shows some results of RTSC pull-out tests for different embedment lengths.

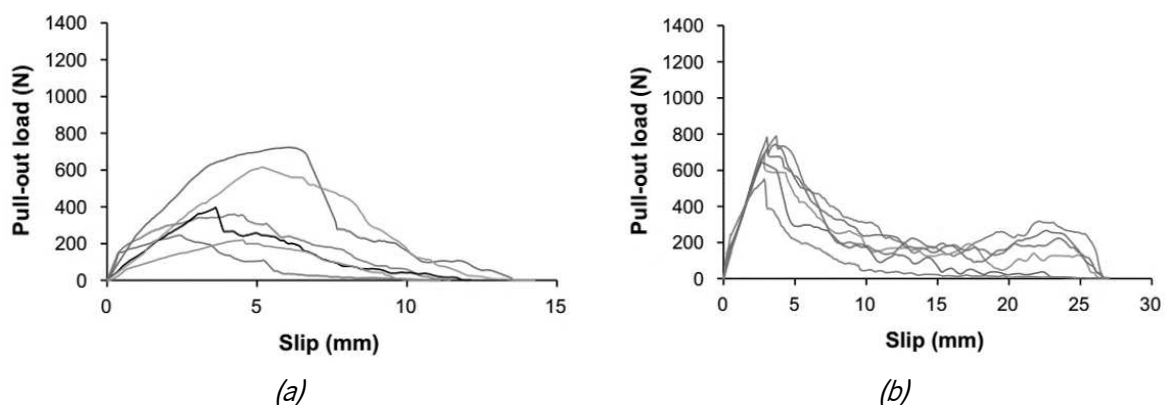


Figure 2.15 – Pull-out load-slip responses for RTSC (nominal cord diameter of 0.75 mm) with different embedment lengths: (a) 10 mm; (b) 25 mm (Hu *et al.*, 2018b)



According to Hu *et al.* (2018b), for RTSC embedment lengths of 10 and 25 mm, all specimens exhibited a similar interfacial bond behavior and failed by cord pull-out (Figure 2.15). For the embedment length of 40 mm, some samples ruptured (Figure 2.14). The authors concluded that the critical embedded length of RTSC should be in the range of 25-40 mm and the RTSC length used in concrete is recommended to be in the range of 50-60 mm, due to the difficulties in mixing high aspect ratio fibers in concrete.

High variability of the results is common due to the voids and flaws unevenly distributed in the steel-concrete ITZ and due to the significant variability of the fibers irregularity, leading to uneven bonding properties along the embedment length (Aiello *et al.*, 2009; Hu *et al.*, 2018b). However, the average pull-out properties of RTSC are comparable to those of ISF (Cunha *et al.*, 2010).

To improve the anchoring and avoid the separating of the wires that form a PRSF, a welding cone is necessary to apply at both ends of the PRSF. Tlemat *et al.* (2003a) recommends using the PRSF in the range of 50-60 mm length, when an end anchorage is not available in PRSF. PRSF with end anchorage and SRSF obtained from twisted tyre cord strands with an embedment length higher than 20 mm have failed in tension during loading. Tlemat *et al.* (2003a) suggested a SRSF length in the range of 20-25 mm for full debonding.

Aiello *et al.* (2009) concluded that all fibers with embedded length of 30 and 40 mm have failed in tension during the linear behavior up to the peak load value. A critical embedded length in the range of 20-30 mm is suggested by these authors.

Caggiano *et al.* (2015) observed that the fiber-to-concrete specimens with an embedded length of 20 mm failed in debonding mechanism, while all fibers with embedded lengths of 40 mm failed in tension, which means that the critical length is between the two aforementioned values.

For specimens failed by pull-out, the average failure load and the dissipated energy increase with the embedment length (Tlemat *et al.*, 2003a; Aiello *et al.*, 2009; Caggiano *et al.*, 2015; Hu *et al.*, 2018b).

The average bond stress at maximum pull-out load,  $\tau_{m\acute{a}x}$ , is evaluated as:

$$\tau_{m\acute{a}x} = \frac{P_{m\acute{a}x}}{L_{ad} \pi d_f} \quad (2.1)$$

where  $P_{m\acute{a}x}$  is the maximum applied load,  $L_{ad}$  is the fiber embedded length and  $d_f$  is the fiber diameter (Aiello *et al.*, 2009). Discrepancies on the obtained results from distinct authors are due to distinct factors considered in the experimental program, namely, concrete matrix properties, fiber embedment length and cross-sectional dimensions, fiber strength, dimensions of the mechanical anchorage, etc. (Abrishambaf, 2015).

The increase of fiber length promotes its tensile rupture, which is a failure mode that should be avoided since detrimentally affect the fiber reinforcement (Barros *et al.*, 2017). Similar effect is reported in the literature when the fiber inclination angle increases towards the crack plane (Barros *et al.*, 2017). Abrishambaf (2015) found that the maximum monotonic pull-out load decreases with the increase of the fiber inclination angle (angle between the fiber and the orthogonal to the crack plane), while the slip at peak load, in general, increases with the angle. This increase of slip at peak load could be ascribed to other additional mechanisms in the pull-out process, which include the matrix spalling and fiber bending in the fiber exit point. The toughness of hooked end fiber pull-out is maximized at an inclination angle between 10-20 degrees (Robins *et al.*, 2002) due to the snubbing effect that occurs for higher pull-out loads (Dupont, 2003). This effect is due to the tendency of the fiber to be aligned with the pull-out load direction (Figure 2.16a). The surrounding concrete at fiber exit point resists to the fiber alignment tendency, originating a stress field in the fiber in this zone composed by normal and shear stress components ( $N_a$  and  $N_b$  - Figure 2.16b). Due to a type of Mohr–Coulomb effect in the zone, the normal stresses increase the pull-out force inducing an increase in the residual strength of the fiber pull-out (Døssland, 2008). For higher fiber orientation angles ( $\theta_f$ ), due to the generation of higher stress concentration, where the fiber is forced to bend ( $\sigma_r$  - Figure 2.16b), concrete spalling at fiber exit point occurs, the stress carried by the fiber is increased and the failure mode is changed to fiber rupture (Dupont, 2003; Abrishambaf, 2015).

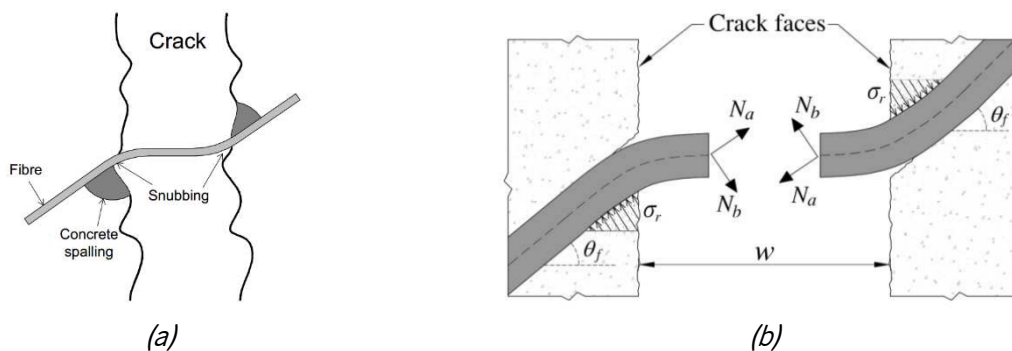


Figure 2.16 – (a) An inclined fiber crossing a crack section (Abrishambaf, 2015)

(b) Components of pull-out force in an inclined fiber (Salehian, 2015)

According to Abrishambaf *et al.* (2017), in general, the long-term and instantaneous ISF pull-out behavior did not differ considerably.

In comparison to the results reported for ISF of similar diameter, the peak pull-out load and dissipated energy of RSF are generally similar or even better (Tlemat, 2004b; Cunha *et al.*, 2010; Abrishambaf, 2015; Hu *et al.*, 2018b). In fact, the irregular wrinkles of RSF confer an effective mechanical contribution to the bond performance comparable to the regular wrinkles of ISF (Aiello *et al.*, 2009). Furthermore, RSF has stiffer initial bond-slip characteristics (formation and propagation of a stable debonding process that ends near the maximum load) than ISF (has no bond along its length, hence resistance is provided only by end anchoring slip) (Tlemat, 2004b). This means that RSF can exhibit consistent pull-out behavior and can provide a reliable way to enhance the post-cracking resistance of concrete.

The experimental pull-out results on RSF can then be used to validate and calibrate models to obtain the local bond slip law of RSF embedded in cementitious matrices, if the purpose is using this information for design and modeling (Caggiano *et al.*, 2015; Barros *et al.*, 2017).

### **2.2.5 Technology of RSFRC manufacturing**

The mix design, with the right selection of concrete ingredients and their optimized proportions, as well as the definition of the optimum mix procedure are essential in order to ensure uniform dispersion of the fibers into the mixture and to prevent segregation and/or fiber balling during mixing. Segregation or balling is affected by many factors, such as aspect ratio and volume content of the fibers, size and volume of the aggregates, water/cement (W/C) ratio and method of mixing (Nawy, 2008). High aspect ratios and high content of fibers, and high volume and large aggregate size (responsible for increasing shear during mixing) tend to interlock the fibers and form balls, which cannot be separated by conventional vibration (Graeff, 2011; Micelli *et al.*, 2014). Neocleous *et al.* (2011) suggests that RSF with an aspect ratio greater than 200 can induce fiber balling even at low fiber dosages. When RSF are added to concrete, the irregular shape of the fibers seems to be another factor influencing the formation of balling, since they tend to interlock more easily, even before added to the mix (Graeff, 2011). The workability of RSFRC can be improved by suitable measures, such as: increasing the fine aggregates fraction and/or reducing the maximum diameter of coarse aggregates; using RSF with low aspect ratio; using high-range water-reducing admixtures, which aids obtaining more fluid mixtures (Micelli *et al.*, 2014).

In the literature, there are several design methods available for proportioning SFRC mixes (Chanh, 2005). One of the most relevant is the packing density optimization method, that has been used on the mix proportion design of steel fiber reinforced self-compacting concrete (SFRSCC) and high performance fiber reinforced concrete (UPFRC) (Barros *et al.*, 2007; Soltanzadeh *et al.*, 2015). According to this method, the design of SFRSCC/UPFRC composition is based on the three following steps: 1) Definition of the

proportion of constituent materials for developing an optimized paste; ii) Determination of the optimum volume percentage of each type of aggregates in the granular skeleton of the concrete; iii) Assessment of an optimum correlation between the binder paste and the solid skeleton in order to obtain SFRSCC/UPFRC with the intended properties at fresh and hardened stages, in accordance with the SFRSCC/UPFRC structural requirements (Barros *et al.*, 2007; Soltanzadeh *et al.*, 2015).

However, the tendency of steel fibers to produce balling during mix stage has been found to be a quite relevant problem, which is more accentuated when using RSF instead of ISF, since RSF are more susceptible to entangle (Aiello *et al.*, 2009). The fresh properties of RSFRC can have a substantial impact on the early age mechanical properties and on the long-term performance of the material (Graeff, 2011). Deficient workability and balling occurrence may lead to excessive voids and non-homogeneous concrete, which can interfere with their transport properties, thus allowing the ingress of aggressive agents (Graeff, 2011). The concentration of fibers near the surface of concrete elements may contribute to reduce their performance due to their higher susceptibility to be corroded (Graeff, 2011). The fact that fibers may not be randomly distributed in concrete may also affect the mechanical behavior of the resulting FRC, leading to higher variability of the results (Graeff, 2011).

Aiello *et al.* (2009) assessed the influence of the type of mixer (traditional and planetary) on the workability of RSFRC and concluded that the planetary vertical mixer is the best equipment to mix RSFRC with good workability. Using a traditional mixer, the maximum fiber content used without bundling of the fibers within the concrete was 0.26%, while with a planetary mixer, an increase in RSF content up to 0.46% by volume of concrete was permitted, obtaining a more uniform fiber distribution and consequently an increase of the mix homogeneity. According to Hu *et al.* (2018b), using a conventional tilting mixer, the maximum dosage of RSF added to concrete without fiber balling was 30 kg/m<sup>3</sup>.

The workability of fluid SFRC is usually measured by the slump flow test. For identical concrete mixtures, the addition of fibers will result in a loss of slump, which does not necessarily mean that there is a corresponding loss of workability, especially when vibration is used during placement. The ACI 544.1R-96 suggests the use of the inverted slump cone test to characterize the workability of fresh SFRC.

Several researchers evaluated the fresh properties of RSFRC by means of slump tests, and confirmed a negative effect on the workability of concrete with the increased percentage of fibers (Tlemat *et al.*, 2006a; Aiello *et al.*, 2009; Centonze *et al.*, 2012; Hu *et al.*, 2018b). When the RSF content is increased, a higher percentage of superplasticizer is added to aid the dispersion of the fibers in the concrete mix, surpassing the technologic problem of their aptitude to tangle (Tlemat *et al.*, 2006a; Centonze *et al.*, 2012; Martinelli *et al.*, 2015; Caggiano *et al.*, 2017; Leone *et al.*, 2018). An increase of the air content is also found in

the fresh mixture of RSFRC, similar to ISFRC, depending on the mixing procedure and fiber content (Smrkić *et al.*, 2017). For small fiber volume contents in concrete mixes (< 0.5%), the addition of fibers does not significantly affect the density of concrete (Smrkić *et al.*, 2017).

### **2.2.6 Compressive behavior of RSFRC**

The incorporation of steel fibers usually has only a minor effect on the compressive strength of concrete (Micelli *et al.*, 2014). However, it is recognized that RSF can control the crack propagation of concrete, mainly for strain levels above the strain at compressive strength, by improving the energy absorption capacity of the material in its compression softening stage (Graeff, 2011; Tlemat *et al.*, 2003b).

The two main factors affecting the compressive strength of SFRC are the matrix properties and the fiber characteristics (type, geometry, aspect ratio, content and distribution) (Yazici *et al.*, 2007). In general, the higher the fiber factor  $V_f l_f / d_f$  (with  $V_f$  fiber volume fraction,  $l_f$  fiber length and  $d_f$  fiber diameter), the greater is the energy absorption capacity in the post-peak stage (Ou *et al.*, 2012; Barros *et al.*, 2017). Studies on the effect of RSF on the compressive strength of concrete are still inconclusive. Leone *et al.* (2018) and Hu *et al.* (2018b) noted that the RSF did not have significant influence on the compressive strength of the reinforced concrete. Tlemat *et al.* (2006a) and Smrkić *et al.* (2017) observed a slight decrease of the compressive strength when shredded RSF were added to concrete, which can be explained by the correspondent decrease in workability and increase of air content. However, various researchers reported that the compressive strength of RSFRC has, generally, increased with the fiber content (Tlemat *et al.*, 2006a; Aiello *et al.*, 2009; Centonze *et al.*, 2012; Rossli and Ibrahim, 2013; Abdul Awal *et al.*, 2013; Caggiano *et al.*, 2017). The randomness of the geometric irregularity of the RSF contributes to limit the lateral strain during loading, delaying the crack propagation and, hence, increasing the compressive strength (Centonze *et al.*, 2012). However, due to the balling effect, this improvement is only observed up to a certain limit volume of RSF, above which the compressive strength tends to decrease due to an increase of the air entrapped in concrete (Pilakoutas *et al.*, 2004, Rossli and Ibrahim, 2013; Smrkić *et al.*, 2017). This threshold of RSF volume depends mainly on the type and size of aggregates and cementitious matrix quality (Caggiano *et al.*, 2017). Pilakoutas *et al.* (2004) suggested that the maximum SRSF content (average diameter of 0.23 mm) that can be effectively used in concrete is 2% (by weight). Rossli and Ibrahim (2013) suggested a value of 0.4% (by volume) for SRSF using a traditional mixer. The presence of rubber (in free form or attached to the steel) can also contribute to the

reduction of compressive strength (Papakonstantinou and Tobolski, 2006). Aiello *et al.* (2009), and Onuaguluchi and Banthia (2018) found that RSF and ISF of identical geometry have similar influence on the compressive strength of concrete.

### **2.2.7 Post-cracking tensile behavior of RSFRC and testing procedures**

The main effect of the incorporation of steel fibers into concrete is to prevent and control the crack propagation. The bridging effect of fibers across cracks provides a significant post-cracking tensile strength and consequently, higher energy absorption of concrete (Abrishambaf, 2017). Different approaches are available for experimental characterization of the tensile post-cracking behavior of SFRC. Currently, flexural tests and indirect tensile tests, coupled with an inverse analysis procedure, have been widely used for the assessment of the tensile constitutive behavior of fiber reinforced cementitious composites (FRCC), which may contribute positively in design approaches for structural elements made with this kind of advanced construction materials. In the next sections these test methods will be reviewed and some representative results observed on the mechanical behavior of RSFRC are provided and discussed.

#### **2.2.7.1 Beam bending test**

The beam bending test, due to their relative simplicity, is widely used to characterize the flexural toughness of SFRC. Two test configurations are generally recommended in the international guidelines: *three-point notched beam bending test*, 3PNBBT (RILEM TC 162-TDF, Vandewalle and Dupont, 2003; EN-14651:2005; MC2010, 2011) and four-point bending tests (UNI 11039-2:2003; JCI-S-003-2007; DBV – Guide to Good Practice, 2007; ASTM C1609/C109M-12, 2012). The UNI 11039-2:2003, JCI-S-003-2007 and ASTM C1609/C109M-12 (2012) prescribe to use un-notched beams, while the DBV – Guide to Good Practice (2007) prescribes beams with 45 mm notch.

The un-notched bending test configuration favors a crack propagation starting from the weakest cross section and multiple cracking may occur, whereas the notched bending test favors a stable propagation of the crack, initiated at the notch located at the mid-span of the beam, that may not be the weakest cross section (Figure 2.17b).

According to the literature, the three-point notched beam bending test (3PNBBT) is the most common alternative for the uniaxial tensile test to define, indirectly, the constitutive laws of SFRC (Salehian, 2015).

Figure 2.17 depicts schematically the 3PNBBT setup, specimen's geometry and the measuring system used to determine the mid-span deflection (LVDT) and the crack mouth opening displacement (CMOD) at the mid-width of the notch (clip gauge). A notch with a depth of 25 mm and a maximum thickness of 5 mm should be executed in the specimens, aiming to control crack initiation and propagation in a pre-defined cross section (MC2010, 2011) (Figure 2.17b).

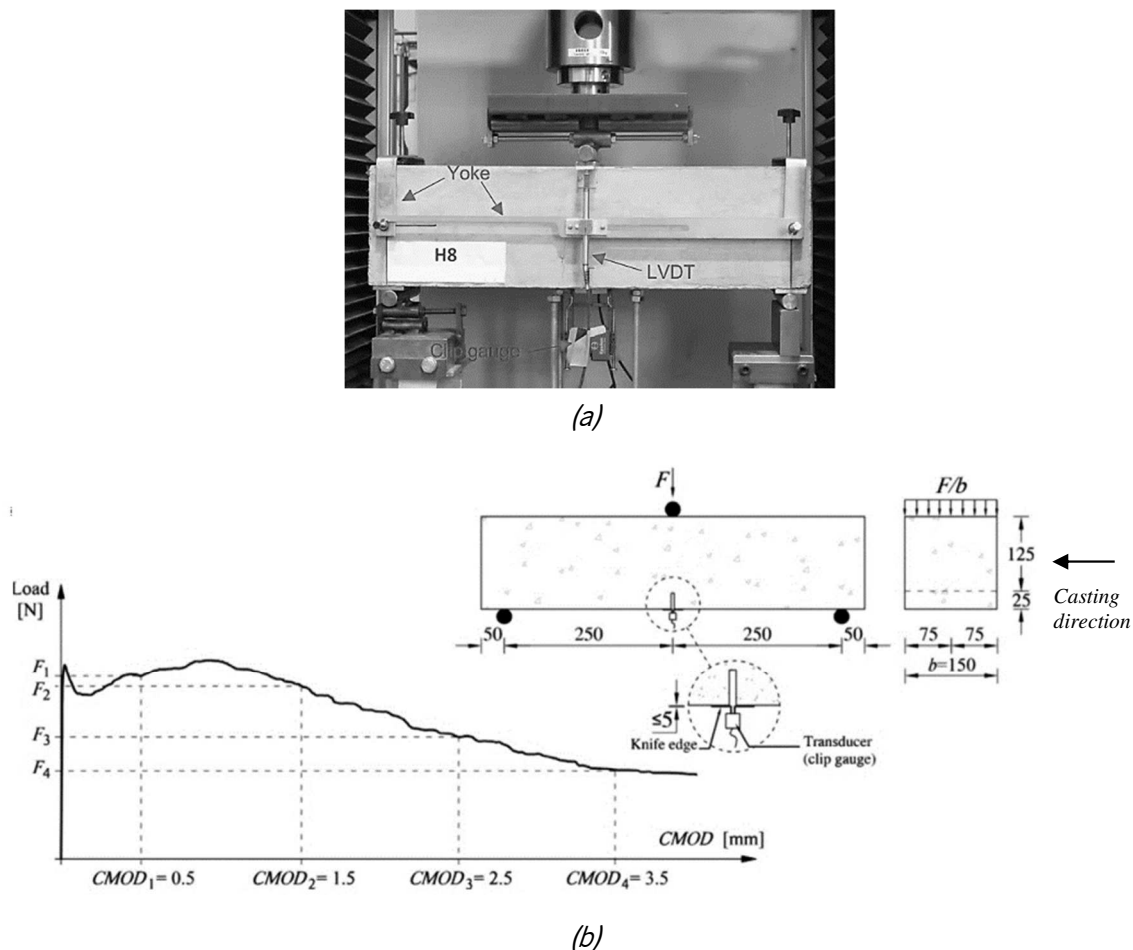


Figure 2.17 – (a) Three-point notched beam bending test setup (Hu *et al.*, 2018)

(b) Typical load-CMOD curve of FRC (dimensions in mm) (adapted from MC2010)

Both the RILEM TC-162 TDF (Vandewalle *et al.*, 2003) and MC2010 (2011) propose the determination of residual flexural strength parameters ( $f_{R,j}$ ) to characterize the post-cracking behavior of FRC. These parameters are determined from the force-CMOD curves obtained from 3PNBBTs (Fig. 2.17b). Based on the load values,  $F_j$ , corresponding to the  $CMOD_j$  ( $j = 1$  to 4), the parameters  $f_{R,j}$  are determined from the following equation:

$$f_{R,j} = \frac{3 F_j L}{2 b h_{sp}^2} \quad (2.2)$$

where  $b$  (=150 mm) and  $L$  (=500 mm) is the width and the span of the specimen, respectively, and  $h_{sp}$  (=125 mm) is the distance between the tip of the notch and the top of the cross section.

Zamanzadeh *et al.* (2015) performed 3PNBBTs with concrete beams reinforced with 45, 60 and 90 kg/m<sup>3</sup> of RSF or ISF. The flexural stress-CMOD curves obtained are depicted in Figure 2.18.

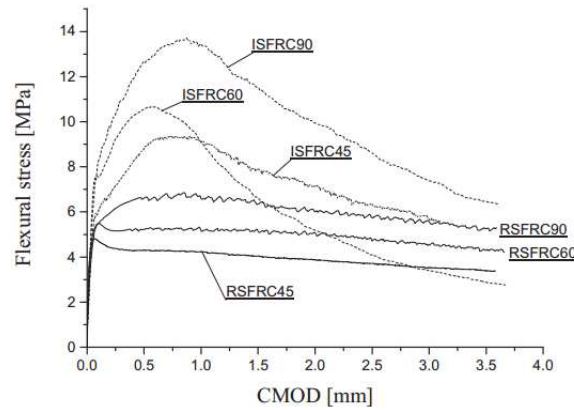


Figure 2.18 – Comparison of the flexural behavior of RSFRC and ISFRC (Zamanzadeh *et al.*, 2015)

From the results presented in Figure 2.18, it was found that the deflection hardening phase of ISFRC specimens was not developed in RSFRC specimens. This indicates that the fiber reinforcement mechanisms for relatively small crack widths were not as effective in the specimens with RSF as were with ISF. This phenomenon is attributed to the different geometry and surface characteristics of RSF fibers. However, contrary to ISFRC, the flexural tensile strength of RSFRC was almost constant up to the ultimate crack width recorded. The results were analyzed in terms of equivalent flexural tensile strength parameters,  $f_{eq}$  (obtained according to the recommendations of RILEM TC-162 TDF (Vandewalle *et al.*, 2003)) and  $f_{R,j}$ . In agreement with previous research on ISFRC (Barros *et al.*, 2005), a clear linear relationship between  $f_{eq,2}$  and  $f_{eq,3}$  was also obtained in RSFRC. In addition, a linear trend was observed between the parameters  $f_{eq,2}$  and  $f_{R,1}$ , and between  $f_{eq,3}$  and  $f_{R,4}$ . From a database containing results of the post-cracking characterization of ISFRC (Moraes Neto, 2013), it was found that the residual flexural strength parameters  $f_{R,j}$  of ISFRC have increased more pronouncedly with the fiber volume percentage ( $v_f$ ) than those of RSFRC, which means that for a certain post-cracking performance a higher  $v_f$  is necessary in RSFRC. In any case, the  $f_{R,j}$  values obtained for the developed RSFRC are sufficiently high



to create good perspectives for the use of these composites in some applications (Zamanzadeh *et al.*, 2015).

Hu *et al.* (2018a) investigated the flexural behavior of SFRC beams under 3PNBBT. Steel fibers recycled from ELTs (RTSF) and two types of manufactured undulated steel fibers (MSF1&MSF2) were used in their study. Figures 2.19a,b shows the load-deflection curves obtained for single-fiber-type reinforced concrete, hybrid SFRC (combining RTSF and MSF) and plain concrete.

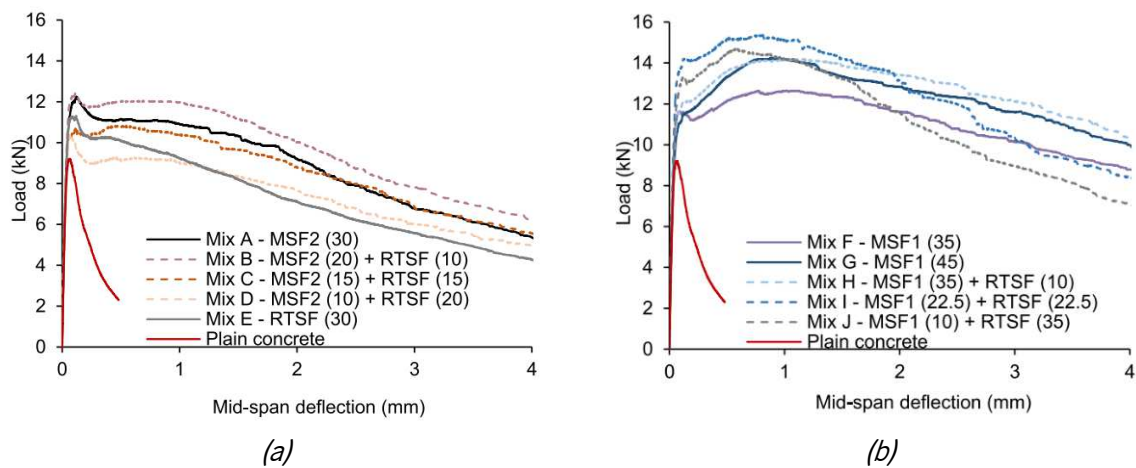


Figure 2.19 – (a) Load-deflection curves for SFRC mixes at 30 kg/m<sup>3</sup> from 3PNBBT  
(b) Load-deflection curves for mixes at 35 and 45 kg/m<sup>3</sup> from 3PNBBT (Hu *et al.*, 2018a)

The two group of results (Figures 2.19a,b) indicated that hybrid SFRC mixes containing 10 kg/m<sup>3</sup> of RTSF showed better flexural performance than MSF-only mixes at the same fiber dosage. For mixes containing more than 22.5 kg/m<sup>3</sup> of RTSF, a sharper descending branch occurs compared to other SFRC mixes. This may be attributed to the less effective macro-crack control of short RTSF than of MSF (can debond or even pull-out at large crack widths, leading to progressive damage). Hu *et al.* (2018a) also verified a high variability of the fracture parameters obtained from bending tests (up to 35%) due to the non-homogeneous fiber distribution of SFRC (Hu *et al.*, 2018a).

Meddah and Bencheikh (2009), Smrkić *et al.* (2017) and Onuaguluchi and Banthia (2018) also demonstrated that a hybrid recycled fiber reinforcement is more effective in terms of post-cracking behavior than adopting exclusively RSF. This is attributed to the multi-level crack stabilization and crack propagation control provided by the shorter fibers (crack-bridging at the micro level) and longer fibers (macro-crack bridging and pull-out resistance) (Onuaguluchi and Banthia, 2018). Meddah and Bencheikh (2009) have recommended to limit the length of these fibers to 10 mm in order to guarantee a homogeneous fiber distribution.

Several authors investigated the flexural behavior of notched RSFRC prisms by means of four-point bending tests (Tlemat *et al.*, 2006a,b; Aiello *et al.*, 2009; Centonze *et al.*, 2012; Rossli *et al.*, 2013; Martinelli *et al.*, 2015; Caggiano *et al.*, 2017; Leone *et al.*, 2018). In four-point bending test of notched FRC beams, the scatter in the maximum flexural stress is significant, compared to 3PNBBT results. This can be justified by the evolution of the moment in four-point bending specimens, which presents a constant moment section that allows the formation of more cracks (Finazzi *et al.*, 2014). Tlemat *et al.* (2006a) and Aiello *et al.* (2009) found that the peak load, and mainly the toughness and the residual strength after cracking increased with the fiber content. However, a fiber volume higher than 0.6% did not provide any further effect on the flexural strength of concrete (Rossli *et al.*, 2013). The ISFRC and RSFRC prisms had similar flexural behavior (Tlemat *et al.*, 2006a; Aiello *et al.*, 2009; Centonze *et al.*, 2012; Caggiano *et al.*, 2017; Leone *et al.*, 2018). The post-cracking behavior of RSFRC was characterized by a more pronounced softening range than ISFRC if the RSF used had a low aspect ratio (47) (Martinelli *et al.*, 2015; Caggiano *et al.*, 2015). The RSFRC specimens failed in bending by mobilizing, in general, the fibers pull-out mechanisms, rather than the tensile rupture of the fibers (Tlemat *et al.*, 2006a). A high variability of the results, referring to post-cracking behavior of RSFRC, was observed due to a non-uniform distribution of RSF (Leone *et al.*, 2018). According to Tlemat *et al.* (2006a), the black carbon on the PRSF surface may have a negative effect in the flexural strength and energy absorption capacity of RSFRC. An inverse finite element analysis based on results obtained from four-point bending tests on notched RSFRC prisms showed that the existing RILEM design guidelines for SFRC (based on 3PNBBT) overestimated the flexural resistance of RSFRC (Tlemat *et al.*, 2006b; Neocleous *et al.*, 2006).

In general, considerable benefits provided by RSFs have been highlighted in terms of post-cracking tensile capacity, energy absorption capacity and deflection performance. They clearly demonstrate that ISF can be replaced by RSF for concrete reinforcement without a significant decay in flexural properties.

## **2.2.7.2 Indirect tensile test**

### **2.2.7.2.1 Splitting tensile test (Brazilian type test)**

The splitting tensile test, also known as Brazilian tensile test, has been widely employed to assess, indirectly, the tensile behavior of concrete, as described in the ASTM C496/C496M-11 (2011). In this test, a compressive load is applied along two diametrically opposite line loads of a cylindrical (or prismatic) specimen, and an almost uniform tensile stress state is induced, perpendicular to the loading plane at the central part of the specimen, as represented in Figures 2.20a,b. However, this test setup is not the most appropriate for deriving the stress-crack opening width ( $\sigma - \omega$ ) relationship, due to the unstable

crack propagation, since the critical region of the specimen is subjected to a biaxial stress field, with compressive stresses acting cross-wise to tensile ones, even executing a notch along the loading plane, as shown in Figure 2.20a (Abrishambaf *et al.*, 2015a). Only using advanced numerical models, capable of simulating both the nonlinear behavior in tension and compression, is possible to derive, with acceptable accuracy, the uniaxial tensile stress-crack opening ( $\sigma - \omega$ ) relationship by performing inverse analysis of the experimental results obtained (Abrishambaf *et al.*, 2015b; Edalat-Behbahani *et al.*, 2016).

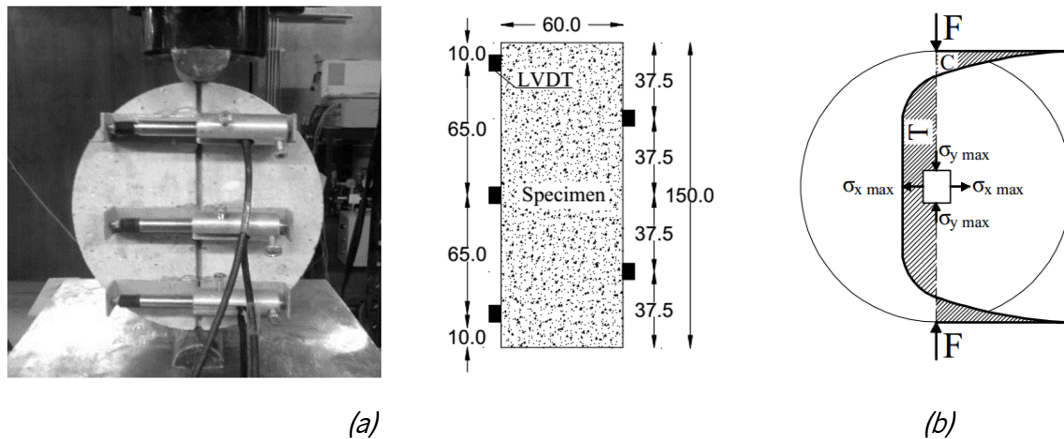


Figure 2.20 – (a) Splitting tensile test setup: front view (left) and lateral view (right) (Dimensions in mm)  
(b) Stress distribution in the loading plane (Abrishambaf, 2015)

Anyway, this test setup has been used by various authors to assess the indirect tensile behavior of RSFRC (Papakonstantinou and Tobolski, 2006; Bdour and Al-Khalayleh, 2010; Rossli and Ibrahim, 2012; Abdul Awal *et al.*, 2013; Ahmadi *et al.*, 2017; Smrkić *et al.*, 2017). Figure 2.21 shows representative results of the splitting tensile tests obtained with RSFRC.

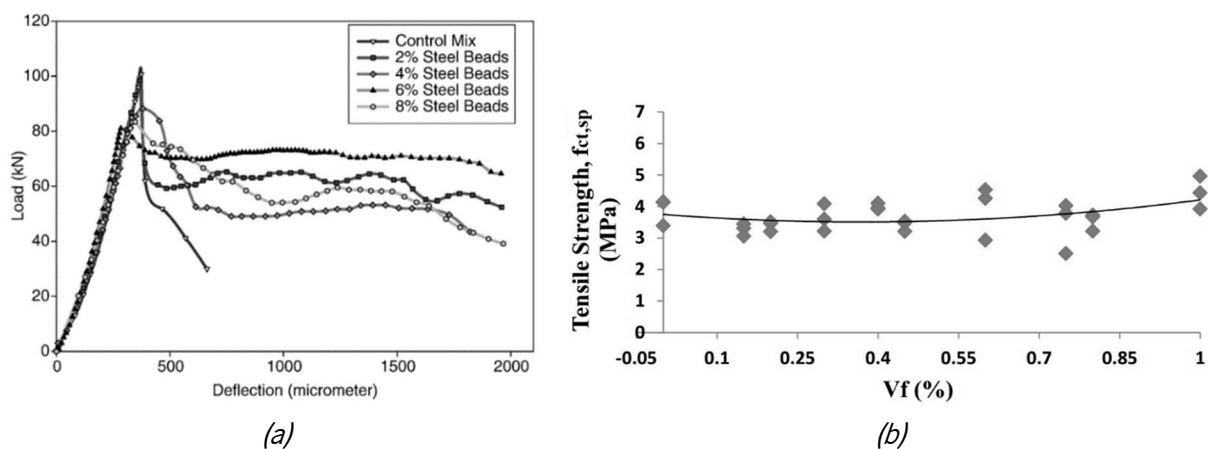


Figure 2.21 – (a) Splitting tension load-deflection curves (Papakonstantinou and Tobolski, 2006)  
(b) Splitting tensile strength ( $f_{ct,sp}$ ) vs. Volume of fibers ( $V_f$ ) (Rossli and Ibrahim, 2012)

The effect of RSF on the splitting tensile strength of concrete is still unreliable. Some authors report a decrease of the splitting tensile strength with the increase of the steel beads content (short steel wires and wires covered by or embedded in rubber pieces obtained from the recycling of waste tires). However, greater toughness is observed in concrete mixtures containing steel beads comparing with plain concrete mixtures (Figure 2.21a) (Papakonstantinou and Tobolski, 2006; Bdour and Al-Khalayleh, 2010). Rossli and Ibrahim (2012) observed an almost null influence of the RSF on the splitting tensile strength of RSFRC (Figure 2.21b), while Abdul Awal *et al.* (2013) and Ahmadi *et al.* (2017) found an increase of the tensile strength of RSFRC with the increasing amount of RSF.

### 2.2.7.2.2 Double Edge Wedge Splitting Test (DEWST)

Currently, this wedge splitting test proposed by di Prisco *et al.* (2013), has been used to determine the tensile stress-crack opening ( $\sigma - \omega$ ) relationship and mode I fracture parameters of fiber reinforced cementitious composites. Figure 2.22a schematically represents this test setup.

The DEWST was conceived in order to deviate the compressive stresses from the ligament between the tips of the two V-notches and, hence an almost pure uniaxial tensile stress state is attained in the fracture surface, aligned with the ligament. Ferrara *et al.* (2012), di Prisco *et al.* (2013) and Salehian *et al.* (2014) proposed an additional notch in the tip of “V” notch in order to better localize the fracture surface (Figure 2.22b).

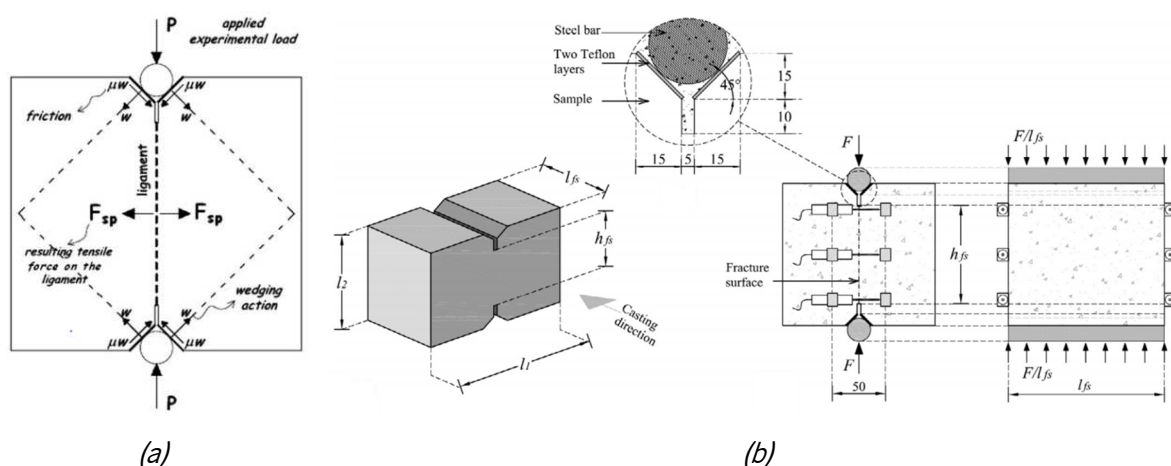


Figure 2.22 – (a) Force diagram in DEWST (di Prisco *et al.*, 2013) (b) Details of the DEWST (sample shape, geometry of the notches and test setup (dimensions in mm)) (Salehian *et al.*, 2014)

The splitting tensile force ( $F_{sp}$ ) induced by the applied compressive load  $P$  can be determined by:

$$F_{sp} = P \frac{\cos \vartheta - \mu \sin \vartheta}{\sin \vartheta + \mu \cos \vartheta} \quad (2.3)$$

where  $\vartheta$  is the inclination angle of the V-notch and  $\mu$  is the concrete-to-steel roller friction coefficient (di Prisco *et al.*, 2013). According to di Prisco *et al.* (2013), the most reliable results were obtained with  $\vartheta = 45^\circ$  and  $\mu = 0.06$ , which resulted in  $F_{sp} = 0.89P$ . The nominal tensile stress ( $\sigma_N$ ) is calculated from Eq. (2.4), where  $h_{fs}$  and  $l_{fs}$  are the ligament depth and the thickness of the fracture surface (Figure 2.22b).

$$\sigma_N = \frac{F_{sp}}{h_{fs} \cdot l_{fs}} \quad (2.4)$$

The DEWST has also been used to study the influence of fiber dispersion and orientation on the mechanical behavior of ISFRC structural elements, since concrete core specimens can be easily cut from these elements, defining the fracture planes with tailored orientations (Ferrara *et al.*, 2012; Salehian *et al.*, 2014; Abrishambaf *et al.*, 2015a; Lameiras *et al.*, 2015). However, so far, no experimental data are still available for RSFRC.

### 2.2.7.2.3 Double Punch Test (Barcelona test)

Another alternative to characterize the residual tensile strength of FRC is the Barcelona test (BCNT) proposed by Molins *et al.* (2009), according to the standard UNE 83515:2010. The BCNT consists of compressing a cylindrical or cubic FRC specimen placed vertically within two circular punches centred at the top and bottom surfaces (Figures 2.23a,b). According to Figure 2.23b, the height and the diameter of the specimen are identical ( $2b/2h=1$ ) and the ratio between the diameters of the punches and the specimen is one fourth ( $2a/2b=0.25$ ). A load is applied to the punches at a constant displacement rate and a conical triaxial state is formed from the center to the edges of the specimen, leading to internal tensile stresses (Galeote *et al.*, 2017) (Fig. 2.23c). The failure mechanism normally presents three radial cracks, although in some cases four cracks can be observed (Fig. 2.23c).

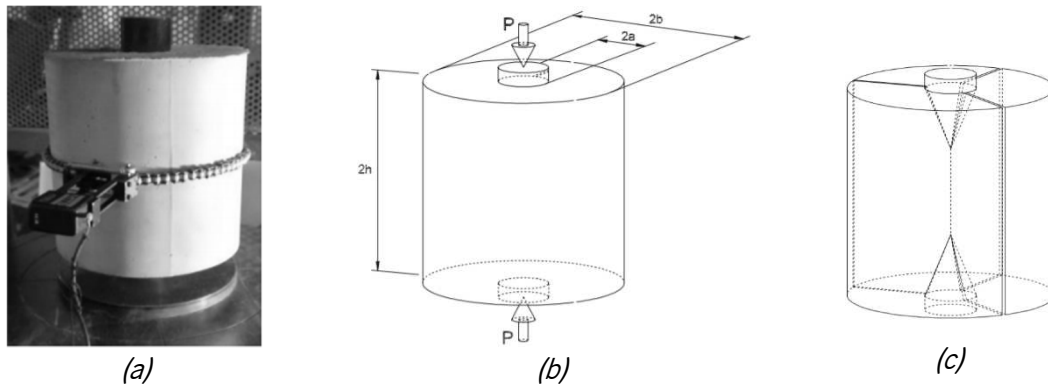


Figure 2.23 – (a) (b) BCN test setup in cylindrical specimen; (c) Mechanism of failure of BCN test (Molins *et al.*, 2009; Galeote *et al.*, 2017)

BCNT was later enhanced by Pujadas *et al.* (2013, 2014), by proposing an analytical model to generalize the BCNT using axial displacement and also by establishing a framework to predict the fiber orientation efficiency in a cubic specimen subjected to BCN test. Additionally, Blanco *et al.* (2014) proposed a constitutive model to characterize the tensile properties of FRC derived from BCNT results.

The results obtained in BCNT may be represented through a Load-Total Circumferencial Opening Displacement (TCOD measured at mid height of the specimen) curve or Load-Axial Displacement relationship (Galeote *et al.*, 2017).

BCNT may represent a suitable method for the quality control of FRC due to its simplicity, the reduced scatter of the results and low material consumption (environment friendly) compared to 3PNBBT. However, the use of the BCNT for the characterization of the post-cracking behavior of FRC is hindered by the lack of acceptable correlations with the 3PNBBT, due to the differences in the crack mechanism observed in both tests. The fracture mechanism of the 3PNBBT is purely dominated by Mode I, while in the BCN test, the propagation of the crack is a mixed response between Modes I and II, as represented in Figure 2.24 (Galeote *et al.*, 2017).

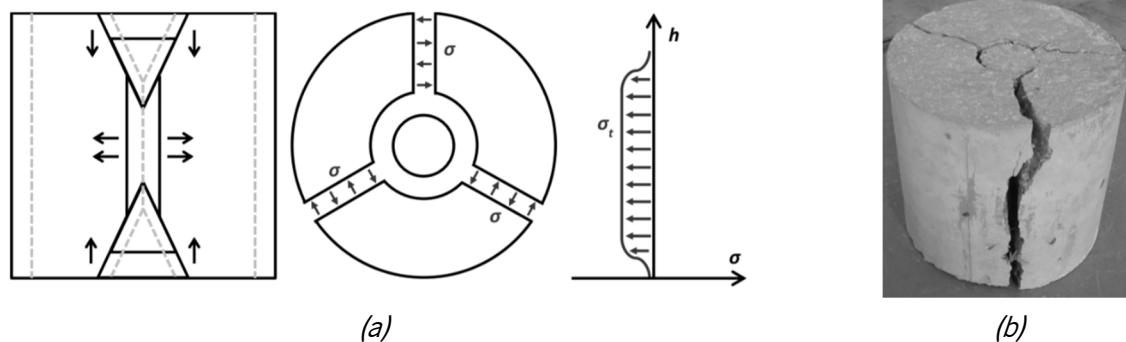


Figure 2.24 – (b) Cracking mechanism and distribution of stresses in BCN test (Galeote *et al.*, 2017)  
(a) Cylindrical specimen after BCN test (Molins *et al.*, 2009)

In Figure 2.25 are presented results from 3PNBBT and BCNT obtained with FRC specimens produced with 30, 45 and 60 kg/m<sup>3</sup> (SCC\_H60\_SF\_30&45&60) of hooked-end steel fibers.

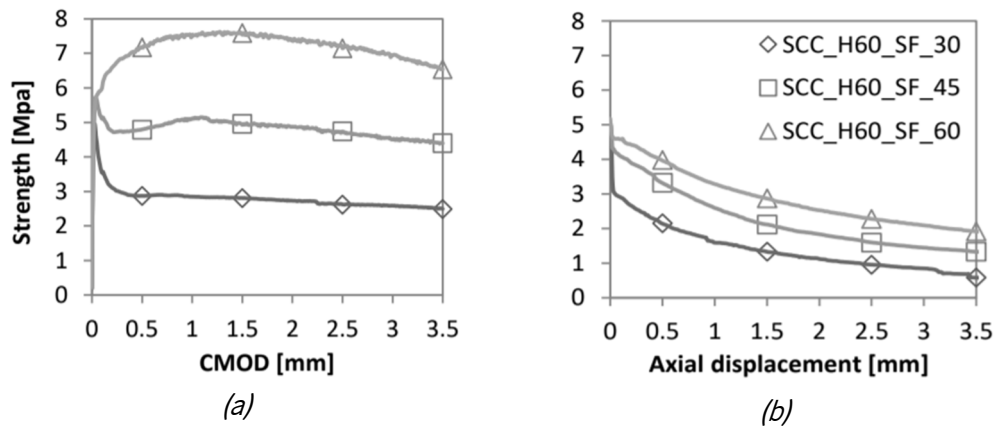


Figure 2.25 – (a) Residual strength vs. CMOD obtained from 3PNBBT;  
(b) Residual strength vs. Axial displacement obtained from BCNT (Galeote *et al.*, 2017)

For both tests (3PNBBT and BCNT), the residual strength increased with the increase of fiber content (Figs. 2.25a,b). However, the residual strength obtained from BCNT is in general, lower than from 3PNBBT, mainly for higher fiber content (SCC\_H60\_SF\_60), since hardening behavior in 3PNBBT appeared after the first crack, while in BCNT, all the FRC mixtures showed softening behavior (Figs. 2.25a,b). This difference is mainly attributed to the cracking mechanism that takes place in each test. In the BCNT, the cracks form abruptly, and the load is almost instantaneously transferred to the fibers, while in the 3PNBBT, the crack is localized and a more gradual load transfer from the matrix to the fibers occurs at crack plane (Galeote *et al.*, 2017).

### 2.2.7.3 Round panel test (RPT-3ps)

The round panel test recommended by ASTM C1550-08 (2008) consists in determining the flexural toughness of FRC expressed as energy absorption (area under the force-deflection curve) in the post-crack range, from a round panel supported on three symmetrically arranged pivots (RPT-3ps) and subjected to a central load  $P$  (Figure 2.26). This test is appropriate to evaluate the fiber reinforcement efficiency for slab and shell type FRC structures, since the crack formation with different orientation reported in the round panels (Figure 2.26) mobilizes more representatively the fiber reinforcement mechanisms really occurred in this type of structures (Salehian and Barros, 2015).

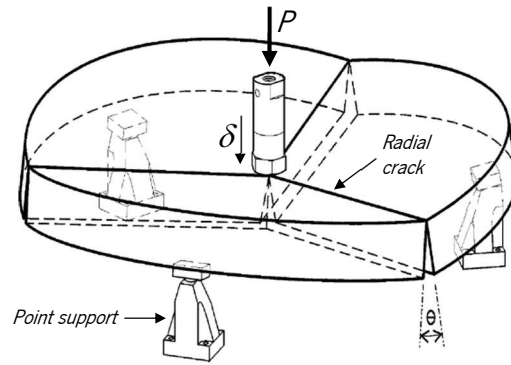


Figure 2.26 – RPT setup with three point support and normal failure mode (Tran *et al.*, 2005)

Hu *et al.* (2018a) examined the flexural performance of SFRC round panels with steel fibers dosages ranging between 30 and 45 kg/m<sup>3</sup>, using manufactured undulated steel fibers (MSF1&MSF2) and recycled tire steel fibers (RTSF) on their own or blended together. The SFRC mixes were the same as those employed in the SFRC beams for 3PNBBT (produced by Hu *et al.* (2018a), as reported in Section 2.2.7.1) in order to analyze the correlation between the two flexural tests. Each round panel was centrally loaded and supported on three symmetrically (120°) arranged pivots on a pitch circle diameter of 750 mm. Figures 2.27a,b show the load-deflection curves obtained for the round panel tested.

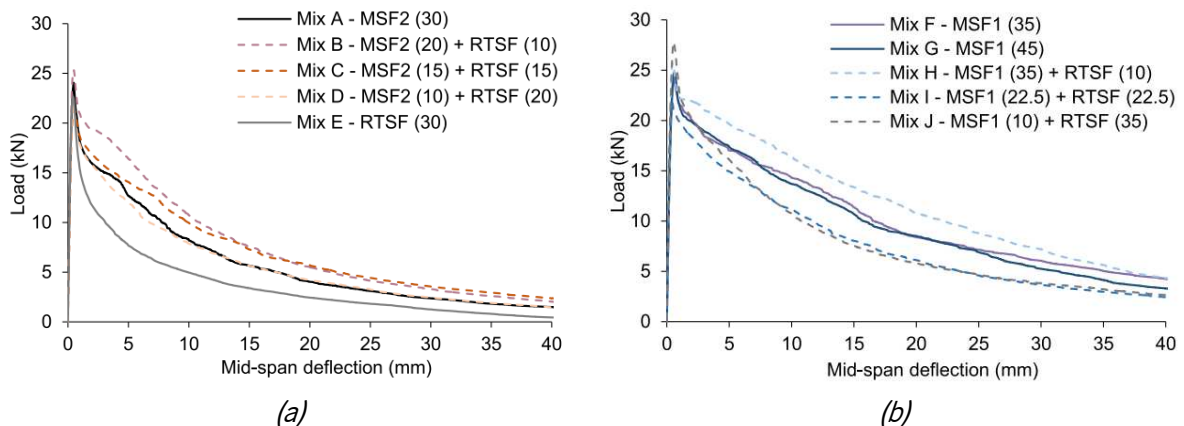


Figure 2.27 – (a) Load-deflection curves for SFRC mixes at 30 kg/m<sup>3</sup> from RPT-3ps  
(b) Load-deflection curves for mixes at 35 and 45 kg/m<sup>3</sup> from RPT-3ps (Hu *et al.*, 2018a)

According to Figures 2.27a,b, only deflection softening behavior was observed in the RPT, contrary to the beam bending tests (Figure 2.19). However, it was verified a beneficial effect of increasing the total fiber content on the flexural toughness of round panels, and the best overall flexural performance was observed for the hybrid SFRC mixes containing 10 kg/m<sup>3</sup> of RTSF, similarly to what was found in SFRC beams (Section 2.2.7.1). The lowest post-cracking capacity was obtained in round panels with RTSF-only mix at



30 kg/m<sup>3</sup> (Figure 2.27a) and in hybrid mixes with a total fiber content of 45 kg/m<sup>3</sup>, of which 10 kg/m<sup>3</sup> are MSF and 35 kg/m<sup>3</sup> are RTSF (Figure 2.27b). These results confirmed a synergy in blending RTSF with MSF, which is able to combine the benefits of the individual fiber types at controlling cracks at different stages. The synergetic effect in hybrid SFRC mixes depends on the test type and the dosage of fibers. There are reasonable correlations between the flexural tensile strength and the fracture parameters of the SFRC prisms and the round panels, which indicates that the two tests approximately provide the same information, however, a wide testing database is still required. For all mixes, the variability in the energy absorption capacity of round panels increased (up to 20%) with the increase in deflection and crack opening, which indicates a more predominant effect of the fiber-matrix interaction and fiber distribution and orientation as cracks open (Hu *et al.*, 2018a). According to Bernard and Xu (2008), the location of the three radial cracks in a round panel submitted to RPT-3ps has a relatively small effect on the post-cracking flexural performance, however, the low variability observed in load resistance is mainly caused by the location of the three radial cracks.

Tests with square panel supported on its contour, as proposed by EFNARC specifications (1996), are also appropriate to evaluate the energy absorption of FRC in slab and shell type structures. Centonze *et al.* (2012) evaluated the energy absorption capacity of RSFRC by executing flexural tests on square panels (600x600x100 mm<sup>3</sup>) of RSFRC reinforced with 0.46% by volume of RSF and square panels of ISFRC for comparison purposes. The effectiveness of RSF in improving the toughness of concrete matrix was also confirmed by these authors, since the experimental results in terms of load and toughness were comparable for both RSFRC and ISFRC panels (the maximum load recorded for RSF panels was about 18% lower than that of ISF panels). A significant scatter on the results was observed due to the different distribution of the fibers in the crack surfaces, among the tested panels (Centonze *et al.*, 2012). Micelli *et al.* (2014) compared the load carrying capacity of RSFRC square panels with those of plain concrete reinforced with a traditional steel mesh (SM panels). Both the maximum load and the total energy absorption of RSF panels were higher (19.9% and 33.2%, respectively) than those of SM panels.

Analytical and numerical models of the flexural performance of FRC panel tests have been proposed to predict the constitutive laws of FRC that can be used on design approaches for SFRC structures (Tran *et al.*, 2005; Nour *et al.*, 2011; Salehian *et al.*, 2014). Salehian *et al.* (2014) have proposed a numerical model that takes into account the stress-crack width relationship of SFRC for the prediction of the force-deflection response from the panel test results by inverse analysis. By adopting a moment-rotation approach (Barros *et al.*, 2015b), this model has demonstrated to be appropriated for deriving the fracture

mode I parameters used in the material nonlinear analysis of slab and shell type structures (Salehian *et al.*, 2014).

However, so far, no numerical simulations are still available for the derivation of the stress-crack width of RSFRC from inverse analysis with the experimental tests with RSFRC panels.

### **2.2.8 Durability of SFRC exposed to chloride attack**

Durability is one of the most important aspects of concrete due to its fundamental incidence on the service lifetime of concrete structures. Chloride-induced reinforcement corrosion has been reported to be the leading cause for degradation of reinforced concrete structures, particularly those which are exposed to coastal/marine environments. In environments containing chlorides, SFRC structures are subjected to chloride attack that can promote steel depassivation and initiate corrosion of steel fibers, with eventual pernicious consequences in terms of structural and durability performance.

Corrosive agents may penetrate the concrete through one of the four main transport mechanisms: Diffusion; Capillary Suction; Permeation and Migration (Bertolini *et al.*, 2004). The chloride penetration depends of the SFRC pore structure and all the factors that determine it, such as, mix design parameters (water to cement (W/C) ratio, type and proportion of mineral admixtures and cement, type and proportion of steel fibers, compaction, curing, etc.) and presence of cracks (Shi *et al.*, 2012). An increase in the crack width leads to a more permeable concrete, providing ingress of water, chlorides and other corrosive agents that enhance the possibility of fiber corrosion. However, the concrete permeability may decrease significantly by increasing the fiber content due to the reduction of shrinkage cracks and the breaking of continuity of pores and inter-connectivity of porous channels by the fiber reinforcement mechanisms (Singh and Singhal, 2011).

Steel fibers are used in concrete to limit the crack width and retain the crack growth. In fact, the fiber reinforcement mechanisms may contribute to reduce the ingress of chlorides with beneficial consequences in terms of concrete durability (Sadeghi-Pouya *et al.*, 2013; Berrocal *et al.*, 2013, 2015, 2016). However, corrosion can affect the fibers bridging the cracks by reducing their sectional area, which has negative consequences in terms of their performance (Granju and Balouch, 2005). Furthermore, steel fiber corrosion affects negatively the appearance of SFRC structures and may produce micro-spalling of concrete. This damage is, nevertheless, less severe than the spalling caused by the corrosion of conventional steel bars used in reinforced concrete structures (Granju and Balouch, 2005; Balouch *et al.*, 2010).

### 2.2.8.1 Corrosion susceptibility of steel fibers

The phenomenon of steel corrosion in aqueous environment is an electrochemical process, which can be understood as two half-cell reactions, iron oxidation reaction (anodic) and oxygen reduction reaction (cathodic), taking place at the surface of the corroding metal, in the presence of moisture and oxygen (Figure 2.28) (Berrocal, 2015). Initial attack occurs at anodic areas on the steel surface, where the chloride ions depassivated the reinforcing steel, and the ferrous ions go into solution while the electrons are released to the adjacent cathodic sites on the surface, where they combine with oxygen and water to form hydroxyl ions. These react with the ferrous ions from the anode to produce ferrous hydroxide, which itself is further oxidised in air to produce hydrated ferric oxide, i.e. red-brown mixture of iron oxides - rust (Kropp and Hilsdorf, 1995).

Low levels of chloride tend to cause general attack corrosion while high levels of chloride induce localized corrosion (Song *et al.*, 2017). Localized or pitting corrosion is defined as the selective removal of metal by corrosion at small areas and takes place when small local sites are attacked by much higher chlorides than the remaining original surface. Figure 2.28 represents, schematically, the overall process of chloride induced pitting corrosion in concrete.

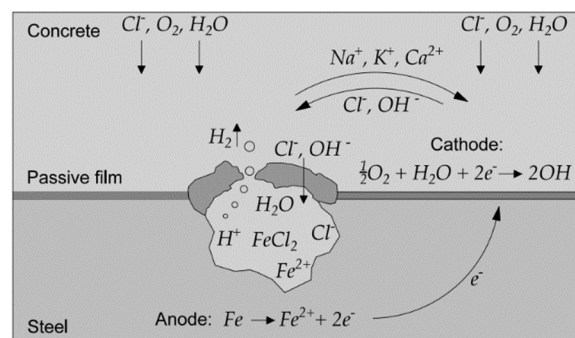


Figure 2.28 – Schematic representation of chloride induced localized corrosion (Berrocal, 2015)

Chen *et al.* (2015) investigated the corrosion effects on the tensile strength of corroded low carbon steel fibers. They concluded that the steel fibers corroded to 0.47-32.49% in weight loss by wetting and drying cycles in 3.5 wt% NaCl solution, exhibiting pitting corrosion, while the steel fibers corroded to 1.81-87.48% by galvanostatic method (applying a designed current density of 20 mA/cm<sup>2</sup>) showed a relatively uniform corrosion. As the corrosion degree increased, the weight loss increased, and the nominal tensile strength of the corroded fibers decreased. The tensile strength of steel fibers was reduced in the case of pitting corrosion, while it was marginally affected by uniform corrosion, even for higher corrosion degree (87%

in weight loss) due to a proportional decrease of cross section with ultimate load. The local section loss of steel fibers at the pits may cause further degradation of the mechanical properties of steel fibers, leading to a brittle failure (Chen *et al.*, 2015).

Electrochemical techniques can be used to assess, control and investigate the corrosion of steel fibers caused by corrosive attack of chloride ions. Frazão *et al.* (2016) assessed the corrosion resistance of ISF through some electrochemical techniques, namely, corrosion potential monitoring and potentiodynamic and linear polarization measurements. Based on open circuit potential ( $E_{ocp}$ ) measurements, the corrosion probability of steel fibers immersed in a 3.5 wt% NaCl solution was higher than 90%. The steel fibers indicated to have a high risk of corrosion in a chloride environment, derived from the high values of corrosion current density ( $i_{corr}$ ) and the small values of polarization resistance ( $R_p$ ) obtained in potentiodynamic and linear polarization tests. Scanning electron microscopy (SEM) analysis have shown that corrosion was uniform on the entire fiber surface and the main corrosion products were iron oxides (Frazão *et al.*, 2016).

### **2.2.8.2 Chloride-induced corrosion of uncracked SFRC**

#### **2.2.8.2.1 Chloride diffusion in SFRC**

Steel embedded in uncontaminated concrete remains passive due to the high alkalinity of concrete. However, in a chloride-laden environment, the ingress of chloride ions into the matrix disrupts the passive layer of steel film, reduces the pH at the steel surface and cause the initiation and propagation of corrosion (Marcos-Meson *et al.*, 2018). In saturated state, chloride ions penetrate in concrete by ionic diffusion, due to concentration gradient between the exposed surface and the pore solution inside concrete. This process is often described by Fick's second law, whose diffusion equation is the most convenient mathematical model to describe the non-steady diffusion processes of chloride ingress into a concrete structure (Wang *et al.*, 2018a,b). Assuming the chloride diffusion coefficient constant, the well-known analytical solution of the Fick's second law is expressed by:

$$C(x,t) = C_s \left( 1 - \operatorname{erf} \frac{x}{2\sqrt{Dt}} \right) \quad (2.5)$$

where  $C(x,t)$  is the chloride concentration at depth  $x$  and immersion time  $t$ ,  $C_s$  is chloride concentration at the surface,  $x$  is the penetration depth,  $t$  is the immersion time, and  $D$  is the chloride diffusion coefficient.

The chlorides are in concrete both in free or combined form (physically adsorbed or chemically bonded to cement hydration products in the form of Friedel's salt (Mohammed and Hamada, 2003)). The free chloride content in the pore solution is responsible for the initiation of corrosion, however, the chloride content required for steel depassivation in reinforced concrete, designated by critical chloride content, is commonly expressed as total chloride content relative to the weight of the cement or concrete, due to the difficulties in evaluating the free chloride content in concrete (Mohammed and Hamada, 2003; Angst *et al.*, 2009). The critical chloride content has been reported in the range of 0.4 - 1.0% (by weight of cement) for conventional reinforced concrete structures, but greatly depends on various factors: e.g. oxygen concentration, binder type, W/C ratio, steel grade, test conditions (e.g. temperature, measurement technique) (Angst *et al.*, 2009). However, the critical chloride content has been found to be much higher in steel fibers (Berrocal *et al.*, 2013). Janotka *et al.* (1989) found that the necessary concentration of chloride to initiate corrosion in steel fibers was at least 3 times higher compared with conventional reinforcing steel. Dauberschmidt and Raupach (2005) reported that fibers embedded in uncracked concrete stay passive up to chloride contents of 2.1 to 4.7% (by weight of cement). Hwang *et al.* (2015) quantified a critical chloride concentration of 0.8% to 1.0% by weight of cement for corrosion initiation of steel fibers embedded in concrete, being higher than for reinforcing steel bar in concrete (0.4%-0.6% by weight of cement, according to EN 1992-1-1 Eurocode 2, 2004). According to Berrocal (2013), the improved corrosion resistance of steel fibers in uncracked concrete is attributed to the combination of two factors: a) The short length of the steel fibers, which impedes large potential differences along the fiber and limits the formation of distinct anode and cathode regions; b) The casting conditions that allow the formation of a very thin well-defined concrete-steel interfacial layer rich in  $\text{Ca(OH)}_2$  with less presence of voids at the interface (Berrocal, 2013). However, some authors have reported the opposite, i.e. higher rate of chloride transport in SFRC, comparing with plain concrete, due to the increased porosity at the interface of steel fibers/matrix, caused by the air bubbles arrested by the fibers during the casting process (Hwang *et al.*, 2015).

Following a generalized conceptual model for corrosion of steel in concrete (Tuutti, 1982), the deterioration of SFRC exposed to chlorides can be divided in two stages: a) *initiation phase*, which is the time required by the chlorides to penetrate into the concrete and reach the steel surface, and b) *propagation phase*, once the chloride threshold at the steel surface is exceeded and the corrosion of the steel embedded in the contaminated concrete proceeds. In Figure 2.29, a schematic representation of the service life of a structure, according to Tuutti's model is shown.

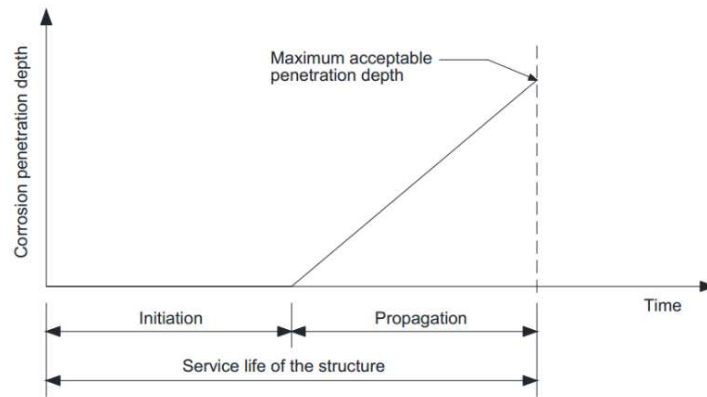


Figure 2.29 – Tuutti's service life model for corrosion of steel in concrete (Berrocal *et al.*, 2013)

The estimation of service lifetime for existing and planning structures is very important for planning future maintenance and repair of the structures. Different models for service life predictions of the chloride ingress, followed by corrosion initiation, in reinforced concrete structures exposed to marine environment, based on the Fick's second law of diffusion, have been proposed by several researchers (Maage *et al.*, 1996; Pillai and Annapareddy, 2013; Safehian and Ramezani-pour, 2015; Khan *et al.*, 2017). However, very few studies in this regard are available for SFRC (Wang *et al.*, 2018a,b). Wang *et al.* (2018a,b) proposed a prediction model for chloride ingress into submerged SFRC under bending load by using the apparent chloride diffusion coefficient. Three concrete mixtures of the same strength grade were considered: plain concrete (C50); concrete reinforced with 1% in volume of steel fibers (SFRC-1) and concrete reinforced with 1.5% in volume of steel fibers (SFRC-1.5). The time-dependent chloride diffusion coefficient,  $D_o$ , was calculated, and the experimental results showed that SFRC had better chloride resistance than plain concrete, when specimens were under bending load (Table 2.5). For SFRC in tension, the chloride diffusion coefficient was 30 ~ 38 % lower than that of plain concrete.

Table 2.5 – Results of chloride diffusion coefficient  $D_o$  ( $\times 10^{-12} \text{ m}^2 \cdot \text{s}^{-1}$ ) (Wang *et al.*, 2018a,b)

Immersion Time (days)	C50		SFRC-1		SFRC-1.5	
	Unstressed	Under tension	Unstressed	Under tension	Unstressed	Under tension
60	3.47	5.29	3.36	3.57	3.14	3.44
90	3.51	5.25	3.30	3.78	3.10	3.18
150	3.48	5.21	3.44	3.69	3.02	3.23
Average of $D_o$	3.49	5.25	3.37	3.68	3.08	3.28

The prediction of the corrosion initiation in submerged concrete structures, with and without bending load, are shown in Figure 2.30. The corrosion initiation was predicted from equation (2.5), adopting the critical chloride concentration,  $C_{cr}$  of 0.05% (by mass of concrete) and the surface chloride concentration,  $C_s$ , of 0.8% (by mass of concrete). The corrosion initiation gets longer as the cover thickness increase (Figure 2.30). For unstressed SFRC, the calculated corrosion initiation of SFRC was 6 ~ 40 % longer compared with plain concrete (C50). For concrete under bending load, the corrosion initiation of SFRC was 2.2 ~ 3.6 times of that for plain concrete, varying with fibers dosage and cover thickness. Therefore, the presence of steel fibers greatly reduced the impact of bending load on the chloride diffusion rate, which means that SFRC can improve the chloride resistance and prolong the service life of concrete structures in chloride environment (Wang *et al.*, 2018a).

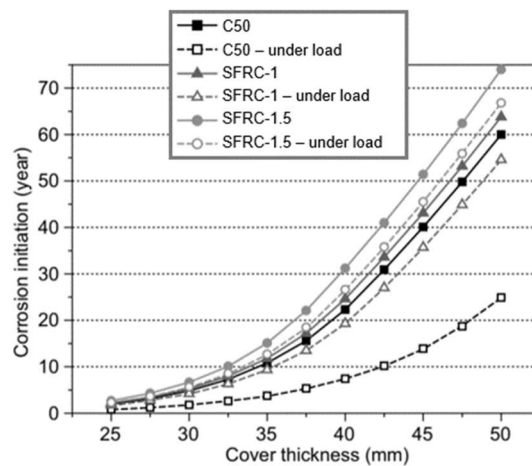


Figure 2.30 – Predicted corrosion initiation of SFRC and plain concrete, with and without applied load (Wang *et al.*, 2018)

### 2.2.8.2.1 Durability of uncracked SFRC

In general, the investigation of SFRC durability in uncracked state showed that minor alterations of the durability indicators of concrete were introduced by the addition of steel fibers (Teruzzi *et al.*, 2004; Roque *et al.*, 2009; Frazão *et al.*, 2015). Teruzzi *et al.* (2004) studied three concrete mixes used for different applications under distinct exposure conditions, with and without steel fiber reinforcement, and found no significant effects on chloride diffusion or oxygen permeability attributable to the presence of fibers in concrete. They concluded that the interfacial zone around the fibers does not act as a preferential path for penetration of detrimental agents (Teruzzi *et al.*, 2004). Roque *et al.* (2009) performed water permeability, water absorption and chloride diffusion tests on SFRC mixes. The results showed that the performance of SFRC was similar or slightly better compared with plain concrete mixes. Frazão *et al.*

(2015) found that adding steel fibers to self-compacting concrete resulted in a very slightly increase of open porosity of SFRSCC; did not significantly change the capillarity pores size and, consequently, the water absorption by capillarity; reduced the electrical resistivity of concrete in 63%; did not significantly affect the chloride diffusion by migration under non-steady state and by natural immersion, as well as the carbonation resistance. According to the results obtained, these authors also concluded that the electrical resistivity test is not suitable to evaluate the durability of SFRC due to the conductivity of steel fibers, and the determination of chloride diffusion coefficient of SFRC is more feasible by natural immersion test in salt solution, since it better represents the mechanism of chloride penetration. The authors also found that in conditions of extreme aggressiveness, not representative of real environmental conditions, corrosion of steel fibers can induce cracking in concrete, leading to a decrease of the SFRC tensile strength (Frazão *et al.*, 2015).

In the last decades, the long-term behavior of SFRC under chloride exposure has been investigated, concerning the chloride-induced corrosion of steel fibers, as well as the impact of steel fiber corrosion on the post-cracking behavior of SFRC (Marcos-Meson *et al.*, 2018). In general, no adverse effects on the structural integrity have been reported for uncracked SFRC when exposed to marine environments (Nemegeer *et al.*, 2003; Bentur and Mindess, 2007; Buratti *et al.*, 2010). The main variables affecting the durability of uncracked SFRC exposed to chlorides are the exposure conditions, type and size of the steel fibers and the quality of the concrete matrix (Marcos-Meson *et al.*, 2018).

The exposure conditions to study the long-term effect of chloride exposure can be divided into field exposure and laboratory exposure under accelerated conditions.

Field tests comprise the exposure of SFRC to in-situ exposure conditions at representative locations for limited exposure time (e.g. 1-20 years) to extrapolate the durability of SFRC to longer exposures. However, in field tests some variables are uncontrolled and may vary, such as the temperature, exposure-cycles and salinity of the aqueous media. Nevertheless, the exposure of SFRC specimens to coastal environment up to 20 years, seawater or de-icing salts showed limited damage for uncracked SFRC (Marcos-Meson *et al.*, 2018). The damage was limited to aesthetics due to the rusting on exposed fibers at concrete surface with a maximum depth of damage of a few millimetres (up to 5 mm) without corrosion-induced cracking or spalling of the matrix. The long-term mechanical properties indicated no deterioration due to possible fiber corrosion (Mangat and Gurusamy, 1988).

In laboratory tests, the variables are better controlled, such as type of exposure, type of salt, salinity, duration of the exposure, temperature, among others (Marcos-Meson *et al.*, 2018). The use of wet-dry cycles has proven to be an effective method to accelerate corrosion damage of SFRC. Shorter exposures



(up to 6 months) and longer exposures (from 6 months to 3 years) of uncracked SFRC specimens to wet-dry cycles at average salinity of 3-5% NaCl, typically show limited damage, usually just some staining on external fibers at concrete surface (sacrificial layer of 0-5 mm) (Marcos-Meson *et al.*, 2018). It seems that corrosion is limited to the exposed fibers at concrete surface and has negligible effect on mechanical behavior of SFRC (Ganesan *et al.*, 2006; Narayan and Ramakrishnan, 2013; Alsaif *et al.*, 2018). In contrast, Alizade *et al.* (2005) found an increase (by 30%) of the toughness in uncracked SFRC exposed for 2 months and a decrease of toughness for an exposure time of 6 months (about 30% compared to specimens subjected to 2 months of exposure (Alizade *et al.*, 2015)). Additionally, a negative effect on the mechanical properties of uncracked SFRC was observed when pre-corroded fibers were used (Waweru, 2011; Alizade *et al.*, 2015). The corrosion characteristics and the effect of corrosion degree in the mechanical properties of steel fibers are directly related to the performance of SFRC. Waweru (2011) conducted mechanical tests on concrete specimens with pre-corroded steel fibers with 0%, 12.5% and 50% reduction in the minimum fiber diameter, induced by drying–wetting cycles. Increasing the degree of corrosion, the failure type of steel fibers changed from typical pull-out to their tensile rupture. The experimental results demonstrated that a 12.5% reduction in the minimum fiber diameter had almost no effect on the shear capacity, while 50% reduction in the minimum fiber diameter led to a decrease of 24% on the beam's shear strength. Furthermore, the toughness and ductility of SFRC were affected by corrosion to a much higher extent than the shear strength (Waweru, 2011). According to Alizade *et al.* (2016), the 50% reduction of fiber diameter due to corrosion can decrease the toughness of SFRC in almost 50%.

The early-age immersion of SFRC specimens to NaCl solution is not recommendable since the curing in this exposure condition increases the chloride activities and the steel fibers can corrode faster (Alizade *et al.*, 2016).

The type of steel fiber used has also a significant influence on the durability of SFRC exposed to chlorides, e.g. stainless steel has proven to increase the resistance to pitting corrosion relative to carbon steel (Mangat and Gurusamy, 1987); galvanized fibers (zinc plated) showed a complete protection against corrosion for long-term exposures, unlike non-coated steel fibers (Nemegeer *et al.*, 2003).

The quality of the concrete matrix is considered as a critical factor to prevent chloride-induced corrosion of conventional steel reinforcement in concrete (Bentur *et al.*, 1997). Assuming the same principle for SFRC, the main design variables “water to binder ratio (W/B)” and “type and quantity of binder” are expected to affect the corrosion durability of uncracked SFRC. A wide range of W/B ratios have been used in SFRC production, from 0.30 to 0.80 (Nordström, 2005; Roque *et al.*, 2009; Balouch *et al.*, 2010).

Balouch *et al.* (2010) proposed an upper limit for W/C of 0.50 and a minimum fiber cover of 0.2 mm to prevent surface corrosion. Marcos-Meson *et al.* (2018) analyzed the influence of the water to binder ratio on the deterioration of SFRC exposed to chlorides, based on the results available in the literature. The results for uncracked SFRC under chloride attack suggest a significant reduction of the compressive strength for W/B > 0.50 and a larger deterioration of the tensile strength, even at a lower W/B ratio (Marcos-Meson *et al.*, 2018).

Supplementary cementitious materials are widely used to improve the durability of concrete subject to aggressive exposures, such as blended cements, fly ash, blast furnace slag or/and silica fume (Shi *et al.*, 2012). However, there is limited information about the efficiency of mineral admixtures on preventing chloride-induced corrosion of SFRC (Marcos-Meson *et al.*, 2018).

Several researchers have investigated the durability of SFRC exposed to chloride environments. However, only some few studies have been focused on RSFRC (Graeff *et al.*, 2009), which are not sufficient to properly understand and attest the corrosion resistance of RSFRC. Graeff *et al.* (2009) investigated the corrosion resistance of RSFRC and ISFRC used for pavement applications. Since corrosion is a long-term process, corrosion accelerating wet-dry cycles in salt solution were implemented to evaluate the losses in terms of flexural and compressive strength. After 5 months of accelerated corrosion, in spite of the occurrence of concrete micro-spalling, the flexural and compressive strength capacity of RSFRC was not reduced by the corrosion attack, when compared to reference concrete (wet cured and tested at 28 days), as can be seen in Figure 2.31. The increased capacity of corroded wet mixes when compared to those at 28 days is probably due to the age of the specimens (Figure 2.31). The ISFRC presented better flexural strength than RSFRC. However, specimens reinforced with RSF showed higher compressive strength than those with ISF (Graeff *et al.*, 2009).

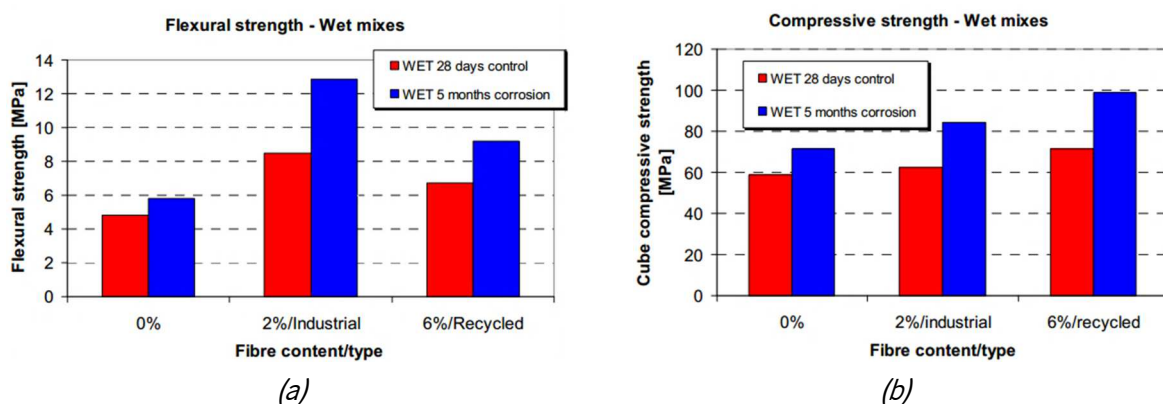








Figure 2.31 – Results obtained with plain concrete, ISFRC and RSFRC, in terms of:  
 (a) Flexural strength (b) Compressive strength (Graeff *et al.*, 2009)

### 2.2.8.2.2 Surface corrosion of SFRC

In SFRC, some of the steel fibers are very close to the concrete surface, with a very small, almost negligible, cover depth. These fibers are highly susceptible to corrosion when exposed to chloride environments, and consequently, high degradation is expected on them.

Graeff *et al.* (2011) visually observed signs of corrosion in the RSF at the surface of RSFRC specimens, which developed as soon as during the curing phase of the specimens. After 5 months of accelerated corrosion, it was noticed that concrete with RSF showed more superficial corrosion effects than those with ISF. From the visual analysis, a scale of deterioration was proposed by Graeff *et al.* (2011), as shown in Table 2.6. The ISFRC usually presented the lowest amount of rust on the surface (in the range of 0-3), whilst RSFRC fall in the highest levels of deterioration (in the range of 2-5) (Graeff *et al.*, 2011).

Table 2.6 – Scale of superficial deterioration of SFRC due to rust (Graeff *et al.*, 2011)

Scale of deterioration	0	1	2	3	4	5
External appearance						

By observing the fracture surface of the samples after testing, it was found that the signs of corrosion in specimens reinforced with RSF were limited to a concrete cover of a thickness not exceeding 10 mm. On the other hand, corrosion signs in concrete with ISF were limited to the fibers at the surface of the samples. This is mainly caused by the high amount and irregular shape of recycled fibers, which caused compaction problems and traps voids (Graeff *et al.*, 2011).

Balouch *et al.* (2010) evaluated the minimum concrete cover of fibers necessary to prevent the appearance of surface spots, which depended on the W/C ratio and the skin porosity of the concrete. After the SFRC prisms have been subjected to cycles of salt fog and drying, the results showed that with high W/C ratio (0.60 and 0.78) all the fibers embedded in concrete less than 1 mm are susceptible to cause corrosion spots at the surface. When the W/C is reduced to about 0.5, the minimum necessary cover to prevent surface corrosion drops to 0.1 or 0.2 mm. Further decrease of W/C does not bring extra significant benefit. The results of corrosion spots counted in the surface of SFRC prisms of different W/C ratio (0.36, 0.48, 0.78) are plotted in Figure 2.32.

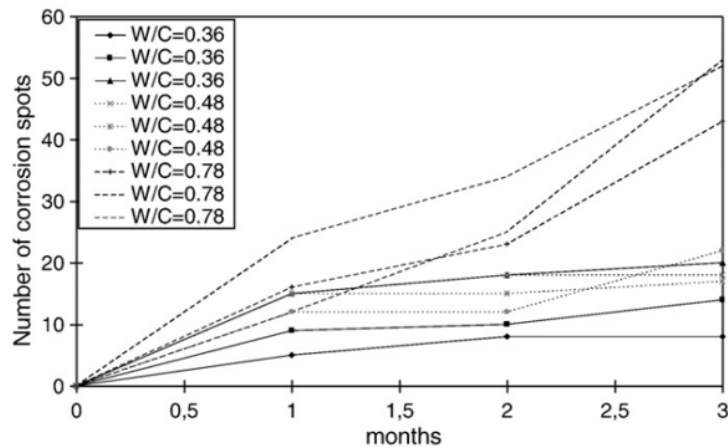


Figure 2.32 – Corrosion spots versus exposure time as a function of W/C (counting area = 100x250 mm<sup>2</sup>) (Balouch *et al.*, 2010)

These results are in agreement with mercury porosimetry analysis of the skin concrete that confirms an important drop in the pore diameters, from  $\approx 7000$  nm to  $\approx 200$  nm, when W/C decrease from 0.78 to 0.48 and a quasi-stability when it is varied from 0.48 to 0.36 (the critical pore diameter stabilized in 200 nm, corresponding to the highest rate of mercury intrusion per change in pressure).

An improved mobility of the fibers in the concrete matrix (higher workability and higher Sand/Gravel ratio) completed by an adequate vibration process (especially by formwork vibration), helps to push the fibers away from the cast surfaces. According to Balouch *et al.* (2010), SFRC must have conjointly  $W/C \leq 0.5$  (which is common) and a minimum cover of the fibers as large as 0.2 mm to prevent surface corrosion. If these two conditions are not fulfilled, the potential surface corrosion of steel fibers may be minimized by using galvanized fibers (Balouch *et al.*, 2010; Marcos-Meson *et al.*, 2018).

### 2.2.8.3 Chloride-induced corrosion of cracked SFRC

The existence of cracks greatly affects the chloride penetration with a significant impact on the durability of SFRC. For SFRC, literature in corrosion resistance induced by chlorides is mainly focused on corrosion arising from cracking process (Mangat and Gurusamy, 1987; Nemegeer *et al.*, 2003; Granju and Balouch, 2005; Nordström, 2005; Solgaard *et al.*, 2010; Yoon, 2012; Marcos-Meson *et al.*, 2018).

Steel fiber reinforcement is effective to reduce chloride penetration through cracks since steel fibers can reduce crack depth significantly (Figure 2.33a). In fact, steel fiber has a function to decrease the effective crack depth,  $d_e$ , which is the depth from concrete surface up to the critical crack width,  $W_{crit}$ , corresponding to the minimum crack width for chloride penetration, and increase the remaining crack

depth,  $d_2 - d_e$  (Figure 2.33b). Therefore, increasing the amount of steel fibers decreases penetration of aggressive substances into concrete.

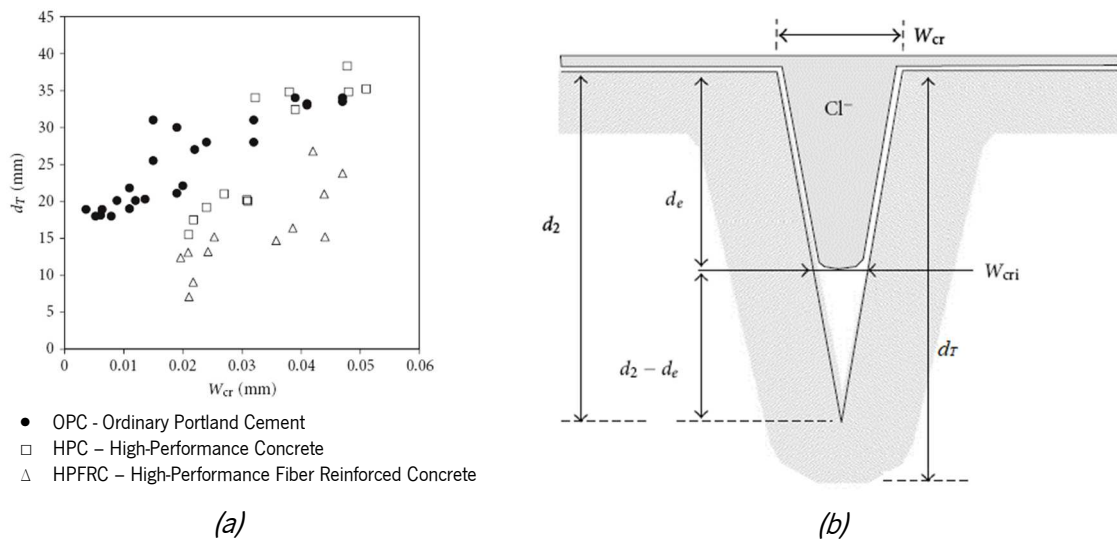


Figure 2.33 – (a) Chloride penetration depth in the fractured zone,  $d_T$ , versus crack width,  $W_{cr}$  (b) Schematic representation of effective crack depth according to critical crack width,  $W_{cri}$  (Yoon, 2012)

There are two main consequences of corrosion in SFRC associated to the cracking process (Granju and Balouch, 2005): 1) The decrease of the carrying capacity and energy absorption performance of the SFRC element (more brittle behavior); 2) The increase of fiber-paste friction due to the rust formation from fiber corrosion process, enhancing the fiber pull-out response, with beneficial effects in terms of load carrying capacity and energy absorption of SFRC elements. If crack width is small enough that self-healing almost restores SFRC integrity, no corrosion of steel fibers is expected from the cracks, which represents a negligible effect in terms of structural and durability performance (Granju and Balouch, 2005). For crack widths higher than 0.1 mm, the chloride penetration is dependent of the crack depth, the concrete quality and the exposure duration. Steel fibers are only corroding if they are in direct contact with the exposed surface or a crack surface (Hansen *et al.*, 1999). According to Granju and Balouch (2005), only the fibers crossing the crack within the distance less than 3 mm from the external surface of the specimens exhibited severe corrosion.

For cracked SFRC, various authors based their conclusions on a critical crack width (e.g.  $W_{cr} \leq 0.20$  mm), where ingress of chlorides and oxygen is limited and autogenous-healing and corrosion products completely seal the crack preventing the evolution of fiber corrosion (Mangat and Gurusamy, 1987; Nordström, 2005). According to Marcos-Meson *et al.* (2018), the damage at the fiber-matrix ITZ induced by the slip of the fibers bridging the crack once the matrix ruptures, promoting fiber corrosion at the

weakest regions, may be explained in four stages, as represented in Figure 2.34: 1) In uncracked SFRC, the steel-matrix ITZ acts as a protective coating of steel fibers surface, preventing the access of aggressive agents (Figure 2.34a); 2) The matrix cracks when the tensile capacity of the concrete is attained, the fiber-matrix bond is “activated”, and the slip of fibers damages the fiber-matrix ITZ, providing a preferential path for transport of chlorides, metal ions and oxygen that promotes corrosion at the areas with greater damage (for ISF, at the level of the hooked end of the fibers and at the area of fibers crossing the crack); 3) If the fibers does not reach a critical slipping up to a critical crack width, the damaged fiber-matrix interface would eventually heal (Homma *et al.*, 2009) (Figure 2.34c). The fiber corrosion and the expansion of the corrosion products increase the fiber roughness, which may increase the fiber-matrix frictional bond (Frazão *et al.*, 2016) and consequently improve the residual tensile capacity (Granju and Balouch, 2005); 4) Larger fiber slipping results in defective healing and excessive damage at the ITZ, which leads to a progressive and localized reduction of the fiber cross-section due to corrosion. When the tensile capacity of the steel is lower than the fiber-matrix bond strength, the failure mode of the SFRC changes from fiber pull-out to fiber tensile rupture, and a decrease of the residual tensile performance is observed (Nordström, 2005) (Figure 2.34d).

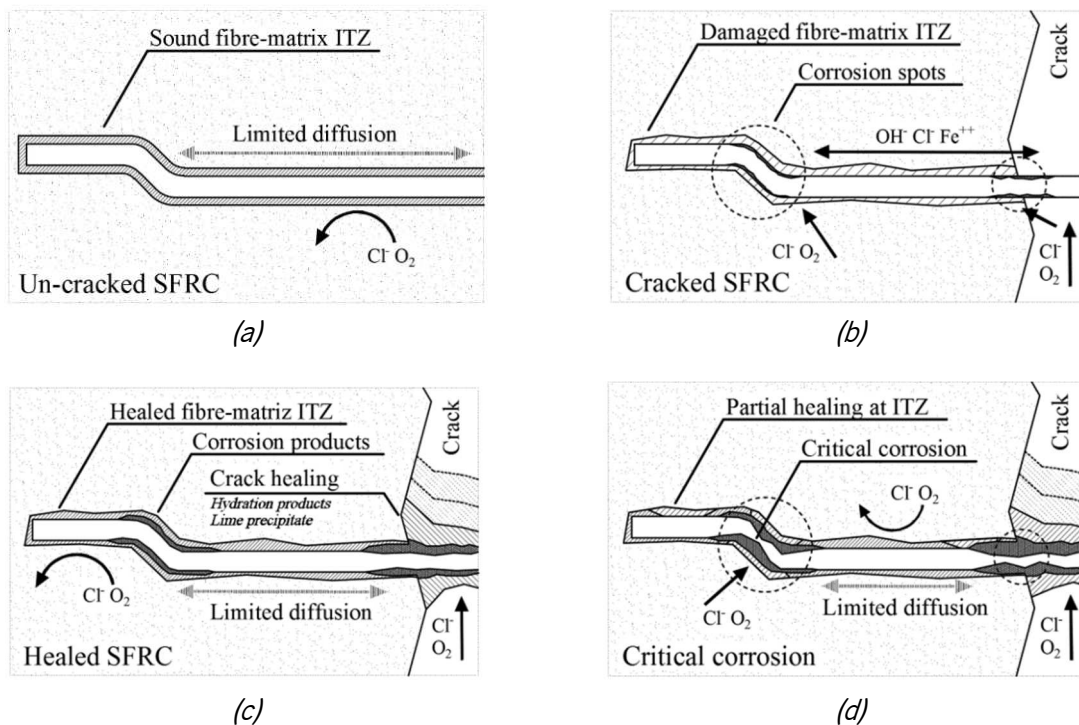


Figure 2.34 – Structure and corrosion mechanisms for SFRC exposed to chlorides for: (a) uncracked SFRC; (b) cracked SFRC at an early stage; (c) cracked SFRC after autogenous healing; (d) cracked SFRC with critical corrosion on fibers (Marcos-Meson *et al.*, 2018)

Field exposure of cracked steel fiber reinforced sprayed concrete (SFRSC) for a period of 5 years to different chloride environments showed heavy corrosion on fibers crossing the crack, that contributed for a decrease of the load bearing capacity of the SFRSC (Nordström, 2005). A loss of 15-20% of the fiber diameter was common in the fibers located into a concrete cover of a thickness of 25 mm. Samples with longer fibers (40 mm) showed almost a double corrosion attack than samples with shorter fibers (30 mm). The self-healing of thin cracks ( $W_{cr} \leq 0.10$  mm) and continued hydration, which increased pull-out resistance of steel fibers, have given an initial increase in residual strength. After long exposures (up to 15 years), the corrosion propagation seemed stagnated and there was little influence of the crack width (0.1-2 mm) (Bernard, 2004; Nordström, 2005). Laboratory studies with accelerated exposure tests showed similar behavior as in field, i.e. the corrosive attack has increased with the crack width and fiber length (Nordström, 2005). For long exposures (from 6 months to 3 years) to wet-dry cycles in seawater, positive results were obtained for smaller cracks ( $W_{cr} \leq 0.20$  mm) in terms of increasing the residual tensile strength, comparing with uncracked SFRC (Mangat and Gurusamy, 1987). However, after reaching a certain degree of corrosion, the corrosion led to a decrease of the cross section of the fibers, which conducted to a decrease in the load carrying capacity of the cracked SFRC elements (Bernard, 2004; Granju and Balouch, 2005; Nordström, 2005; Alizade *et al.*, 2016). In order to improve the durability performance, the cracks can be treated by using surface treatment systems, e.g. combining the application of a sealant followed by a coating, which constituted an effective barrier to chloride penetration into the cracked concrete (Yoon, 2012). Furthermore, the combination of SFRC with a corrosion inhibitor led to reducing crack width and therefore increased the durability of concrete structures in chloride environment (Masmoudi and Bouaziz, 2016).

The mechanisms governing the chloride-induced corrosion of carbon steel fibers in cracked concrete and particularly the influence of fiber corrosion on the post-cracking behavior of SFRC are still unclear. Therefore, more research is needed to explore this issue, not only for ISFRC but especially for RSFRC, whose investigations conducted on chloride-induced corrosion of recycled steel fibers in cracked RSFRC are practically inexistent.

### **2.3 STRUCTURAL ELEMENTS FOR COASTAL BREAKWATERS**

In coastal protective structures, different types of prefabricated PC blocks are used in the construction of breakwaters to dissipate the wave energy and mitigate coastal erosion. Basically, the development of

these elements may attend the following two requisites: 1) Be as simple as possible to reduce the production and placing costs; 2) Have a shape and disposal in coastal areas that optimizes the volume of voids between the PC elements and the internal friction that consequently maximize the dissipation of energy which are subjected (Verhagen, 2004; PIANC/AIPCN, 2005).

Several types of breakwater elements have been developed and patented (217 different elements were identified by a recent PIANC working group), but most of them have been applied for a very limited number of projects. The most commonly used concrete blocks (or “concrete armor units”) for breakwaters are Cube, Antifer cube and Modified cube (own-weight); Tetrapod, Akmon, Dolos and Stabit (own-weight and interlocking); Accropode, Core-loc and Xbloc (interlocking); Cob and Shed (friction); among others (Muttray and Reedijk, 2009).

Tetrapods were the first interlocking armor units, and their main advantages were a slightly improved interlocking as compared to a Cube, and a larger void porosity of the armor layer, which increases wave energy dissipation and reduces the wave run-up (Bakker *et al.*, 2003). Tetrapods have four legs that irradiate from a central point, with leg diameters up to 2m and total tetrapod height over 4m (SOTRAMER, 1978) (Figure 2.35a). The average hydraulic stability and resistance of the Tetrapod are large. However, the structural stability is low, with a large risk of progressive failure (Bakker *et al.*, 2003). The cracking risk of this element is mainly relevant at the surface regions, during the initial setting and hydration of concrete (Azenha *et al.*, 2011). According with Van der Meer (1999), a Tetrapod armor layer has a void ratio of 48%. Tetrapods have been applied for breakwaters, seawalls, beach erosion control, as well as scour and bank protection (SOTRAMER, 1978) (Figure 2.35b).



(a)



(b)

Figure 2.35 – (a) General view of a tetrapod unit; (b) Tetrapod armor layers for breakwaters



During their lifetime, the tetrapods are known to have severe degradation (mainly cracking) and premature rupture of their legs, when located in highly aggressive environments subjected to extreme wave action (as identified in the breakwaters located in the North of Portugal) (Figure 2.36).



(a)



(b)

Figure 2.36 – (a) Rupture of tetrapod legs (b) Cracking of tetrapods

These ruptures are due to an imbalance between the strength (structural integrity) of the Tetrapods and the hydraulic stability (resistance to displacements) of the armor layer and tend to decrease the efficiency of breakwaters as a whole, thus diminishing their capacity to absorb wave energy (PIANC/AIPCN, 2005). The substitution of the damaged tetrapods has significant maintenance costs that justify the study of other solutions that can minimize the need for this kind of intervention (Azenha *et al.*, 2011).

The integrity of the Tetrapods depends on concrete quality, which should be adequate for their use in marine environment (PIANC/AIPCN, 2005). Unreinforced concrete is a brittle material with a low tensile strength (1.5-3.0 MPa) and a high compressive strength, which is one order of magnitude larger (PIANC/AIPCN, 2005). As the failure of Tetrapods is due to tensile stresses, it is therefore important that tensile performance requirements are reflected in the specifications of concrete to be used in their fabrication (PIANC/AIPCN, 2005). Besides stresses caused by mechanical and hydraulic loads, another problem related to the structural integrity of concrete armor units is the thermal stress developed during the curing process (PIANC/AIPCN, 2005). Slender and big-size units are more sensitive to cracking phenomena, due to the temperature gradients created by the hydration process, which promotes the development of tensile stresses that can attain the concrete tensile strength, resulting in widespread surface microcracking (thermal cracking) (PIANC/AIPCN, 2005; Azenha *et al.*, 2011).

The armor units are subjected to different types of loads, namely static loads (weight of units and prestressing of units due to wedge effects and from settlement of underlayers); dynamic loads (pulsating (gradually varying wave forces and earthquake); impact loads (collisions between units, missiles of broken units, collisions during handling, transport and placing, high-frequency occurrence of wave slamming); abrasion loads (impacts of sand, pebbles, etc. in suspension); thermal loads (temperature differences during the hardening process after casting, freeze-thaw); chemical attack (alkali-silica and sulphate reactions and corrosion, if steel reinforcement is provided) (Burcharth, 1992).

Breakage of armor units occurs when the stresses from the static, pulsating and impact loads exceeds the tensile strength of the concrete. Many failures of such breakwaters were caused by unforeseen early breakage of the units, thus revealing an imbalance between the strength structural integrity of the units and the hydraulic stability resistance to displacements of the armor layers (Burcharth *et al.*, 2000). The main parameters that determine the armor unit breakage are the unit mass,  $M$ , the concrete properties (density,  $\rho_a$ , modulus of elasticity,  $E$ , and tensile strength,  $S$ ), the sea action conditions (water depth,  $d$ , significant wave height,  $H_s$ , and peak wave period,  $T_p$ ) and the breakwater geometry parameters (slope, armor unit placement and packing density) (Burcharth *et al.*, 2000).

As previously reported in Section 2.2, steel fibers resulting from the industry of tire recycling can be efficiently employed for the reinforcement of concrete structures. RSFRC is an optimum candidate for the development of ductile, high-strength and durable structural elements, as it is required for the armor units. According to the results obtained by Burcharth (1985), from impact fatigue tests conducted with 30 tons Dolos, a steel fiber content below 70 kg/m<sup>3</sup> has only negligible effect on the tensile strength. To take advantage of the fiber reinforcement mechanisms after initiation of the matrix micro-cracking, the breakwaters should have internal hyperstaticity. Pilot's tests with beams reinforced with various types of steel fibers showed that a fiber length ( $l_f$ ) of approximately 45 mm ensured good toughness (Burcharth, 1985). A fiber diameter smaller than 1 mm would probably be more effective in terms of toughness per kilo of steel (Burcharth, 1985). However, the characteristics of the fibers depend heavily on the maximum size of the aggregate ( $D_{max}$ ) used in the concrete armor units. The  $l_f$  is expected to exceed three times the  $D_{max}$ . The post-cracking behavior of tetrapods is significantly changed by the addition of steel fibers, where an increase of 1.7 of load carrying capacity was obtained by numerical simulation when compared with the PC solution (Azenha *et al.*, 2011). SFRC has been reported as having improved impact and

abrasion resistance as compared with plain concrete, for application in breakwater armor units (Hoff, 1975).

The use of recycled tire materials and the use of by-products for cement replacement, such as fly ash, disclose the adoption of environmental sustainability methodologies in the technology of SFRC production, which seems to have beneficial effects for the development of a new generation of breakwaters with more effective protection of the coastal zone and lower maintenance costs.

---

# Chapter 3

---

## TECHNOLOGY OF RSFRC MANUFACTURING

---

### 3.1 INTRODUCTION

The first part of this chapter presents the characterization of the materials used in the production of Recycled Steel Fiber Reinforced Concrete (RSFRC) specimens for the experimental tests carried out in this research, with especial focus on the characterization of RSF.

The design optimization of RSFRC, regarding the incorporation of Recycled Steel Fibers (RSF), can provide a plurality of reinforcement mechanisms that promotes the increase of post-cracking behavior and durability of RSFRC (Tlemat *et al.*, 2006a; Aiello *et al.*, 2009; Graeff *et al.*, 2012; Zamanzadeh *et al.*, 2015). The efficiency of these strengthening mechanisms is highly dependent on the heterogeneous character of RSF geometry. The chemical composition of steel which influences the microstructure, mechanical and corrosion resistance properties has been widely recognized (Tavares *et al.*, 2007; Romańczuk and Oksiuta, 2017). In this chapter, the characterization of the used RSF is detailed in terms of geometric properties, chemical composition and tensile strength.

The resulting steel fibers from the shredding process of ELTs often contain small amounts of rubber particles attached to their surface, which may influence the mechanical properties of RSFRC (Pilakoutas *et al.*, 2004; Papakonstantinou and Tobolski, 2006). Therefore, in order to assess the influence of this attached rubber in the performance of RSF as concrete reinforcement and in its corrosion resistance, two

distinct methods were adopted: manual polishing of the fiber surface with sandpaper; pre-treatment of the fibers at high temperatures.

In order to assess the influence of these pre-treatment methods in the micro-mechanical properties of RSF, nano-indentation technique was employed to measure the mechanical properties of RSF and monotonic fiber pull-out tests were performed to assess the RSF-concrete bond. The experimental procedures and results obtained are discussed with comparison with ISF.

During SFRC production, the most important factors are to ensure uniform dispersion of the fibers into concrete matrix and to prevent segregation and/or fiber balling during mixing. The technological aspects of RSFRC production, including the mix design, mix procedure, RSFRC compositions and fresh properties are presented in a second part of this chapter. Additionally, the mechanical properties of the developed RSFRC were assessed by three-point notched beam bending tests (3PNBBT) and compressive tests. The fracture mode I parameters of the developed RSFRC were determined by inverse numerical analysis of the 3PNBBT results. Analytical expressions were defined to simulate the experimental curves of the compressive behavior of RSFRC.

## **3.2 MATERIALS**

The following constituent materials were used in concrete production: ordinary Portland cement type CEM I 42.5R, fly ash (FA), limestone filler (LF), fine river sand (FS), coarse river sand (CS), crushed granite (CG), water (W), two types of superplasticizer with the commercial designations ViscoCrete® 3005 from Sika® (SP1) and MasterGlenium SKY 617 from BASF (SP2), and a viscosity modifying admixture (VMA) with the commercial designation CHRYSO®Aquabeton. The characterization of these materials is presented in the following sections.

### **3.2.1 Cement**

The cement (CEM) used was a Portland cement type I class 42.5R (CEM I 42.5R) from Secil – Companhia Geral de Cal e Cimento, S.A., according to EN 197-1 (2011). This is a common cement used in Portugal, which only includes less than 5% minor constituents and at least 95% of clinker. According to the data provided by the supplier, the main physical, mechanical and chemical properties of this cement are those listed in Table 3.1.

Table 3.1 – Main characteristics of CEM I 42.5R

Parameter	Standard	Values
<i>Physical properties</i>		
Specific weight (g/cm <sup>3</sup> )	LNEC E-64	3.12
Blaine specific surface (cm <sup>2</sup> /g)		3656
Residue on the 45 µm sieve (%)	EN 196-6	3.00
Residue on the 32 µm sieve (%)		11.10
Water demand (%)		28.6
Setting time (min)	EN 196-3	Initial: 181; Final: 237
Expansion (mm)		1.0
<i>Mechanical properties</i>		
Compressive strength (2 days)		32.2
Compressive strength (7 days)		47.4
Compressive strength (28 days)	EN 196-1	58.3
Flexural strength (2 days)		6.1
Flexural strength (7 days)		7.6
Flexural strength (28 days)		8.6
<i>Chemical composition</i>		
Loss on ignition (LOI) (%)		2.25
Insoluble residue (%)		1.02
Silicon dioxide, SiO <sub>2</sub> (%)		20.88
Aluminum oxide, Al <sub>2</sub> O <sub>3</sub> (%)		5.13
Ferric oxide, Fe <sub>2</sub> O <sub>3</sub> (%)	EN 196-2	3.06
Calcium oxide, CaO (%)		63.25
Magnesium oxide, MgO (%)		2.05
Sulfates, SO <sub>3</sub> (%)		3.05
Potassium oxide, K <sub>2</sub> O (%)		0.77
Sodium oxide, NaO (%)		0.20
Chlorides, Cl (%)	EN 196-21	0.06

### 3.2.2 Fly Ash

Fly ash (FA) is a type II pozzolanic addition, according to the EN 206:2013+A1 (2016), used as cement replacement in concrete production, with economic, ecological and environmental benefits. The fly ash used in this research work came from the Pego thermoelectric plant, supplied by PEGOP Energia Eléctrica, S.A. The main physical and chemical characteristics of this fly ash are presented in Table 3.2.

Table 3.2 – Main characteristics of fly ash

<b>Parameter</b>	<b>Standard</b>	<b>Values</b>
<i>Physical properties</i>		
Specific weight (g/cm <sup>3</sup> )	LNEC E-64	2.32
Blaine specific surface (cm <sup>2</sup> /g)	EN 196-6	3879
Particles > 45 µm (%)	EN 196-3	27.3
Particles > 75 µm (%)		13.2
Expansion (mm)	-	≤1.0
<i>Mechanical properties</i>		
Activity index at 28 days (%)	EN 450-1	93
Activity index at 90 days (%)		98
<i>Chemical composition</i>		
Loss on ignition (LOI) (%)		4.96
Reactive calcium oxide, CaO (%)	EN 196-2	1.32
Sulphates, SO <sub>3</sub> (%)		0.19
Chlorides, Cl (%)	EN 196-21	<0.01
Free calcium oxide, CaO (%)	EN 451-1	0.04

### 3.2.3 Limestone filler

A limestone filler (LF) with the commercial designation BETOCARB, provided by Omya Comital Minerais e Especialidades, S.A., was used in some concrete compositions. The LF is considered a type I addition according to EN 206:2013+A1 (2016), which was obtained from the fine grinding of limestone, containing nearly 100% of calcium carbonate. This addition is commonly used when paste viscosity is intended to be increased without increasing the amount of cement. According to the data provided by the supplier, the main physical and chemical characteristics of the limestone filler, are those listed in Tables 3.3 and 3.4.

Table 3.3 – Main physical properties of limestone filler

<b>Parameter</b>	<b>Standard</b>	<b>Values</b>
Specific weight (g/cm <sup>3</sup> )	LNEC E-64	2.70
Blaine specific surface (cm <sup>2</sup> /g)	EN 196-6	6200
Particles < 2 mm (%)		100
Particles < 125 µm (%)	EN 933-10	100
Particles < 63 µm (%)		99
Moisture (%)	ISO 787/2	0.1
Apparent density (g/cm <sup>3</sup> )	OMYA LTM 001	0.9

Table 3.4 – Main chemical properties of limestone filler

Parameter	Standard	Values
Calcium carbonate, CaCO <sub>3</sub> (%)	-	99
Sulphates soluble in acid (%)		<0.05
Chlorides (%)	EN 1744-1	<0.001
Total sulfur content (%)		<0.04
Alkali content (%)	-	<0.06
Total silica	-	<0.5
Alkali-silica reactivity	-	NR, Class 1

### 3.2.4 Aggregates

Fine and coarse river sand (FS and CS) obtained by screening of dredged material from the Tejo river, supplied by a company from the district of Santarém, and crushed granite (CG) from a quarry located in Guimarães, were the used aggregates. The results of the granulometric analysis of these aggregates, obtained according to the ASTM C136/C136M-14, by using the ASTM series of square mesh sieves, are listed in Table 3.5.

Table 3.5 – Granulometric analysis of aggregates

ASTM sieve		Material passing (%)		
Number	Opening (mm)	FS	CS	CG
1 1/2"	38.100	100.00	100.00	100.00
1"	25.400	100.00	100.00	100.00
3/4"	19.100	100.00	100.00	97.96
1/2"	12.700	100.00	100.00	23.56
3/8"	9.520	100.00	100.00	1.58
4	4.760	99.97	93.49	0.00
8	2.380	99.85	69.31	0.00
16	1.190	99.58	37.55	0.00
30	0.590	86.70	11.92	0.00
50	0.297	21.19	2.85	0.00
100	0.149	1.44	0.77	0.00
200	0.074	0.24	0.33	0.00
Maximum size (mm)		1.190	4.760	19.100
Minimum size (mm)		0.149	0.297	9.520
Fineness modulus (%)		1.913	3.841	7.005
Specific weight (EN 1097-6) (g/cm <sup>3</sup> )		2.61	2.63	2.61
Water absorption (EN 1097-6) (%)		10.64	5.08	1.58



Figure 3.1 summarizes the granulometric curves of these aggregates.

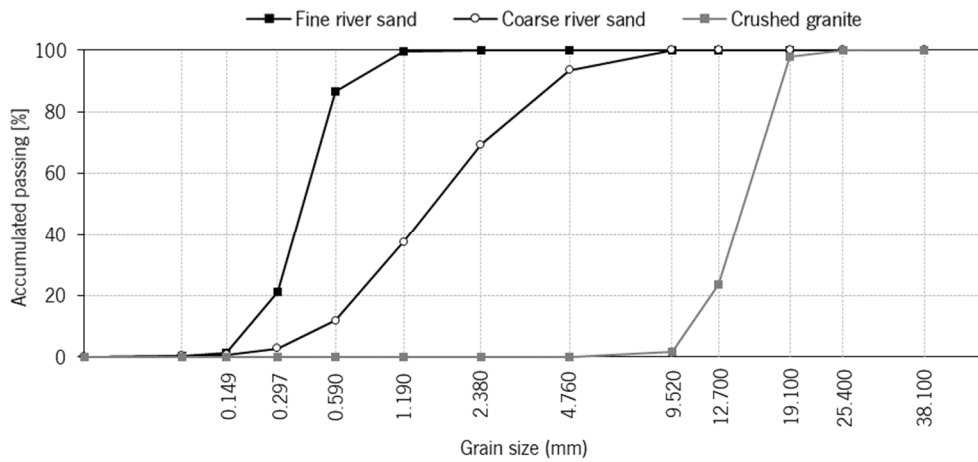


Figure 3.1 – Granulometric curves of used aggregates

### 3.2.5 Water

All concrete specimens for experimental tests of the present work were cast in CiviTest company, located in Jesufrei, Vila Nova de Famalicão. The water (W) used for concrete mixtures was from the public water supply network of Vila Nova de Famalicão, which has an average chloride content of about 10 mg/l (Águas do Norte, 2016, 2017), of irrelevant impact in the durability performance of the developed concretes.

### 3.2.6 Superplasticizers

Two polycarboxylate based superplasticizers (SPs) of third generation were used in concrete production. One was the ViscoCrete® 3005 (SP1) from Sika® and the other was the MasterGlenium® SKY 617 (SP2) supplied by BASF. The reason for using two SPs is because it was decided to keep the type of superplasticizer (SP1) of the known concrete compositions (previously defined by other researchers) used in this study, which was different from the one used in developing new concrete compositions (SP2).

Both SPs promote a very high plastification and water reducing range. The SP2 releases additional polymer chains, which improve the dispersion and stability of the cement particles preventing their flocculation, even when hydration reaction has started. This mechanism allows to maintain a longer workability time; obtain higher mechanical resistance at the early ages, and reduce the water content, compared to traditional SPs. Table 3.6 shows the main characteristics of these two SPs in accordance with EN 934-2, as indicated in the technical data sheet of these products provided by the suppliers. These characteristics are very similar for both SPs.

Table 3.6 – Main characteristics of the superplasticizers

Parameter	ViscoCrete® 3005	MasterGlenium® SKY 617
Density (g/cm <sup>3</sup> ) at (+23 ± 2°C)	1.05 ± 0.02	1.04 ± 0.02
pH (+23 ± 2°C)	4.0 ± 1.0	6.0 ± 1.0
Solid content (%)	25.5 ± 1.2	-
Chloride content (%)	<0.1	<0.1
Brookfield viscosity 20°C Sp00/100rpm	-	<50 cps.
Recommended consumption (% of cement weight)	<1.8 Current dosage: 0.4 to 0.9 SCC: 1.0 to 1.4 S4 or S5 slump flow concrete: 1.0 to 1.6	1.0-1.7

### 3.2.7 Viscosity modifying admixture

A viscosity modifying admixture (VMA) with the commercial designation CHRYSO®Aquabeton was used in some concrete compositions to obtain a concrete mixture with proper viscosity, which enables mixes with higher stability without segregation or bleeding phenomena. Table 3.7 shows the main characteristics of the VMA, indicated in the technical data sheet provided by the supplier.

Table 3.7 – Main characteristics of the VMA

Parameter	CHRYSO®Aquabeton
Brookfield viscosity 20°C in a solution at 1%	150 ± 20 MPa.s
pH in a solution at 1%	8.0 ± 2.0
Recommended consumption (% of cement weight)	0.6 a 1.0; <1.5

## 3.3 CHARACTERIZATION OF RECYCLED STEEL FIBERS

### 3.3.1 Geometric properties

The recycled steel fibers used in this research were supplied by Twincon company from Sheffield, UK and were recovered by a shredding process of post-consumed truck tires. These RSF generally have irregular shapes with various lengths and diameters (Figures 3.2a,b). The steel was separated from the rubber by an electromagnetic separator, and most of the RSF still contain some rubber particles attached on its surface due to the shredding process (Figure 3.2c). Table 3.8 presents the average values of the geometric properties of RSF determined by the supplier from a representative sample of approximately 60 000 fibers by using a photography system that captures images of fibers passing in front of a screen with a high-speed camera (Hu *et al.*, 2008a).

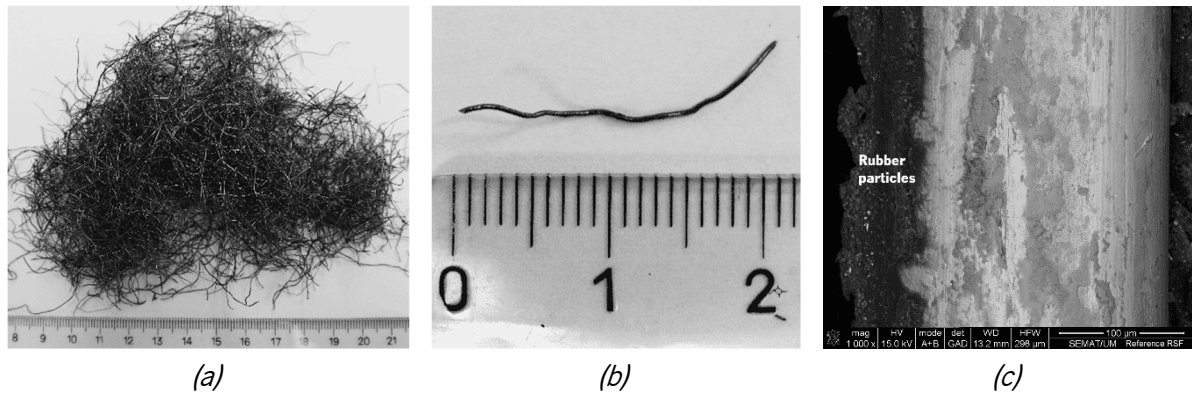


Figure 3.2 - Recycled steel fibers: (a) general view of multi RSF; (b) general view of the geometry of a single RSF; (c) SEM micrograph of the surface of a single reference RSF (Magnification: 1000x)

Table 3.8 – Average geometric properties of RSF obtained by the supplier

Properties	RSF
Diameter, $d_f$ (mm)	0.22
Length, $l_f$ (mm)	23
Aspect ratio, $\lambda$	100

A detailed characterization of the RSF employed in the experimental work was performed on a sample of 2000 fibers in order to evaluate by a statistical analysis, the variability of the geometric properties after the shredding process and without any further treatment. The following parameters were measured for each fiber:

- 1) *Fiber diameter*,  $d_f$  (mm): determined averaging three measures, namely at the two extremities of the fiber and at the mid-point, recorded manually with a micrometer (Figure 3.3a).
- 2) *Fiber length*,  $l_f$  (mm): defined as the distance between the outer ends of the fiber, in accordance with the CNR-DT 204/2006 specifications (Figure 3.3b).
- 3) *Developed length of the fiber*,  $l_d$  (mm): defined as the total “developed” length of the fiber along its axis, in accordance with the CNR-DT 204/2006 specifications (Figure 3.3b).
- 4) *Curvature index*,  $CI$  (%): representing a shape index, namely the fiber curvature, is determined by the following equation:

$$CI = \frac{l_d - l_f}{l_d} \quad (3.1)$$

- 5) *Aspect ratio*,  $\lambda$ : defined as the ratio between the fiber developed length,  $l_d$  and its diameter,  $d_f$ .

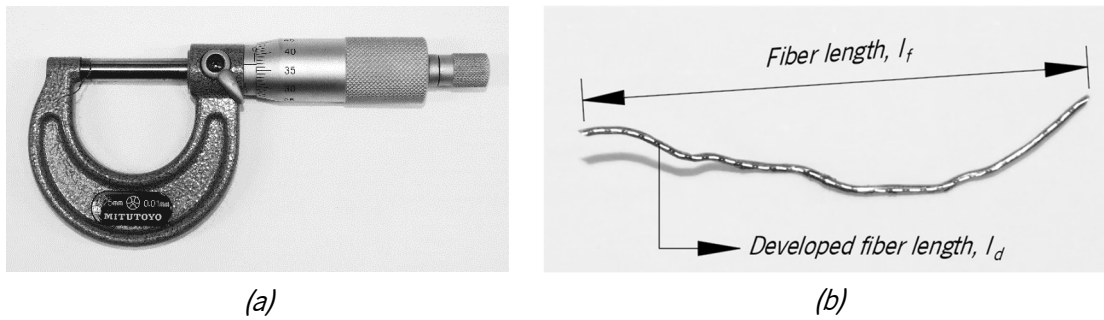


Figure 3.3 – (a) Micrometer to measure the fiber diameter;  
(b) Definitions of fiber length and developed fiber length

Figure 3.4 reports the frequency distribution of the measured fiber diameter. According to Figure 3.4, the diameters of RSF are characterized by a multimodal (two) distribution, in agreement with literature (Martinelli *et al.*, 2015; Caggiano *et al.*, 2017). This fact is probably due to the presence of tires from light and heavy vehicles disposed in the recycling plant (Martinelli *et al.*, 2015). More than one third (43%) of the sampled fibers exhibited a diameter within the range 0.16-0.22 mm.

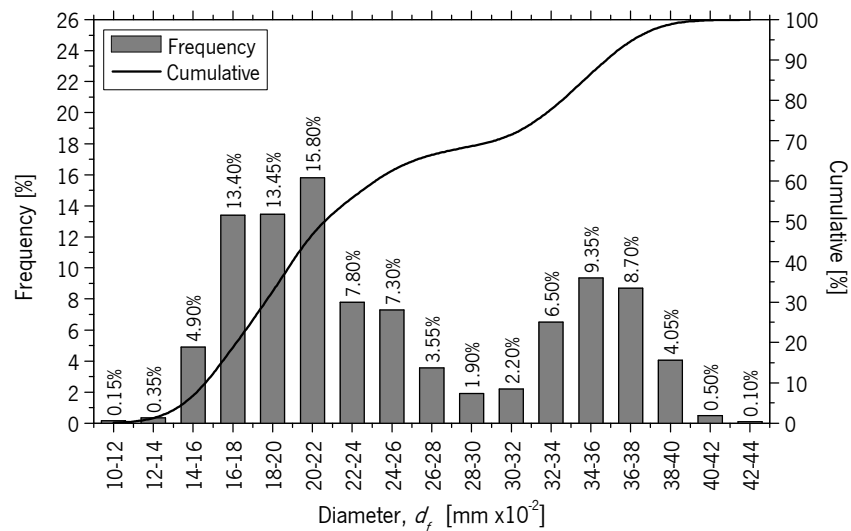


Figure 3.4 – Frequency distribution of fiber diameter ( $d_f$ ) measurements

Figure 3.5 reports the frequency distribution of measured fiber length, while Figure 3.6 presents a comparison between the frequency distribution of measured fiber length and developed fiber length.

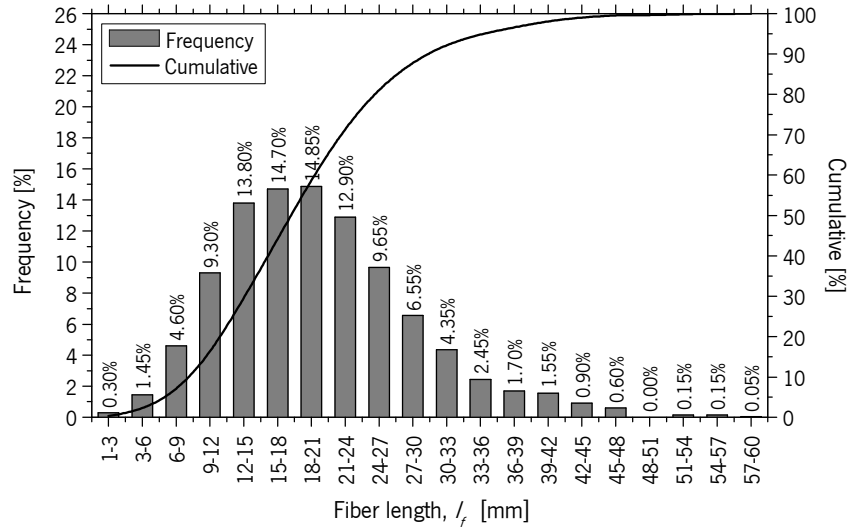


Figure 3.5 – Frequency distribution of fiber length ( $l_f$ ) measurements

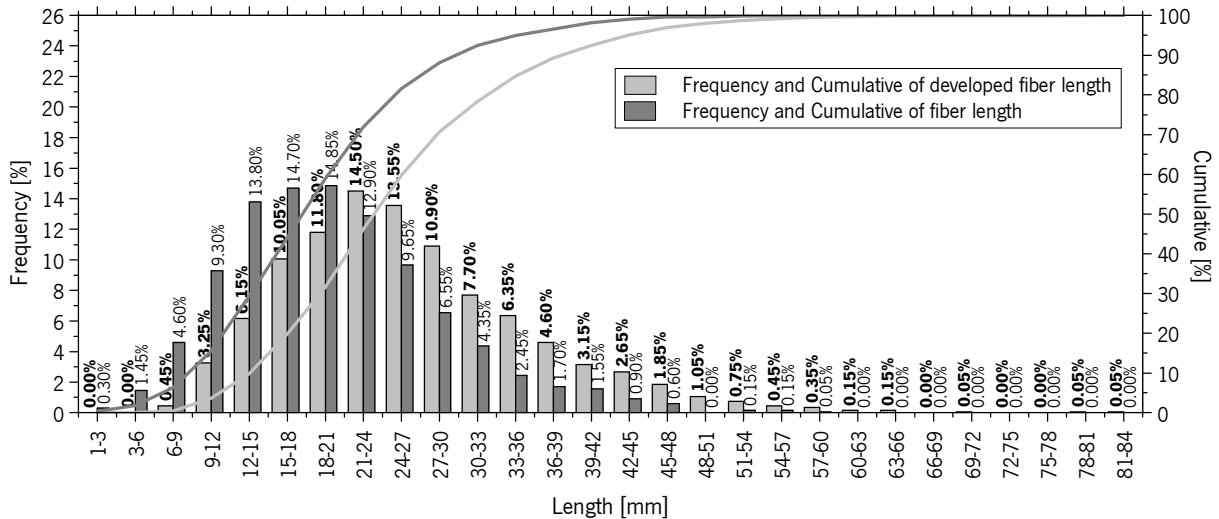
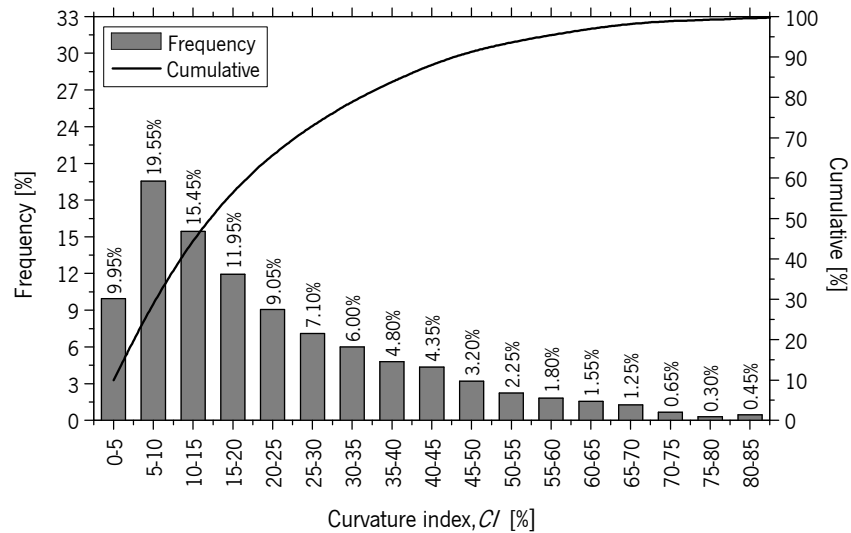


Figure 3.6 – Frequency distribution of fiber length ( $l_f$ ) and developed fiber length ( $l_d$ ) measurements

Figures 3.5 and 3.6 highlight unimodal distributions of fiber length and developed fiber length, which can be attributed to the shredding and cutting procedures performed within the recycling plant (Martinelli *et al.*, 2015). More than one half of the sampled fibers were within the range 15-30 mm (59% for fiber length and 61% for developed fiber length). As expected,  $l_d$  is higher than  $l_f$  due to the presence of curls and/or twists in the RSF geometry. In this regard, further considerations can be obtained by analysing the frequency distribution of the curvature index, showed in Figure 3.7.

Figure 3.7 – Frequency distribution of curvature index ( $CI$ )

The unimodal distribution observed in Figure 3.7 can be justified by the recycling procedures adopted for RSF production, as in the case of the fiber length (Caggiano *et al.*, 2017).  $CI$  values close to 0% corresponds to fairly straight fibers, whereas the higher the  $CI$ , the more curled and twisted the fiber. Values of  $CI$  lower than 20% were obtained in almost 57% of the sampled fibers (Figure 3.7), which means that the RSF can be considered relatively aligned (Caggiano *et al.*, 2017).

Figure 3.8 reports the frequency distribution of the aspect ratio, showing a unimodal distribution. More than one half of the sampled fibers (54%) exhibited a value within the range 70-130.

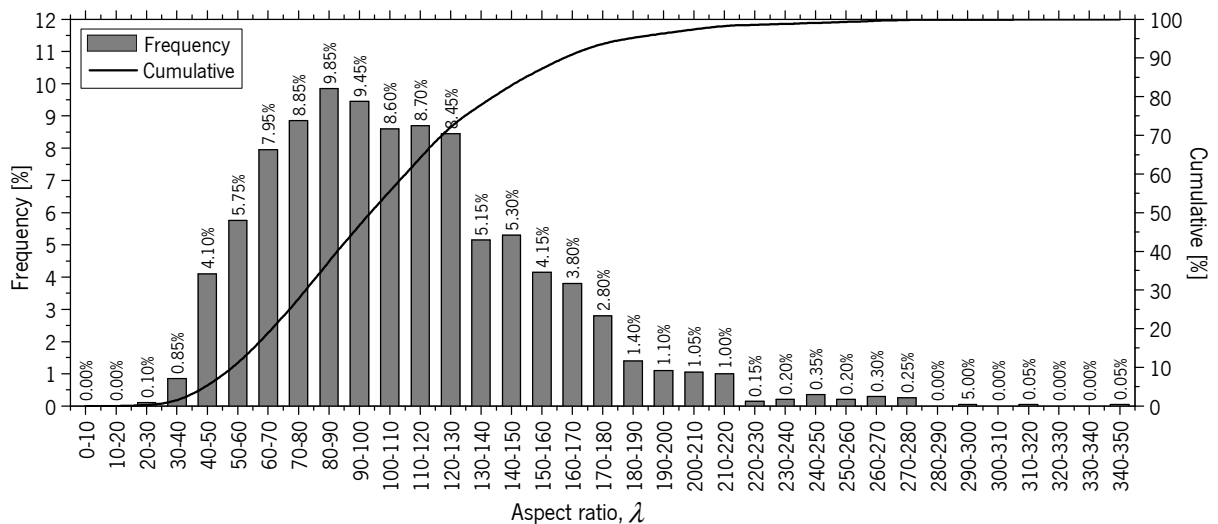
Figure 3.8 – Frequency distribution of the aspect ratio ( $\lambda$ )

Table 3.9 summarizes the main relevant statistical data obtained from the Figures 3.4 to 3.8, for the aforementioned parameters considered for the geometric characterization of RSF. This statistical data includes the following values: the minimum (Min), the maximum (Max), the average, the median, the modal value and range, the standard deviation (StD) and the coefficient of variation (CoV).

Table 3.9 – Geometric characterization of used RSF

Parameters	Min	Max	Average	Median	Mode (value)	Mode (range)	StD	CoV (%)
Diameter, $d_f$ (mm)	0.11	0.43	0.25	0.22	0.20	0.20-0.22	0.08	30.25
Fiber length, $l_f$ (mm)	1	60	20	19	21	18-21	8	41.63
Developed fiber length, $l_d$ (mm)	7	82	26	25	22	21-24	10	37.57
Curvature index, $CI$ (%)	0	93	22	17	12	5-10	17	78.47
Aspect ratio, $\lambda$	28	347	110	104	130	80-90	44	39.93

The average values obtained in terms of  $d_f$ ,  $l_f$  and  $\lambda$  are quite similar to the ones reported by the supplier (Table 3.8). The data sheet of these RSF provided by the supplier indicates a  $d_f$  in the range 0.17-0.35 mm, a  $l_f$  in the range 10-40 mm and a  $\lambda$  in the range 60-210 for 80% by weight of RSF. These ranges are within the corresponding ones indicated in Table 3.8 (for 100% by mass of sampled RSF).

Comparing the obtained results with those already reported in the literature for the geometric properties of other RSF, the obtained average value of  $d_f$  was quite similar to those reported by other authors who used the same procedure for its measurement: 0.258 mm (Aiello *et al.*, 2009), 0.24 mm (Centonze *et al.*, 2012), 0.27 mm (Martinelli *et al.*, 2015), 0.25 mm (Caggiano *et al.*, 2017) and 0.25 mm (Leone *et al.*, 2018). The average results obtained in terms of  $l_f$  are also comparable with some results reported in the literature: 26 mm (Aiello *et al.*, 2009), 31.4 mm (Centonze *et al.*, 2012) and 26.17 mm (Caggiano *et al.*, 2017). However, shorter fibers are also observed by other authors: 12 mm (Martinelli *et al.*, 2015) and 13.94 mm (Leone *et al.*, 2018) of average fiber length. Caggiano *et al.* (2017) obtained similar results in terms of  $CI$ . As in the case of fiber length, the average results obtained of  $\lambda$  are comparable with those obtained by some authors: 131 (Centonze *et al.*, 2012) and 109.1 (Caggiano *et al.*, 2017). However, significant differences are also observed comparing with the average values of  $\lambda$  obtained by other authors: 47 (Martinelli *et al.*, 2015) and 58 (Leone *et al.*, 2018). As expected, higher values of CoV were obtained for all the geometric parameters evaluated, as also reported in the literature (Caggiano *et al.*, 2017; Leone *et al.*, 2018).

### 3.3.2 Chemical composition

The chemical composition of RSF was determined by X-ray Fluorescence spectrometry (XRF) analysis using a Philips X'Unique II spectrometer controlled by the SuperQ software. These chemical analyzes were performed in the Laboratory of Chemical analyzes of TecMinho, located in the Department of Mechanical Engineering of the University of Minho. The basic principle of the XRF technique is based on the use of some excitation radiation to produce ionisation in the inner shells of the atoms presented in the sample due to photoelectric absorption (Marguí and Grieken, 2013).

Table 3.10 presents the chemical composition determined in reference RSF, as were received.

Table 3.10 - Chemical composition for reference RSF determined by XRF analysis

Chemical elements	Concentration (%)	Absolute Error (%)
C	0.77	-
Al	0.23	0.02
Ca	0.07	0.01
Cr	0.02	0.00
Cu	5.41	0.08
Fe	87.40	0.20
Mn	0.50	0.01
P	0.05	0.00
S	1.57	0.03
Si	0.31	0.03
Zn	3.53	0.02

The concentrations of Fe, Mn and Cr are quite similar with those reported by Micelli *et al.* (2014) showed in Table 2.3. A carbon concentration of 0.77% is also in agreement with the composition of steel fibers reported in the literature (Micelli *et al.*, 2014). The presence of high value of Cu and Zn may be associated with the brass coating of the surface of the original steel, aiding the steel to stick to the tire rubber (Micelli *et al.*, 2014).

Figure 3.2c show SEM observations of the surface configuration of RSF taken in the Laboratory for Materials Characterization Services of the University of Minho (SEMAT/UM). A FEI Nova 200 Field Emission Gun Scanning Electron Microscope (FEG-SEM) equipped with EDAX, Energy Dispersive X-Ray Spectroscopy (EDS) was used, which integrates a system for microanalysis by X-ray and diffraction patterns analysis of backscattered electrons. The SEM micrograph of Figure 3.2c evidences the atomic contrast by backscattered electrons of chemical elements presented in the RSF surface. A chemical



analysis (SEM-EDS) was also carried out to identify the main chemical elements presented in some zones of the RSF surface, indicated in Figure 3.9. The chemical composition obtained in these localized zones are presented in Table 3.11.

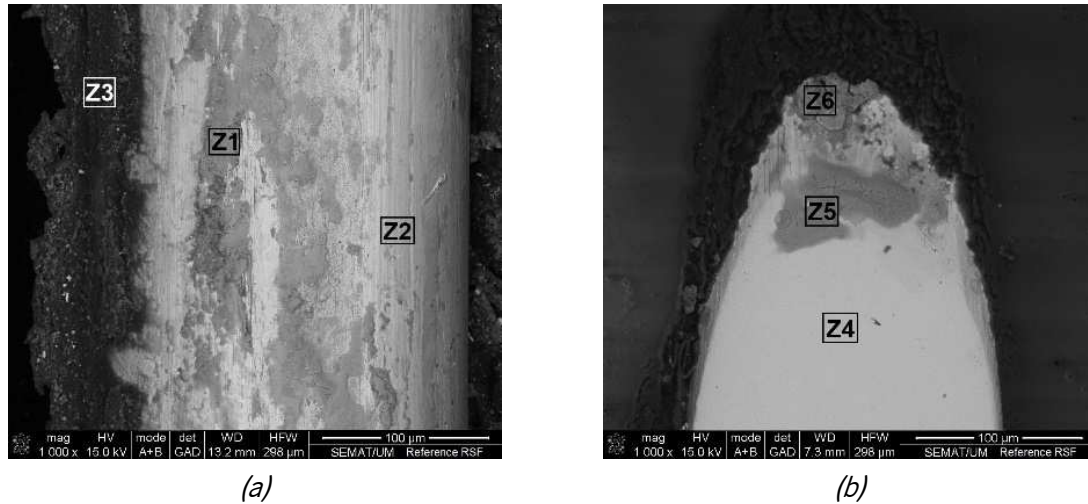


Figure 3.9 –Localization of the zones for chemical analysis by SEM-EDS in a single reference RSF:  
(a) Surface; (b) Transversal section

Table 3.11 – Chemical elements identified in the surface of reference RSF

Zone	Chemical elements (atomic percentage %)				
	C	Fe	O	Cu	Zn
Z1	44.64	25.14	21.11	3.95	2.41
Z2	38.45	41.82	7.19	3.94	2.12
Z3	80.55	1.19	15.27	0.36	0.95
Z4	18.61	81.39	0.00	-	-
Z5	21.77	25.06	46.42	1.00	1.10
Z6	34.86	12.51	52.07	-	0.15

The significant carbon content detected in the RSF surface is related to the presence of rubber residues. A significant difference is observed in the carbon content obtained by SEM-EDS analysis (Table 3.11) and by XRF analysis (Table 3.10). This fact may be justified by the high penetrating power of X-rays used by XRF analyzer for the elemental analysis underneath the surface of the samples (Komatani *et al.*, 2013). Furthermore, SEM-EDS is a semi-quantitative technique and therefore, it is more accurate to use a quantitative technique for the determination of chemical composition of RSF, as the XRF technique. It is also remarkable the presence of Cu and Zn elements, as identified by XRF analysis (Table 3.10) and probably associated with the brass coating.

### **3.3.3 Mechanical properties**

The mechanical behavior of RSF was characterized in terms of tensile strength by performing direct tensile tests and in terms of Young's modulus and hardness determined by means of nano-indentation tests.

As already mentioned in Section 3.2.1, the used RSF contain small rubber particles attached to their surface (Figure 3.2c). In order to assess the influence of this attached rubber in the mechanical performance of RSF as concrete reinforcement, two distinct methods were used to eliminate the small percentage of rubber attached to the fiber surface: pre-treatment of the fibers at high temperatures; manual polishing of the fiber surface with sandpaper. The influence of these pre-treatment methods in the micro-mechanical properties of RSF was evaluated by employing the nano-indentation technique to measure the mechanical properties of RSF, and by means of monotonic fiber pull-out tests performed to assess the RSF-concrete bond behavior.

#### **3.3.3.1 Tensile strength**

The tensile strength of RSF was assessed by means of direct tensile tests carried out under displacement control by an external LVDT installed on the actuator and adopting a displacement rate of 3  $\mu\text{m/s}$ . Prior to testing, two aluminum plates were attached to each end of the RSF (Figure 3.10a) in order to avoid undesired rupture or slippage of the fiber at the gripping system of the testing machine. Furthermore, this also ensures that the tensile force is applied axially minimizing any bending. Since the expected tensile loads were relatively low, a high precision load cell of 10 kN capacity was adopted, installed between the servo-actuator and the loaded grip (Figure 3.10b). It was necessary to select RSF with more than 50 mm in length, which is not representative of the average length (20 mm), to account the anchorage length in the grips (Figures 3.10c,d). A valid tensile test was only considered when the fiber fracture occurred out of the grips (Figure 3.10e).

Figure 3.11 plots the tensile stress-displacement curves of five valid tensile tests. Due to the reduced frequency of RSF with a fiber length higher than 50 mm (Figure 3.5), a limited number of tensile tests were conducted.

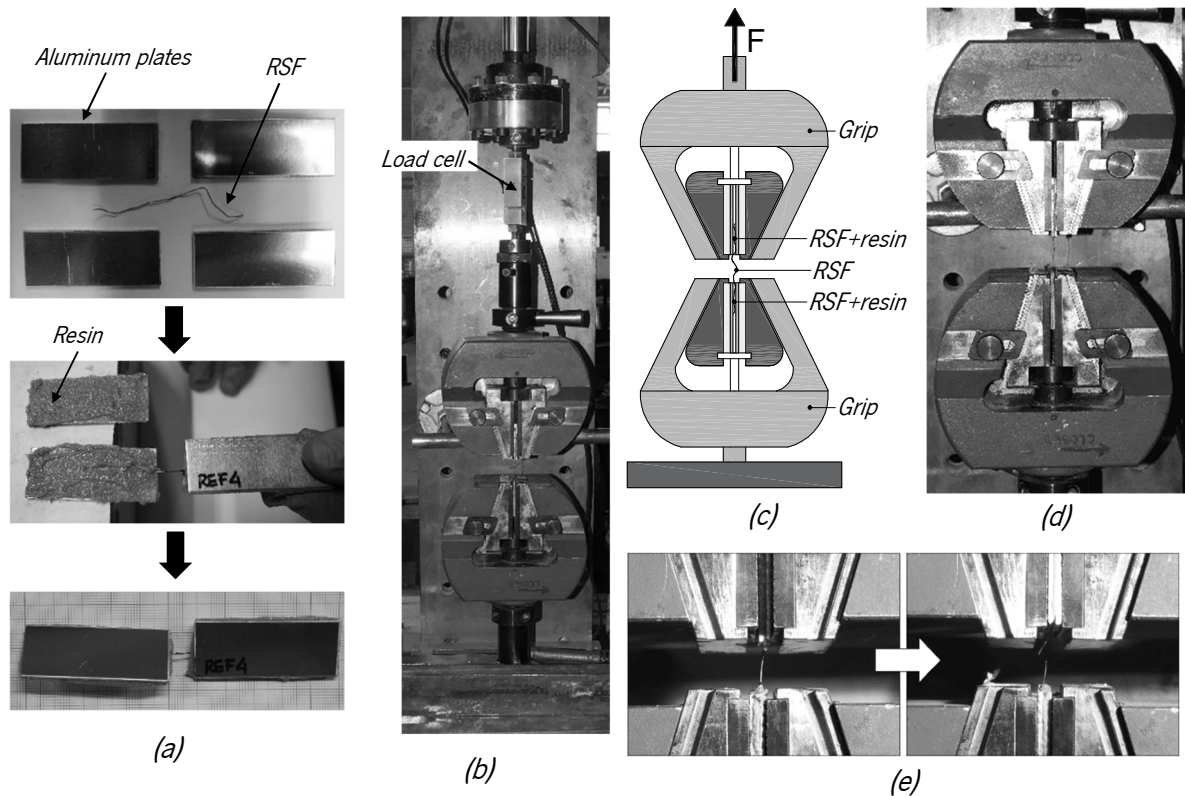


Figure 3.10 – (a) RSF preparation for tensile tests (b) General view of the test setup for RSF tensile tests; (c) and (d) Detail of the RSF fixation between grips for tensile test; (e) RSF failure mode of a valid tensile test

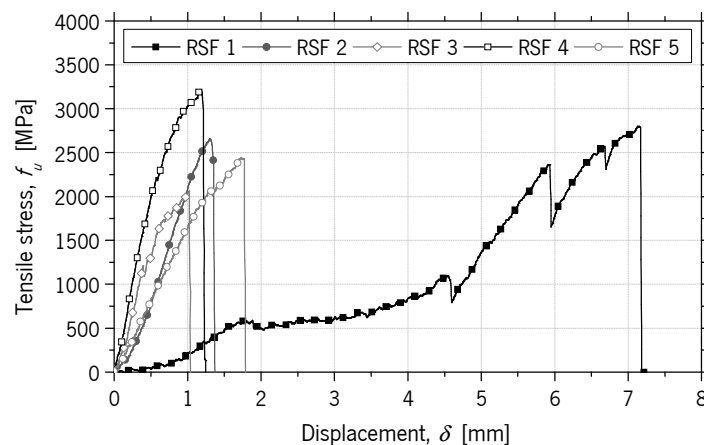


Figure 3.11 – Tensile stress *versus* displacement for the RSF submitted to direct tensile test

According to Figure 3.11, a similar  $f_u - \delta$  behavior was observed for all tested RSF, except RSF 1, due to the higher curvature and fiber length of the fiber between grips of this fiber. As reported in the literature (Section 2.2.3), an initial branch characterized by low level of stress was also observed corresponding to fiber straightening, followed by a “pure tension” stage. Some load drops were recorded in the RSF 1, which would have been caused by fiber slip.

The average geometric properties and tensile strength,  $f_u$ , obtained for the tested fibers, and the correspondent standard deviation (StD) and coefficient of variation (*CoV*) are given in Table 3.12.

Table 3.12 – Geometric properties and tensile strength of tested RSF

	$d_f$ (mm)	$l_f$ (mm)	$l_d$ (mm)	$CI$ (%)	$\lambda$	$l_{df}$ out of the grips (mm)	$f_u$ (MPa)
Average	0.35	61	73	15	209	14	2647.94
StD	0.01	7	13	9	40	8	423.05
<i>CoV</i> (%)	2.16	11.49	17.81	61.59	19.03	58.25	15.98

$l_{df}$  - Free development of fiber length (out of the grips)

The average of  $f_u$  obtained in the RSF tensile tests was slightly higher (3%) than the announced tensile strength value indicated in the technical data sheet provided by the RSF supplier. The results obtained are similar to the  $f_u$  values reported by other authors for RSF (Table 2.4). Comparing with the  $f_u$  values of ISF available in the literature (Table 2.4), the RSF showed higher  $f_u$  values.

### 3.3.3.2 Pre-treatment of RSF to remove rubber debris attached to fiber surface

In order to remove great part of the rubber attached to the RSF surface, two different methods were considered: pre-treatment of fibers at high temperatures, burning the attached rubber of lower melting point; manual polishing of the fiber surface with #180 SiC grinding paper (time consuming method, industrially impracticable).

The range of decomposition temperatures of the rubber waste was settled from thermogravimetric analysis (TGA). Using this technique, the mass loss of RSF *versus* temperature was monitored up to 700°C at a constant heating rate of 10°C/min. Figure 3.12 shows the TGA curve of RSF.

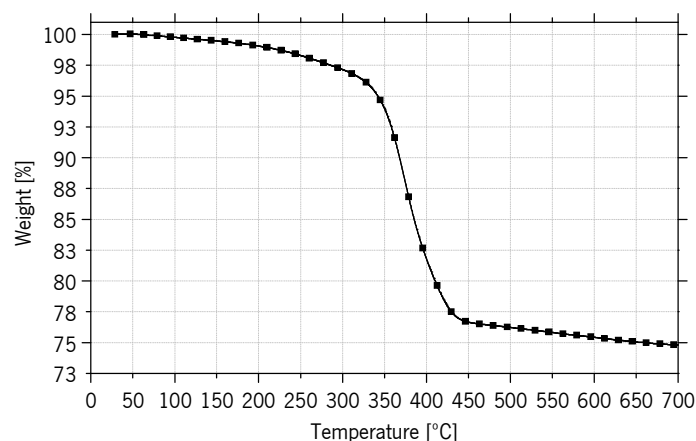


Figure 3.12 – TGA analysis of RSF up to 700°C

The major mass loss occurred between 300°C and 450°C. Considering this preliminary result, RSF were subjected to the following temperatures for 1 hour: 300°C, 350°C, 400°C and 450°C. Figure 3.13 shows the pictures taken with a digital microscope after each of these heat treatments.

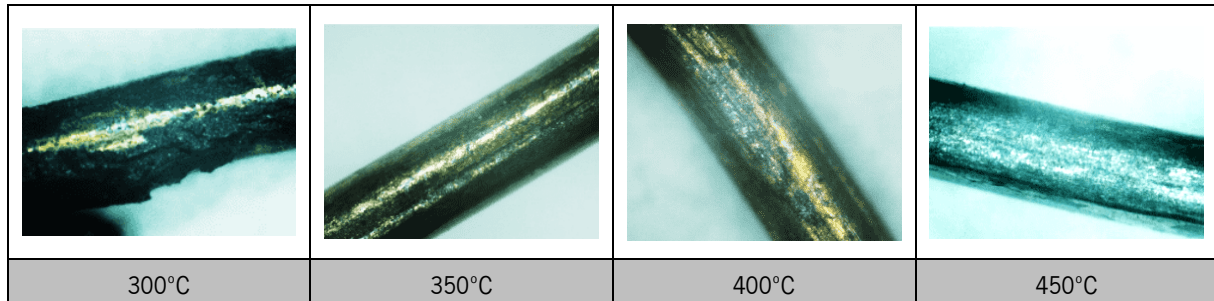


Figure 3.13 – Images of the RSF (magnification: 400x) after firing for 1 hour at the selected temperatures

From visual inspection and weight variation analysis, it was found that heating at 10°C/min up to 350°C followed by 60 minutes at this temperature was effective to remove the rubber waste from the RSF surface. The temperature of 300°C was not effective since part of the rubber still remained on RSF surface (Figure 3.13). For this reason and considering also the economic point of view, the temperature of 350°C was defined for the heat pre-treatment of RSF. Figure 3.14 shows SEM micrographs of the surface configuration of RSF previously submitted to 350°C. This high temperature caused the formation of microcracks in the zones of RSF surface where the rubber particles were attached, as observed in Figure 3.14.

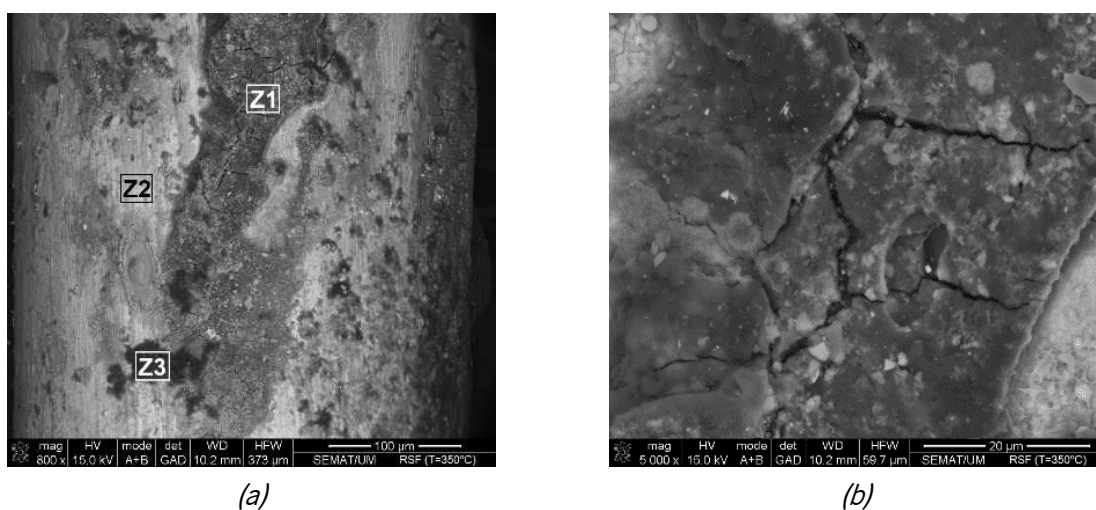


Figure 3.14 - SEM micrographs of the surface of a single RSF submitted to 350°C  
Magnification: (a) 1000x; (b) 5000x

Since Figure 3.14a also evidences the atomic contrast by backscattered electrons of chemical elements presented in the RSF surface, a chemical analysis (SEM-EDS) was carried out to identify the main chemical elements presented in the zones indicated in Figure 3.14a. The chemical composition obtained in these localized zones is presented in Table 3.13.

Table 3.13 – Chemical elements identified in the surface of RSF submitted to 350°C

Zone	Chemical elements (atomic percentage %)				
	C	Fe	O	Cu	Zn
Z1	65.08	3.49	22.64	0.89	2.43
Z2	28.47	28.64	21.69	6.38	4.24
Z3	80.87	2.79	12.49	-	-

According to the results showed in Table 3.13, a significant carbon content was detected in some localized zones of the RSF surface submitted to 350°C, from where rubber particles were removed. Apparently, this high temperature did not affect the presence of Cu and Zn content on the RSF surface.

Polishing of RSF was the most efficient method for removing the rubber particles from RSF surface, leading to the most uniform fiber surface, as shown in the SEM micrograph of Figure 3.15.

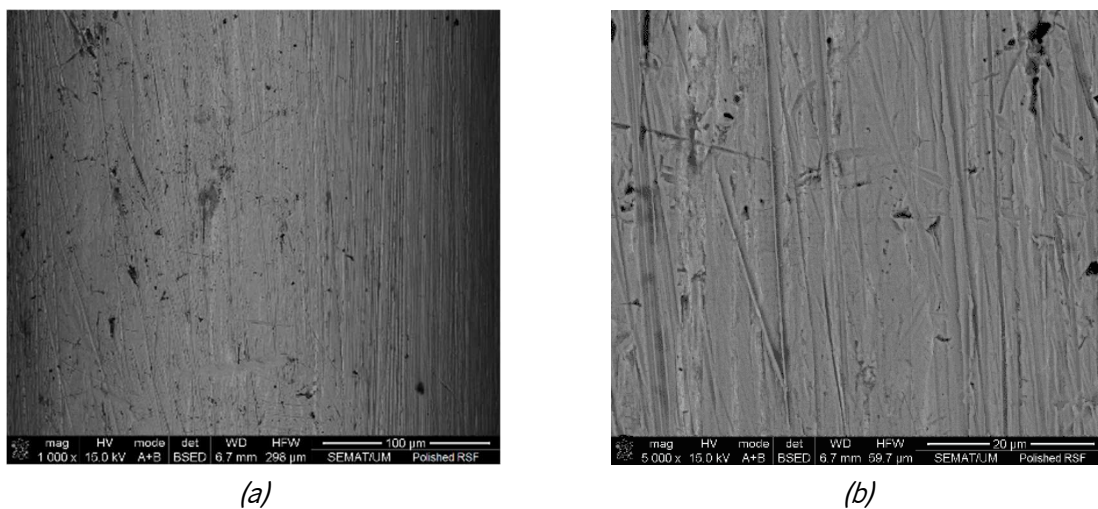


Figure 3.15 - SEM micrographs of the surface of a single polished RSF  
Magnification: (a) 1000x; (b) 5000x

The effectiveness of manual polishing as cleaning process of RSF was proved by analyzing the chemical composition of polished RSF determined by XRF analysis, with comparison to reference RSF. Table 3.14 shows the results obtained in this chemical analysis. Apart from the reduction of the Cu and Zn amounts,

eventually removed during the cleaning process, the atomic content of the other chemical elements remained essentially the same (Tables 3.9 and 3.13). Thus, the manual polishing was able to remove the brass coating as well as the rubber residues that cover the RSF.

Table 3.14 - Chemical composition for polished RSF determined by XRF analysis

Chemical elements	Concentration (%)	Absolute Error (%)
C	0.85	-
Al	0.43	0.04
Ca	-	-
Cr	-	-
Cu	2.77	0.06
Fe	93.30	0.20
Mn	0.56	0.02
P	0.04	0.01
S	0.38	0.02
Si	0.33	0.03
Zn	1.41	0.02

In sum, the following three classes of RSF were considered in the experimental program: *Class 1* – Reference RSF, without pretreatment, as were received; *Class 2* – RSF pre-treated at 350°C; *Class 3* – Polished RSF.

### 3.3.3.3 Young's modulus and Hardness

The Young's modulus and hardness of the three classes of RSF were determined by means of nano-indentation tests carried out in the Scientific and Technological Research Assistance Centre (CACTI) of the University of Vigo. For comparison purposes, the same hooked-ends ISF adopted by Frazão *et al.* (2016) to study their corrosion susceptibility were used. These fibers, herein designated by "ISF type 1", had 60 mm length ( $l_f$ ), 0.90 mm diameter ( $d_f$ ), an aspect ratio ( $\lambda$ ) of 67, 5.1 mg/mm and a tensile yield stress ( $f_u$ ) of 1000 MPa, according to the catalog of steel fibers Dramix® from Bekaert company (Figure 3.16).

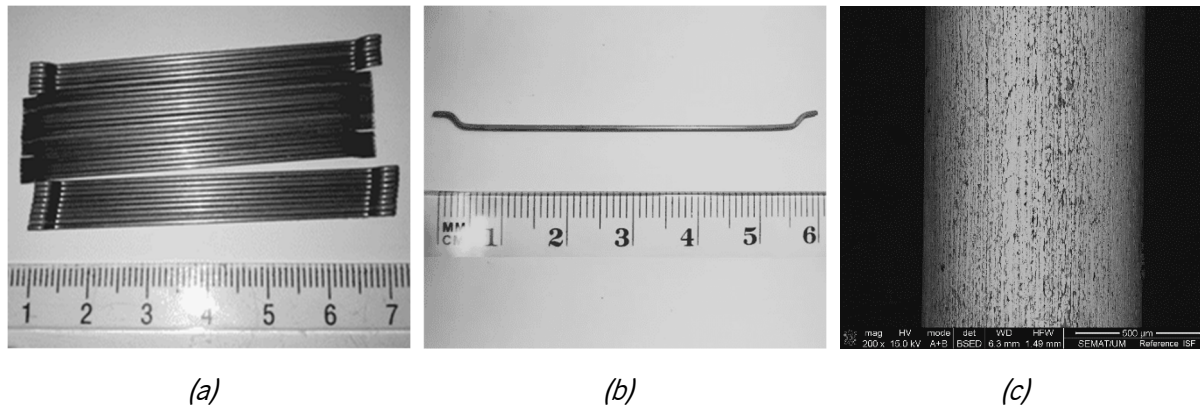


Figure 3.16 – ISF type 1: general view of (a) multi fibers and (b) single ISF; (c) SEM micrograph of the surface of a single reference ISF (Magnification: 200x)

According to the technical manual elaborated by Maccaferri company for the use of steel fibers as concrete reinforcement, these ISF of low carbon percentage have the chemical composition showed in Table 3.15.

Table 3.15 – Chemical composition of ISF according to Italian standard UNI 11037:2003 (Maccaferri, 2008)

Type of steel	C	Mn	Si	S <sub>max</sub>	P <sub>max</sub>
Low C content	≤ 0.20	≤ 0.60	≤ 0.30	0.045	0.045

The following two classes of ISF were considered for nano-indentation tests: *Class 1* – Reference ISF, as were received; *Class 2* – ISF pre-treated at 350°C.

The hardness test determines the materials resistance to the constant penetration of a non-deformable indenter with a shape of a ball, pyramid, or cone (Broitman, 2017). In metals, the hardness is related to the plastic deformation of the surface or the penetration depth of the indenter, under a given load, and within a specific period of time (Broitman, 2017). Hardness has also a close relation to other mechanical properties, such as strength, ductility and fatigue resistance (Broitman, 2017).

A standard Berkovich nanoindenter was forced into a particular site of the sample (steel fibers) by applying an increasing load. A new continuous stiffness measurement (CSM) technique on an MTS Nano Indenter XP system was employed for this analysis. In this technique the mechanical properties are obtained by applying a small oscillating force to the indenter and measuring the resulting amplitude and phase shift of the oscillations. The indenter was forced to penetrate into the surface to a depth of 1000 nm, low enough to avoid any interference. The Nano Indenter XP system records stiffness data along with load



and displacement data dynamically, allowing Young's modulus and hardness of steel fibers to be automatically calculated at every data point acquired during the indentation procedure.

This technique seems to be the most convenient for the studied fibers, which have relatively small size to be tested by other traditional hardness tests. The nano-indentation methodology guarantees a minimum deformation in the sample, so a reliable hardness value representative of the fiber can be determined. In addition, the influence of the high-angle grain boundaries of the sample is not detected at the recorded values, which means that the true matrix hardness is measured (Ohmura *et al.*, 2003).

A recent study of Baldenebro-Lopez *et al.* (2015) showed that the Young's modulus and hardness measured by nano-indentation are influenced by the precise size of the material samples, in particular when comparing fibers and larger specimens. The authors measured higher values of these properties in single fibers than in samples of bulk materials. Therefore, as most of published works include data obtained from bulk samples, the comparison with the results obtained in this study must be cautious (Baldenebro-Lopez *et al.*, 2015).

Various RSF and ISF have been multiple indented (Table 3.16) to guarantee an appropriate reproducibility and reliability. Figures 3.17 and 3.18 show the load-displacement curves obtained for tested fibers.

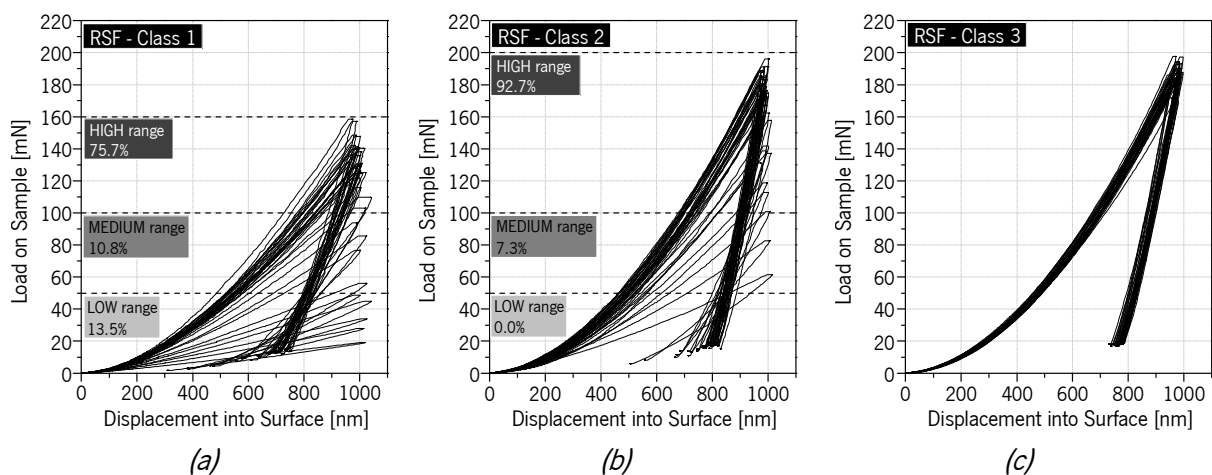


Figure 3.17 – Load-Displacement curves obtained in nano-indentation tests of RSF:  
(a) Class 1 (REF); (b) Class 2 (350°C); (c) Class 3 (polished)

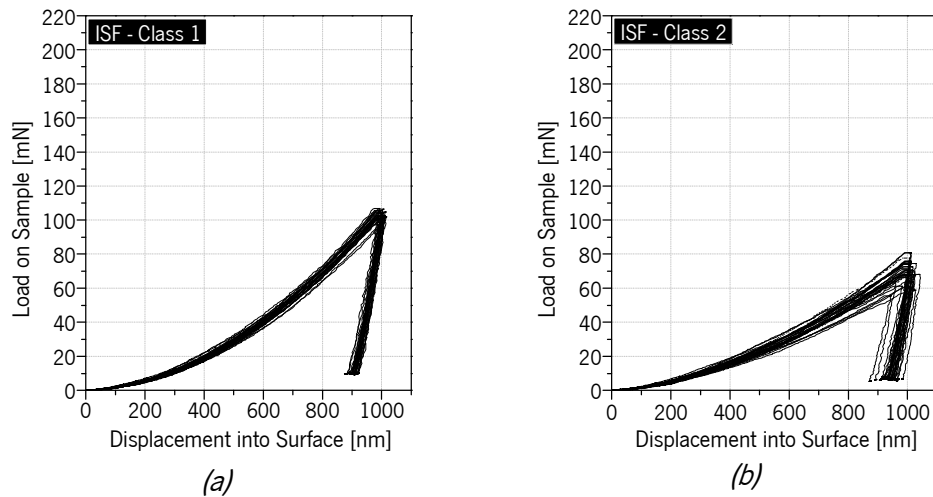


Figure 3.18 – Load-displacement curves obtained in nano-indentation tests of ISF:  
 (a) Class 1 (reference) (b) Class 2 (350°C)

In case of class 1 RSF (reference), three different load ranges were discernible, the HIGH range (100-160 mN), the MEDIUM range (50-100 mN) and the LOW range (0-50 mN), with 75.7%, 10.8% and 13.5% of the total number of indentations in each range, respectively. For class 2 RSF (pre-heated at 350°C), no indentations were recorded within the LOW load range, indicating to have occurred a homogenization of the steel structure due to temperature influence. In fact, 92.7% of the indentations are within the HIGH load range. The load-displacement curves corresponding to class 3 RSF (polished) lie in the same load range, as well as ISF, suggesting the existence of a more homogeneous matrix in comparison to the RSF of class 1 and 2.

A summary of the average values of Young's Modulus and hardness is presented in Table 3.16. According to Oliver and Pharr (2004) and Broitman (2017), the basic principles of the method developed to measure the hardness and elastic modulus of a material from indentation load-displacement data are presented in Appendix A. To calculate the average values of Young's Modulus and hardness, an indentation length range was selected for each fiber class, where the values were more stable (200-900 nm) in order to avoid influence of possible fiber surface heterogeneity.

Table 3.16 – Average values (*and standard deviation*) of Young's modulus and hardness obtained by nano-indentation tests

	<b>Fibers</b>	<b>Young's modulus (GPa)</b>	<b>Hardness (GPa)</b>	<b>Number of indentations</b>
RSF	Class 1 (REF)	131.967 (47.916)	6.407 (1.096)	37
	Class 2 (350°C)	193.828 (46.773)	7.262 (0.954)	41
	Class 3 (Polished)	200.860 (9.026)	9.159 (0.373)	35
ISF	Class 1 (REF)	212.766 (12.223)	4.098 (0.197)	36
	Class 2 (350°C)	192.943 (17.362)	2.937 (0.238)	30

The RSF have a carbon content around 0.70%, according to its chemical composition determined by XRF analysis (Table 3.10). Although the precise microstructure of the RSF could not be yet identified, the hardness measured (6.4 GPa for RSF class 1) agrees to the existence of martensitic and/or bainitic structure, according to the literature (Krauss, 2015).

The lower hardness of ISF than that of RSF was expected due to the lower carbon content of ISF (Table 3.16). The carbon content is a well-known factor that influences the hardness of the martensite. The obtained hardness values of ISF agree with the existence of a low-carbon (0.20%) martensitic structure (Krauss, 1999).

Different trends were found when RSF and ISF were pre-treated at 350°C. In fact, while the hardness increased in RSF, the opposite occurred in ISF. For the RSF, with a high carbon content, a significant amount of retained austenite is expected in the supplied quenched state (Krauss, 1999). Actually, for an AISI 1070 steel, the percentage of retained austenite is about 10% (Krauss, 2015). A possible reason for the increase of hardness in class 2 RSF can be related to the transformation of the retained austenite during the heat treatment used to remove the superficial rubber. The treatment at 350°C eventually assisted the transformation of this retained austenite of the RSF (austenite that had not been transformed to martensite upon quenching), at least partially, into lower bainite (Brooks, 1999), whose refinement of the microstructure leads to an increase in their properties (Schade *et al.*, 2016). This increment of hardness may have a negative effect on ductility since it becomes a more brittle material.

On the other hand, the heat treatment reduced the hardness of ISF. For such a low carbon steel, no retained austenite is expected (Krauss, 1999), and then, the obtained hardness changes suggest a tempering of the existing martensite, which led to a softer tempered martensite (Ohmura *et al.*, 2003; Brooks, 1999; Callister and Rethwisch, 2007). In comparison to RSF of class 1 and 2 (Figures 3.17a,b), the ISF had a more homogeneous microstructure, with a single distinguished phase (Figures 3.18a,b). Accordingly, a greater variability were found among the data obtained for the RSF of class 1 and 2 in comparison to the RSF of class 3 and ISF, as compiled in Table 3.16.

According to Figure 3.17c and Table 3.16, the treatment by manual polishing (RSF of class 3) caused a homogenization of the RSF microstructure and increased the hardness of RSF. This increase in hardness can be explained by the transformation of the retained austenite into martensite due to the strain induced by plastic deformation that occurs during the polishing process (referenced in the literature by “strain-induced martensitic transformation” (Mertinger *et al.*, 2008).

Concerning the Young’s Modulus values, they are in the same range as those reported in the literature (Chen *et al.*, 2016), except for RSF of class 1. As also reported by ASM International (2002) in the *Atlas*

of *Stress-Strain Curves*, the Young's Modulus did not significantly vary with temperature. The unexpected low value for the untreated RSF (132 GPa) can be just a consequence of the great variability observed in the indentations performed to this material (Figure 3.17a). The large number of indentations in the low load range recorded for the as-received RSF, in comparison to the other fibers, has an influence in the obtained average Young's Modulus value. A great variability was also observed in the Young's Modulus values obtained for RSF of class 2 since the high temperatures were not fully effective in homogenizing the steel structure of all the fibers. The data discussed in this section allow to conclude that the RSF of class 1 and 2 are particularly heterogeneous from a microstructural point of view.

### 3.3.3.4 Fiber pull-out behavior

In steel fiber reinforced composites materials, fiber and matrix are bonded together through a weak interface, and the study of this interfacial behavior is important for understanding the mechanical behavior of such composites (Cunha *et al.*, 2010). In this sense, monotonic RSF pull-out tests were carried out with the aim of studying the adhesive bond between single RSF and concrete.

The materials used for concrete production, as well as the pull-out specimen's dimensions and test setup, were identical to the ones used in previous research works carried out to access the fiber pull-out bond-slip behavior on a SFRSCC medium (Cunha, 2010; Abrishambaf, 2015; Frazão *et al.*, 2016).

A fluid concrete mixture (close to a self-compacting concrete) was produced with CEM I 42.5R (CEM), limestone filler (LF), water (W), superplasticizer ViscoCrete 3005 (SP1), fine and coarse river sand (FS and CS), crushed granite (CG), and the VMA CHRYSO®Aquabeton. The concrete composition is presented in Table 3.17. The mix design was based on the packing density optimization method suggested in Barros *et al.* (2007). The fresh properties of concrete, namely the slump-flow was determined according to EN 12350-8:2010. An average slump-flow of 521 mm was achieved without significant segregation. The composition of this fluid concrete with low maximum aggregate size was in order to have similar characteristics of those used in RSFRC production (Section 3.4.1).

Table 3.17 – Mix design for 1 m<sup>3</sup> of concrete

CEM (kg)	LF (kg)	W (L)	SP1 (L)	FS (kg)	CS (kg)	CG (kg)	VMA (kg)	W/C
380.6	326	158	8.6	368	568	510	0.3	0.42

The compressive strength and the elastic modulus of the hardened concrete were determined at 28 days in four cylinders of 150 mm diameter and 300 mm height according to the EN 12390-3:2011 and EN

12390-13: 2013, respectively. Details about the test procedures will be presented in Section 3.5.2. The average compressive strength ( $f_{cm}$ ) was 31.5 MPa with a coefficient of variation (CoV) of 1.62% and the average Young's modulus ( $E_{cm}$ ) was 23.6 GPa, with a CoV of 1.71%. These compressive results were abnormally low considering the concrete composition presented in Table 3.17. In fact, the density of concrete determined in hardened state, was 9.5% lower than expected (2098.5 kg/m<sup>3</sup>), which means that the compactness of the concrete was reduced, probably due to poor compaction or unintentional air entrainment into concrete.

For the pull-out tests a single RSF was centrally embedded on a cylindrical concrete specimen with 88 mm diameter and 80 mm height. The RSF was positioned as perpendicular as possible, with an embedded length of 20 mm, as recommended by other authors (Aiello *et al.*, 2009; Caggiano *et al.*, 2015) (Figure 3.19a). Prior to testing, two aluminum plates were attached to the free loaded end of the RSF with epoxy (Figure 3.19b) in order to avoid undesired rupture or slippage of the fiber at the gripping system of the testing machine.

The pull-out test setup was defined according to Cunha (2010) and Abrishambaf (2015a) (Figures 3.19c,e). Monotonic single fiber pull-out tests were performed until a sufficiently high level of slip ( $\delta > 6$  mm) occurred in the pull-out load-slip response ( $F - \delta$ ). Since the maximum pull-out loads were relatively low, a high precision load cell of 10 kN capacity was adopted. This load cell was installed between the servo-actuator and the grip (Figure 3.19d). The single pull-out specimen was accommodated in a steel frame to fix it (Figure 3.19d), which was designed to prevent the confinement of the fiber due to friction forces developed in the steel reaction plate (Cunha, 2010). This frame incorporated one bottom steel plate bolted to the testing frame and a steel ring mounted on the upper face of the specimen and fixed to the bottom steel plate using three screws disposed around the specimen forming an angle of 120°. The test control procedure guaranteed a stable response during the debonding process of the fiber. To measure the fiber's slip during the pull-out procedure, three Linear Variable Differential Transformers (LVDTs with linear stroke +/- 5 mm) were installed on the back side of the grip to exclude measuring deformation of the test rig, by means of aluminum cubic supports (Figures 3.19e,f). A VMS-004 20-400x USB Microscope with a 2 Mega Pixels camera was used to verify if the fiber slip at the grip was null during the pull-out process (Figure 3.19d). Figure 3.20 shows some images captured during the debonding process of one RSF that confirms a null slip between a "red mark", that represents the lower limit of the fiber length fixed to the grip, and the fiber length embedded into concrete.

Finally, the test was controlled by an LVDT installed on the actuator and adopting a displacement rate of  $3 \mu\text{m/s}$  up to the slip of 3 mm, followed by  $10 \mu\text{m/s}$  until the end of the test.

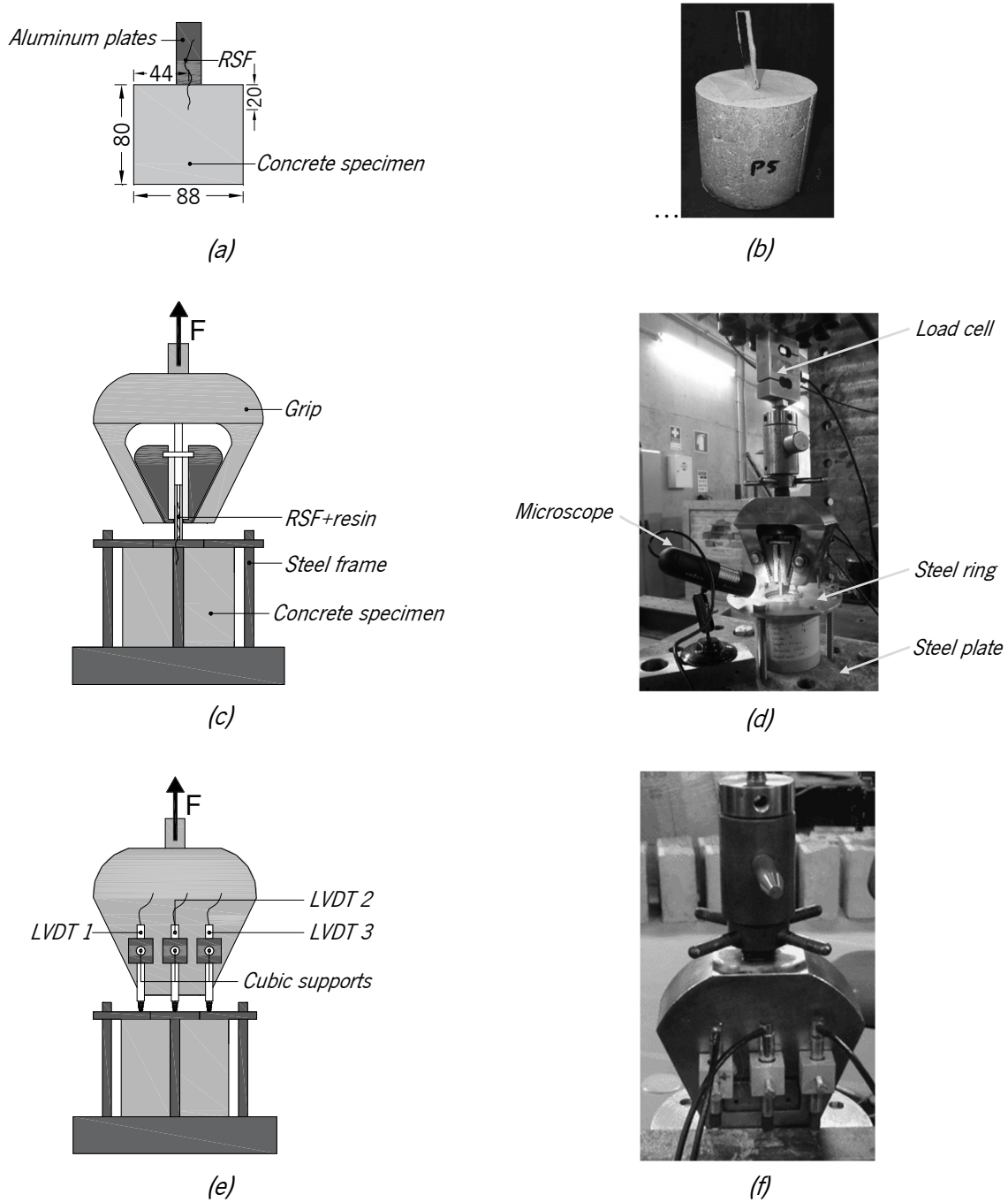


Figure 3.19 – Test setup for fiber pull-out tests: (a) (b) Preparation of fiber pull-out concrete specimens; (c) (d) Specimen front view; (e) (f) Specimen back view

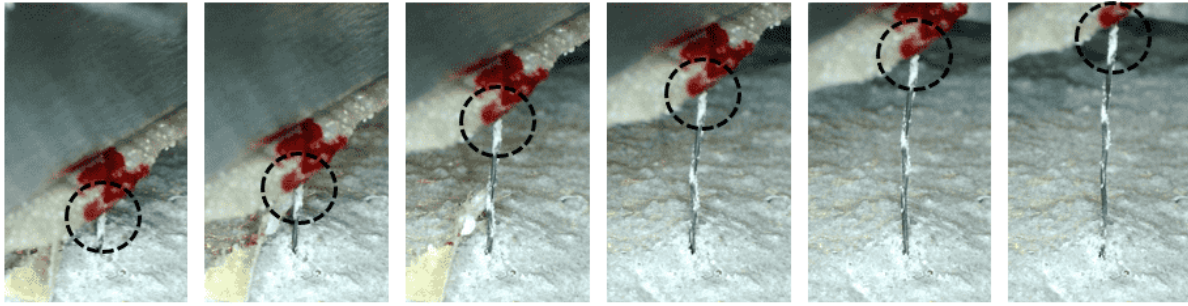


Figure 3.20 – Observation of the debonding process of RSF from concrete with an USB microscope

A total of 47 fiber pull-out tests (18 of Class 1, 15 of Class 2 and 14 of Class 3 RSF) were performed using RSF selected with average developed length of 57 mm (approximately 3 times the embedded length) and aspect ratio of 162 (not representative of the average length and aspect ratio, 26 mm and 110, respectively (Table 3.8)). Figure 3.21 includes the envelope and the average Pull-out load vs End slip curves for the three tested classes of RSF. The slip was determined by averaging the readouts recorded in the three LVDTs installed on the grip (Figure 3.19f).

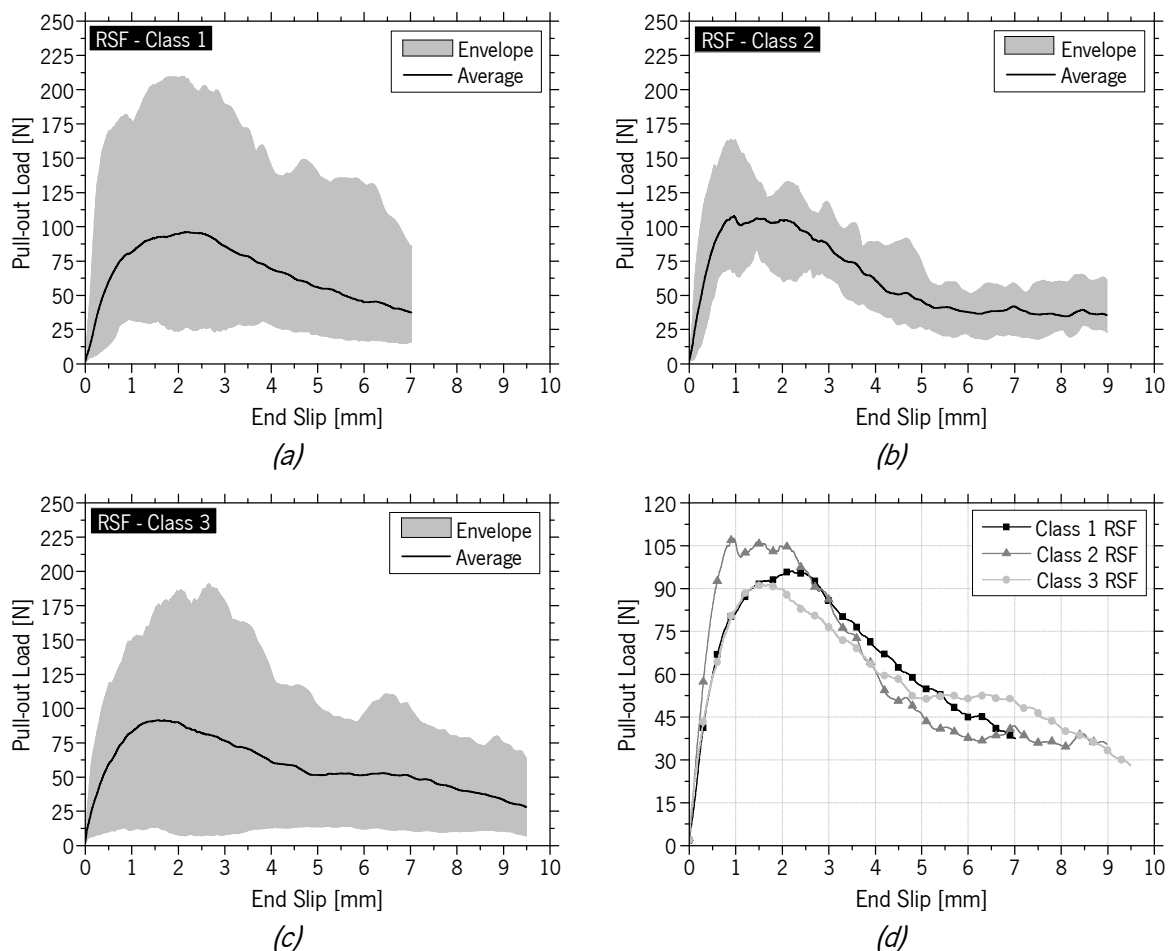


Figure 3.21 – Envelope and average Pull-out load-End slip relationship obtained in RSF pull-out tests: (a) Class 1 (reference); (b) Class 2 (350°C); (c) Class 3 (polished) (d) Classes 1, 2 and 3

Table 3.18 reports the average values of the maximum bond stress ( $\tau_{max}$ ) determined according to equation 2.1, and the corresponding coefficients of variation (CoV) for each class of RSF.

Table 3.18 – Average values of bond stress obtained in RSF pull-out tests

<b>RSF</b>	<b>Tested specimens</b>	<b>Peak pull-out load (N)</b>	<b><math>\tau_{max}</math> (MPa)</b>	<b>CoV (%)</b>
Class 1 (REF)	14	110.29	4.87	43.74
Class 2 (350°C)	5	144.52	6.50	36.86
Class 3 (Polished)	11	105.68	4.81	47.26

As reported in the literature for RSF pull-out behavior (Aiello *et al.*, 2009; Hu *et al.*, 2018b), high dispersion of the results was obtained in the pull-out tests of class 1 and 3 RSF, being essentially affected by two main factors: the amount of attached rubber (class 1 RSF) and the fiber geometry (class 1 and 3 RSF). Except for class 2 RSF, the failure mode of fibers always occurred by pull-out. In some cases, local spalling of the concrete matrix was observed at the fiber bending point due to the snubbing effect (Section 2.2.4). For the pre-treated RSF at 350°C (class 2) it was found that about 67% of the fibers had broken during the pull-out tests (these results are not included in Figure 3.21b). Therefore, since a smaller number of pull-out tests was considered, tests with class 2 RSF showed lower dispersion (Table 3.18). On the one hand, higher average bond strength was attained with the elimination of the rubber debris by pre-treatment of RSF at 350°C (Table 3.18). This can be also attributed to the effect of higher temperatures on the fiber surface, which promoted the formation of microcracks and extra micro roughness on the fiber surface (Figure 3.14b).

Taking only into account the average Pull-out load-End slip curves, it is possible to derive that the low amount of rubber debris attached on the RSF surface (class 1) had a minor effect in the pull-out behavior of RSF, since the average pull-out load was similar to those of “cleaned” RSF (classes 2 and 3) (Figure 3.21d). However, this should be valid only when the rubber debris attached to the fiber surface do not cover a significant surface area. In fact, considering the Pull-out load-End slip curves of five types of class 1 RSF, but with very different rubber contents, it was found that for relevant amounts of rubber debris there was a significant decrease of the pull-out strength with the increase of rubber content (F1 and F2 – Figure 3.22). For low amounts of rubber, which was more common, slight variations on rubber content was not significant (F3 and F4 – Figure 3.22). In addition, the irregular shape of RSF had also a significant influence in the fiber pull-out behavior, as reported by other authors (Tlemat *et al.*, 2003a; Aiello *et al.*,



2009; Caggiano *et al.*, 2015, Hu *et al.*, 2018b). Comparing F4 with F5, which are practically free of rubber (Figure 3.22), the RSF with more irregular and twisted embedded length showed higher fiber pull-out load and greater probability of fiber rupture, since straightening the RSF during the debonding process mobilizes high frictional resistance between the RSF and the surrounding matrix.

The values of  $\tau_{max}$  found in these RSF pull-out tests are comparable to those reported by Aiello *et al.* (2009), in which a  $\tau_{max}$  value of 5.98 MPa was registered for RSF with an average diameter of 0.258 mm, with an embedded length of 20 mm. In comparison to the results reported in literature for straight or hooked-end ISF (Cunha *et al.*, 2010), the maximum peak pull-out load obtained for RSF (Table 3.18) is, in general, higher than that recorded for straight ISF ( $\approx 75$  N) and lower than that for hooked-end ISF ( $\approx 350$  N) (Cunha *et al.*, 2010). However, this comparison must be cautious since some factors, such as concrete matrix properties and fiber diameter, were different in both tests.

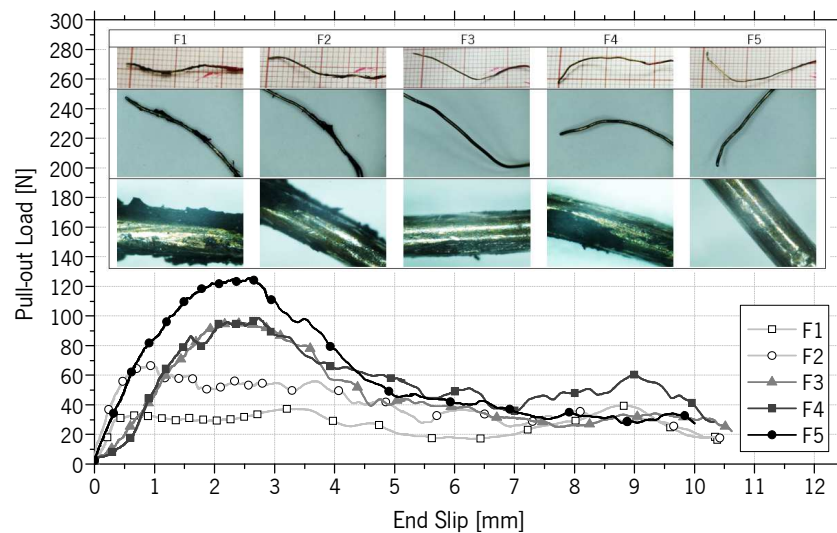


Figure 3.22 – Average Pull-out load-End slip curves obtained from five different types of class 1 RSF (the level of rubber attached to the fibers decreases from F1 to F5)

### 3.4 MIX DESIGN METHODOLOGIES FOR RSFRC PRODUCTION

#### 3.4.1 Mix Compositions

The RSFRC mixtures used in the experimental tests of the next chapters are presented in this section. All the concrete castings were produced with the collaboration of CiviTest company.

At the beginning of this research, a mix composition previously developed by other researchers of the research group (using the same materials) was used for the production of RSFRC specimens. This

composition considered the direct influence of RSF on the mix design methodology (Zamanzadeh *et al.*, 2015) and was produced with a fiber content ( $C_f$ ) of 60 kg/m<sup>3</sup> of RSF (0.8% in volume). The mix proportions of this RSFRC composition, herein designated by “RSFRC0.8%”, are indicated in Table 3.19. The RSFRC0.8% was used to cast the specimens produced for the DEWST tests that are presented in Chapter 6.

In order to produce more efficient and sustainable concrete, a new RSFRC composition was studied. To this end, a high content of recycled fibers and the partial replacement of binder with fly ash was considered. The mix design was defined by using a packing density optimization method, proposed by Pereira (2006) to achieve the optimum composition of SFRSCC.

The definition of the new composition of RSFRC was based on an experimental aggregate packing method (Barros *et al.*, 2007), involving three main steps as described in Section 2.2.5. In the first step, the paste composition was defined based on cement and one more fine addition. To improve the sustainable character of RSFRC, a high percentage of fly ash was adopted (40% of binder volume) in order to avoid excess of cement on paste composition and to enhance packing density and fresh concrete stability. Fly ash also improves the fresh concrete flowability, due to the spherical shape of their constituting particles that act as micro-rollers, decreasing friction and flow resistance (Pereira, 2006). A high dosage of superplasticizer (1.8% of cement weight) was also used to promote the dispersion and deflocculation of the fine particles in suspension, allowing the reduction of the mixing water and the improvement of concrete flowability.

In the second step, the proportions of the three types of aggregates (FS, CS and CG) were obtained executing mixes of distinct quantities of each type of aggregate and weighing 5 dm<sup>3</sup> volume for each mixture. The highest packing density was assumed to be achieved in the aggregate blend of the highest loose bulk density. This is valid when aggregate fractions have similar density, as is the case. Initially, only coarse sand and crushed granite were mixed. After finding the optimum relation between these two aggregates' types, the fine sand was added in distinct volumetric percentages, keeping constant the relation between the two first aggregates. In every mixture was included an estimated portion of fibers equivalent to 76 kg of RSF per m<sup>3</sup> of concrete (assuming that the total volume of aggregates and fibers is around 55% in concrete) in order to take into account the high perturbation that fibers introduce in the aggregate's skeleton organization (Pereira *et al.*, 2008). The results indicated that the optimum solid skeleton was composed, in volume, by 10% of fine sand, 49.5% of coarse sand and 40.5% of crushed granite.

The third phase was dedicated to the evaluation of the final composition of RSFRC resulting from this optimization of solid skeleton. The concrete mixture was prepared with a paste volume of 33% with an effective w/c ratio of 0.43 (the water content corresponds to 50% of paste volume and 78% of the binder volume). The added water was corrected taking into account the aggregate's saturation degree. The paste and water content were adopted taking into account the recommendation of Pereira (2006) to obtain SFRSCC with good homogeneity and cohesion, without signs of segregation.

Table 3.19 includes the resulting RSFRC composition for the adopted RSF content of 1% in volume, herein designated by "RSFRC1%". This RSFRC1% was used to cast the specimens produced for the experimental tests presented in Chapters 7 and 8.

For comparison purposes about the reinforcement performance of RSF in the RSFRC1%, an ISFRC mixture of equal composition was produced with 1% of ISF by volume of concrete, herein designated by "ISFRC1%". Hooked-end steel fibers, herein designated by "ISF type 2", were used with geometry properties as similar as possible with RSF. On average, these ISF had a  $l_f$  of 33 mm, a  $d_f$  of 0.55 mm, an  $\lambda$  of 60 and a  $f_u$  of 1230 MPa (Figure 3.23). This ISFRC1% mixture was used to cast the specimens produced for the experimental tests presented in Chapter 8.

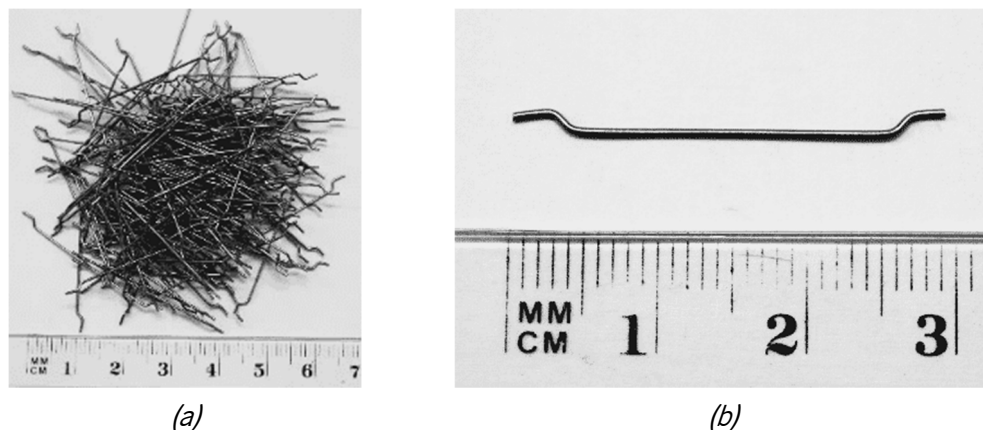


Figure 3.23 – ISF type 2: general view of (a) multi fibers, and (b) single ISF

Table 3.19 – Mix proportions for 1 m<sup>3</sup> of concrete

Concrete mixture	CEM (kg)	FA (kg)	LF (kg)	W (L)	SP1 (L)	SP2 (L)	FS (kg)	CS (kg)	CG (kg)	Cf (kg)	W/C
RSFRC0.8%	381	-	353	140	7.8	-	237	710	590	60	0.37
RSFRC1%	400	200		173	-	7.2	148	735	597	75.8	0.43
ISFRC1%	400	200		173	-	7.2	148	735	597	78.6	0.43

### 3.4.2 Mixing procedure and fresh concrete properties

Planetary mixer of vertical axis was used to manufacture the RSFRC mixtures, with a volumetric capacity adequate to the quantity of concrete needed to produce the specimens. For every mixture, cement, fly ash, limestone filler, fine and coarse river sand, crushed granite, water, superplasticizer and RSF were weighed separately. The aggregates were first introduced into the mixer from the highest to the lowest aggregate dimension, i.e. first the crushed granites were added, then the coarse river sand and the fine river sand. After mixing for one minute, the necessary quantity of water was added to saturate the aggregate one more minute. The cement and fly ash/limestone filler were added, and later the remaining water. The superplasticizer was dissolved in the mixing water. Finally, without stopping the mixer, the RSF were gradually added to the mix by a metal grid where they were separated by hand, as can be seen in Figure 3.24. This process of RSF addition was crucial to assure a suitable distribution of RSF into the concrete matrix. After all the fibers have been added, the concrete was mixed during about five minutes, until it started to exhibit good homogeneity.



Figure 3.24 – Introduction of RSF into the concrete mixer

After concrete producing and before casting the specimens, the workability of fresh fluid concretes (RSFRC0.8%) was determined by the slump-flow test, according to EN 12350-8:2010 while the workability of the remaining fresh concretes was determined by the slump test according to EN 12350-2:2009. Figure 3.25 depicts the final state of performed slump tests for a fresh mixture of RSFRC1%, before and after the addition of RSF, where an average flow reduction of 165 mm was observed after the addition of the fibers. The average slump-flow and slump values obtained for each produced RSFRC are presented in Table 3.20.



Figure 3.25 – Slump tests for a concrete reinforced with  $76 \text{ kg/m}^3$  of RSF  
 (a) Before and (b) After the addition of the RSF

Table 3.20 – Slump and flow of fresh RSFRC

Concrete	Fibers	Number of castings	Average slump (mm)	Average slump-flow (mm)
RSFRC0.8%	RSF class 1 (REF)	1	-	522
RSFRC0.8%	RSF class 2 (350°C)	2	-	494
RSFRC0.8%	RSF class 3 (Polished)	1	-	522
RSFRC1%	RSF class 1 (REF)	6	103	-
ISFRC1%	ISF type 2	1	130	-

According to the EN 206:2013+A1 (2016), the RSFRC1% and ISFRC1% are of Class S3 consistency.

Due to its high fluidity, RSFRC0.8% was not vibrated. However, the remaining RSFRC mixtures were vibrated with an internal vibrator of high frequency. After casting, the filled moulds were kept for 24 hours under the laboratory environment, with the exposed surface protected with black plastics to avoid significant moisture losses. After this period, the specimens were demoulded and cured in the fog room up to 28 days of age at 99% RH and  $\approx 20^\circ\text{C}$ , as recommended by EN 12390-3:2011.

In the experimental program to be presented in Chapter 7, due to the large size of the round panels and the high number of produced specimens (including the beams and cylinders for material characterization), it was not possible to cure them into the fog room. In this case, these specimens were cured in laboratory environment up to 28 days of age (average temperature of  $21^\circ\text{C}$  and relative humidity of 60%) protected with plastics.

## 3.5 MECHANICAL CHARACTERIZATION OF RSFRC

### 3.5.1 Flexural behavior

#### 3.5.1.1 Test procedures

The flexural tensile behavior of RSFRC produced with RSF volume content of 1% was assessed by testing notched beams with 600 mm in length and 150x150 mm<sup>2</sup> cross section under three point loading conditions (3PNBBT), as shown in Figure 3.26. The method of casting the specimens and curing procedure, the position and dimensions of the notch and the load and specimen support conditions were those recommended by RILEM TC 162-TDF (2003) and MC2010 (2011), which are explained in detail in Section 2.2.7.1. These tests were carried out under closed-loop displacement control at a constant rate of 3 μm/s, using the deflection measured at midspan as control variable (Fig. 3.26a). One additional LVDT was used to measure the crack mouth opening displacement (CMOD) placed on the bottom face of the beam at the mid-span (Fig. 3.26b).

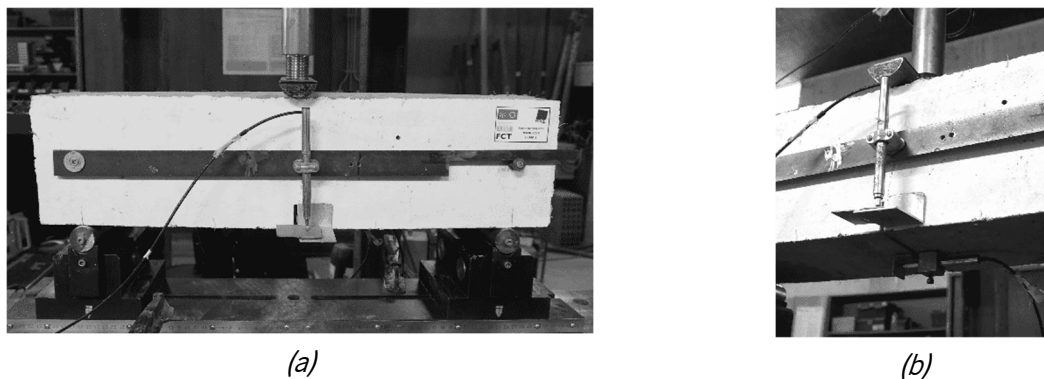


Figure 3.26 – Test setup for 3PNBBT: (a) Specimen front view (b) Specimen bottom view

The 3PNBBT were conducted at different ages to characterize the tensile behavior under flexure of each concrete type, namely, considering the six castings of RSFRC1%, herein designated by “RSFRC1%\_1 to 6”. Additionally, 3PNBBT of plain concrete and ISFRC1% were also tested for comparison purposes.

#### 3.5.1.2 Experimental results

##### Force-Deflection curves

In Figure 3.27 are depicted the envelope and the average  $F/f_{ct,fl} - \delta$  relationship, obtained with the notched beams of RSFRC1%\_1 at 8 and 28 days.

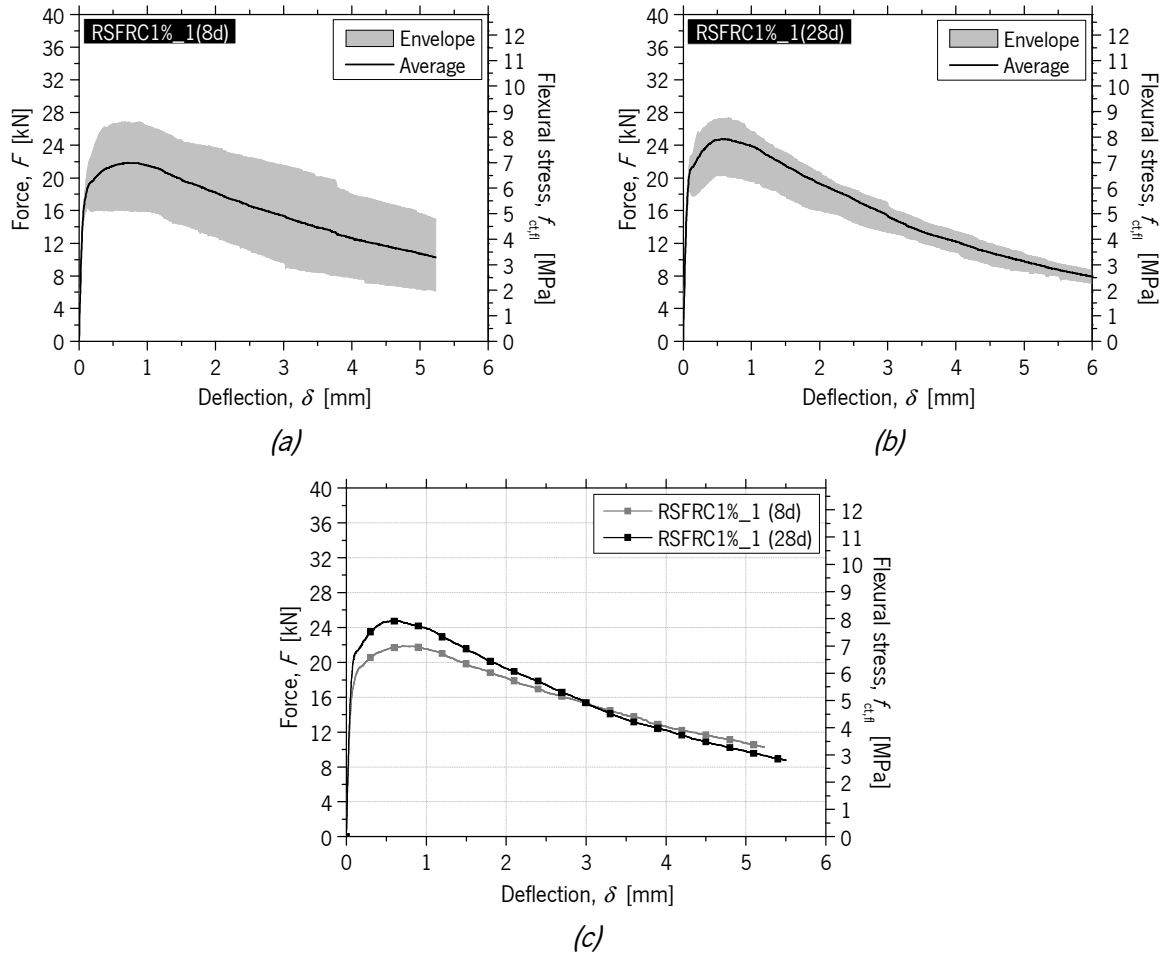


Figure 3.27 – Envelope and average load/flexural stress-deflection curves for beams of:  
 (a) RSFRC1%\_1 (8 days); (b) RSFRC1%\_1 (28 days); (c) RSFRC1%\_1 (8 and 28 days)

As expected, the RSFRC1% composition showed higher peak load at 28 days than at 8 days, however, the post-cracking residual strength was similar for both ages.

Figure 3.28 represents the envelope and the average  $F/f_{ct,fl} - \delta$  relationship, obtained with the notched beams of RSFRC1%\_2 to 5 at 38 and 120 days. The RSFRC1%\_2 to 5 mixtures were used to produce the round panels for round panel tests to be presented in Chapter 7. These 3PNBBT were carried out to characterize the flexural behavior of RSFRC1% at the same age as round panel testing. For this reason, the notched beams were tested at 38 and 120 days.

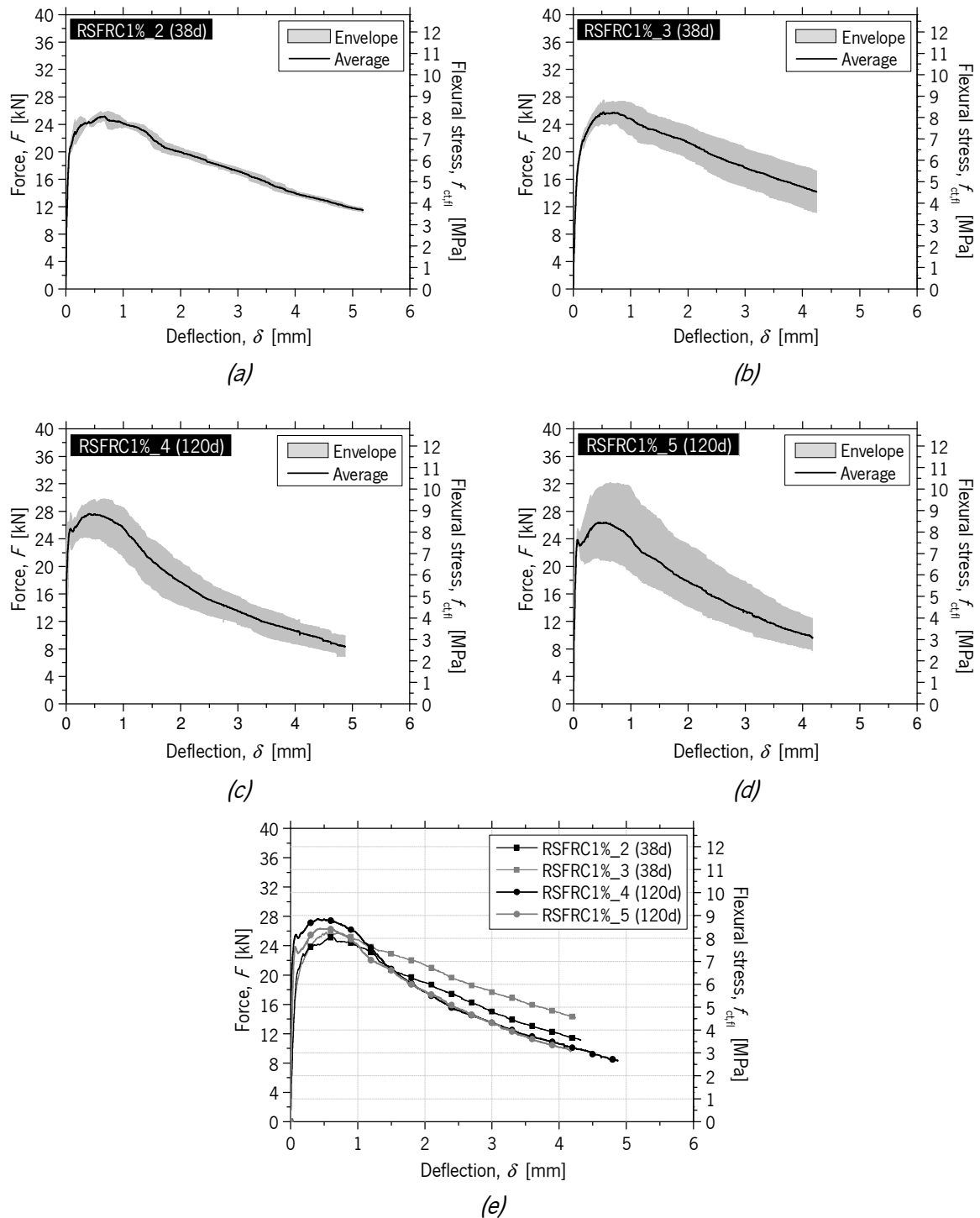


Figure 3.28 – Envelope and average load/deflection and flexural stress-deflection curves for beams of:  
 (a) RSFRC1%\_2 (38 days); (b) RSFRC1%\_3 (38 days); (c) RSFRC1%\_4 (120 days);  
 (d) RSFRC1%\_5 (120 days); (e) RSFRC1%\_2&3&4&5 (38 and 120 days)

At 120 days of age, the RSFRC1% composition showed higher peak load and slightly lower post-cracking residual strength than at 38 days. This is possibly justified by the failure of a higher number of fibers in RSFRC1% at 120 days, due to the higher bond strength of concrete matrix, which is the basis of its



compressive strength. Regarding the pre-peak behavior at 120 days of age, the RSFRC1% beams, after attaining the cracking load, revealed a very small decrease indicative of tensile failure of some fibers, followed by deflection-hardening phase due to the mobilization of the fiber reinforcement mechanisms. At 38 days of age, a markedly non-linear behavior was visible up to the peak load and a load decay was not observed before reaching the peak load.

Figure 3.29 represents the envelope and the average  $F/f_{ct,fl} - \delta$  relationship, obtained with the notched beams of PC, RSFRC1%\_6 and ISFRC1% at 28 days.

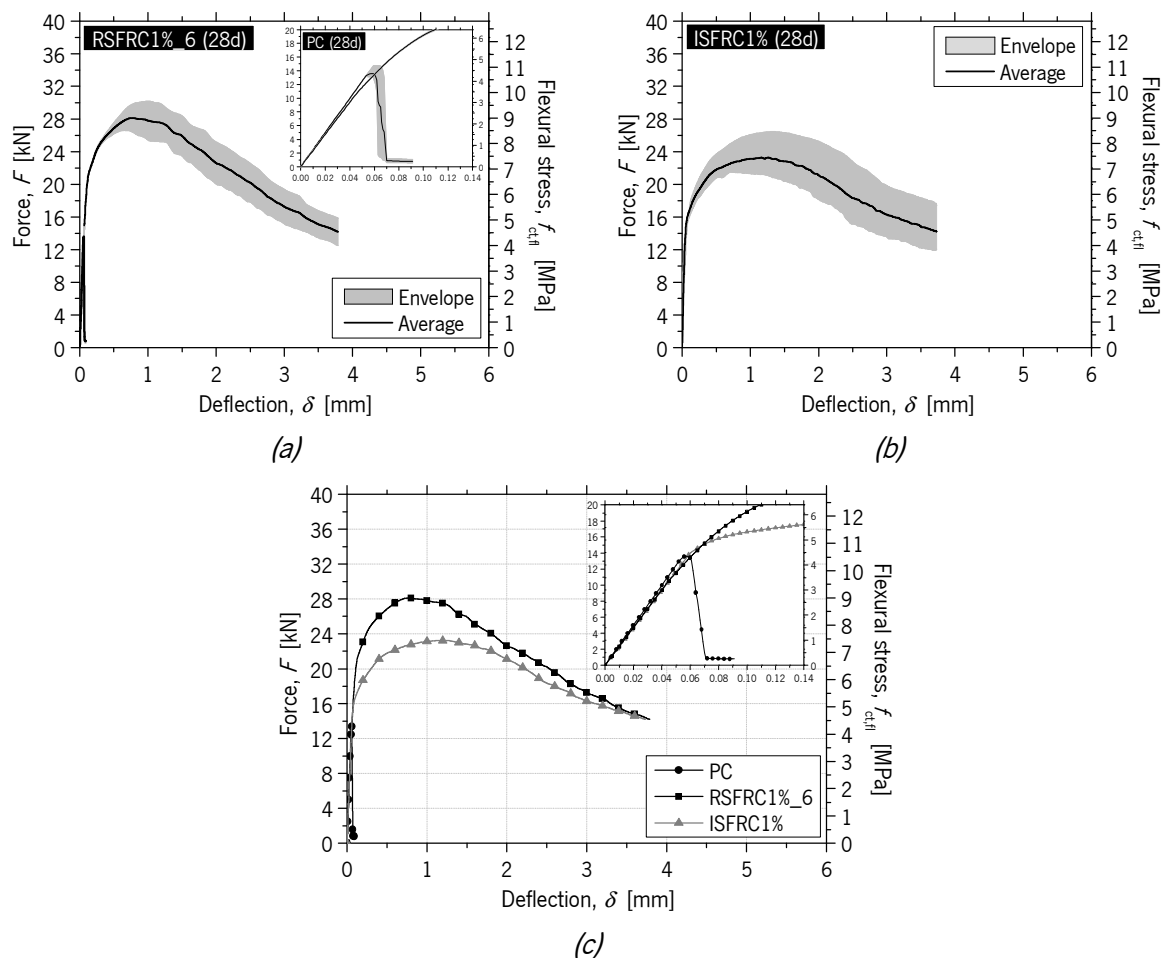


Figure 3.29 – Envelope and average load/flexural stress-deflection curves for beams (28 days) of:  
 (a) PC and RSFRC1%\_6; (b) ISFRC1%; (c) PC, RSFRC1%\_6 and ISFRC1%

Up to a deflection of about 3.5 mm, the RSFRC1% presented higher flexural capacity and energy absorption performance than ISFRC1% (Fig. 3.29c). Regarding the pre-peak stage, the beams made of RSFRC1% and ISFRC1% exhibited a deflection hardening behavior in bending, which is characterized by an increase of the force with the deflection up to the peak load. For PC beams, it is verified that just after

the peak load, an abrupt load decay has occurred due to the brittle character of this material. The increase in ductility provided by the incorporation of fibers is clear, being effective in terms of increasing the flexural strength, the post peak resistance, and the energy absorption capacity.

### Flexural tensile strength parameters

From the 3PNBBTs, the following results were computed: limit of proportionality ( $f_{ct,L}$ ) and equivalent flexural tensile strengths parameters ( $f_{eq,2}$  and  $f_{eq,3}$ ) according to RILEM TC 162-TDF (2003), residual flexural tensile strength parameters ( $f_{R,i}$ ) according to *fib* Model Code 2010 recommendations. The  $f_{ct,L}$  was computed by Eq. (2.2) considering the load at the limit of proportionality,  $F_L$ , corresponding to the highest load value up to a deflection of 0.05 mm (Figure 3.30).

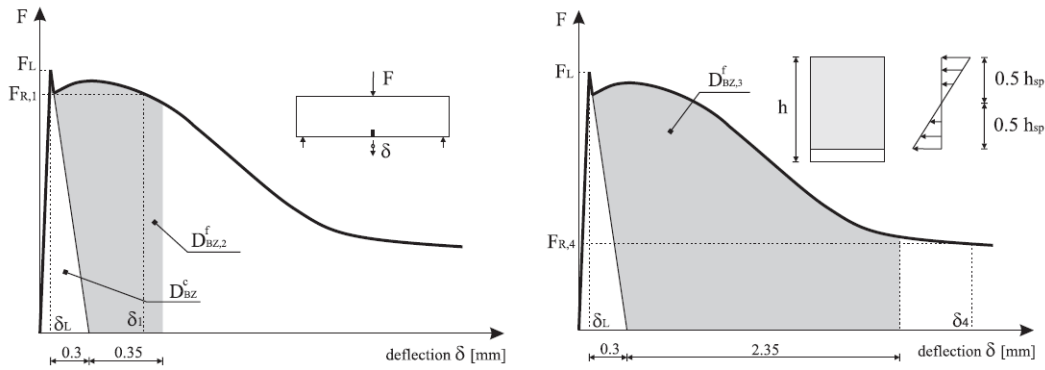


Figure 3.30 – Load-deflection diagrams for the determination of the equivalent and residual flexural tensile strengths according to RILEM TC 162-TDF (2003) (Cunha, 2010)

The contribution of steel fibers in terms of energy absorption capacity of concrete,  $D_{BZ,2}^f$  and  $D_{BZ,3}^f$ , can be evaluated by measuring the area under the load-deflection curve up to certain limit deflections,  $\delta_2 (= \delta_L + 0.65 \text{ mm})$  and  $\delta_3 (= \delta_L + 2.65 \text{ mm})$ , where  $\delta_L$  is the deflection corresponding to  $F_L$ , and then, by subtracting the parcel  $D_{BZ}^c$ , corresponding to the contribution of plain concrete (Figure 3.30). Assuming a linear stress distribution on the cross section at midspan, the equivalent flexural tensile strengths,  $f_{eq,2}$  and  $f_{eq,3}$ , can be determined by:

$$f_{eq,2} = \frac{3}{2} \left( \frac{D_{BZ,2}^f}{0.50} \right) \frac{L}{b h_{sp}^2} f \quad (3.2)$$

$$f_{eq,3} = \frac{3}{2} \left( \frac{D_{BZ,3}^f}{2.50} \right) \frac{L}{b h_{sp}^2} \quad (3.3)$$

The residual flexural tensile strength parameters,  $f_{R,i}$ , were determined from the Eq. (2.2) where  $F_j$  is the load corresponding to  $CMOD_j$  equal to 0.5, 1.5, 2.5 and 3.5 mm (Figure 2.17). The force/flexural stress-CMOD relationships,  $F/f_{ct,fl} - \omega$  obtained by the performed 3PNBBT are shown in Figures 3.31 and 3.32.

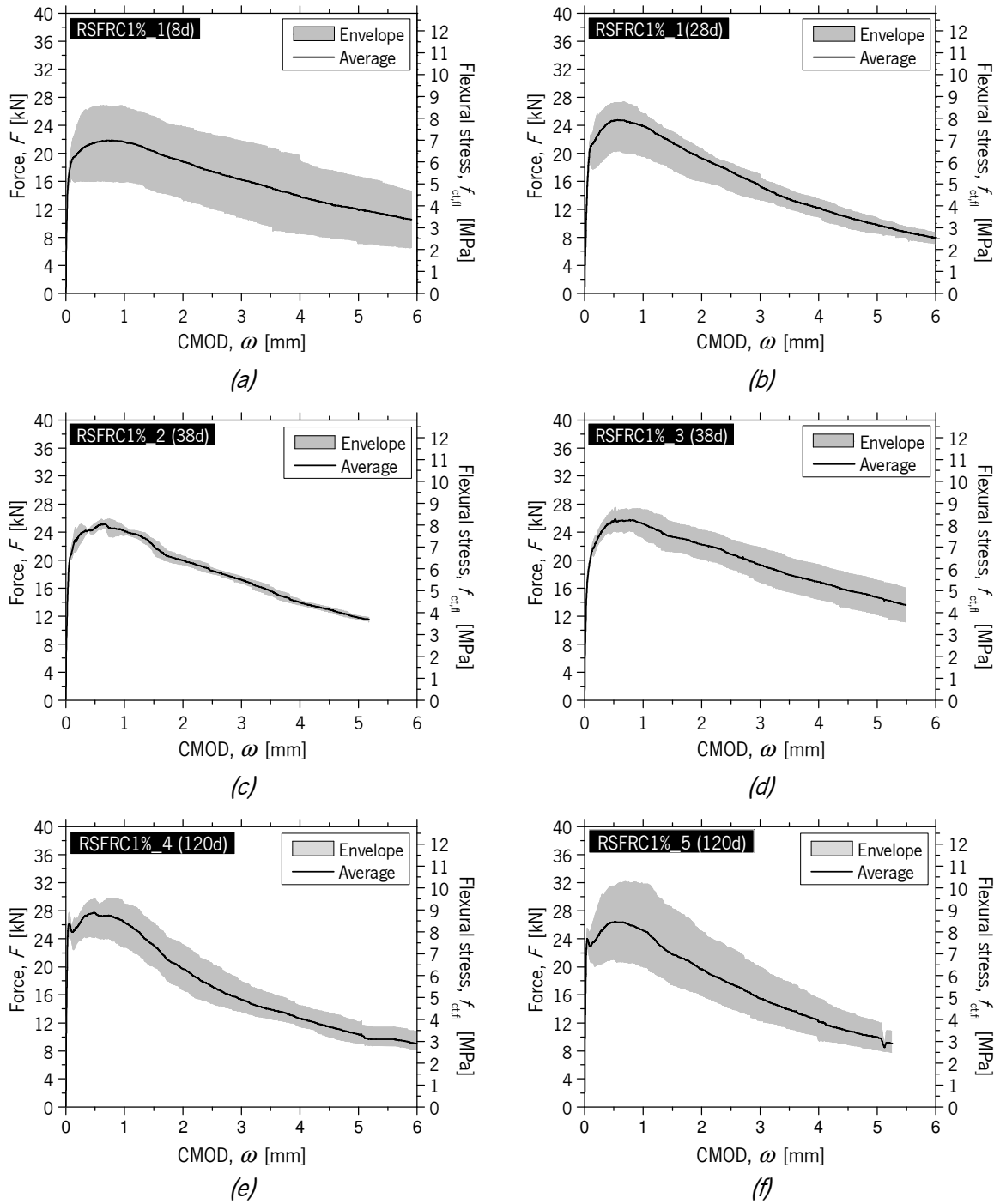


Figure 3.31 – Envelope and average load/flexural stress-CMOD curves for beams of:  
 (a) RSFRC1%\_1 (8 days); (b) RSFRC1%\_1 (28 days); (c) RSFRC1%\_2 (38 days);  
 (d) RSFRC1%\_3 (38 days); (e) RSFRC1%\_4 (120 days); (f) RSFRC1%\_5 (120 days)

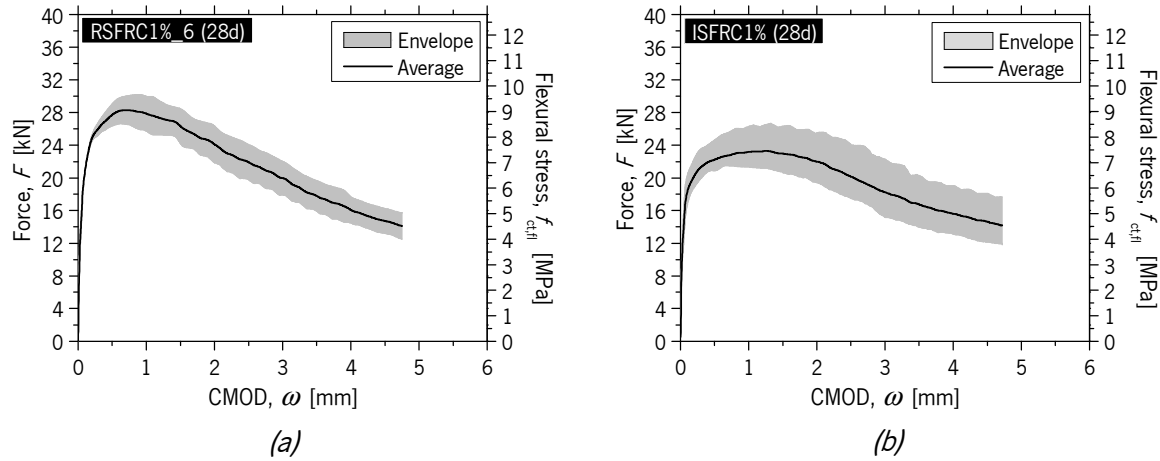


Figure 3.32 – Envelope and average load/flexural stress-CMOD curves for beams of:  
 (a) PC and RSFRC1%\_6; (b) ISFRC1%

The average and envelope of deflection-CMOD relationship obtained for all the performed 3PNBBTs with RSFRC are presented in Figure 3.33. A relatively high dispersion of the experimental results was obtained for this relationship. It was also verified that the average  $\delta$  vs CMOD relationship of experimental results fits very well the corresponding equivalence between  $\delta$  and CMOD proposed by RILEM TC 162-TDF (2002), which gives support on the reliability of this equation:

$$CMOD = 1.18 \delta + \beta \quad \text{with} \quad \beta = -0.0416 \text{ mm} \quad (3.4)$$

It is also observed in Fig. 3.33, that the average  $\delta$  is similar to CMOD for CMOD lower than 0.5 mm and is lower than CMOD for CMOD higher than 0.5 mm, being the decrease more pronounced with the increase of crack opening.

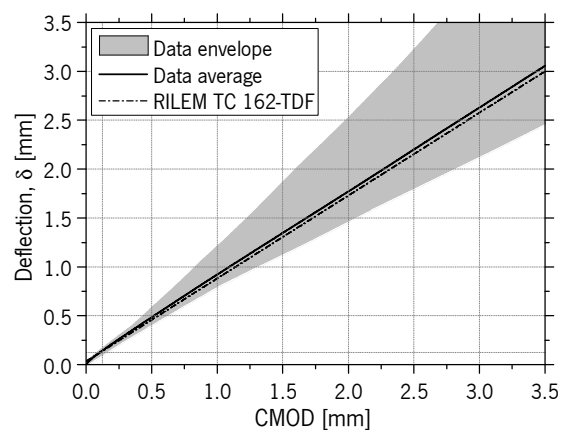


Figure 3.33 – Deflection-CMOD relationship for all the performed 3PNBBT

Table 3.21 shows the average values and the corresponding coefficients of variation (CoV) of the flexural tensile strength parameters,  $f_{ct,L}$ ,  $f_{eq,2}$ ,  $f_{eq,3}$ ,  $f_{R,1}$ ,  $f_{R,2}$ ,  $f_{R,3}$  and  $f_{R,4}$ . The results are presented taking into account different concrete castings and testing age.

Table 3.21 – Average results (and CoV) of 3PNBBTs

Concrete mixtures	Age (days)	Number of beams	$f_{ct,L}$ (MPa)	$f_{eq,2}$ (MPa)	$f_{eq,3}$ (MPa)	$f_{R,1}$ (MPa)	$f_{R,2}$ (MPa)	$f_{R,3}$ (MPa)	$f_{R,4}$ (MPa)
RSFRC1%_1	8	5	4.49 (3.07)	7.16 (21.12)	6.34 (23.26)	6.88 (20.64)	6.49 (22.82)	5.57 (26.35)	4.83 (29.39)
	28	5	5.11 (6.79)	8.18 (11.81)	6.94 (10.12)	7.87 (10.93)	7.13 (9.96)	5.98 (9.04)	4.94 (7.69)
RSFRC1%_2	38	2	4.57 (1.29)	8.37 (1.52)	6.90 (4.07)	7.80 (3.86)	7.30 (4.10)	6.10 (4.66)	5.20 (5.68)
RSFRC1%_3	38	2	4.53 (5.41)	8.47 (7.08)	7.39 (13.11)	8.17 (9.23)	7.64 (11.03)	6.99 (10.82)	6.23 (11.87)
RSFRC1%_4	120	3	7.85 (6.75)	8.80 (11.54)	7.15 (8.84)	8.86 (10.89)	7.57 (13.62)	5.71 (16.58)	4.60 (14.83)
RSFRC1%_5	120	3	7.09 (8.12)	8.38 (20.76)	6.72 (24.93)	8.43 (19.89)	7.14 (25.73)	6.18 (18.54)	4.66 (23.93)
Plain concrete	28	3	3.92 (3.27)	-	-	-	-	-	-
RSFRC1%_6	28	2	3.77 (0.00)	9.21 (2.46)	8.08 (11.14)	8.87 (6.78)	8.41 (11.87)	7.02 (13.74)	5.72 (14.27)
ISFRC1%	28	5	4.77 (9.21)	6.99 (5.07)	6.90 (10.38)	7.12 (6.51)	7.39 (10.36)	6.58 (13.99)	5.42 (13.86)

From the data presented in Table 3.21, in general, no significant differences were observed between the equivalent and residual strengths of RSFRC1% after 28 days of age. In what concerns to  $f_{eq,2}$  and  $f_{R,1}$ , which are used in the design verifications for the serviceability limit states (SLS), it was observed a maximum increase of 8% and 13%, from 28 to 120 days of age, respectively. On the other hand, the parameters  $f_{eq,3}$  and  $f_{R,4}$ , corresponding to the ultimate limit state (ULS) design, have decreased a maximum percentage of 7% from 28 to 120 days of age. This fact is probably due to the higher probability of fibers to suffer tensile rupture at crack plane for higher crack widths. By increasing the rotation between the faces of the cracked plane, it increases the shear force component actuating at the exit point of an inclined fiber (de Oliveira, 2010), which due to snubbing effect decreases the tensile strength of the fibers (Barros and Foster, 2018).

The obtained results also confirmed the higher effectiveness of RSF comparing with ISF in terms of bending behavior. The higher aspect ratio and tensile strength of RSF can justify this better performance of RSFRC1%. The highest difference has occurred for crack width levels corresponding to SLS conditions. The reinforcement performance of both FRCs has become closer with the increase of the crack width, which indicates that they will have similar performance for ULS conditions.

Figure 3.34 shows a linear trend between  $f_{eq,2}$  and  $f_{eq,3}$  obtained for all the tested beams, which is in agreement with previous research on ISFRC (Barros *et al.*, 2005). Therefore, it is enough to analyze the evolution of the  $f_{eq,2}$  and  $f_{eq,3}$ , since the observations attributable to one of them can be also applied to the other. Fig. 3.34 reveals slightly lower values of  $f_{eq,3}$  than  $f_{eq,2}$ . A linear trend between  $f_{eq,2}$  and  $f_{R,1}$ , and  $f_{eq,3}$  and  $f_{R,4}$  was also obtained, as observed in Figures 3.35a,b respectively.

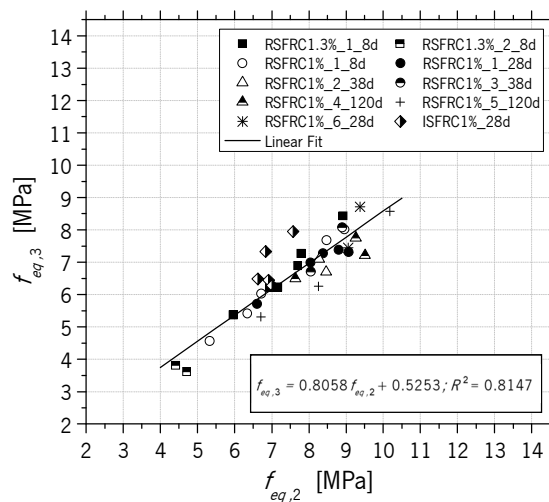


Figure 3.34 – Relationship between  $f_{eq,2}$  and  $f_{eq,3}$

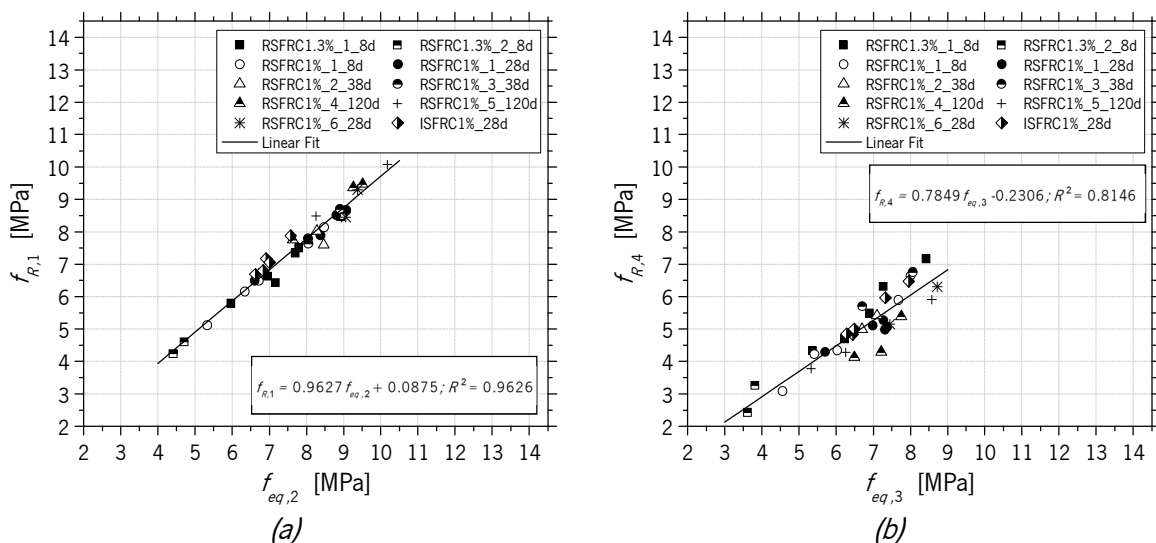


Figure 3.35 – Relationship between (a)  $f_{eq,2}$  and  $f_{R,1}$ ; and (b)  $f_{eq,3}$  and  $f_{R,4}$

In order to classify the post-cracking strength of FRC, the MC2010 proposed a FRC classification assuming a linear elastic behavior and considering the characteristic values of the residual strengths for serviceability ( $f_{R,1k}$ ) and for ultimate ( $f_{R,3k}$ ) conditions. In Table 3.22 are depicted the toughness classes obtained for the developed FRC mixtures.

Table 3.22 –Toughness class obtained for tested FRC beams

Concrete mixtures	$f_{R,1k}$ (MPa)	$f_{R,3k}$ (MPa)	Toughness class
RSFRC1%_1_8d	4.33	3.01	4a
RSFRC1%_1_28d	6.32	4.44	6b
RSFRC1%_2_38d	7.20	5.49	7b
RSFRC1%_3_38d	6.65	5.48	6b
RSFRC1%_4_120d	7.04	3.89	7a
RSFRC1%_5_120d	5.26	3.01	5a
RSFRC1%_6_28d	7.66	5.81	7b
ISFRC1%_28d	6.29	5.74	6c

### Influence of the number of fibers

After testing the RSFRC1%\_1 beams at 8 and 28 days of age, one face of the fracture surface was divided in nine equal regions in order to evaluate the fiber distribution, as shown in Figure 3.36a. The fiber distribution was evaluated by counting the total number of RSF crossing the fractured surface of 10 beams. The results from the fiber counting of RSFRC1%\_1 beams, presented in Figure 3.36b, show that, on average, a uniform distribution of the fibers was ensured, although the large dispersion of results registered.

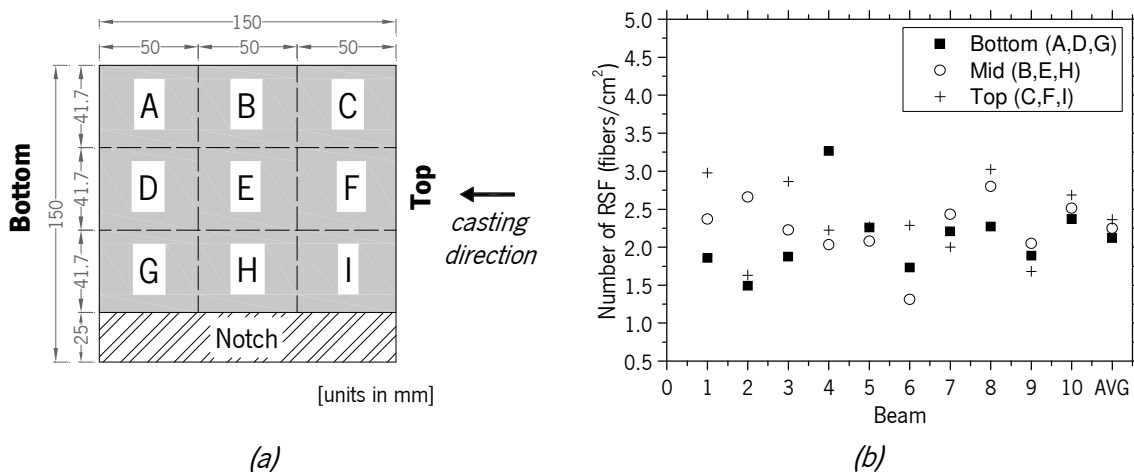


Figure 3.36 – (a) Schematic representation of the regions in the fractured zone of specimens for the fiber distribution assessment; (b) Fiber distribution at the fracture section of the RSFRC1%\_1 beams

### 3.5.1.3 Numerical study: determination of the $\sigma - \omega$ law by inverse analysis

In this section, the post-cracking behavior of RSFRC1% is assessed by inverse analysis taking the results from the 3PNBBTs. For this purpose, the experimental force-CMOD curves obtained with RSFRC1%\_2&3&4&5 notched beams at 38 and 120 days of age were simulated using a numerical model developed in previous research (Cunha, 2010), implemented by the finite element program FEMIX (Azevedo *et al.*, 2003). Due to the geometry, support and loading conditions used in the 3PNBBTs, a plane stress state installed in the beam was assumed. For the numerical simulation of the crack initiation and propagation, 2D line interface elements of 6 nodes located on the symmetry axis of the specimen were used. The remaining part of the specimen was modelled with a mesh of 8-node Serendipity plane stress finite elements, assuming a linear elastic behavior for the material.

The Gauss-Legendre integration scheme with  $2 \times 2$  integration points (IP) was used in all elements, with exception of the interface finite elements at the symmetry axis of the specimen, where a  $1 \times 2$  Gauss-Lobato IP were used in order to assure the crack progress along the symmetry axis. Figure 3.37 depicts the mesh used in the numerical simulations. The values of the material properties used in the inverse analysis are indicated in Table 3.23.

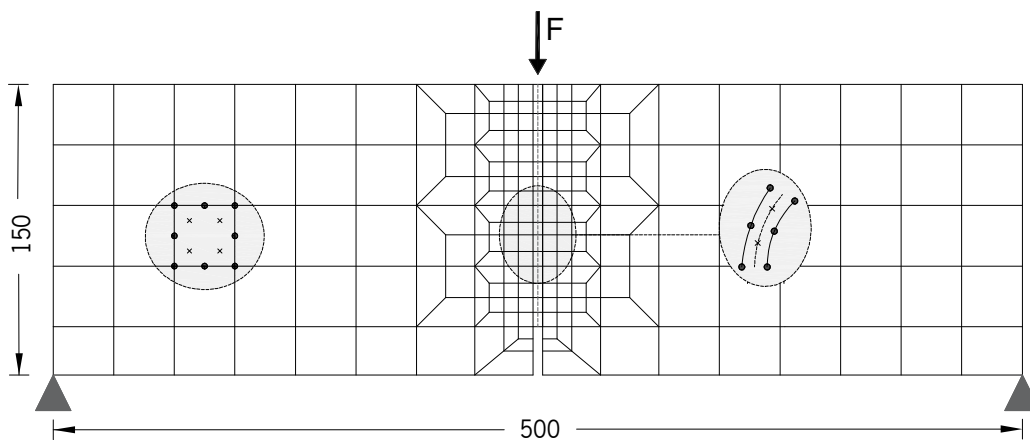


Figure 3.37 – Finite element mesh used in the simulation of the 3PNBBTs (Cunha, 2010)

Table 3.23 – RSFRC properties used in the numerical simulation of the 3PNBBTs

Density	$\rho = 2.34 \times 10^{-5} \text{ N/mm}^3$
Poisson's ratio	$\nu_c = 0.20$
Young's modulus	$E_c = 28510 \text{ MPa}$
Tensile strength	Inverse analysis
Fracture mode I parameters	Inverse analysis



The fracture mode I propagation of FRC was simulated by a trilinear tensile-softening diagram, stress-crack width,  $\sigma - \omega$ , whose parameters that define the shape of the diagram, namely, fracture energy,  $G_f$ , and the values of crack opening,  $\omega_f$  and tensile stress,  $\sigma_f$ , were obtained performing inverse analysis with the force-CMOD relationship obtained by the performed 3PNBBT. The objective of the inverse analysis is to evaluate the fracture mode I parameters leading to the minimization of the error parameter,  $e$ , which is the ratio between the area limited by the experimental and the numerical curves and the area underneath the experimental curve. In Figure 3.38 are depicted both the experimental and numerical force-CMOD curves for the RSFRC1%\_2&3&4&5 notched beams at 38 and 120 days of age. The agreement between the numerical and the experimental curves is very good for all the RSFRC1% beams, which indicates that the trilinear  $\sigma - \omega$  relationship is capable of simulating accurately the post-cracking behavior of RSFRC1%.

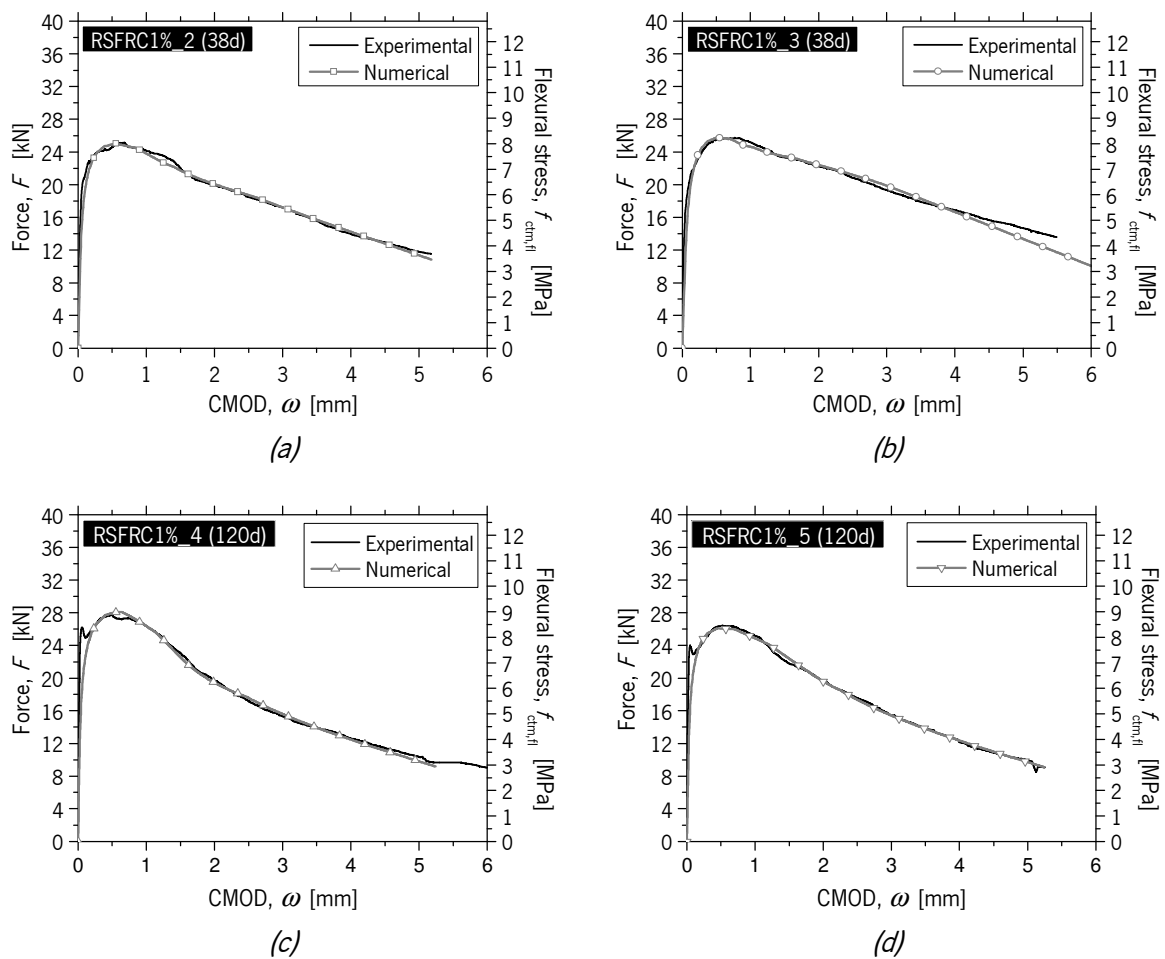
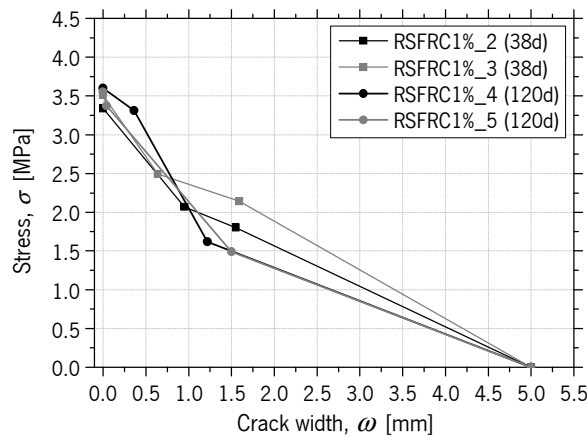


Figure 3.38 – Numerical simulation of the 3PNBBT with: (a) RSFRC1%\_2 (38 days); (b) RSFRC1%\_3 (38 days); (c) RSFRC1%\_4 (120 days); (d) RSFRC1%\_5 (120 days)

The obtained parameters defining the  $\sigma - \omega$  relationship, and the equivalent fitting error ( $e$ ), are indicated in Table 3.24, where  $f_{ct}$  is the tensile strength,  $\sigma_1$  and  $\sigma_2$  are respectively, the stress at the first and second post-peak point of the crack opening,  $\omega_1$  and  $\omega_2$ , and  $\omega_u$  is the ultimate post-peak point of the crack opening. The graphical representation of these  $\sigma - \omega$  laws is presented in Figure 3.39.

Table 3.24 – Parameters of the  $\sigma - \omega$  relationship obtained by inverse analysis

Concrete mixtures	$f_{ct}$ (MPa)	$\sigma_1$ (MPa)	$\sigma_2$ (MPa)	$\omega_1$ (mm)	$\omega_2$ (mm)	$\omega_u$ (mm)	$G_f$ (N/mm)	$e$ (%)
RSFRC1%_2	3.34	2.07	1.80	0.95	1.55	5.00	6.84	0.62
RSFRC1%_3	3.51	2.49	2.14	0.64	1.59	5.00	7.99	0.26
RSFRC1%_4	3.60	3.31	1.62	0.36	1.22	5.00	6.43	1.15
RSFRC1%_5	3.55	3.37	1.49	0.04	1.50	5.00	6.30	0.71

Figure 3.39 –  $\sigma - \omega$  relationships obtained by inverse analysis from 3PNBBTs

The  $\sigma - \omega$  parameters obtained for RSFRC1% at 38 (RSFRC1%\_2&3) and 120 days of age (RSFRC1%\_4&5) were quite different between the crack width levels analyzed,  $\omega_1$  and  $\omega_2$ . However, for the same crack width level, the parameters were not so different for RSFRC1% at 38 and 120 days. The highest difference was observed at  $\omega = 1.5$  mm, where the RSFRC1% at 120 days in average showed a reduced post-cracking behavior than at 38 days, as already discussed in the previous section.

### 3.5.2 Compressive behavior

#### 3.5.2.1 Test procedures

The compressive strength and elasticity modulus of the six hardened mixtures of RSFRC1% were assessed at different ages, by testing cylindrical specimens with 150 mm diameter and 300 mm height. The

uniaxial compressive tests were carried out in a servo-controlled equipment of maximum load carrying capacity of 2250 kN. The elasticity modulus and the stress-strain relationship were obtained in sets of four specimens at each age, according to EN 12390-13:2014 and EN 12390-3:2011, respectively. The procedure adopted consisted on determining the compressive strength in one specimen, in order to establish the maximum load value of the load-unload cycles to be carried out for the determination of the modulus of elasticity (Figure 3.40a). For the three remaining specimens, the modulus of elasticity was determined in a first phase, and then tested up to an axial strain level higher than the strain at peak stress in order to determine the stress-strain response of the RSFRC not only in the pre-peak but also in the post-peak phase.

According to EN 12390-13:2014, the determination of the stabilized secant modulus of elasticity was carried out under force control over three loading cycles. For each one of the three cycles, the stress is increased at a velocity of 0.6 MPa/s until an upper stress level  $\sigma_a = f_{cm} / 3$  is reached, where  $f_{cm}$  is the compressive strength previously determined. The stress  $\sigma_a$  is maintained during 20 seconds, and then reduced at the same rate to the lower stress  $\sigma_b = f_{cm} / 9$ , under which is maintained for 20 seconds. During the final 10 seconds of the upper stress phase of the third cycle the corresponding strain  $\varepsilon_{a,3}$  is recorded. The strain  $\varepsilon_{b,2}$  is recorded during the final 10 seconds of the lower stress phase of the second cycle. The modulus of elasticity is defined as:

$$E_{C,S} = \frac{\sigma_a - \sigma_b}{\varepsilon_{a,3} - \varepsilon_{b,2}} \quad (3.5)$$

In order to accomplish the axial displacement measurement, two steel rings distanced of 100 mm were installed at central region of the specimen, as depicted in Figure 3.40a. In the top ring, three LVDTs were placed around the specimen at 120° from each other to measure the axial displacement of the specimen at the test region (Figure 3.40a). The strain was calculated by dividing the average displacement measured by the three LVDTs, by the length of the test region.

To obtain the entire stress-strain curve,  $\sigma_c - \varepsilon_c$ , the uniaxial compressive test was executed using the axial displacement as control variable, measured by an external LVDT installed on the actuator (Figure 3.40b). The tests were carried out with a displacement ratio of 5  $\mu\text{m/s}$  and the strain was determined by dividing the displacement measured by the LVDT by the length of the test region.

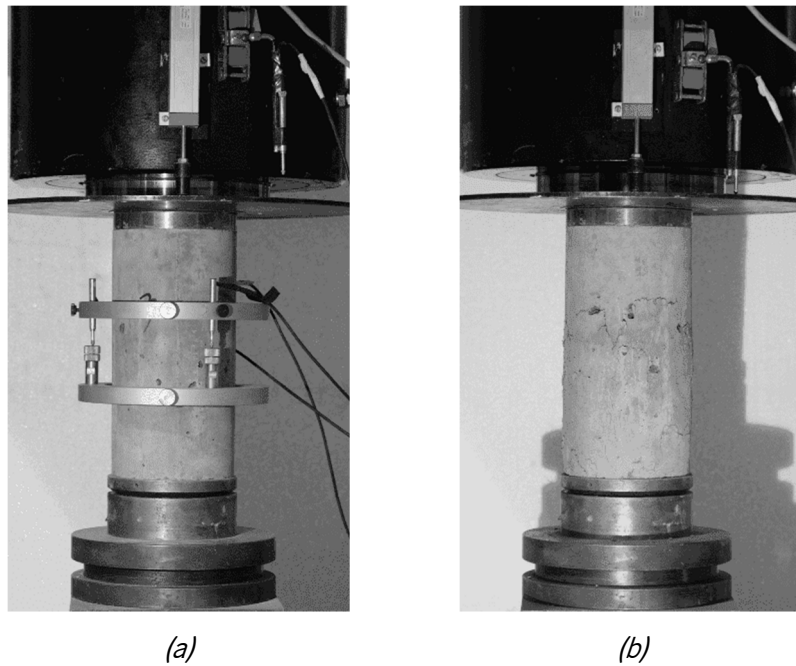


Figure 3.40 – Test configuration for the determination of the:  
 (a) Compressive strength; (b) Modulus of elasticity

### 3.5.2.2 Experimental results

The average  $\sigma_c - \varepsilon_c$  curves obtained from a set of four concrete specimens at each age are depicted in Figure 3.41. In Figure 3.41a are presented the average  $\sigma_c - \varepsilon_c$  curves obtained with the first and sixth RSFRC1% mixtures, RSFRC1%\_1 and RSFRC1%\_6, respectively. In case of RSFRC1%\_6, before the addition of RSF, cylindrical specimens were produced with plain concrete, in order to evaluate its compressive behavior separately. In Figure 3.41b are presented the average  $\sigma_c - \varepsilon_c$  curves obtained with the remaining RSFRC1% mixtures, RSFRC1%\_2 to 5, whose concrete was used in the production of round panels for the tests presented in Chapter 7. In this case, the compressive behavior was evaluated at the same age of conducting round panel tests (38 and 120 days).

Table 3.25 includes the average values and the corresponding coefficients of variation (*CoV*) of the hardened density, the elasticity modulus,  $E_{cm}$ , the compressive strength,  $f_{cm}$ , the strain at peak load,  $\varepsilon_{c1}$ , and the energy dissipated under compression,  $G_c$ , calculated as the area under the stress-strain curve,  $\sigma_c - \varepsilon_c$ , until an ultimate deformation,  $\varepsilon_u$ , of 0.005, where the residual strength was small.

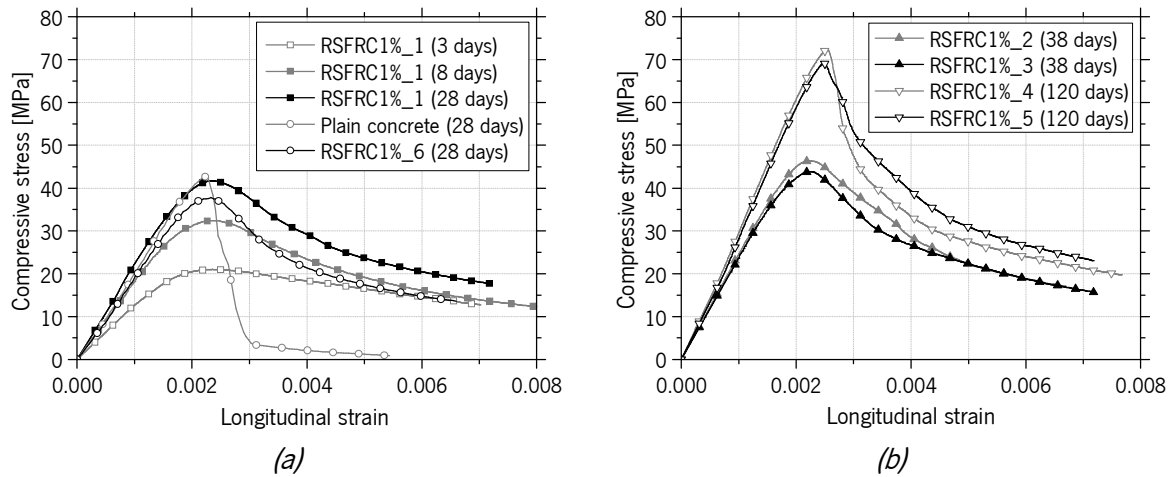


Figure 3.41 – Average Compressive stress-Longitudinal strain curves obtained in compression tests of: (a) RSFRC1%\_1 mixtures (3, 8, 28 days), plain concrete (28 days) and RSFRC1%\_6 mixture (28 days); (b) RSFRC1%\_2&3 mixtures (38 days) and RSFRC1%\_4&5 mixtures (120 days)

Table 3.25 – Average results (and  $CoV$ ) of compression tests

Concrete mixtures	Age (days)	Density (kg/m <sup>3</sup> )	$E_{cm}$ (GPa)	$f_{cm}$ (MPa)	$\epsilon_{c1}$	$G_c$ (MPa)
RSFRC1%_1	3	2300.88 (0.21)	21.22 (0.60)	21.27 (3.97)	0.002 (12.56)	0.08 (1.33)
	8	2290.63 (0.48)	22.63 (3.27)	32.58 (2.24)	0.002 (5.37)	0.11 (3.68)
	28	2297.74 (0.26)	26.76 (6.95)	42.51 (0.13)	0.002 (6.38)	0.14 (5.19)
RSFRC1%_2	38	2318.44 (0.30)	28.14 (12.24)	47.27 (1.35)	0.002 (9.58)	0.15 (4.21)
RSFRC1%_3	38	2285.67 (0.13)	28.94 (0.86)	44.44 (0.94)	0.002 (3.90)	0.14 (6.72)
RSFRC1%_4	120	2335.68 (1.04)	34.68 (8.22)	72.90 (2.41)	0.003 (2.89)	0.19 (10.53)
RSFRC1%_5	120	2330.69 (0.61)	32.74 (4.98)	68.96 (3.37)	0.003 (4.65)	0.20 (5.83)
Plain concrete	28	2241.28 (0.81)	25.76 (3.49)	43.92 (5.57)	0.002 (6.95)	0.07 (14.71)
RSFRC1%_6	28	2269.40 (2.08)	24.31 (10.04)	37.83 (6.78)	0.002 (0.53)	0.12 (5.86)
ISFRC1%	28	2296.01 (0.59)	26.80 (3.11)	48.63 (2.44)	0.002 (2.41)	-

As expected, the  $f_{cm}$  increased with age. At 3 days of age, the energy dissipated by the pull-out of the fibers after crack initiation is only a small part of the energy at older ages, since the bond strength and

the stiffness of the fiber/concrete interface is still relatively low at this age (Cunha, 2010). Throughout the concrete ageing up to 120 days, the increase of the compressive strength caused an increase in the fiber/concrete bond strength and, consequently, an increase in the energy dissipated in the fiber pull-out process ( $G_c$ ). The average values of the strain at peak stress,  $\varepsilon_{c1}$ , slightly increased at 120 days. The values of  $E_{cm}$  also increased with age, except for RSFRC1%\_4 at 120 days of age, where the value was similar to that at 38 days of age, probably due to the high strain values recorded.

A slight decrease of  $E_{cm}$  and  $f_{cm}$  was observed in RSFRC1%\_6 comparing with the control mix (plain concrete). This may have been caused by the heterogeneous fiber geometry in the RSFRC that increase the volume of the interfacial transition zone (ITZ) between fiber and matrix, and may also have increased the void percentage in the matrix. Furthermore, the addition of RSF to concrete caused a reduction in slump of fresh concrete (average slump of 250 mm for plain concrete and 100 mm for RSFRC1%) which affects negatively the compressive strength of concrete. The  $f_{cm}$  of RSFRC1%\_6 was lower than of RSFRC1%\_1 at 28 days, probably due to the higher amount of air voids presented in RSFRC1%\_6, as proved by the lower density determined in hardened state (Table 3.25), and due to the heterogeneous fiber geometry of RSF. However, a significant increase of energy dissipated under compression was provided by the RSF reinforcement in RSFRC1% compared with the corresponding concrete matrix, as proved by the toughness index (ratio between the energy dissipated by the FRC up to a given strain limit, and the energy dissipated by the correspondent plain concrete) of 1.7, obtained with RSFRC1%\_6 mixture up to a strain of 0.005.

A significant increase of  $f_{cm}$  was observed from RSFRC cylinders with 38 days (RSFRC1%\_2&3) to RSFRC cylinders with 120 days (RSFRC1%\_4&5) of age due to the incorporation of fly ash in the concrete mixture. No significant differences were observed between the RSFRC1% mixtures tested at the same age.

In the case of ISF1% concrete mixture, it was not possible to determine  $G_c$  since by mistake the tests were performed under force control, and therefore the  $\sigma_c - \varepsilon_c$  curves obtained with the displacement sensor of the actuator are not comparable with the  $\sigma_c - \varepsilon_c$  curves obtained for RSFRC (Figure 3.41). The average value of  $E_{cm}$  obtained for ISFRC1% was similar than that of RSFRC1%\_1. However, an increase of the  $f_{cm}$  was observed in ISFRC comparing with plain concrete and RSFRC1%\_1, probably due to better fiber distribution in concrete, and consequently mix homogeneity.

In general, low CoV values were obtained for all the evaluated parameters in the compression tests, which

attests the adequate homogeneity of produced concrete.

### 3.5.2.3 Analytical expressions

To estimate the compressive strength and the elasticity modulus of plain concrete at various ages,  $f_{cm}(t)$  and  $E_{ci}(t)$ , respectively, the CEB *fib* Model Code 2010 (MC2010) suggests the following equations:

$$f_{cm}(t) = f_{cm}(28) \cdot \exp \left\{ a \left[ 1 - \left( \frac{28}{t} \right)^b \right] \right\} \quad (3.6)$$

$$E_{ci}(t) = E_{ci}(28) \cdot \left\{ \exp \left[ a \left( 1 - \left( \frac{28}{t} \right)^b \right) \right] \right\}^c \quad (3.7)$$

where  $f_{cm}(28)$  and  $E_{ci}(28)$  are the average compressive strength and the elasticity modulus values at 28 days of age, respectively, while  $a$ ,  $b$  and  $c$  are dimensionless parameters. For plain concrete, the MC2010 suggests  $a = 0.2$  (for a cement class of 42.5 R),  $b = 0.5$  and  $c = 0.5$ . Using the  $f_{cm}(28)$  and  $E_{ci}(28)$  obtained in the tested RSFRC1%\_1 cylinders, the  $f_{cm}(t)/f_{cm}(28)$  and  $E_{ci}(t)/E_{ci}(28)$  functions, evaluated according to the MC2010 proposal, are depicted in Figure 3.42.

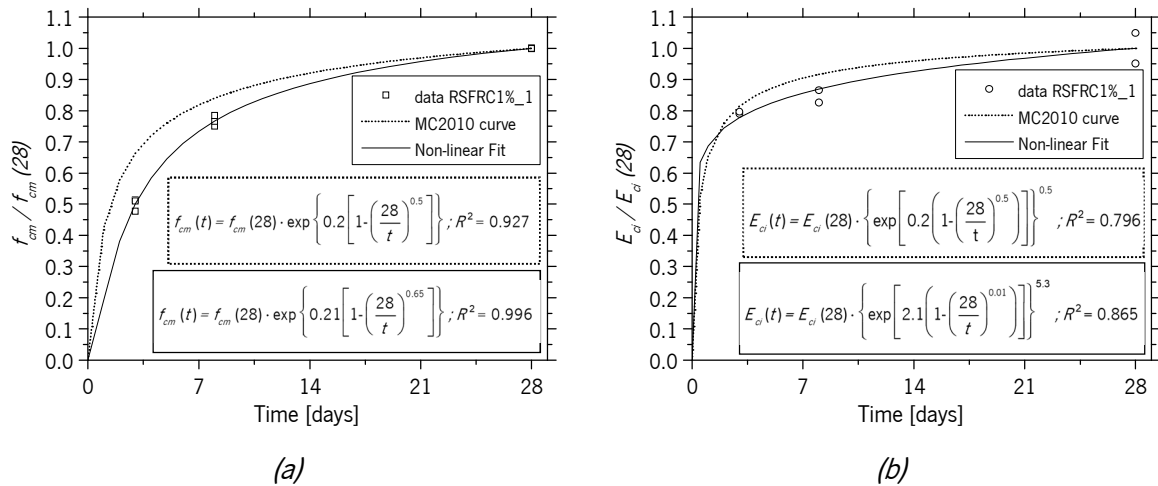


Figure 3.42 – Time dependance of:  
(a) Compressive strength; (b) Elasticity modulus

According to Fig. 3.42a, the obtained correlation factor  $R^2$  is quite high, however, the compressive strength predicted by Eq. (3.6) at the ages of 3 and 8 days is overestimated. Using a non-linear fitting

method, the parameters  $a$  and  $b$  of Eq. (3.6) were determined in order to improve its capability of simulating the time effect on the compressive strength of the developed RSFRC. The degree of the simulation of the fitted curve increased, especially at the ages of 3 and 8 days, as can be seen in Fig. 3.42a.

The elasticity modulus predicted by Eq. (3.7) (Fig. 3.42b) showed also a high correlation factor. This approach overestimates the elasticity modulus at 8 days of age. Fitting the parameters  $a$ ,  $b$  and  $c$  of Eq. (3.6), the accuracy of the fitted curve increased, as showed by the  $R^2$  values indicated in Fig. 3.42b. It is also important to refer that these analytical expressions were obtained by fitting few values of experimental data, which also justifies the high correlation factors obtained.

The MC2010 also proposes an analytical expression to predict the  $\sigma_c - \varepsilon_c$  relationships for plain concrete, given by the following equation:

$$\sigma_c = \left( \frac{k \cdot \eta - \eta^2}{1 + (k - 2) \cdot \eta} \right) \cdot f_{cm} \quad \text{for } \varepsilon_c < \varepsilon_{c,lim} \quad (3.8)$$

where  $\eta = \varepsilon_c / \varepsilon_{c1}$  and  $k = E_{ci} / E_{c1}$ .  $E_{c1}$  is the secant modulus from the origin to the peak compressive stress (Figure 3.43).

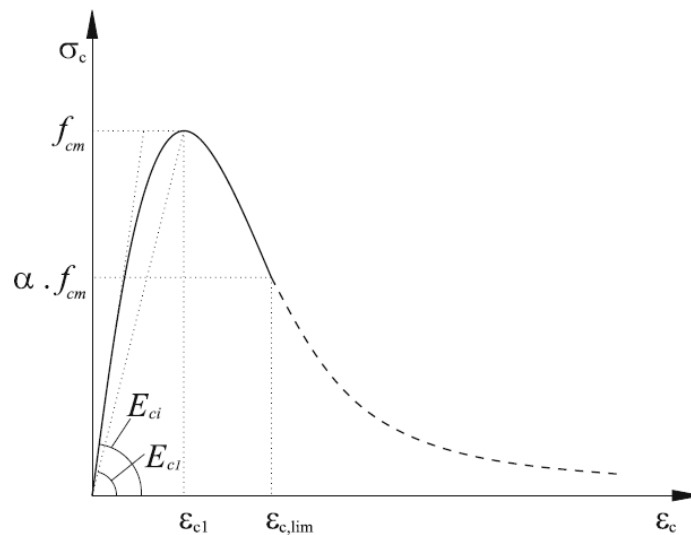


Figure 3.43 – Stress-strain diagram for uniaxial compression (Cunha *et al.*, 2008)



Since the strain  $\varepsilon_{c,lim}$  limits the applicability of Eq. (3.8) (Fig. 3.43), Cunha *et al.* (2008) proposed the following equation to define the descending branch of the  $\sigma_c - \varepsilon_c$  diagram for  $\varepsilon_c > \varepsilon_{c,lim}$ :

$$\sigma_c = \left[ \left[ \frac{1}{\frac{\varepsilon_{c,lim}}{\varepsilon_{c1}}} \xi \cdot \left( \frac{1}{2\alpha} \right)^2 - \frac{1}{\left( \frac{\varepsilon_{c,lim}}{\varepsilon_{c1}} \right)^2} \cdot \frac{1}{\alpha} \right] \left( \frac{\varepsilon_c}{\varepsilon_{c1}} \right)^2 + \left[ \frac{1}{\frac{\varepsilon_{c,lim}}{\varepsilon_{c1}}} \cdot \frac{2}{\alpha} - \xi \cdot \left( \frac{1}{2\alpha} \right)^2 \right] \frac{\varepsilon_c}{\varepsilon_{c1}} \right]^{-1} \cdot f_{cm} \quad \text{for } \varepsilon_c > \varepsilon_{c,lim} \quad (3.9)$$

with

$$\varepsilon_{c,lim} = \left[ \frac{1}{2} \left[ (1 - \alpha) \cdot \frac{E_{ci}}{E_{c1}} + 2\alpha \right] + \left[ \frac{1}{4} \left[ (1 - \alpha) \cdot \frac{E_{ci}}{E_{c1}} + 2\alpha \right]^2 - \alpha \right]^{0.5} \right] \cdot \varepsilon_{c1} \quad (3.10)$$

$$\xi = \frac{4 \left[ \left( \frac{\varepsilon_{c,lim}}{\varepsilon_{c1}} \right)^2 \cdot \left( \frac{E_{ci}}{E_{c1}} - 2 \right) + 2 \frac{\varepsilon_c}{\varepsilon_{c1}} - \frac{E_{ci}}{E_{c1}} \right]}{\left[ \frac{\varepsilon_{c,lim}}{\varepsilon_{c1}} \left( \frac{E_{ci}}{E_{c1}} - 2 \right) + 1 \right]^2} \quad (3.11)$$

In order to evaluate the applicability of the equations (3.8) and (3.9) to obtain the  $\sigma_c - \varepsilon_c$  relationship for RSFRC, the following assumptions were taken in the present research: (a) the experimental values of the elastic modulus,  $E_{ci}$ , compressive strength,  $f_{cm}$  and strain at peak stress,  $\varepsilon_{c1}$ , obtained for RSFRC were used in the analytical simulation; (b) the parameter  $\alpha$  was determined with the exponential function (Eq. (3.12)) proposed by Cunha *et al.* (2008) to estimate the evolution of the parameter  $\alpha$  with the age:

$$\alpha(t) = 0.9 \cdot \exp \left\{ 0.005 \left[ 1 - \left( \frac{28}{t} \right)^{1.16} \right] \right\} \quad (3.12)$$

The analytical stress-strain curves obtained are depicted in Figure 3.44 and are composed by two branches, one for  $\varepsilon_c < \varepsilon_{c,lim}$  (MC2010) and other for  $\varepsilon_c > \varepsilon_{c,lim}$  (Non-linear fit). For comparison purposes, the experimental data obtained with each RSFRC are also represented in these graphs.

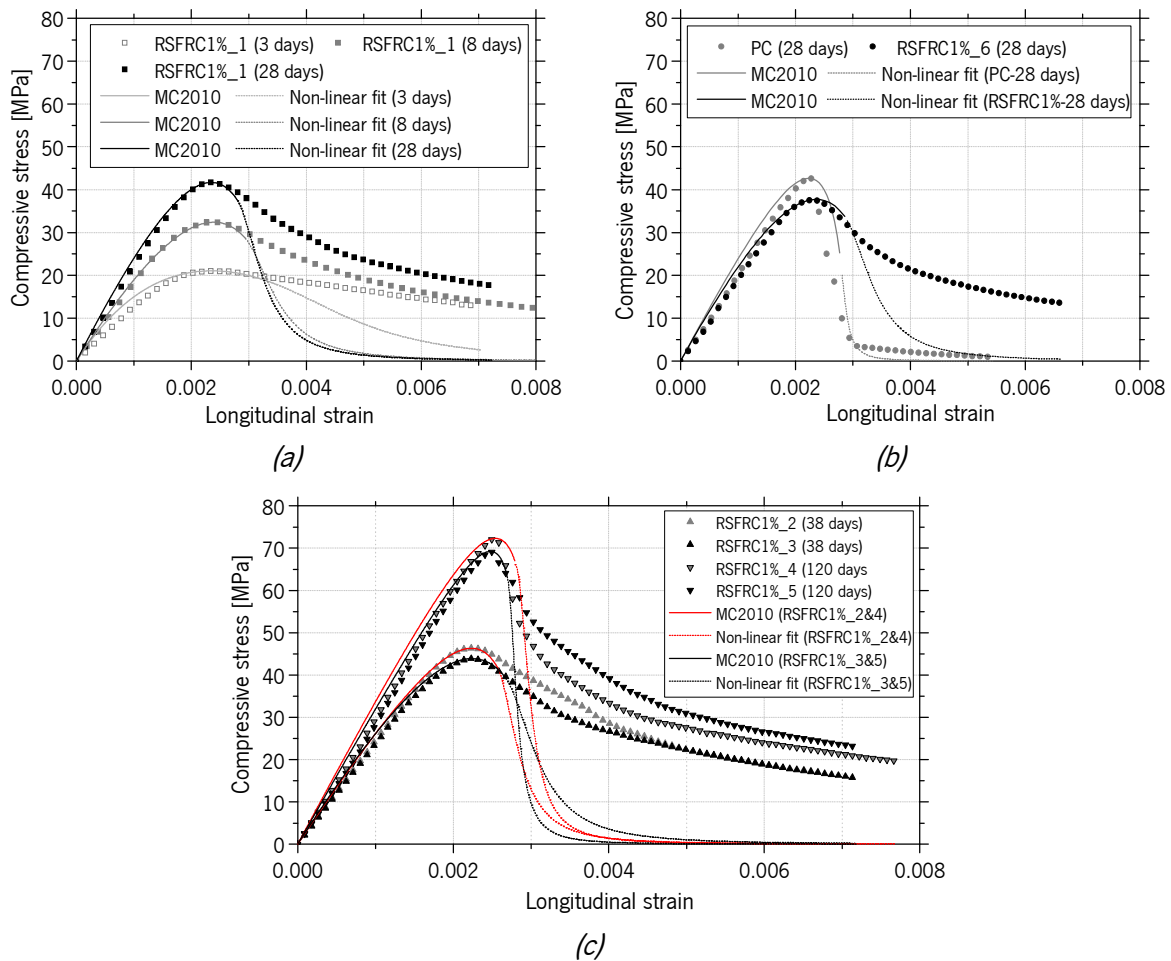


Figure 3.44 – Experimental and analytical (MC2010 & Cunha *et al.*, 2008) relationships for the concrete mixtures: (a) RSFRC1%\_1; (b) PC and RSFRC1%\_6; (c) RSFRC1%\_2 to 5

According to Figure 3.44, the analytical expression proposed by MC 2010 for plain concrete (eq. (3.8)) is appropriated to simulate the pre-peak compressive behavior of RSFRC1%. However, the post-peak phase of compressive behavior of RSFRC1% was underestimated by the non-linear fitting method proposed by Cunha *et al.* (2008) to simulate the compressive strength of Steel Fiber Reinforced Self-Compacting Concrete (SFRSCC).

A second non-linear fit methodology was used to predict the experimental compressive curves of RSFRC1%, based on a law that already proved to be adequate to simulate the uniaxial compressive behavior of FRC, as described in Barros (1995). This law proposed by Mebarkia and Vipulanandan (1992) is defined by the following equation:

$$\sigma_c = f_{cm} \frac{\frac{\varepsilon_c}{\varepsilon_{c1}}}{(1-p-q) + q \left( \frac{\varepsilon_c}{\varepsilon_{c1}} \right) + p \left( \frac{\varepsilon_c}{\varepsilon_{c1}} \right)^{\frac{1-q}{p}}} \quad (3.13)$$

where were considered the experimental values obtained for  $f_{cm}$ ,  $\varepsilon_{c1}$  and  $E_{c1}/E_{ci}$ , and the parameter  $p$  was changed from 0 to 1, to find the  $p$  value that leads to the lowest quadratic deviation,

$$e^2 = \sum_{i=1}^n \left( \frac{\sigma_{ci}^r - \sigma_{ci}^c}{f_{cm}} \right)^2 \quad (3.14)$$

where  $\sigma_{ci}^r$  and  $\sigma_{ci}^c$  are the experimentally recorded stress and the analytical stress determined with the equation (3.13), respectively, and  $n$  is the number of readings recorded in the compression test under analysis. The value of  $p$  must also comply the following conditions:

$$\left. \frac{d\sigma_c}{d\varepsilon_c} \right|_{\varepsilon_c=0} = E_{ci} = \frac{E_{c1}}{1-p-q} \quad (3.15)$$

so that the parameter  $q$  comes as a function of  $p$  and  $E_{c1}/E_{ci}$ , that is:

$$q = 1 - p - \frac{E_{c1}}{E_{ci}} \quad (3.16)$$

$$\frac{d\sigma_c}{d\varepsilon_c} > 0 \quad \text{when} \quad \varepsilon_c < \varepsilon_{c1} \quad (3.17)$$

$$\frac{d\sigma_c}{d\varepsilon_c} = 0 \quad \text{when} \quad \varepsilon_c = \varepsilon_{c1} \quad (3.18)$$

$$\frac{d\sigma_c}{d\varepsilon_c} < 0 \quad \text{when} \quad \varepsilon_c > \varepsilon_{c1} \quad (3.19)$$

$$p+q \in ]0,1[ \quad (3.20)$$

$$\frac{1-q}{p} > 0 \quad (3.21)$$

In Figure 3.45 are depicted the analytical stress-strain curves obtained with the expression (3.13) compared to the adjusted experimental curves. According to these results, the expression (3.13) is more adequate to define simulation laws of uniaxial compressive behavior of RSFRC from experimental responses than those tried before.

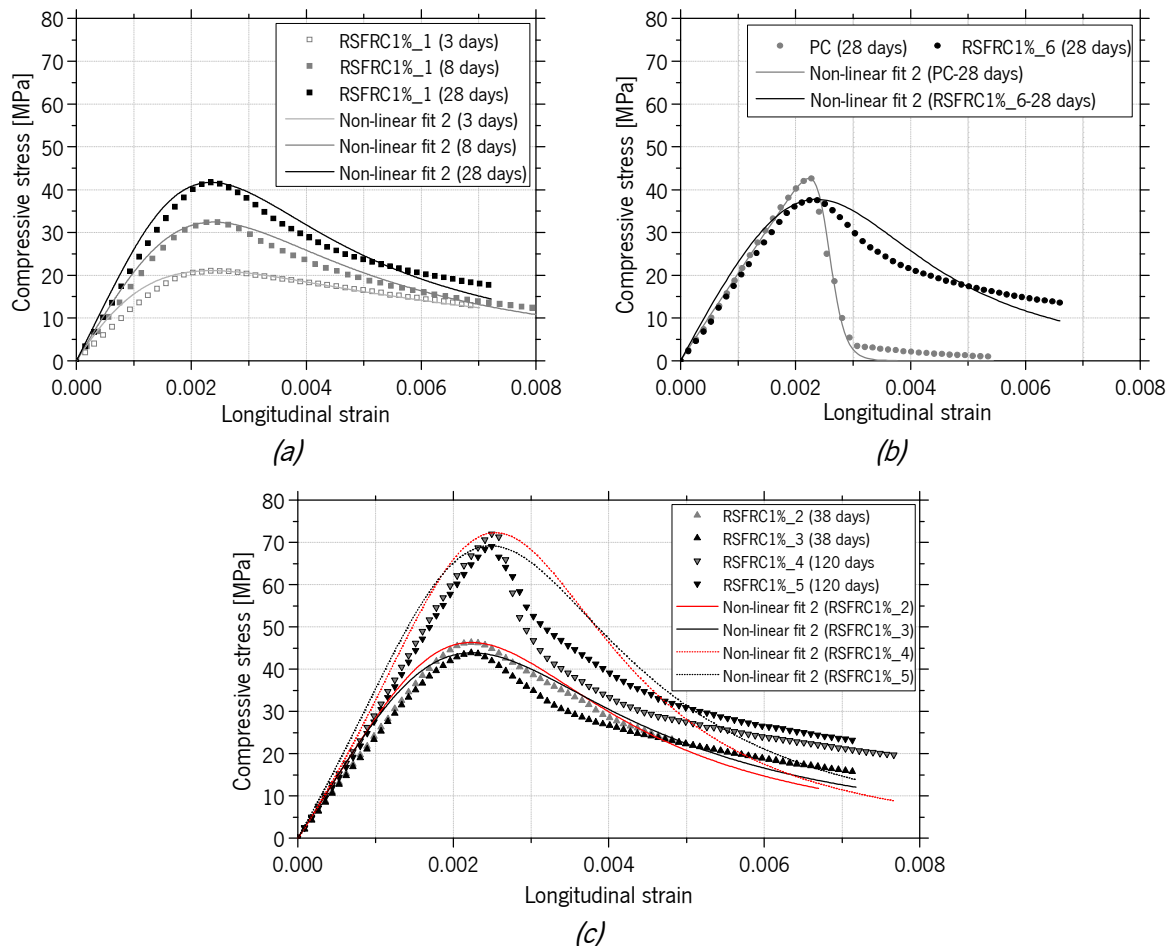


Figure 3.45 – Experimental and analytical (Barros, 1995) relationships for the concrete mixtures: (a) RSFRC1%\_1; (b) PC and RSFRC1%\_6; (c) RSFRC1%\_2 to 5

### 3.6 CONCLUSIONS

In a first part of the present chapter, an experimental work was carried out to characterize the geometry, chemical composition and the mechanical properties of RSF used in the production of RSFRC. Additionally, it was analyzed the influence of the small amount of rubber particles attached to RSF surface in the mechanical properties of RSF and in the concrete-RSF bond behavior. To this end, two distinct pre-treatment methods for rubber removal from RSF surface. In a second part, experimental, numerical and analytical work were performed to characterize the flexural and compressive behavior of RSFRC. From the results presented in this chapter, the following concluding remarks can be highlighted:

- 1) The geometric characterization of RSF pointed to a multimodal distribution of the fiber diameter and a unimodal distribution of the fiber length and aspect ratio. The recycling process used to obtain RSF had a significant contribution for the variability of RSF length. In this case, the RSF used for RSFRC production were quite aligned. The average results obtained in terms of RSF geometry (diameter, length and aspect ratio) and tensile strength are comparable with those obtained by other authors (Aiello *et al.*, 2009; Centonze *et al.*, 2012; Martinelli *et al.*, 2015; Caggiano *et al.*, 2017; Leone *et al.*, 2018).
- 2) When compared to ISF, the RSF showed higher tensile strength and more complex and heterogeneous microstructure. RSF also presented higher hardness and more retained austenite than ISF, due to the higher carbon content. Contrary to what was observed in ISF, the heating of RSF at 350°C slightly increased its hardness, due to the eventual transformation of retained austenite into bainite, which may have a negative effect on ductility.
- 3) Polishing of RSF was the most efficient method for removing the rubber particles from RSF surface, leading to the homogenization of the RSF microstructure and to the increase of the hardness of RSF due to the transformation of the retained austenite into martensite caused by the strain induced by plastic deformation.
- 4) The rubber content attached to the RSF surface can lead to a decrease of the pull-out load if the rubber particles cover a significant area of the fiber surface. However, on average, this amount of rubber is low and, consequently, had a minor effect in the pull-out behavior of RSF from concrete. The fiber shape of the embedded length has a significant influence in the fiber pull-out behavior, since the more irregular and twisted it is, the higher the fiber pull-out load and the greater the probability of fiber rupture, as already reported by other authors (Tlemat *et al.*, 2003a; Aiello *et al.*, 2009; Caggiano *et al.*, 2015; Hu *et al.*, 2018b).
- 5) A more sustainable mix composition of RSFRC (RSFRC1%) was attained by using a packing density optimization method (Pereira, 2006), with a fiber content of 1% in volume and 40% of binder volume replaced by fly ash. This composition was selected as the best performed in terms of mixing homogeneity and mechanical characterization to cast the RSFRC specimens for the experimental tests of Chapters 7 and 8.
- 6) From the 3PNBBTs, it was analyzed the increase of ductility provided by the addition of RSF in plain concrete. The RSFRC1% showed higher flexural capacity and energy absorption than ISFRC1%

for reduced crack width levels corresponding to SLS conditions, and similar reinforcement performance for ULS conditions. In general, the equivalent and residual strength of RSFRC1% had marginal variation after 28 days of age. A linear trend between  $f_{eq,2}$  and  $f_{eq,3}$ ,  $f_{eq,2}$  and  $f_{R,1}$ , and  $f_{eq,3}$  and  $f_{R,4}$  was obtained for all the 3PNBBTs. The agreement between the numerical and the experimental curves was very good for all the RSFRC1% beams, which indicates that the trilinear  $\sigma - \omega$  relationship obtained is capable of simulating the post-cracking behavior of RSFRC1%.

- 7) The effectiveness of RSF as concrete reinforcement was also verified by the increase of toughness observed in the compressive tests. The compressive strength of RSFRC1% increased with the age, specially from 38 days to 120 days due to the incorporation of fly ash. From the analytical study, to predict the compressive stress -strain relationship of RSFRC1%, it was verified that the analytical expression proposed by MC2010 is appropriate to simulate the pre-peak compressive behavior of RSFRC1%. However, the non-linear fitting method proposed by Cunha *et al.* (2008) for SFRSCC underestimated the post-peak compressive behavior of RSFRC1%. The non-linear fit methodology used by Barros (1995) to simulate the uniaxial compressive behavior of FRC showed to be more appropriate to simulate the post-peak compressive behavior of RSFRC1%.

---

# Chapter 4

---

## CHARACTERIZATION OF RSF CORROSION

---

### 4.1 INTRODUCTION

Steel corrosion is a natural phenomenon that involves the gradual destruction of metal by chemical and/or electrochemical reaction with its surrounding environment. The insufficient knowledge on the deterioration mechanisms caused by steel fiber corrosion limits the mobilization of the full potential of Steel Fiber Reinforced Concrete (SFRC) (Solgaard *et al.*, 2010). Steel fibers corrosion displays itself most often in aqueous medium where the corrosive mechanism is essentially electrochemical. This chapter presents the characterization study of the corrosion resistance of Recycled Steel Fibers (RSF) caused by chloride attack, and its relative behavior compared with Industrial Steel Fibers (ISF). To this end, Open Circuit Potential ( $E_{OCP}$ ) measurements, Potentiodynamic Polarization and Linear Polarization Resistance tests, as well as SEM analysis, were carried out. In addition, two experimental programs were carried out to evaluate the mass loss of a single RSF by corrosion after exposure to chloride attack for a certain period of time, and the corrosion effects on the tensile strength of RSF by performing direct tensile tests.

### 4.2 RSF PREPARATION AND ELECTROCHEMICAL CELL

The RSF used for electrochemical tests were selected with similar geometric properties in order to reduce the dispersion of results. The length ( $l_f$ ) of the selected RSF varied between 49 to 63 mm, with an

average diameter of 0.34 mm and an average mass of 0.86 mg/mm. RSF was selected with a higher length than the average of 20 mm, in order to ensure sufficient fiber length immersed in chloride solution. The corrosion resistance of RSF was measured in accordance to the electrochemical methods adopted by Frazão et al. (2016) to assess the corrosion resistance of ISF type 1 (Section 3.2.3.3).

Before testing, the RSF surface must be carefully prepared such that the initial condition of the measurement is well defined and does not vary from test to test. In this context, the fibers were washed with distilled water and ultrasonically cleaned in propanol for 15 minutes to decontaminate the surface of the fibers. The RSF were weighed before and after the electrochemical tests to quantify the loss of fiber mass by corrosion. About half length of the fiber surface, which was not in contact with the chloride solution, was sealed with Lacomit varnish to avoid its corrosion. The remaining length was immersed in the 3.5 wt% NaCl solution. The NaCl concentration was chosen to reflect usual chloride concentrations found in sea water. To perform these electrochemical tests, an electrochemical cell was prepared on a particular RSF/solution system (Figure 4.1). This cell consisted on: the RSF to be investigated (working electrode); the 3.5 wt% NaCl solution; the counter electrode to provide the applied current, which is composed by a highly corrosion resistant material (platinum); the reference electrode (SCE - Saturated Calomel Electrode) that provides a stable reference for measuring the applied potential to the working electrode; the potentiostat/galvanostat (Voltalab, Radiometer Analytical PGZ100) controlled by the software VoltaMaster for monitoring electrochemical tests. The SCE is a mercury electrode covered by a paste of mercurous chloride,  $\text{Hg}_2\text{Cl}_2$ , which is saturated with potassium chloride, KCl, and its potential with respect to the standard hydrogen electrode is equal to +0.242V.

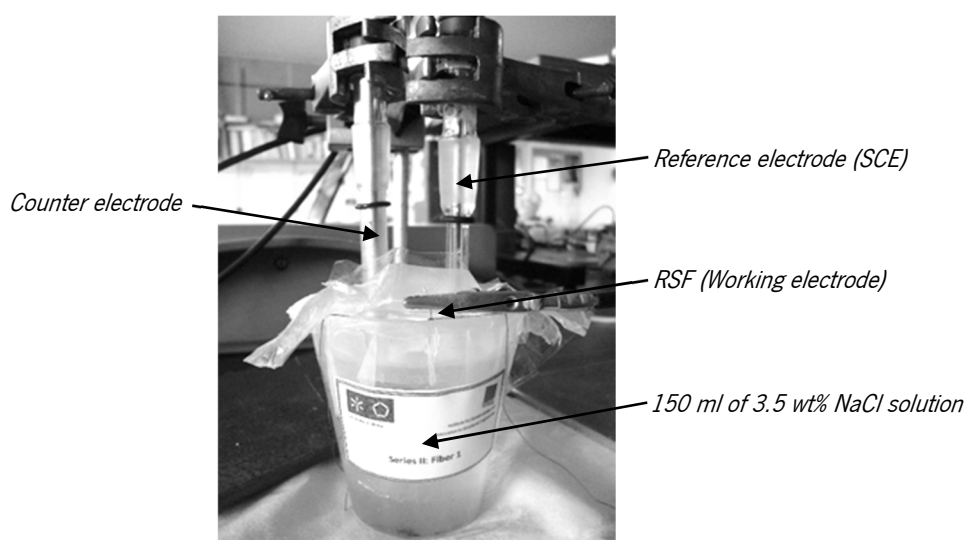


Figure 4.1 – Electrochemical cell prepared on a particular RSF/3.5 wt% NaCl solution system



### 4.3 EXPERIMENTAL PROCEDURES OF ELECTROCHEMICAL TESTS

The  $E_{OCP}$ , which is the equilibrium potential (the equilibrium between oxidation/reduction of a metal in some solution) of the working electrode (RSF) at which there is no current applied to the cell (because the circuit is open), was measured relative to the reference electrode (SCE). The free end of the RSF (out of immersion) and the reference and counter electrodes (after being introduced in the solution) were connected directly to the terminals of the potentiostat in order to measure the potential. The  $E_{OCP}$  was monitored along time, allowing to know the time necessary for its stabilization and corresponds to the corrosion potential. However, the  $E_{OCP}$  is a thermodynamic parameter that indicates the thermodynamic tendency of a metallic material to corrode. For the corrosion process, the kinetics is also important. In order to have a kinetic consideration, the most commonly used technique is potentiodynamic polarization.

A Potentiodynamic Polarization technique was used to generate polarization curves and provide continuous potential at constant speed, starting with a potential in which cathodic reactions predominate (lowest corrosion potential). The counter electrode was properly controlled with the potentiostat, which imposes the desired potential relative to reference electrode and records the polarization current as a function of the potential,  $E$ . The potential was scanned through a potential range about the  $E_{OCP}$  (Enos and Scribner, 1997). The current density,  $i$ , can be expressed as a function of the overpotential,  $\eta$ , where  $\eta = E_{applied} - E_{OCP}$  is obtained from the Tafel equation:

$$\eta = \beta \log \frac{i}{i_0} \quad (4.1)$$

where  $\beta$  is the Tafel slope,  $i$  the applied current density, and  $i_0$  the exchange current density (Enos and Scribner, 1997). The Tafel slope for the anodic and cathodic reactions,  $\beta_a$  and  $\beta_c$ , may be obtained from the linear regions of the polarization curve, as illustrated in Figure 4.2. Once these slopes are established, their interception provides the point of equivalent anodic and cathodic reaction rates (i.e, current densities) (Enos and Scribner, 1997; Wolyneec, 2003). The current density at that point is the corrosion current density ( $i_{corr}$ ) and the potential at which it falls is the corrosion potential ( $E_{corr}$ ) (Figure 4.2).

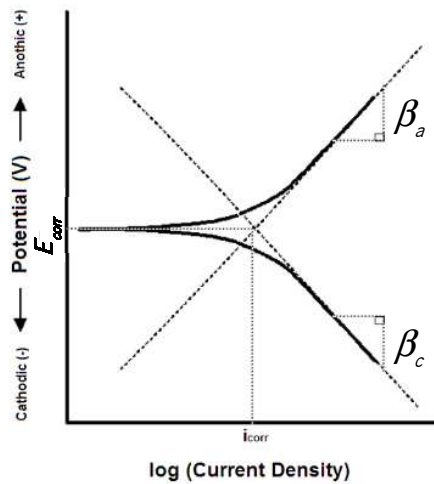


Figure 4.2 – Tafel slope calculation of the polarization curve (Enos and Scribner, 1997)

This test method is also useful to assess the polarization resistance,  $R_p$ , defined by the ratio of the applied potential to the applied current (equation 4.2, ASTM G59-97, 2014) and corresponds to the slope of the experimental curve  $\Delta E$  vs.  $\Delta i$  (remember Ohm's law:  $V = I \times R$ , where  $V$  is the voltage,  $I$  is the current and  $R$  is the resistance) (Figure 4.3).

$$R_p = \left( \frac{\partial \Delta E}{\partial \Delta i} \right)_{\Delta i=0, dE/dt \rightarrow 0} \quad (4.2)$$

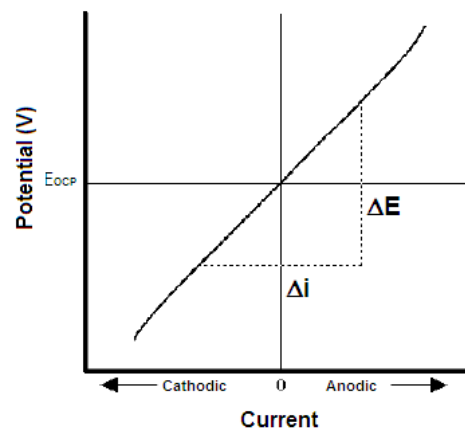


Figure 4.3 – Determination of polarization resistance (Enos and Scribner, 1997)

The polarization resistance is an accurate and rapid way to measure the general corrosion rate. The  $R_p$  indicates the oxidation resistance of a material immersed in an electrolyte and submitted to an external potential. Therefore, a high  $R_p$  indicates that the material has a relatively high resistant to corrosion. The

polarization resistance,  $R_p$  is related to the corrosion current density,  $i_{corr}$ , through the Stern-Geary equation:

$$R_p = 10^6 \frac{\beta_a \beta_c}{2.303 (i_{corr}) (\beta_a + \beta_c)} \quad (4.3)$$

where  $\beta_a$  and  $\beta_c$  are the Tafel slopes illustrated in Figure 4.2. This equation was derived by assuming the anodic and cathodic portions of the total current in the electrochemical system are equal, around the corrosion potential, which means a zero overall current density.

The  $i_{corr}$  ( $\mu\text{A}/\text{cm}^2$ ) may be combined with the Faraday's law and be directly related to the corrosion rate in mpy (milli-inches of penetration per year) through the following equation:

$$\text{Corrosion Rate (mpy)} = \frac{0.13 i_{corr} (E.W.)}{d} \quad (4.4)$$

where  $E.W.$  and  $d$  are the equivalent weight (g) and the density ( $\text{g}/\text{cm}^3$ ) of the corroding species, respectively.

The Potentiodynamic Polarization technique was used at the beginning of these electrochemical tests to rapidly analyze the localized corrosion susceptibility due to the wide range of the scanning potential (Esmailzadeh *et al.*, 2018). The voltage was first increased in the anodic direction and then reversed at some chosen voltage to progress in the cathodic direction up to the starting potential (reverse scan). The sample was immersed for 1 hour to ensure the steady state conditions of the corrosion potential. The corrosion behavior was then predicted from the polarization scan configuration.

Linear polarization resistance was evaluated through a technique that is less intrusive than the potentiodynamic polarization, due to a smaller magnitude of the applied potential. In this technique, the potential was slowly scanned through a potential range of  $\pm 30$  mV of the open circuit potential ( $E_{OCP}$ ), in order to obtain approximately linear current responses. The determination of the  $i_{corr}$  is based on the Stern-Geary equation (4.3). Applying small differences of potential around the  $E_{OCP}$  and measuring the respective currents, it was possible to determine the linear polarization resistance ( $R_p$ ) of the electrode, according to equation (4.2).

Table 4.1 summarizes the tests carried out considering the three RSF classes (Section 3.2.3.2). The tests were divided in ten series that also take into account different periods of chloride immersion, as well as distinct electrochemical procedures. In each series, at least three RSF of the same class were tested under the same conditions.

Table 4.1 – Experimental program of electrochemical tests

Series	RSF	Chloride immersion	Procedure
I	Class 1 (REF)	60 minutes	OCP → Cyclic Polarization
II	Class 3 (Polished)	60 minutes	OCP → Potentiodynamic Polarization
III		7 days	
IV		7 days	
V	Class 1 (REF)	30 minutes	OCP → Linear Polarization
VI		7 days	
VII	Class 2 (350°C)	30 minutes	
VIII		7 days	
IX	Class 3 (Polished)	30 minutes	
X		7 days	

In series I, the class 1 RSF (REF) were immersed in chloride solution and the  $E_{OCP}$  was recorded during 60 minutes before the cyclic potentiodynamic polarization has been implemented. The cyclic polarization tests consisted on a continuous sweep upward and downward potential at a constant rate of 0.6 mV/s, from the cathodic potential -300 mV below the  $E_{OCP}$  up to the anodic potential +250 mV above the  $E_{OCP}$ , and then in the reverse direction, returning to the initial cathodic potential. This cyclic polarization was initially performed in order to identify the type of corrosion attack, i.e., uniform (general) or non-uniform (localized) attack.

In Series II and III, potentiodynamic polarization tests were performed on polished RSF of class 3, after 60 minutes and 7 days of immersion, respectively. In the tests of Series II, a continuous sweep and upward potential was conducted from -300 mV below the value of  $E_{OCP}$  up to 1000 mV, at a constant rate of 0.6 mV/s. After 7 days of immersion, the tests of Series III were similar to those of Series II tests, i.e. the same continuous sweep and upward potential was performed. In this series, the range of continuous sweep and upward potential was reduced, because during the Series II tests the RSF had broken due to the high applied current. Prior to these polarization tests, the  $E_{OCP}$  was recorded for 60 minutes (Series II) and 7 days of immersion (Series III).

The series IV had the purpose of evaluating the weight loss of polished RSF after 7 days of immersion in 3.5 wt% NaCl solution. In this case, RSF were weighed before and after the immersion period.

In series V, VII and IX tests, each RSF class was tested for linear polarization after 30 minutes of immersion in 3.5 wt% NaCl solution, in which  $E_{OCP}$  was first recorded. In these tests, a continuous sweep

upward and downward potential of an amplitude of  $\pm 30$  mV was executed in turn of  $E_{OCF}$ , at a constant rate of 0.1 mV/s. This procedure for linear polarization tests was also adopted in series VI, VIII and X, but after 7 days of immersion (Table 4.1). Prior to these polarization tests and after 7 days of immersion, the  $E_{OCF}$  was recorded for 30 minutes in series VI and VIII. In Series X, the  $E_{OCF}$  was also recorded prior to polarization tests, after the following periods of immersion: 0.5 hours, 24 hours, 48 hours, 3 days, 4 days and 7 days.

This experimental program of electrochemical tests was performed in the Laboratory of Materials located in the Department of Mechanical Engineering of the University of Minho.

After the electrochemical tests, SEM analysis were carried out in some selected fibers to analyze the effect of the corrosion action on their surface, using the same equipment presented in Section 3.2.2.

## 4.4 ELECTROCHEMICAL MEASUREMENTS

### 4.4.1 Open Circuit Potential

The average values of  $E_{OCF}$  during the immersion period of series I, II and X are presented in Figure 4.4.

The values of RSF are compared with those of ISF reported in Frazão *et al.* (2016).

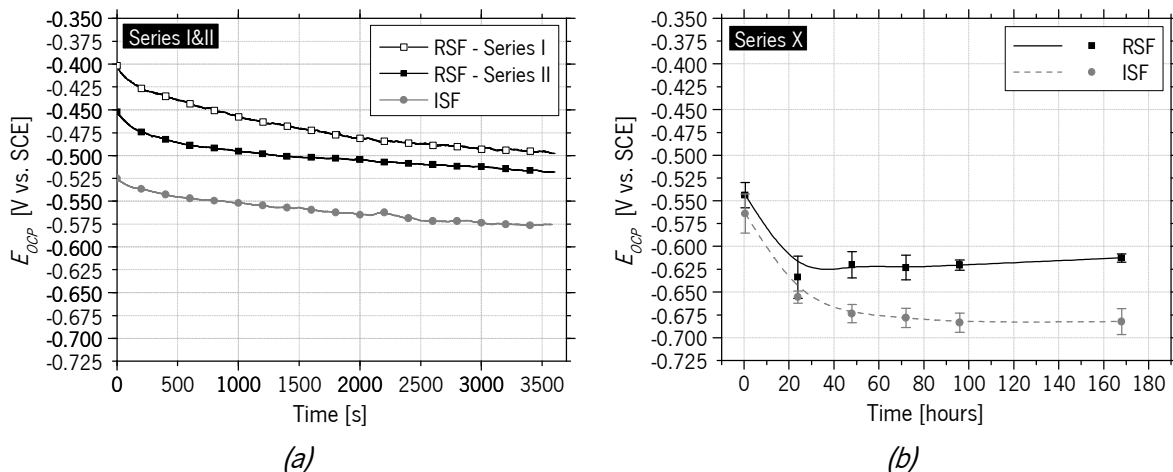


Figure 4.4 – Evolution of  $E_{OCF}$  in RSF over the immersion period of: (a) 60 minutes (Series I&II); (b) 7 days (Series X). Results are compared with those of ISF reported in Frazão *et al.* (2016)

After 60 minutes of chloride immersion, it was found that the  $E_{OCF}$  does not guarantee to be constant, both in RSF and ISF (Fig. 4.4a). In Series X, the  $E_{OCF}$  of RSF and ISF sharply decreased after one day of immersion, indicating an increased tendency of fibers to corrode. Afterwards, the potential of RSF shifted

to the anodic direction and it was not fully stabilized after 7 days of immersion. On the other hand, the  $E_{OCP}$  of ISF fully stabilized after 4 days of immersion.

According to Figures 4.4a,b, it was found that  $E_{OCP}$  decreases by increasing the immersion period of the fibers in 3.5 wt% NaCl solution, which means that both fibers (RSF and ISF) are progressively more prone to corrode. The values of  $E_{OCP}$  recorded for RSF are higher than for ISF, which apparently indicates that RSF are less susceptible to corrode than ISF.

According to the ASTM C876-15 (2015), the probability of reinforcing steel corrosion in concrete is greater than 90% if potential is lower than -0.35 V vs. CSE (corresponding to the potential of the saturated copper-copper sulfate reference electrode - CSE). Following the ASTM G3-89 (Reapproved 1999), as suggested by ASTM C876-15 (2015) for the conversion between reference electrodes, the potential difference between CSE and SCE is +0.06 V, which means that -0.35 V vs. CSE corresponds to -0.29 V vs. SCE. Assuming that this criterion is also valid for steel fibers, as considered in other research studies (Frazão *et al.*, 2016; Aperador-Chaparro *et al.*, 2017), a high probability of corrosion can be concluded for RSF and ISF.

#### 4.4.2 Potentiodynamic Polarization Resistance

Figure 4.5 shows the polarization curves obtained in the cyclic polarization tests performed on three RSF of class 1, after 1 hour of chloride immersion (Series I).

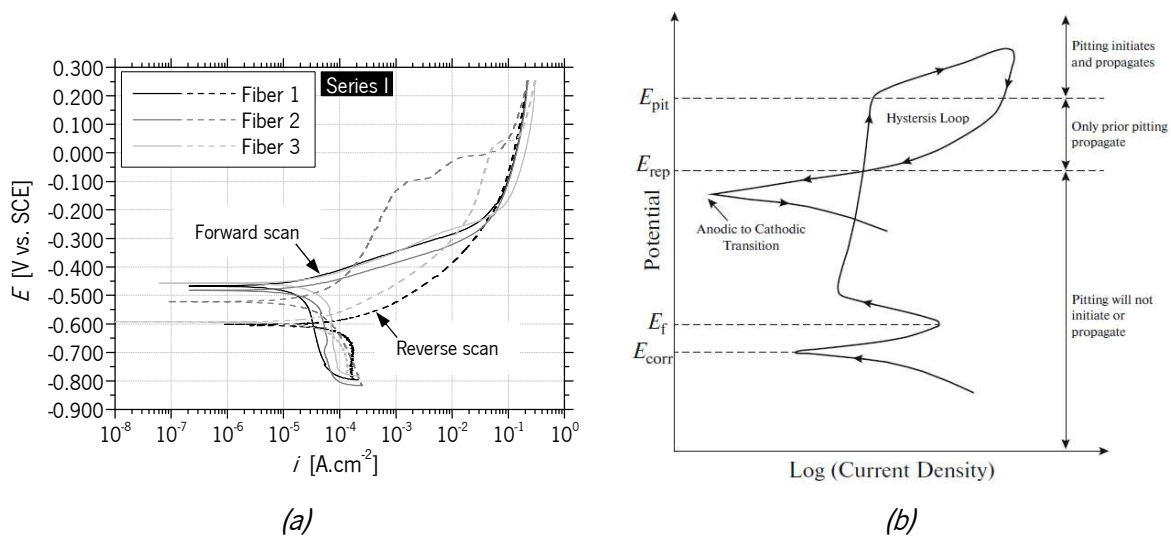


Figure 4.5 – (a) Cyclic polarization curves in three RSF of class 1 – Series I (forward & reverse scan); (b) Schematic illustration of a cyclic potentiodynamic polarization curve of a susceptible material to pitting corrosion (Esmailzadeh *et al.*, 2018)

Small differences were found between the three RSF tested. The obtained curves show no evidence of pitting corrosion since there was no rapid increase in current density with further increase in the potential in the passive region (Figure 4.5b), i.e. complete reversibility of the current during the reverse potential scan of the cyclic polarization curves was found for the NaCl solution (Esmailzadeh *et al.*, 2018; Ma *et al.*, 2019). According to Esmailzadeh *et al.* (2018), which reported a similar cyclic potentiodynamic polarization curve for an Al alloy in 3.5 wt% NaCl at 1 mV/s, the presence of chloride ions in the solution only decreases the stability of the passive film by lowering the breakdown potential (surface potential at which the surface's passive film breaks down) and does not cause pitting corrosion. The reverse scan from the anodic to the cathodic point showed to be more active than the forward scan (greater decrease of the corrosion potential) due to the generalized corrosion in the RSF surface.

Figure 4.6 shows the polarization curves obtained for one fiber in test series II and III comparing with the homologous curves obtained with ISF (Frazão *et al.*, 2016).

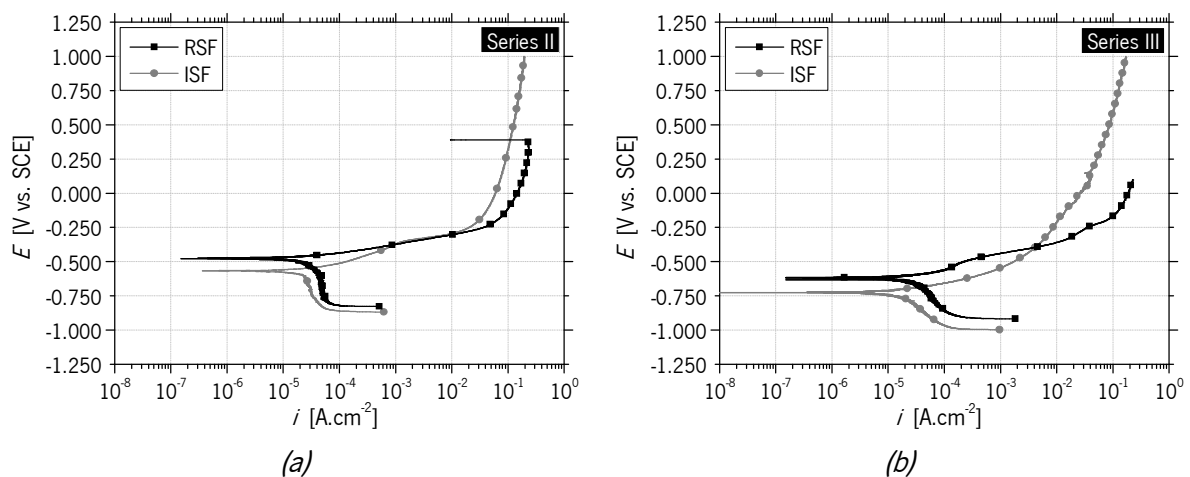


Figure 4.6 – Potentiodynamic polarization curves after the immersion period of: (a) 1 hour (Series II) (b) 7 days (Series III). Results are compared with those of ISF reported in Frazão *et al.* (2016)

In the potentiodynamic experiments, the polarization scan started from cathodic potential (negative potential) and progressed into the anodic direction (positive potential). The cathodic reaction represents the oxygen reduction reaction (depending on the pH and dissolved oxygen concentration in the solution) and the anodic reaction corresponds to metal oxidation (Enos and Scribner, 1997). The intersecting point of the anodic and cathodic polarization curves represents the state of corrosion, namely, the corrosion potential,  $E_{corr}$ , and the corrosion current density,  $i_{corr}$  (Figure 4.2). Due to the reduced diameter of RSF compared with that of ISF, the rupture of RSF occurred during the anodic polarization where the maximum

anode current density was reached (Figure 4.6a;  $E = 391.1$  mV). To avoid this phenomenon, in Series III, the upward potential was limited to up 100 mV.

The polarization curves were examined with Tafel fitting (Eq. (4.1), Figures 4.2 and 4.3) by using the VoltaMaster analysis software to obtain automatically the corrosion parameters, namely, the zero-current potential,  $E_{(i=0)}$  (corrosion potential obtained from potentiodynamic polarization), the corrosion current density,  $i_{corr}$ , and the polarization resistance,  $R_p$ , as presented in Figure 4.7.

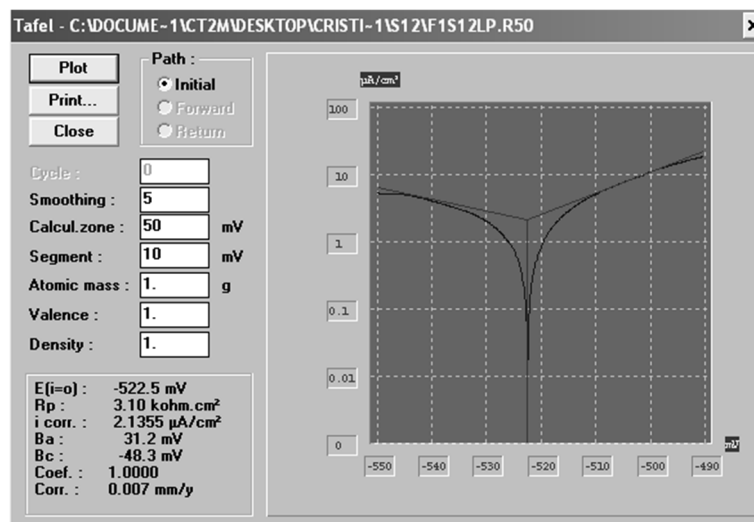


Figure 4.7 – Tafel fitting of the polarization curve using the software VoltaMaster

Table 4.2 summarizes the average values (Avg), standard deviation (StD) and the corresponding coefficients of variation (*CoV*) of the corrosion parameters obtained from the potentiodynamic polarization curves of Series II and III and also the fiber mass loss due to polarization tests.

Table 4.2 – Results obtained in the potentiodynamic polarization tests. Results are compared with those of ISF reported in Frazão *et al.* (2016)

Series	Fibers		$E_{(i=0)}$ (mV)	$i_{corr}$ ( $\mu\text{A}/\text{cm}^2$ )	$R_p$ ( $\text{k}\Omega.\text{cm}^2$ )	Mass loss (%)
II (60 min Cl)	Class 3 RSF (Polished)	Avg±StD <i>CoV</i> (%)	$-477.7 \pm 13.1$ (2.75)	$15.567 \pm 3.430$ (22.03)	$0.646 \pm 0.563$ (87.06)	28.16 (28.63)
	Class 1 ISF type 1 (60 min Cl)	Avg±StD <i>CoV</i> (%)	$-573.5 \pm 7.5$ (1.31)	$10.933 \pm 6.490$ (59.37)	$0.871 \pm 0.255$ (29.29)	26.47 (16.25)
III (7 days Cl)	Class 3 RSF (Polished)	Avg±StD <i>CoV</i> (%)	$-603.8 \pm 17.6$ (2.92)	$13.606 \pm 1.972$ (14.50)	$2.161 \pm 1.795$ (83.09)	-
	Class 1 ISF type 1 (7 days Cl)	Avg±StD <i>CoV</i> (%)	$-711.3 \pm 15.5$ (2.19)	$9.659 \pm 1.082$ (11.20)	$4.011 \pm 2.878$ (71.74)	-



In both Series II and III, the  $E_{(i=0)}$  of RSF was higher than that of ISF, as also shown for  $E_{OCP}$  in Figure 4.4. However, RSF presented relatively higher corrosion rates than ISF, because they showed higher values of  $i_{corr}$  and lower values of  $R_p$  (Table 4.2). These two results are apparently contradictory, but they could be explained if differences in the cathodic reaction are assumed, related to the different composition of the fibers (Freire *et al.*, 2008), and/or as a result of the formation of corrosion products (Wang *et al.*, 2010). It seems that the chemical composition of RSF surface, in particular the Cu species (5.41%, Table 3.9) and/or the formation of rust layers, could have some influence on the slightly lower corrosion susceptibility in RSF (Freire *et al.*, 2008; Wang *et al.*, 2010). Those Cu species could have participated through a parallel cathodic reaction that shifts the corrosion potential in the anodic direction, resulting in more anodic  $E_{(i=0)}$  (Freire *et al.*, 2008). In addition, the reduced diameter of RSF associated with the higher specific surface area of RSF in contact with the chloride solution (1.24 mm<sup>2</sup>/mg) comparing with ISF (0.55 mm<sup>2</sup>/mg), may conduct to higher corrosion rates.

Regardless of the type of fiber (RSF or ISF), the coefficients of variation of some potentiodynamic polarization parameters were very high, being difficult to interpret the results (Table 4.2). Therefore, it was decided to further perform linear polarization tests, which implied lower mass loss and, consequently, lower variability (Wolyneć, 2003). In fact, this test may provide more precise results, since they are carried out within a smaller range of potential sweep and at a lower scan speed, in order to obtain the current response as linear as possible. These experiments are significantly less destructive and provide a more realistic assessment of the corrosion rate (Wolyneć, 2003).

#### 4.4.3 Linear Polarization Resistance

Figure 4.8 shows the polarization curves obtained for one fiber in test series IX and X comparing with the homologous curves obtained with ISF (Frazão *et al.*, 2016). The RSF of class 3 are more appropriate to compare with ISF because the polished RSF showed the most uniform RSF surface (Figure 3.15), similar to ISF type 1 (Figure 3.16).

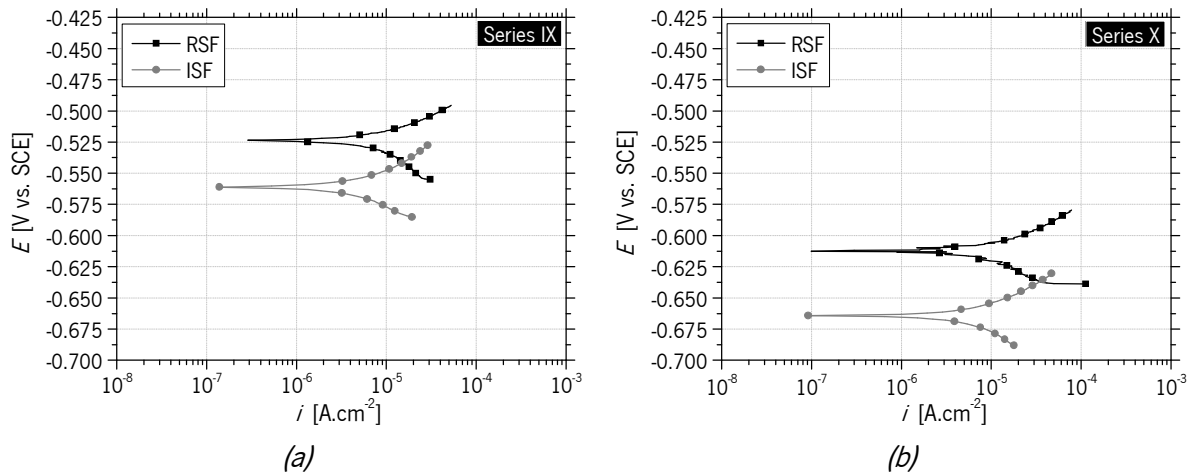


Figure 4.8 – Linear polarization curves after the immersion period of: (a) 30 minutes (Series IX) (b) 7 days (Series X). Results are compared with those for ISF reported in Frazão *et al.* (2016)

Table 4.3 shows the values of  $E_{(i=0)}$ ,  $i_{corr}$  and  $R_p$  obtained in linear polarization tests from Series V to X. As found for ISF (Frazão *et al.*, 2016), the values of  $i_{corr}$  were greater than  $0.2 \mu\text{A}/\text{cm}^2$  and hence, according to the literature (Alonso and Andrade, 1990; González *et al.*, 2004), all RSF classes evidenced high risk of corrosion. In addition, the high risk of corrosion is confirmed by the fairly low values of  $R_p$ . From the linear polarization technique, it was also found that the obtained values of  $i_{corr}$  did not vary significantly with the immersion time. Smaller values of  $CoI$  were obtained in the linear polarization tests when compared to potentiodynamic polarization tests.

As found in potentiodynamic tests, RSF exhibited higher  $i_{corr}$ , showing higher corrosion susceptibility than ISF (Figure 4.8). Taking into account the obtained values of  $i_{corr}$  from the linear polarization, the corrosion rates in mpy were directly determined by the Faraday's Law (Eq. (4.4)). It was found that the level of corrosion in RSF has varied between 3.27 and 5.98 mpy (0.08-0.15 mm/year) under these extreme environmental conditions, which are not representative of the real exposure of the fibers embedded in concrete. These values are of the same order of those found by Ismail *et al.* (2010) in conventional 20 mm-diameter steel bar used for concrete reinforcement, in which the corrosion rate obtained in similar conditions was 2.99 mpy. The level of corrosion obtained in RSF is also within the range of corrosion rate for carbon steel determined in similar test conditions by other authors (Salamci *et al.*, 2017; Yang *et al.*, 2018). The RSF showed similar performance regardless of their class, which means that the pre-treatment had little influence on the corrosion behavior of RSF. Therefore, the results suggest that the removal of the small amount of rubber debris from the fibers surface does not significantly affect the corrosion resistance of RSF.

Table 4.3 – Results obtained in the linear polarization tests

Series	Fibers		$E_{(i=0)}$ (mV)	$i_{corr}$ ( $\mu\text{A}/\text{cm}^2$ )	$R_p$ ( $\text{k}\Omega.\text{cm}^2$ )	Mass loss (%)	Corrosion rate (mpy)
V (30 min Cl)	Class 1 RSF (REF)	Avg $\pm$ StD CoV (%)	-523.6 $\pm$ 4.6 (0.88)	8.679 $\pm$ 1.764 (20.33)	0.609 $\pm$ 0.030 (4.98)	1.63 (60.25)	4.009 $\pm$ 0.815 (20.33)
VII (30 min Cl)	Class 2 RSF (350°C)	Avg $\pm$ StD CoV (%)	-465.0 $\pm$ 17.0 (3.65)	12.937 $\pm$ 1.477 (11.42)	0.683 $\pm$ 0.153 (22.45)	1.39 (54.20)	5.975 $\pm$ 0.682 (11.42)
IX (30 min Cl)	Class 3 RSF (Polished)	Avg $\pm$ StD CoV (%)	-493.8 $\pm$ 22.5 (4.55)	7.077 $\pm$ 1.751 (24.74)	0.778 $\pm$ 0.104 (13.43)	0.48 (35.76)	3.268 $\pm$ 0.809 (24.74)
	Class 1 ISF type 1 (30 min Cl)	Avg $\pm$ StD CoV (%)	-566.5 $\pm$ 4.5 (0.80)	3.738 $\pm$ 0.627 (16.77)	1.383 $\pm$ 0.123 (8.93)	0.50 (20.99)	1.727 $\pm$ 0.290 (16.77)
VI (7 days Cl)	Class 1 RSF (REF)	Avg $\pm$ StD CoV (%)	-631.1 $\pm$ 2.2 (0.35)	8.043 $\pm$ 1.969 (24.48)	1.210 $\pm$ 0.270 (22.32)	3.32 (33.82)	3.715 $\pm$ 0.909 (24.48)
VIII (7 days Cl)	Class 2 RSF (350°C)	Avg $\pm$ StD CoV (%)	-605.8 $\pm$ 32.8 (5.42)	7.998 $\pm$ 2.746 (34.34)	1.304 $\pm$ 0.488 (37.38)	2.47 (55.08)	3.694 $\pm$ 1.268 (34.34)
X (7 days Cl)	Class 3 RSF (Polished)	Avg $\pm$ StD CoV (%)	-609.1 $\pm$ 3.8 (0.63)	11.198 $\pm$ 3.298 (29.45)	0.548 $\pm$ 0.162 (29.52)	4.27 (19.92)	5.172 $\pm$ 1.523 (29.45)
	Class 1 ISF type 1 (7 days Cl)	Avg $\pm$ StD CoV (%)	-677.5 $\pm$ 21.7 (3.20)	3.677 $\pm$ 0.995 (27.06)	1.207 $\pm$ 0.047 (3.88)	0.69 (32.79)	1.698 $\pm$ 0.398 (23.43)

It is worth to mention that it was very difficult to perform the electrochemical tests with the RSF of class 1 and 2, due to the non-uniformity of the fiber surface comparing with that of RSF of class 3 (as shown in SEM micrographs of Figures 3.2c and 3.14a). In this case, only fibers of type F3, F4 and F5 in Figure 3.22 could be tested. Therefore, no accurate conclusions can be drawn regarding the effect of high amounts of rubber debris in the corrosion behavior of RSF.

Regarding the tests of Series IV, the average mass loss that occurred in RSF due to non-induced corrosion was 3.54% ( $CoV = 59.86\%$ ), that is much higher than that of ISF, which was only 0.34% ( $CoV = 27.26\%$ ). According to the values of  $CoV$ , a much higher dispersion of the results was also obtained for RSF than for ISF due to all the aspects already mentioned, namely, the irregular geometry and the non-uniform surface caused by the attached rubber debris. Nevertheless, the difference of mass loss between RSF and ISF, obtained after 7 days of chloride immersion (Series IV) and after the linear polarization tests (Table 4.3 – Series X for RSF), corroborates the results of  $i_{corr}$  determined for these types of fibers.

The mass loss of RSF was larger in Series II due to the greater severity of the destructive potentiodynamic polarization test, where the applied potentials induced higher corrosion rates. In the linear polarization tests, the mass loss of RSF was similar between the different test Series for the same immersion time. In

general, it was found a good correlation between the corrosion current density,  $i_{corr}$ , and the percentage of mass loss, which shows the validity of these tests. The RSF showed a greater increase of mass loss with the chloride immersion than ISF, except for Series IX where the mass loss was lower than expected, probably due to a higher initial adhesion of the corrosion products to RSF, which after 7 days of immersion was not observed. This greater increase of mass loss observed for RSF can be explained by the higher specific surface area of RSF in contact with the chloride solution ( $1.24 \text{ mm}^2/\text{mg}$ ) comparing with ISF ( $0.55 \text{ mm}^2/\text{mg}$ ), and the higher carbon content of RSF, since an increase in the carbon content of steel up to a given level increases the corrosion rate (Feilong *et al.*, 2014).

#### 4.4.4 SEM Fiber Analysis

After the performed tests, SEM analysis were carried out in some fibers to analyze the influence of corrosion in terms of surface configuration. SEM micrographs of corroded polished RSF are shown in Figures 4.9 and 4.10. It is found that the corrosion of RSF is generalized, forming a homogeneous layer of iron oxides in their surface. The presence of corrosion products, along with the significant reduction of the fiber diameter (Figures 4.9 and 4.10a), proves the severe damage produced in the RSF after the potentiodynamic polarization test (Series II).

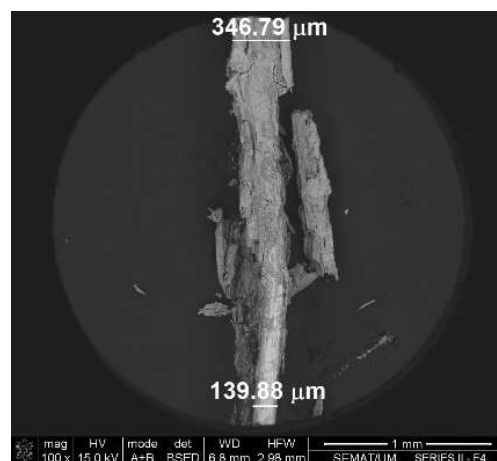


Figure 4.9 – SEM micrographs of the surface of one corroded polished RSF after potentiodynamic polarization (Series II). Magnification: 100x

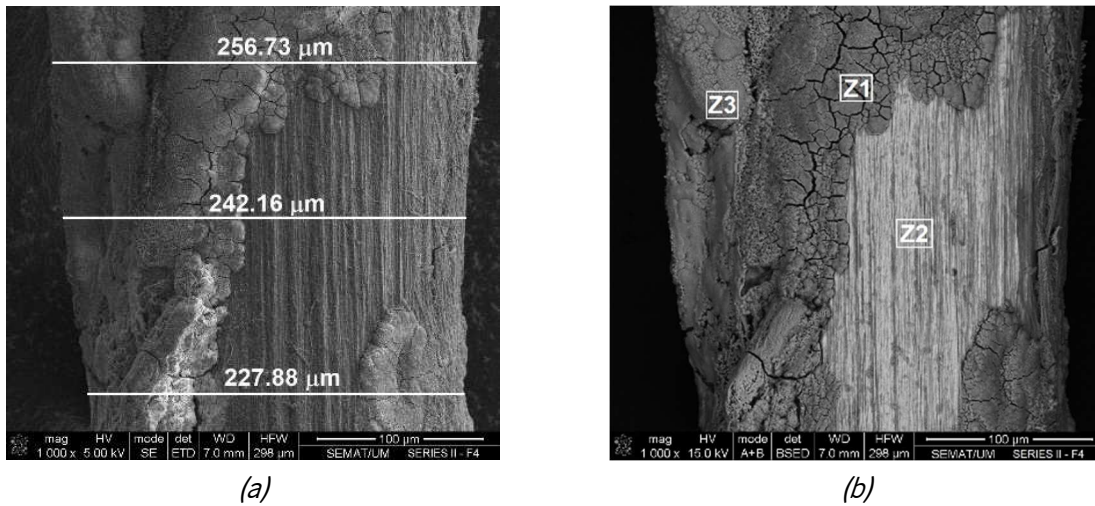


Figure 4.10 – SEM micrographs of the surface of one corroded polished RSF after potentiodynamic polarization (Series II). Magnification: (a) 1000x; (b) 1000x (atomic contrast by backscattered electrons of chemical elements)

After 7 days of chloride immersion and before performing polarization tests, the presence of corrosion products is also remarkable, confirmed throughout the rough, irregular and porous appearance of RSF surface (Figure 4.11), which is in accordance with the high corrosion probability pointed out by the ASTM C876-15 (2015). The appearance of RSF after linear polarization tests revealed the greater progress of corrosion phenomenon after longer periods of chloride immersion (7 days), as observed by the release of the accumulated products (Figure 4.12c).

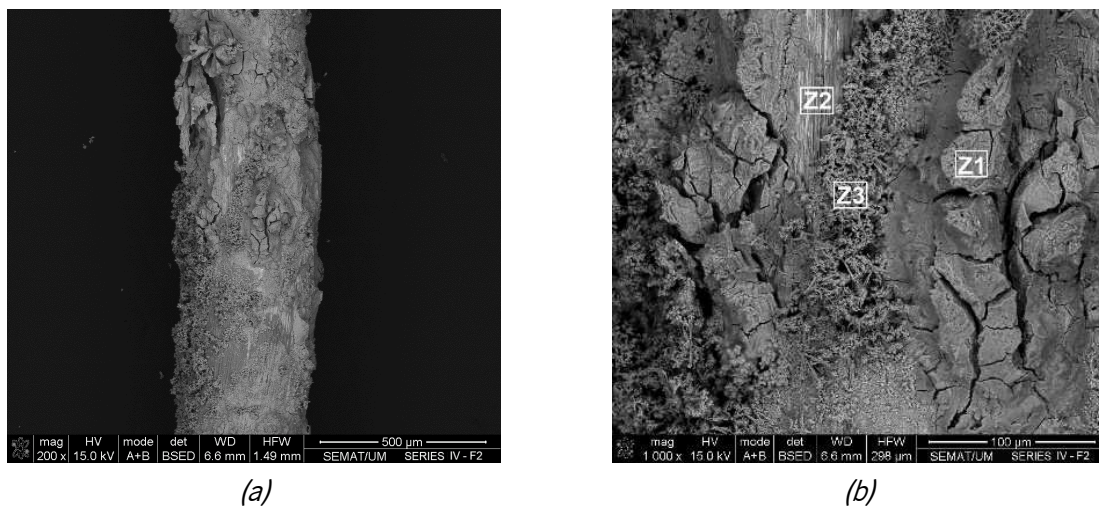


Figure 4.11 – SEM micrographs of the surface of one corroded polished RSF after: Chloride immersion (Series IV): Magnification: (a) 200x (b) 1000x

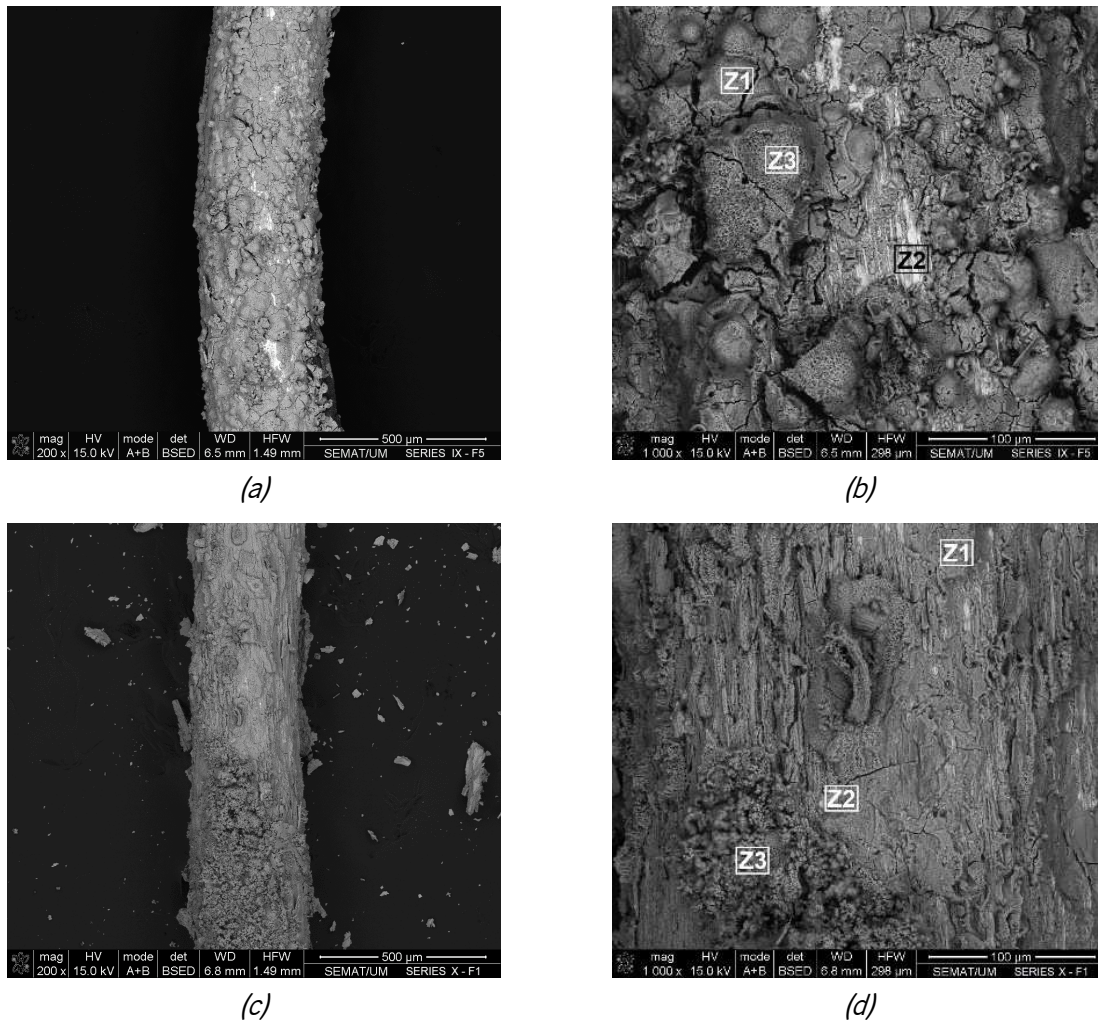


Figure 4.12 – SEM micrographs of the surface of one corroded polished RSF after:  
 Linear polarization (Series IX): Magnification: (a) 200x (b) 1000x  
 Linear polarization (Series X): Magnification: (c) 200x (d) 1000x

Figures 4.10b, 4.11b and 4.12b,d evidence the atomic contrast by backscattered electrons of chemical elements presented in the corrosive products. Through these micrographs, a chemical analysis (SEM-EDS) was carried out to identify the main chemical elements present in the identified zones. The chemical composition obtained in these localized zones are presented in Table 4.4.

The main chemical elements resulted from the corrosion process were carbon, C, oxygen, O, and iron, Fe, and when combined formed higher concentration of iron oxides, as observed in Z1 and Z3 zones. A lower concentration of corrosion products was observed in Z2 zones, associated to a lower content of oxygen.

It was also remarkable the presence of Cu and Zn elements in the RSF not subjected to polarization, as identified in non-corroded RSF (Section 3.2.2), which should be related with the brass coating deposited to increase the bonding steel/rubber in tires. These elements were almost inexistent in the polarized RSF

(Table 4.4) due to the significant formation of corrosion products that removed the brass coating from the RSF surface.

Table 4.4 – Chemical elements identified in the surface of polished RSF tested

Fiber	Zone	Chemical elements (atomic percentage %)						
		C	Fe	O	Cu	Zn	Na	Cl
F4 Series II	Z1	12.25	30.82	53.29	-	-	3.64	-
	Z2	23.98	48.01	23.25	-	-	3.86	-
	Z3	12.08	30.02	53.07	-	-	-	4.83
F2 Series IV	Z1	18.25	27.46	47.13	1.99	0.83	3.41	0.43
	Z2	32.12	57.40	7.11	2.59	0.77	-	-
	Z3	27.31	32.29	32.83	2.53	1.96	2.61	-
F5 Series IX	Z1	22.89	27.18	49.93	-	-	-	-
	Z2	19.84	28.59	38.18	8.21	3.78	-	-
	Z3	32.61	19.07	47.24	-	-	-	1.09
F1 Series X	Z1	8.93	28.18	60.02	-	-	2.58	0.29
	Z2	12.48	51.91	30.48	-	-	4.66	-
	Z3	24.14	33.50	34.67	1.01	0.82	3.99	-

## 4.5 CORROSION RATE AND ITS EFFECT ON THE MECHANICAL PROPERTIES OF RSF

To complement the characterization study of the corrosion resistance of RSF caused by chloride attack, two experimental campaigns were carried out with single RSF to evaluate the mass loss of RSF by corrosion, after immersion in a 3.5 wt% NaCl solution for a certain period. In addition, the corrosion effects on the tensile strength of RSF were also assessed by means of direct tensile tests.

### 4.5.1 Evaluation of RSF mass loss by corrosion

In this experimental program (1), single class 1 RSF were submitted to chloride attack by exposure in 150 ml of 3.5 wt% NaCl solution to induce RSF corrosion. The adopted period for chloride exposure was 3 months and two different exposure conditions were considered: continuous immersion and dry-wet cycles of 3 days wetting and 4 days drying. In order to simulate the exposure of RSF in a concrete crack with 1 and 0.5 mm, some fibers were painted with lacomit varnish to avoid its corrosion, except for a fiber length of 1 and 0.5 mm, located at half-length of RSF. For comparison purposes, RSF were also exposed with their total length. This is a simplified test, because corrosion does not occur in the concrete environment and the fiber is not tensioned. In this case, it is assumed that the concrete crack is sufficiently wide to neglect the beneficial effect of concrete pore solution. Table 4.5 summarizes the exposure

conditions of RSF adopted for the tests that were divided in six series. In each series, three RSF were tested under the same conditions. The mass loss of RSF was evaluated over the exposure period by using a balance with 0.001 g of precision.

Table 4.5 – Experimental program to evaluate the RSF mass loss by corrosion

Series	Chloride exposure	Exposed RSF length
I	Continuous immersion	Total length
II		1 mm
III		0.5 mm
IV	Dry-wet cycles	Total length
V		1 mm
VI		0.5 mm

The evolution of RSF mass loss over the exposure period, assessed in the six series of tests, is depicted in Figures 4.13, 4.14 and 4.15.

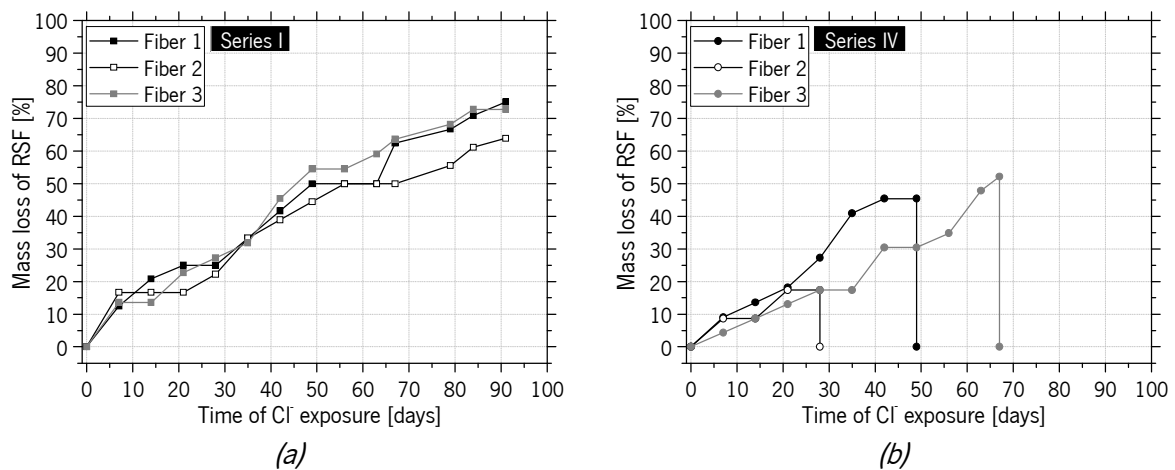


Figure 4.13 – Evolution of RSF mass loss under chloride exposure of its total length:  
(a) Series I; (b) Series IV

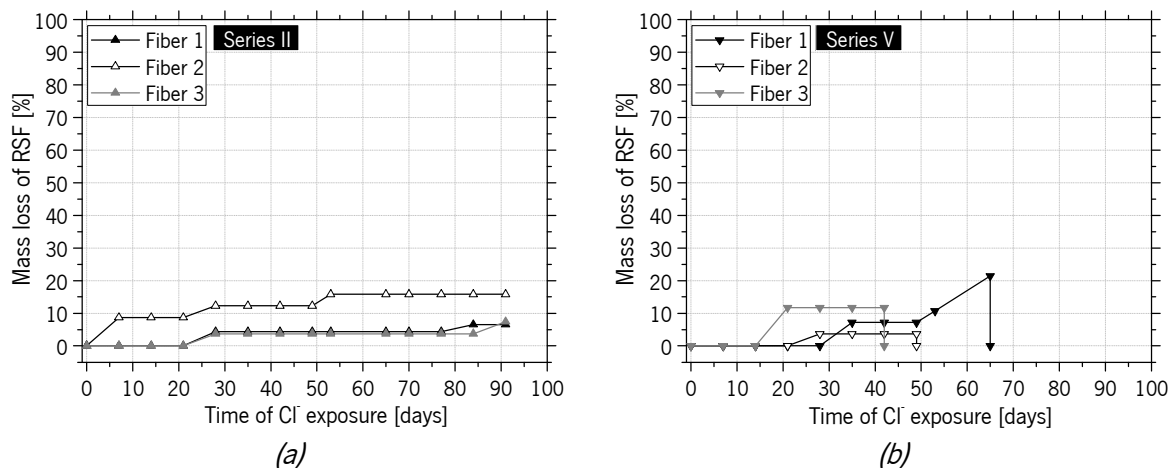


Figure 4.14 – Evolution of mass loss of RSF under chloride exposure of 1 mm of its length:  
(a) Series II; (b) Series V



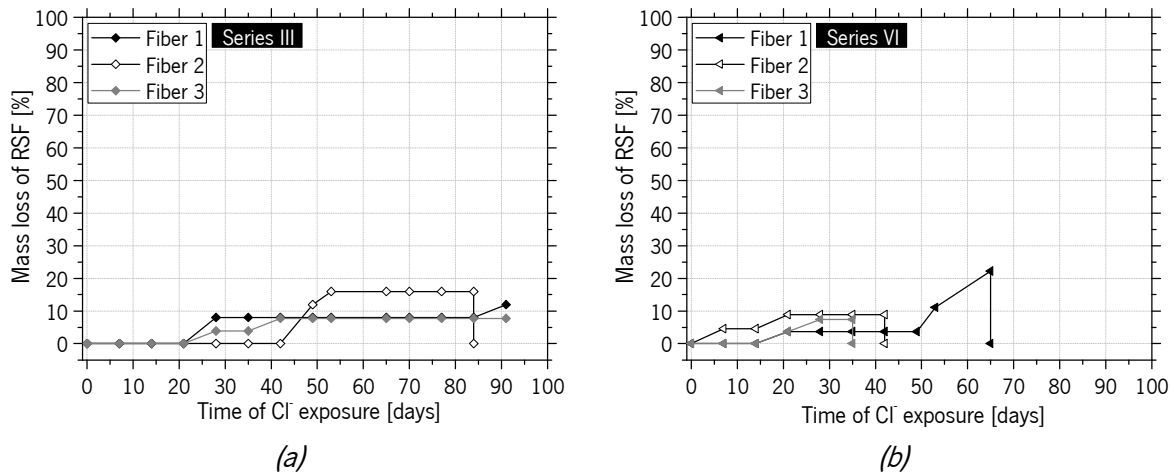


Figure 4.15 – Evolution of mass loss of RSF under chloride exposure of 0.5 mm of its length:  
(a) Series III; (b) Series VI

The corrosion progress of one RSF of each test series during the chloride immersion can be visually observed in the pictures presented in Appendix B.

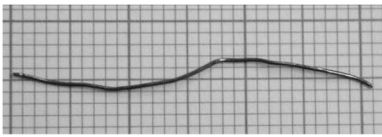
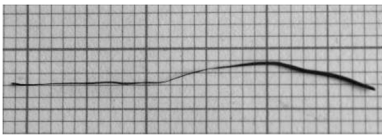
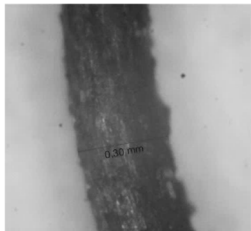
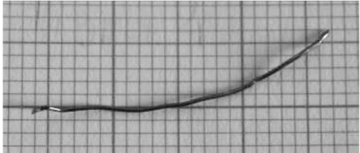
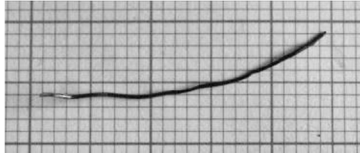
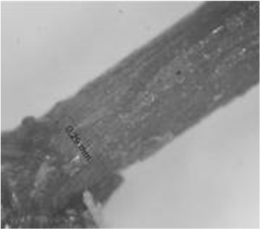
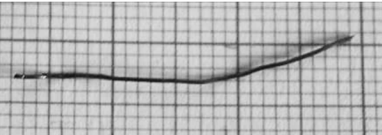
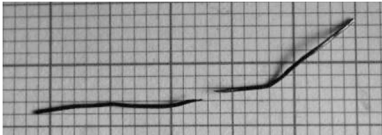
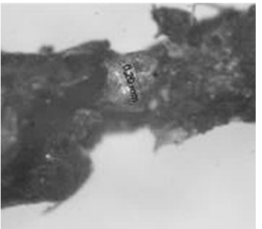
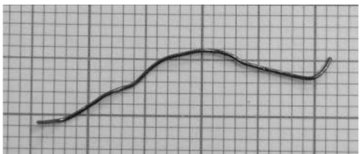
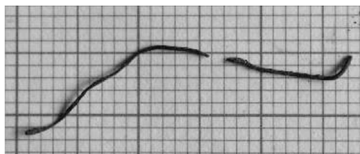
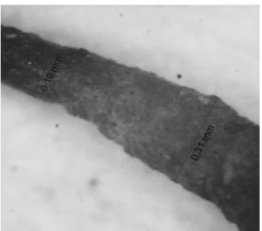
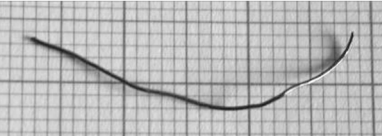
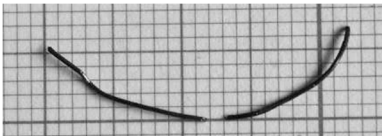
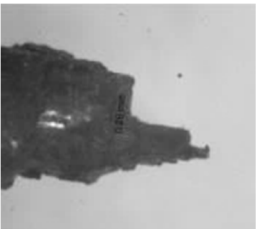
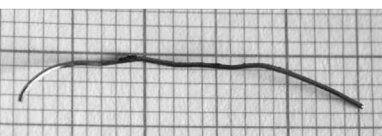
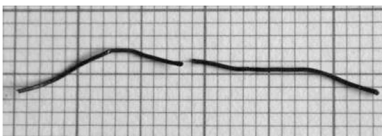
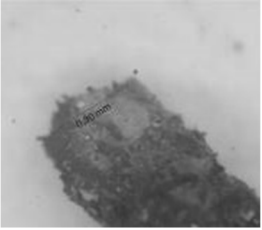
In Table 4.6 are presented the average results obtained in these tests, namely, the exposed fiber length to chloride immersion, the diameters measured before and after chloride exposure, the RSF weight before and after chloride immersion, and the corresponding mass loss of RSF per unit length of exposed fiber. In addition, the exposure period of RSF to chloride attack is indicated in Table 4.6 since some fibers, especially those submitted to dry-wet cycles, ruptured during the exposure period, not completing the three months of chloride exposure, as observed in Figures 4.13b, 4.14b and 4.15b.

Table 4.6 – Relevant results of tests to evaluate RSF mass loss by corrosion

Series		Exposed fiber length (mm)	RSF Diameter (mm)		RSF Mass (g)		Mass loss (mg/mm)	Time of Cl <sup>-</sup> exposure (days)
			Before Cl <sup>-</sup>	After Cl <sup>-</sup>	Before Cl <sup>-</sup>	After Cl <sup>-</sup>		
I	Avg	28.89	0.36	0.24	0.021	0.006	0.52	91
	CoV (%)	(11.49)	(1.41)	(4.17)	(14.32)	(4.68)	(11.82)	(0.00)
II	Avg	1.03	0.36	0.26	0.020	0.018	5.31	91
	CoV (%)	(5.50)	(2.78)	(27.99)	(7.77)	(7.06)	(39.84)	(0.00)
III	Avg	0.58	0.37	0.28	0.018	0.015	1.78	89
	CoV (%)	(8.20)	(8.61)	(27.13)	(6.54)	(10.41)	(18.11)	(4.56)
IV	Avg	31.03	0.35	0.32	0.023	0.014	0.31	48
	CoV (%)	(5.77)	(0.48)	(13.14)	(2.55)	(31.13)	(56.05)	(40.67)
V	Avg	1.02	0.33	0.20	0.018	0.015	4.65	52
	CoV (%)	(7.40)	(15.75)	(28.00)	(30.04)	(35.92)	(79.91)	(22.67)
VI	Avg	0.62	0.36	0.25	0.019	0.016	2.94	47
	CoV (%)	(8.93)	(1.62)	(20.40)	(9.12)	(22.53)	(89.51)	(33.16)

Table 4.7 show some pictures taken on the fibers before and after the exposure to chloride attack.

Table 4.7 – Visual observation of RSF surface before and after chloride exposure

Series	Before Chloride exposure	After Chloride exposure	
I			
II			
III			
IV			
V			
VI			

The RSF exposed in total length to continuous immersion in chloride solution (Series I) showed a uniform reduction in cross section along its length during the immersion period (smooth fiber surface – Table 4.7; Figure 4.13a). For the RSF exposed with the total length to dry-wet cycles in chloride solution (Series IV),

an irregular reduction of cross section was observed along its length due to a more localized corrosion and occurred fixation of corrosion products at RSF surface during the drying phase due to oxidation (rough fiber surface - Table 4.7). In case of RSF subjected to dry-wet cycles, since the corrosion action was more localized on the fiber surface caused the rupture of the fibers for a shorter period of exposure (Figure 4.13b, Table 4.7).

For RSF with an exposed length of 1 mm and 0.5 mm, the dry-wet cycles proved to be more aggressive environmental conditions than continuous immersion, since it caused similar average mass loss for a shorter exposure time and the rupture of all fibers. Significant dispersion of the results was verified for the mass loss of RSF, mainly for those subjected to dry-wet cycles (Table 4.7). However, the mass loss of RSF measured was higher than expected, according to the reduction of fiber cross section assessed for the exposed fiber length, which means that the corrosion process must have occurred beyond the fiber exposure length. However, it should also be noted that the balance used may not have been sufficiently accurate to evaluate the mass loss of the fiber.

Considering the difference between the RSF diameter before and after chloride exposure (Table 4.6), a corrosion rate of RSF was determined by dividing the value corresponding to the reduction of the RSF diameter by the exposure period. In Table 4.8 are presented the average values (Avg) and the coefficients of variation (*CoV*) of the corrosion rates obtained for each test series.

Table 4.8 – Corrosion rate values obtained in RSF submitted to chloride attack

<b>Series</b>	<b>Corrosion rate (mm/year)</b>	
I	Avg	0.47
	<i>CoV (%)</i>	<i>(7.53)</i>
II	Avg	0.39
	<i>CoV (%)</i>	<i>(56.97)</i>
III	Avg	0.41
	<i>CoV (%)</i>	<i>(70.72)</i>
IV	Avg	0.72
	<i>CoV (%)</i>	<i>(89.35)</i>
V	Avg	0.84
	<i>CoV (%)</i>	<i>(57.43)</i>
VI	Avg	1.11
	<i>CoV (%)</i>	<i>(53.09)</i>

The average values of corrosion rate were similar for the three series (I, II and III) of RSF submitted to continuous immersion, which means that the chloride attack caused a similar effect to the exposed fiber length, in terms of reducing the cross section by corrosion (continuous process). However, for RSF

submitted to dry-wet cycles, it seems that the corrosion process was accelerated when the exposed length was reduced to 1 and 0.5 mm, probably due to a more localized corrosion process. A significant dispersion of the results was observed, except for Series I, which indicates an irregular character of RSF to corrosion susceptibility when the fibers are partially exposed to aggressive environment conditions. Comparing with the values of corrosion rate obtained in the linear polarization tests (Section 4.4.3 -Table 4.3), the average corrosion rate obtained in Series I was higher, probably due to a poor diameter measurement of RSF with the USB microscope after chloride immersion, since the presence of corrosion products made it difficult to accurately measure the diameter.

#### 4.5.2 Tensile strength of corroded RSF

In this experimental program (2), the tensile strength of single class 1 RSF previously subjected to corrosion action was assessed by means of direct tensile tests, according to the test setup presented in Section 3.2.3.1. As in the previous tests, continuous immersion and dry-wet cycles in 150 ml of 3.5 wt% NaCl solution were adopted for RSF to induce corrosion, considering the exposed fiber length of 1 mm and 0.5 mm. Two periods for chloride exposure were adopted, 4 and 10 days. In this experimental program (2), the duration of the chloride exposure was reduced to the maximum of 10 days, since it was found in the experimental program (1) (4.5.1) that for 90 days of chloride exposure, a significant number of fibers broke without any mechanical action.

The mass of each RSF was evaluated before and after chloride attack by using a balance with 0.0001 g of precision. For comparison purposes in terms of mass loss due to corrosion, RSF with the total length exposed to continuous immersion and dry-wet cycles for 10 days were also considered.

Table 4.9 summarizes the experimental program carried out divided in six series of tests. In each test series, at least two fibers were tested for each exposure period.

Table 4.9 – Experimental program to evaluate the tensile strength of corroded RSF

Series	Chloride exposure	Exposed RSF length	Exposure time (days)
I		Total length	10
II	Continuous immersion	1 mm	4; 10
III		0.5 mm	4; 10
IV		Total length	10
V	Dry-wet cycles	1 mm	4; 10
VI		0.5 mm	4; 10

In Table 4.10 are presented the average results obtained to evaluate the mass loss of RSF by corrosion before being submitted to tensile tests.

Table 4.10 – Relevant results to evaluate the mass loss of corroded RSF before tensile tests

Series	Time of Cl exposure (days)		Exposed fiber length (mm)	RSF Diameter (mm)		RSF Mass (g)		Mass loss (mg/mm)
				Before Cl	After Cl	Before Cl	After Cl	
I	10	Avg	27.53	0.37	0.35	0.0219	0.0201	0.07
		CoV (%)	(12.14)	(8.22)	(11.66)	(17.34)	(17.23)	(16.33)
II	4	Avg	0.96	0.35	0.32	0.0338	0.0336	0.26
		CoV (%)	(1.56)	(6.90)	(8.15)	(60.17)	(60.43)	(75.97)
II	10	Avg	0.95	0.37	0.34	0.0405	0.0398	0.95
		CoV (%)	(4.28)	(6.04)	(13.78)	(36.01)	(36.48)	(66.33)
III	4	Avg	0.67	0.36	0.34	0.0350	0.0347	0.48
		CoV (%)	(11.88)	(1.63)	(2.99)	(40.14)	(39.78)	(181.22)
III	10	Avg	0.65	0.34	0.27	0.0346	0.0346	1.51
		CoV (%)	(5.05)	(1.59)	(10.83)	(38.18)	(38.31)	(50.65)
IV	10	Avg	30.68	0.35	0.35	0.0233	0.0227	0.0292
		CoV (%)	(14.71)	(15.43)	(15.43)	(38.27)	(38.85)	(37.88)
V	4	Avg	0.95	0.34	0.31	0.0308	0.0303	0.54
		CoV (%)	(2.78)	(4.99)	(6.70)	(50.83)	(50.48)	(98.31)
V	10	Avg	1.01	0.36	0.32	0.0346	0.0339	0.65
		CoV (%)	(2.68)	(1.40)	(11.97)	(46.30)	(46.52)	(73.53)
VI	4	Avg	0.53	0.35	0.35	0.0363	0.0358	0.92
		CoV (%)	(13.40)	(2.33)	(1.67)	(58.90)	(59.48)	(30.72)
VI	10	Avg	0.59	0.36	0.34	0.0358	0.0352	1.01
		CoV (%)	(4.85)	(3.93)	(4.80)	(48.31)	(48.76)	(20.55)

Higher mass loss was obtained for RSF with its total length submitted to continuous immersion than to dry-wet cycles (Table 4.10), similar to what was observed for 3 months of chloride exposure (Table 4.6). The same behavior in terms of mass loss was observed for fibers with a exposure length of 1 and 0.5 mm for 10 days. For 4 days of chloride exposure, no significant differences were expected in terms of mass loss of RSF since the fiber surface was exposed to similar exposure conditions (RSF submitted to cycles was immersed for 3 days and drying for 1 day, no significant oxidation occurred during drying phase). However, for this case, the dry-wet cycles caused higher mass loss than the continuous immersion. Considering the abnormal values of the coefficients of variation, no reliable conclusions could be drawn for 4 days of chloride exposure.

Comparing with the results of RSF mass loss presented in Figures 4.13a,b, for 10 days of chloride exposure (around 15% and 10% for Series I and IV), lower percentage values of mass loss were obtained

in Series I and IV (respectively, 8.42% and 2.92% by mass of total length), probably due to the accuracy of the balance.

There is no clear relationship between the RSF mass loss and the exposed fiber length for exposed lengths lower than 1 mm. As observed, for 3 months of chloride exposure, the results of RSF mass loss after 10 days of chloride exposure also present significant dispersion, probably due to the irregular geometry and fiber surface of exposed length of RSF. The higher dispersion observed for the values of “RSF Mass”, before and after Cl<sup>-</sup> (Table 4.9) are due to the differences in RSF length, since short (representative of the average fiber length) and long (to account the anchorage length in the grips for direct tensile tests) fibers were considered. The mass loss of RSF measured was also higher than expected, according to the reduction of fiber cross section assessed for the exposed fiber length, which means that the corrosion of RSF occurred beyond the fiber exposed length.

After submitting the RSF to chloride attack, the tensile strength of the RSF with an exposed length of 1 and 0.5 mm was assessed by performing direct tensile tests. Table 4.11 presents the relevant results obtained in the tensile tests of corroded RSF. Considering the RSF diameter measured after chloride exposure (Table 4.10), the tensile strength of RSF was determined from the maximum tensile load registered in tensile tests (Table 4.11). With the values obtained of RSF tensile strength, the maximum tensile load of RSF before Cl<sup>-</sup> immersion was also determined (Table 4.11), considering the diameter of RSF measured before Cl<sup>-</sup> (Table 4.10). The influence of the corrosion effects in the tensile strength of RSF was quantified by calculating the loss of maximum tensile load (in %) after chloride attack (Table 4.11).

During the preparation of RSF for direct tensile tests, some RSF previously submitted to dry-wet cycles suffered rupture which confirms the aggressiveness of the environmental exposure by dry-wet cycles compared to the continuous immersion, as observed in Section 4.5.1. As expected, a decrease in tensile load was observed with the increase of exposure time in chloride solution, more pronounced for RSF submitted to dry-wet cycles. The loss of tensile load calculated (Table 4.11) was proportional to the estimated loss of cross section (difference between the RSF diameter, before and after chloride attack – Table 4.10).

Table 4.11 – Relevant results of direct tensile tests of corroded RSF

Series	Time of Cl <sup>-</sup> exposure (days)		Fiber length between grips (mm)	Maximum tensile load after Cl <sup>-</sup> (N)	Tensile strength of RSF (MPa)	Maximum load before Cl <sup>-</sup> (N)	Loss of tensile load (%)
II	4	Avg CoV (%)	16 (8.84)	211.50 (25.14)	2523.75 (2.02)	249.80 (2.02)	15.5 (126.10)
	10	Avg CoV (%)	14 (28.57)	174.30 (9.17)	2492.54 (14.92)	240.58 (18.90)	25.6 (80.89)
III	4	Avg CoV (%)	15 (4.88)	182.60 (16.50)	2160.39 (23.39)	207.85 (23.39)	11.4 (54.55)
	10	Avg CoV (%)	14 (28.57)	134.95 (1.31)	2671.59 (12.41)	249.75 (12.41)	45.6 (13.25)
V	4	Avg CoV (%)	8 (9.43)	147.10 (9.61)	1925.62 (7.15)	190.91 (11.12)	22.9 (5.10)
	10	Avg CoV (%)	13 (28.28)	197.30 (-)	3331.10 (-)	339.06 (-)	41.8 (-)
VI	4	Avg CoV (%)	13 (-)	205.60 (-)	2332.62 (-)	224.42 (-)	8.4 (-)
	10	Avg CoV (%)	13 (39.60)	164.70 (-)	2022.52 (-)	229.38 (-)	28.2 (-)

## 4.6 CONCLUSIONS

This chapter compiles the experimental work carried out to characterize the chloride-induced corrosion performance of RSF and its relative behavior compared with ISF. From the employed electrochemical techniques, the following conclusions can be drawn:

- 1) According to the criteria of ASTM C876-15 (2015), the corrosion probability of RSF and ISF immersed in a 3.5 wt% NaCl solution is higher than 90%.
- 2) The polarization curves showed that the corrosion of RSF is generalized in its surface, and it seems that the RSF are slightly more susceptible to corrosion than ISF. The RSF showed higher corrosion rate and mass loss than ISF, probably due to the higher specific surface area and carbon content of RSF. The values of  $i_{corr}$  obtained for RSF did not vary significant with the immersion time, as for ISF (Frazão *et al.*, 2016).
- 3) Low amounts of small rubber debris attached to RSF surface had a negligible influence in terms of fiber corrosion resistance. Therefore, from this point of view the pre-treatment methods used to clean RSF may be dispensed.
- 4) The SEM analysis of corroded RSF confirmed that corrosion was uniform on the entire fiber surface and reveals the greater progress of the corrosion phenomenon with the immersion time. The main

corrosion products were iron oxides. The Cu and Zn detected in non-corroded polished RSF, from the brass coating existing on the original tire steel, were eliminated with the formation and release of the corrosion products.

- 5) The RSF subjected to continuous immersion in chloride solution showed a uniform mass loss due to a homogeneous corrosion action at fiber surface, while the RSF submitted to dry-wet cycles in chloride solution showed an irregular mass loss due to a localized corrosion action at fiber surface that may cause fiber rupture.
- 6) The dry-wet cycles in chloride solution are more aggressive environmental conditions than the continuous immersion, for RSF corrosion.
- 7) For exposed fiber lengths lower than 1 mm, there was no clear relationship between the RSF mass loss by corrosion and the exposed fiber length to chloride immersion. Higher dispersion of the results was obtained for RSF after chloride attack, in terms of mass loss by corrosion and tensile strength, probably due to the irregular character of the exposed fiber length. An increased loss of tensile strength was observed for RSF with the increase of exposure time in chloride solution, with more relevance in mainly for those RSF submitted to dry-wet cycles.



---

# Chapter 5

---

## **RSF PULL-OUT BEHAVIOR UNDER CORROSIVE ACTION**

### **5.1 INTRODUCTION**

In environments containing chlorides, Steel Fiber Reinforced Concrete (SFRC) structures are subjected to chloride penetration that can initiate corrosion of steel fibers, with eventual pernicious consequences in terms of structural and durability performance. The chloride diffusivity depends on the concrete pore structure, which is affected by various factors, such as the mix design, compaction, curing, placing and presence of cracks (Shi *et al.*, 2012). Cracks in concrete are known to hasten initiation of steel reinforcement corrosion in reinforced concrete structures (Granju and Balouch, 2005; Frazão *et al.*, 2016). The investigation of the impact of cracks on the corrosion initiation is important for understanding the mechanical behavior and durability performance of cracked RSFRC under chloride environments.

With the outcome of new cement-based materials with improved mechanical properties, such is the case of RSFRC, the study of the fiber/matrix interface is important for understanding the mechanical behavior of such cementitious composites. The main benefits of fibers are effective after matrix cracking has occurred, since fibers crossing the crack ensure a certain level of stress transfer between both faces of the crack, providing to the composite a residual strength, which magnitude depends on the fiber, matrix and fiber–matrix bond properties (Cunha *et al.*, 2010).

After the investigation concerning the corrosion susceptibility of RSF caused by chloride attack (presented in the Chapter 4), this chapter is focused on the innovative non-standard experimental fiber pull-out tests of RSF embedded in cracked concrete specimens previously exposed to corrosive environment. This test

procedure was previously developed within the framework of a research project, in order to investigate the corrosion effects of Industrial Steel Fibers (ISF) on the fiber reinforcement mechanisms developed during the fiber pull-out from a self-compacting concrete (SCC) medium (Frazão *et al.*, 2016).

The present research intends to contribute for a better understanding of the corrosion of RSF on the fiber pull-out force-slip response, based on the deep observation and interpretation of the interface between fiber and surrounding paste when RSFRC is submitted to environmental conditions that favor the occurrence of fiber corrosion, as well as on the evaluation and analysis of the fiber-slip response under these circumstances.

Two relevant parameters controlling the phenomenon of corrosion are the crack width and the critical concentration of chlorides required to initiate corrosion. At the material level, it is intended to investigate the fiber corrosion for different crack widths of concrete subjected to an aggressive environment containing chlorides. At the structural level, it is intended to assess the effect of fiber corrosion on the mechanical behavior of cracked RSFRC, namely on the RSF pull-out load vs. slip response. This information can be relevant for numerical models where the fiber reinforcement mechanisms are simulated by the stress-slip response derived from fiber pull-out tests, such is the case of the model proposed by Cunha *et al.* (2012).

In the present chapter, it was also assessed the possibility of using the X-ray Micro-computed Tomography methodology to investigate the corrosion effects of RSF on the fiber reinforcement mechanisms developed during the RSF pull-out tests under corrosion action.

## **5.2 EXPERIMENTAL PROGRAM**

### **5.2.1 Specimens manufacture**

For comparison purposes, the concrete specimens considered in the RSF pull-tests were produced with the same SCC composition used in ISF pull-out tests previously carried out by the author (Frazão *et al.*, 2016), also under corrosive action. In this way, the materials used for concrete production, as well as the pull-out specimen's geometry were identical to the those considered by Frazão *et al.* (2016).

The SCC mixture was produced with CEM I 42.5R (CEM), limestone filler (LF), water (W), superplasticizer ViscoCrete 3005 (SP1), fine and coarse river sand (FS and CS) and crushed granite (CG). Details about the material properties were presented in Section 3.2. Table 5.1 includes the SCC composition used, which has best fitted self-compacting requirements, according to EFNARC (2005) recommendations. The mix-design, which is based on packing density optimization, the mixing procedures and the main fresh

state properties of the SCC, can be found elsewhere (Barros *et al.*, 2007). In Table 5.1, W/C is the water/cement ratio.

Table 5.1 – Mix design for 1 m<sup>3</sup> of SCC

<b>CEM (kg)</b>	<b>LF (kg)</b>	<b>W (L)</b>	<b>SP1 (L)</b>	<b>FS (kg)</b>	<b>CS (kg)</b>	<b>CG (kg)</b>	<b>W/C</b>
413	353	128	7.8	198	722	648	0.31

The fresh properties of concrete, namely the slump-flow and V-funnel time were determined according to EN 12350-8: 2010 and EN 12350-9:2010, respectively. An average slump-flow of 732 mm and a flow time of 3.5 s for the concrete to reach the 500 mm spread circle were achieved with no visual signs of segregation. The average time taken for the concrete to flow through the V-funnel was 12.9 s, showing good homogeneity and cohesion.

According to the EN 12390-3:2011 and EN 12390-13: 2013, the compressive strength and the elastic modulus of the hardened SCC were determined at 28 days from four cylinders of 150 mm diameter and 300 mm height. The test procedures are detailed in Section 3.5.2. The average compressive strength ( $f_{cm}$ ) was 68.2 MPa with a coefficient of variation (CoV) of 4.51%, and the average Young's modulus ( $E_{cm}$ ) was 35.1 GPa with a CoV of 4.55%.

For the RSF pull-out tests, cylindrical specimens with 88 mm diameter and 160 mm height were molded with just one RSF embedded in the SCC matrix, bridging the two parts that form this type of specimens (Figure 5.1c). RSF were selected with a length ranging from 34 to 57 mm, in order to ensure sufficient fiber length embedded in each part of the specimens.

To produce a pseudo-cracked specimen, the two equal parts forming the specimen were molded in two phases, each one of 80 mm height casted with fresh SCC in each phase (Figures 5.1a,c). The fiber was embedded in the part of the specimen casted in the 1<sup>st</sup> phase, by about 1/3 of its average length (Figures 5.1a,b). The remainder fiber's length was embedded in the other part of the specimen, casted in the 2<sup>nd</sup> phase (Figures 5.1c,d). With these two quite different fiber embedment lengths in the two parts of the specimen, it was assured that the fiber pull-out would always occur in the half part of the specimen with smaller embedment length. Before casting the second part of the specimen (in the 2<sup>nd</sup> phase), an adherent film with 0.2  $\mu\text{m}$  of thickness was applied on the top surface of the first part of the specimen (casted in the 1<sup>st</sup> phase) in order to prevent any adhesion between the two parts of the specimen, and to materialize the artificial pseudo-crack bridged by the fiber (Figure 5.1e).

The influence of the crack width,  $\omega$ , was investigated by considering samples with different crack width. Samples with null crack width were also considered for comparison purposes. The concrete cover thickness of the fiber, which is the distance from the fiber to the sample surface, was 10 mm (Figure 5.1c).

In order to induce the fiber corrosion, the specimens were previously subjected to continuous immersion in a 3.5 wt% NaCl solution. To monitor the electrochemical fiber corrosion during immersion, a coated copper wire was welded to the steel fiber, with the region near the welding point sealed with beeswax (Figures 5.1a-d). This coated copper wire had the other extremity outside the specimen and was sufficiently long to stay out of solution during the immersion period.

In the 1<sup>st</sup> phase a PVC mold with 80 mm in height was used to cast the 1<sup>st</sup> part of the specimen. In the 2<sup>nd</sup> phase this 1<sup>st</sup> part of the specimen was introduced into a mold of a total height of 160 mm in order to allow the casting of the second part of the specimen (Figures 5.1a-e).

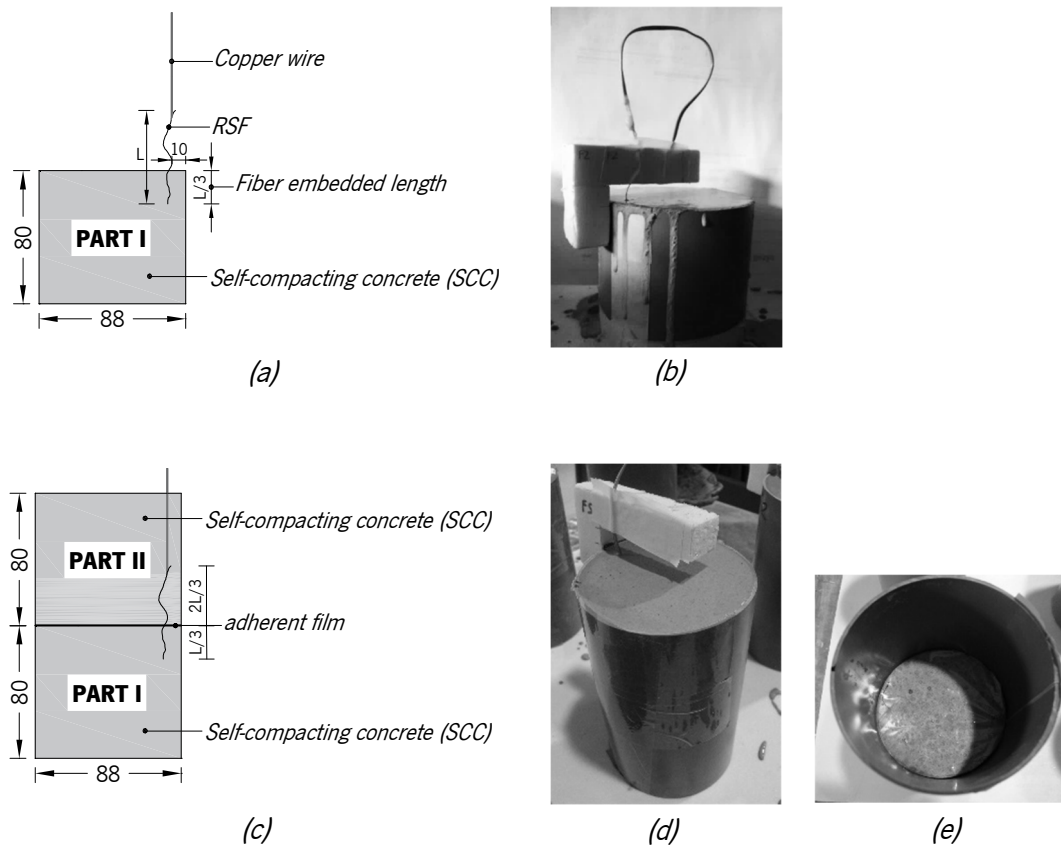


Figure 5.1 – Appearance of the SCC specimen in the: (a) (b) 1<sup>st</sup> Phase; (c) (d) (e) 2<sup>nd</sup> Phase (units in mm)

## 5.2.2 Experimental setup and procedures

### 5.2.2.1 Implementation of the crack width

The width of the pseudo-crack was induced on the specimens after 28 days of curing and before they have been submitted to immersion in 3.5 wt% NaCl solution. The following procedure was followed for each implemented crack width:

- i) The specimen was installed under simple support conditions (Figure 5.2a).
- ii) The specimen and the supporting system were then moved to the immersion tank.
- iii) The load system presented in Figure 5.2b was applied. Due to the irregular shape of the fibers it was very difficult to set the necessary static load (very small loads) for a target crack width. Therefore, it was decided to perform the tests with two different levels of applied load, 265 N and 183 N. Three specimens were tested simultaneously at each load level. The crack width was measured using microscopic devices. The force was kept constant during the immersion period, in order to simulate realistic conditions representative of a cracked structural RSFRC element under service loading conditions. The reference samples were immersed without any applied load, since in uncracked RSFRC the mechanisms of fiber reinforcement are not mobilized.

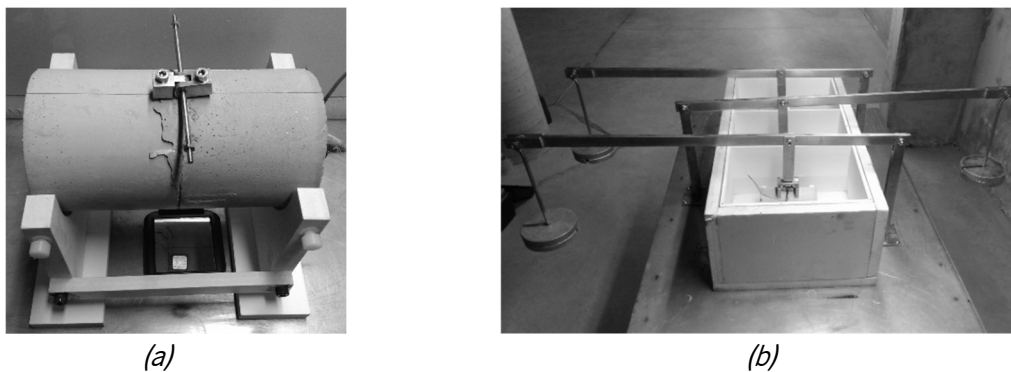


Figure 5.2 – (a) Supporting system for cracked SCC specimens;  
(b) Load application system for cracked SCC specimens

### 5.2.2.2 Chloride immersion and electrochemical monitoring

After the crack width has been assured, the specimens were subjected to 10 days of immersion in 3.5 wt% NaCl solution in the tank (Figure 5.3a). The purpose of this immersion was to accelerate the process of corrosion of steel fibers, simulating a marine environment. Research on the creep behavior of cracked Steel Fiber Reinforced Self-Compacting Concrete (SFRSCC) has demonstrated that for the fiber stress level installed, fiber slip creep is marginal (Abrishambaf *et al.*, 2015c).

During the immersion period, the fiber behavior within the specimen was monitored by electrochemical measurements, including the measurement of open circuit corrosion potential,  $E_{OCP}$ . The electrochemical cell used for this purpose was the one described in Section 4.2 (Figure 5.3b).

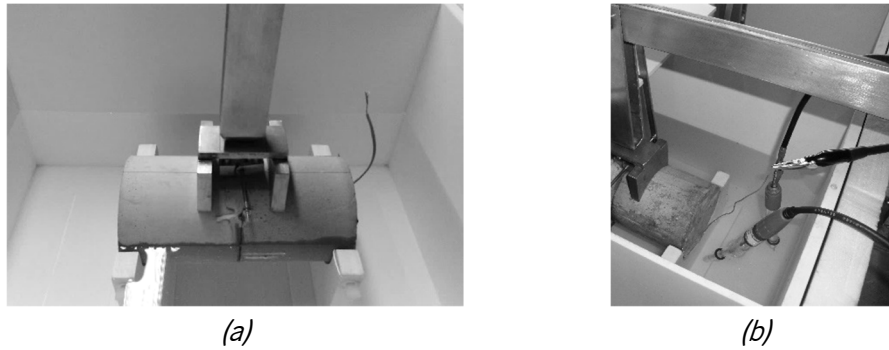


Figure 5.3 – (a) Chloride immersion of cracked SCC specimen under tension; (b) Electrochemical monitoring of embedded RSF into SCC specimen

Samples that were not subjected to chloride immersion were also part of this experimental program for comparison purposes. These samples, with the minimum crack width (approximately 0.1 mm), were kept in the lab environment and were not subjected to accelerated corrosion environmental conditions. After the 10 days of immersion, the fiber pull-out tests were carried out, including the reference samples free from corrosion.

In the present experimental program, four series of tests were considered, as presented in Table 5.2. Four each test series, three specimens (SP) were tested.

Table 5.2 – Experimental program of fiber pull-out bending tests

Series	Specimens	Exposure conditions of specimens before pull-out test
I	SP1, SP2, SP3	Applied load of 265 N
II	SP4, SP5, SP6	Applied load of 183 N
III	SP7, SP8, SP9	Lab environment (free of corrosion)
IV	SP10, SP11, SP12	No load applied

### 5.2.2.3 Fiber pull-out bending test

After the period of immersion, the fiber pull-out tests were performed under the four-point load bending test configuration presented in Figures 5.4a,b.

The tests were conducted with a servo-controlled equipment under displacement control, using for this purpose the signal of the displacement transducer (LVDT1) that measures the mid-span deflection of the specimen, by imposing a displacement rate of 0.001 mm/s. The applied load was measured using a load cell of 10 kN capacity.

The crack width was recorded at the crack mouth by using a LVDT2 mounted on the specimen in the alignment of its bottom generatrix, orthogonal to the pseudo-crack surface (Figures 5.4a,b).

Due to the statically determinate character of this test, the fiber pull-out force,  $F_p$ , can be obtained from the following equation (Figure 5.4a):

$$\frac{F_a}{2} \times (b - c) = F_p \times d \quad (5.1)$$

where  $F_a$  is the applied load,  $b$  is the distance from the specimen's support to the midspan (80 mm),  $c$  is the distance between the loading system and the cracked surface (25 mm), and  $d$  is the distance from the fiber to the top generatrix of the specimen (75.5 mm), as shown in Figure 5.4a.

To assure the constant internal arm underlying equation (5.1), a steel element was installed in the top part of the pseudo-fracture surface in order to transmit the compressive force through a well-defined contact area of the two parts of the specimen (Figures 5.4a,b).

The fiber slip was determined based on the displacement read in the LVDT2 and taking into account the relative position between the fiber and the axis of the LVDT2, applying a geometric transformation law supported on the principle that two rigid bodies that form the specimen rotate around the contact point of the aforementioned steel element.

It was also assumed that the crack width recorded in the LVDT2 is a realistic approach of the fiber slip, neglecting the fiber strain induced by elastic deformation.

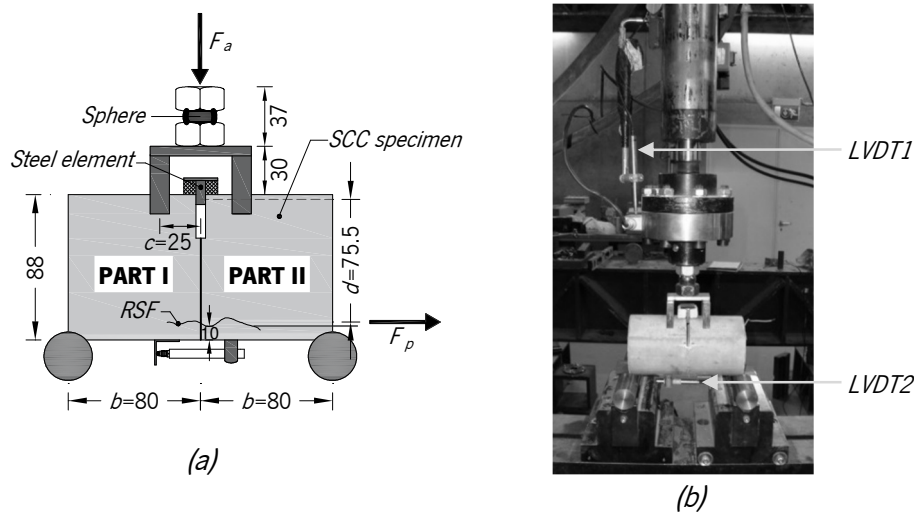


Figure 5.4 – (a) (b) Configuration of the steel fiber pull-out bending test (dimensions in mm)

## 5.3 RESULTS AND DISCUSSION

### 5.3.1 Characterization of fiber corrosion by electrochemical tests

Figure 5.5 shows the  $E_{OCP}$  variation in RSF during the immersion period of the SCC specimens in chloride solution. It is indicated the pre-crack widths,  $\omega_{cr}$ , implemented on each specimen of Series I and II. As reported in Section 4.4.1, according to the ASTM C876-15 (2015) there is more than 90% probability that reinforcing steel corrosion occurs for potentials lower than -0.35 V vs. CSE (-0.29 V vs. SCE). In addition, for corrosion potentials over -0.20 V vs. CSE (-0.14 V vs. SCE) there is more than 90% probability that reinforcing steel corrosion does not occur. A corrosion potential value in the range of -0.20 V to -0.35 V vs. CSE (marked in Figures 5.5a-c) represents uncertain corrosion activity. According to these criteria of ASTM C876-15 (2015) and considering the average values of  $E_{OCP}$  registered on RSF during the immersion period (Figure 5.5), the RSF of specimens 1, 2, 6 and 12 showed a probability of corrosion higher than 90%, while the RSF of the remaining specimens (3, 4, 5, 10 and 11) presented an uncertain corrosion activity.

In cracked specimens (Figure 5.5a,b – Series I&II), the  $E_{OCP}$  was lower for higher crack width levels (1.6 and 1.7 mm) than at low levels of crack width (0.3-0.7 mm). This fact corroborates the results obtained for ISF, reported by Frazão *et al.* (2016), where a decrease of  $E_{OCP}$  was observed with the increase of crack width. However, for the same applied load level, the crack width greatly varied due to the irregular geometry of RSF, as confirmed by the high variability obtained in the monotonic RSF pull-out tests presented in Section 3.2.3.4 (Figure 3.21).



The curled and twisted character of RSF length also gave rise to variable thickness of concrete cover along RSF length (Figure 5.4a). For SP12 (Series IV), due to the difficulties in positioning the RSF into the uncracked concrete specimen with a concrete cover of 10 mm (only one part with 88 mm diameter and 160 mm height - Figure 5.4a), the RSF was very close to the exposed surface (the concrete cover was less than 3 mm). Therefore, this sample was very susceptible to corrosion, as observed in Figure 5.5c. For the remaining uncracked specimens (10 and 11), the concrete cover of 10 mm was guaranteed. In this case, the influence of corrosion phenomena is uncertain (Figure 5.5c).

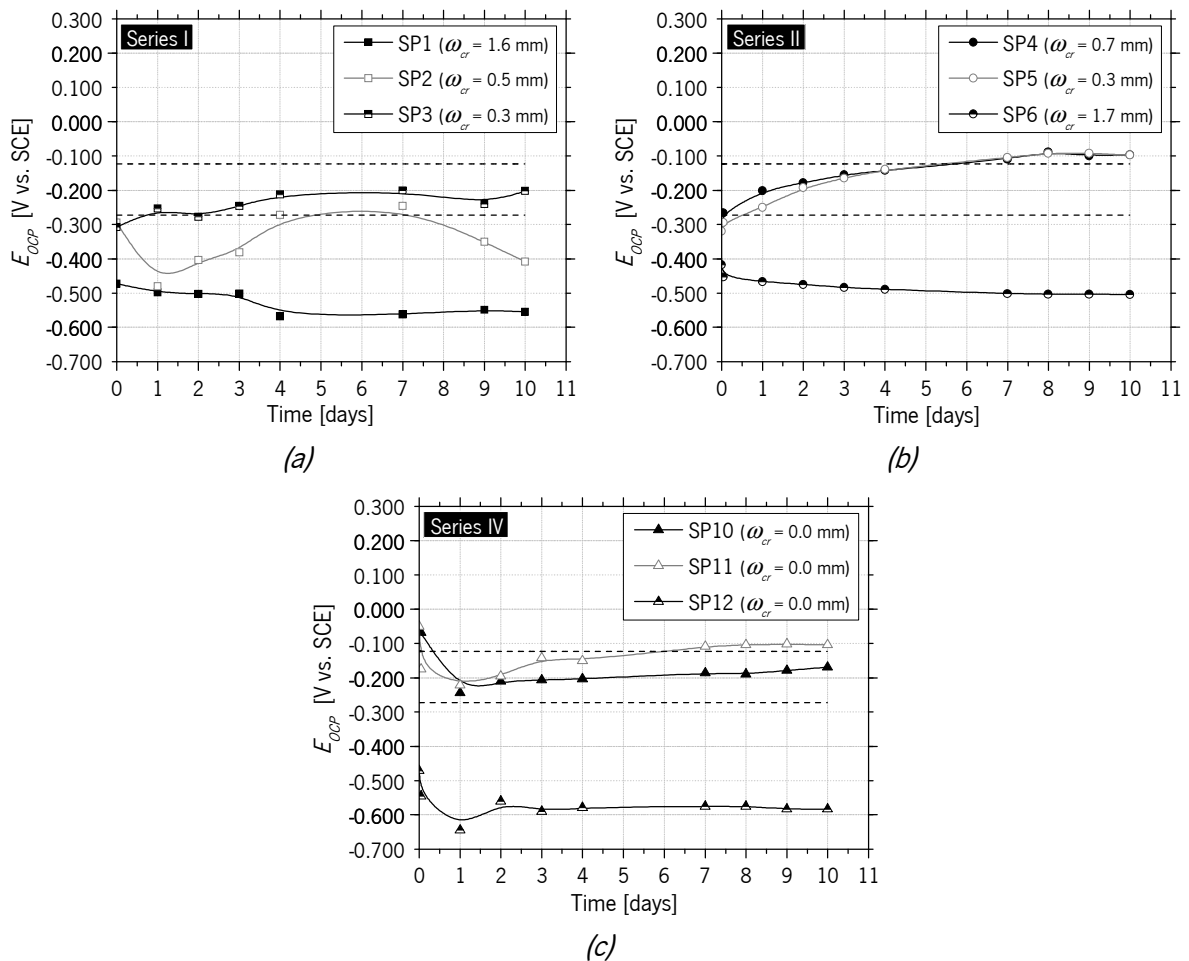


Figure 5.5 – Variation of the  $E_{OCP}$  in RSF during the immersion period of the specimens of:

(a) Series I; (b) Series II; (c) Series IV

### 5.3.2 Pull-out behavior of corroded steel fibers

Figure 5.6 presents the Pull-out load vs. End slip curves obtained from RSF pull-out tests of cracked specimens (Series I&II&III), with the pull-out load determined from equation 5.1.

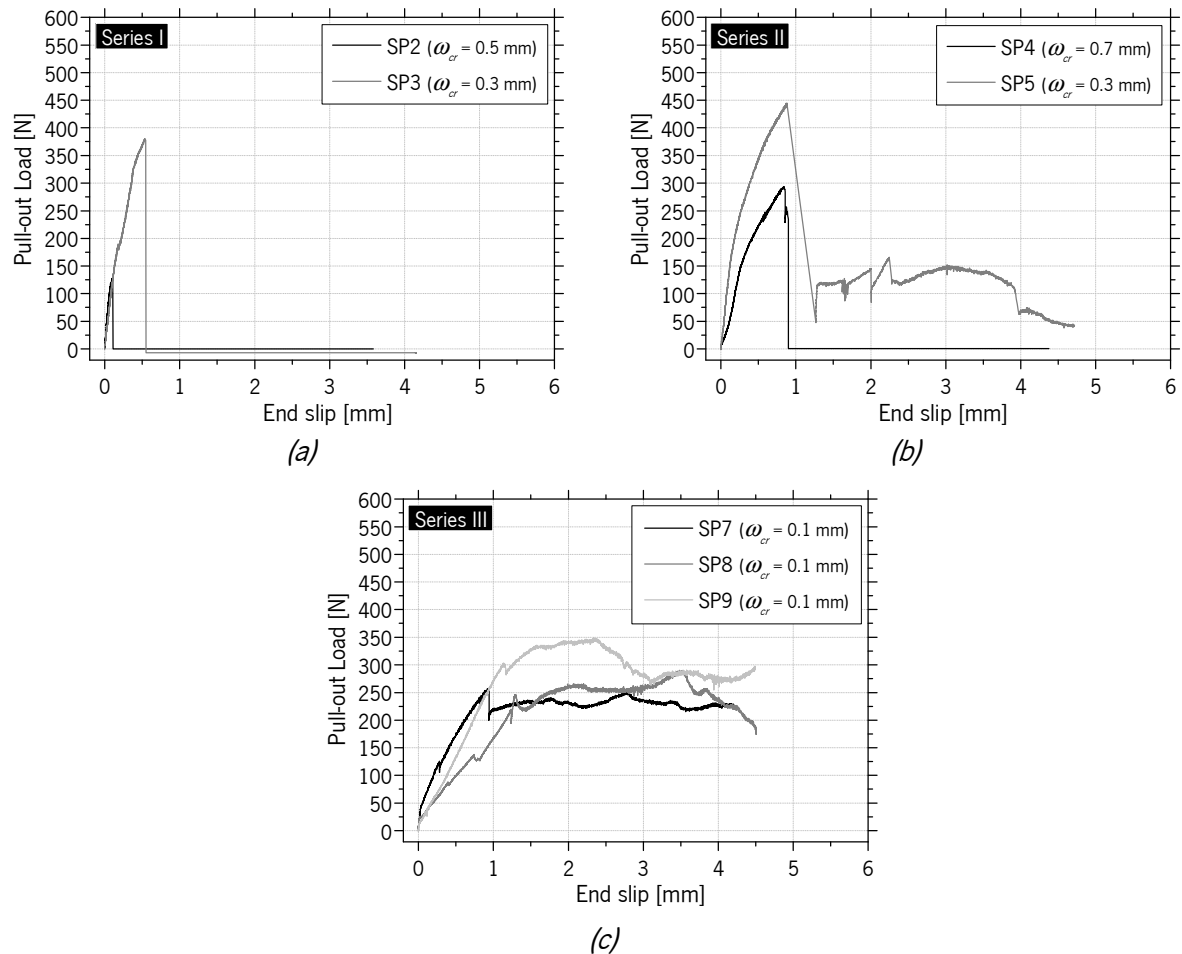


Figure 5.6 – Pull-out load-End slip relationship obtained in RSF pull-out tests of cracked SCC specimens of: (a) Series I; (b) Series II; (c) Series III

The obtained results evidence the occurrence of fiber failure in all cracked specimens submitted to corrosion action, except for SP5, whose failure mode was by fiber pull-out (Series I&II – Figs. 5.6a,b). For SP1 and SP6, the fiber failure occurred during the immersion period of the specimens in 3.5 wt% NaCl solution, due to its high crack width values, 1.6 mm and 1.7 mm, respectively. In Series III corresponding to cracked specimens not subjected to corrosion action, the failure mode of RSF was the fiber pull-out (Fig. 5.6c).

The uncracked SCC specimens previously submitted to corrosion action (Series IV) were also subjected to four-point load bending test, according to the test configuration presented in Figure 5.4. Since these specimens were not cracked, a small notch with 5 mm of depth was implemented in the bottom part of the specimen (mid-length) in order to induce the crack surface crossing the embedded RSF (Fig. 5.7).



Figure 5.7 – Specimen of Series IV after four-point load bending test

For the three specimens 10, 11 and 12, three distinct scenarios were obtained. For the SP10, the failure mode was by fiber pull-out, however, it was not possible to register the fiber pull-out load after cracking the concrete specimen (Fig. 5.8a). In the SP11 (Fig. 5.8a), the failure mode was also by fiber pull-out and the fiber pull-out load (determined with equation (5.1)) vs. End slip after cracking the concrete specimen was registered, as depicted in Fig. 5.8b. It was not possible to test the SP12, since the fiber was cut when the small notch was implemented in the bottom part of the specimen (concrete cover less than 5 mm).

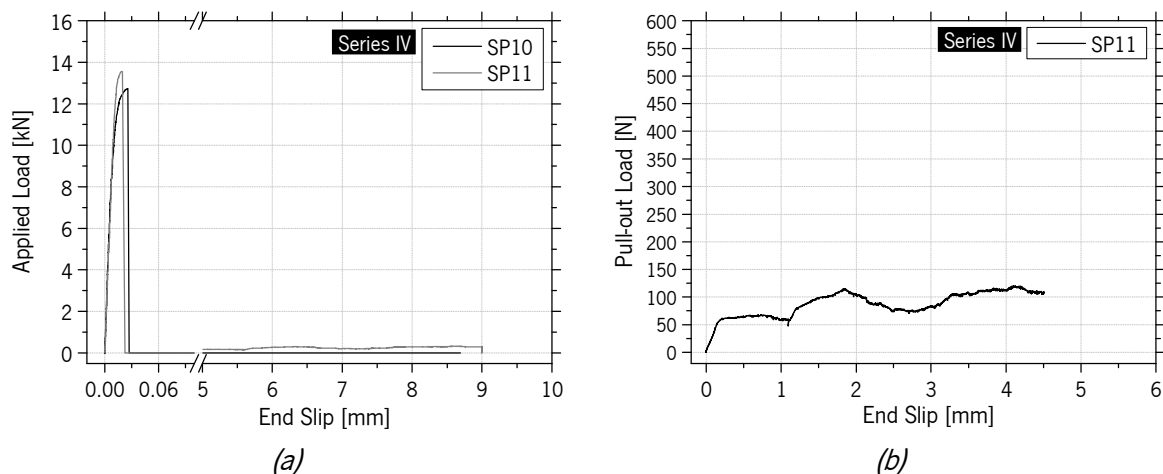


Figure 5.8 – (a) Applied load-End slip relationship obtained in uncracked SCC specimens;  
(b) Pull-out load-End slip relationship obtained in SP11

After performing all RSF pull-out tests in SCC specimens previously subjected to chloride immersion, corrosion products of RSF were visually observed at cracked surfaces, as shown in Figure 5.9a. On the other hand, no significant signs of corrosion were detected at RSF surface in uncracked specimens 10 and 11 (Figure 5.9b).



Figure 5.9 – Aspect of RSF after fiber pull-out test of: (a) SP1 (Series I); (b) SP11 (Series IV)

The diameter of RSF was measured before specimen's production (before Cl<sup>-</sup>) and after the fiber pull-out tests (after Cl<sup>-</sup>). The tensile strength of three failed RSF was determined from the maximum load registered at fiber level in the pull-out tests,  $F_p$ , and with the RSF diameter after Cl<sup>-</sup> (Table 5.3). The influence of the corrosion effects in the tensile strength of RSF was quantified according to the procedure adopted in Section 4.5.2, i.e. by calculating the loss of maximum tensile load (in %) after chloride attack. The maximum tensile load of RSF before Cl<sup>-</sup> immersion was determined with the tensile strength of RSF, considering the diameter of RSF measured before Cl<sup>-</sup> (Table 5.3). For these three cracked specimens submitted to 10 days of chloride immersion, a high variability of the loss of tensile load was observed (from 0.4% to 63.4%) due to chloride attack. However, it is also important to mention that the fiber pull-out bending tests were not performed immediately after the end of the immersion period in chloride solution. After this immersion period, the specimens were left in the fog room until the test date, which may have further contributed for the fiber oxidation.

There is no clear relationship between the crack width and the loss of tensile load due to corrosion action, probably due to the irregular geometry of the RSF that caused an irregular chloride attack at the exposed length of RSF in the crack, and consequently variable susceptibility to fiber corrosion. In addition, crack widths were over 0.3 mm, which are wide enough to allow the easy access of chloride solution. According to Jang *et al.* (2011) above about 0.1 mm, a further increase in the crack opening has less influence on the diffusion rate of chloride ions in concrete.

Table 5.3 – Relevant results of RSF pull-out tests

Series	Specimen	$\omega_{cr}$ (mm)	RSF Diameter (mm)		Maximum load after CI, $F_p$ (N)	Tensile strength of RSF (MPa)	Maximum load before CI (N)	Loss of tensile load (%)
			Before CI	After CI				
I	SP2	0.5	0.39	0.24	127.88	2926.95	349.33	63.4
I	SP3	0.3	0.36	0.36	380.22	3830.65	381.84	0.4
II	SP4	0.7	0.36	0.32	293.36	3576.01	366.53	20.0

Figure 5.10 depicts the comparison between the envelope (ENV) and the average (AVG) fiber Pull-out load-End slip curves obtained from fiber bending tests of Series III (free of corrosion) and from direct fiber pull-out tests presented in Section 3.2.3.4.

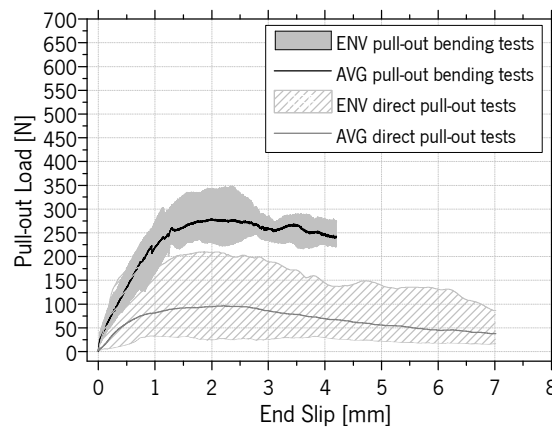


Figure 5.10 – Envelope and average Pull-out load-End slip relationship obtained from four-point load bending tests (Series III) and from direct fiber pull-out tests (Figure 3.21a)

A higher pull-out load and higher post peak residual resistance was obtained in pull-out bending tests compared to direct fiber pull-out tests.

During the pull-out bending test, the opening process of the pseudo-crack introduces some deviation to the initial orthogonality between the fiber and the surface of these cracks that increases with the crack opening. Due to this deviation the concrete surrounding the fiber, in a region close to the fiber-loaded end slip, applies normal stresses to the fiber, which increase the resistance to the fiber sliding. This mechanism is currently designated by snubbing effect (Døssland, 2008). This effect is due to the tendency of the fiber to be aligned with the pull-out load direction. Since the pull-out load is not aligned with the embedded length of RSF, an increase of the pull-out resistance occurred. For the inclined fibers, the surrounding concrete nearby the crack offers resistance to the aforementioned fiber alignment tendency, originating a stress field composed by normal and shear stress components in the fiber in this zone. Due

to a type of Mohr-Coulomb effect, the normal stresses increase the pull-out force inducing an increase in the residual strength of the fiber pull-out (Døssland, 2008).

#### 5.4 RSF PULL-OUT TESTS UNDER CORROSIVE ACTION USING X-RAY MICRO-COMPUTER TOMOGRAPHY

The X-Ray Micro-computer Tomography (3D- $\mu$ XCT) is a non-destructive 3D imaging technique that can be used to provide 3D images of the internal microstructure of cement-based materials (Vavřík *et al.*, 2012; Skarżyński and Tejchman, 2016). This technique uses X-rays to create cross sections of a specimen by means of a 2D-projection (radiography). By a step-by-step rotation of the specimen, numerous single projections are acquired, which are then reconstructed to a 3D-data set (tomography). As the X-ray penetrates the specimen, it is exponentially attenuated according to the material along its path. Every 3D-data set consists of a single volume segments (voxels) which are assigned by a specific attenuation coefficient,  $\mu$ , to different grayvalue depending on the density and the thickness of the specimen. Local differences of density in the specimen can be non-destructively and contactless visualized as 2D- or 3D-images. The resolution of the images is limited by the system-specific parameters of the devices and especially by the geometry and density of the specimen. The smaller the specimen geometry, the higher the resolution limit.

In this work, some experiments were carried out to analyze the potential of employing X-ray imaging to better understand the effects of RSF corrosion on the fiber reinforcement mechanisms developed during the fiber pull-out from the matrix. This investigation was carried out at the Institute of Mineralogy, Crystallography and Materials Science (IMCM) of the Faculty of Chemistry and Mineralogy at the University of Leipzig, Germany. The 3D- $\mu$ XCT was employed by using the Fraunhofer-Gesellschaft-system (FhG-IKTS-MD, Germany) presented in Figure 5.11 that can achieve a maximum resolution limit of 10  $\mu$ m for specimens with a maximum diameter of 10 mm.

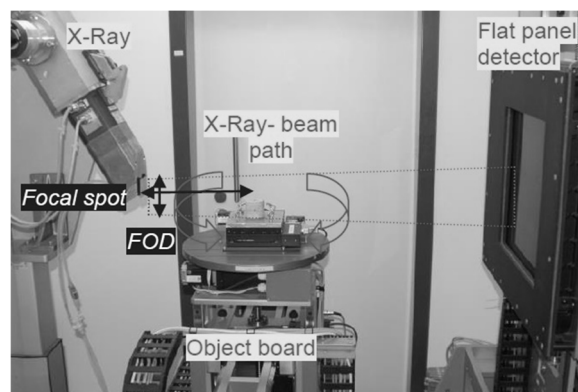


Figure 5.11 – Configuration of measurement setup of 3D- $\mu$ XCT device

The main objective of these experiments was to develop a non-standard experimental fiber pull-out tests, by using 3D- $\mu$ XCT to examine the specimens during the fiber pull-out process in order to assess the corrosion effects on the fiber pull-out force-slip response. The principle of the fiber pull-out tests under corrosion action was similar to that presented in Section 5.2, in terms of the specimens' manufacture, implementation of the crack width, chloride immersion, electrochemical monitoring, and the fiber pull-out bending test. However, in order to increase the resolution limit of the 2D- and 3D-images at fiber level, the dimensions of the specimens were reduced as much as possible, and the test setup was redesigned according to the new dimensions of the specimens and in order to use the 3D- $\mu$ XCT, as will be presented in the following sections.

#### **5.4.1 Specimens manufacture**

For these RSF pull-out tests, cylindrical specimens with 25 mm diameter and 50 mm height were molded similarly to the procedure shown in Figure 5.1, with just one RSF bridging the two parts that form this type of specimens (Figures 5.12a,c). To create the pseudo-crack, the two parts forming the specimen were molded in two phases, each one of 30 mm height. The RSF was embedded in part I with an embedment of about 1/3 of its length and the remaining fiber length was embedded into part II in order to assure the fiber pull-out by part I (Figs. 5.12a,b). To monitor the electrochemical fiber corrosion in the period of specimen immersion, a coated copper wire was welded to RSF, with the region near the welding point sealed with beeswax, and with the other extremity outside the specimen (Figs. 5.12b,d). Before casting the part II, a plastic sphere was installed in the top of part I (pseudo-fracture surface) to assure the constant internal arm underlying to equation (5.1) by a well-defined contact area of the two parts of the specimen through which the compressive force is transmitted during the fiber pull-out test (Fig. 5.12b,e). An adherent polyethylene film with 0.2  $\mu$ m of thickness was applied on the top surface of part I in order to prevent adhesion between the two parts of the specimen, and to materialize the surface for the propagation of the pseudo-crack bridged by the fiber. The crack width,  $w$ , was measured in this surface (Figs. 5.12c,e).

A mortar composition was used to cast these specimens due to their reduced dimensions. The mortar mixture was produced with Portland cement CEM I 42.5R, fly ash, fine and coarse river sand and water. In order to obtain a fluid mortar to facilitate the casting process, the mortar mix ratio was 1:1.5:0.4 (binder:sand:water). The binder (cement+fly ash) and sand (fine sand+coarse sand) contents were used in the same proportions of these materials in RSFRC1% composition (Table 3.18). The workability of the

mortar was assessed by measuring the consistency according to ASTM C1437-07 (2007) and an average flow value of 82.5% was obtained.

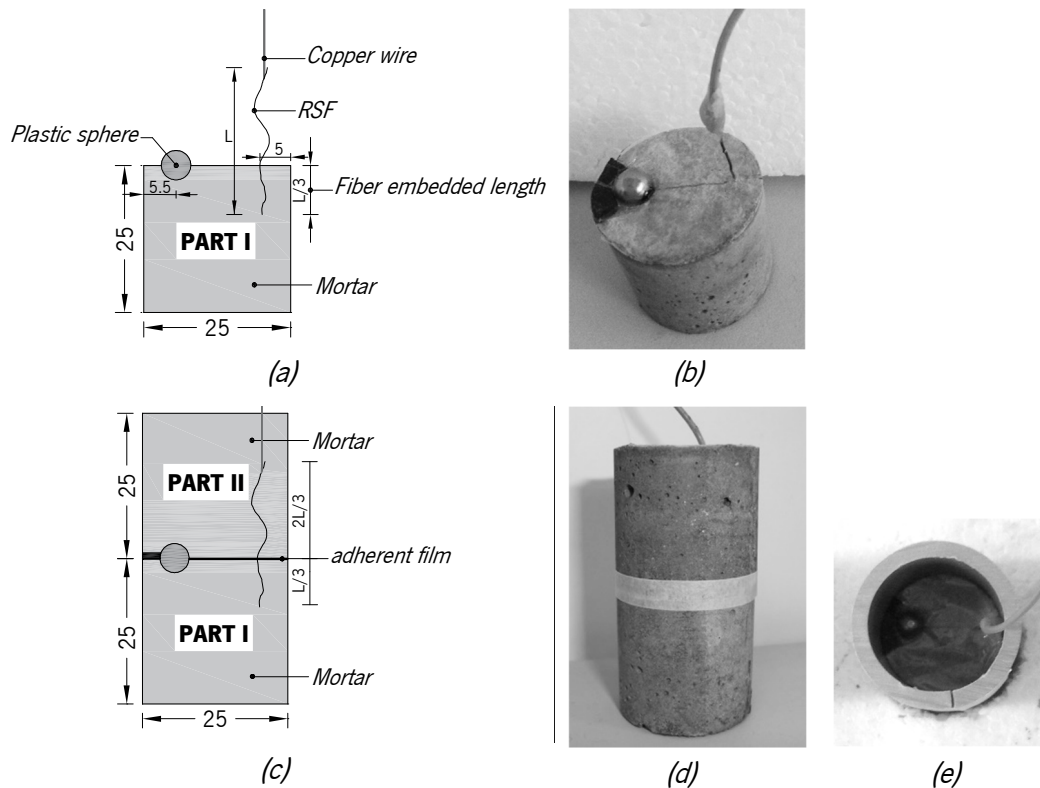


Figure 5.12 – Appearance of the mortar specimen in the:  
(a) (b) 1<sup>st</sup> Phase; (c) (d) (e) 2<sup>nd</sup> Phase (units in mm)

#### 5.4.2 Experimental setup and methodology

This section describes the experimental procedure of the fiber pull-out test, using 3D- $\mu$ XCT.

After 28 days of curing, the specimen was installed in a supporting system capable of assuring simple support conditions (Figure 5.13a). Then, by means of a load application system (Fig. 5.13a), a force was applied to the specimen with a torque wrench in order to implement the crack width, that is measured with a USB microscope, as shown in Figure 5.13b.

After the target crack width was assured, the specimen was immersed in a 3.5 wt% NaCl solution for a certain exposure period, aiming to accelerate the process of RSF corrosion (Figure 5.14a). During the immersion period, the applied load for crack implementation was kept constant and the corrosion potential of RSF was monitored by electrochemical measurements (Figure 5.14b), including the Open Circuit Potential,  $E_{OCP}$ . Since the specimens showed significant amount of pores at exposed surfaces, and in order to guarantee the chloride penetration only across the crack width, the faces of each



cylindrical specimen were waterproofed with a single layer coating based on polyurethane resin, except at 5 mm thick around the pseudo-crack (Figs. 5.12d,5.13b).

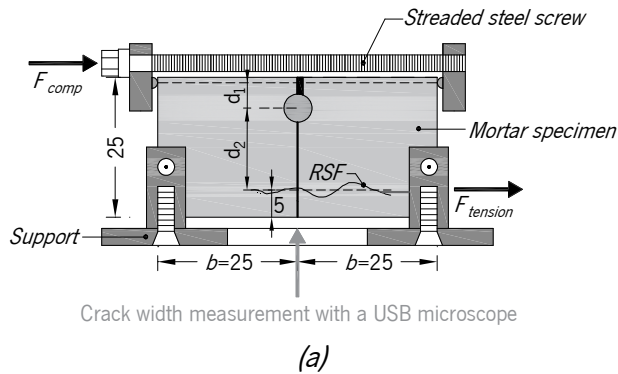


Figure 5.13 – (a) Supporting and load application systems for cracked mortar specimens; (b) Measurement of crack width with a microscope (units in mm)

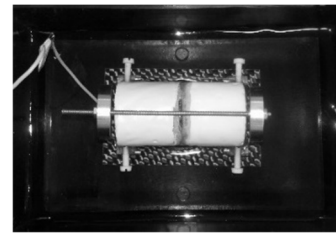
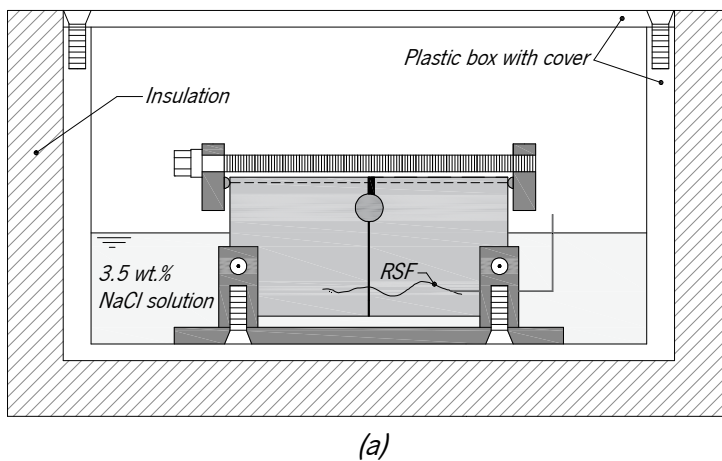


Figure 5.14 – (a) (b) Chloride immersion of cracked mortar specimen under tension; (c) Electrochemical monitoring of embedded RSF into mortar specimen

After the end of the immersion period, the specimens were submitted to fiber pull-out tests, performed under a four-point load bending test configuration. Figure 5.15a presents the test setup defined to employ the 3D- $\mu$ XCT in order to capture internal images of the specimens during the fiber pull-out process. In this sense, the pull-out bending tests were executed in a vertical position by fixing the support and the load application systems to an acrylic base, which is then attached to the rotating metal base (Object Board – Figure 5.11) of the 3D- $\mu$ XCT device (Figure 5.15b). To evaluate the fiber pull-out load-end slip response, successive load increments are applied to the specimen with a torque wrench and the loaded

end slip is measured along the fiber bond length with respect the longitudinal axis of the fiber by means of a 2D-projection (radiography) and 3D-data set (tomography). Due to the statically determinate character of this test, the fiber pull-out force,  $F_{tension}$ , can be obtained from the following equation (Figure 5.13a):

$$F_{comp} \times d_1 = F_{tension} \times d_2 \quad (5.2)$$

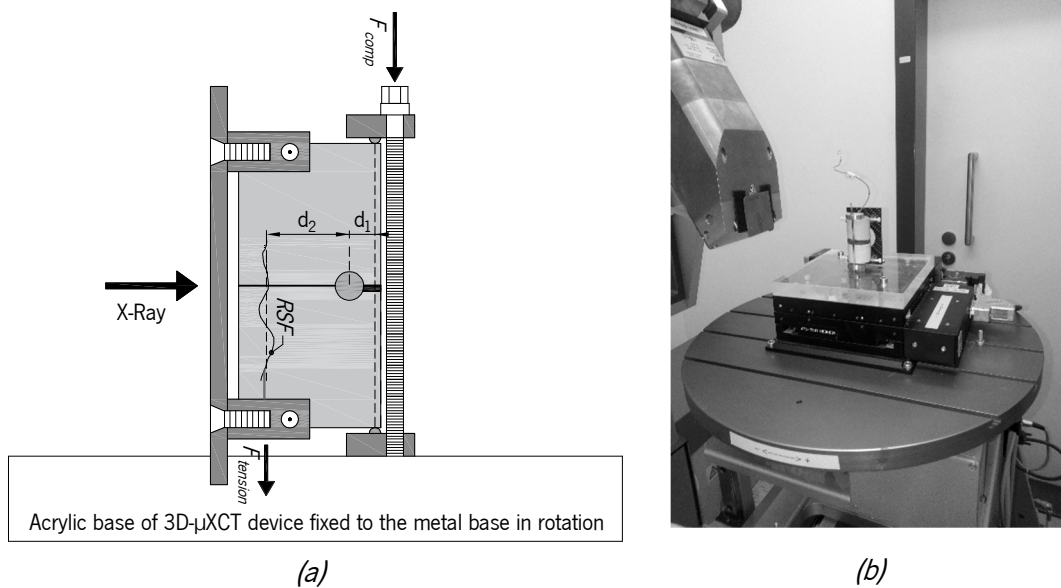


Figure 5.15 – (a) Fiber pull-out test setup defined to employ 3D- $\mu$ XCT; (b) Positioning of the mortar specimen for fiber pull-out test on the 3D- $\mu$ XCT device to be examine with X-ray imaging

Some preliminary tests were carried out to assess the effectiveness of the fiber pull-out test setup proposed using 3D- $\mu$ XCT. One cracked mortar specimen with a single embedded RSF, as presented in Figure 5.12c, was scanned with X-ray for the following five different states:

- 1 – Cracked specimen at initial state with a crack width of 0.1 mm (after its production and before crack width implementation);
- 2 – Cracked specimen with a crack width of 0.5 mm (after 1<sup>st</sup> applied load and before chloride immersion);
- 3 – Corroded cracked specimen with a crack width of 0.5 mm (after 24 hours of chloride immersion);
- 4 – Corroded cracked specimen with a crack width of 0.8 mm (after 2<sup>nd</sup> applied load for fiber pull-out);
- 5 – Corroded cracked specimen with a crack width of 1.2 mm (after 3<sup>rd</sup> applied load for fiber pull-out).

The X-ray computer tomography scan was performed with a beam energy of 140 kV, a flux of 140  $\mu$ A, a Copper foil (0.5 mm thickness) at the focal spot of the beam and a 360° rotation with a step size of 0.2 degrees. The resolution was 18.8  $\mu$ m, which means that for the evaluation of end slip of RSF and

RSF/matrix transition zones, only displacements higher than the resolution could be accurately measured.

The 3D-radiographs were reconstructed by the software *VoIex 6.2* and the image analysis was done with the softwares *Image J 1.47v* and *VGStudio Max 2.0*.

### 5.4.3 Results and discussion

The three-dimensional result of computed tomography measurement was given as an image stack of around 1800 single images of specimen cross section (“slices”). The RSF was located in a significant number of these images and a montage of multiple images was made to visualize the whole fiber in two-dimensional pictures, where the grayvalue were summarized. The 2D-projection of the whole fiber was done in the x- and y-direction, as represented in Figure 5.16.

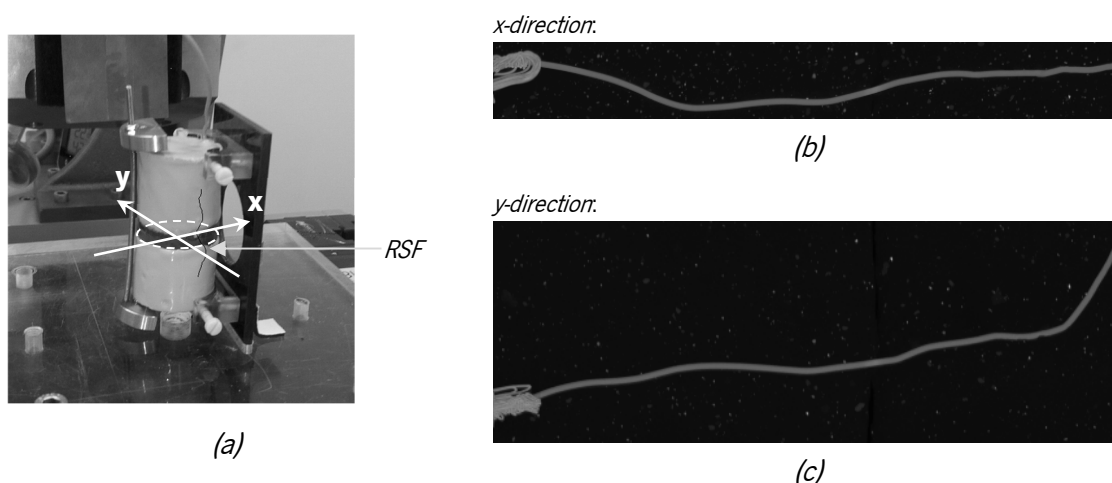


Figure 5.16 – (a) Identification of x- and y- direction defined for 2D-projection of the specimens; (b) 2D-Projection of RSF in x-direction; (c) 2D-Projection of RSF in y-direction

For the cracked mortar specimen examined with 3D- $\mu$ XCT, the following acquisition parameters are possible to measure/identify by image analysis: crack width at fiber level, fiber diameter, fiber deformation, fiber slip and porosity.

#### Crack width at fiber level

To determine the crack width, a plot profile of grayvalue was determined in four areas near the fiber location, two in the x-direction and the other two in the y-direction. As an example, Figures 5.17a-d show the 2D-images selected near the fiber, where the areas defined to calculate the plot profiles are marked.

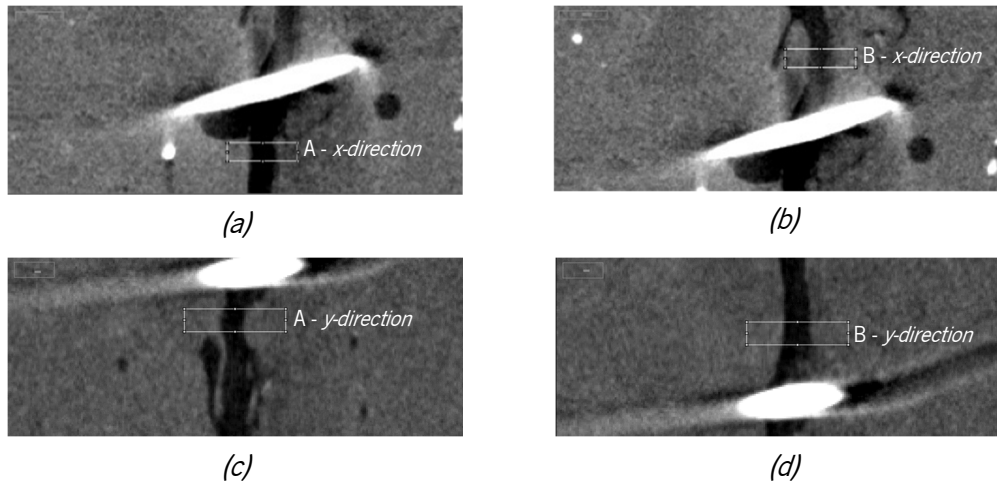


Figure 5.17 – 2D-projection for determination of initial crack width (state A) in:  
 (a) (b) Zones A and B in x-direction; (c) (d) Zones A and B in y-direction

By calculating a plot profile for each defined area, the density appears in grayscale (y-axis) along the length of the marked area (Figure 5.18a). The grayvalue was analyzed in a 16-bit colour depth [0-65535]. By fitting the given curve, the beginning and ending grayvalue of the crack are defined at the half height of the peaks, as represented in Figure 5.18b. The distance in x-axis between these two points corresponds to the crack width,  $\omega_{cr}$  (Figure 5.18b).

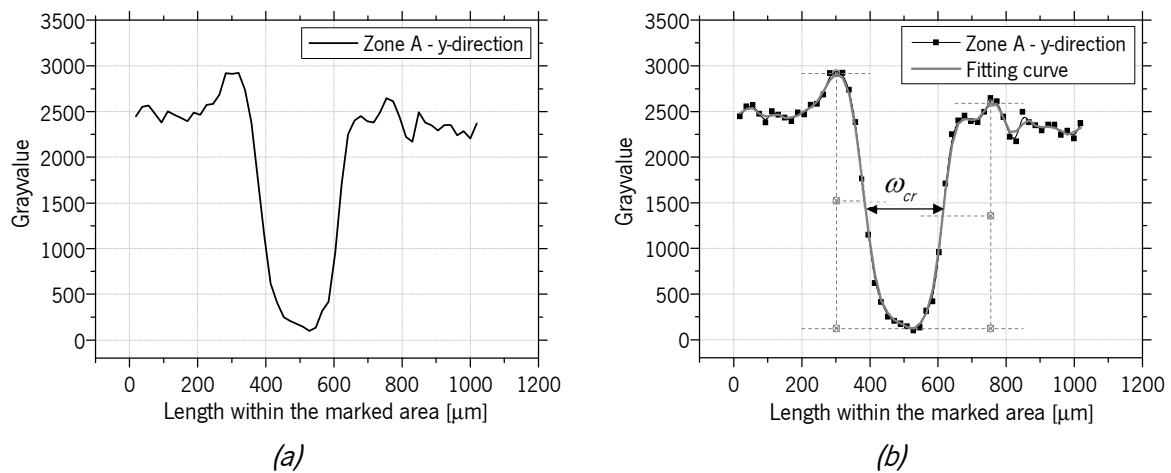


Figure 5.18 – (a) Plot profile of grayvalue obtained for zone A in y-direction;  
 (b) Determination of the crack width in zone A in y-direction

The crack width was determined for each state of the cracked specimen mentioned above (1-5), and for each state corresponded to the average of the measurements at the four marked areas (Fig. 5.17). The plot profiles obtained at zone A in y-direction for the five states of cracked specimen are depicted in Figure 5.19. The average values of the crack width 1-5 are presented in Table 5.4.

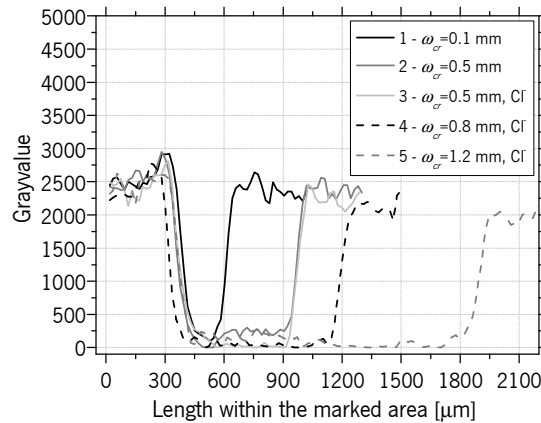


Figure 5.19 – (a) Plot profile of grayvalue obtained at zone A in y-direction for the five states of cracked mortar specimen

Table 5.4 – Average crack width values obtained with 3D- $\mu$ XCT

State of cracked mortar specimen	$\omega_{cr}$ ( $\mu$ XCT) ( $\mu$ m)
1 – 0.1 mm crack width (Initial state)	266
2 – 0.5 mm crack width	563
3 – 0.5 mm crack width, corroded	596
4 – 0.8 mm crack width, corroded	866
5 – 1.2 mm crack width, corroded	1454

The 3D- $\mu$ XCT is a more accurate technique to measure the crack width at fiber level since it allows to visualize the fiber inside the concrete matrix.

The results of crack width measurements with 3D- $\mu$ XCT revealed, at the initial state (“1”), an average crack width of approximately 0.3 mm at the fiber level, which is higher than that measured with the microscope (lower than 0.1 mm) at the exposed surface of the specimen. Slight high crack widths at fiber level were measured with the 3D- $\mu$ XCT compared to the microscope measurements at exposed surface of specimen, for the remaining states of the cracked mortar specimen. However, the opposite should have happened since the crack width tends to be higher at exposure face of the specimen than at fiber level. This may be indicative of inaccurate measurements of crack width performed by the microscope due to the reduced crack width values.

The measures with the 3D- $\mu$ XCT have also confirmed a negligible effect of chloride immersion in the crack width at fiber level (States “2” and “3”).

### Fiber diameter

Analogous to the crack width, the fiber diameter,  $d_f$ , was determined with the plot profiles of grayvalue calculated in two areas per fiber, one in the x-direction and the other in the y-direction. Figure 5.20 shows the 2D-images of RSF obtained with 3D- $\mu$ XCT in x-direction for each state of cracked specimen, with the analyzed areas marked for the calculation of the corresponding grayvalue plot profiles, presented in Figure 5.21.

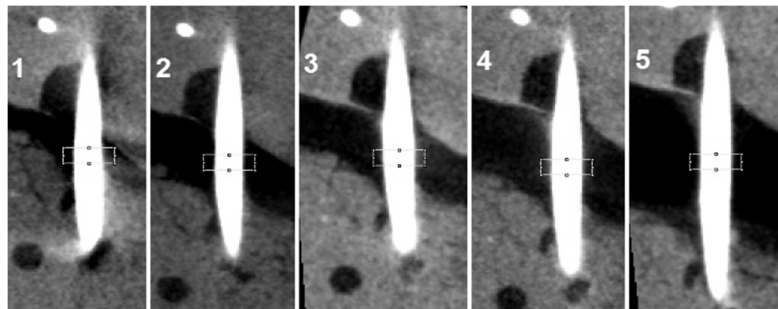


Figure 5.20 – 2D-projection obtained in x-direction with marked areas for fiber diameter determination at the five states of cracked specimen

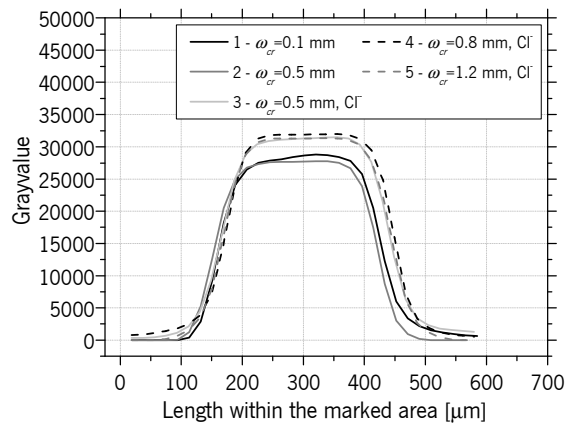


Figure 5.21 – Plot profiles of grayvalue obtained in x-direction for the five states of cracked specimen

The fiber diameter was determined for each specimen state in two directions, adopting the same procedure used for crack width measurement represented in Figure 5.18b. According to Fig. 5.21, in this case a smoothing of the curves was not required. For each specimen state, the RSF diameter corresponded to the average of the two measurements, in x- and y-directions. In Table 5.5 are presented the average values of the fiber diameter obtained for the five cracked states, 1-5.

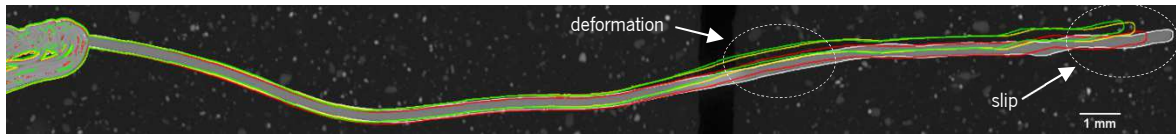
Table 5.5 – Average fiber diameter values obtained with 3D- $\mu$ XCT

State of cracked mortar specimen	$d_f$ ( $\mu$ XCT) ( $\mu$ m)
1 – 0.1 mm crack width (Initial state)	276
2 – 0.5 mm crack width	277
3 – 0.5 mm crack width, corroded	274
4 – 0.8 mm crack width, corroded	275
5 – 1.2 mm crack width, corroded	274
Average	275
CoV (%)	0.47

An accurate measurement of the RSF diameter was obtained with the 3D- $\mu$ XCT technique since a similar average value of fiber diameter was observed with the microscope before the specimen production (272  $\mu$ m). Apparently, the cross section of the RSF was not affected by the short period of chloride attack, since no significant differences occurred in the cross section of the fiber after chloride immersion of the specimen. However, according to the electrochemical monitoring of  $E_{OCP}$  ( $E_{OCP} = -0.505$  V vs. SCE), the embedded RSF showed a corrosion probability higher than 90% after 24 hours of chloride immersion (ASTM C876-15 2015). It should also be noted in this case that due to the resolution limit of the 3D- $\mu$ XCT measurements, only losses in fiber diameter higher than 18.8  $\mu$ m (edge length of a pixel) can be accurately detected and measured in these specimens. According to the results obtained in the tests presented in Section 4.5.1, in terms of the reduction of RSF diameter by corrosion after 90 days of continuous chloride immersion (Series I&II&III - Table 4.6), a maximum cross-sectional reduction of 1-2  $\mu$ m/day is expected in RSF. This means that for the specimen under study immersed for 24 hours, the corrosion effects in terms of the reduction of RSF diameter would not be detectable by 3D- $\mu$ XCT measurements.

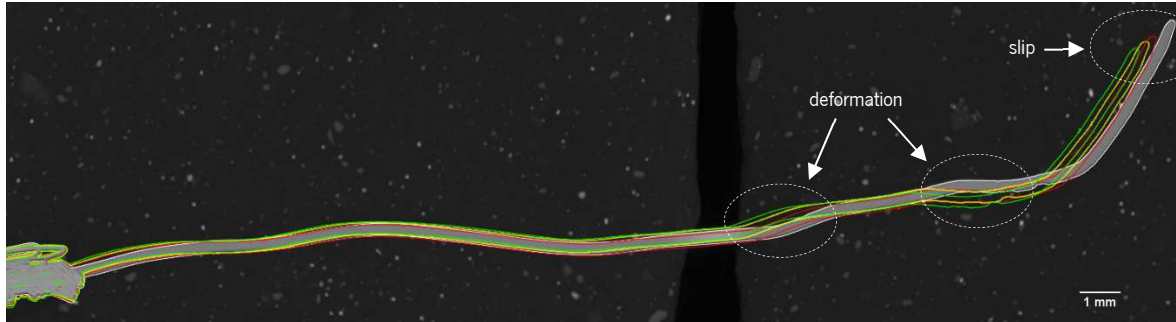
### Fiber deformation and slip

In Figure 5.22 are depicted an overlay of 2D-projection of RSF in x- and y-direction for four cracked states of the specimen (1, 3, 4 and 5), which correspond to successive increments of applied load. In Figures 5.22a,b, the cracked states 1 (green), 3 (yellow), 4 (red) and 5 (white) correspond, respectively, to the average crack widths at the fiber level of 0.3, 0.6, 0.9 and 1.5 mm measured by 3D- $\mu$ XCT.

*x-direction.*

Legend: State 1 ( $\omega_{cr} = 0.3$  mm): Green; State 3 ( $\omega_{cr} = 0.6$  mm): Yellow; State 4 ( $\omega_{cr} = 0.9$  mm): Red; State 5 ( $\omega_{cr} = 1.5$  mm): White

(a)

*y-direction.*

Legend: State 1 ( $\omega_{cr} = 0.3$  mm): Green; State 3 ( $\omega_{cr} = 0.6$  mm): Yellow; State 4 ( $\omega_{cr} = 0.9$  mm): Red; State 5 ( $\omega_{cr} = 1.5$  mm): White

(b)

Figure 5.22 –2D-projection overlay of RSF for cracked specimen under successive increments of applied load: (a) X-direction; (b) Y-direction

As observed in Figures 5.22a,b, the fiber deformation and slip were visualized in 2D-projection of RSF in x- and y-direction. By analyzing these images, it is possible to determine the end slip of the RSF by calculating the displacement of the RSF at the extremity for the different cracking states. From cracking state 1 to 5, an approximate end slip values of 1.2 mm and 0.8 mm were measured in x- and y-directions, respectively. However, to obtain the corresponding fiber pull-out load -end slip response, some difficulties occurred in quantifying the fiber pull-out load since due to the very reduced specimen geometry, a torque wrench was used to apply increments of load to the specimen. These load increments were very low and were out of the torque range of the wrench used (minimum 0.3 N.m). In this regard, further research is needed to improve the configuration of this test for use with 3D- $\mu$ XCT technique, in terms of defining a better load application system (maybe using more than one fiber in the crack plane), more appropriate and accurate for low levels of applied load (less than about 300 N), considering that the applied load is maintained during the x-ray scan image and the fiber pull-out test setup is fixed to the rotating metal base of 3D- $\mu$ XCT device.

### Specimen porosity

The 3D- $\mu$ XCT technique is also useful for visualizing the pore distribution in the cracked mortar specimen, as represented in Figure 5.23. The pore network with a volume bigger than 1 mm<sup>3</sup> (red colour) is



remarkable, mainly in the part I of the specimen (Fig. 5.12), probably due to the fact that the fiber was embedded in part I after filling the mold with mortar, which caused significant air entrainment. However, this pore network obtained seems to be overestimated, probably due to the influence of the resolution and depending on how the pixel is considered as pore. Assuming that this estimation of absolute porosity is not correct, only the regions of highest porosity in the specimen should be analyzed. In this case, according to Figure 5.23, the fiber/matrix interface tends to be more porous, which may affect the durability of RSFRC. For example, this increases the chloride penetration in uncracked concrete.

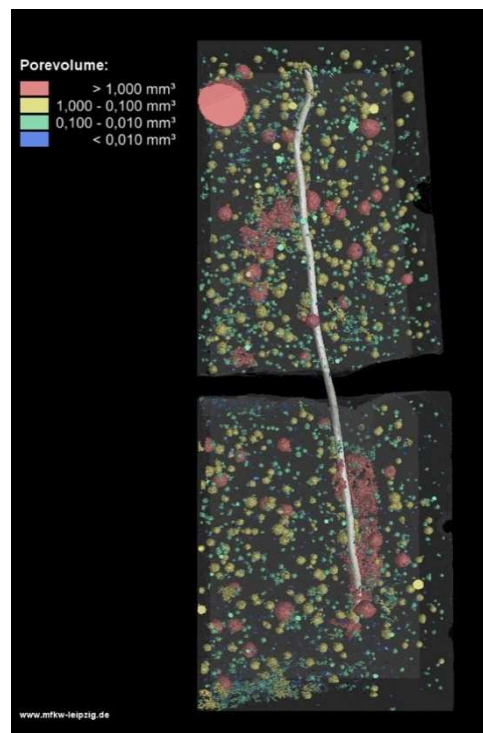


Figure 5.23 – Pore distribution in the cracked mortar specimen

## 5.5 CONCLUSIONS

An innovative non- standard test procedure was considered in this chapter to investigate the pull-out behavior of RSF embedded in cracked concrete specimens previously exposed to chloride environment. In addition, the potentiality of using X-ray Micro-computed Tomography (3D- $\mu$ XCT) technique to investigate the fiber reinforcement mechanisms developed during the fiber pull-out from cracked RSFRC under corrosion action was analyzed. From these studies, the following conclusions have been drawn:

- 1) There is no clear relationship between the corrosion susceptibility of RSF crossing a pseudo-crack in self-compacting concrete (SCC) and the crack width, for crack widths lower than 0.7 mm. The corroded RSF from cracked specimens submitted to chloride attack showed higher variability in

terms of cross section loss, probably due to the irregular geometry of the RSF that caused an irregular chloride attack at the exposed length of RSF in the crack, and consequently variable susceptibility to fiber corrosion. For the higher levels of crack widths ( $> 1.6$  mm), a high probability of RSF corrosion was observed, similar to ISF.

- 2) A high variability was obtained in the crack width implemented in the SCC specimens for the same applied load due to the irregular geometry of RSF that leads to significant differences in the fiber reinforcement mechanisms developed during the RSF pull-out from SCC matrix.
- 3) Fiber failure occurred for most pull-out tests of RSF embedded in cracked SCC specimens after subjected to 10 days of immersion in 3.5 wt% NaCl solution. This fact was due to the reduction of the sectional area of RSF caused by corrosion action. The failure mode of RSF not subjected to corrosion action was fiber pull-out.
- 4) Corrosion products of RSF were visually observed at cracked surfaces of the pre-cracked specimens subjected to chloride immersion. No significant signs of corrosion were detected at the surface of RSF from uncracked specimens.
- 5) The results of fiber pull-out bending tests showed higher pull-out load and higher residual resistance in the post peak behavior compared to direct fiber pull-out tests due to the mechanism of snubbing effect developed by the pull-out bending character of the adopted test that increases the fiber/matrix shear friction with the crack opening process.
- 6) The X-Ray Micro-computer Tomography (3D- $\mu$ XCT) showed to be a promising technique to measure, with high accuracy, the crack width at fiber level, the fiber diameter, the fiber slip and the specimen porosity during the fiber pull-out tests. However, the adopted equipment had some limitations to study the corrosion mechanisms of RSF due to the limit of resolution of the measurement device. Moreover, further research is needed to improve the fiber pull-out test configuration proposed in order to obtain the fiber pull-out load -end slip response under corrosion action.

---

# Chapter 6

---

## **POST-CRACKING BEHAVIOR OF RSFRC UNDER CHLORIDE ATTACK CHARACTERIZED FROM SPLITTING TENSILE TESTS**

### **6.1 INTRODUCTION**

In uncracked Steel Fiber Reinforced Concrete (SFRC), steel fibers are protected by the high alkalinity ( $\text{pH} > 13.5$ ) of the pore solution of concrete that causes the formation of a protective oxide film on the steel fibers surface, passivating them (Chen *et al.*, 2015). This film can be destroyed when the chloride ions penetrate the SFRC and exceed the critical threshold chloride content (Chen *et al.*, 2015). However, in a corrosive environment, such as deicing salt and sea water containing chloride ions with relatively high concentration, it has been reported that only steel fibers near the concrete surface are susceptible to corrosion (Balouch *et al.*, 2010).

The main objective of this chapter is to assess the post-cracking behavior of recycled steel fiber reinforced concrete (RSFRC) under chloride attack from double edge wedge splitting tests (DEWSTs). DEWSTs were conducted according with a new test method (Lameiras *et al.*, 2015) that arose from the combination of the methodology proposed by di Prisco *et al.* (2013) for indirect evaluation of the mode I fracture properties of FRC (Section 2.3.7.2.2) and the Modified Splitting Tensile Test (MSTT) introduced by a group of researchers from the University of Minho (Abrishambaf *et al.*, 2015a,b) (Section 2.2.1.2.2). These tests were divided in two parts. The first part was dedicated to the study of the influence of small rubber particles attached to recycled steel fiber (RSF) surface in the performance of RSF as concrete reinforcement and in its corrosion resistance by immersion in a chloride solution for a certain period. In

this sense, the two distinct pre-treatment methods used to eliminate the attached rubber from RSF, presented in the Section 3.2.3.2, were considered. In the second part of this experimental program, the long-term effects of chloride attack on the post-cracking response of RSFRC was evaluate by adopting different periods for chloride immersion, namely 10 days, and 3 and 6 months.

In FRC structures, the cracking control provided by the fiber reinforcement mechanisms can promote high levels of stress redistribution, leading to higher load carrying capacity and deformability levels. In fact, the energy dissipated on the concrete fracture propagation is the concrete property that most benefits from fiber reinforcement effects. However, this dissipated energy is quite dependent on the fiber orientation and distribution (Cunha, 2010; de Oliveira, 2010). The dispersion and orientation of fibers in concrete depends of several factors, namely, mixing and placing technology of FRC (e.g. vibration and wall-effect introduced by the formwork), rheology of FRC, geometric properties of FRC constituents, especially of fibers, and geometry of the structure (Lameiras, 2015). The fiber efficiency is highly dependent of the fiber orientation towards the active crack plane (Cunha, 2010; Abrishambaf, 2015). Fiber density (number of fibers per unit area crossing a certain section) is influenced by the boundaries that affect the fibers orientation and by the vibration that tends to re-orient the fibers in horizontal planes (Cunha, 2010). The increase of the vibration time induces a fiber re-orientation to a more anisotropic fiber orientation, however, it also increases the segregation degree (Cunha, 2010). The increase of the vibration time induces a fiber re-orientation to a more isotropic fiber orientation, however, it also increases the segregation degree (Cunha, 2010). Consequently, fiber distribution and orientation should be considered for structural design, especially when their variability increases the heterogeneity of the mechanical properties of FRC (Abrishambaf, 2015). In this chapter, the influence of the distribution and orientation of fibers on the post-cracking behavior of RSFRC after exposed to chloride immersion is also assessed by image analysis (Cunha, 2010; Abrishambaf, 2015).

Additionally, the tensile stress-crack width ( $\sigma - w$ ) relationship and mode I fracture parameters of the tested RSFRC are determined by performing inverse numerical analysis of the DEWSTs results with a nonlinear 2D finite element model.

## **6.2 EXPERIMENTAL PROGRAM**

### **6.2.1 Specimens manufacture and environmental exposure**

For each test series, two  $\phi 150 \times 300$  mm cylinders were casted with RSFRC0.8% mixture (Table 3.18). The mixing and fresh properties of RSFRC0.8%, and the curing procedure of specimens are described in Section 3.4.1. After 28 days of curing, one cylinder was immersed in a 3.5 wt% NaCl solution in order to

induce chloride attack, and other reference cylinder was only cured in water saturated with calcium hydroxide, for comparison purposes.

Four specimens of  $\phi 150 \times 60$  mm were obtained from each cylindrical specimen for the DEWST, as shown in Figure 6.1. A thickness layer of 10-12.5 mm was discarded from the upper and lower end of each  $\phi 150 \times 300$  mm cylinder. Following the procedure adopted by di Prisco *et al.* (2013), a V-shaped groove with  $45^\circ$  inclination was executed at the extremities of the notched plane, as illustrated in Figure 6.1 (Notch 1). This V-shaped groove has the objective of inducing a stress field corresponding to an almost pure mode I fracture in the notched plane. In each specimen, 5 mm deep notches were executed parallel to the loading direction, in order to set the specimen's fracture surface along the notched plane (Notch 2 in Figure 6.1). These two notches were implemented in the specimens after the environmental exposure indicated in Table 6.1.

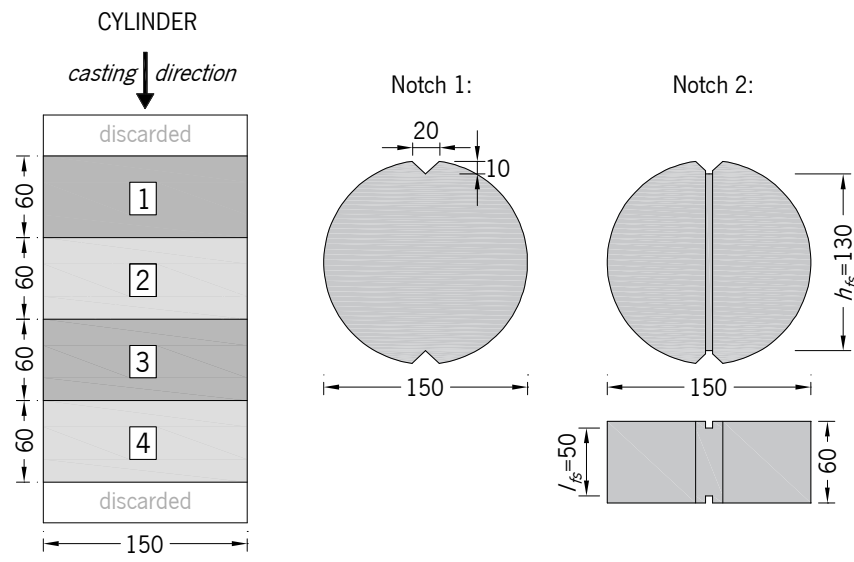
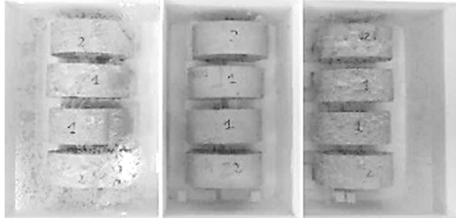
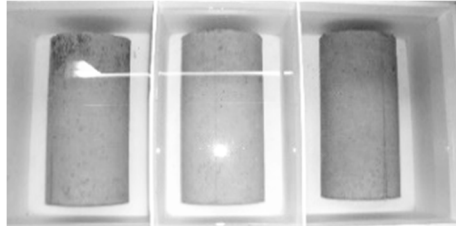


Figure 6.1 – Schematic representation of the preparation process of DEWST specimens from  $\phi 150 \times 300$  mm cylinders (units in mm)

The DEWSTs were divided in six series considering the three classes of RSF (Section 3.2.3.2) and different immersion periods of the specimens before being tested, as presented in Table 6.1. Different exposure conditions of the cut faces of the specimens were also adopted (Table 6.1). In Series I, II and III, the faces of the  $\phi 150 \times 60$  mm cylindrical specimens were directly exposed to immersion. In Series IV, V and VI, the  $\phi 150 \times 300$  mm cylinders were subjected to immersion and the DEWST specimens were obtained by cutting the cylinders after they have been subjected to environmental exposure (the faces of the  $\phi 150 \times 60$  mm specimens were not directly in contact with the solution).

In the second part of the experimental program (Series IV, V and VI), only RSF previously submitted to 350°C (Class 2) were used to produce the RSFRC specimens. This decision was taken after the analysis of the results obtained in the first part of the experimental program, Series I, II and III (Section 6.3.1), where it was found that using RSF of Class 2 and 3, the RSFRC presented an improved pos-cracking behavior after chloride attack. Furthermore, the Class 3 RSF showed lower corrosion rate in the linear polarization tests (Section 4.4.3) and the pre-treatment of fibers at high temperatures is easier and faster to apply than polishing them.

Table 6.1 – Experimental program of DEWSTs

Series	RSF	Exposure conditions of specimens before DEWST	
		Period	Immersion
I	Class 1 (REF)		<p>For each Series:</p> <ul style="list-style-type: none"> <li>➤ Chloride immersion (Cl): 4 <math>\phi</math>150x60 mm</li> <li>➤ Water immersion (REF): 4 <math>\phi</math>150x60 mm</li> </ul> <p>Specimens cut from <math>\phi</math>150x300 mm before exposure</p>
II	Class 2 (350°C)	10 days	<p>Exposed cut faces:</p> 
III	Class 3 (Polished)		
IV		10 days	<p>For each Series:</p> <ul style="list-style-type: none"> <li>➤ Chloride immersion (Cl): 1 <math>\phi</math>150x300 mm</li> <li>➤ Water immersion (REF): 1 <math>\phi</math>150x300 mm</li> </ul> <p>Specimens <math>\phi</math>150x60 mm cut after exposure</p>
V	Class 2 (350°C)	3 months	<p>Unexposed cut faces:</p> 
VI		6 months	

### 6.2.2 Experimental setup and procedures

The splitting tests were conducted under displacement control using an external LVDT that was positioned on the actuator to control the vertical deformation of the specimen. The tests were performed with relatively low displacement rates enabling to obtain a stable response once the crack process was initiated. The following displacement rates were adopted: 1.0  $\mu$ m/s up to the displacement of 2.0 mm; 2.0  $\mu$ m/s from 2.0 mm up to 3.0 mm; 4.0  $\mu$ m/s until the end of the test.

Each specimen was positioned between two rigid supports and subjected to a diametral compressive line load applied along the thickness of the specimen (Figure 6.2). For an accurate detection and tracking of the crack propagation, five LVDTs were used to measure the crack opening displacement along the fracture surface (Figure 6.2) - three on the front face and two on the rear face of the specimen. The load was registered by means of a 150 kN load cell. The test setup was defined based on the combination of DEWST and MSTT, aiming to overcome the limitations of each test method, deviating the crosswise compressive stresses from the fractured section while a unique fracture plane is likely to be obtained (Lameiras *et al.*, 2015).

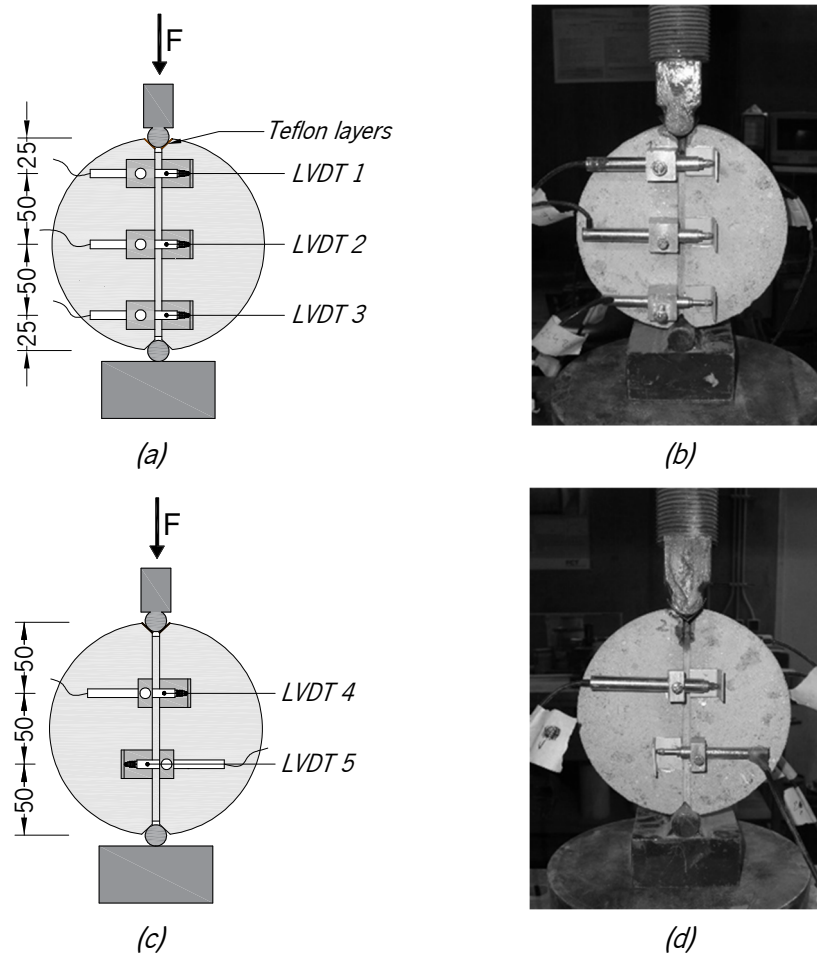


Figure 6.2 – Test setup for DEWST:

(a) (b) Specimen front view; (c) (d) Specimen back view (units in mm)

After testing, each of the two fracture surfaces of the split specimen was divided in four equal regions in order to evaluate the fiber distribution (Figure 6.3). The fiber density was evaluated by counting the number of effective fibers crossing the fractured surfaces. A fiber was considered effective when its length was visible, therefore assuming this fiber has failed by pull-out.

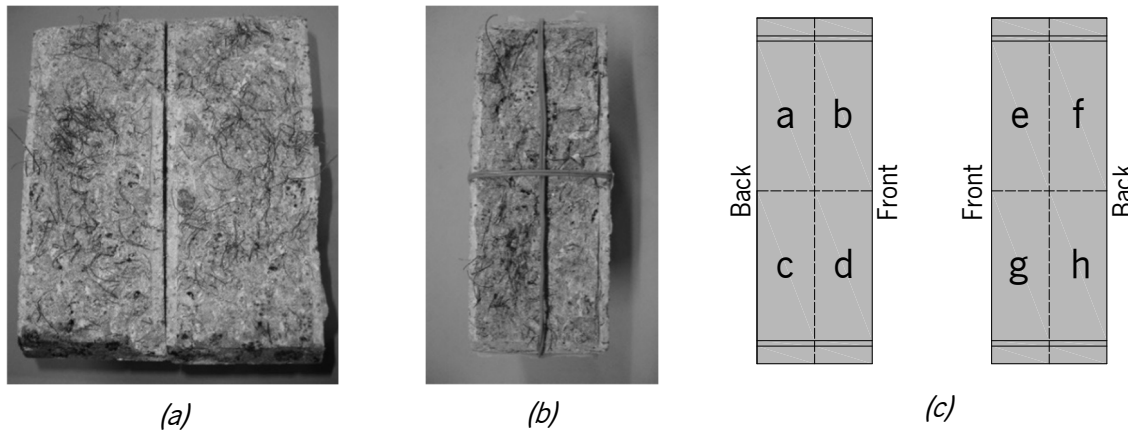


Figure 6.3 – Assessment of the fiber density in the fractured zone of specimens:  
 (a) Overall view of fracture surface; (b) (c) Schematic representation of the regions of fibers counting, identifying the front and back faces of the tested specimens

### 6.3 EXPERIMENTAL RESULTS AND DISCUSSION

To assess the influence of the pre-treatments methods used for removing rubber particles from RSF surface (Section 3.2.3.2) in the corrosion resistance of RSFRC, the tests of Series I, II and III, of the first part of this experimental program, were carried out after the specimens have been subjected to chloride immersion for 10 days in 3.5 wt% NaCl solution. To evaluate the long-term effects of chloride attack on the post-cracking behavior of RSFRC, the tests of Series IV, V and VI, of the second part of this experimental program, were conducted after the specimens have been subjected to 10 days, and 3 and 6 months of immersion in 3.5 wt% NaCl solution.

#### 6.3.1 Effect of the rubber content attached to fibers surface in the corrosion resistance of RSFRC (Series I, II and III)

After 10 days of chloride immersion, it was possible to observe corroded material in the 3.5 wt% NaCl solution (Figure 6.4a) and corrosion spots at exposed surfaces of the specimens, especially in the specimens of Series II, produced with concrete reinforced with RSF of Class 2, previously submitted to high temperatures (Figure 6.4b). This fact corroborates with the results obtained in the linear polarization tests of RSF after 30 minutes of chloride immersion (Table 4.3), where the Class 2 RSF showed higher corrosion rates than RSF of Class 1 and 3. However, after performing the DEWST, no significant signs of corrosion were observed in the RSF crossing the fracture surface of all specimens (Figure 6.4c). That is, only fiber ends in direct contact with the solution on the cut surfaces of concrete specimens were significantly corroded after the 10 days of chloride exposure.



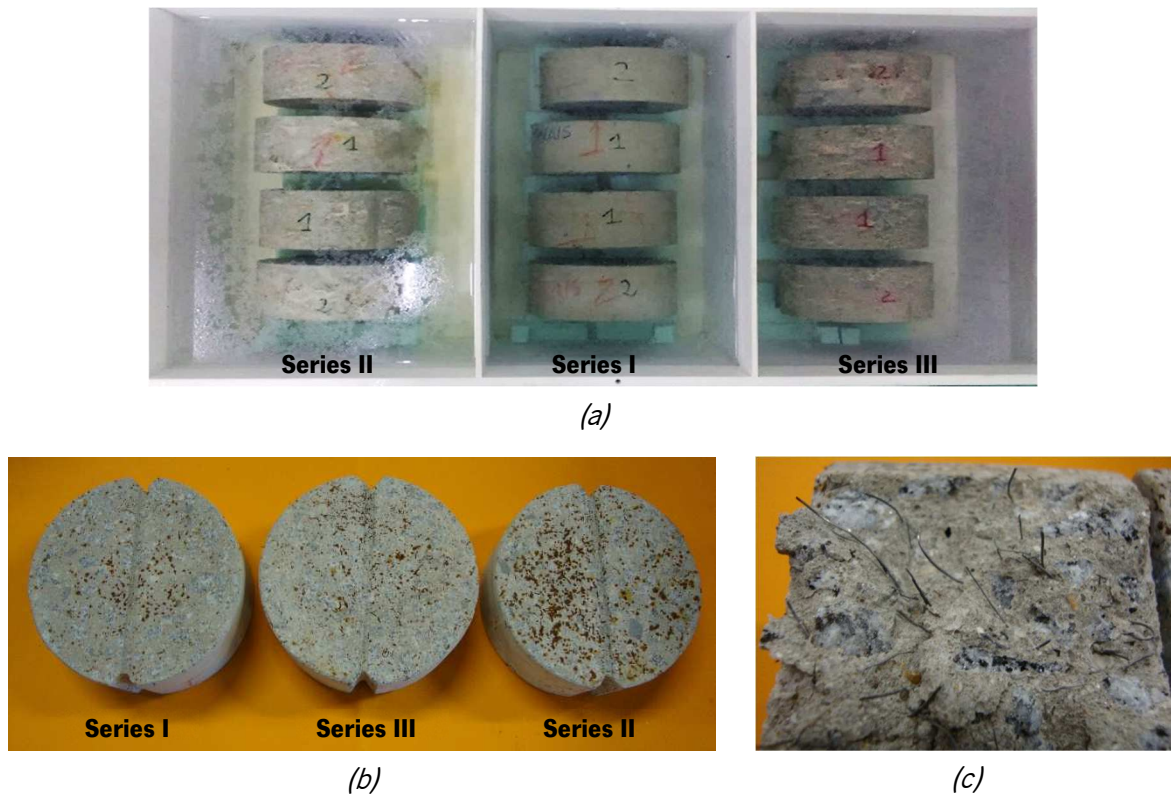


Figure 6.4 – Specimens subjected to 10 days of chloride immersion (Series I, II and III):  
 (a) Aspect of 3.5% NaCl solution; (b) Corrosion spots at exposed faces of the specimens (cut surfaces);  
 (c) RSF at crack surface of a specimen after DEWST with no visible signs of corrosion

Figure 6.5 and 6.6 show the average splitting tensile stress-CMOD curves,  $\sigma_{t,split} - \omega$ , obtained in tests of Series I, II and III, after chloride attack (Cl) and only cured in water (REF). The  $\sigma_{t,split}$  was determined from the equation (2.4) proposed by di Prisco *et al.* (2013) (Section 2.2.1.2.2), where  $h_{fs}$  and  $l_{fs}$  are the thickness and the effective length of the notched region that defines the plan of failure (Figure 6.1), respectively. The crack width in X-axes,  $\omega$ , corresponds to the average values measured by the five LVDTs during the loading stage of the specimens, as shown in Figure 6.2.

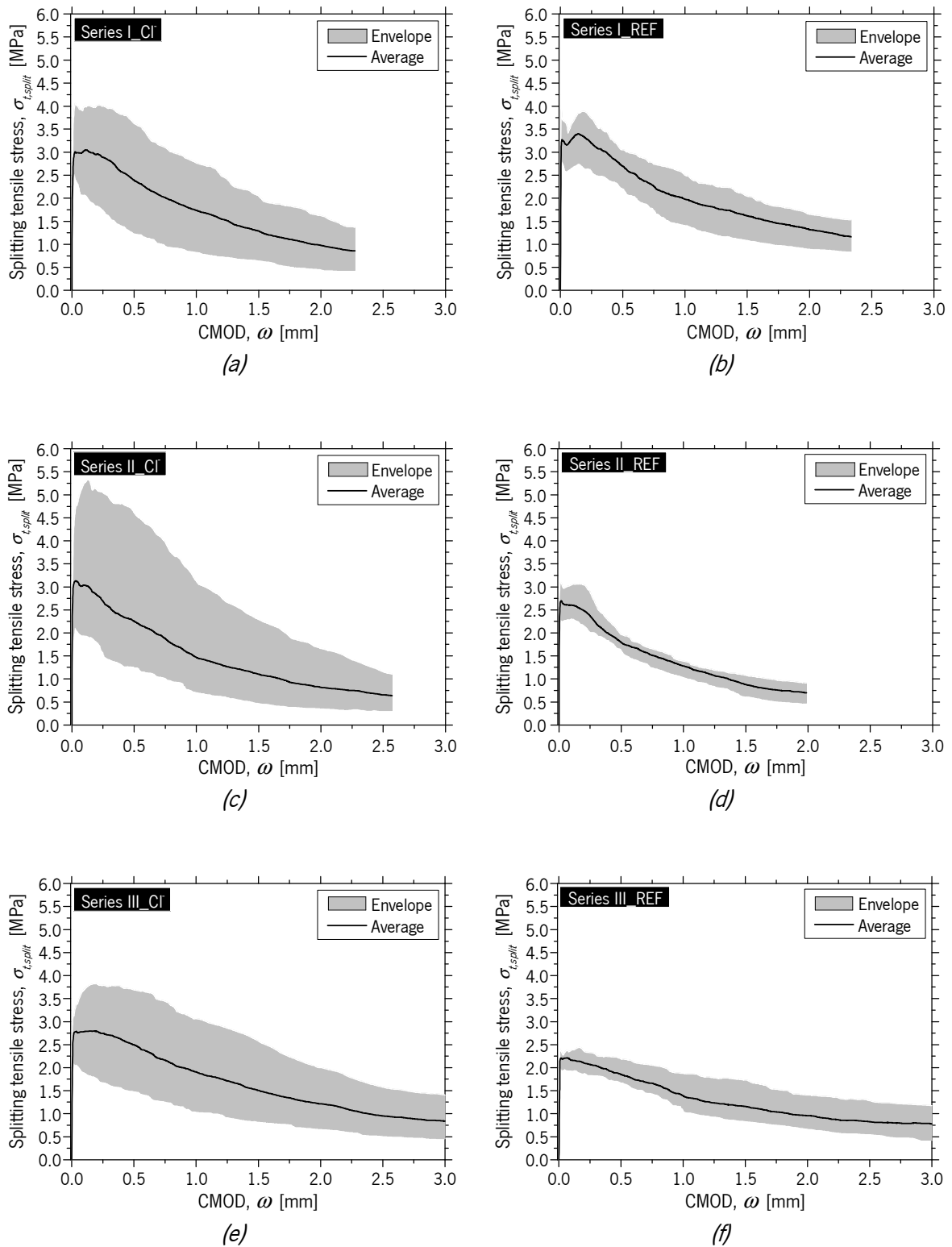


Figure 6.5 – Envelope and average splitting tensile stress-CMOD curves for specimens of: (a) Series I\_Cl; (b) Series I\_REF; (c) Series II\_Cl; (d) Series II\_REF; (e) Series III\_Cl; (f) Series III\_REF

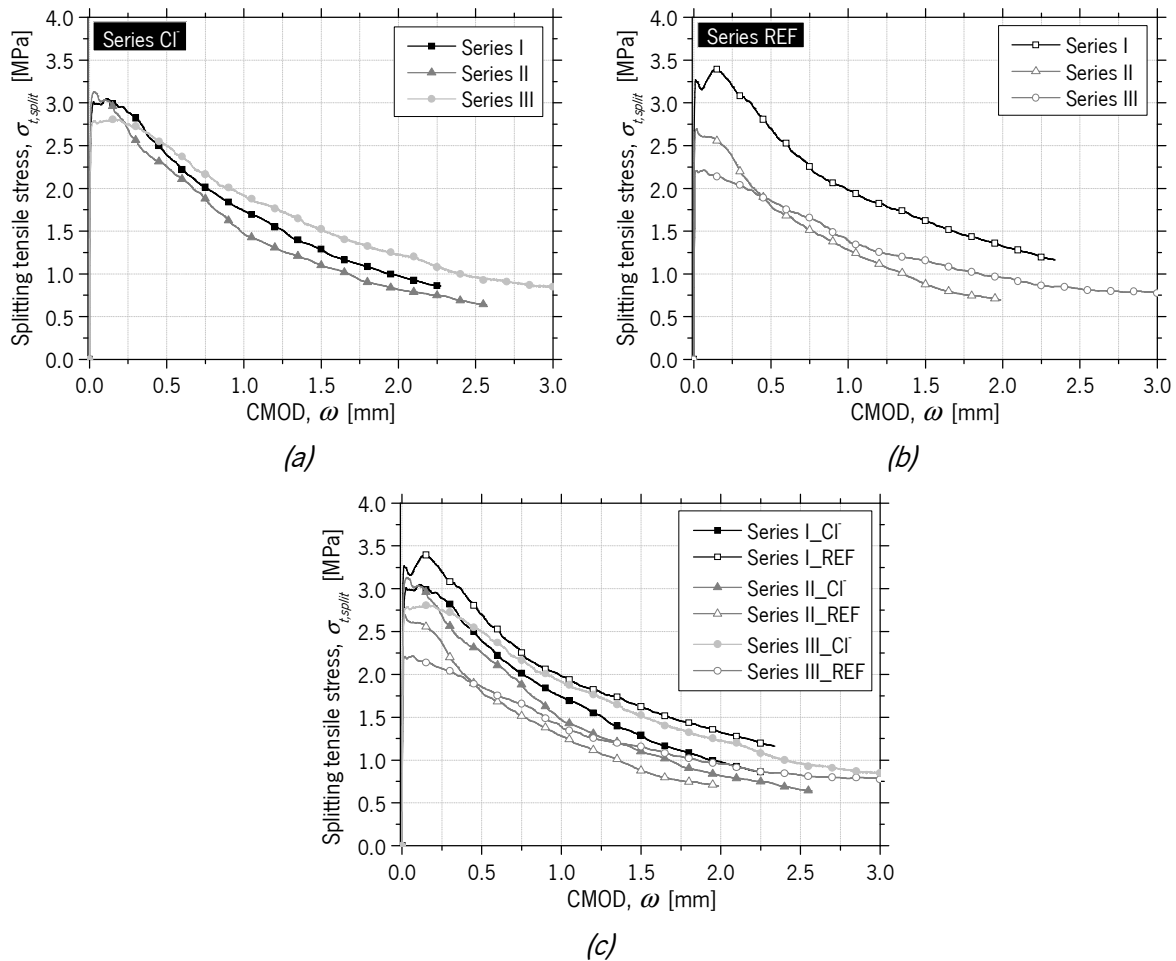


Figure 6.6 – Average splitting tensile stress-CMOD curves for specimens of: (a) Series I&II&III\_Cl; (b) Series I&II&III\_REF; (c) Series I&II&III\_Cl&REF

According to Figures 6.5a,c,e, the dispersion of the results has increased significantly with the chloride immersion, probably due to the irregular geometry of the fibers and the fiber distribution/orientation profile that caused an irregular chloride attack at the fiber-matrix interfacial transition zone (ITZ), and consequently, variable susceptibility to fiber corrosion. For specimens of Class 1 RSF (REF), the chloride attack caused a slight decrease of the average stress at crack initiation (7.9%) and the average post-cracking tensile strength (10.3%) (Figure 6.6c). However, for specimens of Class 2 and 3 RSF, the chloride attack led to the opposite trend, i.e. to an increase of the average stress at crack initiation (16.2% in Class 2 and 26.2% in Class 3) (Figure 6.6c). Apparently, an increase in fiber bonding may have occurred for Class 2 and 3 RSF after chloride attack, which could be associated to the increased roughness at fiber surface caused by corrosion (Granju and Balouch, 2005; Frazão *et al.*, 2016). However, no significant signs of corrosion were visible in the RSF at crack surface after DEWST, even on fibers near the exposed surface, where the chloride penetration was greater than 1 mm, as shown in Section 6.3.2.1. A superficial

corrosion occurred in the fibers near the exposed surface, which was only detected at microscopic level, as presented in Section 6.3.2.2. However, this very low level of fiber corrosion does not explain the significant difference between the  $\sigma_{t,split} - \omega$  curves of Series II and III. Moreover, as reported in literature, only fibers near the concrete surface are expected to be corroded for short exposed periods (Marcos-Meson *et al.*, 2018). Considering the results obtained in the linear polarization tests after 7 days of immersion (Table 4.3 – Series VI and VIII), where similar values of  $i_{corr}$  were obtained for RSF of Class 1 and 2, it was not expected the significant influence of the chloride attack on the splitting tensile strength in the tests of Series I. Assuming that no significant corrosion phenomena occurred at the fiber surface level, the differences between  $\sigma_{t,split} - \omega$  relationships obtained for specimens submitted to chloride attack and reference specimens were mainly due to the irregular geometry and the distribution and orientation of fibers. It is also possible that the corrosion products from the corroded fibers near the exposed surface had a beneficial effect in terms of fiber pull-out behavior during the splitting tests. From the results of non-corroded specimens, it was found that the most effective fibers were those of Class 1, followed by those of Class 2 and 3. The Class 1 RSF had a more irregular fiber surface than Class 2 and 3, as shown in Figures 3.2c, 3.14a and 3.15a, which may justify the results obtained with reference specimens (Fig. 6.6b), since the irregularity of the RSF surface contributes to the increase of fiber pull-out force. The reference specimens of class 1 RSF showed the highest average stress at crack initiation (3.27 MPa for a  $\omega$  of 0.012 mm) and the highest average post-cracking tensile strength (3.40 MPa for a  $\omega$  of 0.145 mm), which means that the two methods used to remove the small percentage of rubber from the fibers surface led to a decrease of the splitting tensile strength of the RSFRC specimens (Figure 6.6b). It is also important to note that the RSF of class 1 used in reference specimens were mostly at the level of F3 and F4 of Fig. 3.22, with few rubber debris attached. Taking also into account the monotonic pull-out tests in Section 3.2.3.4, these results suggest that in specimens of class 2 RSF a significant amount of fibers had broken during the splitting tests. Considering also the higher level of pull-out load achieved by RSF of class 1 than by classes 2 and 3 (Fig. 3.21), the highest average splitting tensile stress showed by class 1 RSF may be justified. The relevant conclusions taken from the stress-crack opening relationships can be also confirmed by determining the residual strength at a given crack width,  $\sigma_{\omega}$ , and the respective energy due to fracture propagation,  $G_{F\omega}$ , which corresponds to the area under the softening curve up to these  $\omega$  values. The average values are presented in Table 6.2 and 6.3.

Table 6.2 – Maximum and residual splitting tensile strength (Series I, II and III)

Series		$\sigma_{max}$ (MPa)	$\sigma_{0.3}$ (MPa)	$\sigma_{0.5}$ (MPa)	$\sigma_{1.0}$ (MPa)	$\sigma_{1.5}$ (MPa)	$\sigma_{3.0}$ (MPa)
I_Cl	Avg	3.19	2.82	2.39	1.73	1.29	0.73
	CoV (%)	(20.47)	(33.64)	(40.68)	(45.69)	(44.78)	(28.65)
I_REF	Avg	3.59	3.08	2.70	1.98	1.63	0.79
	CoV (%)	(13.77)	(14.56)	(13.44)	(23.95)	(26.12)	(30.37)
II_Cl	Avg	3.41	2.56	2.25	1.47	1.10	0.59
	CoV (%)	(40.89)	(63.65)	(70.89)	(76.55)	(74.76)	(55.11)
II_REF	Avg	2.73	2.20	1.79	1.28	0.88	0.57
	CoV (%)	(15.24)	(12.54)	(7.79)	(12.15)	(21.16)	(17.14)
III_Cl	Avg	2.94	2.71	2.49	1.91	1.51	0.84
	CoV (%)	(24.55)	(32.74)	(36.26)	(44.44)	(49.93)	(47.69)
III_REF	Avg	2.28	2.04	1.85	1.39	1.16	0.77
	CoV (%)	(8.56)	(8.68)	(12.53)	(23.98)	(34.15)	(47.40)

Table 6.3 – Energy due to fracture propagation (Series I, II and III)

Series		$G_{F0.3}$ (N/mm)	$G_{F0.5}$ (N/mm)	$G_{F1.0}$ (N/mm)	$G_{F1.5}$ (N/mm)	$G_{F3.0}$ (N/mm)
I_Cl	Avg	0.88	1.40	2.41	3.16	5.18
	CoV (%)	(27.86)	(31.21)	(35.88)	(38.17)	(27.58)
I_REF	Avg	0.97	1.56	2.70	3.59	5.14
	CoV (%)	(12.34)	(12.80)	(15.49)	(18.11)	(23.93)
II_Cl	Avg	0.86	1.34	2.27	2.91	4.60
	CoV (%)	(50.61)	(56.92)	(64.07)	(66.52)	(65.48)
II_REF	Avg	0.75	1.15	1.91	2.45	3.65
	CoV (%)	(14.79)	(12.68)	(11.12)	(10.97)	(3.59)
III_Cl	Avg	0.82	1.34	2.43	3.28	4.94
	CoV (%)	(27.82)	(30.62)	(34.70)	(37.77)	(40.84)
III_REF	Avg	0.64	1.03	1.84	2.47	3.83
	CoV (%)	(8.58)	(8.92)	(12.45)	(16.89)	(23.72)

The Figure 6.7 highlights the relationship between  $\omega$  and  $G_{F\omega}$  in DEWST of Series I, II and III. As observed, it is confirmed that the two pre-treatment methods used to clean the fiber surface from rubber debris, had a negative effect on the  $G_{F\omega}$  for all the crack opening levels at which this property was evaluated. The  $G_{F\omega}$  of RSFRC specimens submitted to 10 days of chloride immersion was similar between the three series of DEWST.

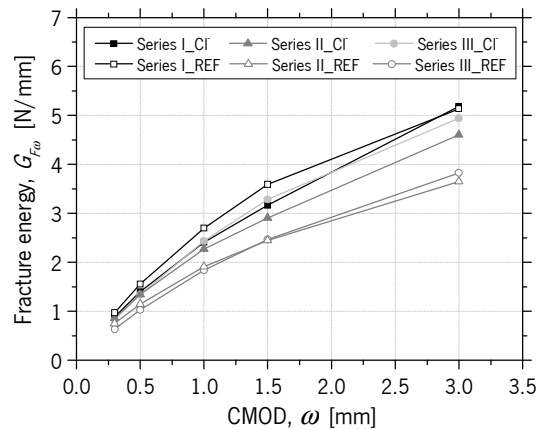


Figure 6.7 – Relationship between the crack width and energy absorption during the fracture propagation in the specimens of Series I, II and III

### 6.3.1.1 Assessment of the number of effective fibers (Series I, II and III)

The results of the average (AVG) effective fiber density at the crack surface for Series I, II and III are presented in Table 6.4, identified according to the casting depth of the  $\phi 150 \times 300$  mm cylindrical specimens shown in Figure 6.1. According to the position of front and back faces of splitting specimens in the DEWST (Fig. 6.3c), the effective fiber density was also determined in two parts of the crack surface: Back (regions a,c,f,h - Fig. 6.3c) and Front (regions b,d,e,g - Fig. 6.3c).

In general, no significant differences were observed between the average number of fibers in the back and front regions at the cracked surface of the tested specimens. The total number of effective RSF at fracture tends to increase from the concrete casting surface to the bottom of the cylinder (Fig. 6.1), which suggests the occurrence of fiber segregation. According to this, the small differences found between the fiber density at back and front faces of the DEWST specimens may be attributed to this segregation phenomenon (Fig. 6.1).

Table 6.4 – Effective fiber counting at fracture surface of splitting specimens of Series I, II and III

Series	Casting depth (Fig. 6.1)	Fiber density (fibers/cm <sup>2</sup> )			AVG	Series	Casting depth (Fig. 6.1)	Fiber density (fibers/cm <sup>2</sup> )			AVG		
		Back*		Front**				Back*		Front**			
		a	b	e				f	a	b		e	f
I_Cl	1	2.55	3.08	3.08	2.82	I_REF	1	3.68	2.14	2.14	2.91		
	2	4.53	3.37	3.37	3.95		2	2.59	4.16	4.16	3.37		
	3	4.43	3.79	3.79	4.11		3	3.12	5.62	5.62	4.37		
	4	4.79	4.22	4.22	4.50		4	5.69	4.26	4.26	4.98		
	Avg	4.08	3.61	3.61	3.84		Avg	3.77	4.05	4.05	3.91		
	CoV (%)	(25.17)	(13.70)	(13.70)	(18.79)		CoV (%)	(35.97)	(35.42)	(35.42)	(24.02)		
II_Cl	1	2.24	2.57	2.57	2.40	II_REF	1	1.61	2.54	2.54	2.08		
	2	3.28	3.16	3.16	3.22		2	3.38	3.41	3.41	3.39		
	3	3.06	3.56	3.56	3.31		3	3.82	4.03	4.03	3.92		
	4	6.69	6.28	6.28	6.48		4	5.23	2.33	2.33	3.78		
	Avg	3.82	3.89	3.89	3.86		Avg	3.51	3.08	3.08	3.29		
	CoV (%)	(51.48)	(42.20)	(42.20)	(46.67)		CoV (%)	(42.49)	(25.53)	(25.53)	(25.56)		
III_Cl	1	4.06	3.48	3.48	3.77	III_REF	1	2.14	3.52	3.52	2.83		
	2	4.82	4.67	4.67	4.75		2	3.22	3.94	3.94	3.58		
	3	5.54	4.47	4.47	5.00		3	5.16	3.44	3.44	4.30		
	4	8.43	6.92	6.92	7.68		4	5.39	5.30	5.30	5.34		
	Avg	5.71	4.89	4.89	5.30		Avg	3.98	4.05	4.05	4.01		
	CoV (%)	(33.44)	(29.74)	(29.74)	(31.54)		CoV (%)	(39.34)	(21.26)	(21.26)	(26.69)		

\*Average of areas “a”, “c”, “f” and “h”; \*\*Average of areas “b”, “d”, “e” and “g”

The relationships between the effective fiber density and the  $G_{F\omega}$  of specimens of Series I, II and III are presented in Figures 6.8 and 6.9.

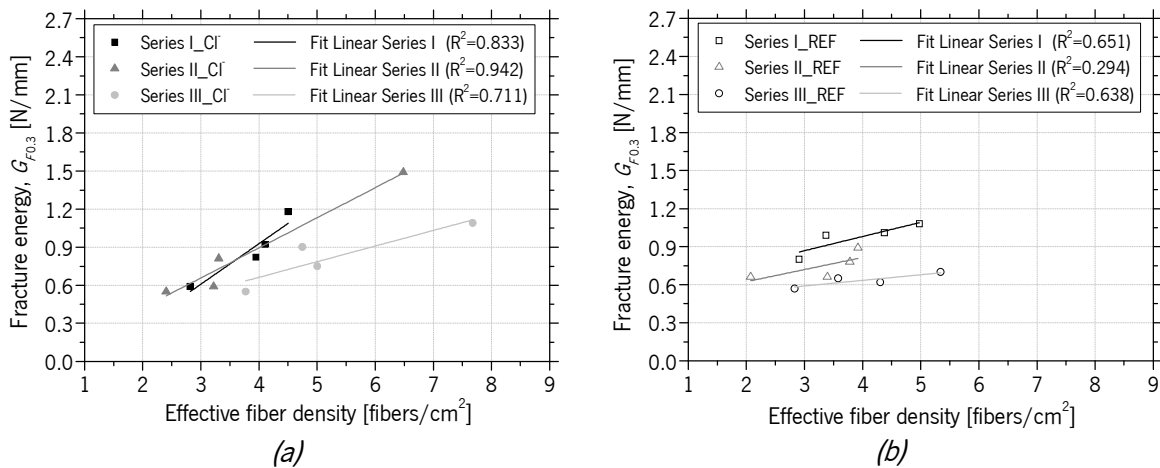


Figure 6.8 – Relationships between the effective fiber density and  $G_{F\omega}$  of specimens of:

(a) Series I&II&III\_Cl:  $G_{F0.3}$ ; (b) Series I&II&III\_REF:  $G_{F0.3}$

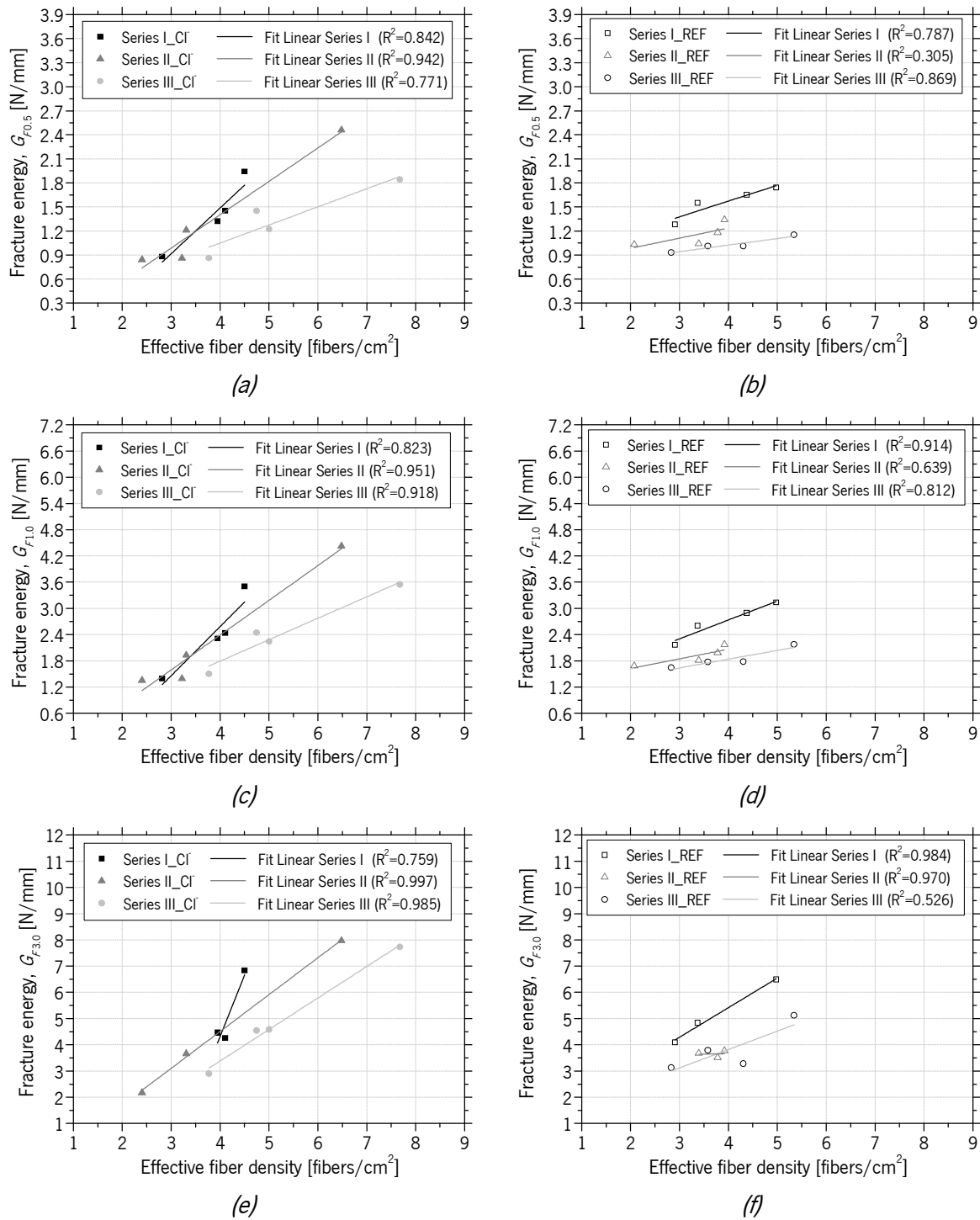


Figure 6.9 – Relationships between the effective fiber density and  $G_{F\omega}$  of specimens:

(a) Series I&II&III\_Cl:  $G_{F0.5}$ ; (b) Series I&II&III\_REF:  $G_{F0.5}$

(c) Series I&II&III\_Cl:  $G_{F1.0}$ ; (d) Series I&II&III\_REF:  $G_{F1.0}$

(e) Series I&II&III\_Cl:  $G_{F3.0}$ ; (f) Series I&II&III\_REF:  $G_{F3.0}$

The Figures 6.8 and 6.9 highlights an almost linear correlation between the energy absorption due to crack propagation of the specimens and the effective fiber counting at the fracture surface. It seems that the differences between the Cl and REF specimens are little related to the chloride attack. A higher



variability of the average number of effective fibers at crack surface was observed for specimens subjected to chloride immersion than in reference specimens (Series II and III), which justifies the higher dispersion of the results presented in Figures 6.5c,e. For Series I, the higher dispersion of  $G_{F\omega}$  in Figure 6.5a is not corroborated with the variability of the number of fibers at crack surface (Table 6.4). In this case, the irregular geometry of the fibers and the fibers orientation may be the main reasons for the higher dispersion of  $\sigma_{\omega}$  and  $G_{F\omega}$  in the specimens after have been submitted to chloride immersion.

### 6.3.2 Long-term corrosion effects on the post-cracking behavior of RSFRC

#### 6.3.2.1 RSFRC subjected to 10 days of chloride immersion (Series IV)

The  $\phi 150 \times 300$  mm cylinders of Series IV of DEWST were subjected to the same exposure period of the  $\phi 150 \times 60$  mm specimens of Series II in order to analyze the influence of exposing to chloride solution the faces to be notched of the  $\phi 150 \times 60$  mm specimen (Table 6.1). After 10 days of chloride immersion, it was also observed the formation of corroded material in the 3.5 wt% NaCl solution, and corrosion spots at the exposed surfaces of  $\phi 150 \times 300$  mm cylinders (Figure 6.10a). After DEWST, one half of the  $\phi 150 \times 60$  mm specimen subjected to chloride attack was broken orthogonally to the crack surface in order to assess the chloride penetration depth by spraying with silver nitrate solution, as observed in Figures 6.10b,c. An average internal depth of chloride penetration of 6.1 mm was measured, which means it did not reach the crack surface, considering the thickness of the notch 1, 10 mm (Figure 6.10b). No significant signs of corrosion were visible in the RSF at crack surface (Figure 6.11a,b), only few casual corrosion spots were detected by microscopic inspection, near the exposed surface (Figure 6.11c).

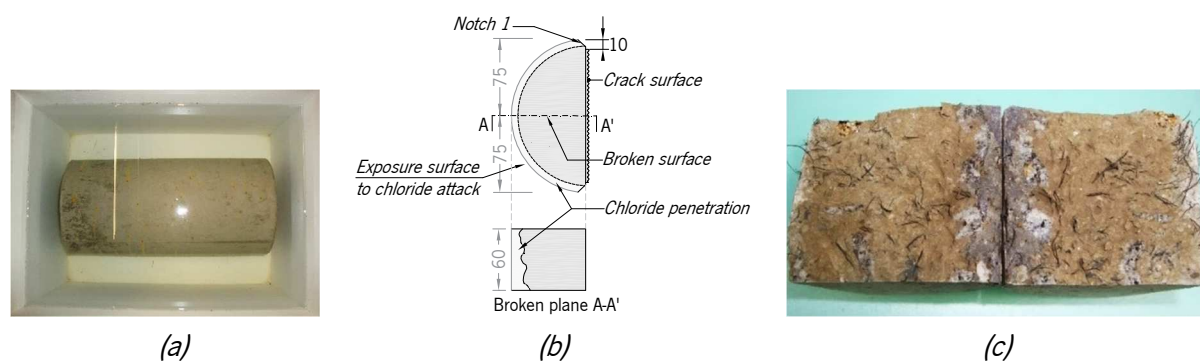


Figure 6.10 – Specimens after 10 days of chloride immersion (Series IV): (a) Aspect of 3.5% NaCl solution and corrosion spots at exposed faces; (b) Chloride penetration measurement (units in mm) (c) Chloride penetration depth

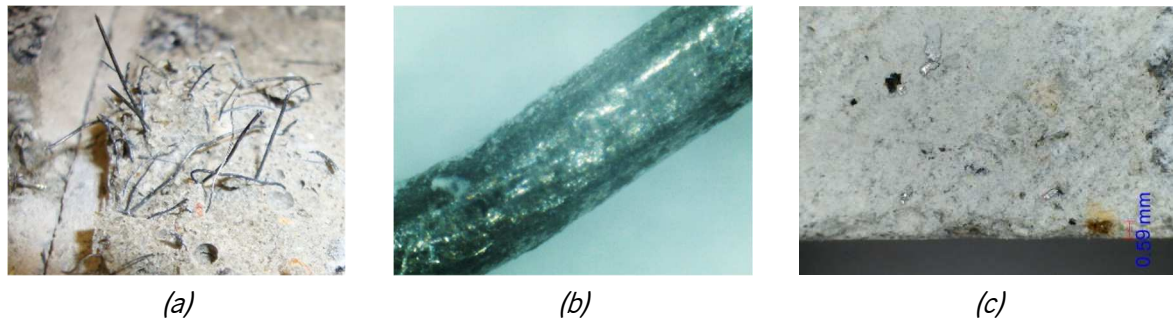


Figure 6.11 – Cracked surface of specimens after 10 days of chloride immersion (Series IV):  
 (a) General aspect of RSF; (b) Microscopic analysis of one pulled RSF;  
 (c) Corrosion sign on RSF near the exposed surface

Figure 6.12a,b shows the average and envelope of splitting tensile stress-CMOD curves,  $\sigma_{t,split} - \omega$  obtained in tests of Series IV, after chloride attack (Cl) and after cured in water (REF). These curves were determined following the same assumptions adopted in those of Figures 6.5 and 6.6 (Section 6.3.1). A low dispersion of the results was obtained for the  $\sigma_{t,split} - \omega$  curves of Series IV, which means that a better uniformity of fiber distribution was guaranteed. The comparison between the  $\sigma_{t,split} - \omega$  curves of Series III and IV is depicted in Figure 6.13. Moreover, contrary to series I, II and II tests, the variability was similar in series IV\_Cl and Series IV\_REF, which confirms that the chloride attack should have been less significant than in series II.

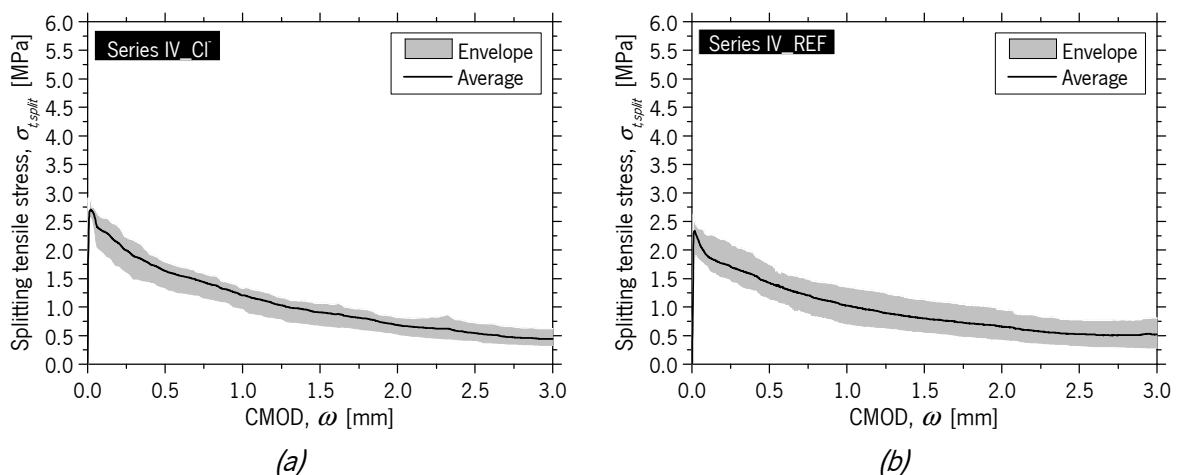


Figure 6.12 – Envelope and average splitting tensile stress-CMOD curves for specimens of:  
 (a) Series IV\_Cl; (b) Series IV\_REF

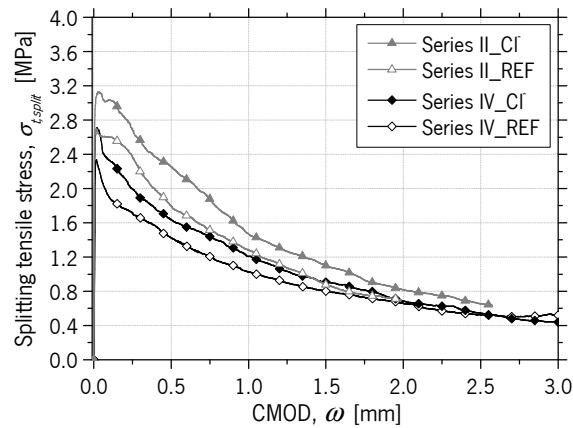


Figure 6.13 – Average splitting tensile stress-CMOD curves for specimens of Series II&IV\_CI&REF

In the Series IV, it seems that the chloride attack also led to a slight increase of the average  $\sigma_{t,split}$  at crack initiation (15.9%), similar to Series II (16.2%), when compared with reference specimens. These differences may also be explained by the fiber distribution and orientation at cracked surface, as will be discussed in Section 6.3.2.5. It was also found that the  $\sigma_{t,split}$  was higher in Series II for both environmental exposures (chloride and water immersion), which may be justified by the age of the specimens at DEWST. Due to unavailability of the test machine after chloride immersion, the specimens of Series II were tested 28 days older (75 days) than those of Series IV (47 days), having been kept in the fog room until the test date.

### 6.3.2.2 RSFRC subjected to 3 months of chloride immersion (Series V)

After 3 months of chloride immersion, no significant increase was observed in terms of corroded material in the 3.5 wt% NaCl solution and corrosion spots at the exposed surfaces of  $\phi 150 \times 300$  mm cylinders (Figure 6.14a). An average internal depth of chloride penetration of 19.5 mm was measured by spraying with silver nitrate solution, which corresponds to 9.5 mm at crack surface, as observed in Figure 6.14b.



Figure 6.14 – Specimens after 3 months of chloride immersion (Series V): (a) Aspect of 3.5% NaCl solution and corrosion spots at exposed faces (b) Chloride penetration depth

Similar to Series IV, there were no significant signs of corrosion in the RSF at crack surface (Fig. 6.15a) and only few fibers near the exposed surface appeared to be corroded, as detected by microscopic analysis (Fig. 6.15b).



Figure 6.15 – Crack surface of specimens after 3 months of chloride immersion (Series V):  
 (a) General aspect of RSF (b) Corrosion sign on RSF near the exposed surface

SEM analysis were carried out in some pulled fibers extracted from the fractured surface of specimens subjected to chloride attack. These pulled fibers were selected from the depth where occurred chloride penetration in order to obtain information on the surface configuration of RSF after chloride attack, before and after the fibers have been pulled out, in an attempt of getting better understanding on their influence in the pull-out reinforcement mechanisms. SEM micrographs of two selected RSF are shown in Figure 6.16.

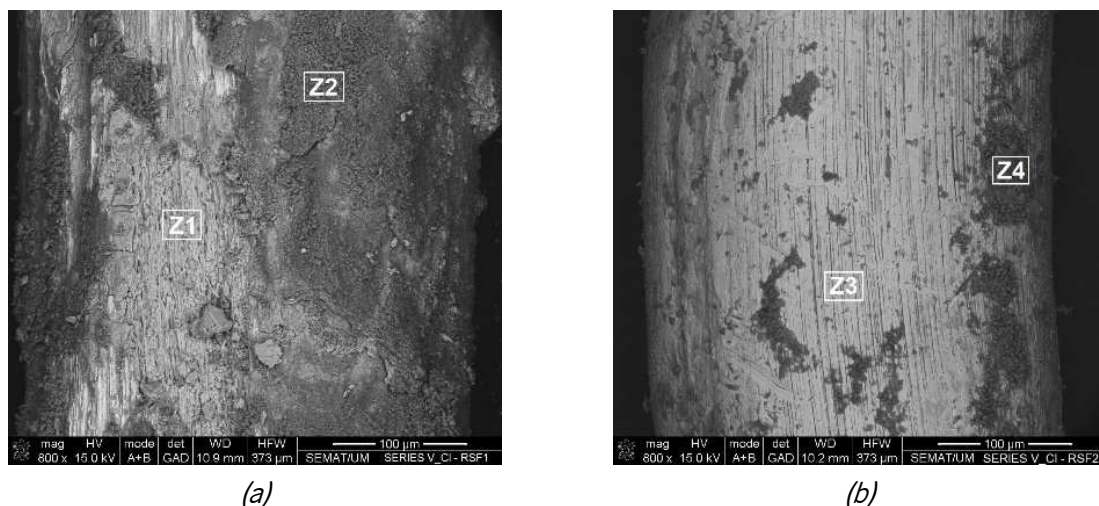


Figure 6.16 – SEM micrographs of Class 2 RSF from the fracture surface of RSFRC specimens subjected to 3 months of chloride attack: (a) RSF1; (b) RSF2

The micrograph presented in Figure 6.16a seems to show signs of corrosion in the RSF surface. According to the micrograph presented in Figure 6.16b, it seems that if the fiber was corroded, the corrosion products were released during the pull-out of the fiber. The micrographs evidence the atomic contrast by backscattered electrons of chemical elements presented in the fiber surface, than could be from the corrosive products and cement hydration products. Through these micrographs, a chemical analysis (SEM-EDS) was carried out to identify the main chemical elements present in the identified zones Z1-Z4 (Figs. 6.16a,b). The chemical composition obtained in these localized zones are presented in Table 6.5.

Table 6.5 – Chemical elements identified in the surface of RSF (T=350°C) from the fracture surface of the splitting specimens previously submitted to 3 months of chloride immersion

Fiber	Zone	Chemical elements (atomic percentage %)				
		C	Fe	O	Ca	Cl
RSF1	Z1	1.15	89.51	3.54	0.31	5.43
	Z2	5.52	21.66	17.41	48.32	0.34
RSF2	Z3	2.91	95.55	0.54	0.68	0.09
	Z4	24.46	20.25	15.02	37.47	-

In zones Z2 and Z4, the chemical elements calcium, Ca, and oxygen, O may be from the cementitious matrix. It seems that no significant corrosion process occurred since the presence of iron, Fe, is limited. Due to the limited presence of oxygen in zones Z1 and Z3, no signs of corrosion products were evident in these areas. The presence of Cu and Zn elements identified in the surface of non-corroded RSF submitted to 350°C (Table 3.12), which should be related with the brass coating, were not detected in the chemical analysis of these RSF, which means that this brass coating of the RSF was removed due to pull-out processes.

Figures 6.17a,b show the average and envelope of splitting tensile stress-CMOD curves,  $\sigma_{t,split} - \omega$ , obtained in tests of Series V, after submitted the specimens to chloride immersion (Cl) and to curing in water (REF) for 3 months. A higher dispersion of the results was obtained in the reference specimens. Moreover, comparing the average curves and the dispersion of the results in Series V (Cl and REF), the chloride attack for 3 months did not cause a significant influence on the  $\sigma_{t,split}$  at crack initiation (increase of 1.64%). This may confirm that no significant corrosion occurred during 3 months of chloride attack.

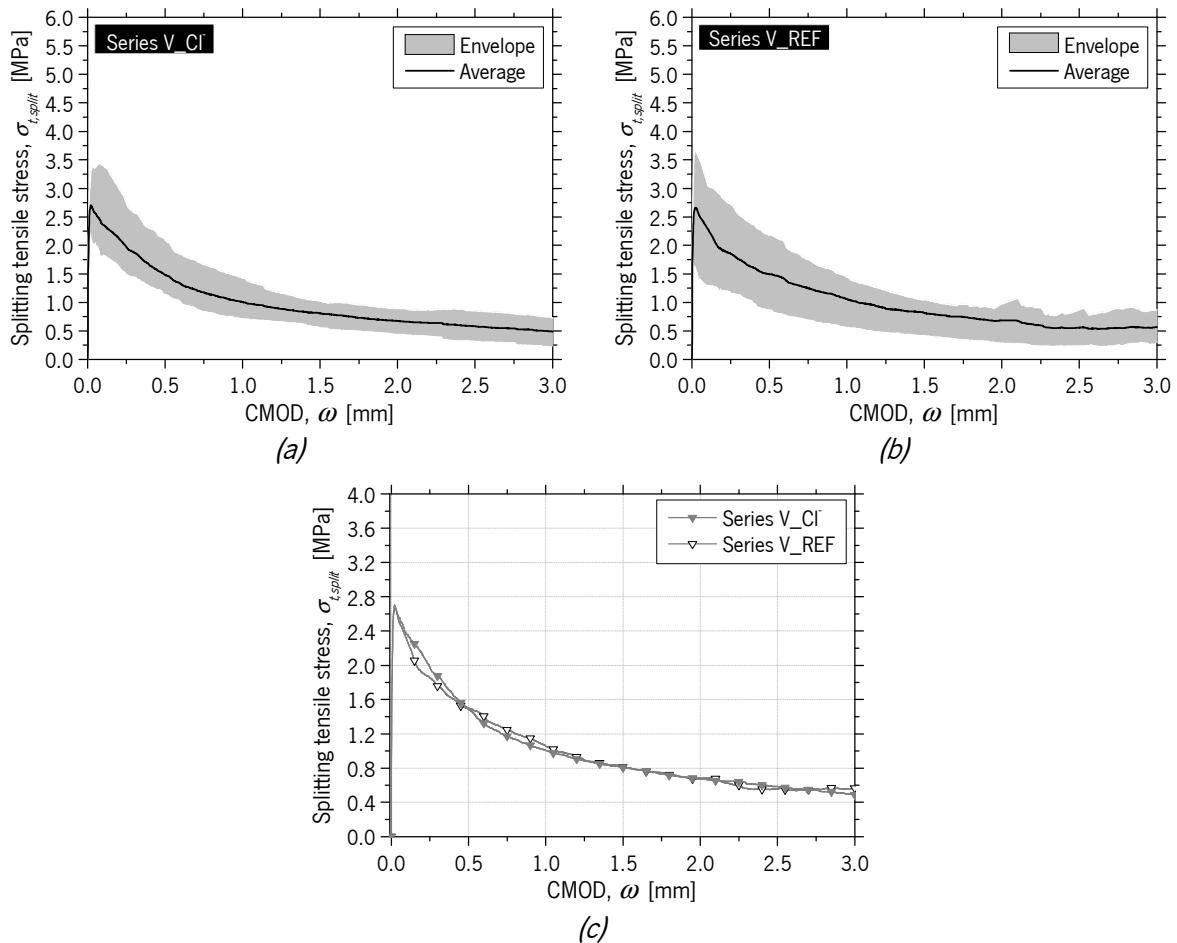


Figure 6.17 – Envelope and average splitting tensile stress-CMOD curves for specimens of:  
 (a) Series V\_CI; (b) Series V\_REF; (c) Series \_CI&REF

### 6.3.2.3 RSFRC subjected to 6 months of chloride immersion (Series VI)

The aspect of 3.5 wt% NaCl solution after 6 months of chloride immersion was similar to the previous series of tests, without significant increase of corrosion products. Corrosion spots at the exposed surfaces of  $\phi 150 \times 300$  mm cylinders were visible due to the RSF that are directly exposed to the solution, without concrete cover (Figure 6.18a). An internal depth of chloride penetration of 28.1 mm, which corresponds to 18.1 mm at crack surface (Figure 6.18b), was measured according to Figure 6.18b.

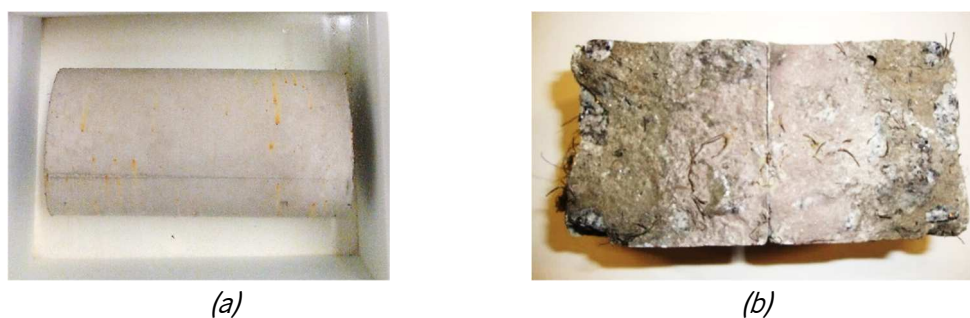


Figure 6.18 – Specimens after 6 months of chloride immersion (Series VI): (a) Aspect of 3.5 wt% NaCl solution and corrosion spots at exposed faces; (b) Chloride penetration depth

No significant signs of corrosion in the RSF at crack surface were detected (Fig. 6.19a), and similar to Series IV and V, only a few fibers near the exposed surface appeared to be corroded (Fig. 6.19b).



Figure 6.19 – Crack surface of specimens after 6 months of chloride immersion (Series VI):  
 (a) General aspect of RSF; (b) Corrosion sign on RSF near the exposed surface

Figures 6.20a,b show the average and envelope of splitting tensile stress-CMOD curves,  $\sigma_{t,split} - \omega$ , obtained in tests of Series VI, after submitted the specimens to chloride immersion (CI) and to curing in water (REF) for 6 months. Figures 6.20 and 6.21 depict the average  $\sigma_{t,split} - \omega$  curves obtained in Series IV, V and VI. The chloride immersion for 6 months (Series VI) led to a slight decrease of the average  $\sigma_{t,split}$  at crack initiation (11.78%). The post-cracking tensile capacity of reference specimens was similar in the tests of Series IV, V and VI (Fig. 6.21), however, a higher dispersion of the results was observed in these tests, probably due to a higher irregular fiber distribution (Fig. 6.21).

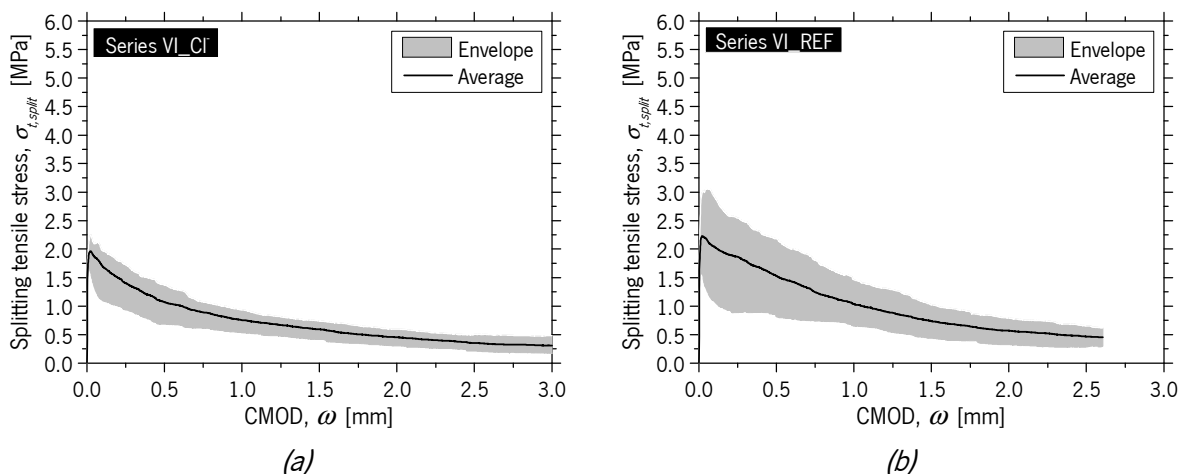


Figure 6.20 – Envelope and average splitting tensile stress-CMOD curves for specimens of:  
 (a) Series VI\_CI; (b) Series VI\_REF

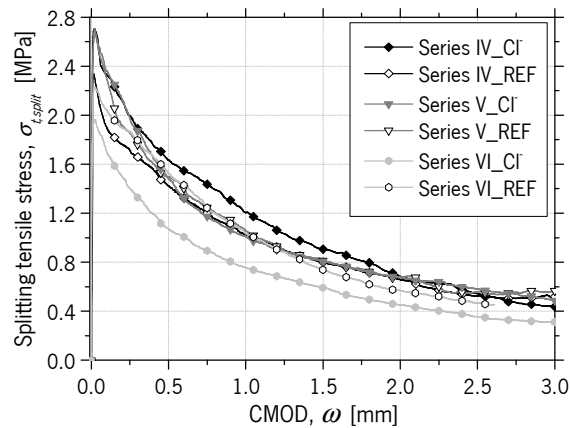


Figure 6.21 – Average splitting tensile stress-CMOD curves for specimens of Series IV&amp;V&amp;VI \_CI&amp;REF

Table 6.6 – Maximum and residual splitting tensile strength (Series IV, V and VI)

Series		$\sigma_{max}$ (MPa)	$\sigma_{0.3}$ (MPa)	$\sigma_{0.5}$ (MPa)	$\sigma_{1.0}$ (MPa)	$\sigma_{1.5}$ (MPa)	$\sigma_{3.0}$ (MPa)
IV_CI	Avg	2.86	1.89	1.63	1.21	0.91	0.44
	CoV (%)	(2.98)	(18.81)	(15.57)	(16.29)	(22.10)	(35.72)
IV_REF	Avg	2.39	1.66	1.42	1.03	0.80	0.52
	CoV (%)	(13.03)	(17.79)	(20.56)	(30.49)	(34.23)	(51.81)
V_CI	Avg	2.78	1.87	1.48	1.01	0.81	0.49
	CoV (%)	(19.30)	(26.62)	(28.75)	(30.88)	(28.44)	(44.61)
V_REF	Avg	2.71	1.76	1.49	1.06	0.82	0.57
	CoV (%)	(31.54)	(37.38)	(37.61)	(33.58)	(32.59)	(40.55)
VI_CI	Avg	2.01	1.33	1.07	0.76	0.59	0.31
	CoV (%)	(12.39)	(23.49)	(26.79)	(24.19)	(25.76)	(42.24)
VI-REF	Avg	2.39	1.80	1.53	1.04	0.74	0.43
	CoV (%)	(32.25)	(41.12)	(40.49)	(41.03)	(43.76)	(33.83)

Table 6.7 – Energy due to fracture propagation (Series IV, V and VI)

Series		$G_{F0.3}$ (N/mm)	$G_{F0.5}$ (N/mm)	$G_{F1.0}$ (N/mm)	$G_{F1.5}$ (N/mm)	$G_{F3.0}$ (N/mm)
IV_CI	Avg	0.67	1.02	1.74	2.26	3.21
	CoV (%)	(12.76)	(13.73)	(14.82)	(16.09)	(18.33)
IV_REF	Avg	0.56	0.87	1.47	1.92	2.84
	CoV (%)	(14.67)	(16.03)	(18.93)	(21.51)	(27.40)
V_CI	Avg	0.67	1.00	1.60	2.05	3.00
	CoV (%)	(25.87)	(26.17)	(27.40)	(26.86)	(26.88)
V_REF	Avg	0.64	0.96	1.59	2.05	2.99
	CoV (%)	(36.79)	(36.68)	(36.00)	(34.80)	(31.72)
VI_CI	Avg	0.52	0.72	1.17	1.51	2.13
	CoV (%)	(7.20)	(23.00)	(23.03)	(22.83)	(24.61)
VI-REF	Avg	0.59	0.92	1.56	2.00	3.08
	CoV (%)	(41.95)	(40.90)	(40.52)	(40.78)	(37.68)



The relationship between the crack width and  $G_{F\omega}$  observed in DEWST of Series IV, V and VI is depicted in Figure 6.22.

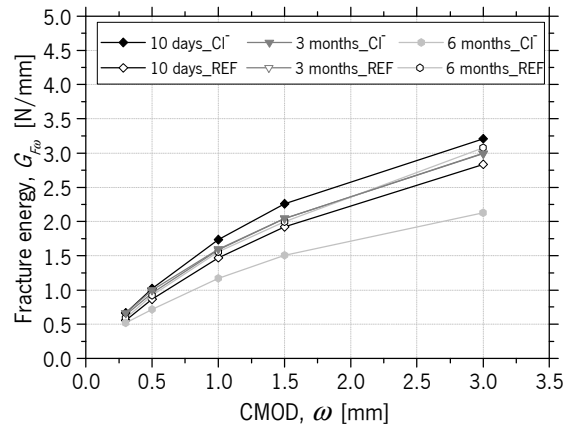


Figure 6.22 – Relationship between the crack width and  $G_{F\omega}$  of specimens of Series IV, V and VI

According to these results (Fig. 6.22), it seems that the chloride attack had not a significant influence on the  $G_{F\omega}$  of specimens submitted to 10 days and 3 months of chloride immersion, compared to reference specimens of Series IV and V. However, after 6 months of chloride immersion, the chloride attack caused a decrease on the  $G_{F\omega}$  for all the crack opening levels at which the energy absorption was evaluated. The  $G_{F\omega}$  in the reference RSFRC specimens was similar for Series IV, V and VI of DEWST.

#### 6.3.2.4 Assessment of the number of effective fibers (Series IV, V and VI)

The average effective fiber density at the crack surface for Series IV, V and VI, identified according to the casting depth (Figure 6.1), are provided in Table 6.8.

The average number of effective RSF at fracture surface of reference specimens (Series IV and V) corroborates with the high dispersion of the results obtained in these specimens (Figures 6.12b, 6.17b). It was not detected an increase tendency of the number of effective RSF with the casting depth of the cylinders, which is indicative of better fiber distribution than in Series I, II and III. According to the coefficients of variation (Table 6.8), it appears that the specimens submitted to chloride attack presented a better distribution of the fibers.

Table 6.8 – Effective fiber counting at fracture surface of splitting specimens of Series IV, V and VI

Series	Casting depth (Fig. 6.1)	Fiber density (fibers/cm <sup>2</sup> )			AVG	Series	Casting depth (Fig. 6.1)	Fiber density (fibers/cm <sup>2</sup> )			AVG
		Back		Front				Back		Front	
		a	b	e				f	a	b	
IV_Cl	1	4.82	2.48	3.65	IV_REF	1	5.45	3.70	4.58		
	2	2.80	3.54	3.17		2	2.39	3.69	3.04		
	3	6.14	3.69	4.92		3	6.12	5.03	5.58		
	4	4.55	4.52	4.53		4	5.58	3.12	4.35		
	Avg	4.58	3.56	4.07		Avg	4.89	3.89	4.39		
	CoV (%)	(30.03)	(23.49)	(19.68)		CoV (%)	(34.60)	(20.84)	(23.81)		
V_Cl	1	3.33	4.43	3.88	V_REF	1	2.69	4.36	3.53		
	2	4.57	4.29	4.43		2	6.84	7.15	7.00		
	3	3.60	6.23	4.92		3	3.93	3.13	3.53		
	4	3.67	2.59	3.13		4	3.23	2.60	2.91		
	Avg	3.79	4.39	4.09		Avg	4.17	4.31	4.24		
	CoV (%)	(14.19)	(33.85)	(18.71)		CoV (%)	(44.42)	(47.15)	(43.45)		
VI_Cl	1	3.09	1.63	2.36	VI_REF	1	4.00	6.24	5.12		
	2	4.32	3.64	3.98		2	5.74	2.95	4.34		
	3	3.87	2.41	3.14		3	2.61	4.59	3.60		
	4	4.43	3.93	4.18		4	2.65	3.62	3.14		
	Avg	3.93	2.90	3.41		Avg	3.75	4.35	4.05		
	CoV (%)	(15.42)	(37.05)	(24.43)		CoV (%)	(39.33)	(32.80)	(21.46)		

Figures 6.23 and 6.24 shows the relationships between the effective fiber density and the  $G_{F\omega}$  of specimens for Series IV, V and VI.

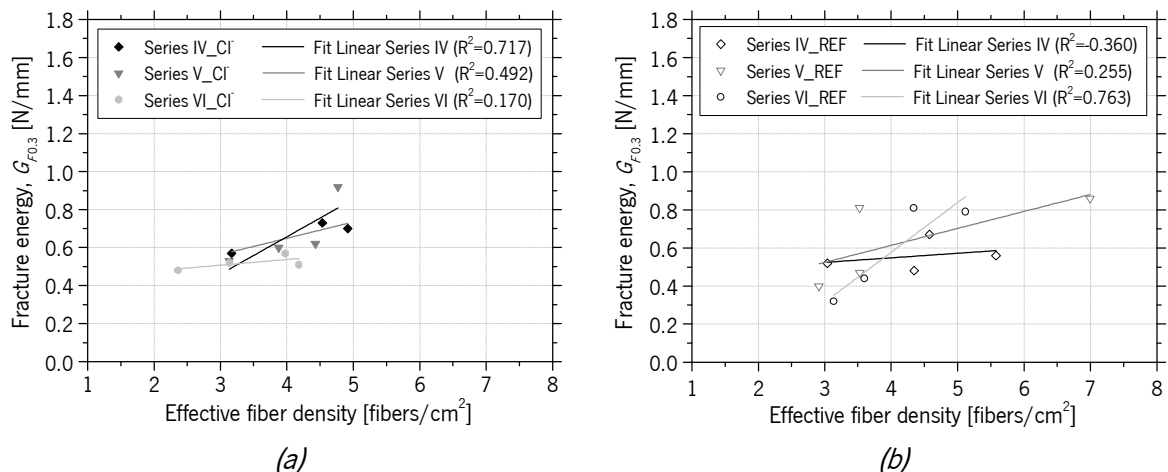


Figure 6.23 – Relationships between the effective fiber density and the toughness of specimens:

(a) Series IV&V&VI\_Cl:  $G_{F0.3}$ ; (b) Series IV&V&VI\_REF:  $G_{F0.3}$

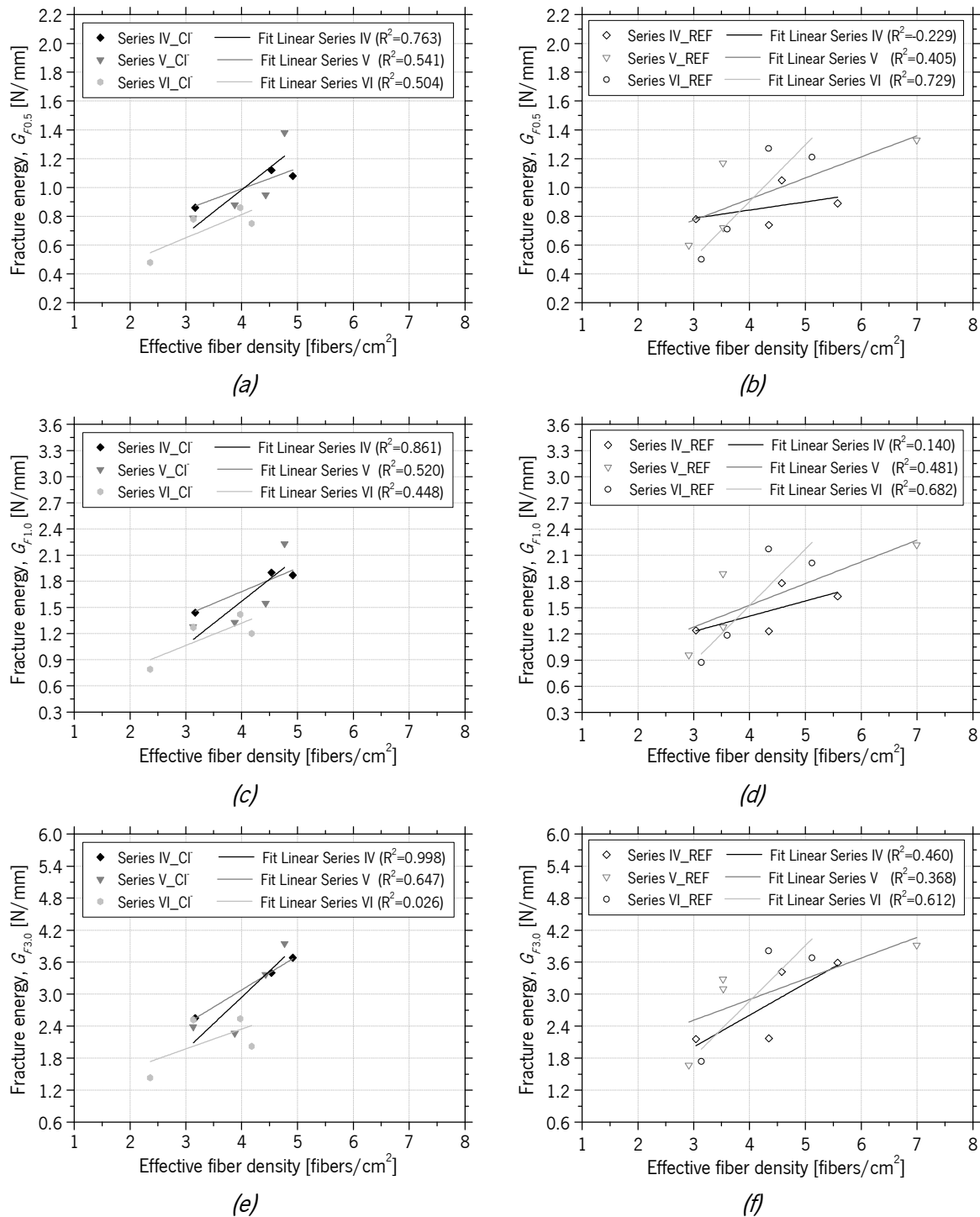


Figure 6.24 – Relationships between the effective fiber density and the toughness of specimens:

(a) Series IV&V&VI\_Cl:  $G_{F0.5}$ ; (b) Series IV&V&VI\_REF:  $G_{F0.5}$

(c) Series IV&V&VI\_Cl:  $G_{F1.0}$ ; (d) Series IV&V&VI\_REF:  $G_{F1.0}$

(e) Series IV&V&VI\_Cl:  $G_{F3.0}$ ; (f) Series IV&V&VI\_REF:  $G_{F3.0}$

Linear correlations are highlighted between  $G_{F,w}$  and the number of effective fibers at the fracture surface.

For all crack opening values evaluated in Series IV and V, Figs. 6.23 and 6.24 also show that the reference specimens have presented higher dispersion of the number of effective fibers at crack surface than the

specimens submitted to chloride attack, which may be caused by the irregular character of fiber geometry and/or due to the orientation of fibers at crack surface. For Series VI, the effective number of fibers at fracture surface was lower in Cl<sup>-</sup> specimens than in REF specimens, which means that the smaller value of  $\sigma_{t,split}$  in Cl<sup>-</sup> specimens may be due to the lower fiber density at crack surface, and not due to chloride effect. Another possibility is the chloride content at the chloride penetration depth exceeded the critical threshold value causing the fiber corrosion. In this case, the fiber corrosion contributes to fiber rupture, decreasing the number of effective fibers and consequently the tensile strength. In order to better clarify these aspects, further research to determine the fiber distribution and orientation parameters was carried out, which is described in the next section.

### **6.3.2.5 Fiber distribution/orientation profile**

For a better understanding of the residual stresses and energy absorption obtained in DEWSTs of Series IV, V and VI, the fiber dispersion and orientation parameters were determined. These parameters were determined by executing image analysis on one plane surface of two tested specimens of Series IV, V and VI (one reference and one submitted to chloride immersion), according to the procedure adopted by Cunha (2010) and Abrishambaf (2015).

The adopted image analysis procedure comprised four main steps (Abrishambaf, 2015). Firstly, half of the tested DEWST specimen was cut parallel to the notch plane and as close as possible to the fracture surface (approximate distance of 5 mm) to obtain a plane surface. This surface was then polished and cleaned with acetone to enhance the reflective properties of RSF. Secondly, pictures of this surface were taken using a high-resolution digital camera (Olympus E-M10 Mark II, 16 effective megapixels). In order to increase the quality of the images, the cut surface of each specimen was divided in twelve areas, with approximately 25x30 mm<sup>2</sup>, and a picture was taken from each one. Afterwards, the obtained images were processed using the software Image J (Ferreira and Rasband, 2012) to recognize the cross section of each RSF intersecting the cut plane. This third step comprises four main tasks: Pre-processing, Segmentation, Classification and Post-processing.

In the first task, the obtained image was converted to an 8 bits picture in grayscale (Figure 6.25a). In the Segmentation task, a black and white image was obtained by defining a threshold and a mask function, distinguishing the cross section of the fibers from the surrounding matrix (Figures 6.25b,c). In the analysis procedure for each picture, the threshold function was set manually with an appropriate value

(Abrishambaf, 2015). Some bright points in the images correspond to crushed granite, that are also reflected by the light of camera's flash, but did not correspond to fibers. In the classification step, only areas higher or equal to the area of the minimum fiber's cross section ( $0.0095 \text{ mm}^2$  with the diameter of  $0.11 \text{ mm}$  (Table 3.8), which represents a perpendicular fiber to the cut surface) were considered. After this classification process, the final images were compared to the initial images by visual inspection (Abrishambaf, 2015). In the post-processing phase, the best circle/ellipse was fitted to each cross section of RSF (Figure 6.21d). If the cross section of a fiber has a circular configuration, the fiber is orthogonal to the cut section, otherwise the fiber has a certain inclination toward this section, and its cross section in this plane has an ellipse format. The number of circles/ellipses, the center of gravity and the minor and major diameters of each individual fitted circle/ellipse were computed and exported to a data file for determining the orientation and segregation factors.

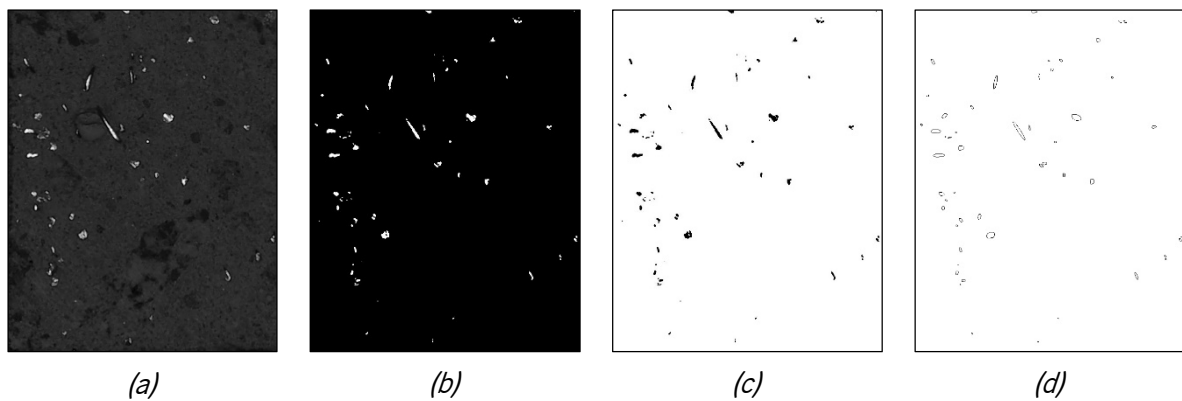


Figure 6.25 – Image processing steps: (a) Converting to grayscale; (b) Adjusting a threshold; (c) Defining a mask; (d) Classification process and fitting the best circle/ellipse to each fiber

After computation of the image analysis results, the following parameters that characterize the fiber structure were derived out: 1) The number of fibers per unit area,  $N^f$ ; 2) Fiber orientation factor,  $\eta$ ; 3) Fiber segregation parameter,  $\xi_{seg}$ .

The number of fibers per unit area,  $N^f$ , is the ratio between the total number of fibers counted in all analyzed images of cut surface,  $N^f$  (number of all the fitted circles/ellipses), and the total area of the cut surface,  $A$ .

The fiber orientation factor,  $\eta$ , was calculated with two different approaches. In the first method, it was calculated based on the image analysis procedure of the cut surface. In the case of ellipse shape of a

single fiber, the average orientation factor for all the fibers intersecting the cut surface,  $\eta_{img}$  can be determined by using the following equation:

$$\eta_{img} = \frac{1}{N_f} \sum_{i=1}^{N_f} \cos \theta_i \quad (6.1)$$

where  $\theta_i$  is the angle between the fiber's longitudinal axis and the orthogonal to the cut section, and can be computed with the major ( $a_f$ ) and minor ( $b_f$ ) axis lengths of the elliptical cross section:

$$\theta_i = \cos^{-1}(b_f / a_f) \quad (6.2)$$

In the second method, the average orientation factor within a cross section,  $\eta_{exp}$  was obtained from Equation (6.3) proposed by Soroushian and Lee (1990):

$$\eta_{exp} = N_f \frac{A_f}{V_f} \quad (6.3)$$

where  $A_f$  and  $V_f$  are, respectively, the cross sectional area of a single RSF and the volumetric percentage of fibers added to concrete. The cross section of RSF was determined with the average value of RSF diameter presented in Table 3.8 (0.25 mm). The obtained results of  $\eta_{img}$  and  $\eta_{exp}$  are presented in Table 3.8.

The degree of segregation along the gravity direction was also determined from equation (6.4), based on the calculation of each Y-coordinate of all the fibers intersecting a certain plane (Babut, 1986):

$$\xi_{seg} = \frac{1}{h.N_f} \sum_{i=1}^{N_f} \bar{y}_i \quad (6.4)$$

where  $\bar{y}_i$  is the coordinate in the Y axis of the center of gravity of each fiber and  $h$  is the height of the specimen in parallel to the vibration direction (Figure 6.26). The value of  $\xi_{seg}$  tends to range between 0 (segregation at the top of surface – Fig. 6.26) and 1 (segregation at the bottom of surface – Fig. 6.26).

Table 6.9 includes the fiber distribution and orientation parameters obtained on the cut surface of one specimen of Series IV, V and VI (Cl and REF).

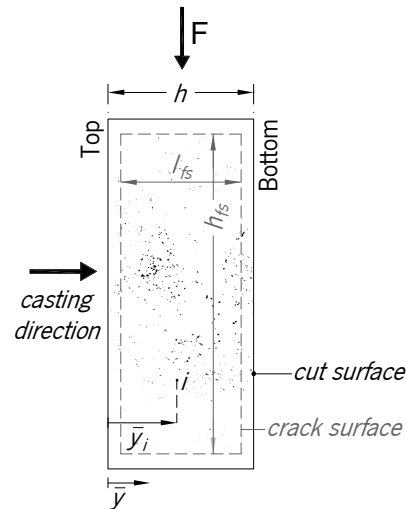


Figure 6.26 – Procedure to determine the fiber segregation degree in DEWST specimens

Table 6.9 – Fiber distribution and orientation parameters for the specimens of Series IV, V and VI after DEWST

Series	Specimen (Fig. 6.1)	$N^f$ (fibers/cm <sup>2</sup> )	$\eta_{img}$	$\eta_{exp}$	$\xi_{seg}$
IV_Cl	3	9.36 (*74%)	0.623	0.574	0.45
IV_REF	2	6.42 (76%)	0.619	0.394	0.44
V_Cl	4	5.95 (*74%)	0.560	0.365	0.40
V_REF	4	8.08 (*82%)	0.562	0.496	0.50
VI_Cl	2	6.17 (*68%)	0.613	0.378	0.49
VI_REF	2	7.04 (*69%)	0.602	0.432	0.47
	Avg	7.17 (*74%)	0.596	0.440	0.46
	CoV (%)	(18.39)	(4.76)	(18.40)	(8.21)

\*Percentage of fibers failed by rupture

For a better analysis of the results obtained for the fiber distribution parameters, the corresponding  $\sigma_{t,split} - \omega$  curves registered in the indicated specimens (Table 6.9) are depicted in Figure 6.27.

In Series IV, the number of RSF per unit area ( $N^f$ ) was higher in the specimen submitted to chloride attack than in the reference specimen, which corroborates with the  $\sigma_{t,split} - \omega$  curves showed in Figure 6.23a. In this sense, the higher values of  $\sigma_{t,split}$  observed in the specimen 3 - Cl compared to specimen 2 - REF (Fig. 6.27a) are justified by the fiber density.

In Series V, the specimen 4 submitted to chloride attack showed a lower number of RSF in the cut surface than the reference specimen 4. However, higher values of  $\sigma_{t,split}$  were observed in the specimen 4 - Cl comparing to specimen 4 - REF (Fig. 6.27b), which may be due to the irregular fiber geometry, and/or to a beneficial effect of chloride attack.

It is also important to mention that the pictures were not taken immediately after the specimens were cut. Since the cutting surface of specimens previously submitted to chloride attack has been exposed to air for some time, this caused the oxidation of some fibers near the exposed surfaces. These oxidized fibers (7% of  $N^f$  on average) have lost their reflective properties and therefore were not accounted for. The specimens of Series VI showed similar fiber density ( $N^f$ ). However, a smaller  $\sigma_{t,split}$  is observed in the specimen submitted to chloride immersion for 6 months (Fig. 6.27c), which may be due to a detrimental effect of chloride attack.

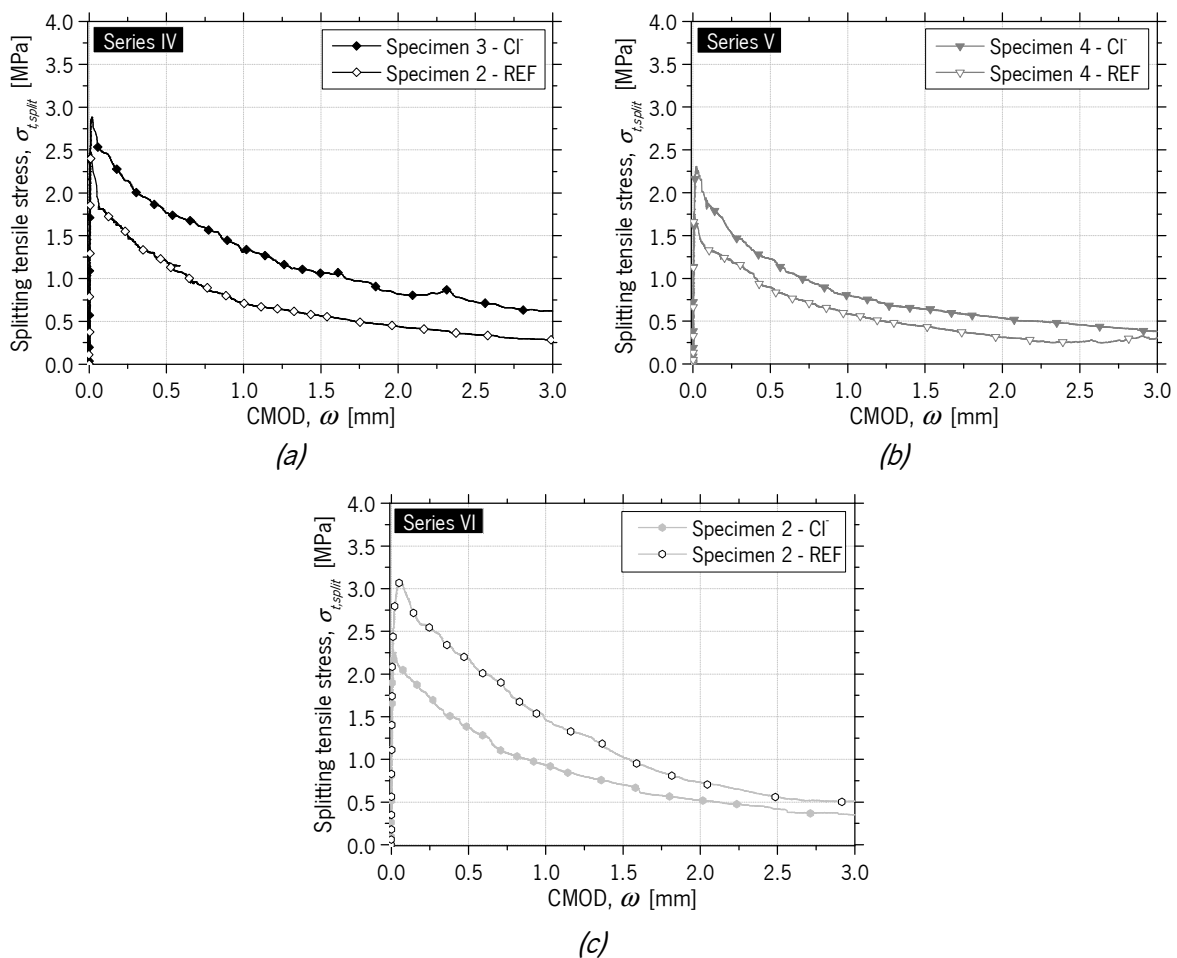


Figure 6.27 – Splitting tensile stress-CMOD curves for specimens:

- (a) 3 of Series IV\_Cl and 2 of Series IV\_REF; (b) 4 of Series V\_Cl and 4 of Series V\_REF;  
(c) 2 of Series VI\_Cl and 2 of Series VI\_REF

The higher values of  $N^f$  (Table 6.9) than the values of effective RSF at fracture surface (Table 6.8) is indicative of a significant number of fibers that were ruptured during the execution of DEWST (not taken into the account as effective RSF) due to the strong bond between recycled fibers and matrix and also due to the rupture tendency of pre-treated RSF at 350°C (class 2) during the pull-out test, as observed in



Section 3.2.3.4. Table 6.9 presents an estimative of the percentage of fibers failed by rupture, which in average corroborates with the percentage (67%) of fibers that had broken during the pull-out tests of Class 2 RSF (Section 3.2.3.4). This percentage of fibers failed by rupture was similar for CI and REF specimens and was the predominant failure mode of fibers in all test series, which means that the beneficial effect of corrosion at ITZ for fibers near the exposed surface, should not be relevant (for example, in the Series V). It seems that when the fibers are submitted to corrosion action, there is a loss of effective cross section of the fibers, and for this reason, the tensile strength tends to decrease. In this case, the corrosion products do not have a beneficial contribution in the pull-out reinforcement mechanisms developed during the RSF pull-out from matrix. In addition, the corrosion effect on the pull-out increment of fibers from matrix should not be also relevant due to the irregularity of fiber geometry, that has a more pronounced influence in the post-cracking behavior of RSFRC.

In terms of the fiber orientation factor obtained by image analysis,  $\eta_{img}$ , similar values were obtained for Series IV and VI. A slight decrease of  $\eta_{img}$  is observed in Series V, which means that the fibers are less aligned perpendicular to the plane surface. This fact corroborates with the lower peak values of  $\sigma_{t,split}$  obtained in the reference specimens. The orientation factor computed from the image analysis approach,  $\eta_{img}$ , is higher than the correspondent  $\eta_{exp}$ .

Concerning the fibre segregation factor,  $\xi_{seg}$ , the obtained values for the studied cross-sectional planes were slightly lower than 0.50. This means that for this RSFRC casting, slightly fiber segregation towards the top of the specimen was observed (Fig. 6.26). This phenomenon was also verified by dividing the cutting surface into 6 layers perpendicular to casting direction (parallel to the applied load) and counting the number of fibers in each layer based on image analysis. Figure 6.28 depicts the average values and the corresponding standard deviation of the number of fibers per unit area crossing the cutting surface. As observed, a larger number of fibers were counted in the layers near the bottom of the specimen.

Considering the cutting surface layered in the other direction, i.e. parallel to casting direction (perpendicular to the applied load), the average number of fibers and the corresponding standard deviation decreased from the center of the cross section to the extremities, as represented in Figure 6.29.

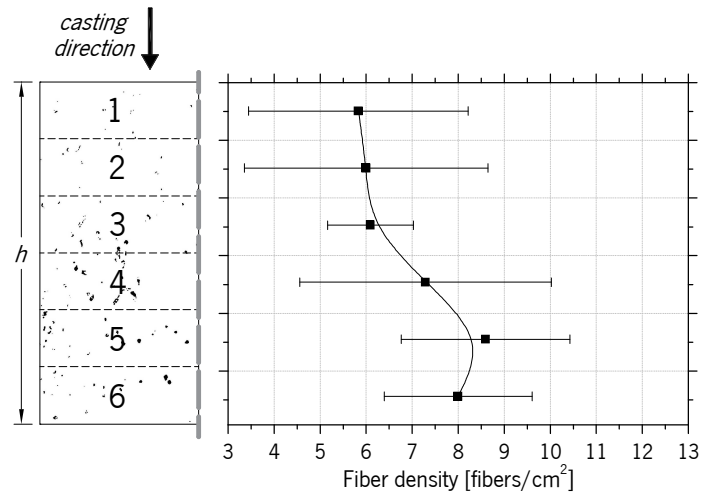


Figure 6.28 – Fiber density in each layer of cutting surface, perpendicular to casting direction

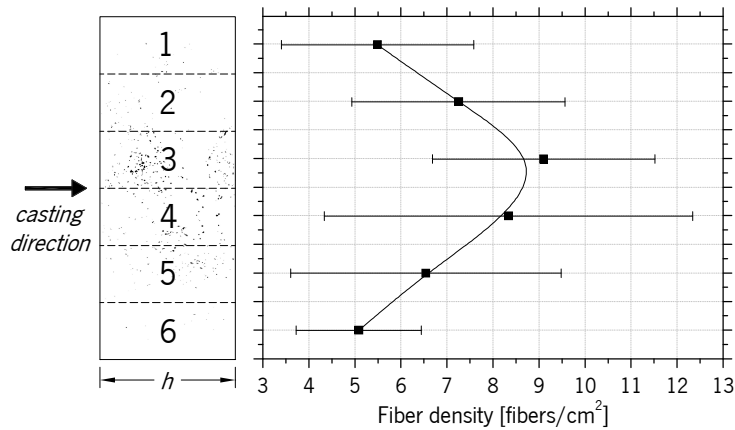


Figure 6.29 – Fiber density in each layer of cutting surface, parallel to casting direction

## 6.4 NUMERICAL SIMULATIONS

In this section, the post-cracking behavior of RSFRC0.8% was assessed by inverse analysis taking the experimental results obtained in DEWSTs into account. In this inverse analysis, the  $\sigma_{t,split} - \omega$  curves obtained in all DEWST Series were fitted as much as possible using a numerical model, implemented by the finite element program FEMIX (Azevedo *et al.*, 2003). Due to the double symmetry condition of the specimen geometry (Figure 6.1), only a quarter of the specimen was modelled. On both axes of symmetry, roller supports were imposed on all nodes to impose null displacements perpendicular to the symmetry axes. A mesh of 8-node Serendipity plane stress finite elements with  $2 \times 2$  Gauss-Legendre integration points (IP) scheme was adopted for the specimen, assuming a linear elastic behavior for the material. The crack initiation and propagation were simulated by using 2D line interface finite elements with  $1 \times 2$  Gauss-Lobato IP, located on the symmetry axis of the specimen in the notched plane. A point load was

applied to the middle of the V-shaped groove edge, orthogonal to this edge, under the displacement control by the arc-length method. Figure 6.30 shows the mesh used in the numerical simulations. The material properties used in the numerical model are indicated in Table 6.10.

Table 6.10 – RSFRC properties used in the numerical simulation of the DEWSTs

Density	$\rho = 2.37 \times 10^{-5} \text{ N/mm}^3$
Poisson's ratio	$\nu_c = 0.20$
Young's modulus	$E_c = 31425 \text{ MPa}$
Tensile strength	Inverse analysis
Fracture mode I parameters	Inverse analysis

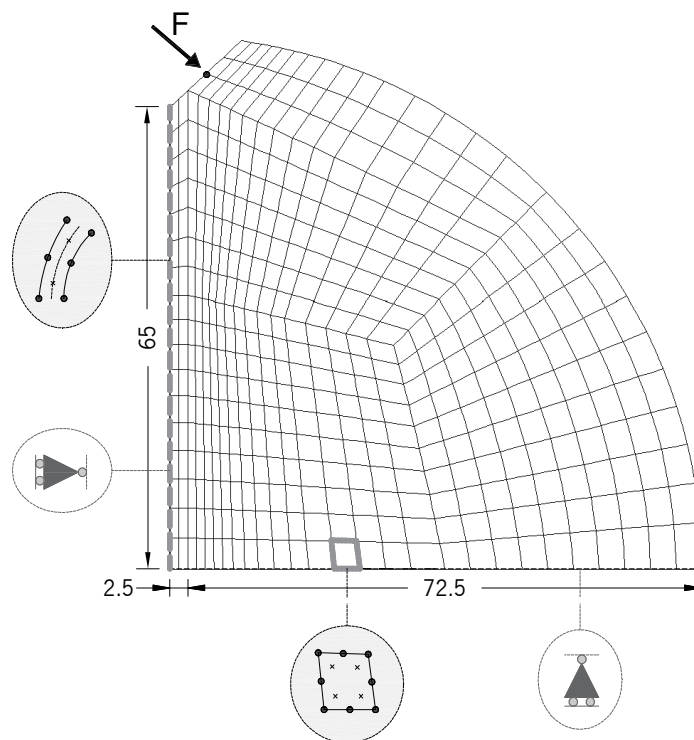


Figure 6.30 – Finite element mesh, support and loading conditions used in the simulation of the DEWST (units in mm)

A trilinear tensile-softening stress-crack width diagram,  $\sigma - \omega$ , was used to simulate the fracture mode I propagation of FRC, and the parameters that define the shape of the diagram, namely, fracture energy,  $G_f$ , and the values of crack opening,  $\omega_f$  and tensile stress,  $\sigma_f$ , that define the  $\sigma - \omega$ , were obtained by performing inverse analysis with the splitting tensile stress-CMOD relationship obtained by the performed DEWSTs. Figure 6.31 presents both the experimental and numerical  $\sigma_{t,split} - \omega$  curves for RSFRC0.8% obtained for all Series of DEWSTs (Table 6.1).

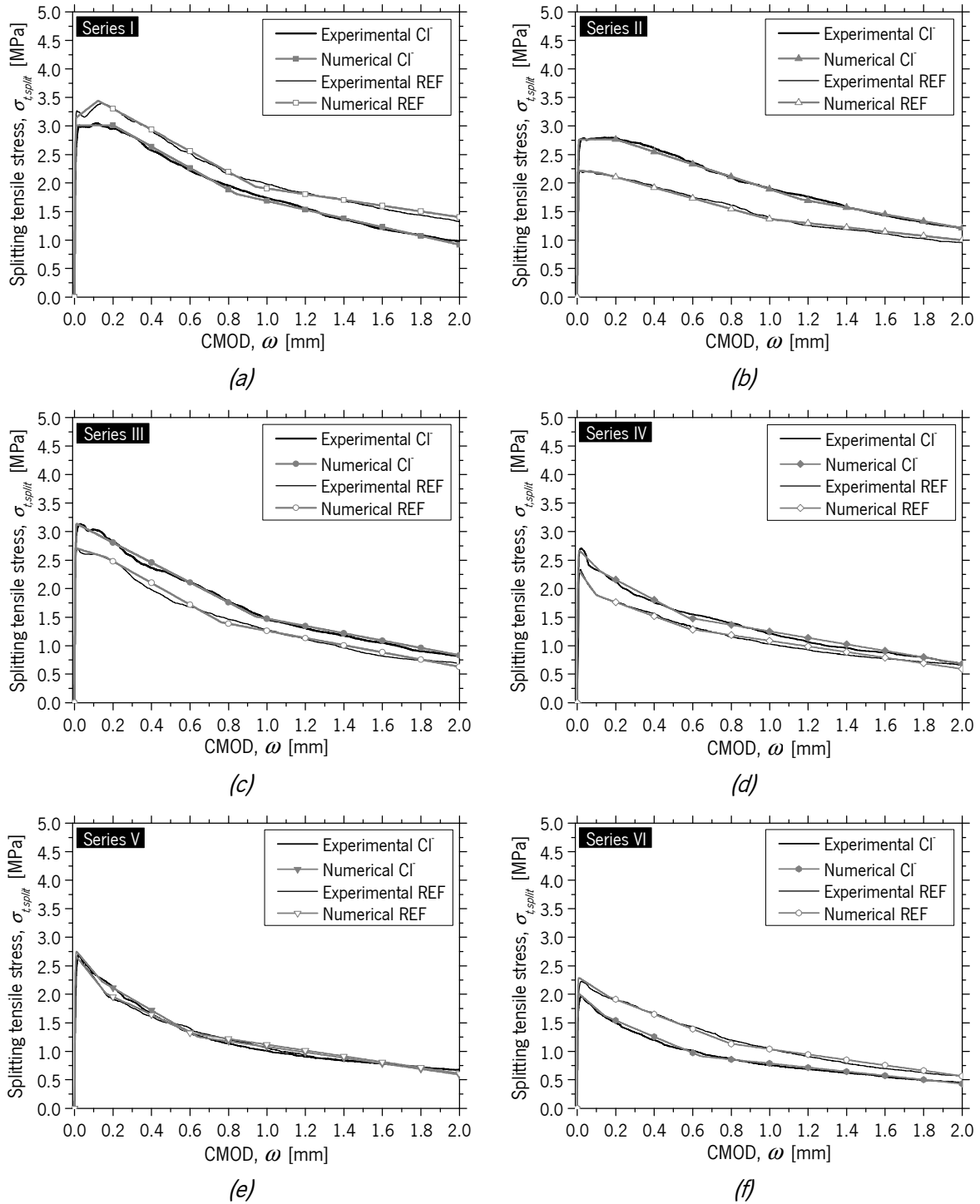


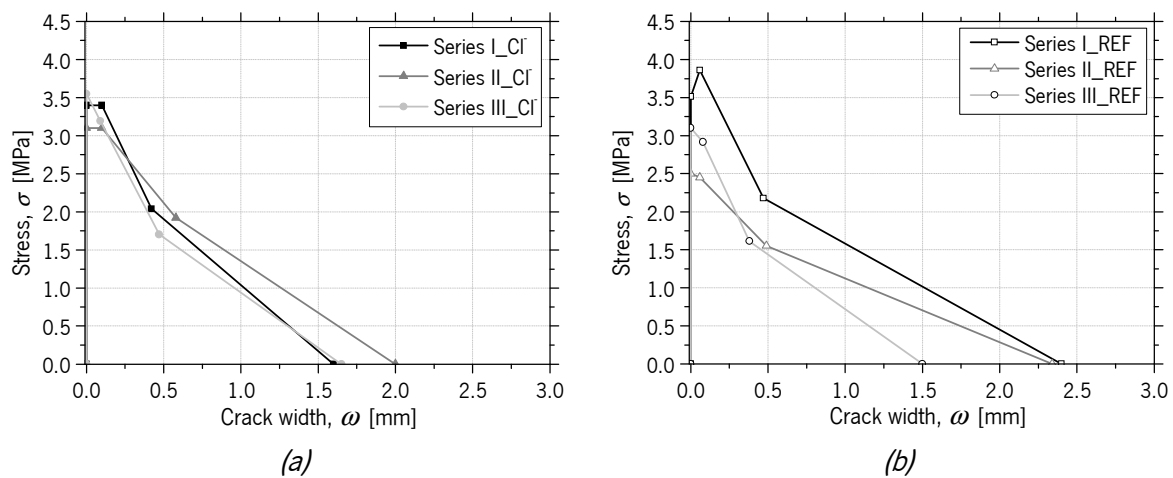
Figure 6.31 – Numerical simulation of the DEWST for:  
 (a) Series I; (b) Series II; (c) Series III; (d) Series IV (e) Series V; (f) Series VI

The numerical values of  $\sigma_{t,split}$  were determined from the equation (2.4) (Section 2.3.7.2.2), considering the compressive load  $P$  corresponding to the sum of the vertical reactions at the nodes located on the horizontal symmetry axis. The numerical values of  $\omega$  correspond to the average of horizontal displacements at the nodes located on the vertical symmetry axis.

The numerical simulations were able of fitting with high accuracy the experimental results up to the average crack width of 2 mm. The obtained parameters defining the  $\sigma - \omega$  relationship, and the normalized fitting error,  $e$  (the difference of the area limited by the experimental and the numerical curves divided by the area underneath the experimental curve), are indicated in Table 6.11. The  $f_{ct}$  corresponds to the tensile strength,  $\sigma_1$  and  $\sigma_2$  are the stress at the first and second post-peak points at the crack opening,  $\omega_1$  and  $\omega_2$ , respectively;  $\omega_u$  is the ultimate crack opening. The graphical representation of these  $\sigma - \omega$  laws are presented in Figures 6.32, 6.33 and 6.34.

Table 6.11 – Parameters of the  $\sigma - \omega$  relationship obtained by inverse analysis (DEWSTs)

Series	$f_{ct}$ (MPa)	$\sigma_1$ (MPa)	$\sigma_2$ (MPa)	$\omega_1$ (mm)	$\omega_2$ (mm)	$\omega_u$ (mm)	$G_f$ (N/mm)	$e$ (%)
I_Cl	3.40	3.40	2.04	0.10	0.42	1.60	2.41	0.65
I_REF	3.51	3.86	2.18	0.06	0.47	2.40	3.56	0.91
II_Cl	3.10	3.10	1.92	0.10	0.58	2.00	2.88	0.80
II_REF	2.50	2.45	1.55	0.06	0.49	2.34	2.44	0.94
III_Cl	3.55	3.20	1.70	0.09	0.47	1.65	2.24	0.69
III_REF	3.10	2.91	1.61	0.08	0.38	1.50	1.82	1.52
IV_Cl	3.05	2.59	1.68	0.06	0.29	1.60	1.76	0.73
IV_REF	2.55	2.04	1.40	0.05	0.29	1.60	1.45	0.73
V_Cl	3.10	2.48	1.40	0.05	0.32	1.60	1.56	0.09
V_REF	3.00	2.25	1.47	0.08	0.30	1.60	1.57	0.18
VI_Cl	2.15	1.72	0.97	0.07	0.32	1.60	1.09	0.99
VI_REF	2.50	2.13	1.23	0.08	0.40	1.60	1.46	0.22

Figure 6.32 –  $\sigma - \omega$  relationships obtained by inverse analysis for splitting specimens of:

(a) Series I&amp;II&amp;III\_Cl; (b) Series I&amp;II&amp;III\_REF

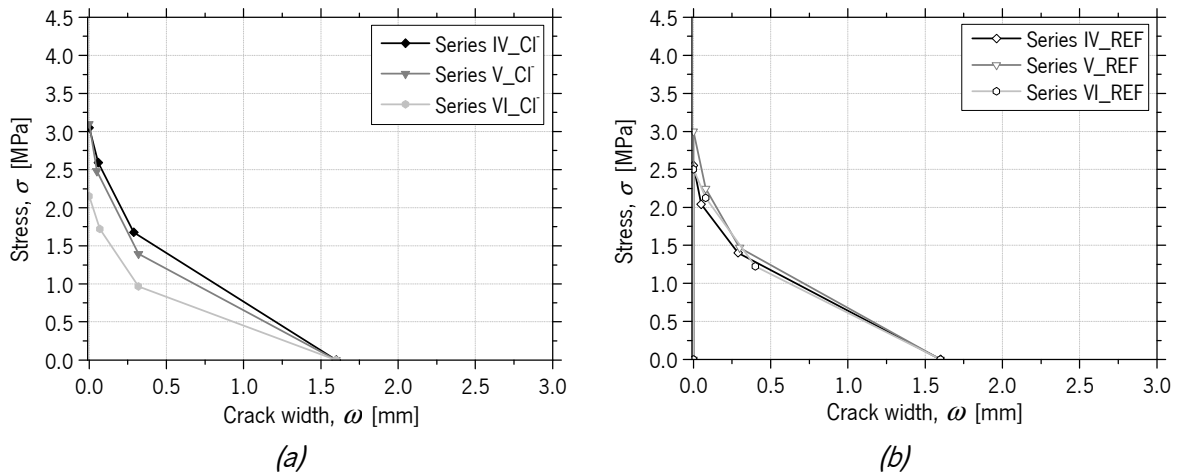


Figure 6.33 –  $\sigma$  -  $\omega$  relationships obtained by inverse analysis for splitting specimens of:  
 (a) Series IV&V&VI\_CI; (b) Series IV&V&VI\_REF

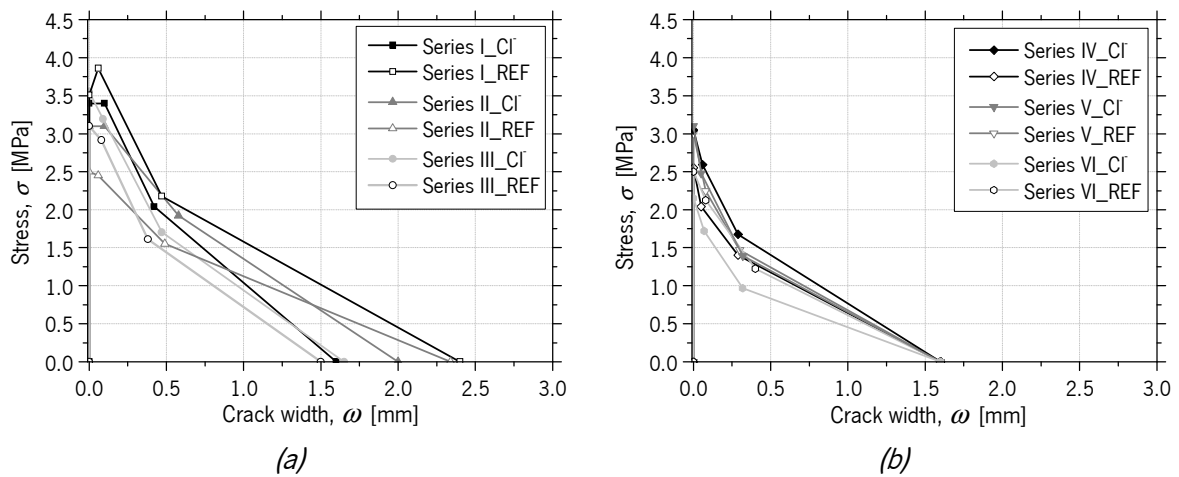


Figure 6.34 –  $\sigma$  -  $\omega$  relationships obtained by inverse analysis for splitting specimens of:  
 (a) Series I&II&III\_CI&REF; (b) Series IV&V&VI\_CI&REF

The predicted splitting tensile stress of RSFRC0.8% reference specimens reinforced with Class 1 RSF attained a short hardening branch followed by a softening stage. For the remaining test Series with long-term effects and chloride attack, a decrease or omission of the hardening branch occurred.

In Series I, II and III, the values of fracture energy,  $G_f$ , obtained for specimens submitted to chloride attack and for reference specimens (Table 6.11) corroborate with the number of effective fibers at the fracture surface (Table 6.4). According to this, the differences between the numerical tensile strength and post-cracking residual stresses obtained for specimens submitted to chlorides and reference specimens may be due to the fiber density.

In Series IV, the values of  $G_f$  and tensile strength obtained numerically for specimens submitted to chloride attack and for reference specimens (Table 6.11) corroborate with the number of fibers counted in the analyzed images of cut surface (Table 6.9).

In Series V, similar results were obtained for Cl- and REF specimens in terms of the numerical tensile strength and post-cracking residual stresses. According to the values of fiber density (Table 6.9), a relatively low number of fibers was counted in the cut surface of Cl- specimens, which means that the higher tensile strength may be justified by the irregular geometry of fibers that provided differences in the pull-out reinforcement mechanisms developed. In Series VI, the values of  $G_f$  obtained for Cl- and REF specimens (Table 6.11) corroborate with the number of effective fibers at the fracture surface (Table 6.9). According to the results of fiber density shown in Table 6.9 and Figure 6.34b, it appears that only after 6 months of chloride immersion, the chloride attack caused some detrimental effect compared to the corresponding reference specimens, since the fiber density and the percentage of fibers failed by rupture were similar in these specimens, and then was expected that the fiber distribution had a similar contribution to the  $G_f$  values. However, the chloride attack led to the decrease of the strength and post-cracking resistance of RSFRC after 6 months of immersion.

## 6.5 CONCLUSIONS

In this chapter, the post-cracking behavior of RSFRC under chloride attack was evaluated by performing DEWSTs. In a first part of the experimental work (Series I, II and III of DEWSTs), the influence of the small amount of rubber particles attached to RSF surface in the splitting tensile stress-crack width response,  $\sigma_{t,split} - \omega$ , obtained from RSFRC specimens previously submitted to 10 days of chloride immersion, was studied by using two distinct pre-treatment methods for rubber removal from RSF surface: pre-treatment of fibers at 350°C and superficial polishing of RSF. In the second part of the experimental work, the long-term effects of chloride immersion on the  $\sigma_{t,split} - \omega$  response of RSFRC were evaluated for three different exposure periods: 10 days, 3 and 6 months. For both parts of the experimental program, the influence of RSF distribution and orientation on the post-cracking behavior of RSFRC was analyzed. Inverse analysis of the DEWSTs were performed to obtain the  $\sigma - \omega$  relationship and mode I fracture parameters of the RSFRC0.8%, by using FEM-based numerical simulations, where in the notched plane

interface finite elements were adopted with a cohesive constitutive law. From the experimental and numerical results, the main conclusions are:

- 1) After 10 days, and 3 and 6 months of chloride immersion in 3.5 wt% NaCl solution, no significant signs of corrosion were observed in the RSF on the fracture surface of RSFRC0.8% splitting specimens. However, corrosion spots were observed at exposed surfaces of all specimens.
- 2) The dispersion of  $\sigma_{t,split} - \omega$  curves obtained for specimens submitted to chloride attack and reference specimens were mainly due to the irregular geometry of the fibers and fiber distribution and orientation. Fiber segregation was detected in the tested specimens. A linear correlation was found between the post-cracking response of the specimens and the number of effective fibers at the fracture surface.
- 3) The Class 1 RSF were the most effective fibers at crack initiation and post-cracking tensile strength of RSFRC. The small content of rubber particles attached to RSF surface had a negligible effect in the post-cracking tensile behavior of RSFRC. Therefore, the two distinct pre-treatment methods used to clean fiber surface can be discarded since they had a negative impact on the energy absorbed during the fracture process of DEWSTs specimens reinforced with this type of fiber.
- 4) The  $\sigma_{t,split} - \omega$  curves obtained for the RSFRC specimens and its corresponding fiber distribution analysis revealed a negligible effect of chloride attack after 10 days and 3 months of chloride exposure, and a detrimental effect of chloride attack after 6 months of immersion.
- 5) According to the adopted image analysis procedure, a significant number of fibers have ruptured during the execution of DEWSTs at the cracked surface of specimens submitted to chloride attack and reference specimens. This fact may be indicative that the beneficial effect of corrosion in the fiber pull-out reinforcement mechanisms is irrelevant. When RSF embedded in uncracked concrete are submitted to corrosion action, there is a loss of effective cross section of the fibers, causing the decrease of tensile strength.
- 6) No significant differences were detected in terms of the fiber orientation factor, between reference specimens and specimens submitted to chloride immersion; the fiber orientation factor computed from the image analysis approach is higher than the orientation factor calculated with the equation proposed by Soroushian and Lee (1990); the homogeneous fiber distribution was not completely guaranteed in the cross section of the splitting specimens.
- 7) The tensile post-cracking parameters of RSFRC0.8% were obtained by inverse analysis procedure, by using for this purpose the experimental  $\sigma_{t,split} - \omega$  relationships up to the average crack width



of 2 mm, obtained from DEWST results. The predicted splitting tensile stress of RSFRC0.8% reference specimens reinforced with Class 1 RSF attained a short hardening branch followed by a softening stage. For the remaining test Series with long-term effects and chloride attack, a decrease or omission of the hardening branch occurred.

---

# Chapter 7

---

## **POST-CRACKING BEHAVIOR OF RSFRC UNDER CHLORIDE ATTACK CHARACTERIZED FROM ROUND PANEL TESTS**

### **7.1 INTRODUCTION**

Recycled Steel Fibers (RSF) have been successfully used in concrete to improve its post-cracking load bearing capacity and energy absorption performance, and also to limit the crack width, with beneficial consequences in terms of concrete durability (Graeff *et al.*, 2012; Micelli *et al.*, 2014; Zamanzadeh *et al.*, 2015). For slab and shell type structures, higher potentialities of the post-cracking response of Fiber Reinforced Concrete (FRC) can be effectively mobilized to improve the load carrying capacity of this type of structures. The fiber reinforcement efficiency can be assessed by the conventional material tests, including the three-point notched beam bending test (3PNBBT) or the double edge wedge splitting test (DEWST), as already reported in chapters 3 and 6, respectively. However, the stress-crack width relationship ( $\sigma - \omega$ ), obtained by these tests is noticeably influenced by the number and orientation of fibers crossing the crack (sections 3.5.1.2 and 6.3.2.5). The fiber orientation and dispersion in an FRC element is significantly affected by the shape and the geometry of the element (Švec *et al.*, 2014). In prismatic elements, a larger number of fibers may be preferably oriented orthogonally to the fracture plane due to the wall effects caused by the geometry of the mould, leading to improved post-cracking behavior (Salehian, 2015). Furthermore, the post-cracking response of FRC in the prismatic specimens is governed by a localized crack (Sections 3.5.1.1. and 6.2.1). Furthermore, the post-cracking response

of FRC in the prismatic specimens is governed by a localized crack (Sections 3.5.1.1. and 6.2.1). Therefore, the design methodology of a RSFRC slab based on constitutive models derived from RSFRC panel with cracks propagation of different orientations is more representative of the fiber reinforcement mechanisms in this type of FRC structures.

In the present chapter, an experimental program was carried out to evaluate the effects of chloride attack on the load carrying capacity of round panels made of RSFRC. The influence of the crack width, the chloride exposure period, and the fiber distribution/orientation profile was investigated on the force-deflection and energy dissipation responses obtained in round panel tests (RPTs). Furthermore, the tensile stress-crack width ( $\sigma - \omega$ ) relationship of the RSFRC representative of the RPT was derived by performing an inverse analysis of the RPTs results. For this purpose, numerical simulations of RPTs were developed combining a moment-rotation approach with a numerical model that considers the kinematics conditions of RPT at failure stage and the equilibrium equations.

The diffusion of chlorides into uncracked RSFRC was also studied by determining the resistance to chloride penetration by migration under non-steady state and by natural immersion. Additionally, the long-term chloride penetration depth into a structural element made with RSFRC was estimated based on a simplified prediction of the critical chloride content for the specific environmental conditions considered in performed tests.

## **7.2 EXPERIMENTAL PROGRAM**

### **7.2.1 Specimens manufacture**

According to ASTM C1550-08 (2008), the nominal dimensions of the round panels are 800 mm in diameter and 75 mm in thickness. In order to facilitate handling and placing of the specimens, smaller RSFRC panels were produced with 600 mm in diameter and 60 mm in thickness. According to Minelli and Plizzari (2010), such reduction of the panel's diameter and thickness does not affect the scatter and repeatability of the test results when compared to the standard specimens of ASTM C1550-08 (2008).

The round panels were casted with the RSFRC1% mixture detailed in Table 3.18. Only Class 1 RSF were used since they are the most effective fibers, according to the previous chapter (Section 6.3.1). The mixing and fresh properties of RSFRC1% and curing procedure of specimens are described in Section 3.4.1. Due to the limited panel molds available, four batches with the same composition (RSFRC1% mixture) were produced to cast 36 panels, 9 panels per casting.

For each casting, RSFRC beams with 600x150x150 mm<sup>3</sup> and RSFRC cylindrical specimens with  $\phi$ 150x300 mm dimensions were also casted for mechanical characterization, whose tests were reported

in Chapter 3. The flexural behavior of each RSFRC1% casting was assessed by testing notched RSFRC beams under three-point loading conditions (3PNBBT), as shown in Table 3.20 (concrete mixtures RSFRC1%\_2 to 5). The compressive behavior of each RSFRC1% casting was assessed by testing the RSFRC cylindrical specimens under uniaxial compressive tests, as shown in Table 3.24 (concrete mixtures RSFRC1%\_2 to 5).

Additionally, four cylindrical specimens with  $\phi 100 \times 200$  mm dimensions were casted (two with RSFRC1%\_2 casting and two with RSFRC1%\_4 casting) for the non-steady state accelerated migration tests to evaluate the resistance of RSFRC to chloride penetration. For comparison purposes, four cylindrical specimens ( $\phi 100 \times 200$  mm) of plain concrete (PC) were casted with the same concrete matrix of RSFRC. For the determination of the resistance to chloride penetration by immersion in NaCl solution, two 150 mm cubic specimens for both RSFRC1% (RSFRC1%\_4 casting) and PC (same concrete matrix) were produced.

### 7.2.2 Experimental setup

The RPTs were conducted on round panels supported on three symmetrically arranged pivots (RPT-3ps), as presented in Section 2.2.1.3. The three pivots support system represented in Figure 7.1a was designed and built to be used for both panel diameters of 600 mm and 800 mm. The connection between the panel and each pivot was provided by two round steel plates of 50 mm diameter and 25 mm thickness, with a spherical seat of around 6 mm depth machined into the two surfaces to achieve the ball connection recommended by ASTM C1550-08 (2008), as represented in Figure 7.1b. Two teflon sheets were used between the concrete panel and each round steel plate to reduce friction (Figure 7.1b). More details of the designed system of the RPT-3ps test setup are represented in Appendix C.

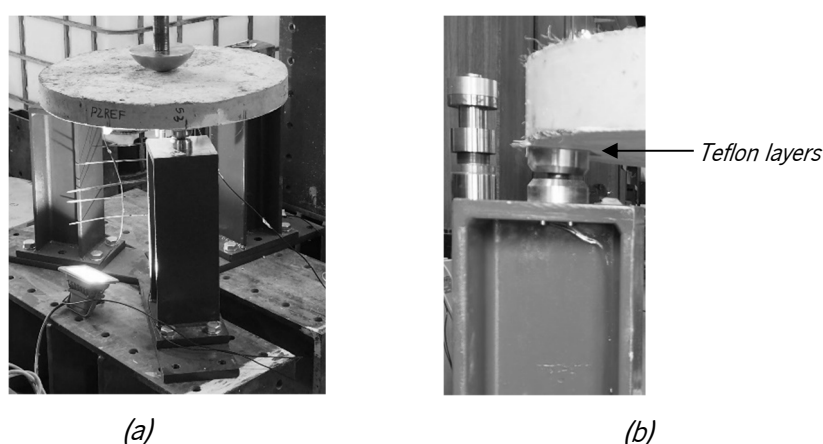


Figure 7.1 – (a) The three pivots support system; (b) Connection between the panel and each pivot

The load was applied to the panel's center through a hemispherical-ended steel piston at a constant rate of displacement. The central deflection of the panel was measured by an LVDT with a linear stroke of  $\pm 50$  mm installed at the bottom surface of the panel (Figure 7.2a,b). Three LVDTs with a linear stroke of  $\pm 5$  mm were also used in the bottom face of the panels to measure the three developed crack widths (Figure 7.2c).

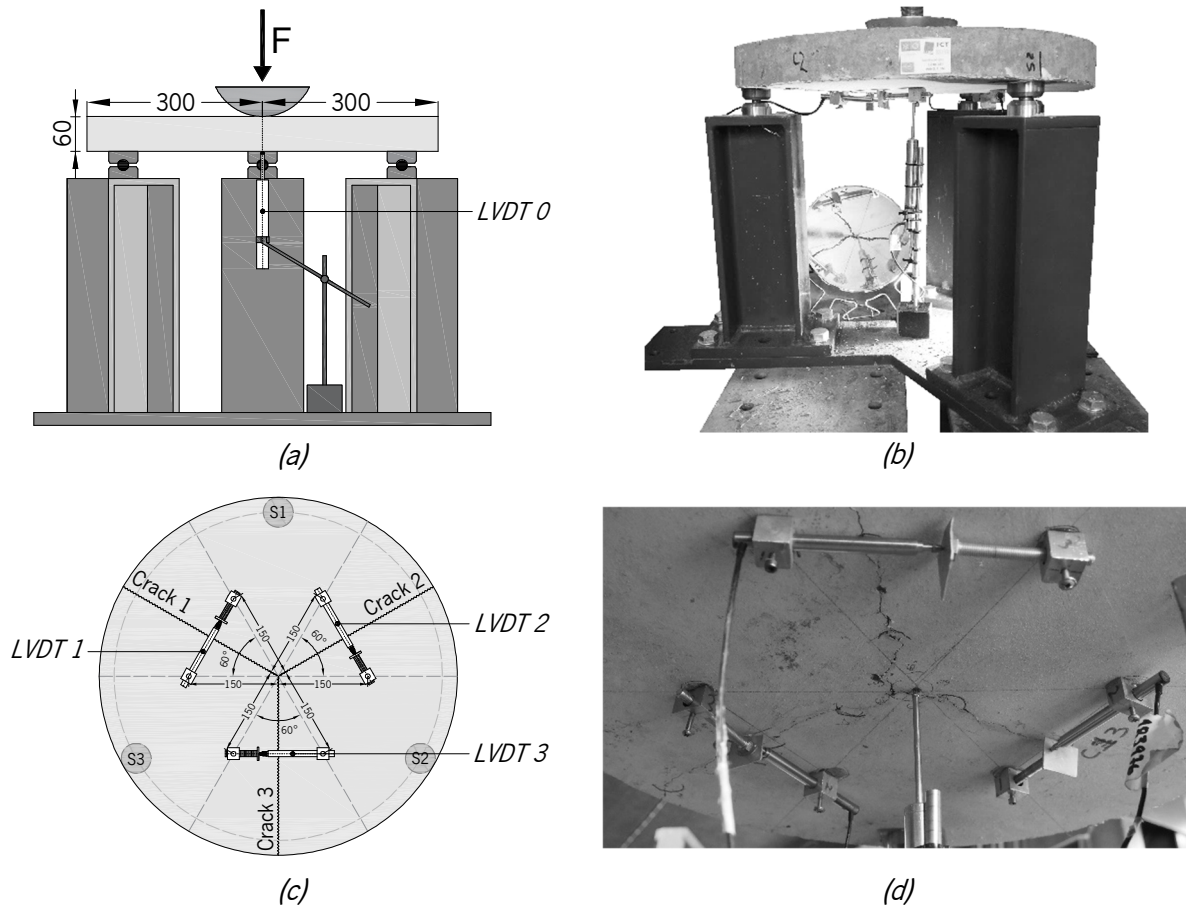


Figure 7.2 – RPT-3ps test setup: (a) and (b) Position of the LVDT for central deflection measurement; (a) and (d) Position of the LVDTs for crack width measurement (units in mm)

### 7.2.3 Parameters in study

In the performed RPT-3ps, different parameters were considered in order to study their influence on the post-cracking behavior of RSFRC under chloride attack, namely, the crack width, the environmental exposure period and the fiber distribution/orientation profile.

#### 7.2.3.1 Crack width

In order to investigate the influence of the crack width, the RPT-3ps were executed with pre- and non-cracked RSFRC panels. The influence of the pre-crack width level,  $\omega_{cr}$ , was investigated by adopting pre-

crack width values of about 0.5 mm and 1.0 mm for the panels, implemented with the RPT-3ps test setup in the bottom face of the panels (Fig. 7.2d). For comparison purposes, non pre-cracked panels were considered. The target pre-crack width was installed in the panels after 28 days of curing and before being subjected to the chloride environment.

In order to define the pre-cracking procedure of the round panels, some preliminary RPT-3ps were carried out in four round panels casted with RSFRC1% mixture (RSFRC1%\_6 casting) to obtain the crack width-central deflection ( $\omega_{cr} - \delta$ ) relationship of RSFRC panels.

### **Preliminary RPT-3ps**

In the preliminary RPT-3ps, one panel was first tested in accordance with the ASTM C1550-08 (2008) using the test setup presented in Section 7.2.2 by imposing a deflection rate of 4.0 mm/min up to a central displacement of at least 45 mm. This test was first performed to obtain the force-central deflection relationship,  $F - \delta$  for one RSFRC panel. According to the result obtained in this RPT-3ps, as will be presented in Section 7.3.1, the crack initiation was assumed at the limit of proportionality that occurred at a central deflection of about 1 mm.

The preliminary RPT-3ps of the remaining three panels were performed in displacement control by imposing a deflection rate of 1.0 mm/min up to reach a central displacement of 1.0 mm (assumed crack initiation). Afterwards, successive increments of central displacement of 0.5 mm were applied at the deflection rate of 1.0 mm/min. The testing machine was stopped at the loaded position between each increment for crack width measurements.

In the RPT-3ps, the ultimate yield line patterns of the panels comprise three radial cracks that propagate in the sectors between two adjacent pivots. The three crack widths were measured with a USB Microscope at three located points (A, B and C) in the bottom face of the panel, as schematically represented in Figure 7.3. After reaching an average crack width (of 9 measurements) close to the target pre-crack width values (0.5/1.0 mm), the panels were unloaded and the average crack width after discharge was measured. According to the results obtained (to be presented in Section 7.3.1), to ensure the target pre-crack widths after the panel discharge, crack widths of approximately 0.8 and 1.3 mm are required to impose a final unloaded pre-crack width of 0.5 and 1.0 mm, respectively.

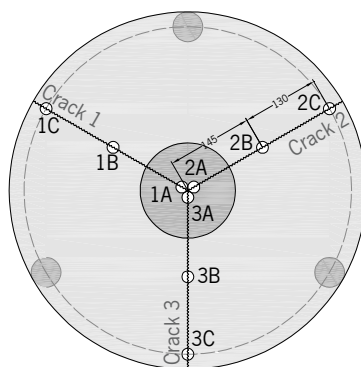


Figure 7.3 – Position of the crack width measurement with a USB Microscope

### Pre-cracking process of round panels

After performing the preliminary tests, the following procedure was defined for pre-cracking RSFRC panels with the target pre-crack width,  $\omega_{cr}$ , of 0.5 or 1.0 mm, using the test setup presented in Section 7.2.2:

1) Impose a deflection rate of 1.0 mm/min up to reach a central displacement of 2.5 mm and unload the panel; 2) Check if the  $\omega_{cr}$  obtained is close to the desired one. The target  $\omega_{cr}$  corresponds to the average value measured by the three LVDTs indicated in Figure 7.2c; 3) If the  $\omega_{cr}$  is not the desired, impose successive increments of 0.25 mm to the installed central displacement, at the same deflection rate, up to obtain the desired pre-crack width. At the end and before submitting the panels to the environmental exposure, the  $\omega_{cr}$  was also measured with a USB microscope in the nine located points (three points at each crack) represented in Figure 7.3. Each test series of different target pre-crack width was composed by three round panels simultaneously tested under the same conditions.

#### 7.2.3.2 Environmental exposure

In order to study the influence of chloride attack in the post-cracking behavior of RSFRC, the panels were immersed in a 3.5 wt% NaCl solution after the pre-cracking process and before final RPT-3ps. Two different periods for chloride exposure were adopted: 10 days of chloride immersion; 3 months of dry-wet cycles. For each period, pre-cracked and non-cracked panels were used. For comparison purposes, pre-cracked and non-cracked reference panels were considered for each test series, immersed in tap water for the same exposure period of chloride environment. The RPT-3ps were divided in six series considering the distinct pre-crack width levels and the environmental exposure periods of the panels before final RPT-3ps, as presented in Table 7.1. For each test series, three RSFRC panels submitted to chloride attack (Cl) and three reference RSFRC panels (REF) were considered. Four RSFRC batches with the same

composition were produced for round panels casting (see Section 7.2.1). Two batches were used to produce the panels submitted to chloride attack and the other two to produce the reference panels.

Table 7.1 – Experimental program of RPT-3ps

Series	Panels		$\omega_{cr}$ (mm)	Exposure conditions of panels before RPT-3ps
	RSFRC casting	Designation		
I_Cl	RSFRC1%_2	P1, P2, P3	1.0	10 days of chloride immersion in 3.5 wt% NaCl solution
II_Cl		P4, P5, P6	0.5	
III_Cl		P7, P8, P9	0.0	
I_REF	RSFRC1%_3	P1, P2, P3	1.0	10 days of tap water immersion
II_REF		P4, P5, P6	0.5	
III_REF		P7, P8, P9	0.0	
IV_Cl	RSFRC1%_4	P1, P2, P3	1.0	3 months of dry-wet cycles in 3.5 wt% NaCl solution
V_Cl		P4, P5, P6	0.5	
VI_Cl		P7, P8, P9	0.0	
IV_REF	RSFRC1%_5	P1, P2, P3	1.0	3 months of tap water immersion
V_REF		P4, P5, P6	0.5	
VI_REF		P7, P8, P9	0.0	

The exposure of RSFRC panels to chloride/water immersion after pre-cracking process was carried out by using individual tanks of 1000 liters per each different exposure conditions, as presented in Figure 7.4c. The Figures 7.4a,b schematically show the arrangement of each 9 panels within the tank. The pre-cracked panels were placed into the tank after pre-cracking, positioned horizontally according to the RPT-3ps test configuration, i.e. supported at the same three points used for the pre-cracking process (Figures 7.4a,b). The non-cracked panels were placed vertically as shown in Figures 7.4a,b. Once placed into the tank, the pre-cracked and non-cracked panels were subjected to the environmental exposure conditions for the adopted periods (Table 7.1).

For the immersion period of 10 days, the 3.5 wt% NaCl solution used was always the same. For the dry-wet cycles of 3 days wetting, 4 days drying during 3 months, the chloride solution was replaced once in the middle of the period (at about 1.5 months). To avoid a significant salt crystallization, two water circulation pumps were placed inside the tank to keep the solution continuously circulated, and the tanks were covered to prevent evaporation.



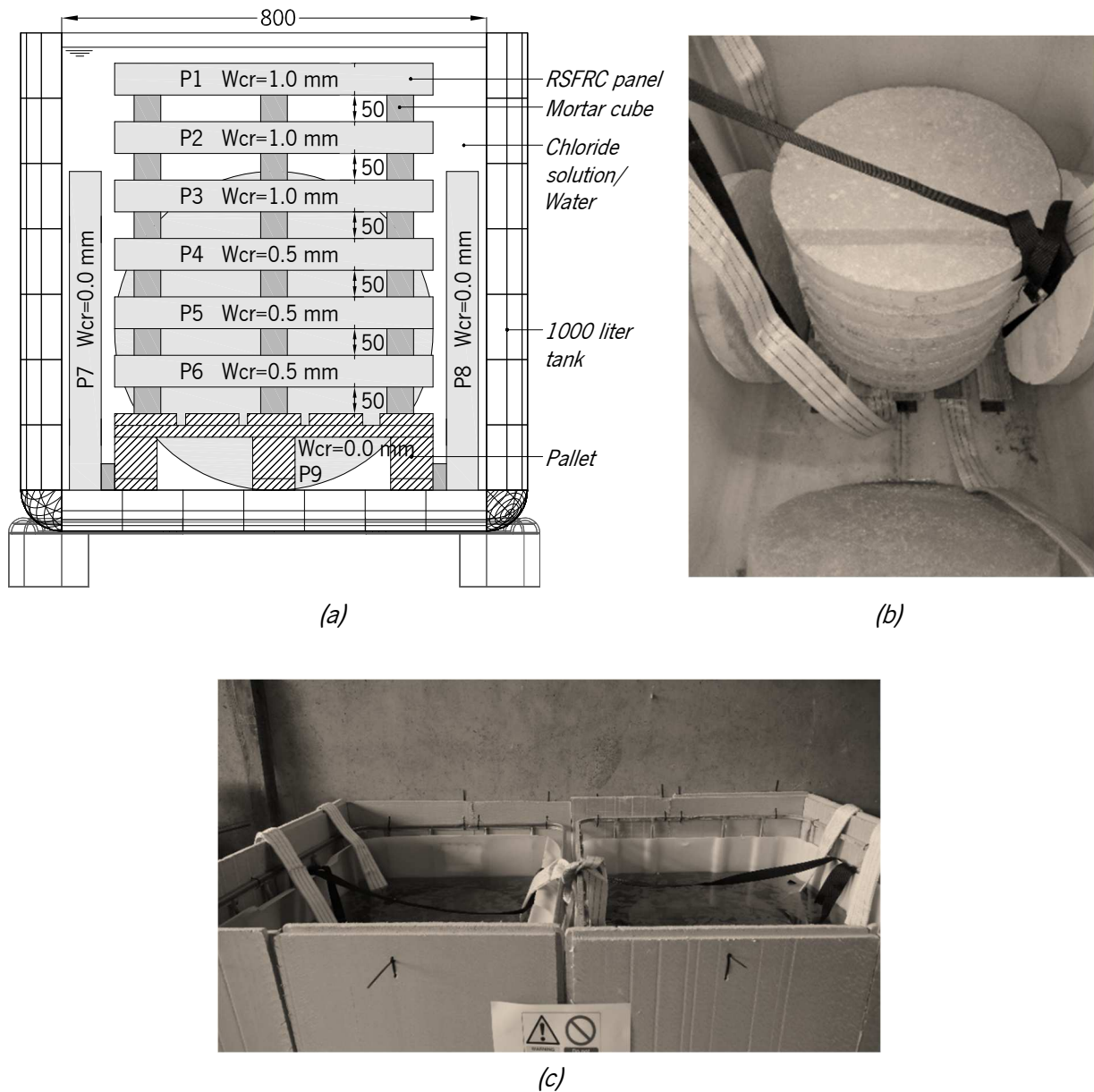


Figure 7.4 – General view of the tanks: (a) Arrangement of the panels inside the tank after pre-cracking process: (b) Before immersion and (c) During immersion

Regarding the temperature of the chloride solutions/water during panel's immersion, two water heaters with thermostat were used per tank to heat and keep the solution/water constant at 20°C. The tanks were also externally insulated with extruded polystyrene plates (Figure 7.4c). The temperature of solutions/water was measured throughout the exposure period of 3 months, as shown in Figure 7.5. As observed, the temperatures of 3.5 wt% NaCl solution and water were similar and almost constant at 21°C.

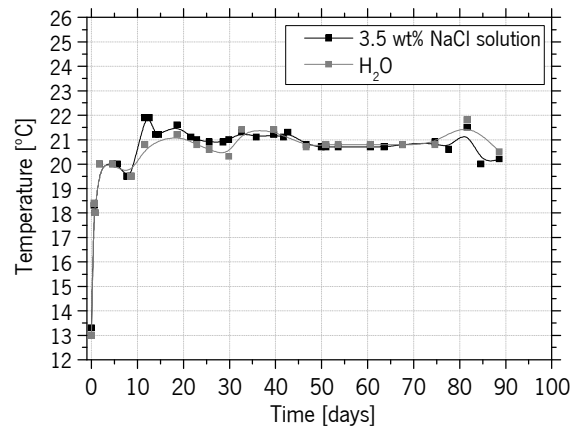


Figure 7.5 – Temperature monitoring of tank solution/water over the 3-month exposure period

After completing the adopted exposure periods, the panels were submitted to the final RPT-3ps to assess the influence of chloride attack in the post-cracking behavior of RSFRC. The panels were supported on the same three-point supports, and a central point load was applied at a constant displacement rate of 4 mm/min up to a central displacement of 40 mm.

### 7.2.3.3 Fiber distribution/orientation profile

For a better understanding of the residual stresses and energy absorption obtained in the final RPT-3ps, the fiber distribution and orientation parameters were determined, adopting the image analysis procedure described in Section 6.3.2.5. After performing the final RPT-3ps, each panel test was divided into three distinct parts corresponding to the delimitation imposed by the crack surfaces. For each test Series, one of these distinct parts from two panels (one reference panel and the other submitted to chloride attack) was cut parallel and as close as possible to one crack surface to obtain a plane surface. Each cut surface was divided in areas of approximately 25x30 mm<sup>2</sup>, and an image analysis was executed on each area, according to the procedure described in Section 6.3.2.5. After computation of the image analysis results, the parameters presented in Section 6.3.2.5 that characterize the fiber structure were derived out, namely: 1) The number of fibers per unit area,  $N^f$ ; 2) Fiber orientation factors,  $\eta_{img}$  and  $\eta_{exp}$ ; 3) Fiber segregation parameter,  $\xi_{seg}$ .

## 7.2.4 Chloride diffusion in RSFRC

### 7.2.4.1 Non-steady state chloride migration tests

An accelerated non-steady state migration test method was applied according to the standard NT BUILD 492 (1999) to assess the resistance of RSFRC against chloride penetration. These tests were carried out in three cylindrical specimens of 100 mm diameter and 50 mm thickness of each RSFRC1% mixture used in the production of round panels submitted to chloride attack (RSFRC1%\_2 and RSFRC1%\_4 castings – see Table 7.1). For comparison purposes, the tests were also carried out in three plain concrete cylindrical specimens ( $\phi 100 \times 50$  mm) of each concrete matrix used in the RSFRC1%\_2 and RSFRC1%\_4 castings (without RSF addition). The specimens were sliced from cast cylinders with  $\phi 100 \times 200$  mm (Section 7.2.1) and were tested at 28 days of age. The test specimens were prepared by first cutting the cylinder into two halves and then cutting a 50 mm thick slice from each half (two specimens). The end surface that was nearer to the first cut (the middle surface) is the one to be exposed to the chloride solution (catholyte) (Figure 7.6).

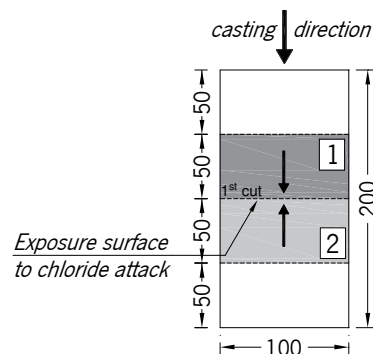


Figure 7.6 – Schematic representation of the preparation process of specimens for chloride migration tests (units in mm)

The principle of this test is to axially apply an external electrical potential across the specimen, by forcing the outside chloride ions to migrate into the specimen (Figures 7.7a,b). The catholyte solution is 10% NaCl by mass in tap water and the anolyte solution is 0.3 N NaOH in distilled water (Figure 7.7a). The tests were carried out with initial temperature solutions of 20-25°C. After the test duration, the specimens are axially split, and a silver nitrate solution (0.1 N  $\text{AgNO}_3$ ) is sprayed on to one of the freshly split sections (Figure 7.7c).

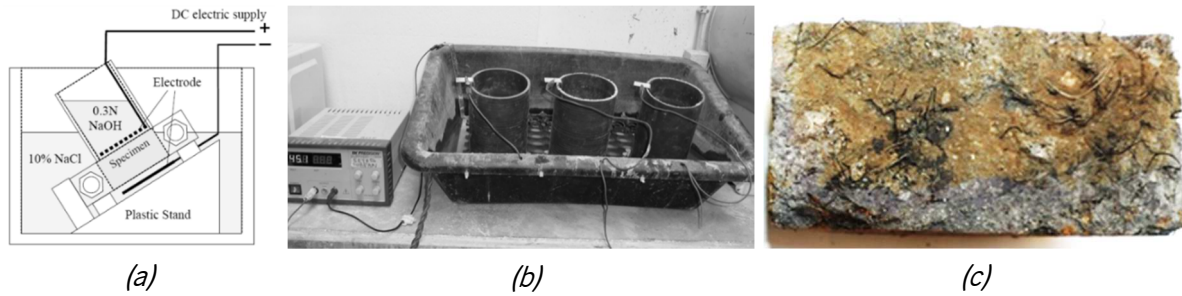


Figure 7.7 – Rapid chloride migration test: (a) and (b) Test setup; (c) Split section of RSFRC specimen

The chloride penetration depth is measured from the visible silver chloride precipitation and the chloride migration coefficient,  $D_m$  ( $\times 10^{-12}$  m<sup>2</sup>/s) is calculated from the following equation:

$$D_m = \frac{0.0239 (273 + T) \times L}{(U - 2) \times t} \left( x_d - 0.0238 \sqrt{\frac{(273 + T) \times L \times x_d}{U - 2}} \right) \quad (7.1)$$

where  $T$  is the mean value between initial and final temperature (°C) of the anolyte solution,  $U$  is the absolute value of the applied voltage (V),  $L$  is the thickness of specimen (mm),  $t$  is the test duration (hours) and  $x_d$  is the average penetration depth (mm).

#### 7.2.4.2 Chloride penetration by immersion

The determination of the resistance to chloride penetration by immersion was performed according to the standards ASTM C1556-03 (2003) and NT BUILD 443 (1995). The method is based on determining parameters related to chloride penetration in hardened concrete, based on measuring the chloride penetration profile in samples after immersion in an aqueous sodium chloride solution (a solution of 3.5 wt% NaCl was adopted). For this test, two 150 mm cubic specimens of both RSFRC1% (RSFRC1%\_4 casting) and the corresponding plain concrete (PC) were used (Section 7.2.1). The faces of each cubic specimen were waterproofed with a single layer coating based on polyurethane resin, except for one that allows the penetration of chlorides (Figure 7.8a).

After 90 days of immersion (Figure 7.8a), the determination of the chloride concentration at different depths in the cubic specimens was performed using the kit RCT-500 (Rapid Chloride Test) of the German Instruments A/S. The RCT-500 consists of a quick and easy-to-use kit for determination of chloride content as a percentage of binder mass. In this case, the acide soluble amount of chlorides (total chlorides = free chlorides + bound chlorides) were measured on 1.5 g powder samples of concrete collected at various depths by drilling the test specimens with a 22 mm drill bit (Figure 7.8b). Each powder sample was mixed with a liquid to extract the chloride ions and the chloride content was obtained by using the

RCT electrode calibrated with four calibration solutions of known chloride content (Figure 7.8c). In each test specimen, one chloride profile was obtained with 10-14 powder samples collected at different depths.

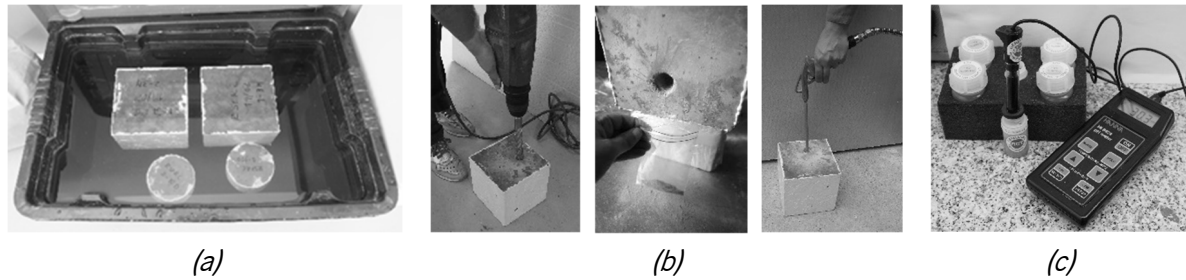


Figure 7.8 – Chloride penetration test by immersion: (a) Immersion of the specimens in chloride solution; (b) Collection of powder samples of concrete at different depths in the specimens; (c) Using the Kit RCT-500 to determine the chloride content

After obtaining the chloride content profile for each concrete specimen, the values of the chloride content at the exposed surface,  $C_s$  (% of binder mass), and the apparent chloride diffusion coefficient,  $D_d$  ( $\times 10^{-12}$  m<sup>2</sup>/s) were determined by curve-fitting the measured chloride-ion contents to an error-function solution of Fick's 2<sup>nd</sup> law, according to the following equation:

$$C_x = C_s - (C_s - C_0) \operatorname{erf} \left( \frac{1/2 x}{\sqrt{D_d \times t}} \right) \quad (7.2)$$

where  $C_x$  is the chloride content (% of binder mass) measured at depth  $x$  (m) for a exposure time of immersion  $t$  (s),  $C_s$  is the chloride content (% of binder mass) calculated by regression analysis at the concrete surface after a time of immersion  $t$  (s), and  $C_0$  is the initial chloride content in concrete prior to submersion in the exposure solution (it was assumed 0% of binder mass) and  $\operatorname{erf}$  is the error-function. Following the recommendations of the NT BUILD 443 (1995), a chloride penetration parameter,  $K_{C_r}$  (mm/year<sup>0.5</sup>) was also calculated according to the equation:

$$K_{C_r} = 2\sqrt{D_d} \operatorname{erf}^{-1} \left( \frac{C_s - C_r}{C_s - C_0} \right) \quad (7.3)$$

where  $C_r$  is a selected reference chloride concentration. For  $C_r$  was adopted the value of 0.05% by concrete mass, recommended by NT BUILD 443 (1995).

#### 7.2.4.2.1 Chloride penetration and aging coefficient by colorimetric method

The aging coefficients of the RSFRC1% and PC were determined considering the chloride diffusion coefficients calculated by the colorimetric method, in order to avoid making the most rigorous and difficult method of chloride profiles. Two cylindrical specimens ( $\phi 100 \times 50$  mm) of both RSFRC1% (RSFRC1%\_2 casting) and the corresponding plain concrete (PC) were submitted to chloride immersion in a 3.5 wt% NaCl solution. For these tests, it was used the same immersion container of the cubic specimens shown in Figure 7.8a. The lateral and upper (end) faces of each cylindrical specimen were waterproofed with a single layer coating, in order to restrict the penetration of chlorides from the bottom surface (sawn face). One specimen of RSFRC and one of PC were submitted to 10 days of continuous immersion and the remaining two specimens (one of RSFRC and one of PC) were subjected to 3 months of continuous immersion. After these exposure periods, the specimens were axially split, and a silver nitrate ( $\text{AgNO}_3$ ) solution was sprayed on to one of the freshly split sections (Figure 7.9).



Figure 7.9 – Split section of PC cylindrical specimens:  
(a) after 10 days of immersion (b) after 3 months of immersion

The chloride penetration depth was measured from the visible white silver chloride precipitation (Fig. 7.9), where free chlorides have penetrated into concrete. The values of the chloride diffusion coefficient,  $D_c$ , were determined according to the assumptions indicated by Yang *et al.* (2014), considering the following equation:

$$D_c = \frac{-x_c^2}{2 \ln \left( \frac{C_c}{C_o} \right) t} \quad (7.4)$$

where  $x_c$  is the colorimetric penetration depth,  $C_c$  is the concentration of free chlorides in the pore solution corresponding to the color change boundary,  $C_o$  is the chloride concentration ponded at the top surface and  $t$  is the exposure time.

The specimens were subjected to continuous ponding with 3.5 wt% NaCl solution, with the chloride

concentration ponded on the top surface of  $C_o = 0.61$  N (considering that  $C_o = 0.52$  N with 3.0 wt.% NaCl solution (Yang *et al.*, 2014)). The free chloride concentration at the colour change boundary was set equal to  $C_c = 0.07$  N as pointed out by Tang (1996), Lay *et al.* (2004) and NT BUILD 492 (1999) for Ordinary Portland Cement (OPC) concrete.

The amount of chlorides diffusing into concrete is referred as total (acid-soluble) chlorides, as evaluated in the previous Section 7.2.4.2. This total amount of chlorides is divided into the free (water soluble) chlorides that are responsible for the reinforcement corrosion, and bound chlorides (Tuutti, 1982). According to the literature (He *et al.*, 2012), the measured concentration of free chlorides at the color change boundary in OPC concrete may vary between 0.28%-1.69% by binder mass or 0.071-0.714 N in pore solution based on the  $\text{AgNO}_3$  method (Sirivivatnanon and Khatri, 1998; Meck and Sirivivatnanon, 2003; He *et al.*, 2008; Yuan, 2009). After immersing in NaCl solution, Otsuki *et al.* (1992) found at the color change boundary, a free chloride content of 0.15% by cement mass and a total amount of chlorides of 0.4 - 0.5% by cement mass.

The aging coefficient,  $n_{cl}$ , was determined considering the following equation (Poulsen and Mejlbro, 2006; Bogas, 2011):

$$n_{cl} = \frac{\ln\left(\frac{D_{c,1}}{D_{c,2}}\right)}{\ln\left(\frac{t_2}{t_1}\right)} \quad (7.5)$$

where  $D_{c,1}$  and  $D_{c,2}$  are the chloride diffusion coefficients corresponding to 10 days ( $t_1$ ) and 3 months ( $t_2$ ) of chloride immersion, respectively.

## 7.3 RESULTS AND DISCUSSION

### 7.3.1 Preliminary RPT-3ps

Figure 7.10 shows the force-central deflection curve,  $F - \delta$ , obtained for Panel 1 of the preliminary RPT-3ps. The  $F - \delta$  response comprises a linear pre-peak ascending branch up to a maximum load. Beyond the peak point, the load decreases with the opening of the formed cracks in a deflection softening response. The crack initiation was assumed at the limit of proportionality that occurred at a central deflection of around 1 mm.

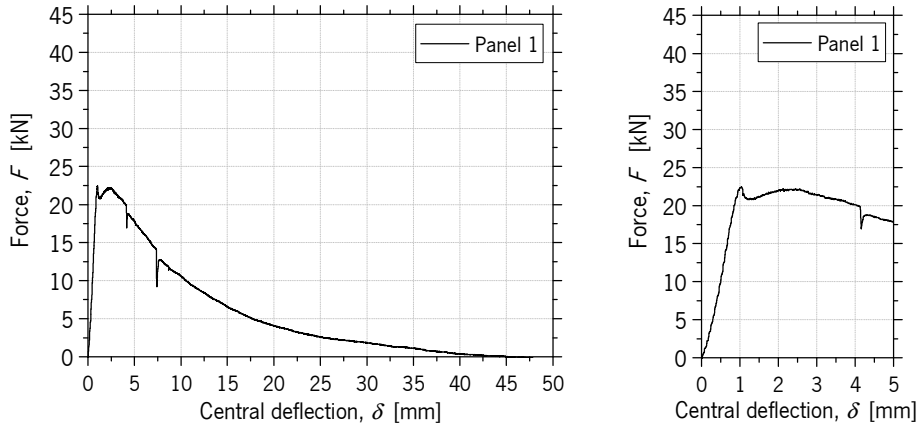


Figure 7.10 – Force-central deflection curve obtained in Panel 1 of preliminary RPT-3ps up to a central deflection of: (a) 50 mm; (b) 5 mm

The average crack width values of cracks 1, 2 and 3, measured with the USB microscope at the located points A, B and C (Fig. 7.3) versus the central deflection for each panel are reported in Figure 7.11.

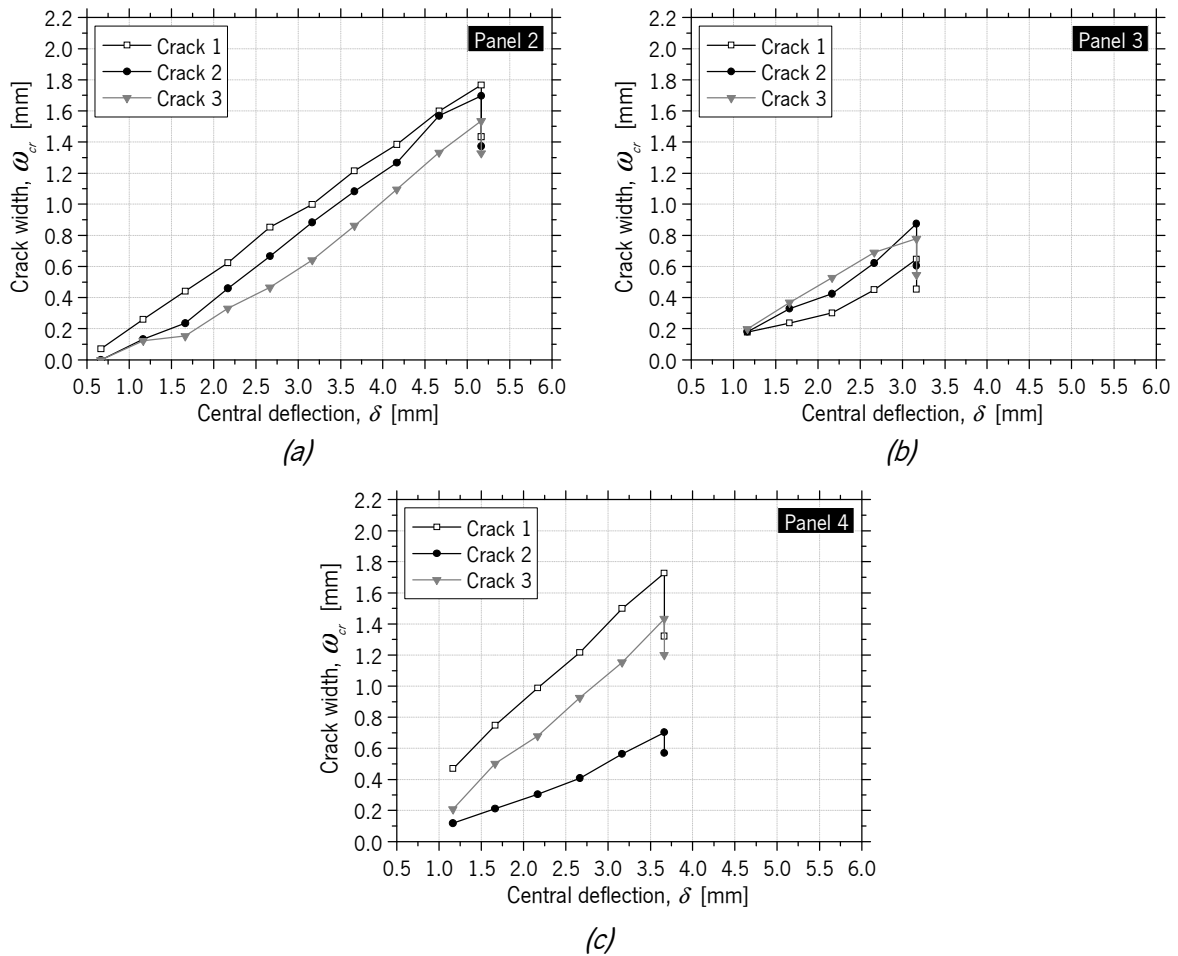


Figure 7.11 – Average crack width - central deflection relationship obtained in preliminary RPT-3ps for cracks 1, 2 and 3 of: (a) Panel 2; (b) Panel 3; (c) Panel 4



It is verified that the progress of the three crack widths was similar in Panels 2 and 3. However, in Panel 4 a significant reduction of the crack 2 progress was observed compared to cracks 1 and 3. These differences are probably due to fiber distribution and orientation that were not so homogeneous in Panel 4 than in the other two panels.

After unloading the panels, an average decrease of 0.3 mm in the crack width was observed with the USB microscope. Considering this, in order to ensure the target pre-crack widths of 0.5 and 1.0 mm after unloading the panels, it was necessary to impose the crack widths of 0.8 and 1.3 mm, respectively. Considering the average crack width of the three cracks in each panel, as represented in Figure 7.12, the minimum value of deflection corresponding to a crack width of 0.8 mm (Panel 3), was 2.5 mm. Based on these results, the procedure defined for pre-cracking panels consisted to first impose a deflection value of 2.5 mm to panels, followed by successive increments of 0.25 mm in deflection up to achieve the desired unloaded pre-crack width.

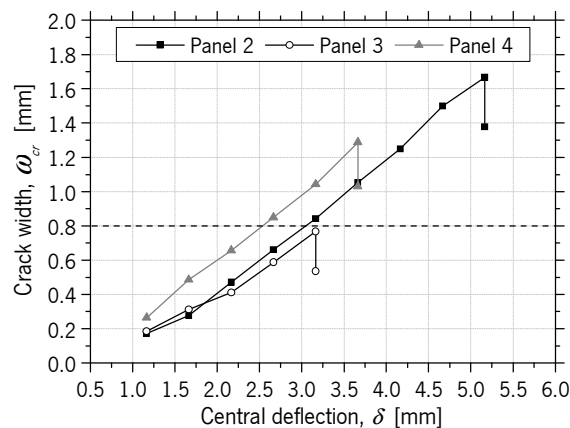


Figure 7.12 – Average crack width - central deflection relationship obtained in Panels 2, 3 and 4 of preliminary RPT-3ps

The relationships between the average measurement at each crack position A, B and C (Fig. 7.3) and the central deflection obtained in tested panels are presented in Figure 7.13. No significant differences in the crack width were observed along its length up to a central deflection of approximately 2.0 mm. The dispersion of the crack width measurements increased for higher central deflections ( $> \approx 3.0$  mm). At the position B, where the LVDTs for crack width measurement were installed, the average central deflection corresponding to a crack width of 0.8 mm was 2.9 mm, and for a crack width of 1.3 mm was 4.1 mm.

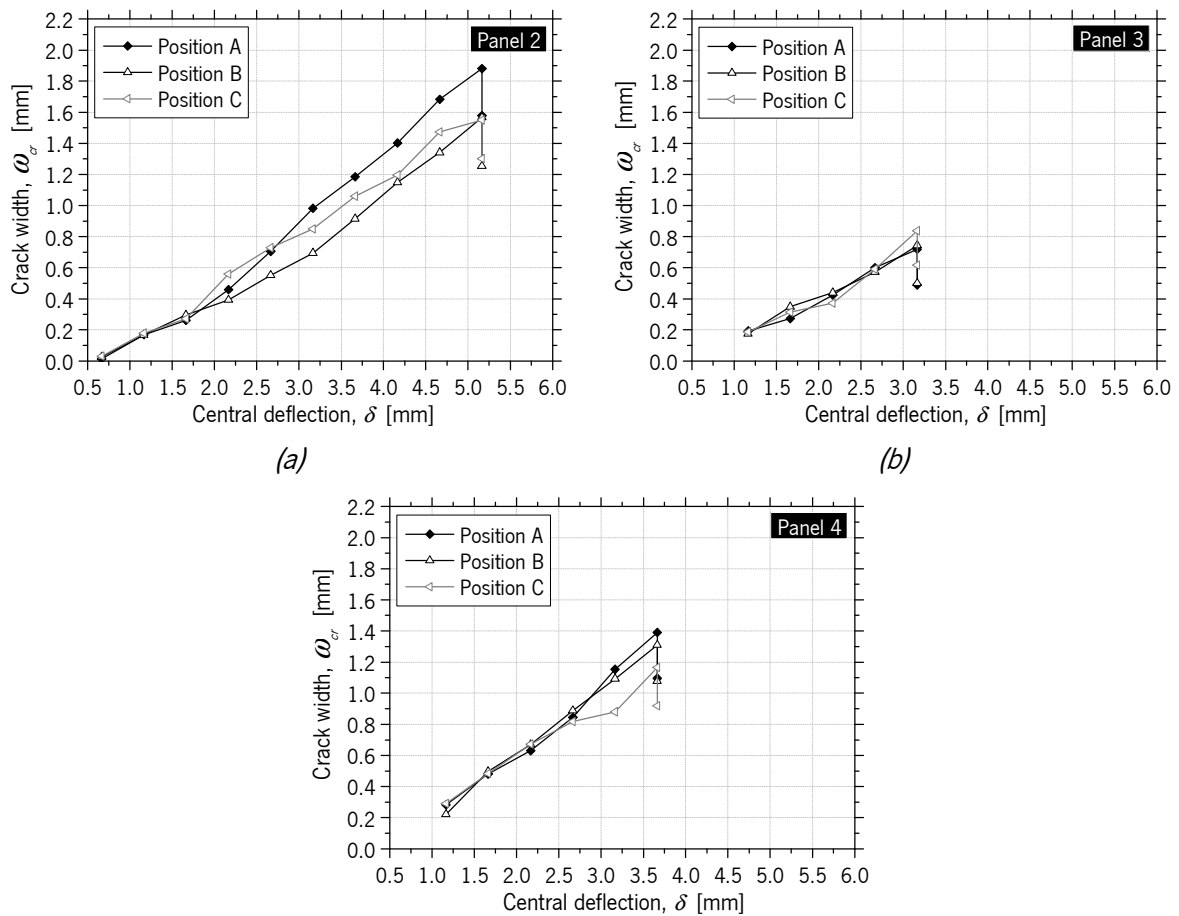


Figure 7.13 – Average crack width - central deflection relationship obtained in preliminary RPT-3ps for position A, B and C of: (a) Panel 2; (b) Panel 3; (c) Panel 4

## 7.3.2 Results of RPT-3ps under chloride attack

### 7.3.2.1 Modes of failure

The ultimate crack patterns at failure conditions of the panels comprise three radial cracks that propagate in the sectors between two adjacent pivots, as represented in Figure 7.14a. The cracks' alignment often deviates from the bisector of the segments due to the influence of fiber dispersion and orientation on the panels, which is very sensitive to the casting procedure (Figure 7.14b). Three round panels presented only two radial cracks, as observed in Figure 7.14c. The ultimate crack patterns of the 36 round panels registered in the performed RPT-3ps are depicted in Appendix D.

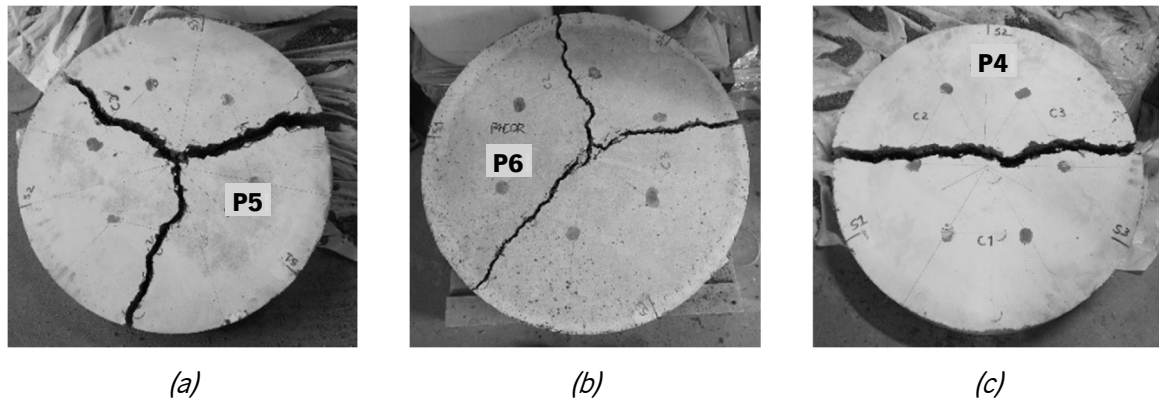


Figure 7.14 – Crack patterns of the panels of:  
 (a) Series II\_REF\_P5; (b) Series V\_Cl\_P6; (c) Series II\_REF\_P4

### 7.3.2.2 Chloride penetration into RSFRC panels

After 10 days of chloride immersion, no significant signs of RSF superficial corrosion were visible in the RSFRC panels. Only some poorly covered and uncovered fibers located on the exposed surfaces appeared to be slightly corroded (Figures 7.15a,b). However, after 3 months of dry-wet cycles in chloride solution, a significant increase in surface corrosion has occurred on the RSFRC panels, and many corrosion spots were visible due to the poorly covered and uncovered RSF directly exposed to the chloride solution (Figures 7.15c,d).

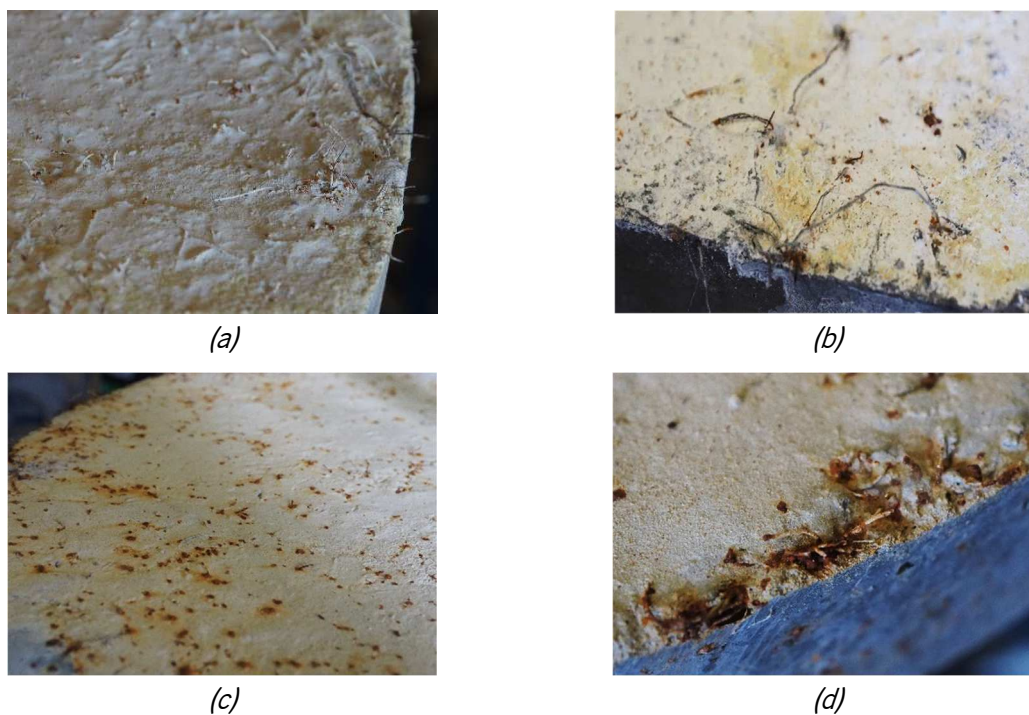
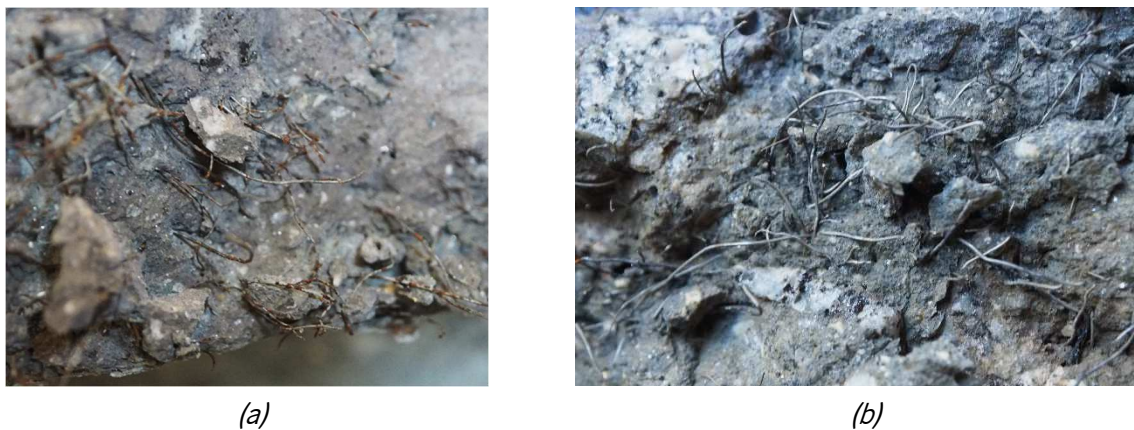
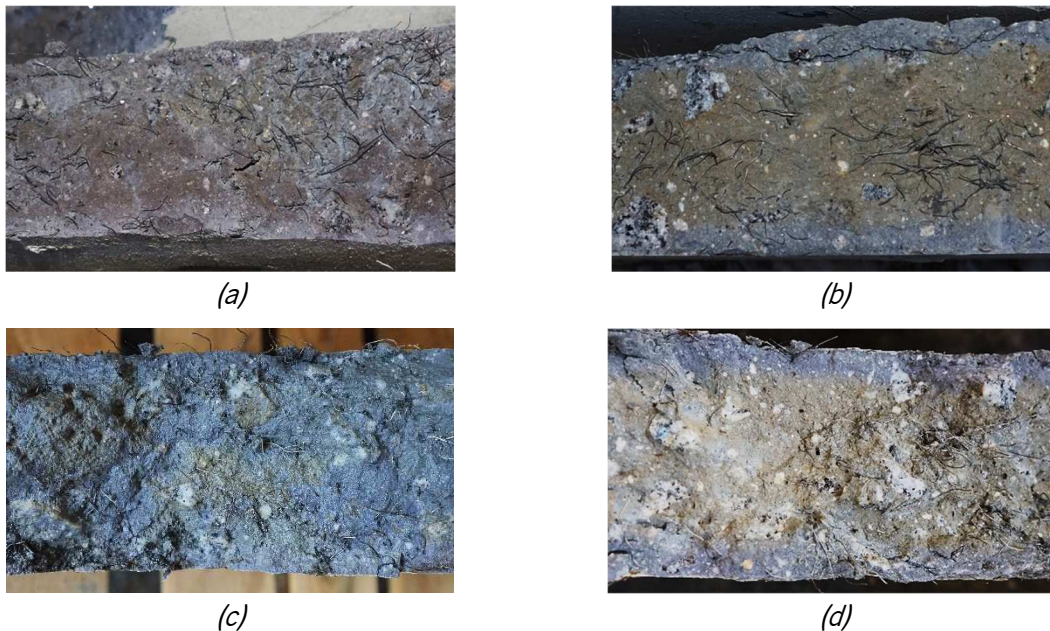


Figure 7.15 – Corrosion spots at exposed surfaces of RSFRC Panels:  
 (a) and (b) After 10 days of chloride immersion;  
 (c) and (d) After 3 months of dry-wet cycles in chloride solution

After performing the final RPT-3ps of the RSFRC panels submitted to chloride immersion, these panels were divided into the three cracked plates, and the cracked surfaces were visually observed. As shown in Figure 7.16a, some RSF at cracked surfaces of pre-cracked panels presented corrosion products, mainly near the exposed lower face of the panels, where the crack width was higher. It seems that the RSF corrosion occurred mainly at the fiber length crossing the crack width (in direct contact with the chloride solution) since a more localized corrosion was detected. Apparently, no signs of corrosion were detected in the RSF at crack surfaces of non-cracked panels (Figure 7.16b). To assess the chloride penetration depth, the cracked surfaces were sprayed with silver nitrate solution, as observed in Figure 7.17.



(a) (b)  
Figure 7.16 – Inspection of RSF at crack surfaces of:  
(a) Pre-cracked panels; (b) Non-cracked panels



(a) (b)  
(c) (d)  
Figure 7.17 – Chloride penetration depth at cracked surfaces:  
After 10 days of chloride immersion: (a) Pre-cracked panels; (b) Non-cracked panels  
After 3 months of dry-wet cycles in chloride solution: (c) Pre-cracked panels; (d) Non-cracked panels



### 7.3.2.3 Force-Central deflection relationships

#### Pre-cracked RSFRC panels

Figures 7.19 and 7.20 present the force-central deflection responses registered in the pre-cracked RSFRC1% panels, during the pre-cracking process (initial load/unload cycle) and after the environmental exposure period (final RPT-3ps) of 10 days of immersion (Series I&II) and 3 months of dry-wet cycles/immersion (Series IV&V). In these figures are indicated the pre-crack widths,  $\omega_{cr}$  (after unloading) implemented on each panel. As observed, the crack width values were close to the target crack widths, 0.5 or 1.0 mm.

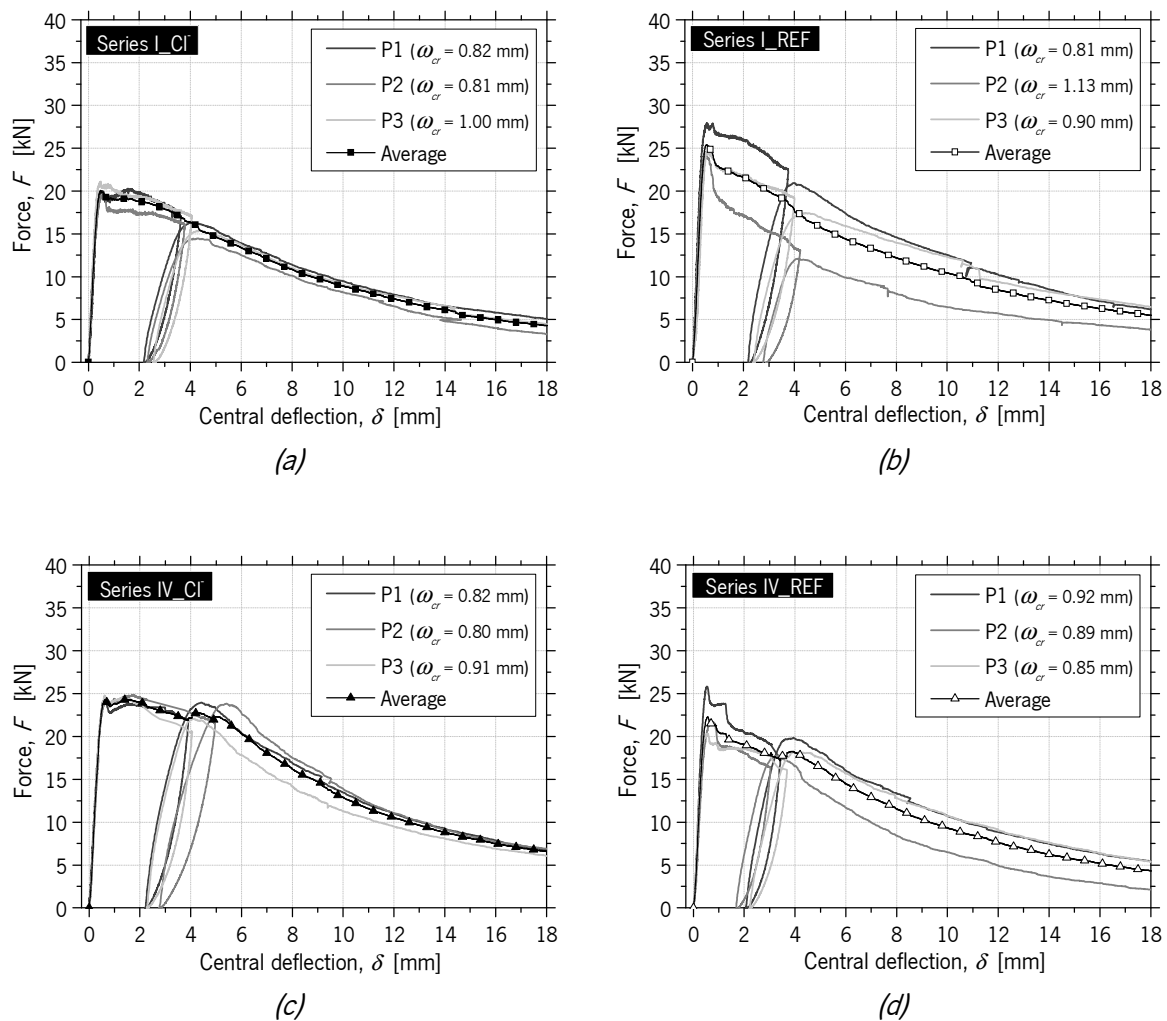


Figure 7.19 – Force-Central deflection relationships of:  
 (a) Series I\_CI; (b) Series I\_REF; (c) Series IV\_CI; (d) Series IV\_REF

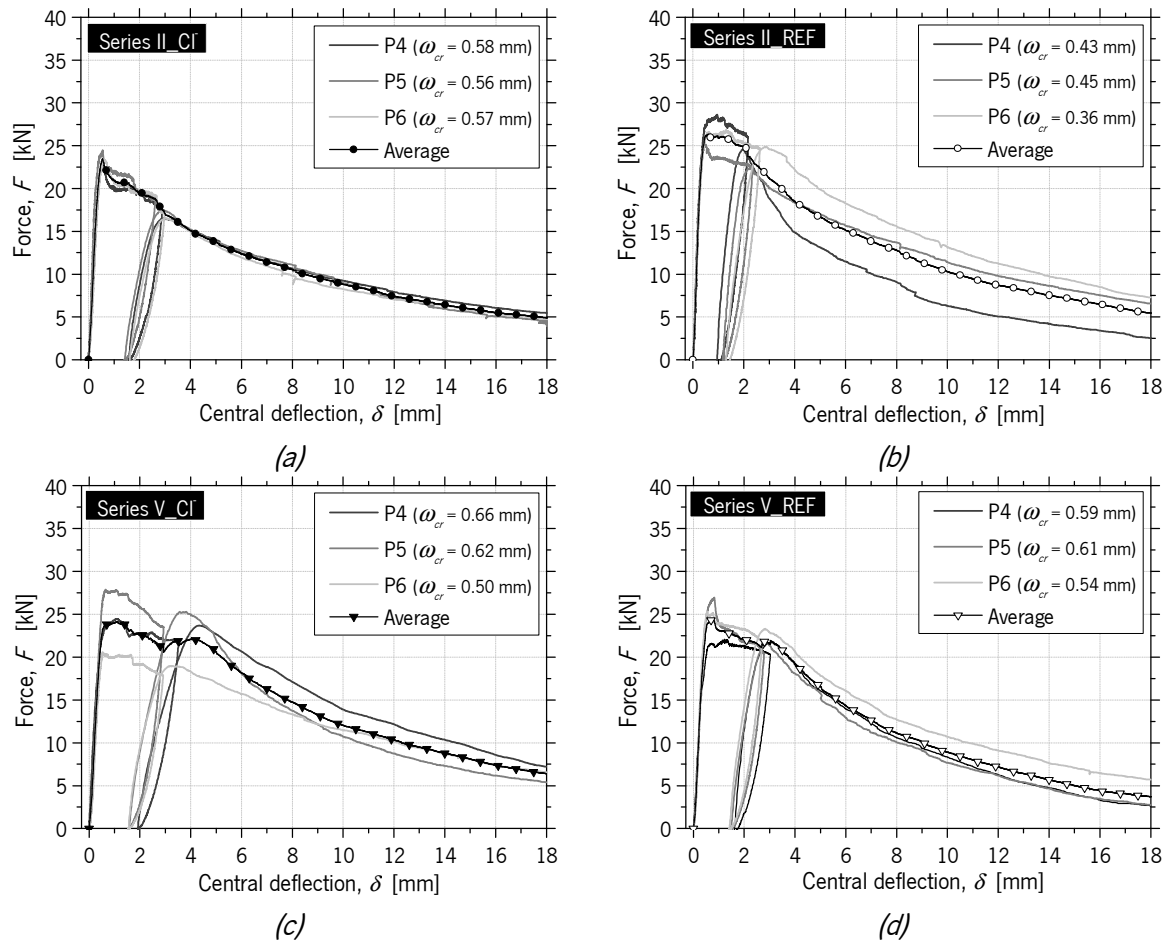


Figure 7.20 – Force-Central deflection relationships of:  
 (a) Series II\_CI; (b) Series II\_REF; (c) Series V\_CI; (d) Series V\_REF

### Stiffness parameters

For the force-central deflection relationship obtained in each pre-cracked panel, the parameters of stiffness represented in Figure 7.21 were determined.

- Initial stiffness,  $K_{ci}$  ;
- Initial unloading tangent stiffness,  $K_{Ou}$  ;
- Final unloading tangent stiffness,  $K_{fu}$  ;
- Initial reloading tangent stiffness,  $K_{Or}$  ;
- Unloading secant stiffness,  $K_{csecu}$  ;
- Reloading secant stiffness,  $K_{csecr}$  ;

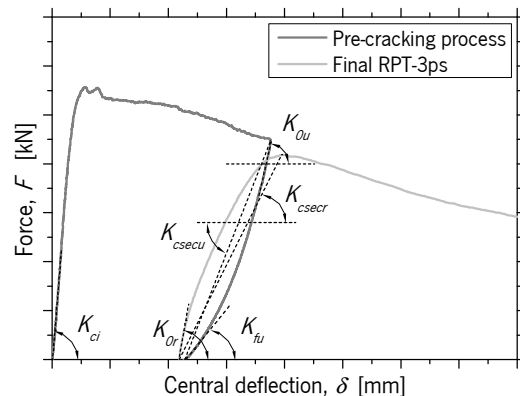


Figure 7.21 – Stiffness parameters determined for each pre-cracked panel using the obtained experimental data

The results obtained of the normalized stiffness parameters are presented in Tables 7.2 and 7.3.

Table 7.2 – Stiffness parameters for Series I&IV (target  $\omega_{cr}$  of 1.0 mm)

Series	Panel	$\omega_{cr}$ (mm)	$K_{ci}$ (kN/mm)	$K_{Ou}/K_{ci}$	$K_{fu}/K_{ci}$	$K_{Or}/K_{ci}$	$K_{csecu}/K_{ci}$	$K_{cseccr}/K_{ci}$
I_CI	P1	0.82	62.40	0.37	0.08	0.40	0.20	0.13
	P2	0.81	67.15	0.36	0.07	0.32	0.17	0.11
	P3	1.00	76.97	0.33	0.06	0.31	0.15	0.10
	Avg	0.88	68.84	0.35	0.07	0.34	0.17	0.11
	CoV (%)	(12.26)	(10.80)	(6.50)	(19.52)	(13.83)	(13.00)	(11.25)
I_REF	P1	0.81	83.51	0.31	0.09	0.40	0.18	0.14
	P2	1.13	74.57	0.27	0.06	0.28	0.13	0.12
	P3	0.90	73.50	0.36	0.06	0.33	0.16	0.12
	Avg	0.95	77.19	0.31	0.07	0.34	0.16	0.13
	CoV (%)	(17.59)	(7.12)	(14.31)	(25.49)	(18.60)	(15.04)	(10.98)
IV_CI	P1	0.82	59.82	0.47	0.09	0.62	0.23	0.19
	P2	0.80	60.23	0.36	0.08	0.38	0.17	0.15
	P3	0.91	66.74	0.42	0.07	0.48	0.18	0.18
	Avg	0.85	62.27	0.42	0.08	0.49	0.19	0.17
	CoV (%)	(6.94)	(6.24)	(13.55)	(12.95)	(24.78)	(16.82)	(10.80)
IV_REF	P1	0.92	83.38	0.36	0.07	0.36	0.16	0.13
	P2	0.89	60.01	0.45	0.08	0.36	0.22	0.19
	P3	0.85	62.91	0.37	0.07	0.41	0.18	0.15
	Avg	0.89	68.77	0.39	0.07	0.38	0.19	0.15
	CoV (%)	(4.39)	(18.52)	(12.95)	(7.93)	(8.46)	(14.10)	(19.64)

Table 7.3 – Stiffness parameters for Series II&V (target  $\omega_{cr}$  of 0.5 mm)

Series	Panel	$\omega_{cr}$ (mm)	$K_{ci}$ (kN/mm)	$K_{Ou}/K_{ci}$	$K_{fu}/K_{ci}$	$K_{Or}/K_{ci}$	$K_{csecu}/K_{ci}$	$K_{cseccr}/K_{ci}$
II_CI	P4	0.58	61.97	0.44	0.10	0.55	0.22	0.13
	P5	0.56	89.25	0.32	0.08	0.30	0.18	0.13
	P6	0.57	63.15	0.41	0.12	0.41	0.23	0.19
	Avg	0.57	71.46	0.39	0.10	0.42	0.21	0.15
	CoV (%)	(1.90)	(21.58)	(16.25)	(16.91)	(29.61)	(11.64)	(21.16)
II_REF	P4	0.43	96.79	0.43	0.14	0.61	0.25	0.24
	P5	0.45	94.27	0.38	0.11	0.61	0.22	0.22
	P6	0.36	81.44	0.46	0.14	0.45	0.26	0.19
	Avg	0.41	90.83	0.42	0.13	0.56	0.24	0.21
	CoV (%)	(11.93)	(9.06)	(9.85)	(12.62)	(17.30)	(8.52)	(11.28)
V_CI	P4	0.66	66.02	0.42	0.09	0.38	0.21	0.14
	P5	0.62	70.73	0.52	0.09	0.41	0.24	0.18
	P6	0.50	60.27	0.44	0.09	0.53	0.22	0.18
	Avg	0.59	65.67	0.46	0.09	0.44	0.23	0.17
	CoV (%)	(13.83)	(7.98)	(11.25)	(0.86)	(17.79)	(7.66)	(12.67)
V_REF	P4	0.59	61.92	0.49	0.12	0.65	0.26	0.23
	P5	0.61	68.99	0.46	0.11	0.49	0.23	0.23
	P6	0.54	83.88	0.43	0.08	0.45	0.21	0.20
	Avg	0.58	71.60	0.46	0.10	0.53	0.23	0.22
	CoV (%)	(5.85)	(15.65)	(6.37)	(23.65)	(19.96)	(9.43)	(8.93)



Comparing the pre-cracked chloride-immersed (CI) panels with the corresponding reference (REF) pre-cracked panels, no significant differences were observed between the stiffness parameters, which means that the corrosion induction conditions of RSF had a negligible effect on the post-cracking behavior of cracked RSFRC up to a crack width of 1 mm for the adopted exposure periods. The small differences observed between the stiffness parameters obtained in the pre-cracked panels are justified by the differences between the pre-crack width levels.

For a better understanding of these results of stiffness, Figure 7.22 shows the relationship between the average pre-crack width level,  $\omega_{cr}$  and the normalized stiffness,  $K_j / K_{ci}$ , where  $K_j$  is the stiffness parameter represented in Figure 7.21. For all pre-cracked panels (CI and REF), there was a clear tendency to decrease the normalized stiffness,  $K_j / K_{ci}$ , with the increase of the pre-crack width,  $\omega_{cr}$ , regardless of the initial stiffness value,  $K_{ci}$ .

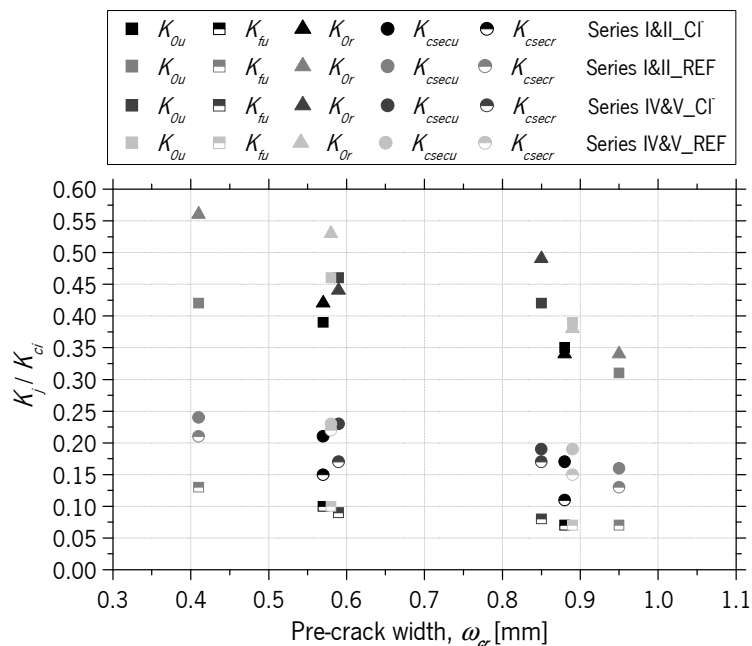


Figure 7.22 – Normalized stiffness- pre-crack width relationship obtained in the pre-cracked panels

### Non pre-cracked RSFRC panels

The force-central deflection responses registered in the non-cracked RSFRC1% panels, after 10 days of immersion (Series III) and 3 months of dry-wet cycles/immersion (Series VI), are depicted in Figure 7.23.

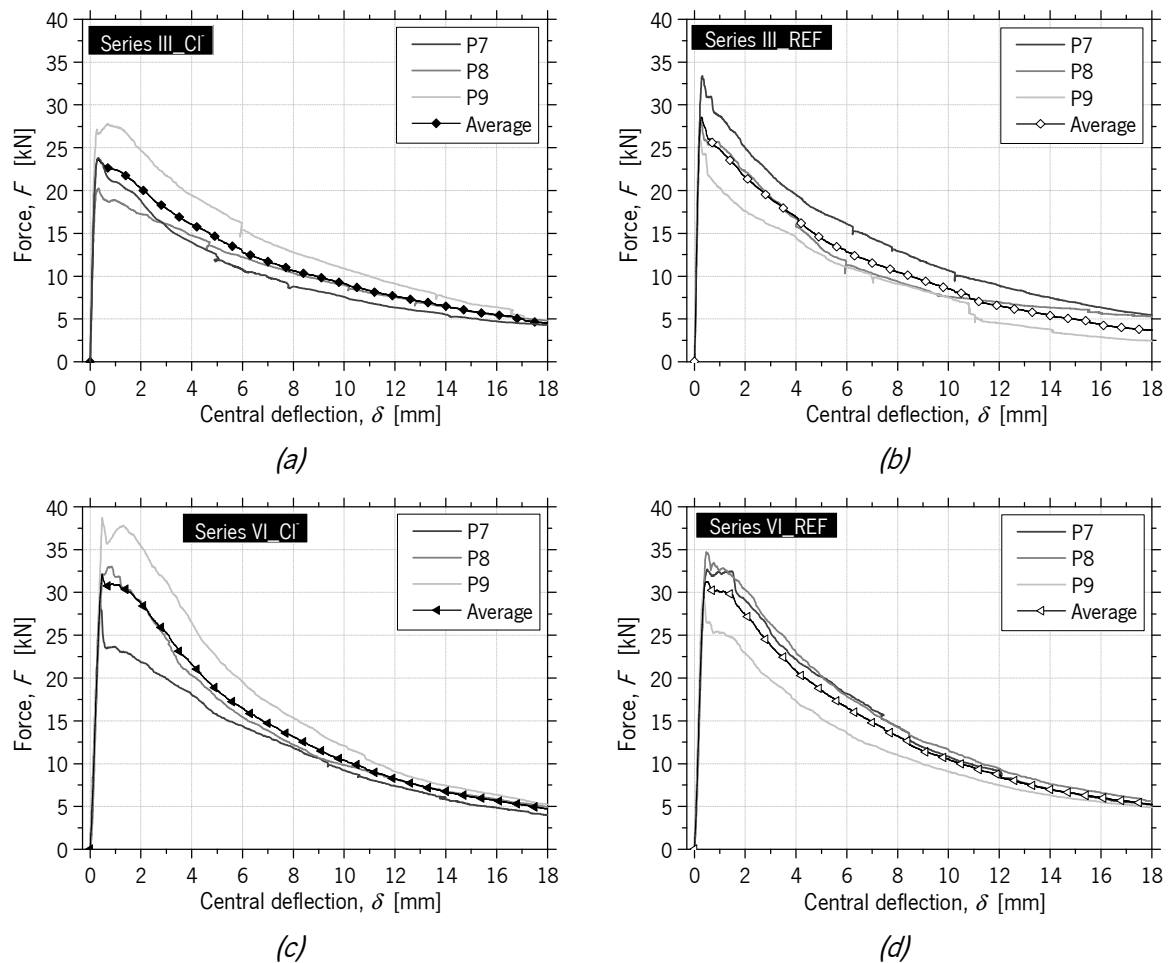


Figure 7.23 – Force-Central deflection relationships of:  
 (a) Series III\_Cl; (b) Series III\_REF; (c) Series VI\_Cl; (d) Series VI\_REF

For Series III (non pre-cracked), the panels submitted to 10 days of chloride immersion showed lower average post-cracking resistance than reference panels, which corroborates with the lower flexural tensile strength parameters,  $f_{eq}$  and  $f_{R,i}$ , obtained in the 3-point notched beam bending tests (3PNBBTs) of RSFRC1%\_2 beams (same RSFRC1% casting as Series III\_Cl panels), comparing to RSFRC1%\_3 beams (same RSFRC1% casting as Series III\_REF panels), as presented in Section 3.5.1.2 (Table 3.20). As pointed out by Barros *et al.* (2015a), a correlation between the post-cracking performance on 3PNBBTs and RPT-3ps was observed. It should be noted that these RSFRC1% beams were tested at the same age as the RSFRC1% panels of Series III (38 days = 28 days of curing + 10 days of immersion).

In the Series VI, the average post-cracking resistance of panels submitted to 3 months of dry-wet cycles of chloride immersion was similar to that of reference panels, which also corroborates with the results obtained in the 3PNBBTs of RSFRC1%\_4 beams (same RSFRC1% casting as Series VI\_Cl panels), comparing to RSFRC1%\_5 beams (same RSFRC1% casting as Series VI\_REF panels), as presented in Section 3.5.1.2 (Figure 3.28). These RSFRC1% beams were also tested at the same age as the RSFRC1%

panels of Series VI (120 days = 28 days of curing + 92 days of dry-wet cycles/immersion). The non-cracked panels of Series VI showed higher maximum load and post-cracking resistance than the non-cracked panels of Series III, mainly due to the age difference of the panels, 120 days and 38 days, respectively. For comparison between pre-cracked and non-cracked panels, the average force-central deflection curves registered in the six series of tests are presented in Figure 7.24.

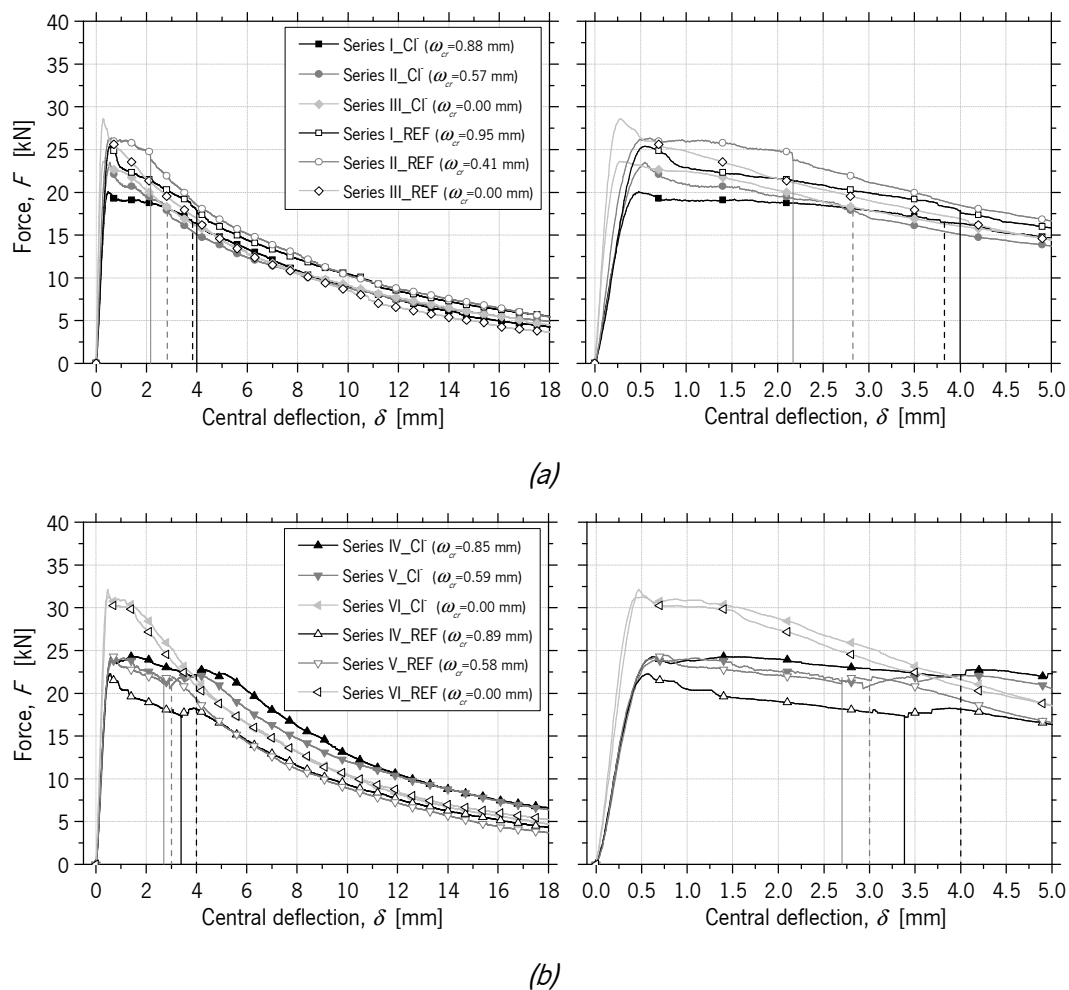


Figure 7.24 – Average Force-Central deflection relationships of:

(a) RSFRC panels submitted to 10 days of  $\text{Cl}^-$ /water immersion (Series I&II&III);

(b) RSFRC panels submitted to 3 months of  $\text{Cl}^-$  wet-dry cycles/water immersion (Series IV&V&VI)

No significant differences were observed between the post-cracking behavior of pre-cracked and non-cracked panels submitted to 10 days of chloride immersion (Fig. 7.24a). In this case, the small differences observed in terms of maximum load and post-cracking strength appear to be due to slight differences in panel thickness and/or due to fiber distribution and orientation. The influence of these two parameters will be discussed in the next sections 7.3.2.4 and 7.3.3, respectively. According to Fig. 7.24a, the

reference panels showed better flexural performance than chloride attacked panels due to differences in flexural tensile strength of the corresponding RSFRC1% castings, as presented in Section 3.5.1.2.

No significant differences were observed in the post-cracking behavior between non-cracked panels submitted to 3 months of dry-wet cycles in chloride solution and the corresponding non-cracked reference panels (the small differences are explained by the differences in flexural strength of the corresponding RSFRC1% castings, see Section 3.5.1.2). However, for the pre-cracked panels submitted to chloride attack for 3 months of dry-wet cycles, a slight increase in the post-cracking load carrying capacity is observed for panels with an average  $\omega_{cr} = 0.59$  mm (Series V\_ Cl) comparing with the respective pre-cracked reference panels (Series V\_REF). During the pre-cracking process, the pre-cracked panels with an average  $\omega_{cr} = 0.85$  mm submitted to 3 months of dry-wet cycles in chloride solution (Series IV\_ Cl) showed better flexural behavior than the corresponding reference pre-cracked panels (Series IV\_REF). For this reason, it was expected to obtain better flexural performance with these pre-cracked panels, assuming no significant influence of chloride attack, which seems to be the case. The influence of chloride attack in the pre-cracked panels will be better clarified in the next sections.

### 7.3.2.4 Energy absorption-Central deflection relationships

The performance of the RSFRC panels tested by RPT-3ps was quantified in terms of the energy absorption,  $W$ , that represents the area under the force-central deflection curves (Figure 7.24) up to a specified central deflection,  $\delta$ . This energy absorbed by the panels is representative of the flexural toughness of RSFRC panels. Figure 7.25 represents the average energy absorption-central deflection responses registered on the tested RSFRC panels up to a  $\delta$  of 18 mm.

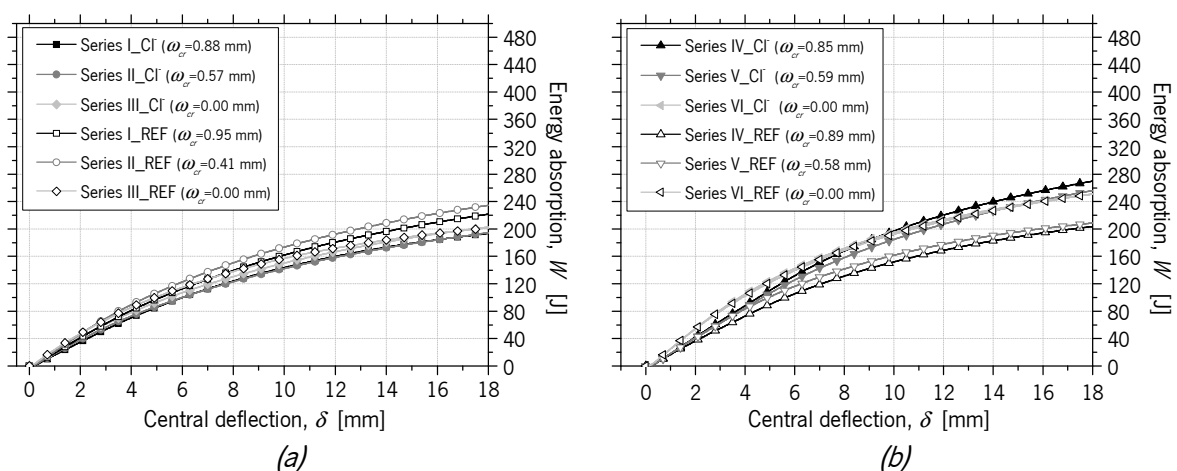


Figure 7.25 – Average Energy absorption-Central deflection relationships of:

(a) RSFRC panels submitted to 10 days of Cl-/water immersion (Series I&II&III);

(b) RSFRC panels submitted to 3 months of Cl- wet-dry cycles/water immersion (Series IV&V&VI)

The ASTM C1550-08 (2008) recommends the determination of flexural toughness of FRC expressed as energy absorbed by the panel up to a specified central deflection. The energy absorbed up to 5 mm central deflection is applicable to situations in which the material is required to hold cracks tightly closed at low levels of deformation. The energy absorbed up to 40 mm is more applicable to situations in which the material is expected to suffer severe deformation in situ. The energy absorbed,  $W$ , was determined up to the central deflections of 5, 10, 20 and 40 mm. In some cases, it was not possible to determine up to 40 mm since for this higher crack opening, the *LVDT O* (Figure 7.2a) tended to move and get inside the cracks, invalidating the measurement of central deflection.

In Table 7.4 are presented the average values of the pre-crack width,  $\omega_{cr}$ , the maximum load (load capacity at first peak),  $F_{max}$ , and the energy absorbed up to a central deflection  $\delta$ ,  $W_{\delta}$ , obtained in all series of RPT-3ps.

Table 7.4 – Pre-crack width, maximum load and energy absorption obtained in RPT-3ps

Series		$\omega_{cr}$ (mm)	$F_{max}$ (kN)	$W_5$ (J)	$W_{10}$ (J)	$W_{20}$ (J)	$W_{40}$ (J)
I_CI	Avg	0.88	20.31	85.91	143.71	198.12	-
	CoV (%)	(12.26)	(4.11)	(5.04)	(5.49)	(10.54)	(-)
I_REF	Avg	0.95	25.74	97.77	162.00	231.90	-
	CoV (%)	(17.59)	(7.34)	(19.08)	(22.54)	(24.00)	(-)
II_CI	Avg	0.57	23.71	87.18	142.21	203.31	266.44
	CoV (%)	(1.90)	(2.79)	(3.00)	(3.17)	(2.62)	(-)
II_REF	Avg	0.41	26.88	107.02	173.55	244.73	266.49
	CoV (%)	(11.93)	(6.46)	(7.84)	(14.03)	(21.28)	(30.65)
III_CI	Avg	0.00	24.02	93.44	150.28	191.26	237.72
	CoV (%)	(-)	(15.69)	(18.68)	(18.36)	(4.43)	(5.63)
III_REF	Avg	0.00	29.13	101.11	157.09	208.56	310.91
	CoV (%)	(-)	(12.98)	(15.78)	(17.32)	(21.78)	(-)
IV_CI	Avg	0.85	24.65	110.26	197.16	282.18	345.86
	CoV (%)	(6.94)	(1.06)	(1.87)	(5.92)	(6.38)	(3.57)
IV_REF	Avg	0.89	22.61	89.96	152.02	211.58	249.07
	CoV (%)	(4.39)	(12.68)	(8.94)	(12.81)	(18.81)	(23.64)
V_CI	Avg	0.59	24.30	106.24	184.78	267.82	363.40
	CoV (%)	(13.83)	(14.94)	(14.26)	(11.96)	(10.10)	(-)
V_REF	Avg	0.58	24.78	101.01	161.74	215.31	240.40
	CoV (%)	(5.85)	(10.00)	(4.73)	(7.17)	(13.42)	(24.27)
VI_CI	Avg	0.00	33.42	124.94	195.15	259.89	310.27
	CoV (%)	(-)	(15.34)	(20.60)	(18.61)	(16.97)	(23.37)
VI_REF	Avg	0.00	32.25	121.83	192.34	260.76	307.48
	CoV (%)	(-)	(8.47)	(13.09)	(13.59)	(12.43)	(10.81)

The obtained values of energy absorption were corrected using the following equation recommended by the ASTM C1550-08 (2008):

$$W' = W \left( \frac{t_0}{t} \right)^\beta \left( \frac{d_0}{d} \right) \text{ with } \beta = 2.0 - (\delta - 0.5)/80 \quad (7.6)$$

where  $W'$  is the corrected energy absorption,  $W$  is the measured energy absorption,  $t_0$  is the nominal thickness of 75 mm,  $t$  is the panel thickness (mm),  $d_0$  is the nominal diameter of 800 mm,  $d$  is the panel diameter (mm) and  $\delta$  is the specified central deflection at which the absorbed energy is measured (mm). In Table 7.5 are presented the average values of the pre-crack width,  $\omega_{cr}$ , maximum load,  $F_{max}$ , panel thickness,  $t$ , and the corrected values of energy absorption. The maximum load values corroborate with the thickness of the panels since higher loads were registered in the panels of higher thickness. According to this, the dispersion observed in force-central deflection curves (Figures 7.19, 7.20 and 7.23) is partly justified by differences in panel thickness,  $t$ .

Table 7.5 – Corrected energy absorption obtained in RPT-3ps

<b>Series</b>		$\omega_{cr}$ (mm)	$F_{max}$ (kN)	$t$ (mm)	$W'_5$ (J)	$W'_{10}$ (J)	$W'_{20}$ (J)	$W'_{40}$ (J)
I_CI	Avg CoV (%)	0.88 (12.26)	20.31 (4.11)	60.56 (2.64)	173.60 (3.61)	286.57 (4.59)	394.70 (9.25)	- (-)
I_REF	Avg CoV (%)	0.95 (17.59)	25.74 (7.34)	65.99 (2.28)	166.53 (15.46)	273.75 (19.75)	385.79 (21.79)	521.63 (-)
II_CI	Avg CoV (%)	0.57 (1.90)	23.71 (2.79)	64.22 (0.57)	157.15 (1.89)	253.88 (2.34)	356.06 (2.87)	451.87 (-)
II_REF	Avg CoV (%)	0.41 (11.93)	26.88 (6.46)	67.10 (2.77)	177.38 (9.09)	286.26 (16.46)	398.84 (23.80)	424.82 (36.21)
III_CI	Avg CoV (%)	0.00 (-)	24.02 (15.69)	65.35 (3.71)	161.83 (11.17)	258.22 (11.46)	337.25 (6.68)	402.87 (7.56)
III_REF	Avg CoV (%)	0.00 (-)	29.13 (12.98)	68.47 (1.50)	160.54 (12.98)	247.92 (14.40)	325.23 (19.04)	463.73 (-)
IV_CI	Avg CoV (%)	0.85 (6.94)	24.65 (1.06)	63.91 (0.88)	200.71 (3.35)	355.46 (7.35)	498.64 (7.63)	589.64 (2.13)
IV_REF	Avg CoV (%)	0.89 (4.39)	22.61 (12.68)	64.62 (1.28)	160.11 (7.25)	268.14 (12.13)	366.40 (18.55)	415.59 (23.50)
V_CI	Avg CoV (%)	0.59 (13.83)	24.30 (14.94)	64.41 (6.12)	189.86 (7.15)	328.35 (10.55)	468.64 (13.14)	627.50 (-)
V_REF	Avg CoV (%)	0.58 (5.85)	24.78 (10.00)	65.00 (2.76)	178.22 (8.08)	282.65 (8.67)	369.57 (14.19)	398.32 (24.88)
VI_CI	Avg CoV (%)	0.00 (-)	33.42 (15.34)	68.94 (6.05)	194.47 (9.03)	302.73 (7.58)	399.44 (6.57)	467.20 (10.65)
VI_REF	Avg CoV (%)	0.00 (-)	32.25 (8.47)	66.46 (1.87)	205.04 (10.13)	321.26 (10.81)	429.11 (9.67)	491.18 (8.44)

For a better understanding of the energy absorption results, the average values of corrected energy absorbed at central deflections of 5, 10 and 20 mm, are graphically represented in Figure 7.26.

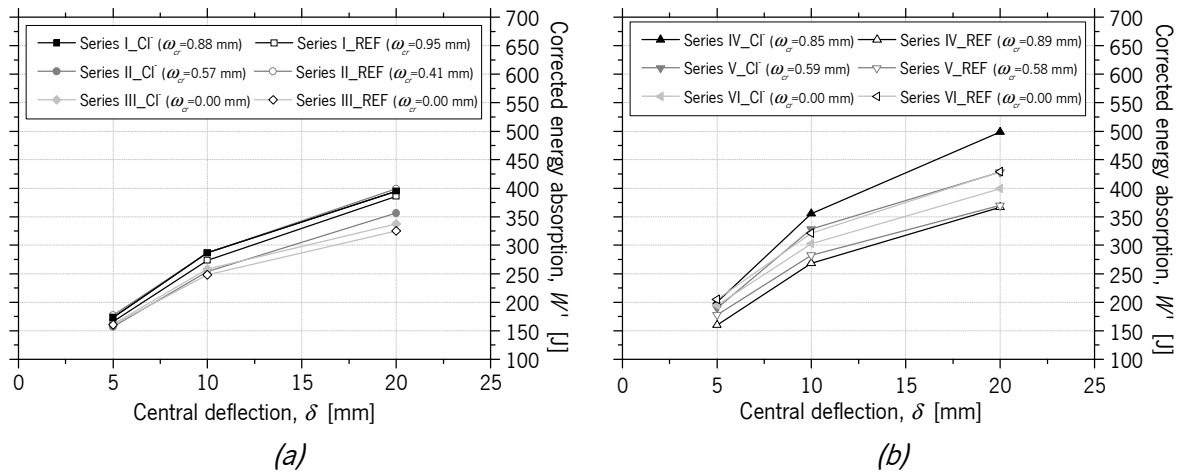


Figure 7.26 – Corrected energy absorption-Central deflection relationships of:  
 (a) RSFRC panels submitted to 10 days of Cl-/water immersion (Series I&II&III);  
 (b) RSFRC panels submitted to 3 months of Cl- wet-dry cycles/water immersion (Series IV&V&VI)

For panels submitted to 10 days of immersion (Fig. 7.26a), due to differences in concrete properties, a higher post-cracking performance would be expected for reference panels compared to panels submitted to chloride immersion, assuming a negligible effect of chloride attack on the energy absorbed by pre-cracked and non-cracked panels (according to the differences in the flexural tensile strength of the corresponding RSFRC1% castings, see Section 3.5.1.2). This was confirmed in the tests of Series II since the pre-cracked panels ( $\omega_{cr} = 0.57$  mm) submitted to chloride immersion showed lower energy absorption than the reference panels ( $\omega_{cr} = 0.41$  mm). However, it seems that the chloride attack had a small beneficial effect for pre-cracked panels with higher level of  $\omega_{cr}$  (0.88 mm), which showed higher energy absorption than the corresponding reference panels ( $\omega_{cr} = 0.95$  mm).

For non-cracked panels submitted to 10 days of chloride immersion, slightly higher energy absorption was also obtained than in non-cracked reference panels. However, as no significant signs of RSF corrosion were visible at crack surfaces of non-cracked panels (Section 7.3.2.2), probably these differences are due to fiber distribution and orientation at crack surfaces.

In Series I, II and III, for a central deflection of 20 mm (Figure 7.26a), the pre-cracked panels showed higher energy absorption performance than non-cracked panels (Cl and REF), which may be justified by the fiber distribution and orientation at crack surfaces.

The RSFRC panels submitted to 3 months of environmental exposure showed higher average values of energy absorption than the RSFRC panels submitted to 10 days of immersion (mainly for chloride attacked

panels) due to age differences of the panels at tests. A higher variability of the results between CI and the corresponding REF panels was also observed for the longest exposure period, which may be due to fiber distribution at crack surfaces and also due to the irregular character of RSF geometry, that causes an irregular susceptibility to fiber corrosion for panels submitted to aggressive environmental conditions, as is the case of dry-wet cycles in chloride solution.

For panels submitted to 3 months of dry-wet cycles in chloride solution, the pre-cracked panels showed higher energy absorbed than reference panels, with a difference that is more pronounced as larger is the pre-crack width. This may be justified by differences in fiber distribution and orientation at crack surfaces. The non-cracked panels submitted to chloride attack for 3 months showed lower energy absorption performance than non-cracked reference panels. This is probably due to fiber distribution at crack surfaces, since no significant differences occurred in the flexural tensile strength of the corresponding RSFRC1% castings (RSFRC1%\_4&5 castings, see Section 3.5.1.2) and no significant signs of RSF corrosion were detected at crack surfaces of non-cracked panels (Section 7.3.2.2).

In Series IV, V and VI, for a central deflection of 20 mm (Figure 7.26b), the pre-cracked panels submitted to chloride attack showed higher energy absorption performance than non-cracked panels. However, the opposite occurred for the reference panels, with non-cracked panels (REF) showing higher energy absorbed than pre-cracked panels (REF). This may also be justified by the fiber distribution and orientation at crack surfaces, and in case of pre-cracked chloride attacked panels, also by the corrosion effects of RSF. According to these results, further research needs to be performed to study the fiber distribution/orientation profile of the tested RSFRC panels, as will be presented in Section 7.3.3 in order to conclude on the effect of chloride attack in the post-cracking behavior of cracked RSFRC.

### **7.3.2.5 Stiffness-Central deflection relationships**

Figure 7.27 shows the average stiffness-central deflection responses that represent the slope determined at each five consecutive points under the average force-central deflection curves of all test Series (Figure 7.24).

The initial stiffness value,  $K_{ci}$ , corresponding to a central deflection,  $\delta_{K_{ci}}$ , is a measure of the elastic deformation of the RSFRC panels (Tables 7.2 and 7.3). The average values of these parameters are presented in Table 7.6, as well as, the average values of the panel thickness,  $t$ , pre-crack width,  $w_{cr}$  and the corresponding central deflection,  $\delta_{cr}$ .



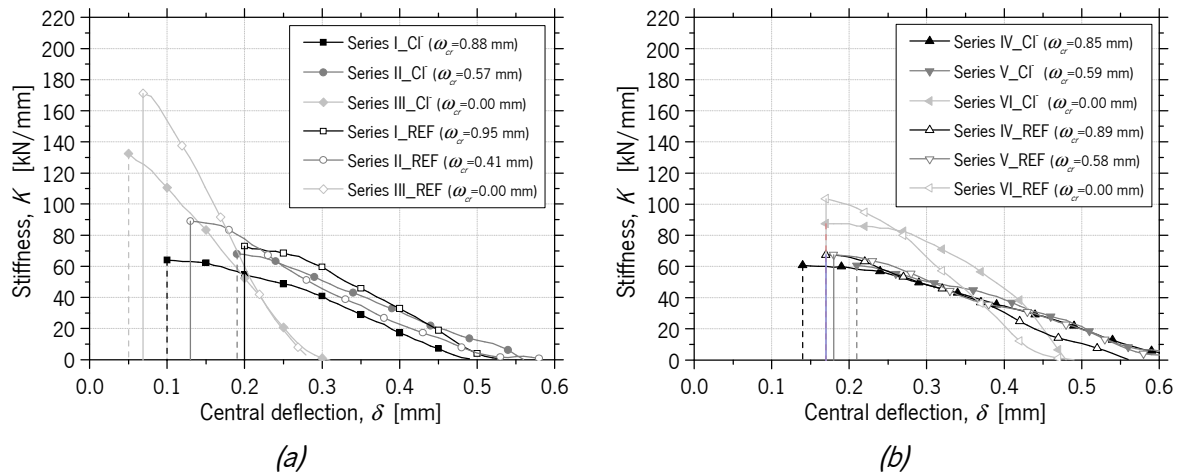


Figure 7.27 – Average Stiffness-Central deflection relationships of:  
 (a) RSFRC panels submitted to 10 days of Cl<sup>-</sup>/water immersion (Series I&II&III);  
 (b) RSFRC panels submitted to 3 months of Cl<sup>-</sup> wet-dry cycles/water immersion (Series IV&V&VI)

Table 7.6 – Parameters  $t$ ,  $K_{ci}$ ,  $\delta_{K_d}$ ,  $\omega_{cr}$  and  $\delta_{cr}$  of the RSFRC panels

Series		$t$ (mm)	$K_{ci}$ (kN/mm)	$\delta_{K_d}$ (mm)	$\omega_{cr}$ (mm)	$\delta_{cr}$ (mm)
I_Cl	Avg	60.56	68.84	0.11	0.88	3.83
	CoV (%)	(2.64)	(10.80)	(50.62)	(12.26)	(5.72)
II_Cl	Avg	64.22	71.46	0.19	0.57	2.83
	CoV (%)	(0.57)	(21.58)	(26.96)	(1.90)	(6.58)
III_Cl	Avg	65.35	133.90	0.06	0.00	0.00
	CoV (%)	(3.71)	(14.89)	(20.38)	(-)	(-)
I_REF	Avg	65.99	77.19	0.21	0.95	4.00
	CoV (%)	(2.28)	(7.12)	(41.24)	(17.59)	(5.89)
II_REF	Avg	67.10	90.83	0.13	0.41	2.38
	CoV (%)	(2.77)	(9.06)	(12.06)	(11.93)	(9.73)
III_REF	Avg	68.47	175.44	0.07	0.00	0.00
	CoV (%)	(1.50)	(8.09)	(28.31)	(-)	(-)
IV_Cl	Avg	63.91	62.27	0.18	0.85	4.31
	CoV (%)	(0.88)	(6.24)	(28.49)	(6.94)	(13.19)
V_Cl	Avg	64.41	65.67	0.17	0.59	3.12
	CoV (%)	(6.12)	(7.98)	(36.64)	(13.83)	(11.08)
VI_Cl	Avg	68.94	88.42	0.11	0.00	0.00
	CoV (%)	(6.05)	(7.86)	(43.53)	(-)	(-)
IV_REF	Avg	64.62	68.77	0.17	0.89	3.38
	CoV (%)	(1.28)	(18.52)	(15.10)	(4.39)	(9.70)
V_REF	Avg	65.00	71.60	0.18	0.58	2.83
	CoV (%)	(2.76)	(15.65)	(38.31)	(5.85)	(5.96)
VI_REF	Avg	66.46	104.65	0.16	0.00	0.00
	CoV (%)	(1.87)	(10.31)	(13.29)	(-)	(-)

According to the results presented in Figure 7.27 and Table 7.6, an increase of the initial stiffness,  $K_{ci}$ , was observed with the decrease of pre-crack width,  $\omega_{cr}$ . However, since these  $K_{ci}$  values were assessed in the initial elastic deformation phase, they are not dependent on pre-crack width and fiber distribution and orientation. In this sense, this increase of  $K_{ci}$  values was observed due to the increase of panel thickness,  $t$ , and also due to their curing conditions. Due to the large size of the round panels, they were cured in laboratory environment up to 28 days of age (as mentioned in Section 3.4.1) and after were subjected to the exposure periods of immersion/dry-wet cycles. This fact justified the higher  $K_{ci}$  values obtained for panels after exposure period (Series III and VI), comparing with the  $K_{ci}$  values obtained for panels during the pre-cracking process, before exposure period (Series I, II, IV and V).

According to the values of  $\delta_{K_G}$ , the elastic deformation of RSFRC panels occurred, on average, up to a central deflection of 0.21 mm. Since this  $\delta_{K_G}$  was much lower than the deflection imposed to implement the target crack width,  $\delta_{cr}$  (from 2.38 mm to 4.31 mm in average), it can be neglected and the vertical deformation of the panel's center is assumed to be obtained by the rigid rotation of the plates in turn of their connecting dominant cracks. This will be an assumption to be adopted in the theoretical approach for deriving the stress-crack width relationship,  $\sigma - \omega$ , by performing inverse analysis with the force-central deflection curves obtained in the RPT-3ps.

### 7.3.2.6 Force-Crack width relationships

Figure 7.28 represents the average force-crack width responses registered on the RSFRC panels. The crack width,  $\omega$ , corresponds to the mean value measured by the three LVDTs used for measuring the three developed crack widths (Figure 7.2). Up to the occurrence of a crack in the measuring stroke of the LVDT, the displacement recorded was an elastic deformation of the intact RSFRC panels.

As observed in the average force-central deflection relationships (Figure 7.24), an increase of the pre- and post-cracking performance of reference panels of Series I, II and III (10 days of water immersion) was observed comparing to panels submitted to chloride immersion for 10 days (Figure 7.28a). This corroborates with the 3PNBBTs results of the RSFRC beams (Section 3.5.1.2), casted with the corresponding RSFRC1% mixtures used for panels production. No significant differences were observed between the average force vs. crack width relationships of pre-cracked and non-cracked panels submitted to 3 months of environmental exposure (Series IV and VI – CI-&REF), except for panels with an average

$\omega_{cr} = 0.59$  mm (Series V\_Cl) that showed a slightly higher post-cracking behavior than the corresponding REF panels (Series V\_REF). This is indicative of a negligible effect of the chloride attack, and, consequently, of the RSF corrosion products on the average progression of crack widths during the RPT-3ps, for the predefined conditions of chloride exposure and pre-crack width level.

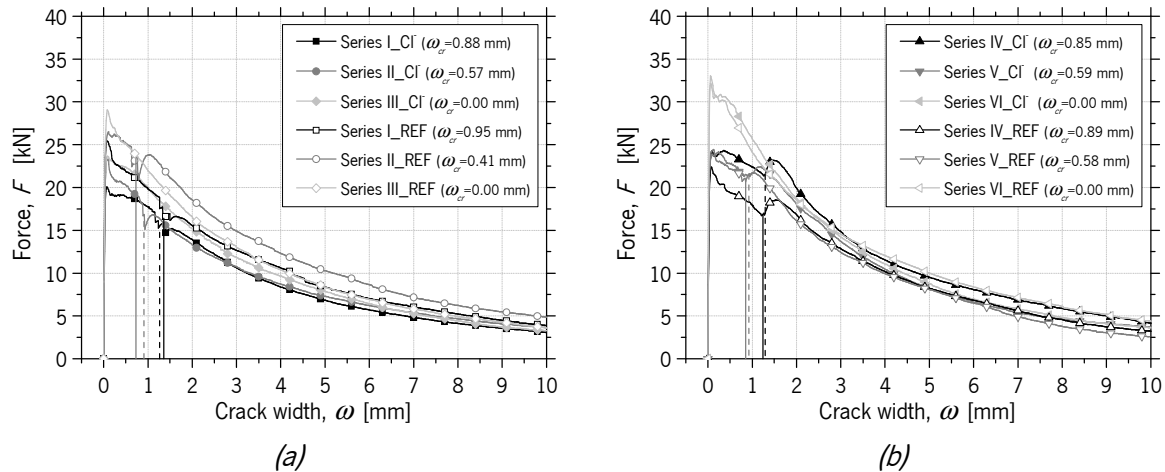


Figure 7.28 – Average Force-CMOD relationships of:

(a) RSFRC panels submitted to 10 days of Cl<sup>-</sup>/water immersion (Series I&II&III);

(b) RSFRC panels submitted to 3 months of Cl<sup>-</sup> wet-dry cycles/water immersion (Series IV&V&VI)

### 7.3.2.7 Evaluation of crack width measurements

As mentioned in Section 7.2.3.1, the crack widths were also measured with a USB microscope before and after submitting the panels to immersion. The measurements were performed at three points of each crack in the bottom surface of the panel, as schematically represented in Figure 7.3. In some of these positions, it was not possible to measure the crack width with the microscope due to the difficulty in capturing a sharp image with well-defined crack boundaries. For this reason, only the reliable results obtained of crack width measurement with the microscope are presented. Figure 7.29 represents the comparison between the crack width measurements performed with the LVDTs and with the microscope at position B (Figure 7.3) after pre-crack width implementation and before submitting to immersion. The results represent the average of the three radial cracks of the panels, except for panels P4 (Series II\_REF), P2 (Series IV\_REF) and P5 (Series V\_REF) that comprised two radial cracks.

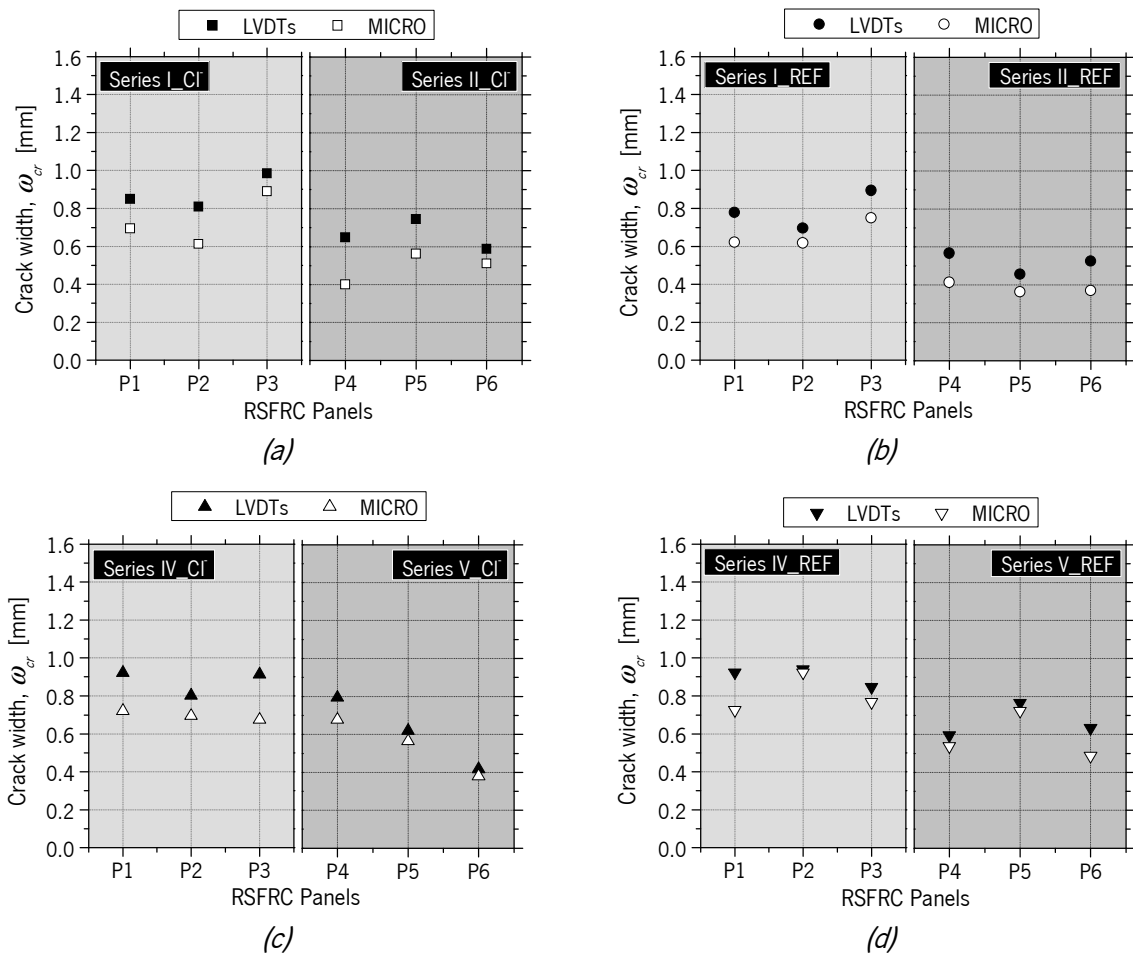


Figure 7.29 – Crack width measurements performed with the LVDTs and the microscope (MICRO) in pre-cracked panels of: (a) Series I&II\_CI; (b) Series I&II\_REF; (c) Series IV&V\_CI; (d) Series IV&V\_REF

According to Figure 7.29, the crack widths measured with the microscope were slightly lower than that measured with the LVDTs, with an average difference of 0.14 mm for the panels with a high pre-crack width level (panels P1, P2 and P3) and 0.11 mm for the panels with a low pre-crack width level (panels P4, P5 and P6). The larger crack width values measured by the LVDTs is caused by the elastic deformation included in the registered measures, as well as due to the kinematic mechanism represented in Figure 7.30 (Spasojević, 2008). Owing to the geometry of the measurement device,  $l_m$  (Figure 7.30), the experimentally captured deformations,  $l_m + \Delta l_{m,device}$ , are higher than the element tensile deformations,  $l_m + \Delta l_m$ , due to the rotation of the measurement base,  $\theta$  (Spasojević, 2008). The error is more pronounced for slender elements due to their higher deformability (Spasojević, 2008).

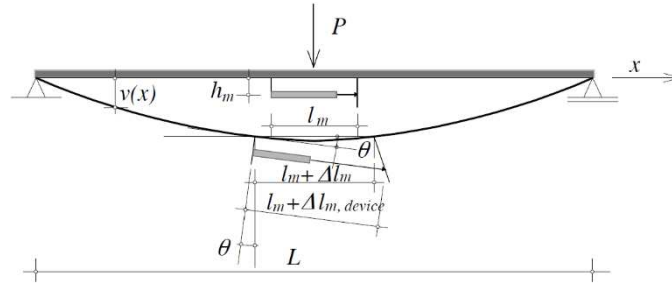


Figure 7.30 – Measurement of non-linear tensile deformations of a beam under 3-point bending test: Initial position of the measurement device and rotation of measurement points caused by rotation of the beam (Spasojević, 2008)

Figure 7.31 represents the comparison between the crack width measurements performed with the microscope for each crack, C1, C2 and C3 (average of the 3 measurements at positions A, B and C – Figure 7.3), before and after continuous immersion/dry-wet cycles, i.e. before introducing the panels into the tanks and after removing them from the tanks and placing in the test setup for the final RPT-3ps.

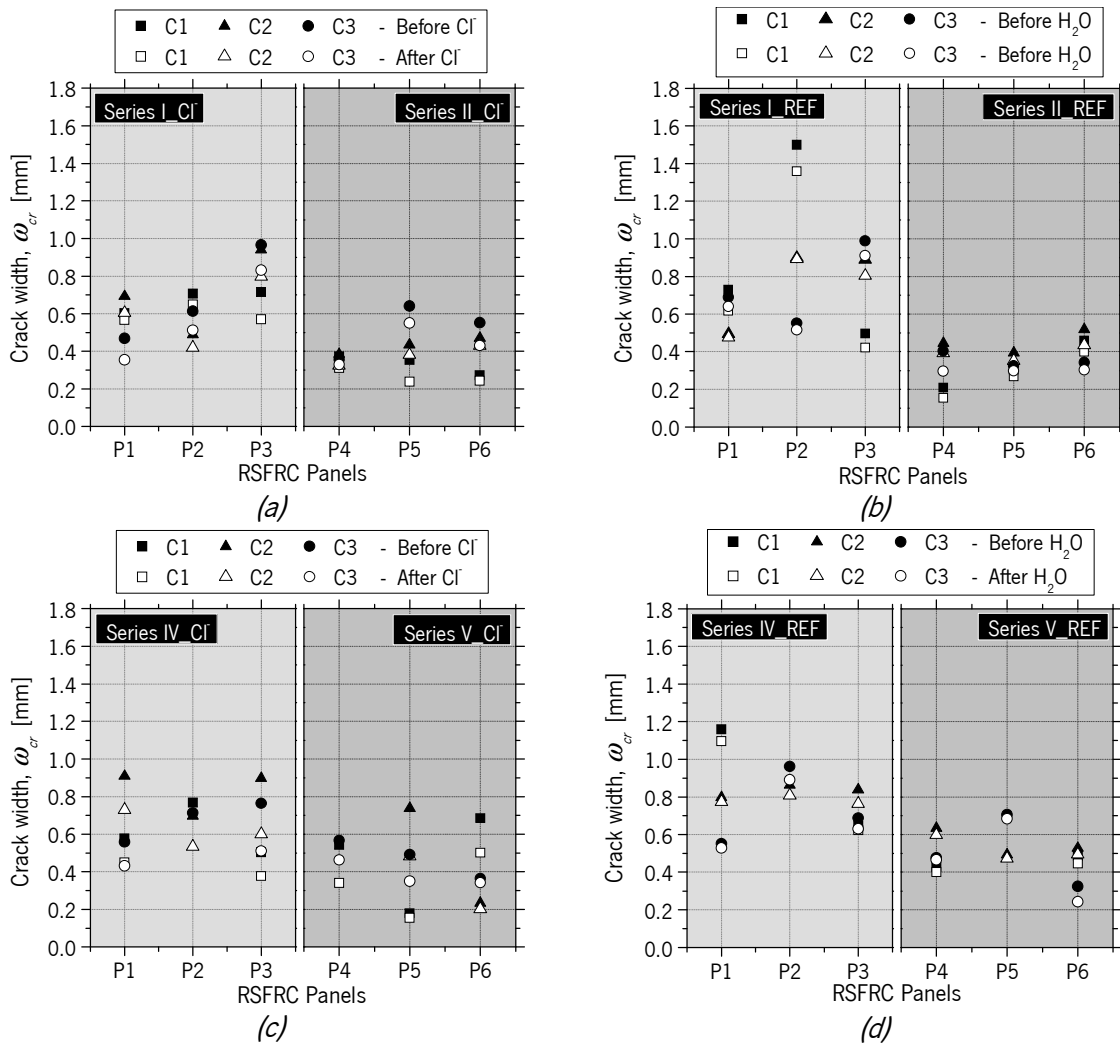


Figure 7.31 – Crack width measurements performed with the microscope at each crack C1,C2 and C3: (a) Series I&II\_Ci; (b) Series I&II\_REF; (c) Series IV&V\_Ci; (d) Series IV&V\_REF

Figure 7.32 shows an example of the crack width measurement performed with the microscope at position 1C (Fig. 7.3) in the bottom face of the pre-cracked panel P4, before and after being submitted to 3 months of dry-wet cycles in chloride solution (Series IV\_Cl).

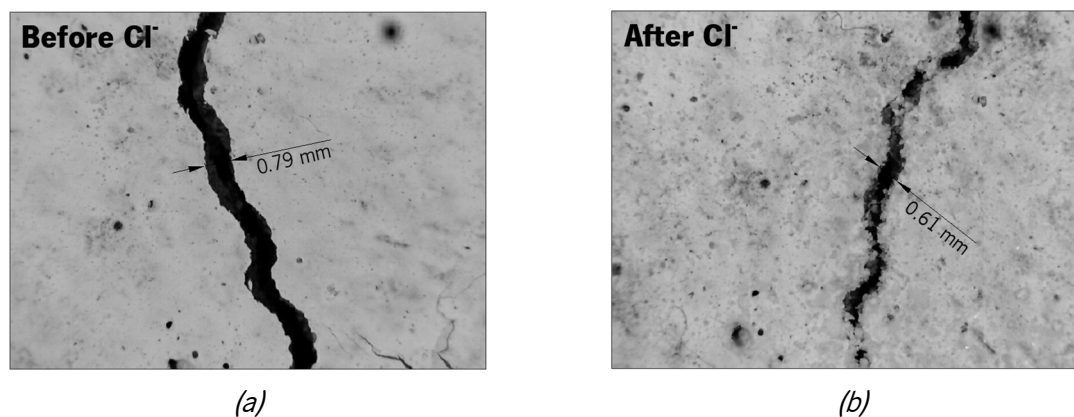


Figure 7.32 – Crack width measurement performed with the microscope at position 1C in the Panel P4 (Series IV\_Cl): (a) Before chloride attack; (b) After chloride attack

According to the results present in Figure 7.31 and Figure 7.32, a slight reduction of the crack width occurred in the three cracks of the panels after performing the environmental exposure (on average, 0.10 mm for the panels with high pre-crack width level (panels P1, P2 and P3) and 0.07 mm for the panels with a low pre-crack width level (panels P4, P5 and P6)).

A high dispersion of the results was observed between the measurements at the three different cracks (Coefficient of variation, CoV, ranging from 3% to 60%), especially for the pre-cracked panels submitted to chloride attack, namely, P4&P5\_Series II\_Cl (CoV=43% and 40%, respectively), P4\_Series II\_Cl (CoV=43%) and P5&P6\_Series V\_Cl (CoV=60% and 54%, respectively).

In Figure 7.32b, it is observed the presence of some salt crystals deposited in the crack boundaries that were formed during panel drying after chloride exposure and before the final RPT-3ps. The high irregularities of the crack boundaries after chloride exposure caused by the salt crystallization/deposition (Figure 7.32b) have increased the difficulty in reading the crack width, which may have contributed to the larger aforementioned CoV.

Figure 7.33 shows the comparison between the crack width measurements performed with the microscope at each position, A, B and C (average of the 3 measurements at cracks C1, C2 and C3 – Figure 7.3), before and after continuous immersion/dry-wet cycles.

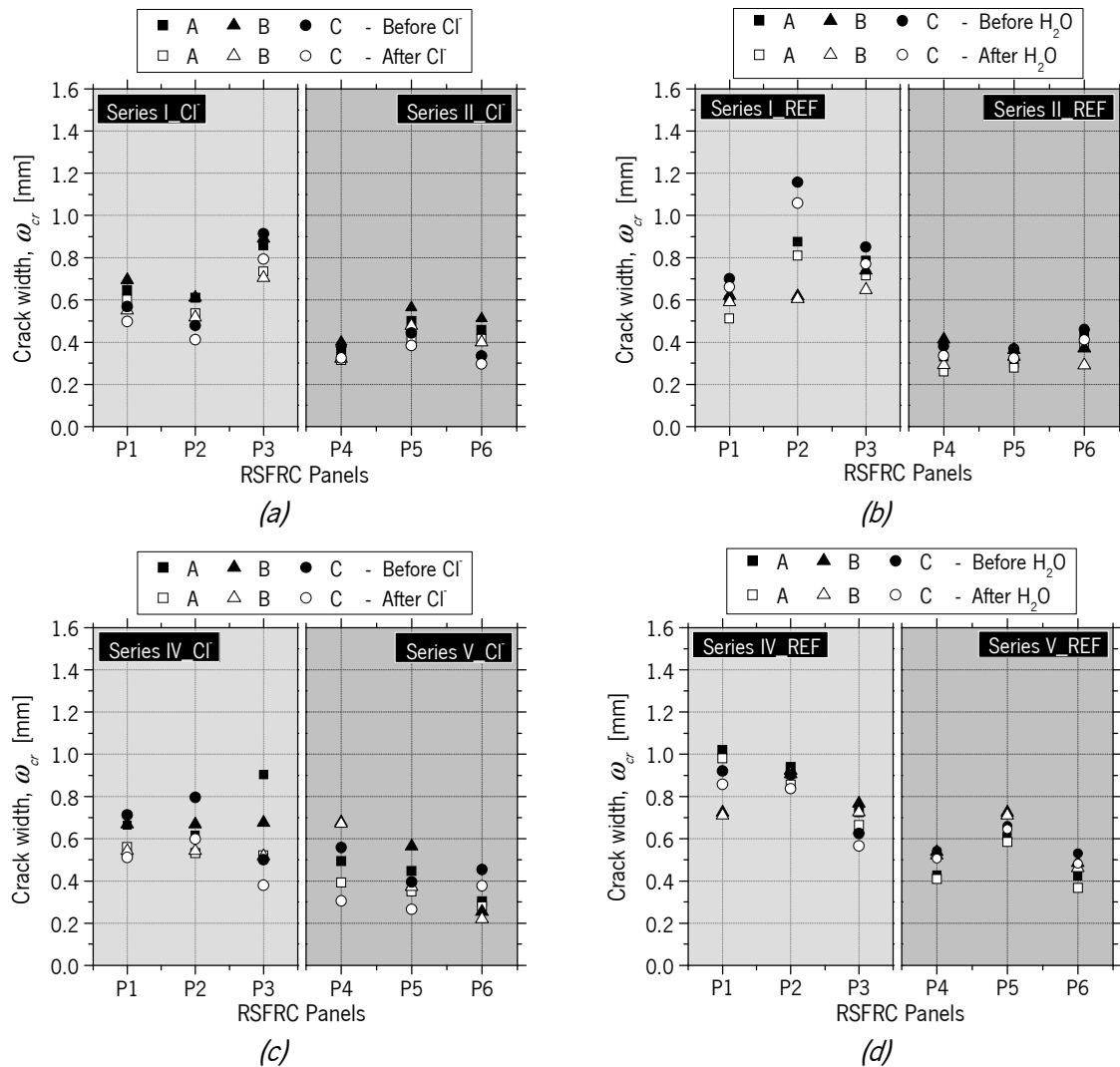


Figure 7.33 – Crack width measurements performed with the microscope at each position A, B and C: (a) Series I&II\_Cl; (b) Series I&II\_REF; (c) Series IV&V\_Cl; (d) Series IV&V\_REF

A slight reduction of the crack width was observed at the three crack positions A, B and C of the panels after performing the environmental exposure (on average, 0.10 mm for the panels with high pre-crack width level (panels P1, P2 and P3) and 0.06 mm for the panels with a low pre-crack width level (panels P4, P5 and P6)).

A high dispersion of the results was also observed between the crack measurements at the three different positions (CoV ranging from 2% to 42%), in particular for pre-cracked panels submitted to 3 months of chloride attack by dry-wet cycles in chloride solution (P3 and P4, CoV=29% and 42%, respectively).

There was also a slight tendency to increase the crack width from the center of the panel (position A) to the edge of the panel (position C). However, as the difference in crack width values was not so significant, the crack width along the crack development length will be assumed constant in the theoretical approach

for deriving the stress vs. crack width by inverse analysis, using the force-central deflection relationships obtained in the RPT-3ps (subject to be addressed in Section 7.3.4).

### 7.3.3 Fiber distribution and orientation parameters

The fiber distribution and orientation parameters were obtained on a plane surface of two tested panels from each test series, one chloride-immersed panel and one reference panel. The segregation degree along the gravity direction was also determined from equation (6.4), considering the coordinate in the Y axis of the center of gravity of each fiber,  $\bar{y}_i$ , and the height of the panel,  $h$ , parallel to the casting direction, as represented in Figure 7.36. The value of  $\xi_{seg}$  tends to range from 0 (segregation at the top of surface) to 1 (segregation at the bottom of surface) (Fig. 7.34).

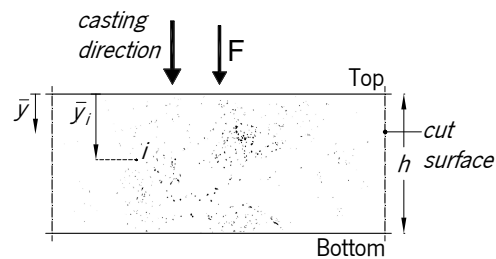


Figure 7.34 – Procedure to determine the fiber segregation degree in round panels

### Panels submitted to 10 days of immersion – Series I, II and III

Table 7.7 includes the fiber distribution and orientation parameters obtained from pre-cracked panels (Series I and II - Cl and REF) and non pre-cracked RSFRC (Series III - Cl and REF). In this Table are indicated the panel designation according to Table 7.1 and Figure 7.4a, the crack identification according to Figure 7.3, the panel thickness,  $t$ , the number of fibers per unit area,  $N^f$ , the fiber orientation factors,  $\eta_{img}$  and  $\eta_{exp}$ , and the fiber segregation degree,  $\xi_{seg}$ .

Since the analyzed pictures of cut surfaces were not taken immediately after cutting, the fibers near the exposed surfaces of panels previously submitted to chloride attack suffered oxidation. These oxidized fibers (16% of  $N^f$  in average) were not accounted for the determination of fiber orientation factor,  $\eta_{img}$ , since they have lost their reflective properties.



Table 7.7 – Fiber distribution and orientation parameters obtained in the analyzed round panels of Series I, II and III

Series	Panel (Fig. 7.4a)	Crack (Fig. 7.3)	$t$ (mm)	$N$ (fibers/cm <sup>2</sup> )	$\eta_{img}$	$\eta_{exp}$	$\xi_{seg}$
I_CI	1	1	59.96	8.87 (*74%)	0.631	0.436	0.45
I_REF	1	1	67.73	7.38 (*73%)	0.661	0.317	0.58
II_CI	5	1	64.63	8.69 (*70%)	0.646	0.427	0.50
II_REF	5	1	65.22	7.94 (*65%)	0.640	0.390	0.54
III_CI	8	1	63.41	10.82 (*76%)	0.625	0.531	0.48
III_REF	9	1	67.65	7.69 (*74%)	0.629	0.377	0.45
	Avg CoV (%)	Avg CoV (%)	64.77 (4.49)	8.57 (*72%) (14.54) (5.49)	0.639 (2.09)	0.413 (17.36)	0.50 (10.35)

\*Percentage of fibers failed by rupture

For a better analysis of the obtained fiber distribution parameters, in Table 7.8 are indicated the corresponding pre-crack width,  $\omega_{cr}$ , and the corrected values of energy absorption (Section 7.3.2.4) registered in the analyzed panels.

Table 7.8 – Corrected energy absorption obtained in the analyzed round panels of Series I, II and III

Series	Panel (Fig. 7.4a)	$\omega_{cr}$ (mm)	$W'_5$ (J)	$W'_{10}$ (J)	$W'_{20}$ (J)	$W'_{40}$ (J)
I_CI	1	0.82	180.83	301.74	420.52	-
I_REF	1	0.81	188.90	312.28	438.64	
II_CI	5	0.56	160.58	259.46	353.77	
II_REF	5	0.45	178.56	299.13	433.80	533.59
III_CI	8	0.00	150.94	248.89	353.18	424.40
III_REF	9	0.00	139.12	216.53	271.36	

The fiber distribution and orientation parameters presented in Table 7.7 were determined for only one cracked surface of each analyzed panel. However, for a better understanding of the influence of fiber distribution/orientation profile in the residual stresses and energy absorption obtained in RPT-3ps, the three crack surfaces of round panels must be considered.

The crack width vs. central deflection relationships obtained in each analyzed panel are represented in Figure 7.35. These graphs provide information on the progress of the three crack openings and their corresponding average in each analyzed panel.

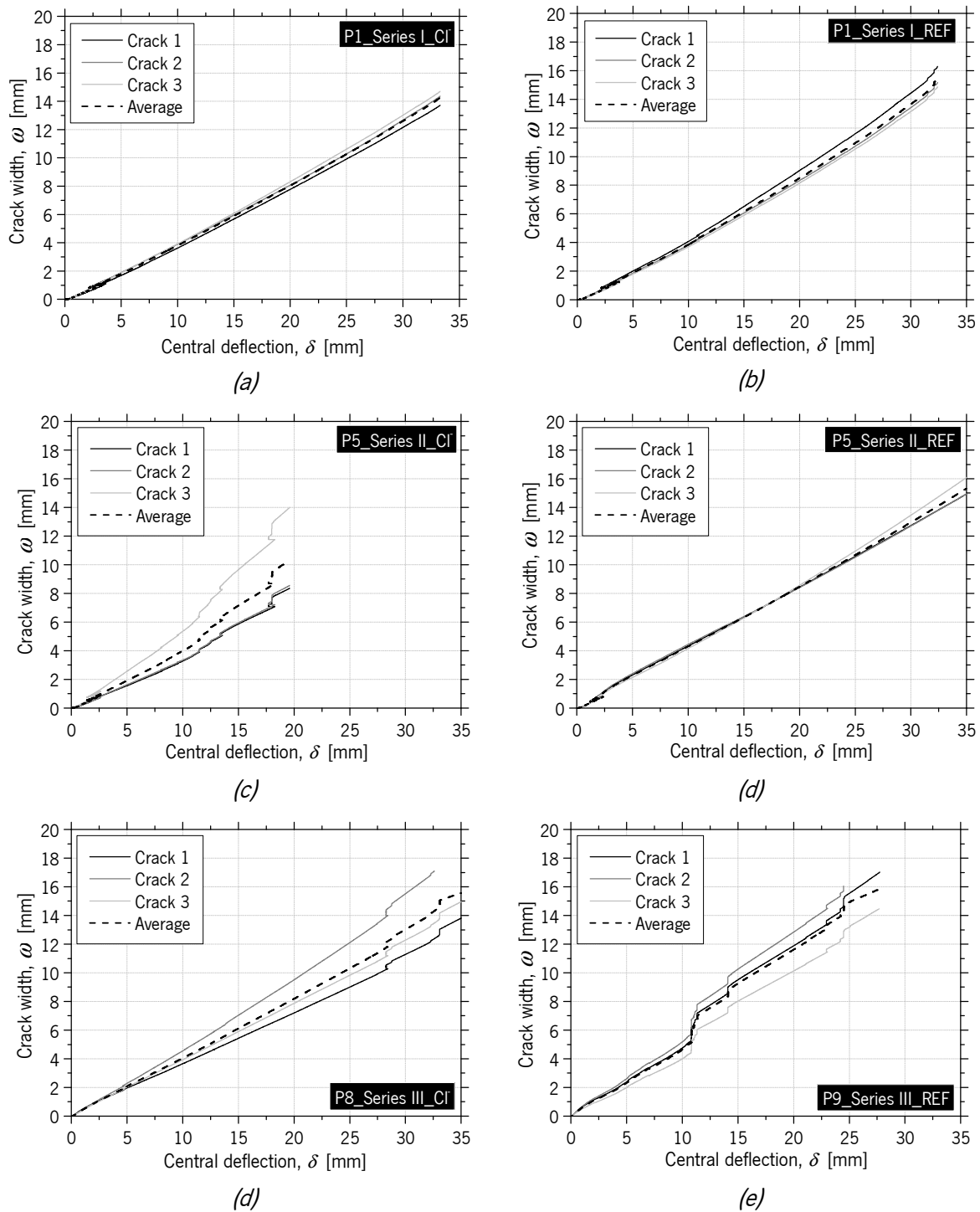


Figure 7.35 – Crack width-Central deflection relationships of:  
 (a) P1\_Series I\_CI; (b) P1\_Series I\_REF; (c) P5\_Series II\_CI; (d) P5\_Series II\_REF;  
 (e) P8\_Series III\_CI; (f) P9\_Series III\_REF

According to the results presented in Table 7.7, the  $N^f$  was similar in the pre-cracked panels (Series I and II - Cl and REF), and higher in the non-cracked panels submitted to chloride attack compared to the reference panels (Series III - Cl and REF).

For non-cracked panel of Series III\_Cl, the higher value of energy absorption obtained, compared to the corresponding reference panel (Series III\_REF, Table 7.8), is justified by the higher fiber density registered in the cut surface (Table 7.7).

A lower value of energy absorption was obtained for panel 9 of Series III\_REF compared to the remaining reference panels, despite having a similar fiber density (Table 7.7). This may be justified by the differences between the three crack widths in each analyzed panel, which is indicative of the different fiber density at each crack surface, as observed in Figure 7.35. For example, for panel 8 of Series III\_Cl, the fiber density at crack 2 (Table 7.7) must be higher than at crack 1 of the corresponding reference panel (P9\_Series III\_REF). In Figures 7.35c,d, for the central deflection of 20 mm, the average crack width was lower in P8\_Series III\_Cl than in P9\_Series III\_REF, which may indicate that, on average, the density of fibers bridging the cracks is higher in P8\_Series III\_Cl (as confirmed in Table 7.7), since the cracking control provided by fibers was higher in this panel. The higher fiber density and the consequent reduced average crack width in P8\_Series III\_Cl allow higher values of energy absorbed compared to P9\_Series III\_REF, as observed in Table 7.8 for a deflection of 20 mm ( $W_{20}$ ).

Due to the strong bond between recycled fibers and matrix, a high percentage of RSF failed by rupture, as indicated in Table 7.7. On average, this percentage is similar to the percentage of pre-treated RSF at 350°C (class 2) that had broken during the splitting tests (Section 6.3.2.5). This percentage of fibers failed by rupture was similar for Cl and REF specimens, which may be indicative of a negligible effect of chloride attack, as already verified in the splitting tensile tests presented in Chapter 6 (Section 6.3.2.5).

In the analyzed cut planes of panels from Series I, II and III, similar values were obtained for the fiber orientation factor,  $\eta_{img}$ . The obtained values of  $\eta_{img}$  were higher than the correspondent fiber orientation factors,  $\eta_{exp}$ , determined from equation (6.3) proposed by Soroushian and Lee (1990). A reduction of  $\eta_{exp}$  was observed with the decrease of the fiber density,  $N^f$ . The values obtained for the fiber segregation factor,  $\xi_{seg}$ , were close to 0.50, meaning that there was no relevant fiber segregation.

**Panels submitted to 3 months of dry-wet cycles/immersion – Series IV, V and VI**

Table 7.9 includes the fiber distribution and orientation parameters obtained from two panels of Series IV, V and VI (Cl and REF). The corresponding pre-crack width,  $\omega_{cr}$ , and the corrected values of energy absorption are indicated in Table 7.10. Figure 7.36 presents the crack width-central deflection relationships obtained in each analyzed panel of Series IV, V and VI.

Table 7.9 – Fiber distribution and orientation parameters obtained in the analyzed round panels of Series IV, V and VI

Series	Panel (Fig. 7.4a)	Crack (Fig. 7.3)	$t$ (mm)	$N^f$ (fibers/cm <sup>2</sup> )	$\eta_{img}$	$\eta_{exp}$	$\xi_{seg}$
IV_Cl	1	1	64.13	8.42 (*73%)	0.614	0.413	0.47
IV_REF	1	2	65.45	8.65 (*78%)	0.595	0.424	0.48
V_Cl	4	2	63.17	7.35 (*88%)	0.628	0.361	0.49
V_REF	6	2	64.92	7.68 (*80%)	0.617	0.377	0.54
VI_Cl	7	2	64.64	9.33 (*77%)	0.619	0.458	0.55
VI_REF	7	2	66.42	8.73 (*81%)	0.628	0.429	0.49
	Avg	Avg	64.74	8.36 (*80%)	0.617	0.410	0.50
	CoV (%)	CoV (%)	(1.72)	(8.70) (6.30)	(1.97)	(8.69)	(6.61)

\*Percentage of fibers failed by rupture

Table 7.10 – Corrected energy absorption obtained in the analyzed round panels of Series IV, V and VI

Series	Panel (Fig. 7.4a)	$\omega_{cr}$ (mm)	$W'_5$ (J)	$W'_{10}$ (J)	$W'_{20}$ (J)	$W'_{40}$ (J)
IV_Cl	1	0.82	200.94	359.01	507.61	598.53
IV_REF	1	0.92	171.95	291.42	407.27	472.62
V_Cl	4	0.66	204.23	368.23	533.69	627.50
V_REF	6	0.54	187.52	306.35	427.24	509.51
VI_Cl	7	0.00	178.78	286.80	379.42	432.00
VI_REF	7	0.00	218.13	344.21	452.90	515.34

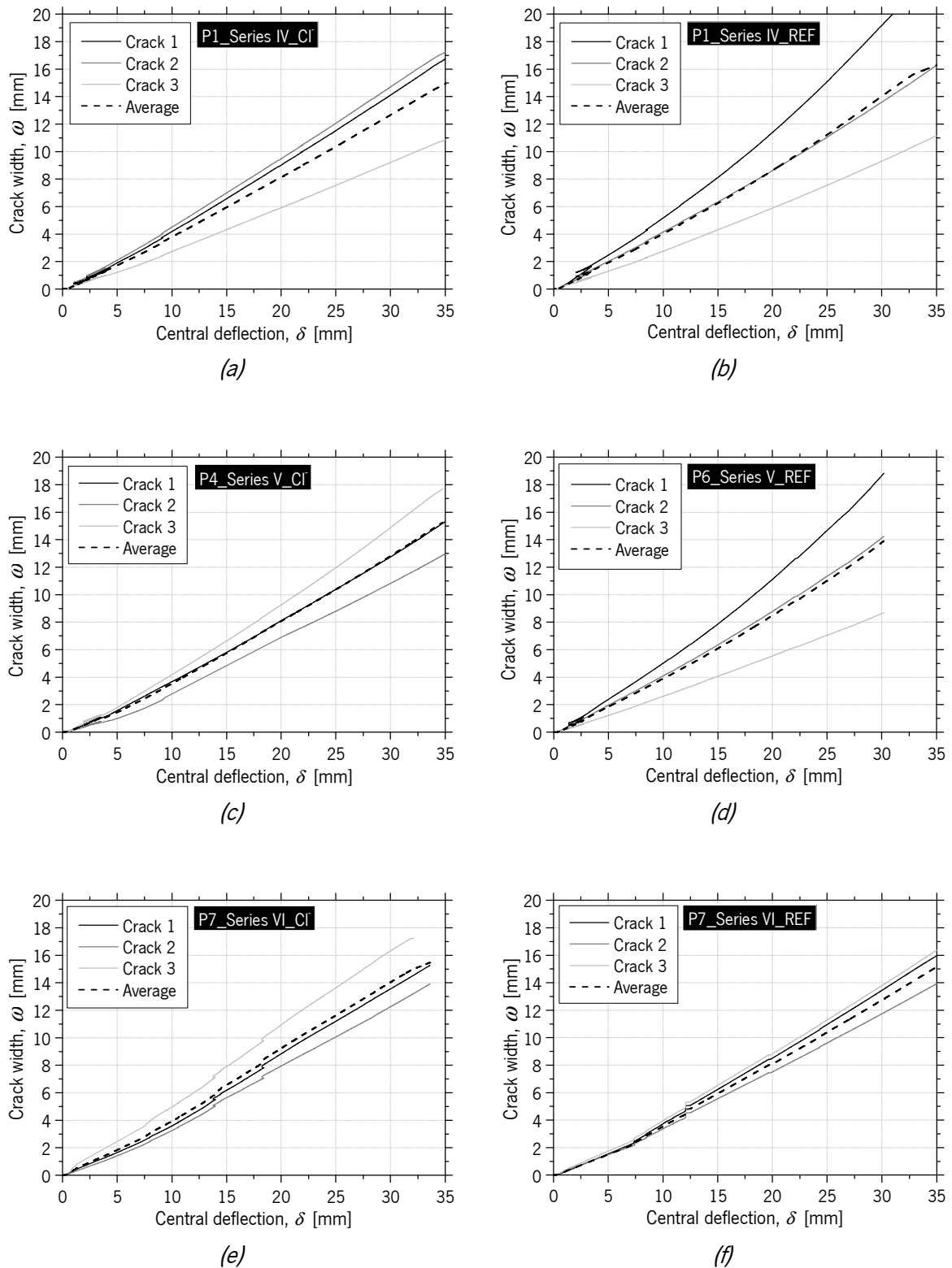


Figure 7.36 – Crack width-Central deflection relationships of:  
 (a) P1\_Series IV\_CI; (b) P1\_Series IV\_REF; (c) P4\_Series V\_CI; (d) P6\_Series V\_REF;  
 (e) P7\_Series VI\_CI; (f) P7\_Series VI\_REF

The values of  $N^f$  presented in Table 7.9 were similar between the panels submitted to chloride attack and the reference panels, which may be indicative that the differences between the corresponding corrected energy absorption (Table 7.10) are due to the differences between the fiber distribution at the three crack widths in each analyzed panel (Fig. 7.36) and/or due to the corrosion effect of RSF crossing the cracks of the pre-cracked panels submitted to 3 months of dry-wet cycles in chloride solution.

The values of  $N^f$  presented in Table 7.9 were similar between the panels submitted to chloride attack and the reference panels, which may be indicative that the differences between the corresponding corrected energy absorption (Table 7.10) are due to the differences between the fiber distribution at the three crack widths in each analyzed panel (Fig. 7.36) and/or due to the corrosion effect of RSF at crack surfaces for pre-cracked panels submitted to 3 months of dry-wet cycles in chloride solution.

For Series IV and V, no significant differences were observed between the average crack width, panel's thickness and the percentage of fibers failed by rupture of chloride-attached panels and the corresponding reference panels (Figs. 7.36a-d and Table 7.9). The energy absorbed obtained in the corroded pre-cracked panels was higher compared to the corresponding reference panels (Table 7.10), which may be explained by the irregularity of fiber geometry, which has also influence on the progress of crack openings in the round panels. According to Figs. 7.36a-d, the panels submitted to chloride attack showed higher variability of the crack width measurements than reference panels, which may be explained by the irregularity of RSF geometry.

For non-cracked panels (Series VI), the chloride attack had a negligible effect since the differences between the values of energy absorption obtained for chloride-attacked and reference panels (Table 7.10) appeared to be due to differences in fiber density at the three fracture surfaces, comparing the average crack width measurements (Figs. 7.36e,f).

The percentage of RSF failed by rupture in Series IV, V and VI (Table 7.9) was slightly higher than in Series I, II and III (Table 7.7), which is indicative of an increased adhesive bond between the fibers and the concrete matrix with the concrete age (from 38 days to 120 days).

For the determination of the fiber orientation factor,  $\eta_{img}$ , the oxidized fibers at cut surfaces due to air exposure (35% of  $N^f$  in average) were not taken into account since they have lost their reflective properties. The obtained values of  $\eta_{img}$  and  $\eta_{exp}$  were similar to those obtained in Series I, II and III

(Table 7.7), which means that no significant differences in fiber orientation occurred in all panels tested. According to the values of  $\xi_{seg}$ , a uniform fiber distribution seems to have been guaranteed.

### **7.3.4 Numerical simulation of the performed RPT-3ps**

#### **7.3.4.1 Numerical model**

An inverse analysis strategy was executed for deriving the stress-crack opening ( $\sigma - \omega$ ) relationship of the RSFRC representative of the RPT-3ps, combining a moment-rotation approach with a numerical model that considers the kinematics conditions of RPT-3ps at failure stage and the equilibrium equations (Salehian, 2015). This strategy allowed to evaluate the influence of the chloride exposure conditions adopted for round panels on the  $\sigma - \omega$  relationship of the pre-cracked and non-cracked RSFRC. This numerical simulation considers the constitutive laws of RSFRC in tension and in compression to determine the moment-rotation relationship, the loading and support conditions of RPT-3ps, kinematic assumptions, and the principle of virtual work in order to derive the stress-crack width ( $\sigma - \omega$ ) law of RSFRC from round panels. In an inverse approach, the post-cracking constitutive laws of the RSFRC representative of the RPT-3ps were determined by fitting the experimental curves of the average force-central deflection relationships obtained in each series of RPT-3ps (Figure 7.24).

For the calculation of the moment-rotation relationship, a cross-section layer model that was implemented into DOCROS computer program was developed. DOCROS is a software to evaluate the moment-curvature of sections of irregular shape and size, composed of different types of materials subjected to an axial force and variable curvature (Basto and Barros, 2008). The model in DOCROS considers the non-linear behavior of the intervening materials, assume that a plane section remains plane after deformation and perfect bond exists between distinct materials. The implemented model considers the panels' cross-section discretized in horizontal layers and attends the equilibrium equations, the compatibility of deformations, and the constitutive laws of the intervening material. In this case a section of 1000 mm wide, and with a height corresponding to the average thickness of the tested panels was considered, discretized in 60 layers of equal thickness.

#### **Cinematic assumptions**

In the numerical model used proposed by Salehian *et al.* (2014), it is assumed that in RPT-3ps, just after the peak load, three dominant cracks propagate in the panel according to a general asymmetric crack

pattern (Figure 2.26). For the sake of simplicity, it is assumed that the cracks are straight and radiate from the center of the panel with random orientation (Figure 2.26) (Salehian, 2015).

In Figure 2.26 is schematized the considered deflection configuration for RPT-3ps, where the propagation of  $n_{cr}$  cracks subdivides the panels into  $n_{cr}$  intact (un-cracked) plates, whose elastic deformation is recovered in the structural softening stage when cracks are opening gradually. Since this elastic deformation was much lower than the deflection due to crack opening (as observed in Section 7.3.2.5), it was neglected, and the vertical deformation of the panel's center,  $\delta$  (Fig. 2.26), was attributed to the rigid rotation of the plates in turn of their connecting dominant cracks.

In case of RPT-3ps, due to its statically determinate nature, three radial cracks often propagate between the point supports and, therefore, the round panel is subdivided in three rigid plates (as observed in the performed tests – Section 7.3.2.1). The rotation axes of the plates in the RPT-3ps are the lines drawn tangent to the slab perimeter at each point support and intersect mutually at the assumed imaginary point located in the alignment of the median crack if the crack propagation is considered quite symmetric (Fig. 7.37) (Salehian *et al.*, 2014). However, when the crack propagation is asymmetric, the intersection of the rotation axes of the two adjacent plates and the median crack will not be attained at the same point. In this case two distinct imaginary pivots should be considered for the rotation axes, being represented with  $p_{i,1}$  and  $p_{i,2}$  (Fig. 7.38) (Salehian, 2015).

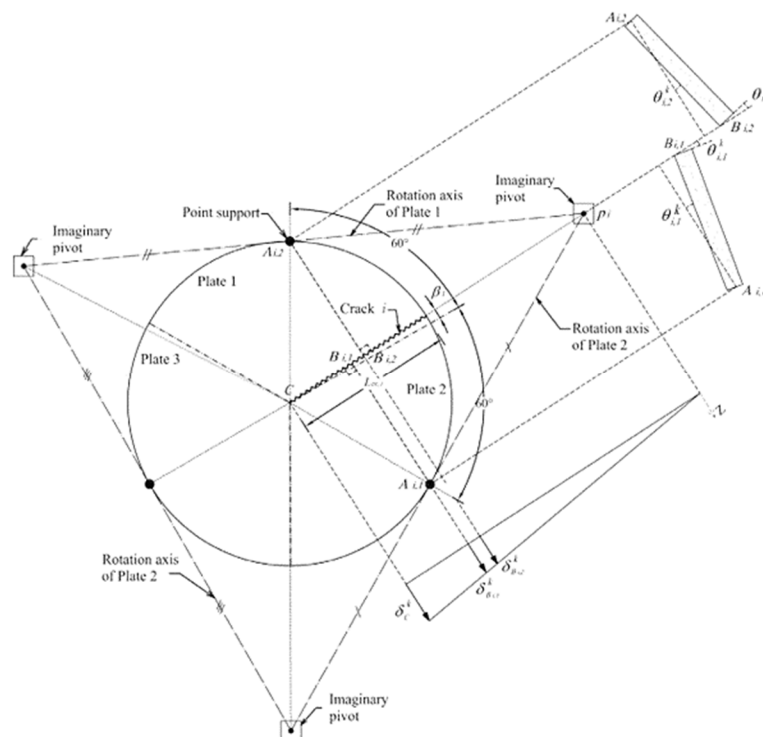


Figure 7.37 – Crack rotation analysis in RPT-3ps (symmetric crack propagation) (Salehian *et al.*, 2014)





$$\theta_{i,1}^k = \left( \frac{\delta_{B_{i,1}}^k}{A_{i,1} B_{i,1}} \right) \quad (7.9)$$

$$\theta_{i,2}^k = \left( \frac{\delta_{B_{i,2}}^k}{A_{i,2} B_{i,2}} \right) \quad (7.10)$$

By adding the rotations of the plates connecting the  $i^{th}$  crack, it is obtained the rotation of this crack due to the imposed deflection  $\delta_c^k$  at the panel center:

$$\theta_i^k = \theta_{i,1}^k + \theta_{i,2}^k \quad (7.11)$$

In the computational algorithm developed by Salehian *et al.* (2014), the overall rotation of  $\theta_i^k$  is imposed on the  $i^{th}$  crack of  $L_{cr,i}$  length in the  $k^{th}$  generic step of loading. Correspondingly, the resisting bending moment per unit width of the panel's cross-section ( $M_i^k$ ) is determined considering the moment-rotation relationship obtained with the cross-section layer model implemented into DOCROS. By applying the principle of the virtual work, the force-central deflection ( $F_c^k - \delta_c^k$ ) relationship for the  $k^{th}$  loading step is obtained from the following equation:

$$F_c^k = \frac{1}{\delta_c^k} \sum_{i=1}^{n_{cr}} (M_i^k \times L_{cr,i}) \theta_i^k \quad (7.12)$$

where  $L_{cr,i}$  represents the length of the  $i^{th}$  crack and  $n_{cr}$  is the total number of cracks.

### 7.3.4.2 Numerical results

#### Pre-cracked RSFRC panels

Figure 7.39 presents both the experimental (EXP) and numerical (NUM) force-deflection ( $F - \delta$ ) relationships for pre-cracked RSFRC1% panels (target crack width of 1.0 mm) of Series I\_CI&REF (submitted to 10 days of immersion) and Series IV\_CI&REF (submitted to 3 months of dry-wet cycles/immersion). For each test Series are presented the results obtained during the pre-cracking process (Figures 7.39a,b) and after the environmental exposure (Figures 7.39c,d).

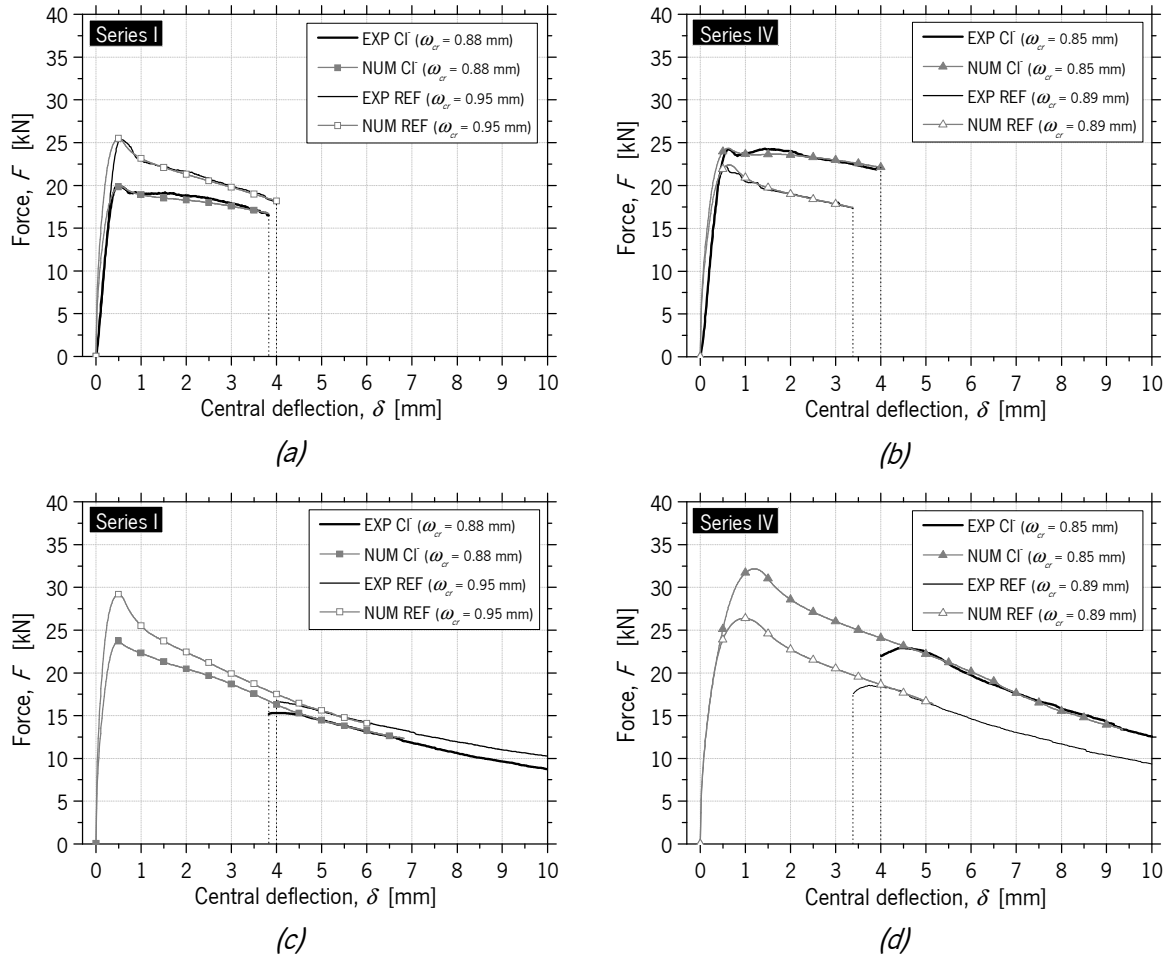


Figure 7.39 – Numerical simulation of RPT-3ps from Series I&IV\_CI&REF for: (a) and (b) Pre-cracking stage; (c) and (d) After environmental exposure

Figure 7.40 presents both the  $F - \delta$  relationships (EXP and NUM) for pre-cracked RSFRC1% panels (target crack width of 0.5 mm) of Series II\_CI&REF (submitted to 10 days of immersion) and Series V\_CI&REF (submitted to 3 months of dry-wet cycles/immersion), obtained for the pre-cracking stage (Figures 7.40a,b) and after the environmental exposure (Figures 7.40c,d).

The numerical simulations were able of fitting with high accuracy the experimental results. A quadrilinear tensile-softening stress-crack width diagram,  $\sigma - \omega$ , was used to simulate the fracture mode I propagation of pre-cracked RSFRC, and the obtained parameters that define the shape of the diagram and the equivalent fitting error,  $e$ , are indicated in Tables 7.11 and 7.12. The  $f_{ct}$  corresponds to the tensile strength,  $\sigma_1$ ,  $\sigma_2$  and  $\sigma_3$  are the stress at the first, second and third post-peak points at the crack opening,  $\omega_1$ ,  $\omega_2$ , and  $\omega_3$ , respectively;  $\omega_u$  is the ultimate crack opening and  $G_f$  is the mode I fracture energy. The graphical representation of these  $\sigma - \omega$  laws is presented in Figure 7.41.

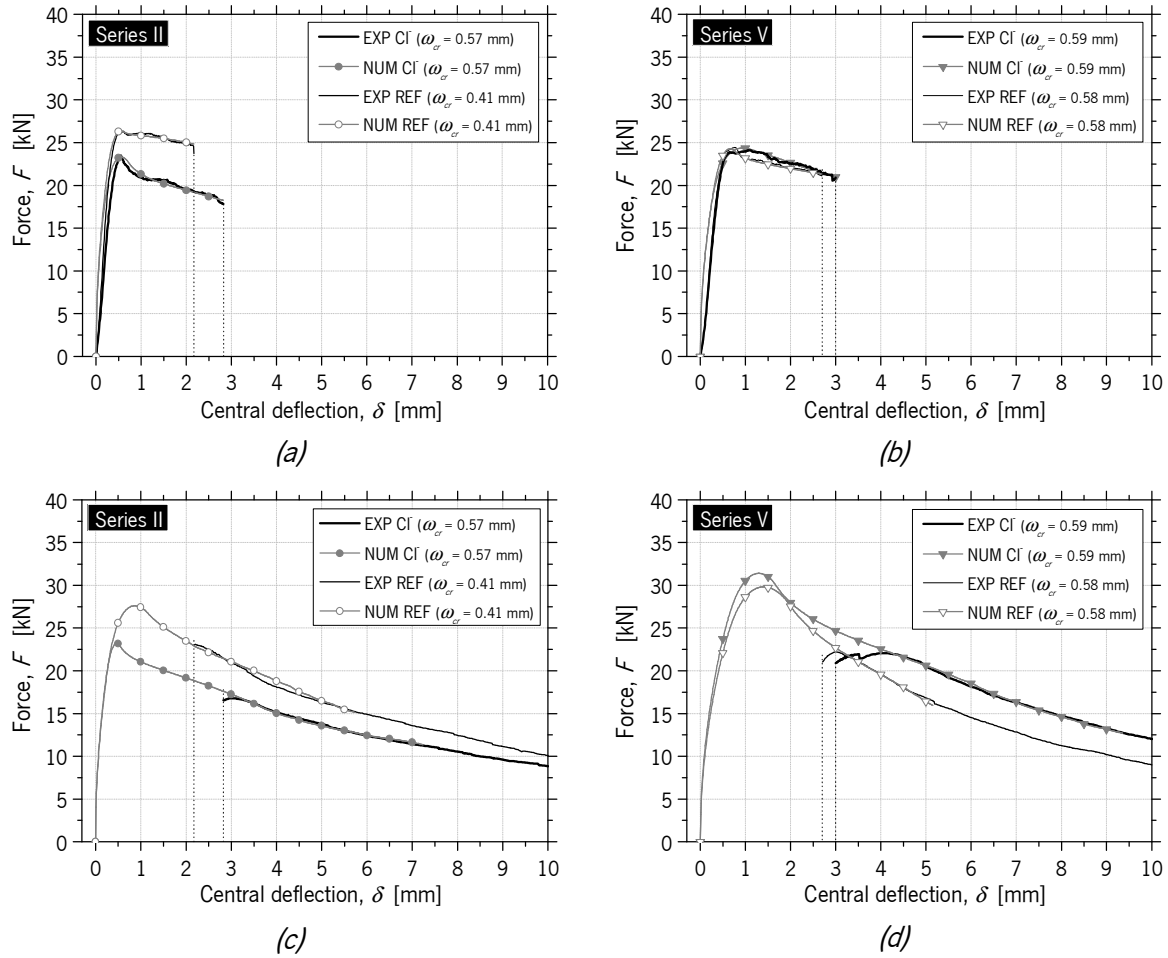


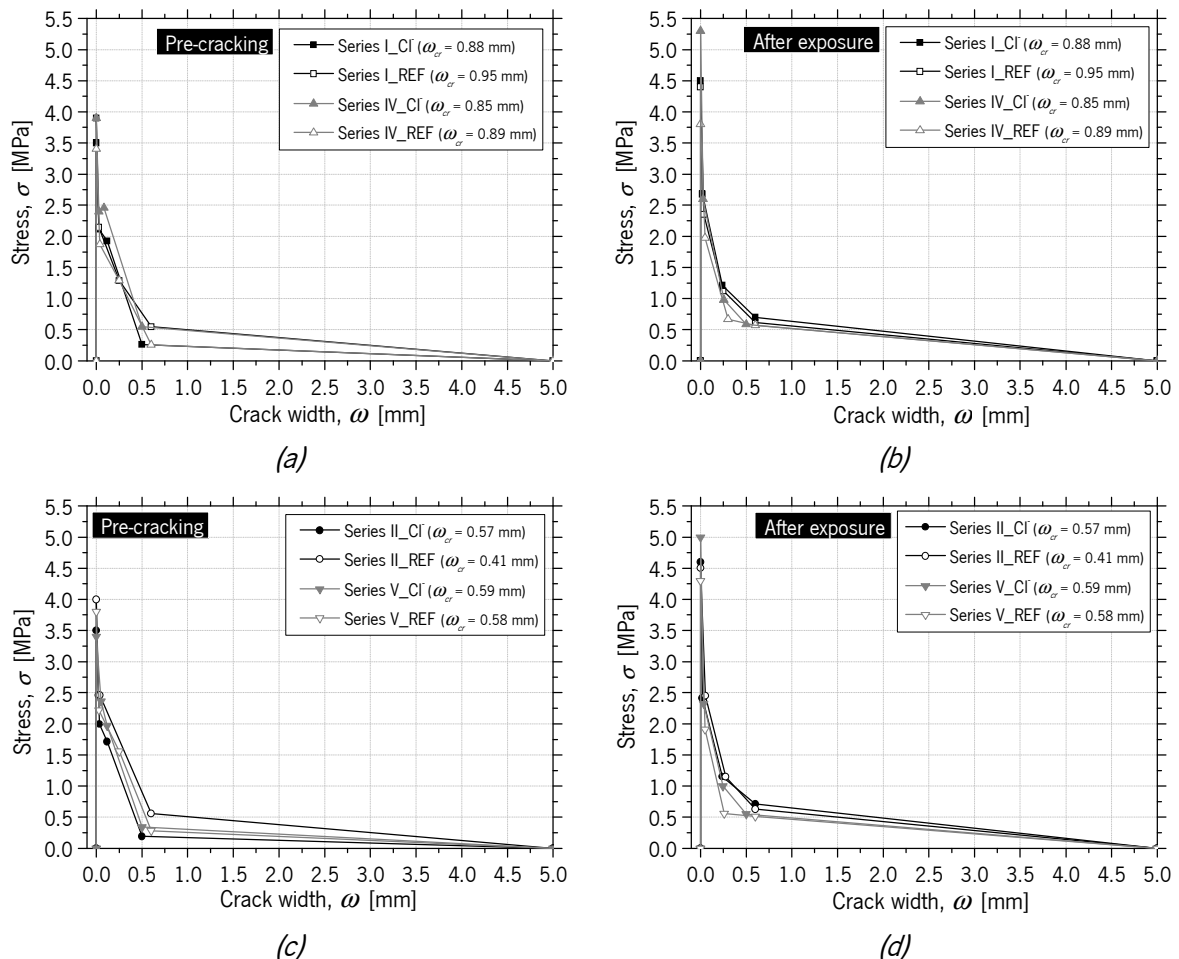
Figure 7.40 – Numerical simulation of RPT-3ps from Series II&V\_CI&REF for: (a) and (b) Pre-cracking stage; (c) and (d) After environmental exposure

Table 7.11 – Parameters of the  $\sigma$ - $\omega$  relationship obtained by inverse analysis (RPT-3ps) for pre-cracked panels (Series I&IV\_CI&REF)

	Series	$f_{ct}$ (MPa)	$\sigma_1$ (MPa)	$\sigma_2$ (MPa)	$\sigma_3$ (MPa)	$\omega_1$ (mm)	$\omega_2$ (mm)	$\omega_3$ (mm)	$\omega_u$ (mm)	$G_f$ (N/mm)	$e$ (%)
Pre-cracking stage $\omega_{cr} = 1.0$ mm	I_CI	3.50	2.12	1.93	0.26	0.03	0.12	0.50	5.00	1.27	0.44
	I_REF	3.90	2.15	1.29	0.55	0.03	0.25	0.60	5.00	1.99	3.09
	IV_CI	3.90	2.40	2.46	0.55	0.03	0.09	0.50	5.00	2.08	2.78
	IV_REF	3.40	1.87	1.29	0.26	0.04	0.25	0.60	5.00	1.27	3.58
After environmental exposure	I_CI	4.50	2.68	1.22	0.70	0.02	0.24	0.60	5.00	2.38	0.95
	I_REF	4.40	2.35	1.12	0.62	0.04	0.25	0.60	5.00	2.15	0.95
	IV_CI	5.30	2.60	0.98	0.58	0.03	0.26	0.50	5.00	2.02	0.38
	IV_REF	3.80	1.98	0.67	0.57	0.05	0.30	0.60	5.00	1.91	0.33

Table 7.12 – Parameters of the  $\sigma$ - $\omega$  relationship obtained by inverse analysis (RPT-3ps) for pre-cracked panels (Series II&V\_CI&REF)

	Series	$f_{ct}$	$\sigma_1$	$\sigma_2$	$\sigma_3$	$\omega_1$	$\omega_2$	$\omega_3$	$\omega_u$	$G_f$	$e$
		(MPa)	(MPa)	(MPa)	(MPa)	(mm)	(mm)	(mm)	(mm)	(N/mm)	(%)
Pre-cracking stage $\omega_{cr} = 0.5$ mm	II_CI	3.50	2.00	1.72	0.19	0.04	0.12	0.50	5.00	1.05	4.18
	II_REF	4.00	2.46	2.46	0.56	0.03	0.04	0.60	5.00	2.20	3.17
	V_CI	3.40	2.36	1.97	0.34	0.06	0.12	0.50	5.00	1.50	3.88
	V_REF	3.80	2.22	1.56	0.29	0.03	0.25	0.60	5.00	1.46	3.41
After environmental exposure	II_CI	4.60	2.42	1.15	0.71	0.02	0.24	0.60	5.00	2.37	0.04
	II_REF	4.50	2.45	1.15	0.63	0.06	0.28	0.60	5.00	2.26	1.22
	V_CI	5.00	2.33	1.00	0.55	0.04	0.25	0.50	5.00	1.91	0.23
	V_REF	4.30	1.91	0.56	0.52	0.05	0.26	0.60	5.00	1.73	0.07


 Figure 7.41 –  $\sigma$ - $\omega$  relationships obtained by inverse analysis for RPT-3ps of:  
 (a) and (b) Series I&IV\_CI&REF (Pre-cracking stage and after exposure);  
 (c) and (d) Series II&V\_CI&REF (Pre-cracking stage and after exposure)

In the pre-cracking stage, the parameters obtained in Series I&II\_CI&REF corroborate with the flexural tensile strength parameters obtained in the 3-point bending tests of the corresponding RSFRC beams (Table 3.21: RSFRC1%\_2 – Series I&II\_CI- and RSFRC1%\_3 – Series I&II\_REF). For series V\_CI-&REF, the parameters also corroborate with the flexural tensile strength parameters (RSFRC1%\_4 – Series IV&V\_CI- and RSFRC1%\_5 – Series IV&V\_REF) (Table 3.21). However, a slight increase of the parameters was observed for Series IV\_CI comparing to the corresponding reference Series, possibly due to higher fiber density on the three cracked surfaces. This fact explained the better pre-cracking performance of CI panels compared to REF panels showed in Figurec 7.19c,d.

Comparing the  $\sigma - \omega$  relationships obtained for pre-cracking stage (Figs. 7.41a,c) and the corresponding  $\sigma - \omega$  obtained after exposure (Figs. 7.41b,d), it seems that the chloride immersion for 10 days had a small beneficial effect on the post-cracking behavior of pre-cracked RSFRC panels, since slightly higher parameter values were obtained in Series I&II\_CI than in Series I&II\_REF (Table 7.11). Considering the results of RSF mass loss by corrosion obtained in section 4.5.1, for 10 days of continuous immersion and an exposed fiber length of 0.5 and 1 mm (Series II&III), the maximum percentage of fiber mass loss was 10% (Figs. 4.14a and 4.15b). This could be indicative of a small reduction of the tensile strength of RSF and in this case, probably the beneficial effect of corrosion products in the fiber pull-out is more pronounced, than the failure of fiber by corrosion.

After the exposure period of 3 months, the dry-wet cycles in chloride solution caused a small detrimental effect on the post-cracking behavior of pre-cracked RSFRC panels of Series IV ( $\omega_{cr} = 1.0$  mm). For Series V ( $\omega_{cr} = 0.5$  mm), a small beneficial effect of the chloride attack was observed. Anyway, the differences in the fracture energy obtained during the pre-cracking stage and after 3 months of environmental exposure for pre-cracked panels were not very significant, so it can be assumed that the action of RSF corrosion was negligible in the post-cracking behavior of cracked RSFRC submitted to these chloride exposure conditions. According to the results of RSF mass loss by corrosion presented in section 4.5.1 for 3 months of dry-wet cycles and an exposed fiber length of 0.5 and 1 mm (Series V&VI), would be expected a significant reduction of the cross section of the fibers and a consequently reduction of the post-cracking behavior of RSFRC1%. However, the variability of the crack width along its length and its V-shape in RSFRC panels probably justified the lower effect of corrosive action in the post-cracking behavior of RSFRC verified in this chapter.

### Non-cracked RSFRC panels

Figure 7.42 presents both the  $F - \delta$  relationships (EXP and NUM) for non-cracked RSFRC1% panels of Series III\_CI&REF (submitted to 10 days of immersion) and Series VI\_CI&REF (submitted to 3 months of dry-wet cycles/immersion). In Table 7.13 are presented the fracture mode I parameters obtained, which define the shape of the quadrilinear  $\sigma - \omega$  diagram shown in Figure 7.43, used to simulate the post-cracking behavior of non-pre-cracked RSFRC panels.

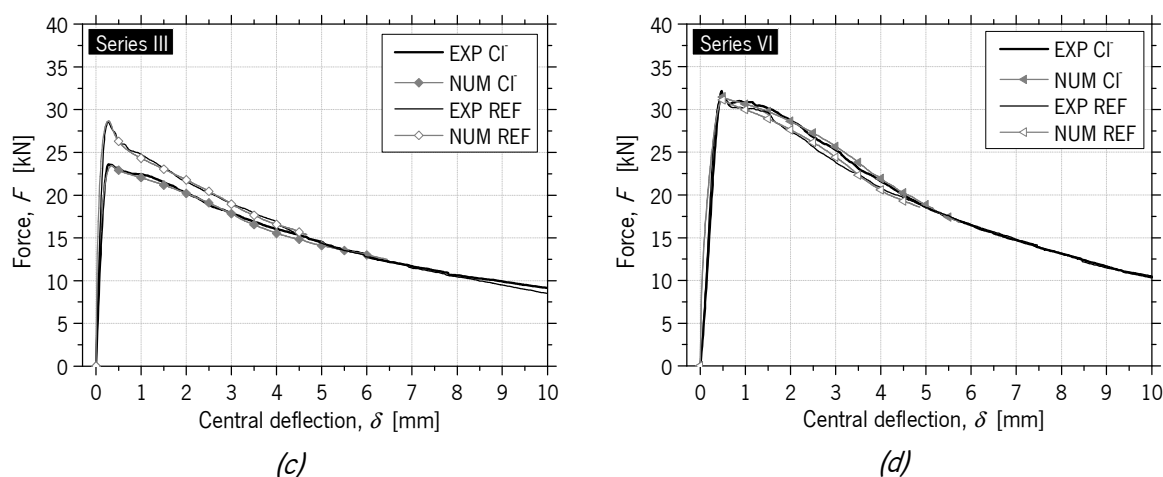


Figure 7.42 – Numerical simulation of RPT-3ps for non-cracked panels of:  
(a) Series III\_CI&REF; (b) Series VI\_CI&REF

Table 7.13 – Parameters of the  $\sigma - \omega$  relationship obtained by inverse analysis (RPT-3ps)  
for non-cracked panels (Series III&VI\_CI&REF)

	Series	$f_{\alpha}$ (MPa)	$\sigma_1$ (MPa)	$\sigma_2$ (MPa)	$\sigma_3$ (MPa)	$\omega_1$ (mm)	$\omega_2$ (mm)	$\omega_3$ (mm)	$\omega_u$ (mm)	$G_f$ (N/mm)	$e$ (%)
After environmental exposure	III_CI	3.70	2.29	1.11	0.67	0.02	0.24	0.60	5.00	2.22	0.70
	III_REF	4.25	2.25	1.11	0.60	0.03	0.25	0.60	5.00	2.07	0.80
	VI_CI	4.80	2.88	1.25	0.48	0.01	0.25	0.60	5.00	1.89	2.21
	VI_REF	4.85	2.96	1.26	0.97	0.02	0.25	0.60	5.00	3.08	1.34

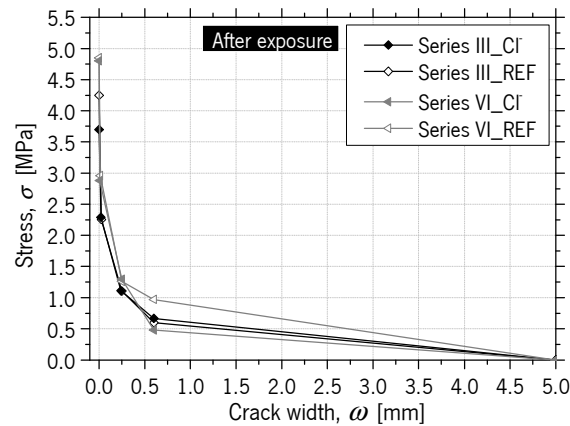


Figure 7.43 –  $\sigma$  -  $\omega$  relationships obtained by inverse analysis for RPT-3ps of Series III&VI\_CI&REF

The numerical simulations were able of fitting with high accuracy the experimental results. For the exposure period of 10 days of immersion, no significant differences occurred between the obtained parameters of the  $\sigma$  -  $\omega$  relationship for non-cracked panels submitted to chloride attack (Table 7.12 and Fig. 7.43 - Series III\_CI) and the corresponding reference parameters (Table 7.12 and Fig. 7.43 - Series III\_REF), which means that the chloride attack had a negligible effect in the post-cracking behavior of uncracked RSFRC for this period of immersion.

For the exposure period of 3 months, it seems that the dry-wet cycles of chloride solution had a detrimental effect on the post-cracking behavior of non-precracked RSFRC panels. The reduced value of fracture energy in the panels submitted to chloride attack (Series VI\_CI) is partially justified by the fiber distribution and orientation at cracked surfaces, as observed in Section 7.3.3. However, although there were no significant signs of RSF corrosion on cracked surfaces of non-precracked RSFRC panels (Section 7.3.2.2), the chloride attack appears to have a slight negative effect on the interfacial bond between recycled fibers and concrete matrix. The results presented in Table 7.13 corroborate with the corrected values of energy absorption determined for panels of Series VI (Table 7.5).

### Constitutive laws of RSFRC obtained from RPT-3ps and 3PNBBTs

Figure 7.44 presents the comparison between the  $\sigma$  -  $\omega$  relationship of the RSFRC1% (for each distinct RSFRC1% castings: RSFRC1%\_2&3&4&5) obtained by inverse analysis from RPT-3ps presented in Figures 7.41a,c, and from 3PNBBTs presented in Figure 3.39 (Section 3.5.1.3). As observed, it is verified that the constitutive laws obtained from 3PNBBT (prismatic specimens with a localized crack) overestimated the post-cracking behavior of RSFRC compared to the constitutive laws obtained from RPT-3ps, which are



more representative of the fiber reinforcement mechanisms developed in thin elements (wall elements, panels, slabs, shotcrete...).

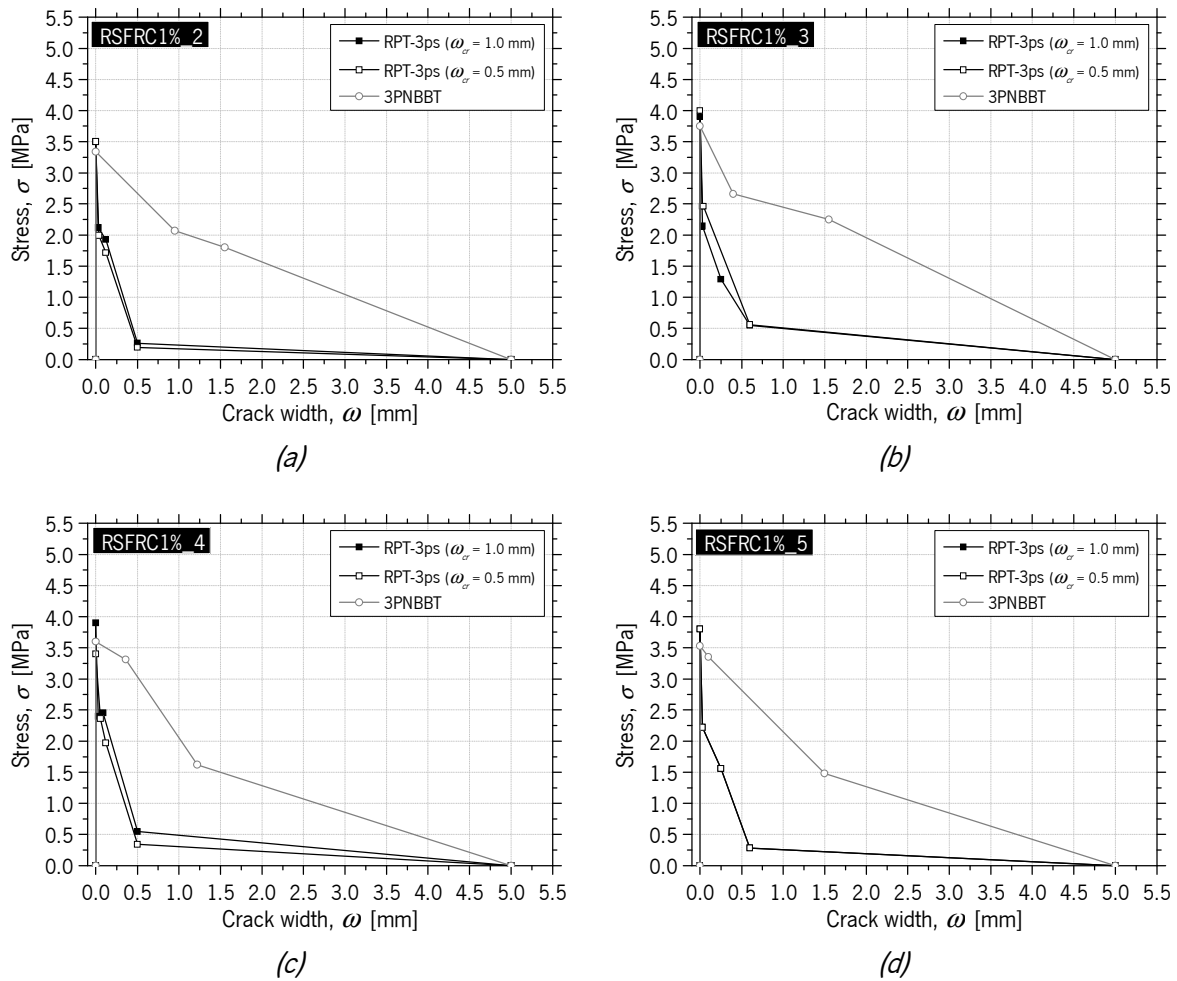


Figure 7.44 –  $\sigma$ - $\omega$  relationships obtained by inverse analysis from RPT-3ps and 3PNBBTs

### 7.3.5 Chloride diffusion in RSFRC

#### 7.3.5.1 Chlorides migration under non-steady state

During the chloride migration tests described in Section 7.2.4.1, an increased formation of corroded material could be observed in the cathodic solution used to test RSFRC specimens, as shown in Figure 7.45. This fact happened due to the corrosion of fibers located on the specimen surface (cut surface) directly exposed to the chloride (catholyte) solution.



Figure 7.45 – Chloride migration tests carried out with specimens made with:  
 (a) The RSFRC1%\_2 casting and (b) The RSFRC1%\_4 casting

The average values of the chloride migration coefficient,  $D_m$ , obtained in RSFRC1% specimens and in the corresponding plain concrete (PC) specimens (RSFRC1%\_2&4 castings) are shown in Table 7.14.

Table 7.14 – Chloride migration coefficients in RSFRC and PC specimens

		RSFRC1%_2 casting		RSFRC1%_4 casting	
		RSFRC	PC	RSFRC	PC
$D_m$ ( $\times 10^{-12}$ m <sup>2</sup> /s)	Avg	14.73	13.22	15.08	10.27
	CoV (%)	(12.87)	(21.12)	(16.75)	(18.30)

The values of obtained  $D_m$  indicate that the RSF decreased the resistance to chloride penetration. On the one hand, this fact may be explained by the slight increase of the open porosity of concrete resulting from the addition of steel fibers (Frazão *et al.*, 2015), which provides higher chloride penetration, mainly through the fiber-matrix interfaces of the fibers located at the exposed surface of the specimens. On the other hand, the method of evaluation of chloride diffusion by migration, despite being faster than the one based on diffusion by natural immersion, has some disadvantages for testing RSFRC. The external electrical potential applied axially across the specimen and the test duration were defined based on the LNEC Specification E463:2004, that establishes the potential difference and the duration of the test according to the initial current intensity applied in plain concrete. However, the presence of steel fibers can influence the electrical field generated due to the high electrical conductivity of steel fibers. In addition, the chloride migration test causes an increase of temperature in concrete specimens, which may favor the chloride penetration process (Isteita and Xi, 2017). Thus, it is more prudent to use methods based on the natural diffusion immersion to evaluate the penetration of chlorides in RSFRC, since, despite requires longer testing periods is more representative of real environment exposure conditions.

### 7.3.5.2 Resistance to chloride penetration by immersion

The chloride profiles obtained in each cubic specimen of RSFRC1% and PC are presented in Figure 7.45, determined as described in Section 7.2.4.2.

The average values obtained of the chloride content at the exposed surface after immersion period,  $C_s$ , and the apparent chloride diffusion coefficient,  $D_d$ , determined by curve-fitting the measured chloride-ion contents to Fick's 2<sup>nd</sup> law (Figure 7.46), are presented in Table 7.15. The obtained values of the chloride penetration parameter,  $K_{C_r}$ , calculated with the equation (7.3), are also presented in Table 7.15.

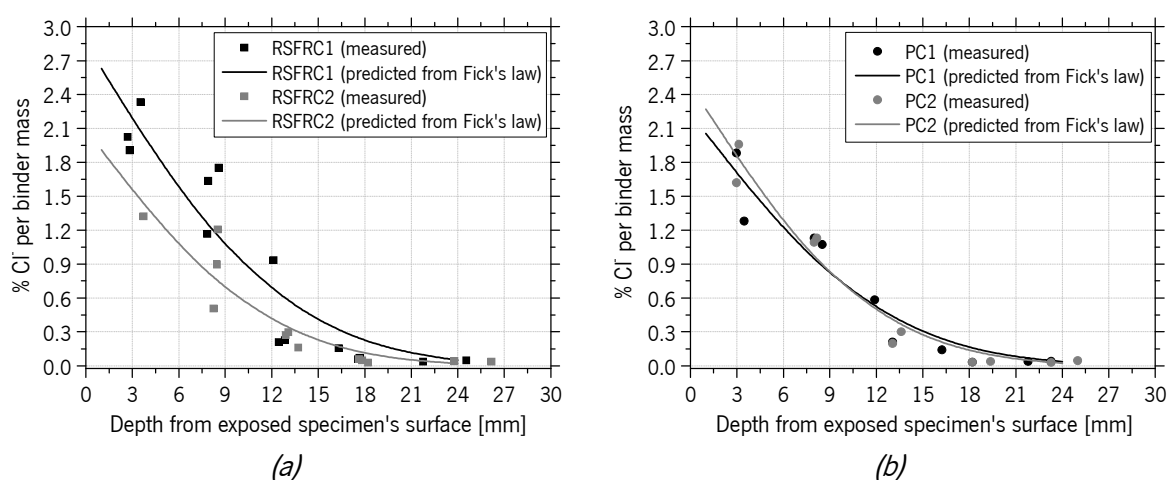


Figure 7.46 – Chloride profiles along specimen depth from exposed surface of:  
(a) RSFRC1% specimens; (b) PC specimens

Table 7.15 – Results of chloride penetration test by immersion

Concrete Specimen	$C_s$ (%)	avg $C_s$ (%)	$D_d$ ( $\times 10^{-12}$ m <sup>2</sup> /s)	avg $D_d$ ( $\times 10^{-12}$ m <sup>2</sup> /s)	$K_{C_r}$ (mm/year <sup>0.5</sup> )	avg $K_{C_r}$ (mm/year <sup>0.5</sup> )
RSFRC1	2.853	2.472	6.59	6.02	37.06	34.05
RSFRC2	2.090		5.46		31.05	
PC1	2.236	2.361	6.35	5.92	34.44	33.69
PC2	2.486		5.49		32.94	

The obtained values of  $D_d$  evidence a similar resistance to chloride penetration between RSFRC and PC specimens, which means that the presence of RSF had a negligible effect in the penetration of chloride ions into concrete.

Comparing  $D_d$  with  $D_m$  (Table 7.14), higher values were obtained for the chloride diffusion coefficients by migration,  $D_m$ , than by natural immersion,  $D_d$ . The same trend is reported by other authors (Tang *et al.*, 2001; Yuan *et al.*, 2008), who also confirmed higher results from NT BUILD 492 (1999) than from NT BUILD 443 (1995) tests, for identical concretes. This is due to the different transport mechanism and maturity of concrete considered in each test.

### 7.3.5.3 Chloride diffusion and aging coefficient by colorimetric method

In Table 7.16 are presented the results obtained for chloride penetration and aging coefficient evaluated by the colorimetric method in RSFRC and PC cylindrical specimens previously submitted to 10 days (RSFRC1 and PC1) and 3 months (RSFRC2 and PC2) of chloride immersion, as described in Section 7.2.4.2.1. In this table,  $x_c$  is the colorimetric penetration depth,  $C_o$  is the chloride concentration ponded at the top surface,  $C_c$  is the concentration of free chlorides in the pore solution corresponding to the color change boundary,  $t$  is the exposure time,  $D_c$  is the chloride diffusion coefficient, and  $n_{cl}$  is the aging coefficient.

Table 7.16 – Results of chloride diffusion and aging coefficients determined by colorimetric method in RSFRC and PC cylindrical specimens after 10 days and 3 months of chloride immersion

<b>Cylindrical specimens</b> (RSFRC1%_2 casting)	$x_c$ (m)	$C_o$ (N)	$C_c$ (N)	$t$ (s)	$D_c$ ( $\times 10^{-12}$ m <sup>2</sup> /s)	$n_{cl}$
<b>RSFRC1</b>	0.0056	0.61	0.07	864000	8.31	0.56
<b>RSFRC2</b>	0.0090			7776000	2.42	
<b>PC1</b>	0.0052	0.61	0.07	864000	7.34	0.49
<b>PC2</b>	0.0091			7776000	2.48	

As expected, the chloride diffusion coefficient,  $D_c$ , decreased with the time of exposure for both RSFRC and PC specimens. No significant differences were observed between the aging coefficients of RSFRC and PC.

This simple colorimetric method was also used for measuring the chloride penetration depth into the 4 cubic specimens of RSFRC and PC used in the tests described in Section 7.2.4.2. After the determination of chloride profiles (Fig. 7.47), the 4 cubic specimens were axially split, and the 0.1 N AgNO<sub>3</sub> solution was sprayed on to one freshly split section (Figure 7.47).



Figure 7.47 – Chloride penetration depth in RSFRC and PC cubes after 3 months of immersion

The values of  $D_c$  were determined according to eq. (7.4) and the results are presented in Table 7.17.

Table 7.17 – Results of chloride diffusion coefficients determined by colorimetric method in RSFRC and PC cubic specimens after 3 months of chloride immersion

Cubic specimens (RSFRC1%_4 casting)	$x_c$ (m)	$C_0$ (N)	$C_c$ (N)	$t$ (s)	$D_c$ ( $\times 10^{-12} \text{ m}^2/\text{s}$ )	Avg $D_c$ ( $\times 10^{-12} \text{ m}^2/\text{s}$ )
<b>RSFRC1</b>	0.0104	0.61	0.07	7776000	3.24	3.26
<b>RSFRC2</b>	0.0105				3.29	
<b>PC1</b>	0.0087	2.26	2.49			
<b>PC2</b>	0.0095	2.71				

After 3 months of chloride immersion, the values of  $D_c$  obtained by the colorimetric method were lower than those of  $D_d$  obtained by Fick's 2<sup>nd</sup> law (Table 7.15). For the determination of  $D_c$ , the chloride concentration ponded at the top surface,  $C_0$ , was assumed equal to the chloride concentration at NaCl solution, which means that no fixation of chloride ions at top surface was assumed, being unrealistic. In this case, higher values of  $D_c$  would be obtained if the real chloride concentration in the reference pore solution was considered.

The chloride concentration corresponding to the chloride penetration depth,  $x_c$  (Table 7.17), in RSFRC and PC cubes was determined by the Fick's 2<sup>nd</sup> law (Equation 7.2) considering the parameters  $C_s$  and  $D_d$  obtained with the chloride profiles of RSFRC cubic specimens, as shown in Table 7.15. For the initial chloride content,  $C_0$  was assumed 0% of binder mass, and the time of immersion  $t$  was 7776000 s (3 months). The average chloride content obtained for the chloride penetration depth,  $x_c$ , was 0.70% per binder mass for RSFRC (0.18% per concrete mass) and 0.80% per binder mass for PC (0.21% per

concrete mass).

Considering that no significant signs of corrosion were detected on the fibers at the freshly split sections of RSFRC cubic specimens, the chloride content corresponding to 2 mm (maximum depth of corroded fibers from exposed surfaces in RSFRC panels – Section 7.3.2.2) was also determined by the same way (Fick's 2<sup>nd</sup> law). The average chloride content obtained for the depth of corroded fibers was 2.07% per binder mass (0.53% per concrete mass). These results reveal that the critical chloride concentration in immersion conditions, corresponding to the beginning of fiber corrosion was higher than 2.07% per binder mass.

#### 7.3.5.4 Resistance to chloride penetration by dry-wet cycles

The following sections describe the procedure adopted for determining the critical concentration of chlorides corresponding to the beginning of fiber corrosion in non-cracked round panels of RSFRC1%, which were subjected to 3 months of dry-wet cycles in 3.5 wt.% NaCl solution (Series IV&V&VI\_Cl in Table 7.1).

##### 7.3.5.4.1 Determination of the chloride diffusion coefficient by colorimetric method

As mentioned in Section 7.3.5.3, for non-cracked panels, an average chloride penetration depth of 9.5 mm was measured after 3 months of dry-wet cycles in chloride solution. Considering this colorimetric penetration depth,  $x_c$ , the average chloride diffusion coefficient,  $D_c$ , was determined according to equation (7.4), and the obtained values are presented in Table 7.18.

Table 7.18 – Chloride diffusion coefficient determined by colorimetric method in non-cracked RSFRC panels after 3 months of dry-wet cycles in chloride solution

<b>Panels</b> (RSFRC1%_4 casting)	$x_c$ (m)	$C_0$ (N)	$C_c$ (N)	$t$ (s)	$D_c$ ( $\times 10^{-12} \text{ m}^2/\text{s}$ )
<b>Non-cracked RSFRC</b>	0.0095	0.61	0.07	7776000	2.69

A slight decrease of  $D_c$  was found in non-cracked RSFRC panels submitted to dry-wet cycles, compared to  $D_c$  obtained in RSFRC cubic specimens (same concrete casting) submitted to continuous immersion (Table 7.17). On one hand, panels subjected to dry-wet cycles were not continuously under maximum

diffusion conditions. On the other hand, the arrangement of specimens inside the immersion containers was different which caused differences in terms of hydrostatic pressure at exposed surfaces. Non-cracked panels were positioned with the surface exposed vertically (Fig. 7.4b) and the cubic specimens with the surface exposed horizontally (Fig. 7.8a), which is more susceptible to chloride penetration than the vertical one.

#### 7.3.5.4.2 Determination of the chloride diffusion coefficient by Fick's 2<sup>nd</sup> law

Chiang and Yang (2007) and Yang and Liang (2014) found a good linear relationship between  $D_d$  obtained from chloride profile method, and  $D_c$ , in which penetration depths were determined from AgNO<sub>3</sub> colorimetric method. Assuming a linear correlation between  $D_d$  and  $D_c$ , the value of  $D_d$  for non-cracked RSFRC panels was derived by linear regression, considering the average values of  $D_d$  (Table 7.14) and  $D_c$  (Table 7.16), obtained in RSFRC and PC cubic specimens after 3 months of chloride immersion. The value of  $D_d$  estimated from this linear regression for non-cracked RSFRC panels was  $5.95 \times 10^{-12} \text{ m}^2/\text{s}$ .

#### 7.3.5.4.3 Determination of surface chloride content by Fick's 2<sup>nd</sup> law

The surface chloride content,  $C_s$  (% of binder mass) for non-cracked RSFRC panels was determined by the Fick's 2<sup>nd</sup> law (equation 7.2), considering for  $C_x$  the chloride content of 0.70% of binder mass obtained in RSFRC cubic specimens (Section 7.3.5.3), corresponding to the chloride penetration depth,  $x_c$  (0.0095 m). The parameter values considered for the estimation of  $C_s$  are presented in Table 7.19.

Table 7.19 – Surface chloride content determined by Fick's 2<sup>nd</sup> law in non-cracked RSFRC panels after 3 months of dry-wet cycles in chloride solution

<b>Panels</b> (RSFRC1%_4 casting)	$x_c$ (m)	$D_d$ ( $\times 10^{-12} \text{ m}^2/\text{s}$ )	$t$ (s)	$C_x$ (%)	$C_s$ (%)
<b>Non-cracked RSFRC</b>	0.0095	5.95	7776000	0.70	2.157

#### 7.3.5.4.4 Determination of the critical chloride concentration corresponding to the beginning of fiber corrosion

The critical content of chlorides,  $C_{cr}$  (% binder mass) corresponding to the beginning of fiber corrosion in the RSFRC panels subjected to dry-wet chloride cycles for 3 months was determined by the Fick's 2<sup>nd</sup> law considering the parameters  $D_d$  and  $C_s$  determined in sections 7.3.5.4.2 and 7.3.5.4.3, respectively. The depth of corroded fibers was measured in the non-cracked panels as represented in Figure 7.18 (Section 7.3.2.2), from the exposed surfaces of non-cracked panels. The value obtained for  $C_{cr}$  for non-cracked panels corresponding to chloride content,  $C_x$  corresponding to the depth of corroded fibers,  $x$ , is presented in Table 7.20.

Table 7.20 – Critical chloride content determined by Fick's 2<sup>nd</sup> law in non-cracked RSFRC panels after 3 months of dry-wet cycles in chloride solution

<b>Panels</b> (RSFRC1%_4 casting)	<b><math>x</math></b> (m)	<b><math>D_d</math></b> ( $\times 10^{-12} \text{ m}^2/\text{s}$ )	<b><math>C_s</math></b> (% binder mass)	<b><math>t</math></b> (s)	<b><math>C_{cr}</math></b> (% binder mass)	<b><math>C_{cr}</math></b> (% concrete mass)
<b>Non-cracked RSFRC</b>	0.00236		2.157	7776000	1.74	0.45

Comparing to the RSFRC cubic specimens subjected to continuous immersion (section 7.3.5.3), lower critical chloride content was obtained for RSFRC round panels (Table 7.20), which means that for 3 months of chloride exposure, the dry-wet cycles was a more aggressive environment for chloride-induced fiber corrosion than the continuous chloride immersion. The same is considered in Duracrete R17 (2000).

#### 7.3.5.5 Chloride penetration prediction into a RSFRC structural element

A prediction of the chloride penetration depth into a RSFRC structural element was made based on the chloride diffusion results obtained for the RSFRC panels. This prediction was determined by the Fick's 2<sup>nd</sup> law (equation 7.2), considering 2.163% of binder mass for  $C_s$ , determined according to LNEC Specification E465:2007 and 1.7% of binder mass for  $C_{cr}$  (section 7.3.5.4.3), which corresponds to chloride content,  $C_x$  for the chloride penetration depth,  $x$ , in RSFRC panels. The chloride diffusion coefficient,  $D_d$ , was defined assuming an average aging coefficient of 0.49 (minimum value according to Table 7.16). The following equation was used to determine  $D_d$  for the time dependency (Song *et al.*, 2013):



$$D(t) = D_{ref} \left( \frac{t_{ref}}{t} \right)^m \quad (7.13)$$

where  $D(t)$  is the diffusion coefficient in  $\text{m}^2/\text{s}$  at the exposure time  $t$  (s),  $D_{ref}$  is the diffusion coefficient at reference time  $t_{ref}$  ( $D_{ref} = 5.95 \times 10^{-12} \text{ m}^2/\text{s}$ ,  $t_{ref} = 7776000 \text{ s}$ ), and  $m$  is the aging coefficient (0.49 – Table 7.16). The obtained results of the chloride penetration prediction in a RSFRC structural element submitted to dry-wet cycles in 3.5 wt% solution is represented in Figure 7.48. After has been exposed to dry-wet cycles in a 3.5 wt.% NaCl solution for 100 years, a chloride penetration depth of about 11 mm was predicted for a RSFRC structural element. Note, that dry-wet exposure (XS3) is usually more aggressive than continuous immersion (XS2). Therefore, it is shown that the RSF corrosion in non-cracked concrete should not be significant.

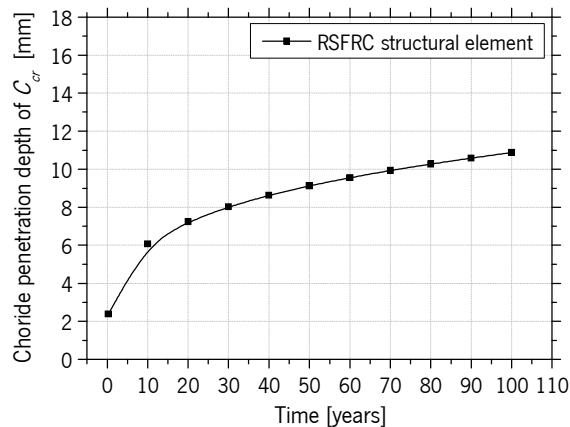


Figure 7.48 – Prediction of chloride penetration depth into a RSFRC structural element

## 7.4 CONCLUSIONS

RPT-3ps were carried out to assess the effects of chloride attack on the post-cracking behavior of RSFRC. The influence of the parameters crack width, chloride exposure period and fiber distribution/orientation profile was assessed in terms of the flexural toughness obtained in RPT-3ps. In addition, an inverse analysis strategy was executed for deriving the  $\sigma - \omega$  relationship and mode I fracture parameters of the RSFRC1% representative of the RPT-3ps, combining a moment-rotation approach with a numerical model that considers the kinematics conditions of RPT-3ps at failure stage and the equilibrium equations (Salehian, 2015). The chloride diffusion in RSFRC was investigated by migration under non-steady state and natural immersion. A simplified prediction of the critical chloride content corresponding to the beginning of fiber corrosion and the long-term chloride penetration depth into a RSFRC structural element

exposed to a maritime environment (dry-wet cycles in chloride solution) was estimated. The main conclusions based on the experimental and numerical results are:

- 1) After 10 days of chloride immersion, no significant signs of superficial corrosion were visible in the RSFRC panels; however, a significant increase in surface corrosion has occurred on the RSFRC panels after 3 months of dry-wet cycles in chloride solution.
- 2) After 10 days and 3 months of chloride attack, no significant signs of corrosion were detected in the RSF at crack surfaces of non pre-cracked RSFRC panels. For pre-cracked RSFRC panels with crack widths up to 1 mm, the cracked surfaces were completely penetrated by chlorides during the immersion period, and corrosion products were visible in the RSF located in the cracked surfaces, mainly near the exposure faces of the panels.
- 3) The stiffness parameters obtained indicate a negligible effect of the adopted corrosion induction conditions of RSF on the post-cracking behavior of cracked RSFRC up to a crack width of 1 mm. For the pre-cracked RSFRC panels, there was a clear tendency to a decrease of the normalized stiffness,  $K_j / K_{ci}$ , with the increase of the pre-crack width,  $\omega_{cr}$ , regardless of the initial stiffness value,  $K_{ci}$ .
- 4) The average force-central deflection responses registered in the RPT-3ps of RSFRC panels revealed small differences between the post-cracking behavior of pre-cracked and non-cracked panels submitted to 10 days of chloride immersion, which can be mainly justified by the differences in panel's thickness and due to fiber distribution and orientation at crack surfaces. After 3 months of dry-wet cycles in chloride solution, the post-cracking behavior of non-cracked panels was similar to that of non-cracked reference panels; For pre-cracked panels, a slight increase in the post-cracking load carrying capacity was observed for panels with an average  $\omega_{cr} = 0.59$  mm, comparing with the corresponding pre-cracked reference panels; However, for higher average  $\omega_{cr}$  (0.85 mm), it seems that the chloride attack had a negligible effect in the post-cracking behavior of RSFRC.
- 5) The values of energy absorption corrected according to the ASTM C1550-08 (2008) indicated that the dispersion observed in force-central deflection curves was partly due to the differences in panel thickness. The differences between the energy absorption obtained for pre-cracked and non pre-cracked panels seems to be due to fiber distribution at crack surfaces. The irregular corrosion

susceptibility of RSF due to its irregular geometry caused a higher dispersion of the results for the longest exposure period (3 months).

- 6) The central deflection corresponding to the elastic deformation of the RSFRC panels can be neglected for numerical simulations by inverse analysis since it was much lower than the central deflection due to crack opening.
- 7) The average force-crack width responses registered on the RSFRC panels indicate a negligible effect of the chloride attack on the average progression of crack widths during the RPT-3ps for the adopted conditions of chloride exposure and pre-crack width level.
- 8) The crack widths measured with the microscope were slightly lower than that measured with the LVDTs due to the elastic deformation and the rotation of the measurement base included in the registered measures by LVDTs.
- 9) Significant differences may occur in the progress of the three crack widths in round panels during RPT-3ps due to fiber distribution of RSF at crack surfaces, with an inherent influence on the energy absorption of RSFRC panels. No significant differences in the crack width were observed along its length up to a central deflection of approximately 2.0 mm. A slight reduction of the crack widths occurred in the pre-cracked panels after performing the environmental exposure.
- 10) A high percentage of RSF failed by rupture in RPT-3ps, as observed in DEWSTs (Section 6.3.2.5), due to the strong bond between recycled fibers and matrix, which is indicative of a negligible effect of chloride attack.
- 11) The results obtained in terms of the fiber orientation factor determined by image analysis were similar to DEWSTs samples, i.e., no significant differences were detected in terms of the fiber orientation factor, between reference panels and panels submitted to chloride attack; the fiber orientation factor computed from the image analysis approach,  $\eta_{img}$  was higher than the orientation factor,  $\eta_{exp}$ , calculated with the equation proposed by Soroushian and Lee (1990). A reduction of  $\eta_{exp}$  was observed with the decrease of fiber density. A uniform fiber distribution seems to have been guaranteed in the RSFRC panels.
- 12) The post-cracking constitutive laws of the RSFRC1% representative of the RPT-3ps were obtained by inverse analysis procedure, by using the experimental curves of the average force-central deflection relationships obtained from RPT-3ps. The strategy adopted combines a moment-rotation approach with a numerical model that considers the kinematics conditions of RPT-3ps at failure stage and the equilibrium equations (Salehian, 2015). Comparing the  $\sigma - \omega$  relationships

obtained for pre-cracking stage and the corresponding  $\sigma - \omega$  obtained after exposure, the chloride attack for 10 days of immersion had a small beneficial effect on the post-cracking behavior of pre-cracked RSFRC panels with crack widths up to 1 mm, while for 3 months of dry-wet chloride cycles, a negligible effect of chloride attack was observed. For uncracked RSFRC, no significant influence of the chloride immersion for 10 days was verified on post-cracking behavior, whereas the dry-wet cycles in chloride solution for 3 months seem to have had a slight negative effect in the post-cracking load carrying capacity.

- 13) The constitutive laws of the RSFRC1% representative of the 3PNBBTs overestimate the post-cracking behavior of RSFRC1% comparing with the constitutive laws of the RSFRC1% representative of the RPT-3ps.
- 14) Determining the diffusion coefficient from the chloride migration test under non-steady state may not be feasible for RSFRC, since the presence of steel fibers seems to have a significant influence in the test methodology, mainly by inducing severe corrosion in RSF. The determination of the diffusion for RSFRC is more prudent by natural immersion test in salt solution.
- 15) The presence of RSF had a negligible effect in the penetration of chloride ions into concrete. No significant differences were observed between the aging coefficients of RSFRC and the corresponding PC. The average chloride content obtained for the chloride penetration depth was 0.70% of binder mass for RSFRC and 0.80% of binder mass for PC, which agrees with the chloride concentration at the color change boundary reported in the literature for OPC concrete. The critical chloride concentration corresponding to the beginning of fiber corrosion is higher than 2.47% of binder mass in uncracked RSFRC submitted to 3 months of continuous immersion.
- 16) The cracked RSFRC with crack widths up to 1 mm is more susceptible to RSF corrosion than the uncracked RSFRC. The dry-wet cycles in salt solution for 3 months are more aggressive environment conditions for chloride-induced fiber corrosion than the continuous chloride immersion for the same exposure period.
- 17) A chloride penetration depth of about 11 mm was predicted into a RSFRC structural element after exposed to dry-wet cycles in a 3.5 wt.% NaCl solution for 100 years.

---

# Chapter 8

---

## **RSFRC AS ALTERNATIVE TO ISFRC FOR REINFORCEMENT OF THE STRUCTURAL ELEMENTS**

### **8.1 INTRODUCTION**

In a world that is becoming increasingly sensitive to the need of protecting the environment, the ability to build concrete structures using sustainable resources is an exciting and attractive proposition with environmental and economic benefits.

Nowadays, pneumatic tires are among the most widespread industrial products and, giving the best use to tires that have reached their end-of-life is still a societal challenge. In recent years, several efforts have been done for using different by-products obtained from the recycling of waste tires, such is the case of deriving constituents for the concrete industry (Tlemat *et al.*, 2003b; Pilakoutas *et al.*, 2004; Micelli *et al.* 2014; Zamanzadeh *et al.*, 2015; Caggiano *et al.*, 2017).

As reported in the previous chapters, steel fibers resulting from industry of tire recycling (RSF – Recycled Steel Fibers) have high potential as an effective reinforcement for concrete, in terms of improving the post-cracking behavior and durability performance. Recycled Steel Fibre Reinforced Concrete (RSFRC) seems to be a promising candidate with technical, environmental and economic benefits for the development of ductile, high strength and durable constructive systems.

In this chapter, the technical, environmental and economic benefits of using the developed RSFRC for application to structural elements, have been assessed at material level and compared to Industrial Steel Fiber Reinforced Concrete (ISFRC).

Double edge wedge splitting tests (DEWSTs) and round panel tests (RPTs) were carried out to evaluate the technical benefits of RSF as concrete reinforcement in terms of indirect tensile strength and flexural toughness. The environmental impact of the incorporation of RSF in concrete in comparison with ISFRC was evaluated using Life Cycle Assessment (LCA) methodology. The economic benefits of using RSF as an alternative to Industrial Steel Fibers (ISF) for concrete reinforcement were simply analyzed.

## **8.2 TECHNICAL BENEFITS OF RSFRC: EXPERIMENTAL INVESTIGATION ON THE POST-CRACKING BEHAVIOR**

RSFRC and ISFRC of equal composition were produced with 1% of fibers by volume of concrete, according to the mix proportions presented in Table 3.18 (RSFRC1% and ISFRC1%). The post-cracking behavior of RSFRC1% and ISFRC1% was analyzed using DEWSTs and RPTs. The flexural behavior of these concretes was also characterized by means of three-point notched beam bending tests (3PNBBT), as already presented in Section 3.5.1 (Figure 3.30).

The DEWSTs were performed on four  $\phi 150 \times 60$  mm cylindrical specimens per each concrete, obtained from molded  $\phi 150 \times 300$  mm specimens, as shown in Figure 6.1. The procedures adopted in terms of position and dimensions of the notches sawn into the specimens, load and specimen support conditions, main characteristics of the equipment and measuring devices, as well as the test setup were described in Section 6.2.2.

The flexural toughness of RSFRC1% and ISFRC1% was characterized in this chapter by conducting RPTs on three round panels with 600 mm diameter and 60 mm thickness of each concrete. The RPTs were carried out with three point supports according to the recommendations of ASTM C1550-08 (2008). The details of the experimental setup of the RPTs were presented in Section 7.2.2.

### **8.2.1 Splitting tensile tests**

Figures 8.1a-c show the average splitting tensile stress-CMOD curves,  $\sigma_{t,split} - \omega$ , obtained for the RSFRC1% and ISFRC1% specimens at 75 days of age, where  $\sigma_{t,split}$  was determined from the equation (2.4) proposed by di Prisco *et al.* (2013) (Section 2.2.1.2.2). In Figure 8.1c are depicted the average  $\sigma_{t,split} - \omega$  curves obtained for the RSFRC1% and ISFRC1% specimens in comparison with the average flexural stress-CMOD curves,  $f_{ct,fl} - \omega$  obtained by the performed 3PNBBTs presented in Section 3.5.1.2 (Figures 3.32a,b).

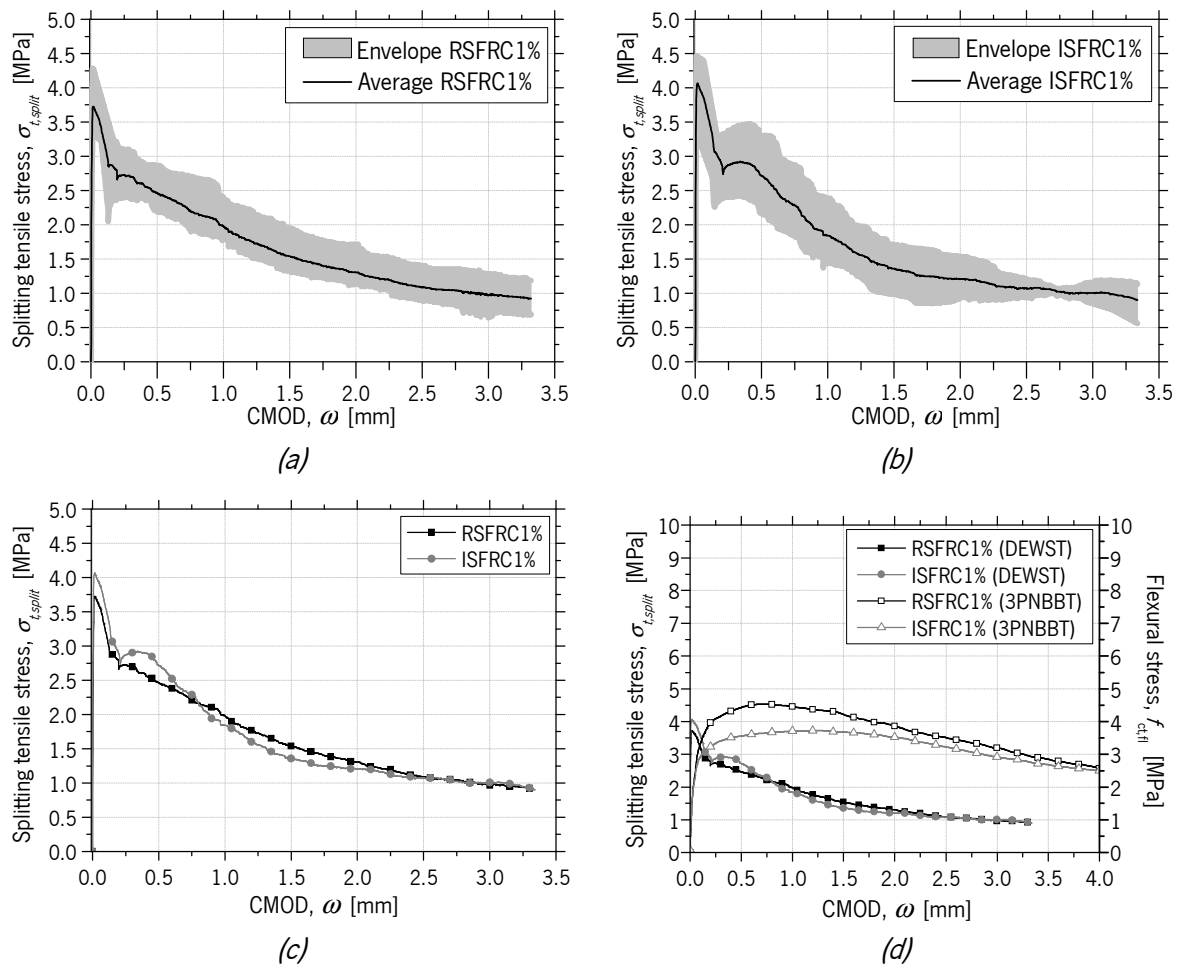


Figure 8.1 – Envelope and average splitting tensile stress-CMOD curves for specimens of:  
 (a) RSFRC1%; (b) ISFRC1%; (c) RSFRC1% and ISFRC1%;  
 (d) RSFRC1% and ISFRC1% (DEWST and 3PNBBT)

According to Figures 8.1a-c, RSFRC1% showed similar indirect tensile strength and post-cracking behavior to those registered in ISFRC1%. The dispersion of the results was also similar in RSFRC1% and ISFRC1%, as observed in Figures 8.1a,b. These conclusions can be confirmed with the average residual strength at a given crack width,  $\sigma_{\omega}$ , and the respective energy due to fracture propagation,  $G_{F\omega}$  (which corresponds to the area under the softening curve up to these  $\omega$  values) taken from the stress-crack opening relationships, as presented in Table 8.1.

As observed in Fig. 8.1d, the flexural capacity and the energy absorption performance of RSFRC1% and ISFRC1% obtained in 3PNBBTs were much higher than the indirect tensile strength and post-cracking behavior obtained in DEWSTs. These differences may be attributed to the differences between the tests setup, particularly with regard to the crack opening process, which is more constant in DEWST than in 3PNBBT, being the fiber reinforcement mechanisms not activated in the same way.

Table 8.1 – Maximum and residual splitting tensile strength and energy due to fracture propagation in RSFRC1% and ISFRC1%

Concrete		$\sigma_{max}$ (MPa)	$\sigma_{0.3}$ (MPa)	$\sigma_{0.5}$ (MPa)	$\sigma_{1.0}$ (MPa)	$\sigma_{1.5}$ (MPa)	$\sigma_{3.0}$ (MPa)
RSFRC1%	Avg CoV (%)	3.74 (12.31)	2.70 (10.76)	2.47 (11.58)	1.98 (14.01)	1.54 (18.41)	0.97 (25.85)
ISFRC1%	Avg CoV (%)	4.10 (13.13)	2.90 (13.96)	2.72 (16.98)	1.84 (24.76)	1.36 (25.14)	1.04 (7.53)

Concrete		$G_{F0.3}$ (N/mm)	$G_{F0.5}$ (N/mm)	$G_{F1.0}$ (N/mm)	$G_{F1.5}$ (N/mm)	$G_{F3.0}$ (N/mm)
RSFRC1%	Avg CoV (%)	0.90 (11.72)	1.42 (10.49)	2.53 (10.84)	3.40 (11.88)	5.21 (13.97)
ISFRC1%	Avg CoV (%)	0.97 (12.34)	1.56 (12.80)	2.70 (15.49)	3.59 (18.11)	5.14 (23.93)

The fiber distribution was evaluated after testing by counting the number of effective fibers crossing the fracture surface considering this surface divided in two parts: Back (regions a,c,f,h) and Front (regions b,d,e,g), as represented in Figure 6.3c. A fiber was considered effective when its length was visible, therefore assuming this fiber has failed by pull-out. The results obtained are presented in Table 8.2, identified according to the casting depth of the  $\phi 150 \times 300$  mm cylindrical specimens shown in Figure 6.1. A lower number of fibers was counted in the ISFRC1% specimens since each ISF has a higher steel volume than the average RSF, resulting in fewer fibers for the same percentage of fibers per concrete volume.

Some variability was observed between the fiber density in the back and front regions at the cracked surface of the RSFRC1% specimens. Slight occurrence of fiber segregation is also suggested in these specimens by the average values of fiber density at fracture considering the casting depth of the specimens (Fig. 6.1). However, for ISFRC1%, a uniform fiber distribution at fracture surface appears to have been guaranteed. These differences in fiber distribution for RSFRC1% and ISFRC1% specimens are mainly justified by the fiber's geometry since the irregular length and longitudinal configuration of RSF make more difficult to ensure a homogeneous distribution of these fibers into the matrix. However, as observed in Fig. 8.1 and Table 8.1, the fiber distribution in RSFRC1% specimens did not significantly influence the indirect tensile strength and post-cracking behavior of the concrete, compared to ISFRC1% specimens. The larger number of RSF seems to have compensated the detrimental impact of this higher non uniform fiber distribution in terms of tensile performance.



Table 8.2 – Effective fiber counting at fracture surface of splitting specimens of RSFRC1% and ISFRC1%

Series	Casting depth (Fig. 6.1)	Fiber density (fibers/cm <sup>2</sup> )			Series	Casting depth (Fig. 6.1)	Fiber density (fibers/cm <sup>2</sup> )				
		Back*		Front**			AVG	Back*		Front**	AVG
		a	b	e				f	g	h	
RSFRC1%	1	5.24	4.82	5.03	ISFRC1%	1	1.27	1.33	1.30		
	2	2.75	4.40	3.58		2	1.73	1.88	1.80		
	3	2.50	6.08	4.29		3	2.08	1.85	1.96		
	4	4.39	5.18	4.79		4	1.26	1.40	1.33		
	Avg	3.72	5.12	4.42		Avg	1.58	1.61	1.60		
	CoV (%)	(35.35)	(13.94)	(14.50)		CoV (%)	(24.97)	(17.78)	(20.87)		

\*Average of areas “a”, “c”, “f” and “h”; \*\*Average of areas “b”, “d”, “e” and “g”

### 8.2.2 Round Panel tests

The average force-central deflection and energy absorption-central deflection relationships of RSFRC1% and ISFRC1% panels are depicted in Figure 8.2. The crack failure pattern of each round panel was formed by three cracks at angles of about 120°, with the panel breaking into 3 pie-shaped wedges at large deflections. Like in the 3PNBBT (Figure 3.30), the RSFRC1% has also provided higher flexural capacity and energy absorption performance than ISFRC1% in the RPTs. The higher aspect ratio and number of RSF can justify this better performance of RSFRC1% (Micelli *et al.*, 2014). In sum, the results obtained in this work suggest that, at least, RSFRC may have the same mechanical strength performance as ISFRC.

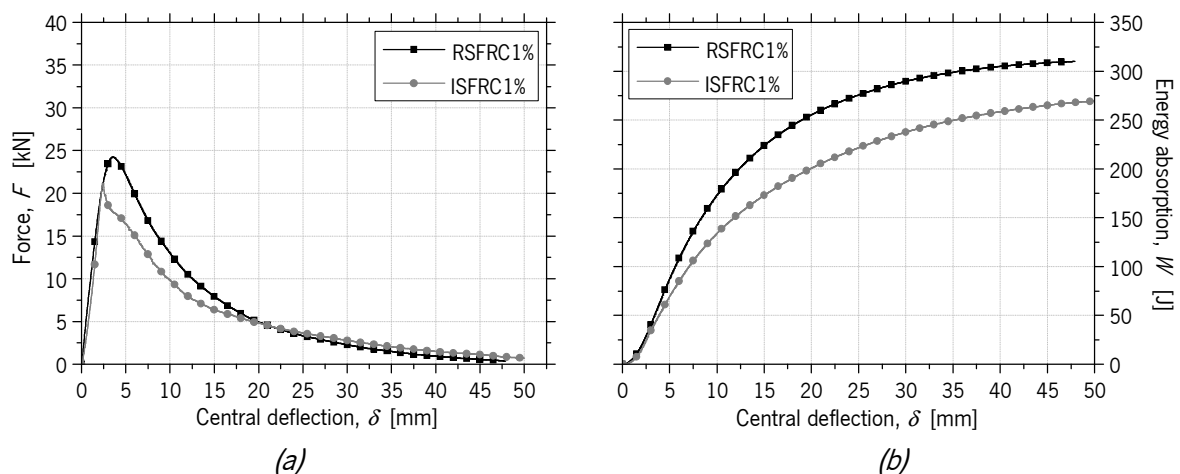


Figure 8.2 – (a) Average force versus central deflection, and (b) Average energy absorption versus central deflection of RSFRC1% and ISFRC1% panels

### 8.3 ENVIRONMENTAL IMPACT OF RSFRC: LIFE CYCLE ASSESSMENT

In this research, the Life Cycle Assessment (LCA) methodology was used to assess the environmental impact of RSFRC in comparison to ISFRC. LCA is an analytical tool thoroughly used to evaluate the environmental sustainability of a product, service or process by quantifying the potential environmental effects during its entire life cycle, from extraction of raw material to production, consumption and recycling or final disposal (Židonienė and Kruopienė, 2015). The LCA was carried out based on ISO standards 14040:2006 and 14044:2006, and on EN 15804:2012+A1. The four main phases involved in an LCA according to ISO 14040:2006 are presented in Figure 8.3.

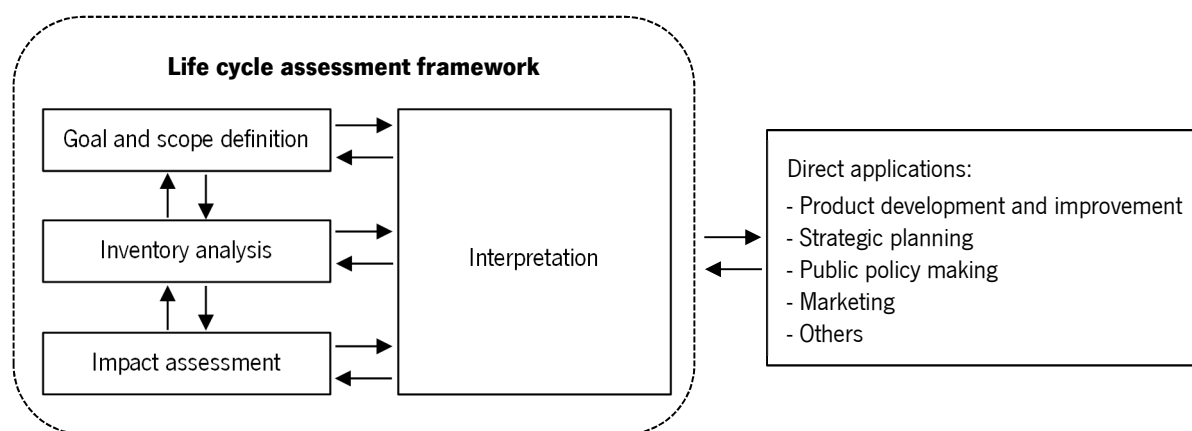


Figure 8.3 – Stages of an LCA according to ISO 14040:2006

In the first stage “goal and scope definition”, the product, process or activity is defined and described, the context of the assessment is established, and the boundaries and the environmental aspects to be considered are identified. The LCA boundary defines the level of detail and can be of three different types: “cradle to gate”, “gate to grave” and “cradle to cradle” (Farinha *et al.*, 2019). The “cradle to gate” boundary is focused only on the product stage of the life cycle. The “gate to grave” boundary includes the construction process, the use and the end-of-life stages. The “cradle to cradle” boundary allows the most complete LCA and includes the life cycle stages of the previous ones and the reuse, recover or recycling options at the materials end-of-life (Farinha *et al.*, 2019).

The inventory analysis consists of input/output data with regard to the system being studied, and involves the collection of the data necessary to meet the goal of the defined study. It is a process that quantifies the energy and raw material requirements (input) and the environmental releases (output), as atmospheric and waterborne emissions, solid wastes, and other releases for the entire life cycles of a product, process, or activity (EPA, 2006). The level of accuracy and detail of the data collected is reflected

throughout the LCA. The inventory of a material based on data collection can be found in environmental product declarations (EPD), collected site-specific data, scientific researches, or in international databases (Farinha *et al.*, 2019).

The impact assessment is the phase of an LCA dedicated to understand and evaluate the magnitude and significance of the potential human and ecological effects quantified in the inventory analysis. The interpretation is the final phase of the LCA procedure, in which the results of the inventory analysis and impact assessment are summarized and discussed as a basis for conclusions.

### 8.3.1 Materials

In the present work, the environmental impacts of RSFRC1% and ISFRC1% of equal composition were evaluated, considering the mix proportions for 1 m<sup>3</sup> of concrete presented in Table 3.18. In addition, two reference ISFRC compositions of the same strength class (C30/37) and commonly used for structural applications (Lourenço, 2012), herein designated by “ISFRC0.3%” and “ISFRC1%\_2”, were also considered with a fiber content of 0.3% and 1% in volume, respectively.

Table 8.3 lists all concrete compositions, including the following constituent materials: ordinary Portland cement type CEM I 42.5R, fly ash (FA), water (W), superplasticizer (SP), fine river sand (FS), coarse river sand (CS) and crushed granite (CG).

Table 8.3 – Mix proportions for 1 m<sup>3</sup> of fiber reinforced concrete (FRC)

<b>Concrete mixture</b>	<b>CEM (kg)</b>	<b>FA (kg)</b>	<b>W (L)</b>	<b>SP (L)</b>	<b>FS (kg)</b>	<b>CS (kg)</b>	<b>CG1 (kg)</b>	<b>CG2 (kg)</b>	<b>Cf (kg)</b>	<b>W/C</b>
RSFRC1%	400	200	173	7.2	148	735	597	-	75.8	0.43
ISFRC1%	400	200	173	7.2	148	735	597	-	78.6	0.43
ISFRC0.3%	368	-	177	1.41	190	581	382	543	20	0.48
ISFRC1%_2	383	-	169	2.60	306	675	376	310	75	0.44

### 8.3.2 Goal and Scope definition

The goal of this LCA is to evaluate the environmental sustainability of the developed concrete reinforced with 1% in volume of recycled steel fibers from end-of-life tires in comparison with concrete reinforced with industrial steel fibers of three different compositions, as presented in Table 8.3.

A “cradle to gate” boundary was considered for each ingredient of the concretes, which means that the stages of construction, use and end-of-life were not taken into account. This boundary includes the analysis of raw materials extraction and processing (A1), their transport to the factory (A2), and the concrete production (A3). In addition, the system boundary was limited at raw material extraction and processing, since the transport of raw materials and the manufacturing process of the concretes were considered identical for the four concrete mixtures. Actually, according to Filippo *et al.* (2019), the raw material stage (A1) represents approximately 94% of the concrete environmental impact at the product stage.

The selection of the functional unit plays a relevant role in the performance of the environmental assessment, especially when products are compared. The functional units selected were a unit of concrete volume (1 m<sup>3</sup>) and a unit of functional performance, i.e. 1 m<sup>3</sup> per 1 MPa of indirect tensile strength (Table 8.1). According to Damineli *et al.* (2010), using a performance indicator as a functional unit allows avoiding the distinction between a material scale, where impacts are expressed in kg or m<sup>3</sup>, and a structural scale, where the effective volume to provide the function is used. In this case, the efficiency of concretes with different performances is better comparable, being being the environmental impact calculated by LCA visible in terms of environmental and economic benefits

The life cycle impact was assessed through the analysis of eight environmental impact categories required for EPD by EN 15804:2012+A1: Global warming potential (GWP) – Climate change, ozone depletion potential (ODP), photochemical ozone creation potential (POCP), acidification potential of land and water (AP), eutrophication potential (EP), abiotic depletion potential (two components: ADP - elements, ultimate reserves and ADP - fossil fuels), total non-renewable primary energy consumption (PE-NRe), and total renewable primary energy consumption (PE-Re). The first six impact categories were analyzed according to the method developed by the Institute of Environmental Sciences (CML - Centrum voor Milieuwetenschappen in Leiden) of the University of Leiden (Netherlands), one of the most commonly applied in practice (Guinée *et al.*, 2002). The last two impact categories (PE-NRe and PE-Re) were analyzed according to the Cumulative Energy Demand (CED) Method.

### **8.3.3 Life Cycle Inventory**

This stage of LCA involves the data collection of input and output of the life cycle phases considered. According to Muralikrishna and Manickam (2017), two types of data are distinguished, foreground and

background data. Foreground data refers to very specific data that generally come from industries. Background data is data for generic materials, energy, transport and waste management systems, typically found in databases and literature. Foreground data results in a more reliable life cycle inventory, however, is not always provided by the companies due to confidentiality issues. The EPD is another source to obtain high quality and suitable data, which are registered documents that provide information about the life cycle environmental impact of products and services with objectivity, comparability and credibility, making the information useful for fair comparisons between the environmental performances of products and services. The “cradle to gate” assessments are sometimes the basis for EPD (Muralikrishna and Manickam, 2017), which have identical system boundary of this LCA. The standards recommend extract data following the next order to get the most reliable LCA: 1° Industries; 2° EPDs; 3° Public data bases; 4° Environmental reports (ERs).

### **Raw materials**

The input data for LCA of RSF and ISF was provided by the suppliers (for confidentiality reasons, this data is not presented in this document), in terms of allocated energy and material consumptions, waste and transport, and their environmental impact was calculated with the OpenLCA software. The environmental impact of cement was obtained from the European Life Cycle Database (ELCD) denominated “ELCD 3.2: Portland cement (CEM I); CEMBUREAU production mix, at plant, CEMBUREAU technology mix, EN 197-1”. The environmental impact of fly ash and superplasticizer was obtained from International EPDs. The EPD of used fly ash is owned by BauMineral GmbH (Germany) since 2017 and refers to 1 ton hard coal fly ash from the coal-fired power station Maasvlakte, Block 3 near Rotterdam. The EPD of superplasticizer belongs to European Federation of Concrete Admixtures Associations Ltd. (EFCA, 2015). The LCA of the aggregates and water was obtained from scientific papers published in literature, since the EPDs of these materials were not available. The environmental impact of fine and coarse river sand and water was obtained using site-specific data adapted from a research study of Kurda *et al.* (2018). The LCA data of crushed granites was adapted by a site-specific data from a research study by Braga *et al.* (2017) in Portuguese companies. In Tables 8.4 and 8.5, the environmental impacts results for the production of 1 ton of each raw material are presented, obtained by CML and CED methods.

Table 8.4 – Baseline CML method results for raw materials (for 1 ton)

Raw Materials	GWP kg CO <sub>2</sub> -eq.	ODP kg CFC11-eq.	POCP kg ethen-eq.	AP kg SO <sub>2</sub> -eq.	EP kg PO <sub>4</sub> <sup>-3</sup> -eq.	ADP	
						Elements kg Sb-eq.	Fossil fuels MJ
RSF	54.74	8.63×10 <sup>-6</sup>	1.62×10 <sup>-2</sup>	3.27×10 <sup>-1</sup>	1.72×10 <sup>-2</sup>	1.36×10 <sup>-6</sup>	641.99
ISF	1095.88	7.97×10 <sup>-7</sup>	5.00×10 <sup>-1</sup>	2.98	3.07×10 <sup>-1</sup>	0	11370.00
CEM	903.23	4.37×10 <sup>-5</sup>	1.66×10 <sup>-1</sup>	2.21	2.59×10 <sup>-1</sup>	1.43×10 <sup>-5</sup>	3472.05
FA	0.20	1.21×10 <sup>-13</sup>	-1.36×10 <sup>-5</sup>	3.84×10 <sup>-4</sup>	6.50×10 <sup>-5</sup>	1.72×10 <sup>-9</sup>	2.08
W	0.26	3.01×10 <sup>-8</sup>	5.88×10 <sup>-5</sup>	1.31×10 <sup>-3</sup>	7.28×10 <sup>-4</sup>	5.83×10 <sup>-7</sup>	-
SP	1880.00	2.30×10 <sup>-7</sup>	2.12×10 <sup>-1</sup>	2.92	1.03	1.10×10 <sup>-3</sup>	29100.00
FS	1.73	0	1.25×10 <sup>-4</sup>	9.58×10 <sup>-3</sup>	2.49×10 <sup>-3</sup>	0	-
CS	4.56	2.33×10 <sup>-7</sup>	1.33×10 <sup>-3</sup>	6.22×10 <sup>-2</sup>	1.37×10 <sup>-2</sup>	6.56×10 <sup>-9</sup>	-
CG	24.40	2.43×10 <sup>-7</sup>	7.83×10 <sup>-3</sup>	1.44×10 <sup>-1</sup>	3.18×10 <sup>-2</sup>	1.09×10 <sup>-6</sup>	-

Table 8.5 – Cumulative Energy Demand (CED) results for raw materials (for 1 ton)

Raw Materials	PE-NRe MJ	PE-Re MJ
RSF	990.72	15.27
ISF	12100.00	219.28
CEM	4111.57	132.20
FA	2.08	2.99×10 <sup>-2</sup>
W	5.08	6.83×10 <sup>-1</sup>
SP	31400.00	1510.00
FS	17.60	0
CS	62.30	0
CG	344.00	3.81×10 <sup>-1</sup>

### 8.3.4 Life Cycle Impact Assessment

The LCA of the four fiber reinforced concretes considered (Table 8.3) were assessed by analyzing the above-mentioned environmental impact categories, as presented in Tables 8.6 and 8.7.

Table 8.6 – Baseline CML method results for 1 m<sup>3</sup> of concrete

Concrete	GWP kg CO <sub>2</sub> -eq.	ODP kg CFC11-eq.	POCP kg ethen-eq.	AP kg SO <sub>2</sub> -eq.	EP kg PO <sub>4</sub> <sup>-3</sup> -eq.	ADP	
						Elements kg Sb-eq.	Fossil fuels MJ
RSFRC1%	397.24	1.85×10 <sup>-5</sup>	7.47×10 <sup>-2</sup>	1.06	1.42×10 <sup>-1</sup>	1.45×10 <sup>-5</sup>	1647.42
ISFRC1%	479.22	1.79×10 <sup>-5</sup>	1.13×10 <sup>-1</sup>	1.27	1.65×10 <sup>-1</sup>	1.44×10 <sup>-5</sup>	2492.44
ISFRC0.3%	382.55	1.65×10 <sup>-5</sup>	7.93×10 <sup>-2</sup>	1.05	1.41×10 <sup>-1</sup>	7.92×10 <sup>-5</sup>	1546.15
ISFRC1%_2	453.41	1.71×10 <sup>-5</sup>	1.08×10 <sup>-1</sup>	1.22	1.57×10 <sup>-1</sup>	9.18×10 <sup>-6</sup>	2258.21

Table 8.7 – Cumulative Energy Demand (CED) results for 1 m<sup>3</sup> of concrete

<b>Concrete</b>	<b>PE-NRe MJ</b>	<b>PE-Re MJ</b>
RSFRC1%	2200.86	65.26
ISFRC1%	3076.83	81.34
ISFRC0.3%	2157.97	55.64
ISFRC1%_2	2848.15	71.38

As expected, for 1 m<sup>3</sup> of concrete, the RSFRC1% showed lower environmental impact than ISFRC1% with the same concrete matrix, especially on the environmental impact categories of GWP, PE-Re, PE-NRe, POCP and ADP-Fossil fuels, with an impact reduction of 17%, 20%, 28%, 34% and 34%, respectively. Comparing to “commercial mixtures” of ISFRC, the RSFRC1% showed also lower environmental impact than ISFRC with similar fiber volume content, ISFRC1%\_2 and slightly higher environmental impact than ISFRC0.3%.

For example, considering the application of recycled or industrial steel fibers in in a tetrapod for breakwaters made with 16 m<sup>3</sup> of concrete, each RSFRC1% tetrapod would present approximately less 1300 kg CO<sub>2</sub> equivalent in GWP impact, 250 MJ in PE-NRe and 14000 MJ in PE-Re than that of ISFRC1%.

#### **8.3.4.1 Global warming potential**

Global warming potential (GWP), also known as “Greenhouse effect”, is a measure of the amount of the “greenhouse gases” emitted to the atmosphere relative to carbon dioxide. At a global scale, the heat trapped by the greenhouse gases results in an increase of the global medium temperature, which further rises with the increase of the concentration of these gases. This global warming may results in several climate changes with significant influence in the ecosystems and human health, since it is responsible for several environmental impacts, such as polar melting, soil moisture loss, longer seasons, forest loss/change, and change in wind and ocean patterns (EPA, 2006; Farinha *et al.*, 2019).

For analyzed concretes, cement was the component that contributed the most to the global warming impact, being responsible for more than 75% of the GWP impact, as observed in Figure 8.4. The ISF also contributed at a smaller scale to this impact (about 18%), especially when were used in high volume percentage (ISFRC1% and ISFRC1%\_2). The remaining concrete ingredients had a negligible effect in the GWP impact (maximum 8%).

The RSFRC1% presented lower GWP impact than ISFRC with the same concrete matrix and fiber content (17% lower than ISFRC1% and 12% lower than ISFRC1%\_2). A slight lower GWP impact (almost 4%) was

obtained for ISFRC0.3% compared to RSFRC1% due to the lower content of cement in ISFRC0.3%. Therefore, this analysis is less valid, since RSFRC with similar composition and fiber content would lead to lower GWP impact, for the same expected mechanical and durability performance.

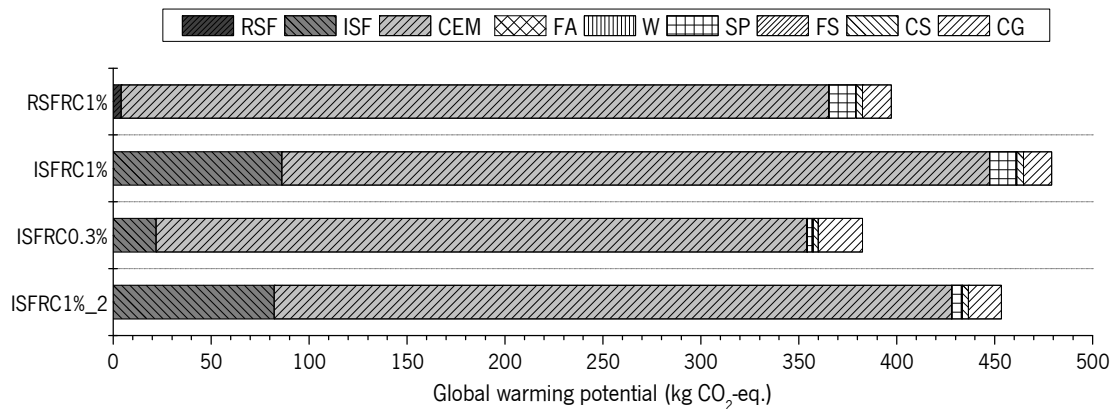


Figure 8.4 – Global warming potential impact

#### 8.3.4.2 Ozone Depletion Potential

The ozone depletion potential (ODP) gives the relative amount of degradation to the ozone layer in the atmosphere by Halocarbons (HCFCs). The depletion of the stratospheric ozone layer increases the vulnerability of the Earth's surface to the ultraviolet radiation, with a negative effect in the ecosystems and human health (Silvestre, 2012). However, as the HCFCs were already banned in Europe and in USA, the analysis of this environmental category is just indicative and does not have a significant influence on the assessment of the environmental sustainability (Farinha *et al.*, 2019).

The main contributor to the ODP impact was also the cement, representing 95% of the total ODP impact produced by the RSFRC1% and 98% of the total ODP impact produced by the remaining concretes (Figure 8.5). The production of RSF from end-of-life tire recycling had a higher ODP impact than the ISF production. Therefore, the RSFRC showed slightly higher ODP impact than ISFRC1% (about 3%). In this case, the incorporation of RSF in FRC, as alternative to ISF, was not beneficial for this environmental impact category.



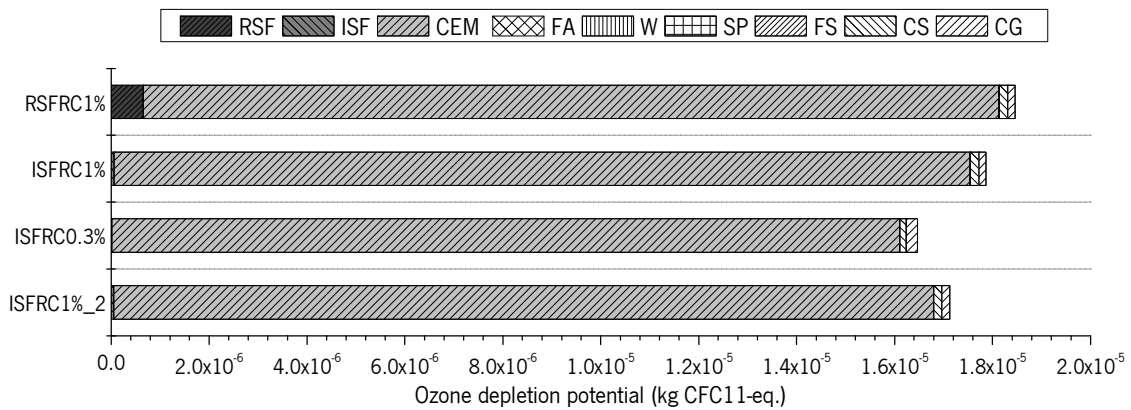


Figure 8.5 – Ozone depletion potential impact

### 8.3.4.3 Photochemical Ozone Creation Potential

Photochemical ozone creation potential (POCP), also known as summer smog, quantifies the relative abilities of volatile organic compounds (VOCs) to produce ground level ozone. The concentrations of ozone are higher in the summer and, due to its toxic nature, can directly affect human health and ecosystems disruption (Farinha *et al.*, 2019).

According to Figure 8.6, cement and ISF were the components that mostly contributed to the POCP impact in the concretes analyzed, increasing the concentration of ozone at the ground level. Cement was responsible for 89% of the POCP impact in RSFRC1% and from 59% to 77% in the ISFRC mixtures. The production of ISF had a significant contribution to POCP impact when used at high content (about 35% in ISFRC1% and ISFRC1%\_2).

The RSFRC1% presented lower POCP impact than all ISFRC mixtures, with a decrease between 6% and 34%.

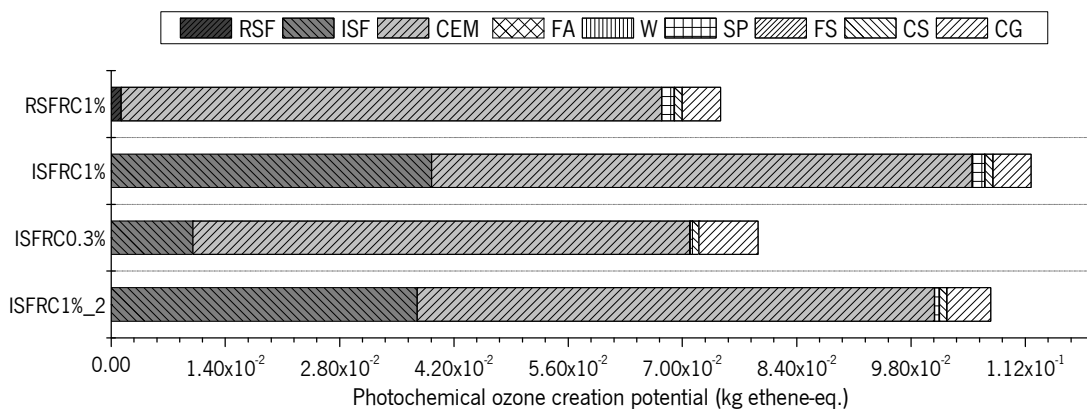


Figure 8.6 – Photochemical ozone creation potential impact

#### 8.3.4.4 Acidification Potential of Land and Water

Acidification Potential (AP) is a consequence of acids being emitted to the atmosphere and subsequently deposited in surface soils and waters. The main gases responsible for acidification are produced by the combustion of fossil fuels, and cause a wide range of impacts on soil, ground and surface water, organisms, ecosystems, and materials (EPA, 2006; Silvestre, 2012).

Figure 8.7 shows the total impact of the analyzed concretes in the AP impact category. The AP impact produced by the concretes was influenced mainly by cement and ISF. In RSFRC1%, the impact of cement was around 83% while in ISFRC1% was 70% of the total. The production of ISF had a significant contribution to AP impact (about 18% in ISFRC1% and ISFRC1%\_2). For this reason, the total AP impact was lower in RSFRC1% compared to ISFRC1%.

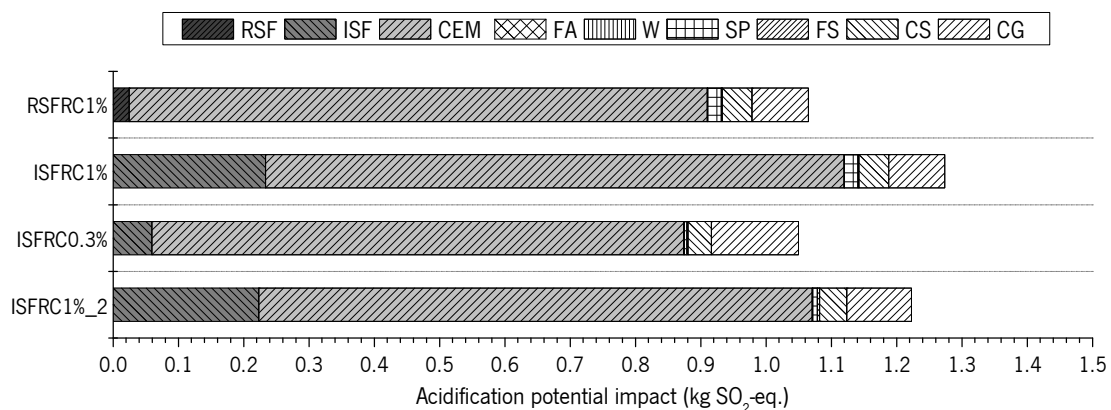


Figure 8.7 – Acidification potential impact

#### 8.3.4.5 Eutrophication Potential

Eutrophication is often induced by the discharge of mainly nitrogen and phosphorus from polluting emissions, wastewater and fertilizers, originating the enrichment with minerals and nutrients of a body of water (aquatic environment), which induce excessive growth of algae and plants. This process may result in oxygen depletion of the water body, and causes the contamination of plants and groundwater in terrestrial eutrophication (EPA, 2006).

Figure 8.8 presents the impacts produced by each concrete in the Eutrophication Potential (EP) environmental impact category. Similar to AP impact, the EP impact was mainly influenced by cement (73% in RSFRC1% and 63% in ISFRC1%). The total EP impact was lower in RSFRC1% compared to ISFRC1% due to the higher influence of ISF production compared to RSF (about 15% in ISFRC1% and ISFRC1%\_2).

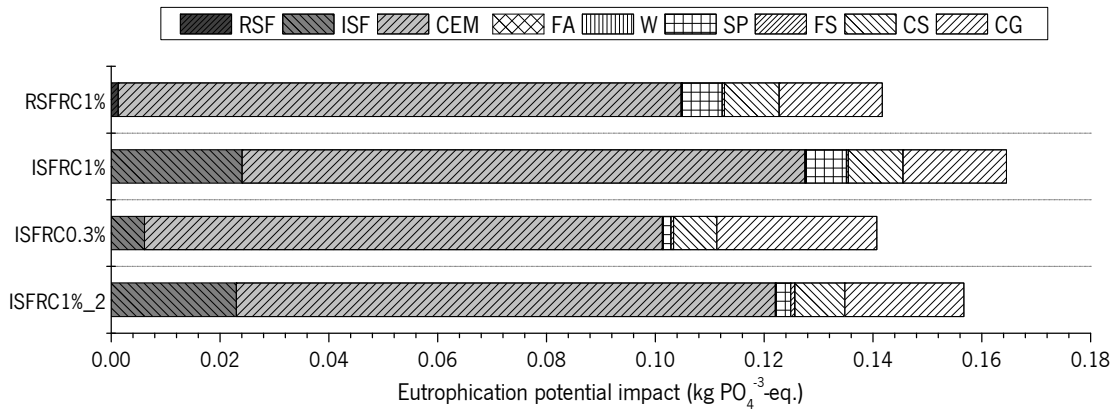


Figure 8.8 – Eutrophication potential impact

### 8.3.4.6 Abiotic Depletion Potential

Abiotic depletion potential (ADP) refers to the depletion of nonliving (abiotic) natural resources such as minerals and fossil fuels. This environmental category is divided in two components: a material component, *ADP – Elements* for non-fossil resources (in kg Sb equivalent) and an energy component, *ADP – Fossil fuels* for fossil resources (in MJ).

#### ADP-Elements

Cement and superplasticizer were the constituents with higher influence on the ADP impact category (Figure 8.9). The cement and the superplasticizer were responsible for about 40% and 55%, respectively, of the total impacts of RSFRC1% and ISFRC1%. In ISFRC0.3% and ISFRC1%\_2, a lower impact of this category was obtained due to the lower content of superplasticizer (the SP was responsible for 20% of the total impacts in ISFRC0.3% and for 31% in ISFRC1%\_2). A very slight influence of RSF production was observed in ADP - Elements impact category, which caused a slight increase of the total impact of RSFRC1% compared to ISFRC1%.

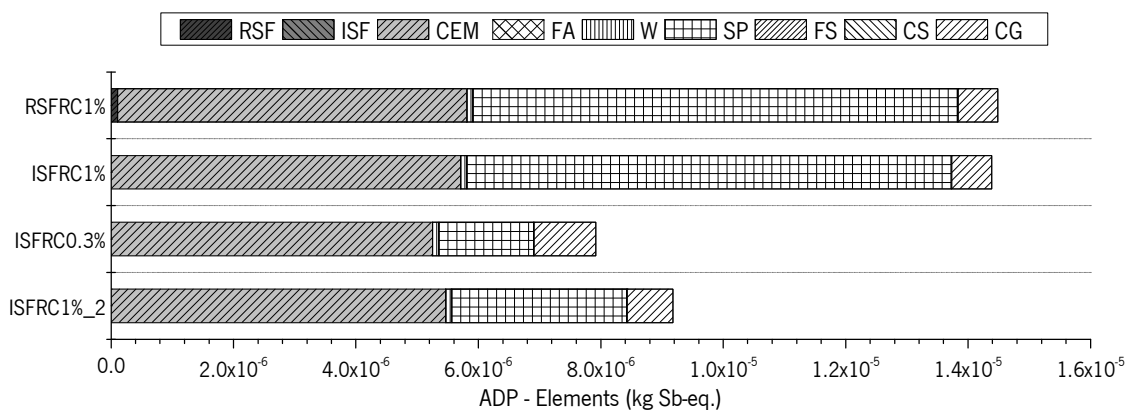


Figure 8.9 – ADP - Elements

### **ADP-Fossil fuels**

In this environmental impact category, the concretes' constituents that most contribute were cement and ISF (Figure 8.10). The cement was responsible for 56% to 84% of the total impact. The ISF production in a volume content of 1% greatly contributes to this environmental impact category compared to RSF production, being about 36% in ISFRC1% and 38% in ISFRC1%\_2. The RSFRC1% showed a total ADP-fossil fuels impact 34% lower than ISFRC1% and 32% lower than ISFRC1%\_2. However, due to the higher content of superplasticizer, the RSFRC1% showed a slightly higher total impact of ADP-fossil fuels than ISFRC0.3% (around 7%).

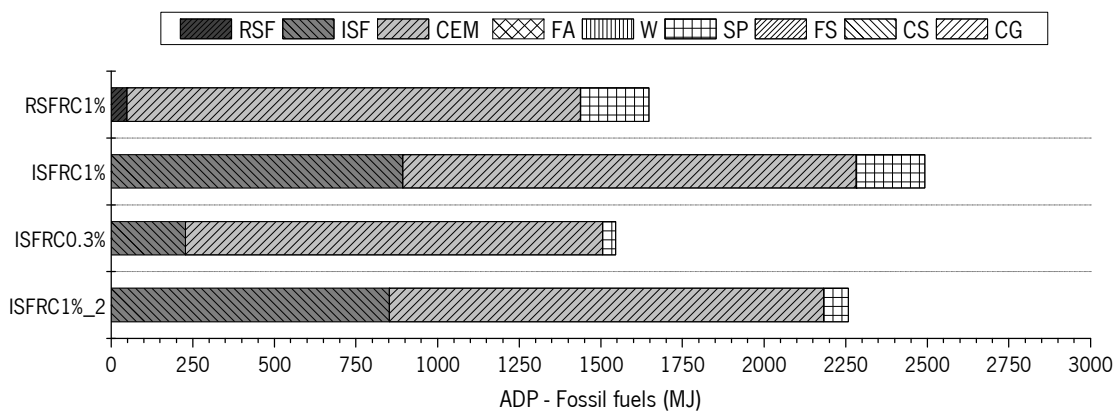


Figure 8.10 – ADP-Fossil fuels impact

#### **8.3.4.7 Use of Non-renewable Primary Energy Resources**

The non-renewable primary energy (PE-NRe) is produced by resources that cannot be replenished on human time scale (EN 15804:2012+A1). Figure 8.11 presents the PE-NRe impacts produced by each analyzed concrete composition. Cement was responsible for 53% to 75% of the total PE-NRe impacts. The production of ISFRC with 1% of ISF in concrete volume had a significant contribution for the total PE-NRe impact of ISFRC1% (around 32%), similar to the influence of ISF in the previous environmental impact categories, GWP, POCP and ADP – Fossil fuels. The amounts of superplasticizer and crushed granite were the main responsible for the remaining PE-NRe impact of the concretes. The RSFRC1% showed lower PE-NRe impact than ISFRC1% and ISFRC1%\_2 and slightly higher PE-NRe impact than ISFRC0.3%.

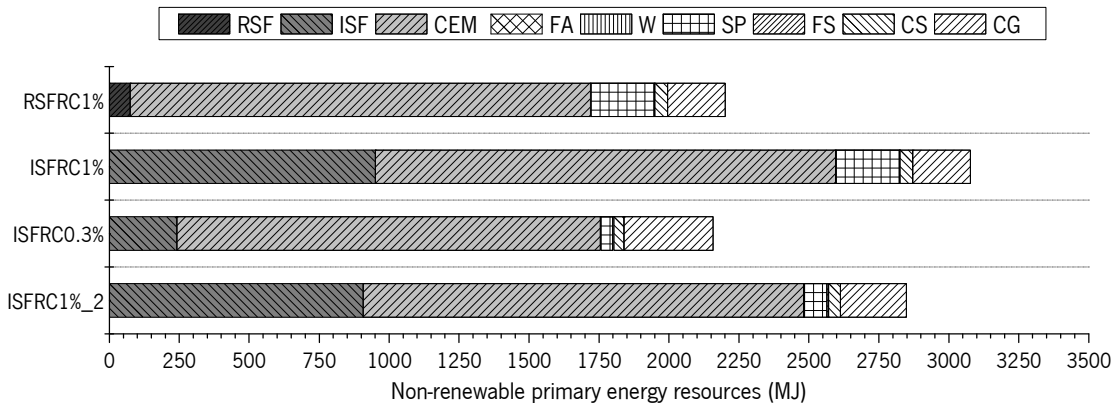


Figure 8.11 – Non-renewable primary energy (PE-NRe) resources impact (in MJ)

### 8.3.4.8 Use of Renewable Primary Energy Resources

The renewable primary energy (PE-Re) comes from renewable sources (typically non-fossil sources) that grown naturally, are replenished or cleansed on a human time scale (EN 15804:2012+A1).

ISF, cement and superplasticizer productions were the components that most influenced the PE-Re impact, as observed in Figure 8.12. ISF production is responsible for more than 20% of the total PE-Re impact in ISFRC1% and ISFRC1%\_2. The cement was the component with more renewable energy consumption (from 65% to 87% of the total renewable energy spent). The superplasticizer was responsible for 17% of the total PE-Re impact in RSFRC1% and for 13% in ISFRC1%.

The concrete with less PE-Re impact was ISFRC0.3% with around 15% less impact than RSFRC1%. The RSFRC1% showed a reduction of energy spent of more than 24% than ISFRC1% and more than 9% than ISFRC1%\_2.

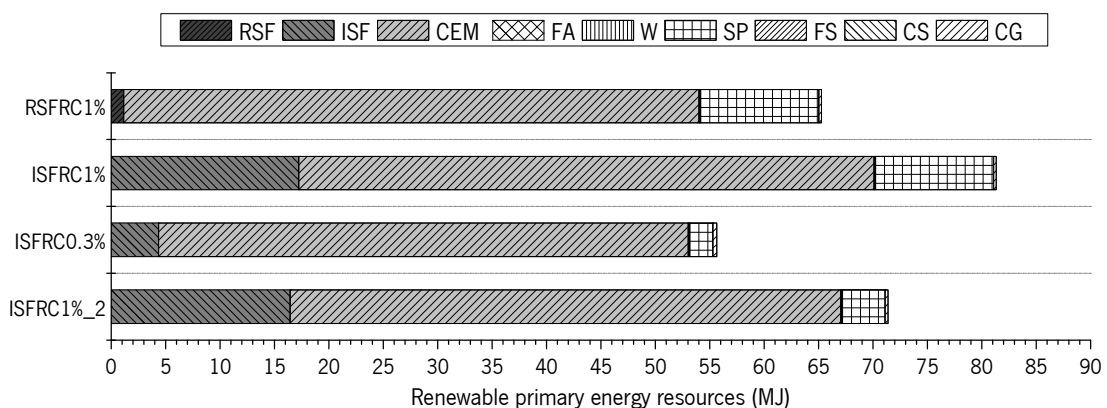


Figure 8.12 – Renewable primary energy resources impact

The results obtained for the environmental impact categories, considering the functional unit of 1 MPa of indirect tensile strength are presented in Tables 8.8 and 8.9. These results were obtained by dividing the impact values presented in Tables 8.6 and 8.7 for RSFRC1% and ISFRC1% by the maximum splitting tensile strength of these concretes (Table 8.1).

In general, for 1 MPa of indirect tensile strength, the RSFRC1% showed similar or lower environmental impact than ISFRC1% for the impact categories obtained by baseline CML method (Table 8.8). Regarding the results obtained for the cumulative energy demand, the RSFRC1% showed an PE-NRe impact lower than ISFRC1%. For PE-Re impact, the RSFRC1% is comparable to ISFRC1%.

Table 8.8 – Baseline CML method results for 1 MPa of indirect tensile strength

Concrete	GWP kg CO <sub>2</sub> -eq.	ODP kg CFC11-eq.	POCP kg ethen-eq.	AP kg SO <sub>2</sub> -eq.	EP kg PO <sub>4</sub> <sup>-3</sup> -eq.	ADP	
						Elements kg Sb-eq.	Fossil fuels MJ
RSFRC1%	106.21	4.94 × 10 <sup>-6</sup>	2.00 × 10 <sup>-2</sup>	0.39	6.21 × 10 <sup>-2</sup>	3.87 × 10 <sup>-6</sup>	440.49
ISFRC1%	116.88	4.36 × 10 <sup>-6</sup>	2.75 × 10 <sup>-2</sup>	0.41	6.22 × 10 <sup>-2</sup>	3.51 × 10 <sup>-6</sup>	607.91

Table 8.9 – Cumulative Energy Demand (CED) results for 1 MPa of indirect tensile strength

Concrete	PE-NRe	PE-Re
	MJ	MJ
RSFRC1%	588.47	17.45
ISFRC1%	750.45	19.84

## 8.4 ECONOMIC BENEFITS OF RSFRC

According to the information provided by the suppliers of steel fibers, the RSF used in this research are about 30% cheaper than ISF.

Considering the application of RSFRC1% and ISFRC1% in structural elements subjected to chloride attack, as for example in a tetrapod for breakwaters made with 16 m<sup>3</sup> of concrete, savings of 400€ per each tetrapod is achieved in its production by using RSFRC1% over ISFRC1%.

## 8.5 CONCLUSIONS

The technical and environmental benefits of using RSFRC compared to ISFRC for application to structural elements were investigated in this chapter. The technical benefits were evaluated by performing double

edge wedge splitting tests (DEWSTs) and round panel tests (RPTs) to assess the post-cracking behavior of RSFRC compared to ISFRC with the same concrete matrix. The environmental impacts of RSFRC and ISFRC were evaluated using Life Cycle Assessment (LCA) methodology by baseline CML (Institute of Environmental Sciences) and CED (Cumulative Energy Demand) methods, limited at raw material extraction and processing. In addition, the economic benefits of using RSF as an alternative to ISF for concrete reinforcement is also addressed. From this research, the main conclusions obtained are:

- 1) From DEWSTs, RSFRC produced with 1% of RSF by volume of concrete (RSFRC1%) presented similar indirect tensile strength and post-cracking behavior than ISFRC produced with the same concrete matrix and 1% of ISF by volume of concrete (ISFRC1%). The irregular character of RSF geometry made difficult to distribute homogeneously the fibers into RSFRC1%, compared to ISFRC1% where a uniform fiber distribution was guaranteed. However, the fiber distribution in RSFRC1% specimens did not influence the indirect tensile strength and post-cracking behavior of the concrete, compared to ISFRC1% specimens.
- 2) From RPTs, the RSFRC1% showed higher flexural capacity and energy absorption performance than ISFRC1%, probably due to the higher aspect ratio and number of RSF.
- 3) Based on the LCA results, the reduction of the environmental impact of the production of 1 ton of RSF compared to ISF is clear for almost all environmental impact categories analyzed.
- 4) For 1 m<sup>3</sup> of concrete, the RSFRC1% showed lower environmental impact than ISFRC1% with the same concrete matrix, especially on the environmental impact categories of GWP, PE-Re, PE-NRe, POCP and ADP-Fossil fuels, with a corresponding lower impact of 17%, 20%, 28%, 34% and 34%, respectively. Comparing to “commercial mixtures” of ISFRC, the RSFRC1% showed also lower environmental impact than ISFRC for similar fiber volume content, ISFRC1%\_2 and slightly higher environmental impact than ISFRC0.3%.
- 5) Cement was the component that most contributed in all environmental impact categories analyzed for RSFRC and ISFRC. However, the ISF production also had a significant contribution to environmental impact when used at high content into concrete, namely in the impact categories of GWP, POCP, AP, EP, ADP-Fossil fuels, PE-NRe and PE-Re. The ADP-Elements impact was significantly influenced by the content of superplasticizer.
- 6) Considering the performance functional unit of 1 MPa of indirect tensile strength, the RSFRC1% showed similar or lower environmental impact than ISFRC1% for the impact categories obtained by baseline CML method. Regarding the results obtained for the cumulative energy demand, the

RSFRC1% showed an PE-NRe impact lower than ISFRC1%. For PE-Re impact, the RSFRC1% is comparable to ISFRC1%.

- 7) A significant economic benefit can be achieved when RSFRC1% is applied in large volumetric quantities to structural elements compared to the application of ISFRC1%.



---

# Chapter 9

---

## 9 CONCLUSIONS AND FUTURE PERSPECTIVES

### 9.1 MAIN CONCLUSIONS

The present thesis involves both experimental and analytical/numerical research regarding the behavior of Recycled Steel Fiber Reinforced Concrete (RSFRC) under chloride attack. The main purpose was to achieve, as much as possible, a consistent comprehension of the mechanical behavior and durability performance of this composite material under chloride environment. In addition, it was also intended to collect data for future calibration of analytical formulations and FEM-based numerical models in order to predict the long-term performance of RSFRC under aggressive chloride exposure conditions.

The experimental research covered two main fields: the first one dedicated to the technology of RSFRC manufacturing, and the second one dedicated to the investigation of RSFRC behavior under chloride environment.

#### **Technology of RSFRC manufacturing**

The first part of this research field included an experimental program dedicated to characterizing the recycled steel fibers (RSF) obtained from the recycling of end-of-life tires, used in this work for RSFRC production. This RSF characterization was detailed in terms of geometry, chemical composition and mechanical properties, and the results were compared with industrial steel fibers (ISF). Due to the recycling process, the used RSF have irregular shape with unimodal distribution of the fiber length and

aspect ratio, and multimodal distribution of the fiber diameter. When compared to ISF, RSF showed higher carbon content and tensile strength.

The used RSF were recovered by a shredding process of post-consumed truck tires, and the steel was separated from the rubber by an electromagnetic separator. Due to the shredding process, most of the RSF still contain some rubber particles attached on their surface, which may influence the mechanical properties of RSFRC. Therefore, in order to assess the influence of this attached rubber in the performance of RSF as concrete reinforcement and in its corrosion resistance, two distinct methods were adopted, manual polishing of the fiber surface, and pre-treatment of the fibers at high temperatures.

The influence of these pre-treatment methods in the micro-mechanical properties of RSF was assessed by nano-indentation tests. Monotonic fiber pull-out tests were performed to assess the RSF-concrete bond. Polishing of RSF was the most efficient method for removing the rubber particles from RSF surface, but too time consuming for industrial use of RSF. RSF showed more complex and heterogeneous microstructure and higher hardness than ISF. The heating of RSF at 350°C may have a negative effect on the ductility of concrete. The rubber content attached to the RSF surface had a minor effect in the pull-out behavior of RSF from concrete. The fiber shape of the embedded length had a significant influence in the fiber pull-out behavior.

The second part of this research field was dedicated to the assessment of the potentialities of RSF as concrete reinforcement. A sustainable mix composition of RSFRC was attained by using a packing density optimization method, with a fiber content of 1% in volume and 40% of binder volume replaced by fly ash. An experimental program was conducted to evaluate the mechanical properties of the developed RSFRC by three-point notched beam bending tests (3PNBBT) and compressive tests. The 3PNBBT results were also used to determine the fracture mode I parameters of the developed RSFRC by inverse numerical analysis. The experimental curves of the compressive behavior of RSFRC were simulated by analytical expressions.

The RSFRC showed higher flexural capacity and energy absorption than ISFRC1% for reduced crack width levels corresponding to serviceability limit states (SLS) conditions, and similar reinforcement performance for ultimate limit state (ULS) conditions. The agreement between the numerical and the experimental curves was very good for all the RSFRC1% beams, which indicates that the trilinear  $\sigma - \omega$  relationship obtained is able of simulating the post-cracking behavior of RSFRC1% representative of 3PNBBTs.

The effectiveness of RSF as concrete reinforcement was also confirmed by the increase of toughness observed in the compressive tests. The analytical expression proposed by MC2010 is appropriate to simulate the pre-peak compressive behavior of RSFRC1% and the non-linear fit methodology used by

Barros (1995) to simulate the uniaxial compressive behavior of FRC showed to be more appropriate to simulate the post-peak compressive behavior of RSFRC1% than the non-linear fitting method proposed by Cunha *et al.* (2008).

The technical benefits of using the developed RSFRC for application to structural elements were assessed at material level in comparison with Industrial Steel Fiber Reinforced Concrete (ISFRC). In this sense, 3PNBBTs, double edge wedge splitting tests (DEWSTs) and round panel tests (RPTs) were carried out with specimens of RSFRC and ISFRC, produced with equal concrete matrix and fiber content (1% in volume) in order to evaluate the indirect tensile strength and flexural toughness. From DEWSTs, RSFRC and ISFRC presented similar indirect tensile strength and post-cracking behavior. From 3PNBBTs and RPTs, RSFRC showed higher flexural capacity and energy absorption performance than ISFRC, probably due to the higher aspect ratio and number of RSF per concrete volume.

### **Corrosion susceptibility of RSFRC**

For structural elements exposed to chloride environments, an important aspect of RSFRC durability is the corrosion resistance. In this research field was intended to acquire new competences on corrosion susceptibility of RSF, and evaluate its effect on the post-cracking performance of pre-cracked and non pre-cracked RSFRC under long-term exposure to chloride environment.

Steel fibers corrosion displays itself most often in aqueous medium where the corrosive mechanism is essentially electrochemical. In this sense, an experimental program was carried out to characterize the corrosion resistance of RSF caused by chloride attack, based on Open Circuit Potential measurements, Potentiodynamic Polarization and Linear Polarization Resistance tests, and SEM analysis.

The electrochemical results of RSF were compared with those of ISF and revealed that the corrosion probability of RSF and ISF immersed in a 3.5 wt% NaCl solution is higher than 90%, and the RSF are slightly more susceptible to corrosion than ISF. The low amounts of small rubber debris attached to RSF surface had a negligible influence in terms of fiber corrosion resistance.

Additionally, some experiments were carried out to evaluate the corrosion rate of single RSF after exposure to chloride attack, as well as the corrosion effects on the direct tensile strength of RSF. The RSF subjected to continuous immersion in chloride solution showed uniform mass loss, while the RSF submitted to more aggressive dry-wet cycles in chloride solution showed uneven mass loss due to a localized corrosion action. The loss of tensile strength of RSF has increased with the exposure time in chloride solution.

The investigation of the impact of cracks on the corrosion initiation is important for understanding the mechanical behavior and durability performance of cracked RSFRC under chloride environments. An

innovative non-standard experimental fiber pull-out tests of RSF was adopted to investigate the corrosion effects of RSF on the fiber reinforcement mechanisms developed during the fiber pull-out from a cracked concrete specimen previously exposed to corrosive environment. Furthermore, the potentiality of using X-ray Micro-computed Tomography (3D- $\mu$ XCT) technique in this investigation was explored. From this study, no clear relationship was obtained between the corrosion susceptibility of RSF crossing a pseudo-crack in self-compacting concrete (SCC) and the crack width, for crack widths lower than 0.7 mm.

The corroded RSF from cracked specimens submitted to chloride attack showed higher variability in terms of cross section loss, probably due to the irregular geometry of the RSF that caused an irregular chloride attack at the exposed length of RSF in the crack and, consequently, variable susceptibility to fiber corrosion. Fiber failure occurred for most pull-out tests of RSF embedded in cracked SCC specimens after subjected to 10 days of immersion in 3.5 wt% NaCl solution. The 3D- $\mu$ XCT showed to be a promising technique to monitor, with high accuracy, the crack width at fiber level, the fiber diameter, the fiber slip and the specimen porosity during these fiber pull-out tests.

The post-cracking behavior of uncracked RSFRC exposed to chloride immersion was investigated from DEWSTs. The influence of the small amount of rubber particles attached to RSF surface and the long-term effects of chloride immersion were studied. The fiber distribution and orientation at crack surfaces were evaluated by image analysis. After 10 days, and 3 and 6 months of chloride immersion in 3.5 wt% NaCl solution, no significant signs of RSF corrosion were observed on the fracture surface of RSFRC splitting specimens. However, corrosion spots were observed at exposed surfaces of all specimens. The small content of rubber particles attached to RSF surface had a negligible effect in the post-cracking tensile behavior of RSFRC. The average splitting tensile stress-CMOD curves obtained for the RSFRC specimens and its corresponding fiber distribution analysis revealed a negligible effect of chloride attack after 10 days and 3 months of chloride exposure, and a detrimental effect of chloride attack after 6 months of immersion. Additionally, the tensile stress-crack width relationship and mode I fracture parameters of the tested RSFRC were determined by performing inverse numerical analysis of the DEWSTs results with a nonlinear 2D finite element model.

An experimental program was also carried out to evaluate the effects of chloride attack on the load carrying capacity of round panels made of RSFRC. The influence of the crack width, the chloride exposure period, the panel's thickness and the fiber distribution/orientation profile was investigated on the force-deflection and energy dissipation responses obtained in round panel tests (RPTs). The results were compared to those of reference panels submitted to water immersion. In addition, an inverse analysis

methodology was carried out for deriving the tensile stress-crack width relationship and mode I fracture parameters of the RSFRC1% representative of the RPT-3ps.

Surface corrosion has occurred on the RSFRC panels after 10 days of immersion and 3 months of dry-wet cycles in chloride solution. For pre-cracked RSFRC panels with crack widths up to 1 mm, the cracked surfaces were completely penetrated by chlorides during the immersion period, and corrosion products were visible in the RSF located in the cracked surfaces, mainly near the exposure faces of the panels.

From experimental and numerical results, the chloride attack for 10 days of immersion had a small beneficial effect on the post-cracking behavior of pre-cracked RSFRC panels with crack widths up to 1 mm, while for 3 months of dry-wet chloride cycles, a negligible effect of chloride attack was observed. For uncracked RSFRC, no significant influence of the chloride immersion for 10 days was verified on post-cracking behavior, whereas the dry-wet cycles in chloride solution for 3 months showed a slight negative effect in the post-cracking load carrying capacity. The dispersion of the results obtained are mainly justified by the irregularity of fiber geometry, and by the differences in panel's thickness and fiber distribution and orientation at crack surfaces. A significant and similar percentage of fibers failed by rupture in chloride attacked and reference panels, which is indicative of a negligible effect of chloride environment. In general, it can be concluded that uncracked RSFRC was not significantly affected by chloride attack.

Additionally, the long-term chloride-induced RSF corrosion depth of an uncracked structural element made with RSFRC was estimated based on a simplified prediction of the critical chloride content for the specific environmental conditions considered in performed tests. The predicted critical chloride penetration depth into a RSFRC structural element was only about 11 mm after exposed to dry-wet cycles in a 3.5 wt.% NaCl solution for 100 years. Therefore, it is concluded that RSF corrosion in uncracked concrete should be essentially a surface phenomenon.

### **Life Cycle Impact Assessment of RSFRC**

The environmental benefits of using the developed RSFRC for application to structural elements have been assessed at material level by using Life Cycle Assessment (LCA) methodology. The LCA results showed a clear reduction of the environmental impact of the RSF production compared to ISF production. In the same way, the RSFRC showed lower environmental impact than ISFRC with the same concrete matrix, considering the functional units of 1 m<sup>3</sup> of concrete and 1 MPa of indirect tensile strength. A significant economic benefit can be achieved when RSFRC1% is applied in large volumetric quantities to structural elements compared to the application of ISFRC1%.

## 9.2 RECOMMENDATIONS FOR FUTURE RESEARCH

The work conducted in this thesis can be further developed, and the following list of recommendations are proposed for future research:

- Further experimental program for a more comprehensive assessment of the long-term effects of chloride attack in pre-cracked and non pre-cracked RSFRC by adopting longer exposure periods for chloride environment, namely for continuous immersion (> 6 months) and dry-wet cycles (> 3 months) in chloride solution.
- More accurate determination of the critical chloride content and corrosion rate of RSF for concretes with distinct compositions under different chloride exposure environments.
- Further research to improve the fiber pull-out test configuration proposed in Section 5.4 in order to obtain the fiber pull-out load-end slip response under corrosion action and for distinct crack width levels by using X-Ray Micro-computer Tomography. These experimental pull-out load-slip responses can be used to predict the local bond stress-slip relationship developed in RSFRC under fiber corrosion conditions by numerical analysis.
- Prediction of the load carrying capacity of a structural element under chloride attack, like a breakwater element, produced with the developed RSFRC in comparison with one produced with ISFRC and plain concrete, supported on advanced numerical modelling that considers thermo-hygro-chemical-mechanical phenomena.
- Assessment of the long-term corrosion resistance of cracked and uncracked RSFRC exposed to carbonation action.
- Assessment of the post-cracking behavior and durability performance of RSFRC under natural chloride environment.
- Development of an analytical model to evaluate the influence of chloride attack on the post-cracking behavior of RSFRC structures.

---

# Chapter 10

## 10 REFERENCES

- Abdul Awal, A.S.M.; Lim Lion Yee; Zakaria Hossain, M. (2013). *Fresh and hardened properties of concrete containing steel fibre from recycled tire*. Malaysian Journal of Civil Engineering, 25(1), 20-32.
- Abraham, E., Cherian, B.M.; P A, E.; Pothen, L.A.; Thomas, S. (2011). *Recent advances in the recycling of rubber waste*. Chapter 2 in book "Recent developments in Polymer Recycling", Transworld Research Network, Eds: A. Fainleib; O. Grigoryeva, 47-100.
- Abrishambaf, A. (2015). *Creep Behaviour of Cracked Steel Fibre Reinforced Self-Compacting Concrete Laminar Structures*. Doctoral Thesis, Department of Civil Engineering, School of Engineering of the University of Minho, Guimarães, Portugal.
- Abrishambaf, A.; Cunha, V.M.C.F.; Barros, J.A.O. (2015a). *The influence of fibre orientation on the post-cracking tensile behaviour of steel fibre reinforced self-compacting concrete*. Fracture and Structural Integrity, 31, 38-53.
- Abrishambaf, A.; Barros, J.A.O.; Cunha, V.M.C.F. (2015b). *Tensile stress-crack width law for steel fibre reinforced self-compacting concrete obtained from indirect (splitting) tensile tests*. Cement and Concrete Composites, 57, 153-165.
- Abrishambaf, A.; Barros, J.A.O.; Cunha, V.M.C.F. (2015c). *Time-dependent flexural behaviour of cracked steel fibre reinforced self-compacting concrete panels*. Cement and Concrete Research, 72, 21-36.
- Abrishambaf, A.; Barros, J.A.O.; Cunha, V.M.C.F.; Frazão, C. (2017). *Time dependent behaviour of fibre pull-out in self-compacting concrete*. Cement and Concrete Composites, 77, 14-28.
- ACI 544.1R-96, (2009). *State-of-the-Art Report on Fiber Reinforced Concrete*. Reported by American Concrete Institute, Committee 544, Farmington Hills, MI.
- ACI 544.5R-10, (2010). *Report on the Physical Properties and Durability of Fiber-Reinforced Concrete*. ACI Committee 544, USA.
- Ahmadi, M.; Farzin, S.; Hassani, A.; Motamedi (2017). *Mechanical properties of the concrete containing recycled fibers and aggregates*. Construction and Building Materials, 144, 392-398.
- Aiello, M.A.; Leuzzi F.; Centonze, G.; Maffezzoli, A. (2009). *Use of steel fibers recovered from waste tyres as*

- reinforcement in concrete: Pull-out behaviour, compressive and flexural strength*. Waste Management, 29, 1960-1970.
- Aiello, M.A.; Leuzzi, F. (2010). *Waste tyre rubberized concrete: Properties at fresh and hardened state*. Waste Management, 30, 1696–1704.
- Alizade, E.; Alaei, F.J.; Zabihi, S. (2016). *Effect of steel fiber corrosion on mechanical properties of steel fiber reinforced concrete*. Asian Journal of Civil Engineering, 17(2), 147-158.
- Alonso, C.; Andrade, C. (1990). *Effect of nitride as a corrosion inhibitor in contaminated and chloride-free carbonated mortars*. ACI Materials Journal, 87(2), 130–137.
- Alsaif, A.; Bernal, S.A.; Guadagnini, M.; Pilakoutas, K. (2018). *Durability of steel fibre reinforced rubberised concrete exposed to chlorides*. Construction and Building Materials, 188, 130-142.
- Alwan, J.M.; Naaman, A.E. and Hansen, W. (1991). *Pull-Out Work of Steel Fibers From Cementitious Composites: Analytical Investigation*. Cement and Concrete Composites, 13, 247-255.
- Angelakopoulos, H.; Waldron, P. (2015). *Tyre Wire in Concrete Leading to Environmental Sustainability*. CIP Eco-innovation project, Twincletoes project - Layman's report, Twincon Ltd, Sheffield, UK.
- Angst, U.; Elsener, B.; Larsen, C.K.; Vennesland, Ø. (2009). *Critical chloride content in reinforced concrete – A review*. Cement and Concrete Research, 39, 1122-1138.
- Antoniou, N.; Zabaniotou, A. (2013). *Features of an efficient and environmentally attractive used tyres pyrolysis with energy and material recovery*. Renewable and Sustainable Energy Reviews, 20, 539–558.
- Aperador-Chaparro, W.; Carrillo, J.; Cárdenas-Pulido, J. (2017). *Effect of Chloride Ion on the Durability Properties of RC-65/35-BN Steel Fiber Reinforced Concrete*. Ingeniería. Investigación y Tecnología, 18(2), 139-147.
- ASM International (2002). *Atlas of Stress-Strain Curves*. 2<sup>nd</sup> Edition, Moosbrugger, C. (Technical Editor), 816 pages.
- ASTM C496/C496M-11 (2011). *Standard Test Method for Splitting Tensile Strength of Cylindrical concrete specimens*. ASTM International, USA.
- ASTM C876-15 (2015). *Standard Test Method for Corrosion Potentials of Uncoated Reinforcing Steel in Concrete*. ASTM International, 1-8.
- ASTM C1437-07 (2007). *Standard Test Method for Flow of Hydraulic Cement Mortar*. ASTM International, USA.
- ASTM C1550-08 (2008). *Standard Test Method for Flexural Toughness of Fiber Reinforced Concrete (Using Centrally Loaded Round Panel)*. ASTM International, USA.
- ASTM C1556-03 (2003). *Standard Test Method for Determining the Apparent Chloride Diffusion Coefficient of Cementitious Mixtures by Bulk Diffusion*. ASTM International, USA.
- ASTM C1609/C1609M-12 (2012). *Standard Test Method for Flexural Performance of Fiber-Reinforced Concrete (Using Beam With Third-Point Loading)*. American Society for Testing and Materials (ASTM), USA.
- ASTM G3-89 (Reapproved 1999). *Standard Practice for Conventions Applicable to Electrochemical Measurements in Corrosion Testing*. ASTM International, USA.
- ASTM G59-97 (2014). *Standard Test Method for Conducting Potentiodynamic Polarization Resistance Measurements*. ASTM International, 1-4.
- Athanassiades, E. (2013). *Waste tyre pyrolysis: Sustainable recovery and reuse of a valuable resource*. Doctoral Thesis, Department of Civil and Environmental Engineering, Imperial College London, UK.
- Azenha M.; Sena Cruz J.; Camões A.; Ferreira, R.M. (2011). *Numerical simulation of the structural behaviour of concrete tetrapods subject to imposed deformations and applied loads*. In Proceedings of the Congress on Numerical Methods in Engineering, 14-17 June, Coimbra, 16 pages.
- Azevedo, A.F.M.; Barros, J.A.O.; Sena-Cruz, J.M.; Gouveia, A.V. (2003). *Software in structural engineering education and design*. In Proceedings of III Portuguese-Mozambican Conference of Engineering, 19-21 August, Mozambique, 81-92.



- Azevedo, F.; Pacheco-Torgal, F.; Jesus, C.; Barroso de Aguiar, J.L.; Camões, A.F. (2012). *Properties and durability of HPC with tyre rubber wastes*. Construction and Building Materials, 34, 186-191.
- Babut, R. (1986). *Structural investigation of steel fibre reinforced concrete*. In *Fracture mechanics and structural aspects of concrete*. Heron, 31(2), 15-44.
- Bakker, P.; Berge, A. van den; Hakenberg, R.; Klabbbers, M.; Muttray, M.; Reedijk, B.; Rovers, I. (2003). *Development of concrete breakwater armour units*. In Proceedings of 1<sup>st</sup> Coastal, Estuary and Offshore Engineering Specialty Conference of the Canadian Society for Civil Engineering, 4-7 June, Moncton, Nouveau-Brunswick, Canada, 12 pages.
- Baldenebro-Lopez, F.J.; Gomez-Esparza, C.D.; Corral-Higuera, R.; Arredondo-Rea, S.P.; Pellegrini-Cervantes, M.J.; Ledezma-Sillas, J.E.; Martinez-Sanchez, R.; Herrera-Ramirez, J.M. (2015). *Influence of Size on the Microstructure and Mechanical Properties of an AISI 304L Stainless Steel - A Comparison between Bulk and Fibers*. Materials 8(2), 451-461.
- Balouch, S.U.; Forth, J.P.; Granju, J.-L. (2010). *Surface corrosion of steel fibre reinforced concrete*. Cement and Concrete Research, 40, 410-414.
- Barros, J.A.O. (1995). *Comportamento do betão reforçado com fibras. Análise experimental e simulação numérica. Behavior of fiber reinforced concrete. Experimental analysis and numerical simulation*. Doctoral Thesis, Faculty of Engineering, University of Porto, Portugal. [in Portuguese]
- Barros, J.A.O.; Figueiras, J.A. (1999). *Flexural Behavior of SFRC: Testing and Modeling*. Journal of Materials in Civil Engineering, 11(4), 331-339.
- Barros, J.A.; Cunha, V.M.; Ribeiro, A.F.; Antunes, J.A. (2005). *Post-cracking behaviour of steel fibre reinforced concrete*. Materials and Structures, 31(1), 47-56.
- Barros J.; Pereira E.; Santos S. (2007). *Lightweight panels of steel fibre reinforced self-compacting concrete*. Journal of Materials in Civil Engineering, 19(4), 295-304.
- Barros, J.A.O.; di Prisco, M.; di Prisco, C. (2009). *Modelling FRC Infrastructures taking into account the soil-structure interaction*. In Proceedings of the Congress on Numerical Methods in Engineering 2009, 29 Jun-2 Jul, Barcelona, Spain.
- Barros, J.A.O.; Taheri, M.; Salehian, H.; Mendes, P.J.D. (2012). *A design model for fibre reinforced concrete beams prestressed with steel and FRP bars*. Composite Structures, 94, 2494-2512.
- Barros, J.; Lourenço, L.; Soltanzadeh, F.; Taheri M. (2013). *Steel fibre reinforced concrete for elements failing in bending and in shear*. Advances in Concrete Construction, 1(1), 1-27.
- Barros, J.A.O.; Moraes Neto, B.N.; Melo, G.S.S.A.; Frazão, C.M.V. (2015a). *Assessment of the effectiveness of steel fibre reinforcement for the punching resistance of flat slabs by experimental research and design approach*. Composites Part B, 78, 8-25.
- Barros, J.A.O.; Taheri, M.; Salehian, H. (2015b). *A model to simulate the moment-rotation and crack width of FRC members reinforced with longitudinal bars*. Engineering Structures, 100, 43-56.
- Barros, J.A.O.; Frazão, C.; Caggiano, A.; Folino, P.; Martinelli, E.; Xargay, H.; Zamanzadeh, Z.; Lourenço, L. (2017). *Cementitious Composites Reinforced with Recycled Fibres*. Chapter 8 in book "Recent Advances on Green Concrete for Structural Purposes – The Contribution of the EU-FP7 Project EnCoRe", Springer book, Eds: J.A.O. Barros; L. Ferrara; E. Martinelli, 141-195.
- Barros and Foster (2018). *An integrated approach for predicting the shear capacity of fibre reinforced concrete beams*. Engineering Structures, 174, 346-357.
- Basto, C.A.A.; Barros, J.A.O. (2008). *Numeric Simulation of Sections Submitted to Bending*. Technical report 08-DEC/E-46, Dep. of Civil Engineering, School of Engineering, University of Minho, 73 pages.
- BauMineral GmbH (2017). *Environmental Product Declaration (EPD) Report. EFA-füller® MR3*. BCS Öko-Garantie GmbH – Ecobility Experts, Germany.
- Bdour, A.N. and Al-Khalayleh, Y.A. (2010). *Innovative Application of Scrap-tire Steel Cords in Concrete Mixes*.

- Jordan Journal of Civil Engineering, 4(1), 55-61.
- Bentur, A.; Mindess, S. (2007). *Fibre Reinforced Cementitious Composites*. 2<sup>nd</sup> Edition, Taylor & Francis, London, UK and New York, USA.
- Bentur A.; Berke N.; Diamond S. (1997). *Steel Corrosion in Concrete: Fundamentals and Civil Engineering Practice*. First Edition, CRC Press, London, UK, 202 pages.
- Bernard, E.S. (2004). *Durability of cracked fibre reinforced shotcrete*. Shotcrete: More Engineering Developments. In Proceedings of the Second International Conference on Engineering, Eds: E.S. Bernard, CRC Press, Cairns, Queensland, Australia, 8 pages.
- Bernard, E.S.; Xu, G.G. (2008). *The Effect of Radial Crack Locations in Load Resistance in C1550 Panel Tests*. Journal of ASTM International, 5(10), 1-14.
- Berrocal, C.; Lundgren, K.; Löfgren, I. (2013). *Influence of steel fibres on corrosion of reinforcement in concrete in chloride environments: A review*. In Proceedings of the International Conference: FC2013-Fiber Concrete 2013, 12-13 September, Prague, Czech Republic.
- Berrocal, C.G. (2015). *Chloride Induced Corrosion of Steel Bars in Fiber Reinforced Concrete*. Thesis for the degree of Licentiate of Engineering, Department of Civil and Environmental Engineering, Chalmers University of Technology, Göteborg, Sweden.
- Berrocal, C.G.; Lundgren, K.; Löfgren, I. (2016). *Corrosion of steel bars embedded in fibre reinforced concrete under chloride attack: State of the art*. Cement and Concrete Research, 80, 69-85.
- Bertolini, L.; Elsener, B.; Pedeferri, P.; Polder, R.P. (2004). *Corrosion of Steel in Concrete - Prevention, Diagnosis, Repair*. 1<sup>st</sup> edition, Wiley-VCH, Weinheim, Germany.
- Blanco, A.; Pujadas, P.; Cavalaro, S.; de la Fuente, A.; Aguado, A. (2014). *Constitutive model for fibre reinforced concrete based on the Barcelona test*. Cement and Concrete Composites, 53, 327-340.
- Bogas, J. (2011). *Characterization of structural lightweight expanded clay aggregate concrete*. Doctoral Thesis, Instituto Superior Técnico, University of Lisboa, Portugal.
- Boudaoud, Z.; Beddar, M. (2012). *Effects of Recycled Tires Rubber Aggregates on the Characteristics of Cement Concrete*. Open Journal of Civil Engineering, 2, 193-197.
- Braga, A.M.; Silvestre, J.D.; Brito, J. de (2017). *Compared environmental and economic impact from cradle to gate of concrete with natural and recycled coarse aggregates*. Journal of Cleaner Production, 162, 529-543.
- Bravo, M.; de Brito, J. (2012). *Concrete made with used tyre aggregate: durability-related performance*. Journal of Cleaner Production, 25, 42-50.
- Broitman, E. (2017). *Indentation Hardness Measurements at Macro-, Micro-, and Nanoscale: A critical Overview*. Tribology Letters, 65:23.
- Brooks, C.R. (1999). *Principles of Heat Treatment of Plain Carbon and Low-Alloy Steels*. ASM International, USA.
- Buratti, N.; Mazzotti, C.; Savoia, M. (2010). *Long-term behaviour of cracked SFRC beams exposed to aggressive environment*. In Proceedings of IA-FraMCoS - Fracture Mechanics of Concrete and Concrete Structures - High Performance, Fiber Reinforced Concrete, Special Loadings and Structural Applications, Eds: B.H. Oh *et al.*, 23-28 May, Jeju, Korea.
- Burcharth, H.F. (1985). *Fatigue in Breakwater Concrete Armour Units*. In Proceedings of the 19<sup>th</sup> International Conference on Coastal Engineering: ICCE '84, 3-7 September, Houston, Texas.
- Burcharth, H.F. (1992). *Design of Rubble Mound Breakwaters: Structural Integrity*. In Design and Reliability of Coastal Structures: Proceedings of the Short Course on Design and Reliability of Coastal Structures, attached to the 23<sup>rd</sup> International Conference on Coastal Engineering, Eds: A. Lamberti, 1-3 October, Venice, Italy, 511-546.
- Burcharth, H.F.; Angremond, K. d'; Meer, J.W. van der; Liu, Z. (2000). *Empirical formula for breakage of Dolosse and Tetrapods*. Coastal Engineering, 40(3), 183-206.
- Caggiano, A.; Cremona, M.; Faella, C.; Lima, C.; Martinelli, E. (2012). *Fracture behaviour of concrete beams*

- reinforced with mixed long/short steel fibres*. Construction and Building Materials, 37, 832-840.
- Caggiano, A.; Xargay, H.; Folino, P.; Martinelli, E. (2015). *Experimental and numerical characterization of the bond behavior of steel fibers recovered from waste tires embedded in cementitious matrices*. Cement & Concrete Composites, 62, 146-155.
- Caggiano, A.; Folino, P.; Lima, C.; Martinelli, E.; Pepe, M. (2017). *On the mechanical response of Hybrid Fiber Reinforced Concrete with Recycled and Industrial Steel Fibers*. Construction and Building Materials, 147, 286-295.
- Callister, W.D.; Rethwisch, D.G. (2007). *Materials Science and Engineering: An Introduction*. 8<sup>th</sup> Edition, John Wiley & Sons, Inc., USA.
- CEN/TS 14243:2010. *Materials produced from end of life tyres. Specification of categories based on their dimension(s) and impurities and methods for determining their dimension(s) and impurities*. European Technical Specification. European Committee for Standardization, Brussels, 2010.
- Centonze, G.; Leone, M.; Aiello, M.A. (2012). *Steel fibers from waste tires as reinforcement in concrete: A mechanical characterization*. Construction and Building Materials, 36, 46-57.
- Chanh, N.V. (2005). *Steel fibre reinforced concrete*. In Proceedings of JSCE-VIFCEA Joint Seminar on Concrete Engineering, 8-9 December, Ho Chi Minh City University of Technology, Vietnam, 108–116.
- Chen, G.; Hadi, M.N.S.; Gao, D.; Zhao, L. (2015). *Experimental study on the properties of corroded steel fibres*. Construction and Building Materials, 79, 165-172.
- Chen, Z.; Gandhi, U.; Lee, J.; Wagoner, R.H. (2016). *Variation and consistency of Young's modulus in steel*. Journal of Materials Processing Technology, 227, 227-243.
- Chiang, C.T.; Yang, C.C. (2007). *Relation between the diffusion characteristic of concrete from salt ponding test and accelerated chloride migration test*. Materials Chemistry and Physics, 106(2-3), 240-246.
- CNR-DT 204/2006. *Guide for the Design and Construction of Fiber-Reinforced Concrete Structures*. CNR Advisory Committee on Technical Recommendations for Construction, Rome, 2007, 55 pages.
- Council Directive 75/442/EEC of 15 July 1975 on waste*. Official Journal of the European Communities L194, 1-39.
- Council Directive 91/156/EEC of 18 March 1991 amending Directive 75/442/EEC on waste*. Official Journal of the European Communities L78, 32-37.
- Council Directive 1999/31/EC of 26 April 1999 on the landfill of waste*. Official Journal of the European Communities L192, 1-19.
- Cunha, V.M.C.F. (2010). *Steel Fibre Reinforced Self-Compacting Concrete (from Micro-Mechanics to Composite Behaviour)*. Doctoral Thesis, Department of Civil Engineering, School of Engineering of the University of Minho, Guimarães, Portugal.
- Cunha, V.M.C.F.; Barros, J.A.O.; Sena-Cruz, J.M. (2008). *Modelling the influence of age of steel fibre reinforced self-compacting concrete on its compressive behaviour*. Materials and Structures, 41, 465-478.
- Cunha, V.M.C.F.; Barros, J.A.O.; Sena-Cruz, J.M. (2010). *Pullout Behavior of Steel Fibers in Self-Compacting Concrete*. Journal of Materials in Civil Engineering, 22(1), 1-9.
- Cunha, V.M.C.F.; Barros, J.A.O.; Sena-Cruz, J.M. (2012). *A finite element model with discrete embedded elements for fibre reinforced composites*. Computers and Structures Journal, 94-95, 22-33.
- Damineli, B.L.; Kemeid, F.M.; Aguiar, P.S.; John, V.M. (2010). *Measuring the eco-efficiency of cement use*. Cement and Concrete Composites, 32, 555-562.
- Dauberschmidt C.; Raupach M. (2005). *Passivity and Depassivation of Steel Fibres and Cold-Drawn Steel Wires in Artificial Pore Solution and Concrete Containing Chlorides*. In Proceedings of EUROCORR 2005, the European Corrosion Congress, 4-8 September, Lisbon, Portugal.
- DBV – Guide to Good Practice (2007). *Steel Fibre Concrete*. German Society for Concrete and Construction Technology, Berlin, Germany.

- de Oliveira, F. (2010). *Design-oriented constitutive model for steel fiber reinforced concrete*. Doctoral Thesis, Department d'Enginyeria de la Construcció, Universitat Politècnica de Catalunya, Barcelona, Spain.
- de Wilde, P.; Coley, D. (2012). *The implications of a changing climate for buildings*. Building and Environment, 55, 1-7.
- di Prisco, M.; Ferrara, L.; Lamperti, M.G.L. (2013). Double edge wedge splitting (DEWS): an indirect tension test to identify post-cracking behaviour of fiber reinforced cementitious composites. Materials and Structures, 46, 1893-1918.
- Ding, Y.; Kusterle, W. (1999). *Comparative study of steel fibre-reinforced concrete and steel mesh-reinforced concrete at early ages in panel tests*. Cement and Concrete Research, 29, 1827-1834.
- Directive 2008/98/EC of the European Parliament and of the Council of 19 November 2008 on waste and repealing certain Directives*. Official Journal of the European Union L312, 3-30.
- Døssland, A. (2008). *Fibre Reinforcement in Load Carrying Concrete Structures*. Doctoral Thesis, Department of Structural Engineering, Faculty of Engineering Science and Technology, Norwegian University of Science and Technology, Norway.
- Dupont, D. (2003). *Modelling and experimental investigation of the constitutive law (stress-strain) and cracking behaviour of steel fibre reinforced concrete*. Doctoral Thesis, Catholic University of Leuven, Belgium.
- Duracrete R17 (2000). *Duracrete – Final technical report*. The European Union – Brite EuRam III. Probabilistic Performance based Durability Design of Concrete Structures. Document BE95-1347/R17.
- Ecopneus (2014). *Ecopneus in the Green economy Sustainability Report 2013*. Prepared by Ecopneus scpa, Milano, Italy. Downloaded on 4<sup>th</sup> April, 2019 from [http://www.ecopneus.it/\\_public-file/Ecopneus%20sustainability%20Report%202013.pdf](http://www.ecopneus.it/_public-file/Ecopneus%20sustainability%20Report%202013.pdf)
- Edalat-Behbahani, A.; Barros, J.A.O.; Ventura-Gouveia, A. (2016). *Application of plastic-damage multidirectional fixed smeared crack model in analysis of RC structures*. Engineering Structures, 125, 374-391.
- Edvardsen, C.; Jepsen, M.T. (2000). *Chloride migration coefficients from non-steady-state migration experiments at environment-friendly "Green" concrete*. In Proceedings of 2<sup>nd</sup> International RILEM Workshop on Testing and Modelling the Chloride Ingress into Concrete, RILEM Publications SARL, 203-209.
- EFCA (2015). Environmental Product Declaration (EPD) Report. Concrete admixtures – Plasticisers and Superplasticisers. European Federation of Concrete Admixtures Associations Ltd. (EFCA).
- EFNARC (1996). *European Specification for sprayed concrete*. 30 pages.
- EFNARC (2005). *The European Guidelines for Self-compacting Concrete*. Specification, Production and Use, 63 pages.
- Elnour, M.G.; Laz, H.A. (2014). *Tire Hazardous, Disposal and Recycling*. Journal of Applied and Industrial Sciences, 2(2), 63-74.
- EN 197-1:2011 (2011). *Cement – Part 1: Composition, specifications and conformity criteria for common cements*. CEN, Brussels.
- EN 206:2013+A1 (2016). *Concrete – Specification, performance, production and conformity*. CEN, Brussels.
- EN 1992-1-1 (2004). *Eurocode 2: Design of concrete structures – Part 1-1: General rules and rules for buildings*. CEN, Brussels, 225 pages.
- EN 12350-2:2009. *Testing fresh concrete – Part 2: Slump test*. CEN, Brussels.
- EN 12350-8:2010. *Testing fresh concrete – Part 8: Self-compacting concrete – Slump-flow test*. CEN, Brussels.
- EN 12350-9:2010. *Testing fresh concrete – Part 9: Self-compacting concrete – V-funnel test*. CEN, Brussels.
- EN 12390-3:2011. *Testing hardened concrete – Part 3: Compressive strength of test specimens*. CEN, Brussels.
- EN 12390-13:2013. *Testing hardened concrete – Part 13: Determination of secant modulus of elasticity in compression*. CEN, Brussels.

- EN 14651 (2005). *Test method for metallic fibered concrete – Measuring the flexural tensile strength (limit of proportionality (LOP), residual)*. CEN, Brussels.
- EN 15804:2012+A1. *European Standard. Sustainability of Construction Works - Environmental Product Declarations - Core Rules for the Product Category of Construction Products*. CEN, Brussels, Belgium.
- Enos, D.G.; Scribner, L.L. (1997). *The Potentiodynamic Polarization Scan*. Technical Report 33. Solartron Instruments, a division of Solartron Group Ltd, UK.
- Environmental Protection Agency (EPA), 1999. *State Scrap Tire Programs: A Quick Reference Guide:1999 Update*. Document N.º EPA-530-B-99-002, prepared by EPA, USA. Downloaded on 4<sup>th</sup> April, 2019 from <https://nepis.epa.gov/>
- EPA, 2006. *Life Cycle Assessment: Principles and Practice*. Report EPA/600/R-06/060, EPA, Washington D.C., USA.
- Esmailzadeh, S.; Aliofkhazraei, M.; Sarlak, H (2018). *Interpretation of Cyclic Potentiodynamic Polarization Test Results for Study of Corrosion Behavior of Metals: A Review*. Protection of Metals and Physical Chemistry of Surfaces, 54 (5), 976-989.
- ETRMA, 2015. *End-of-life Tyre Report 2015*. Prepared by ETRMA, Brussels, Belgium. Downloaded on 11<sup>th</sup> March, 2019 from [www.etrma.org/uploads/Modules/Documentsmanager/elt-report-v9a-final.pdf](http://www.etrma.org/uploads/Modules/Documentsmanager/elt-report-v9a-final.pdf)
- ETRMA, 2016. *Statistics Edition 2016*. Prepared by ETRMA, Brussels, Belgium. Downloaded on 4<sup>th</sup> April, 2019 from <http://www.etrma.org/uploads/Modules/Documentsmanager/20161208-statistics-booklet-2016-final5.pdf>
- ETRMA, 2017a. *Statistics Edition 2017*. Prepared by ETRMA, Brussels, Belgium. Downloaded on 4<sup>th</sup> April, 2019 from <http://www.etrma.org/uploads/Modules/Documentsmanager/20180329-statistics-booklet-2017-alternative-rubber-section-final-web.pdf>
- ETRMA, 2017b. *The European Tyre Industry – Facts and Figures*. Prepared by ETRMA, Brussels, Belgium. Downloaded on 4<sup>th</sup> April, 2019 from <http://www.etrma.org/uploads/Modules/Documentsmanager/20170912-facts-and-figures-leaflet-2017.pdf>
- ETRMA, 2018. *ELT Management figures 2016*. Prepared by ETRMA, Brussels, Belgium. Downloaded on 4<sup>th</sup> April, 2019 from [http://www.etrma.org/uploads/Modules/Documentsmanager/20180502-2016-elt-data\\_for-press-release.pdf](http://www.etrma.org/uploads/Modules/Documentsmanager/20180502-2016-elt-data_for-press-release.pdf)
- Farinha, C.B.; Silvestre, J.D.; de Brito, J.; Veiga, M. do R. (2019). *Life Cycle Assessment of Mortars with Incorporation of Industrial Wastes*. Fibers, 7, 59, 19 pages.
- Feilong, S.; Xiaogang, L.; Xuequn, C. (2014). *Effects of Carbon Content and Microstructure on Corrosion Property of New Developed Steels in Acidic Salt Solutions*. Acta Metallurgica Sinica, 27(1), 115-123.
- Ferrara, L.; Faifer, M.; Toscani, S. (2012). *A magnetic method for non destructive monitoring of fiber dispersion and orientation in steel fiber reinforced cementitious composites. Part 2: Correlation to tensile fracture toughness*. Materials and Structures, 45, 591-598.
- Ferreira, T.; Rasband, W. (2012). ImageJ User Guide - IJ 1.46.
- Fiksel, J.; Bakshi, B.R.; Baral, A.; Guerra, E.; DeQuervain, B. (2011). *Comparative life cycle assessment of beneficial applications for scrap tires*. Clean Technologies and Environmental Policy, 13(1), 19-35.
- Filippo, J. D.; Karpman, J.; DeShazo, J.R. (2019). *The impacts of policies to reduce CO<sub>2</sub> emissions within the concrete supply chain*. Cement and Concrete Composites, 101, 67-82.
- Finazzi, S.; Paegle, I.; Fisher, G.; Minelli, F. (2014). *Influence of bending test configuration on cracking behavior of FRC*. In Proceedings of the 3<sup>rd</sup> All- Russia (International) Conference on Concrete and Reinforced Concrete, Vol. 3, 196-205.
- Frazão, C.; Camões, A.; Barros, J.; Gonçalves, D. (2015). *Durability of steel fiber reinforced self-compacting concrete*. Construction and Building Materials, 80, 155-166.

- Frazão C.; Barros, J.; Camões, A.; Alves, A.C.; Rocha, L. (2016). *Corrosion effects on pullout behavior of hooked steel fibers in self-compacting concrete*. Cement and Concrete Research, 79, 112-122.
- Freire, L.; Nóvoa, X.R.; Pena, G.; Vivier, V. (2008). *On the corrosion mechanism of AISI 204Cu stainless steel in chlorinated alkaline media*. Corrosion Science, 50 (11), 3205–3212.
- Galeote, E.; Blanco, A.; Cavalaro, S.H.P.; de la Fuente, A. (2017). *Correlation between the Barcelona test and the bendig test in fibre reinforced concrete*. Construction and Building Materials, 152, 529-538.
- Ganesan, N.; Indira, P.V; Kumar, P.T.S. (2006). *Durability aspects of steel fibre-reinforced SCC*. Indian Concrete Journal, 80(5), 31–37.
- González, J.; Miranda, J.; Feliu, S. (2004). *Considerations on reproducibility of potential and corrosion rate measurements in reinforced concrete*. Corrosion Science, 46, 2467–2485.
- Graeff, A.; Pilakoutas, K.; Lynsdale, C.; Neocleous, K. (2009). *Corrosion Durability of Recycled Steel Fibre Reinforced Concrete*. Article No.7, Intersections/Intersec\_ii, 6(4).
- Graeff, A.G. (2011). *Long-term performance of recycled steel fibre reinforced concrete for pavement applications*. Doctoral Thesis, Department of Civil and Structural Engineering, Faculty of Engineering of the University of Sheffield, UK.
- Graeff, A.; Pilakoutas, K.; Lynsdale, C.; Neocleous, K.; Peres, M. (2012). *Fatigue resistance and cracking mechanism of concrete pavements reinforced with recycled steel fibres recovered from post-consumer tyres*. Engineering Structures, 45, 385-395.
- Granju, J.-L.; Balouch, S.U. (2005). *Corrosion of steel fibre reinforced concrete from the cracks*. Cement and Concrete Research, 35, 572–577.
- Guinée, J.B. (2002). *Handbook on Life Cycle Assessment: Operational guide to the ISO standards*. Kluwer Academic Publishers.
- Hansen, E.J. de P.; Ekman, T.; Hansen, K.K. (1999). *Durability of cracked fibre reinforced concrete structures exposed to chlorides*. In the proceedings of Durability of Building Materials and Components 8: Service life and durability of materials and components, Eds: M.A. Lacasse, D.J. Vanier, NRC Research Press, Vancouver, Canada, 280–289.
- He, F.; Shi, C.; Yuan, Q.; Zheng, K.; Zou, Q. (2008). *Factors influencing chloride concentration at the color change boundary using  $AgNO_3$  colorimetric method*. Journal of the Chinese Ceramic Society, 36(7), 890-895.
- He, F.; Shi, C.; Yuan, Q.; Chen, C.; Zheng, K. (2012).  *$AgNO_3$ -based colorimetric methods for measurement of chloride penetration in concrete*. Construction and Building Materials, 26, 1-8.
- Herrera-Sosa, E.S.; Martínez-Barrera, G.; Barrera-Díaz, C.; Cruz-Zaragoza, E.; Ureña-Núñez, F. (2015). *Recovery and Modification of Waste Tire Particles and Their Use as Reinforcements of Concrete*. Hindawi Publishing Corporation, International Journal of Polymer Science, Article ID 23469, 8 pages.
- Hoff, G.C. (1975). *Use of fiber-reinforced concrete in hydraulic structures and marine environments*. In Proceedings of 1<sup>st</sup> RILEM International Symposium on Fiber-Reinforced Cement and Concrete, 14-17 September, London, UK.
- Homma, D.; Mihashi, H.; Nishiwaki, T. (2009). *Self-healing Capability of Fibre Reinforced Cementitious Composites*. Journal of Advanced Concrete Technology, 7(2), 217-228.
- Hu, H.; Papastergiou, P.; Angelakopoulos, H.; Guadagnini, M.; Pilakoutas, K. (2018a). *Mechanical properties of SFRC using blended manufactured and recycled tyre steel fibres*. Construction and Building Materials, 163, 376-389.
- Hu, H.; Papastergiou, P.; Angelakopoulos, H.; Guadagnini, M.; Pilakoutas, K. (2018b). *Mechanical properties of SFRC using blended Recycled Tyre Steel Cords (RTSC) and Recycled Tyre Steel Fibres (RTSF)*. Construction and Building Materials, 187, 553-564.
- Hwang, J.P.; Jung, M.S.; Kim, M.; Ann, K.Y. (2015). *Corrosion risk of steel fibre in concrete*. Construction and Building Materials, 101, 239-245.
- Hylands, K.N.; Shulman, V. (2003). *Civil engineering applications of tyres*. Viridis Report VR5. Prepared by Viridis,

- TRL (Transport Research Laboratory) Limited and ETRA (European Tyre Recycling Association), Crowthorne, UK. Project funded by Biffaward under the Landfill Tax Credit Scheme, with contributions from the Institution of Civil Engineers (ICE). Downloaded on 11<sup>th</sup> March, 2019 from <https://trl.co.uk/reports/VR5>
- IEA and the United Nations Environment Programme, 2018. *2018 Global Status Report: towards a zero-emission, efficient and resilient buildings and construction sector*. Prepared by the IEA for the Global Alliance for Buildings and Construction (Global ABC). Coordinated by the United Nations Environment Programme. Downloaded on 8<sup>th</sup> March, 2019 from <https://www.unenvironment.org/resources/report/global-status-report-2018>
- Ismail, M.; Hamzah, E.; Chun Guan, G.; Abd Rahman, I. (2010). *Corrosion performance of dual-phase steel embedded in concrete*. Arabian Journal for Science and Engineering, 35 (2B), 81-90.
- ISO 14040:2006. *International Standard. Environmental Management - Life Cycle Assessment - Principles and framework*; ISO: Geneva, Switzerland.
- ISO 14044:2006. *International Standard. Environmental Management - Life Cycle Assessment – Requirements and guidelines*; ISO: Geneva, Switzerland.
- Isteita, M.; Xi, Y. (2017). *The effect of temperature variation on chloride penetration in concrete*. Construction and Building Materials, 156, 73-82.
- Jang, S.Y.; Kim, B.S.; Oh, B.H. (2011). *Effect of crack width on chloride diffusion coefficients of concrete by steady-state migration tests*. Cement and Concrete Research, 41, 9–19.
- Janotka, I.; Krajci, L.; Komlos, K.; Frtalová, D. (1989). *Chloride corrosion of steel fibre reinforcement in cement mortar*. International Journal of Cement Composites and Lightweight Concrete, 11(4), 221–228.
- JCI-S-003-2007 (2007). *Method of test for bending moment-curvature of FRCC*. Japan Concrete Institute Standard.
- Khan, M.U.; Ahmad, S.; Al-Gahtani, H.J. (2017). *Chloride-Induced Corrosion of Steel in Concrete: An Overview on Chloride Diffusion and Prediction of Corrosion Initiation Time*. International Journal of Corrosion, Article ID 5819202, 1-9.
- Komatani, S.; Aoyama, T.; Nakazawa, T.; Tsuji, K. (2013). *Comparison of SEM-EDS, Micro-XRF and Confocal Micro-XRF for Electric Device Analysis*. e-Journal of Surface Science and Nanotechnology, 11, 133-137.
- Krauss, G. (1999). *Martensite in steel: strength and structure*. Materials Science and Engineering, A273–275, 40–57.
- Krauss, G. (2015). *Steels: Processing, Structure, and Performance*. 2<sup>nd</sup> Edition, ASM International, USA.
- Kropp, J.; Hilsdorf, H. (1995). *Performance Criteria for Concrete Durability*. RILEM Report 12. 1<sup>st</sup> Edition, CRC Press.
- Kurda, R.; Silvestre, J.D.; Brito, J. de (2018). *Life cycle assessment of concrete made with high volume of recycled concrete aggregates and fly ash*. Resources, Conservation & Recycling, 139, 407-417.
- Lameiras, R. de M. (2015). *Sandwich structural panels comprising thin-walled SFRSCC and GFRP connectors: from material features to structural behaviour*. Doctoral Thesis, Department of Civil Engineering, School of Engineering of the University of Minho, Guimarães, Portugal.
- Lameiras, R.; Barros, J.A.O.; Azenha, M. (2015). *Influence of casting condition on the anisotropy of the fracture properties of Steel Fibre Reinforced Self-Compacting Concrete (SFRSCC)*. Cement and Concrete Composites, 59, 60-76.
- Laresgoiti, M.F.; Caballero, B.M.; de Marco, I.; Torres, A.; Cabrero, M.A.; Chomón, M.J. (2004). *Characterization of the liquid products obtained in tyre pyrolysis*. Journal Analytical and Applied Pyrolysis, 71, 917-934.
- Lay, S.; Liebl, S.; Hilbig, H.; Schießl, P. (2004). *New Method to Measure the Rapid Chloride Migration Coefficient of Chloride-Contaminated Concrete*. Cement and Concrete Research, 34 (3), 421–427.
- Leone, M.; Centonze, G.; Colonna, D.; Micelli, F.; Aiello, M.A. (2016). *Experimental Study on Bond Behavior in Fiber-Reinforced Concrete with Low Content of Recycled Steel Fiber*. ASCE Journal of Materials in Civil Engineering, 28(9), 1-13.

- Leone, M.; Centonze, G.; Colonna, D.; Micelli, F.; Aiello, M.A. (2018). *Fiber-reinforced concrete with low content of recycled steel fiber: Shear behaviour*. Construction and Building Materials, 161, 141-155.
- Letelier, V.; Tarela, E.; Muñoz, P.; Moriconi, G. (2017). *Combined effects of recycled hydrated cement and recycled aggregates on the mechanical properties of concrete*. Construction and Building Materials, 132, 365-375.
- Liang, S.B.; Hao, Y.C. (2000). *A novel cryogenic grinding system for recycling scrap tire peels*. Advanced Powder Technology, 11(2), 187-197.
- LNEC E463:2004. *Determination of diffusion coefficient of chlorides by migration under non-steady state*. LNEC, Lisbon, 8 pages. [in Portuguese]
- LNEC E465:2007. *Method for estimating the properties of the concrete performance capable of meeting the design life of reinforced concrete structures or prestressed under environmental expositions XC and XS*. LNEC, Lisbon. [in Portuguese]
- Lourenço, L. (2012). *Betão Reforçado com Fibras: aplicações e técnicas de inspeção e reforço de elementos estruturais afetados pela ação de um fogo*. Doctoral thesis, Department of Civil Engineering, School of Engineering of the University of Minho, Guimarães, Portugal.
- Lourenço, L.; Zamanzadeh, Z.; Barros, J.A.O.; Razazadeh, M. (2018). *Shear strengthening of RC beams with thin panels of mortar reinforced with recycled steel fibres*. Journal of Cleaner Production, 194, 112-126.
- Ma, Y.; Tian, X.; Yin, J.; Chen, J.; Jiang, J. (2019). *The Pitting Corrosion Behavior of Copper with Different Grain Size*. International Journal of Electrochemical Science, 14, 4047-4056.
- Maage, M.; Helland, S.; Poulsen, E.; Vennesland, Ø.; Carlsen, J.E. (1996). *Service Life Prediction of Existing Concrete Structures Exposed to Marine Environment*. ACI Materials Journal, 93(6), 1-8.
- Maccaferri, 2008. *Fibers as Structural Element for the Reinforcement of Concrete*. Technical Manual. 238 pages.
- Mangat, P.S.; Gurusamy, K. (1987). *Permissible crack widths in steel fibre reinforced marine concrete*. Materials and Structures, 20, 338-347.
- Mangat, P.S.; Gurusamy, K. (1988). *Long term properties under marine exposure of steel fibre reinforced concrete containing pfa*. Materials and Structures, 21(5), 352-358.
- Marcos-Meson, V.; Michel, A.; Solgaard, A.; Fischer, G.; Edvardsen, C.; Skovhus, T.L. (2018). *Corrosion resistance of steel fibre reinforced concrete – A literature review*. Cement and Concrete Research, 103, 1-20.
- Marguí, E.; Grieken, R.V. (2013). *State-of-the-art of X-ray fluorescence instrumentation for chemical analysis*. Available online at <https://www.petro-online.com/article/analytical-instrumentation/11>. Accessed on 23<sup>rd</sup> May 2019.
- Martinelli, E.; Caggiano, A.; Xargay, H. (2015). *An experimental study on the post-cracking behaviour of Hybrid Industrial/Recycled Steel Fibre-Reinforced Concrete*. Construction and Building Materials, 94, 290-298.
- Martínez, J.D.; Puy, N.; Murillo, R.; García, T.; Navarro, M.V.; Mastral, A.M. (2013). *Waste tyre pyrolysis – A review*. Renewable and Sustainable Energy Reviews, 23, 179-213.
- Masmoudi, A.; Bouaziz, J. (2016). *Durability of Steel Fibres Reinforcement Concrete Beams in Chloride Environment Combined with Inhibitor*. Hindawi Publishing Corporation, Advances in Materials Science and Engineering, Article ID 1743952, 6 pages.
- MC2010 (2011). CEB fib Model Code 2010 - Final Draft, Switzerland.
- Mebarkia, S.; Vipulanandan, C. (1992). *Compressive behavior of glass-fiber-reinforced polymer concrete*. Journal of Materials in Civil Engineering, 4(1), 91-105.
- Meck, E.; Sirivivatnanon V. (2003). *Field indicator of chloride penetration depth*. Cement and Concrete Research, 33, 1113-1117.
- Meddah, M.S.; Bencheikh, M. (2009). *Properties of concrete reinforced with different kinds of industrial waste fibre materials*. Construction and Building Materials, 23, 3196-3205.



- Mertinger, V.; Nagy, E.; Tranta, F.; Sólyom, J. (2008). *Strain-induced martensitic transformation in textured austenitic stainless steels*. Materials Science and Engineering A, 481-482, 718-722.
- Micelli, F.; Leone, M.; Centonze, G.; Aiello, M. (2014). *Go Green: Using Waste and Recycling Materials*. In: Infrastructure Corrosion and Durability – A Sustainability Study, Yang Lu (Ed.), OMICS Group eBooks, USA, 1-68.
- Michelin (2019). *How is a tire made?*. Available online at <https://www.michelinman.com/US/en/help/how-is-a-tire-made.html>. Accessed on 4<sup>th</sup> April 2019.
- Minelli, F.; Plizzari, G.A. (2010). *Fiber reinforced concrete characterization through round panel test – part I: Experimental study*. Fracture Mechanics of Concrete and Concrete Structures – High Performance, Fiber Reinforced Concrete, Special Loadings and Structural Applications, B.H. Oh *et al.* (eds), Korea.
- Mohammed, T.U.; Hamada, H. (2003). *Relationship between free chloride and total chloride contents in concrete*. Cement and Concrete Research, 33, 1487-1490.
- Molins, C.; Aguado, A.; Saludes, S. (2009). *Double Punch Test to control the energy dissipation in tension of FRC (Barcelona test)*. Materials and Structures, 42, 415-425.
- Moraes Neto, B.N. (2013). *Punching behaviour of steel fibre reinforced concrete slabs submitted to symmetric loading*. Doctoral Thesis, Department of Civil and Environmental Engineering, University of Brasilia, Brasil.
- Morris, J.W.; Glazer, J.; Chan, J.W. (1989). *The Metallurgical Determinants of Toughness at Cryogenic Temperature*. In Proceedings of the International Cryogenic Materials Conference, 24-28 July, Los Angeles, USA.
- Mudadu, A.; Tiberti, G.; Germano, F.; Plizzari, G.A.; Morbi, A. (2018). *The effect of fiber orientation on the post-cracking behavior of steel fiber reinforced concrete under bending and uniaxial tensile tests*. Cement and Concrete Composites, 93, 274-288.
- Muralikrishna, I.V.; Manickam, V. (2017). *Life Cycle Assessment*. Chapter 5 in book “Environmental Management - Science and Engineering for Industry”, Butterworth-Heinemann, 57-75.
- Muttray, M.; Reedijk, B. (2009). *Design of Concrete Armour Layers*. Hansa International Maritime Journal, 146(6), 111-118.
- Narayan, N.T.; Ramakrishnan, S. (2013). *Steel Fibre Reinforced Concrete for Ports Infrastructure*. The Masterbuilder, March 2013, 144–147.
- Nawy, E.G. (2008). *Fiber-Reinforced Composites*. Chapter 22 in book “Concrete Construction Engineering Handbook 2<sup>nd</sup> Edition”, Taylor & Francis Group, 22(1-28).
- Nemegeer, D.; Vanbrabant, J.; Stang, H. (2003). *Brite Euram Program on Steel Fibre Concrete. Subtask: Durability: Corrosion Resistance of Cracked Fibre Reinforced Concrete*. In Proceedings of International RILEM Workshop on Test and Design Methods for Steel Fibre Reinforced Concrete, RILEM Publications SARL 2003, Eds: B. Schnütgen; L. Vandewalle, Bochum, Germany, 47–66.
- Neocleous, K.; Tlemat, H.; Pilakoutas, K. (2006). *Design issues for concrete reinforced with steel fibers, including fibers recovered from used tires*. ASCE Journal of Materials in Civil Engineering, 18(5), 677-685.
- Neocleous, K.; Angelakopoulos, H.; Pilakoutas, K. and Guadagnini, M. (2011). *Fibre reinforced roller-compacted concrete transport pavements*. In Proceedings of the institution of civil engineers – transport, 97–109.
- Neocleous, K.; Maxineasa, S.G.; Dumitrescu, L.; Themistocleous, K.; Taranu, N. and Hadjimitsis, D. (2014). *D1.6 Preliminary LCA*. Anagennisi Project, Anagennisi: innovative use of all tyre components in concrete.
- Neves, R.D. and Almeida, J.C.O.F. (2005). *Compressive behaviour of steel fibre reinforced concrete*. Structural Concrete, 6 (1), 1-8.
- Nordström, E. (2005). *Durability of Sprayed Concrete – Steel fibre corrosion in cracks*. Doctoral Thesis, Department of Civil and Environmental Engineering, Division of Structural Engineering, Luleå University of Technology, Sweden.
- Nour, A.; Massicotte, B.; De Montaignac, R.; Charron, J.-P. (2011). *Derivation of a crack opening deflection relationship for fibre reinforced concrete panels using a stochastic model: Application for predicting the flexural behaviour of round panels using stress crack opening diagrams*. Cement and Concrete Research, 41, 964-974.

- NT BUILD 492 (1999). *Concrete, mortar, and cement-based repair materials: Chloride migration coefficient from non-steady-state migration experiments*. Nordtest method, Finland.
- NT BUILD 443 (1995). *Concrete, hardened: Accelerated chloride penetration*. Nordtest method, Finland.
- OECD, 2012. *Transport Outlook 2012: Seamless Transport for Greener Growth*. Prepared by the International Transport Forum (ITF), Paris, France. Downloaded on 11<sup>th</sup> March, 2019 from <https://www.oecd.org/greengrowth/greening-transport/Transport%20Outlook%202012.pdf>
- Ohmura, T.; Hara, T.; Tsuzaki, K. (2003). *Evaluation of temper softening behavior of Fe-C binary martensitic steels by nanoindentation*. Scripta Materialia, 49, 1157-1162.
- Oliver, W.C.; Pharr, G.M. (2004). *Measurement of hardness and elastic modulus by instrumented indentation: Advances in understanding and refinements to methodology*. Journal of Materials Research, 19(1), 3-20.
- Onuaguluchi, O.; Banthia, N. (2018). *Scrap tire steel fiber as a substitute for commercial steel fiber in cement mortar: Engineering properties and cost-benefit analyses*. Resources, Conservation & Recycling, 134, 248-256.
- Otsuki, N.; Nagataki, S.; Nakashita, K. (1992). *Evaluation of AgNO<sub>3</sub> solution spray method for measurement of chloride penetration into hardened cementitious matrix materials*. ACI Materials Journal, 89(6), 587-592.
- Ou, Y.C.; Tsai, M.-S.; Liu, K.-Y.; Chang, K.-C. (2012). *Compressive behavior of steel fiber-reinforced concrete with a high reinforcing index*. ASCE Journal of Materials in Civil Engineering, 24(2), 207-215.
- Papakonstantinou, C.G. and Tobolski M.J. (2006). *Use of waste tire steel beads in Portland cement concrete*. Cement and Concrete Research, 36, 1686–1691.
- Paris, J.; Roessler, J.; Ferraro, C.; DeFord, H.; Townsend, T. (2016). *A review of waste products utilized as supplements to Portland cement in concrete*. Journal of Cleaner Production, 121, 1-18.
- Pehlken, A.; Essadiqi, E. (2005). *Scrap tyre recycling in Canada*. CANMET Materials Technology Laboratory, Report MTL 2005-08(CF). Downloaded on 4<sup>th</sup> April, 2019 from <https://www.nrcan.gc.ca/sites/www.nrcan.gc.ca/files/mineralsmetals/pdf/mms-smm/busi-indu/rad-rad/pdf/scr-tir-rec-peh-eng.pdf>
- Pereira, E. (2006). *Steel Fibre Reinforced Self-Compacting Concrete: from material to mechanical behaviour*. Dissertation for Pedagogical and Scientific Aptitude Proofs, Department Civil Engineering, University of Minho, 188 pages.
- Pereira, E.B.; Barros, J.A.O. & Cam es, A.F. (2008). *Steel fibre reinforced self-compacting concrete-experimental research and numerical simulation*. Structural engineering, 134(8), 1310-1321.
- Pham, T.-H.; Kim, S.-E. (2015). *Nanoindentation for investigation of microstructural compositions in SM490 steel weld zone*. Journal of Constructional Steel Research, 110, 40-47.
- Pharr, G.; Oliver, W.; Brotzen, F. (1992). *On the generality of the relationship between contact stiffness, contact area, and elastic moduli during indentation*. Journal of Materials Research, 7, 613-617.
- PIANC/AIPCN (2005). *Catalogue of prefabricated elements*. Report produced by the MarCom Working Group 36, Brussels, Belgium, 24 pages.
- Pilakoutas, K.; Neocleous, K.; Tlemat, H. (2004). *Reuse of tyre steel fibres as concrete reinforcement*. In Proceedings of the Institution of Civil Engineers (ICE): Engineering Sustainability, 157(3), 131-138.
- Pillai, R.G.; Annapareddy, A. (2013). *Service life prediction models for chloride-laden concrete structures: a review and nomographs*. International Journal of 3R's, 4(2), 563-580.
- Poulsen, E.; Mejlbro, L. (2006). *Diffusion of chloride in concrete – Theory and Application*. Modern Concrete Technology 14. Taylor & Francis Group, London and New York.
- Presti (2013). *Recycled Tyre Rubber Modified Bitumens for road asphalt mixtures: A literature review*. Construction and Building Materials, 49, 863-881.
- Pujadas, P.; Blanco, A.; Cavalaro, S.; de la Fuente, A.; Aguado, A. (2013). *New Analytical Model to generalize the Barcelona test using axial displacement*. Journal of Civil Engineering and Management, 19:2, 259-271.

- 
- Pujadas, P.; Blanco, A.; Cavalaro, S.H.P.; de la Fuente, A.; Aguado, A. (2014). *Multidirectional double punch test to assess the post-cracking behaviour and fibre orientation of FRC*. Construction and Building Materials, 58, 214-224.
- Quadrini, F.; Bellisario, D.; Santo, L.; Hren, I. (2013). *Direct Moulding of Rubber Granules and Powders from Tyre Recycling*. Applied Mechanics and Materials, 371, 315-319.
- Reschner, K. (2008). *Scrap Tire Recycling*. A Summary of Prevalent Disposal and Recycling Methods. Downloaded on 4<sup>th</sup> April, 2019 from [http://www.entire-engineering.de/Scrap\\_Tire\\_Recycling.pdf](http://www.entire-engineering.de/Scrap_Tire_Recycling.pdf).
- RILEM TC 162-TDF (2002). *Test and design methods for steel fibre reinforced concrete. Bending test. Final Recommendation*. Materials and Structures, 35, 579-582.
- RILEM TC 162-TDF (2003). *Test and design methods for steel fibre reinforced concrete.  $\sigma$ - $\epsilon$ -design method. Final Recommendation*. Materials and Structures, 36, 560-567.
- Robins, P.; Austin, S.; Jones, P. (2002). *Pull out behaviour of hooked steel fibres*. Materials and Structures, 33, 434-442.
- Rodriguez, I.M.; Laresgoiti, M.F.; Cabrero, A.; Torres, A.; Chomón, M.J.; Caballero, B. (2001). *Pyrolysis of scrap tyres*. Fuel Processing Technology, 72(1), 9-22.
- Romańczuk, E.; Oksiuta, Z. (2017). *Comparison of corrosion resistance in physiological saline solution of two austenitic stainless steels – 316LV and REX734*. Acta mechanica et automatica, The Journal of Bialystok Technical University, 11(2), 91-95.
- Roque, R.; Kim, N.; Kim, B.; Lopp, G. *Durability of Fiber-Reinforced Concrete in Florida Environments*. Final Report September 2004-June 2009, UF Project No. 00050493, Dept. of Civil and Coastal Engineering, University of Florida, 2009, 25 pages.
- Rosli, R.A., Ibrahim, I.S. (2013). *Mechanical properties of Recycled Steel Tire Fibres in Concrete*. Technical Report, Faculty of Civil Engineering, University Technology of Malaysia, Johor Bahru, Malaysia.
- RMA, 2019. *Scrap Tire Characteristics*. Available online at <http://www.energyjustice.net/files/tires/files/scrapchn.html#anchor135840>. Accessed on 4<sup>th</sup> April 2019.
- Sadeghi-Pouya, H.; Ganjian, E.; Claisse, P.A.; Muthuramalingam, K. (2013). *Corrosion durability of high-performance steel fibre reinforced concrete*. In Proceedings of the 3<sup>rd</sup> International Conference on Sustainable Construction Materials and Technologies, Coventry University and The University of Wisconsin Milwaukee Centre for By-products Utilization, 18-21 August, Kyoto Research Park, Kyoto, Japan.
- Safehian, M.; Ramezani-pour, A.A. (2015). *Prediction of RC structure service life from field long term chloride diffusion*. Computers and Concrete, 15(4), 589-606.
- Salamci, E.; Candan, S.; Kabakci, F. (2017). *Effect of microstructure on corrosion behavior of dual-phase steels*. Kovove Materialy, 55, 133-139.
- Salehian, H.; Barros, J.A.O.; Taheri, M. (2014). *Evaluation of the influence of post-cracking response of steel fibre reinforced concrete (SFRC) on load carrying capacity of SFRC panels*. Construction and Building Materials, 73, 289-304.
- Salehian, H. (2015). *Evaluation of the Performance of Steel Fibre Reinforced Self-Compacting Concrete in Elevated Slab Systems; from the Material to the Structure*. Doctoral Thesis, Department of Civil Engineering, School of Engineering of the University of Minho, Guimarães, Portugal.
- Salehian, H.; Barros, J.A.O. (2015). *Assessment of the performance of steel fibre reinforced self-compacting concrete in elevated slabs*. Cement and Concrete Composites, 55, 268-280.
- Schade, C.; Murphy, T.; Lawley, A.; Doherty R. (2016). *Microstructure and Mechanical properties of a Bainitic Powder Metallurgy Steel*. International journal of Powder Metallurgy, 52 (2), 37-46.
- Shi, X.; Xie, N.; Fortune, K.; Gong, J. (2012). *Durability of steel reinforced concrete in chloride environments: An overview*. Construction and Building Materials, 30, 125-138.
-

- 
- Shulman, V.L. (ETRA), (2004). *Tire Recycling*. Rapra Review Reports, 15(7). Rapra Technology Limited, Smithers Rapra Press, UK, 144 pages. Downloaded on 4<sup>th</sup> April, 2019 from <http://www.polymerjournals.com/pdfdownload/928289.pdf>
- Shulman, V.L. (ETRA), (2019). *Tire Recycling*. Chapter 26 in book "Waste: A Handbook for Management, Second Edition", Academic Press, Eds: T.M. Letcher; D.A. Vallero, 489-515.
- Sienkiewicz, M.; Kucinska-Lipka, J.; Janik, H.; Balas, A. (2012). *Progress in used tyres management in the European Union: A review*. Waste Management, 32, 1742-1751.
- Silvestre, J.D. (2012). *Life Cycle Assessment "from Cradle to Cradle" of Building Assemblies – Application to External Walls*. Doctoral Thesis, Instituto Superior Técnico, Lisbon, Portugal.
- Silvestre, J.D.; de Brito, J.; Pinheiro, M.D. (2013). *From the new European Standards to an environmental, energy and economic assessment of building assemblies from cradle-to-cradle (3E-C2C)*. Energy and Buildings, 64, 199-208.
- Singh, S.P.; Kaushik, S.K. (2003). *Fatigue strength of steel fibre reinforced concrete in flexure*. Cement & Concrete Composites, 25, 779-786.
- Singh, A.P.; Singhal, D. (2011). *Permeability of Steel Fibre Reinforced Concrete Influence of Fibre Parameters*. Procedia Engineering, 14, 2823–2829.
- Sirivivatnanon, V.; Khatri, R.P. (1998). *Chloride penetration resistance of concrete*. In Proceedings of Concrete Institute of Australia Conference 'Getting a Lifetime out of Concrete Structures', Brisbane, Australia.
- Skarżyński, Ł.; Tejchman, J. (2016). *Experimental Investigations of Fracture Process in Concrete by Means of X-ray Micro-computed Tomography*. Strain, 52, 26-45.
- Smrkić, M.F.; Damjanović, D.; Baričević, A. (2017). *Application of recycled steel fibres in concrete elements subjected to fatigue loading*. GRAĐEVINAR, 69 (10), 893-905.
- Sofi, A. (2018). *Effect of waste tyre rubber on mechanical and durability properties of concrete – A review*. Ain Shams Engineering Journal, 9, 2691-2700.
- Solgaard, A.O.S.; Küter, A.; Edvardsen, C.; Stang, H.; Geiker, M. (2010). *Durability Aspects of Steel Fibre Reinforced Concrete in Civil Infrastructure*. In Proceedings of the 2<sup>nd</sup> International Symposium on Service Life Design for Infrastructure, 4-6 October, Delft, The Netherlands.
- Soltanzadeh, F.; Barros, J.A.O.; Santos, R.F.C. (2015). *High performance fiber reinforced concrete for the shear reinforcement: Experimental and numerical research*. Construction and Building Materials, 77, 94-109.
- Song, L.; Sun, W.; Gao, J. (2013). *Time Dependent Chloride Diffusion Coefficient in Concrete*. Journal of Wuhan University of Technology-Materials Science Edition, 28(2), 314-319.
- Song, Z.; Yang, Y.; Zhao, X.; Sun, J.; Wang, W.; Mao, Y.; Ma, C. (2017). *Microwave pyrolysis of tire powders: Evolution of yields and composition of products*. Journal of Analytical and Applied Pyrolysis, 123, 152-159.
- Sonti, K.; Senadheera, S.; Jayawickrama, P.W.; Nash, P.T.; Gransberg, D.D. (2003). *Evaluate the Uses for Scrap Tires in Transportation Facilities*. Research Report N.º 1808-1, conducted for Texas Department of Transportation by the Center for Multidisciplinary Research in Transportation, Department of Civil Engineering, Texas Tech University. Downloaded on 4<sup>th</sup> April, 2019 from [https://www.depts.ttu.edu/techmrtweb/reports/complete\\_reports/1808\\_Scrap\\_Tire.pdf](https://www.depts.ttu.edu/techmrtweb/reports/complete_reports/1808_Scrap_Tire.pdf)
- Soroushian, P.; Lee, C.D. (1990). *Distribution and orientation of fibers in steel fiber reinforced concrete*. ACI Materials Journal, 87(5), 433-439.
- SOTRAMER (1978). *Tetrapods*. Technical note, Grenoble, France.
- Spasojević, A. (2008). *Structural implications of Ultra-High Performance Fibre-Reinforced Concrete in Bridge Design*. Doctoral Thesis, Faculté de L'Environnement Naturel, Architectural et Construit, École Polytechnique Fédérale de Lausanne, Switzerland.
-

- Švec, O.; Zirgulis, G.; Bolander, J.E.; Stang, H. (2014). *Influence of formwork surface on the orientation of steel fibres within self-compacting concrete and on the mechanical properties of cast structural elements*. Cement and Concrete Composites, 50, 60-72.
- Taheri, M.; Barros, J.A.O.; Salehian, H. (2012). *A parametric study on the use of strain softening/hardening FRC for RC elements failing in bending*. Journal of Materials in Civil Engineering, 24(3), 259-274.
- Tang, L. (1996). *Electrically Accelerated Methods for Determining Chloride Diffusivity in Concrete-Current Development*. Magazine of Concrete Research, 48 (176), 173–179.
- Tang, L.; Sørensen, H.E. (2001). *Precision of the Nodic test methods for measuring chloride transport diffusion/migration coefficients*. Materials and Structures, 34, 479-485.
- Tavares, S.S.M.; Pardal, J.M.; Lima, L.D.; Bastos, I.N.; Nascimento, A.M.; de Souza, J.A. (2007). *Characterization of microstructure, chemical composition, corrosion resistance and toughness of a multipass weld joint of superduplex stainless steel UNS S32750*. Materials characterization, 58, 610-616.
- Tchobanoglous, G.; Kreith, F. (2002). *Handbook of Solid Waste Management*. 2<sup>nd</sup> Edition, McGraw-Hill Handbooks, New York, USA.
- Teruzzi, T.; Cadoni, E.; Frigeri, G.; Cangiano, S.; Plizzari, G., (2004). *Durability aspects of steel fibre reinforced concrete*. In Proceedings of BEFIB'2004 - 6<sup>th</sup> International RILEM Symposium on Fibre-Reinforced Concretes (FRC), 20-22 September, Varenna, Italy, 625–634.
- Thomas, B.S.; Gupta, R.C.; Panicker, V.J. (2016). *Recycling of waste tire rubber as aggregate in concrete: durability-related performance*. Journal of Cleaner Production, 112, 504-513.
- Tlemat, H.; Pilakoutas, K.; Neocleous, K. (2003a). *Pull-out behaviour of steel fibres recycled from used tyres*. In Proceedings of the International Symposium on Celebrating Concrete: People and Practice, Thomas Telford Ltd, 3-4 September, Dundee, Scotland, 175-184.
- Tlemat, H.; Pilakoutas, K.; Neocleous, K. (2003b). *Flexural toughness of SFRC made with fibres extracted from tyres. Recycling and Reuse of Waste Materials*. In Proceedings of International Symposium on Advances in Waste Management and Recycling, Thomas Telford Ltd, 9-11 September, Dundee, Scotland, 365-374.
- Tlemat, H.; Pilakoutas, K.; Neocleous, K. (2004a). *Demonstrating steel fibres from waste tyres as reinforcement in concrete: material characterization*. In Proceedings of the 1<sup>st</sup> International Conference on Innovative Materials and Technologies for Construction and Restoration, 7-9 June, Lecce, Italy.
- Tlemat, H. (2004b). *Steel Fibres from Waste Tyres to Concrete; Testing, Modelling and Design*. Doctoral Thesis, Department of Civil and Structural Engineering, Faculty of Engineering of the University of Sheffield, UK.
- Tlemat, H.; Pilakoutas, K.; Neocleous, K. (2006a). *Stress-strain characteristic of SFRC using recycled fibres*. Materials and Structures, 39, 365-377.
- Tlemat, H.; Pilakoutas, K.; Neocleous, K. (2006b). *Modelling of SFRC using inverse finite element analysis*. Materials and Structures, 39, 221-233.
- Tran, V.N.G.; Bernard, E.S.; Beasley, A.J. (2005). *Constitutive Modeling of Fiber Reinforced Shotcrete Panels*. Journal of Engineering Mechanics, 131(5), 512-521.
- Turer, A. (2012). *Recycling of Scrap Tires*. Chapter 8 in book “Material Recycling-Trends and Perspectives”, InTechOpen, Eds: D. Achilias, 195-212.
- Tuutti K. (1982). *Corrosion of steel in concrete*. CBI Report 4:82, The Swedish Cement and Concrete Institute, 468.
- UNE 83515:2010. *Fiber reinforced concrete. Determination of cracking strength, ductility and residual tensile strength. Barcelona test*. AENOR, Spain.
- UNI 11039-2:2003. *Steel Fiber Reinforced Concrete – Test Method for Determination of First Crack Strength and Ductility Indexes*. UNI Editions, Milan, Italy.
- UNI 11037:2003. *Steel fiber to be used in the preparation of reinforced concrete conglomerate*. UNI Editions, Milan, Italy.

- Undri, A.; Meini, S.; Rosi, L.; Frediani, M.; Frediani, P. (2013). *Microwave pyrolysis of polymeric materials: Waste tires treatment and characterization of the value-added products*. Journal of Analytical and Applied Pyrolysis, 103, 149-158.
- Undri, A.; Rosi, L.; Frediani, M.; Frediani, P. (2014). *Upgraded fuel from microwave assisted pyrolysis of waste tire*. Fuel, 115, 600-608.
- USTMA, 2018. *2017 U.S. Scrap Tire Management Summary*. Prepared by USTMA, Washington, USA. Downloaded on 4<sup>th</sup> March, 2019 from [https://www.ustires.org/system/files/USTMA\\_scrap\\_tire\\_summ\\_2017\\_072018.pdf](https://www.ustires.org/system/files/USTMA_scrap_tire_summ_2017_072018.pdf)
- Van der Meer, J.W. (1999). *Design of concrete armour layers*. In Proceedings of the International Conference on Coastal Structures '99, Santander, Spain, 213-222.
- Vandewalle, L.; Dupont, D. (2003). *Test and Design Methods for Steel Fibre Reinforced Concrete – Background and Experiences: Bending test and interpretation*. In Proceedings of the RILEM TC 162-TDF Workshop, RILEM Publications S.A.R.L., Eds: B. Schnütgen; L. Vandewalle, 20-21 March, Bochum, Germany.
- Vavřík, D.; Fila, T.; Janděšek, I.; Veselý, V. (2012). *X-ray observation of the loaded silicate composite*. In Proceedings of the 18<sup>th</sup> International Conference Engineering Mechanics 2012, 14-17 May, Svratka, Czech Republic, 1485-1491.
- Verhagen, H.J. (2004). *Classical, Innovative and Unconventional Coastline Protection Methods*. In Proceedings of the NATO Advanced Research Workshop on Environmentally Friendly Coastal Protection Structures, 25-27 May, Varna, Bulgaria, 57-71.
- D21V032 (2013). *VoltaLab systems with VoltaMaster 4*. User's Manual (English). HACH LANGE GmbH, Germany.
- Wang, J.; Wang, Z.Y.; W. Ke (2010). *Corrosion behaviour of weathering steel in diluted Qinghai salt lake water in a laboratory accelerated test that involved cyclic wet/dry conditions*. Materials Chemistry and Physics, 124, 952-958.
- Wang, J.; Wang, Z.Y.; Ke, W. (2010). *Corrosion behaviour of weathering steel in diluted Qinghai salt lake water in a laboratory accelerated test that involved cyclic wet/dry conditions*. Material Chemistry and Physics, 124, 952-958.
- Wang, Q.; Sun, W.; Guo, L.; Gu, C.; Zong, J. (2018a). *Prediction of chloride ingress in steel fibre reinforced concrete under bending load*. Ceramics - Silikáty, 62(1), 59-66.
- Wang, Q.; Sun, W.; Guo, L.; Gu, C.; Zong, J. (2018b). *Modeling Chloride Diffusion Coefficient of Steel Fiber Reinforced Concrete under Bending Load*. Advances in Civil Engineering, Article ID 3789214, 1-6.
- Waweru, R. (2011). *The effect of fiber corrosion on shear capacity of steel fiber reinforced concrete beams and an initial investigation on alkali-silica reaction in steel fiber reinforced concrete*. Master Thesis in Civil Engineering, The University of Texas at Arlington.
- Wei, S.; Jiang, Z.; Liu, H.; Zhou, D.; Sanchez-Silva, M. (2013). *Microbiologically induced deterioration of concrete – A Review*. Brazilian Journal of Microbiology, 44, 4), 1001-1007.
- Williams, P. (2013). *Pyrolysis of waste tyres: A review*. Waste Management, 33, 1714-1728.
- Wolyniec S. (2003). *Electrochemical Techniques in Corrosion*. Edusp - Publisher of University of São Paulo, Brasil [in Portuguese].
- World Business Council for Sustainable Development (WBCSD), 2010. *End-of-Life Tires: A framework for effective management systems*. Prepared by the WBCSD Tire Industry Project, Geneva, Switzerland. Downloaded on 8<sup>th</sup> March, 2019 from <http://www.etrma.org/uploads/Modules/Documentsmanager/a-framework-for-effective-elt-management-systems-final-25.6.10.pdf>
- Xu, B.W.; Shi, H.S. (2009). *Correlations among mechanical properties of steel fiber reinforced concrete*. Construction and Building Materials, 23, 3468-3474.
- Yang, C.-C.; Liang, C.-H. (2014). *A modified colorimetric method to determine the chloride profile from the ponding test*. Journal of the Chinese Institute of Engineers, 37:4, 419-427.

- Yang, J.; Lu, Y.; Guo, Z.; Gu, J.; Gu, C. (2018). *Corrosion behaviour of a quenched and partitioned medium carbon steel in 3.5 wt.% NaCl solution*. Corrosion Science, 130, 64-75.
- Yazici, S., Inan, G., Tabak, V. (2007). *Effect of aspect ratio and volume fraction of steel fiber on the mechanical properties of SFRC*. Construction and Building Materials, 21, 1250–1253.
- Yoon, I. (2012). *Chloride Penetration through Cracks in High- Performance Concrete and Surface Treatment System for Crack Healing*. Hindawi Publishing Corporation, Advances in Materials Science and Engineering, ID 294571, 8 pages.
- Yuan, Q.; De Schutter, G.; Shi, C.; Audenaert, K. (2008). *The relationship between chloride diffusion and migration coefficients in concrete*. In Proceedings of 1<sup>st</sup> International Conference on Microstructure Related Durability of Cementitious Composites, Nanjing, China, 13-15 October, 553-563.
- Yuan, Q. (2009). *Fundamental Studies on Test Methods for the Transport of Chloride Ions in Cementitious Materials*. Doctoral thesis, Department of Structural Engineering, Ghent University, Ghent, Belgium; School of Civil Engineering and Architecture, Central South University, Changsha, China.
- Zamanzadeh, Z.; Lourenço, L.; Barros, J. (2015). *Recycled Steel Fibre Reinforced Concrete failing in bending and in shear*. Construction and Building Materials, 85, 195-207.
- Zamanzadeh, Z. (2017). *Cement based materials reinforced with recycled steel fibres: mechanical, durability and structural performance*. Doctoral thesis, Department of Civil Engineering, School of Engineering of the University of Minho, Guimarães, Portugal.
- Zhang, Y.-s.; Bian, T.-t.; Zhang, Y.; Zheng, X.-d.; Li, Z.-y. (2018). *Effective and green tire recycling through microwave pyrolysis*. Journal of Zhejiang University – Science A (Applied Physics & Engineering), 19(12), 951-960.
- Židonienė, S.; Kruopienė, J. (2015). *Life Cycle Assessment in environmental impact assessments of industrial projects: towards the improvement*. Journal of Cleaner Production, 106, 533-540.

---

# Appendix A

---

## **METHODOLOGY TO MEASURE THE HARDNESS AND ELASTIC MODULUS BY NANO-INDENTATION TEST**



## Basic principles

A schematic representation of a typical data set obtained with a Berkovich indenter is presented in Figure A.1a, where the parameter  $P$  is the applied load and  $h$  is the displacement relative to the initial undeformed surface. From the  $P-h$  curves, four parameters are measured: the maximum load,  $P_{max}$ , the maximum displacement,  $h_{max}$ , the elastic unloading stiffness (also designated by contact stiffness),  $S = dP/dh$ , defined as the slope of the upper portion of the unloading curve during the initial stages of unloading, and the permanent depth of penetration after the indenter is fully unloaded,  $h_f$  (Oliver and Pharr, 2004) (Figure 1a).

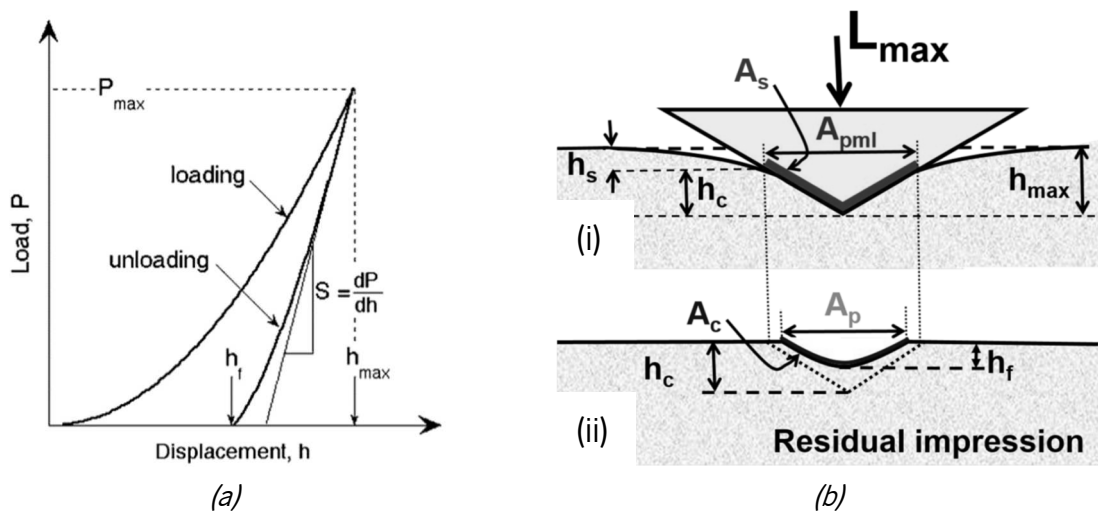


Fig. A.1 – (a) Load-displacement data obtained in nano-indentation test;  
 (b) Elasto-plastic deformation of the sample at the maximum applied load,  $P_{max}$  (i)  
 and plastic deformation after releasing the load (ii) (Oliver and Pharr, 2004; Broitman, 2017)

The hardness of the material is defined as  $H = P/A_{pml}$ , where  $A_{pml}$  is the projected area of contact at the maximum load (Figure A.1b). Since this area is very small (nanometer or few micrometers size), a method developed by Pharr *et al.* (1992) can be used to calculate  $A_{pml}$  directly from the load-unload curve. This method consists in four steps (Broitman, 2017):

- 1) Fit the unloading part of the load-displacement data to the power law relation derived from the elastic contact theory, according to the following equation:

$$P = \beta (h - h_f)^m \quad (\text{A.1})$$

where  $\beta$  and  $m$  are power law fitting constants (Oliver and Pharr, 2004).

- 2) Find the contact stiffness,  $S$ , by differentiating the unloading curve fit, and evaluating the result at the maximum depth of penetration,  $h = h_{m\acute{a}x}$ . This gives the following:

$$S = \left( \frac{dP}{dh} \right)_{h=h_{m\acute{a}x}} = \beta (h_{m\acute{a}x} - h_f)^{m-1} \quad (\text{A.2})$$

- 3) Determine the contact depth,  $h_c$ , which for an elastic contact is smaller than  $h_{m\acute{a}x}$  (Fig. A.1b). Assuming that the material pileup around an indent is negligible, an elastic model shows that the amount of sink-in  $h_s$  (Figure A.1b), is given by:

$$h_s = \varepsilon P_{m\acute{a}x} / S \quad (\text{A.3})$$

where  $\varepsilon$  is a constant that depends on the geometry of the indenter (Pharr *et al.*, 1992). The contact depth,  $h_c$ , is estimated according to the following expression:

$$h_c = h_{m\acute{a}x} - \varepsilon P_{m\acute{a}x} / S \quad (\text{A.4})$$

- 4) Assuming a perfect Berkovich indenter, calculate the projected area as:

$$A_{pmi} = 3\sqrt{3} \tan^2\left(\frac{\alpha}{2}\right) h_c^2 \quad (\text{A.5})$$

where  $\alpha$  is the angle of the Berkovich indenter.

The calculation of the elastic modulus of the material can be done using its relationship to contact area and the measured unloading stiffness through the following fundamental relation (Broitman, 2017):

$$S = \frac{2}{B\sqrt{\pi}} E_{eff} \sqrt{A_{pmi}} \quad (\text{A.6})$$

where  $B$  is a geometrical factor depending on the indenter (Pharr *et al.*, 1992) and  $E_{eff}$  is the effective elastic modulus defined as:

$$\frac{1}{E_{eff}} = \frac{1-\nu^2}{E} + \frac{1-\nu_i^2}{E_i} \quad (\text{A.7})$$























where  $E$  and  $\nu$  are the Young's modulus and Poisson's ratio of the sample, and  $E_i$  and  $\nu_i$ , the elastic modulus and Poisson's ratio of the indenter.

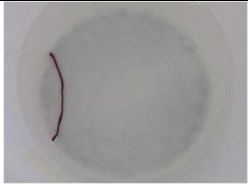























---

























# Appendix B

---

## **RSF EXPOSED TO CHLORIDE IMMERSION**

Exposure time (days)	0.1	3	14	21	28	35	42
<b>Series I</b> (Fiber 1)							
Exposure time (days)	49	56	63	67	79	84	91
<b>Series I</b> (Fiber 1)							
Exposure time (days)	0.1	3	14	21	28	35	42
<b>Series IV</b> (Fiber 1)							
Exposure time (days)	49						
<b>Series IV</b> (Fiber 1)							

Exposure time (days)	0	7	14	21	28	35	42
<b>Series II</b> (Fiber 1)							
Exposure time (days)	49	53	65	70	77	84	91
<b>Series II</b> (Fiber 1)							
Exposure time (days)	0	7	14	21	28	35	42
<b>Series V</b> (Fiber 1)							
Exposure time (days)	49	53	65				
<b>Series V</b> (Fiber 1)							

Exposure time (days)	0	7	14	21	28	35	42
<b>Series III</b> (Fiber 1)							
Exposure time (days)	49	53	65	70	77	84	91
<b>Series III</b> (Fiber 1)							
Exposure time (days)	0.1	7	14	21	28	35	42
<b>Series VI</b> (Fiber 1)							
Exposure time (days)	49	53	65				
<b>Series VI</b> (Fiber 1)							

---

# Appendix C

---

## **DESIGN OF THE TEST SETUP FOR RPT-3PS**

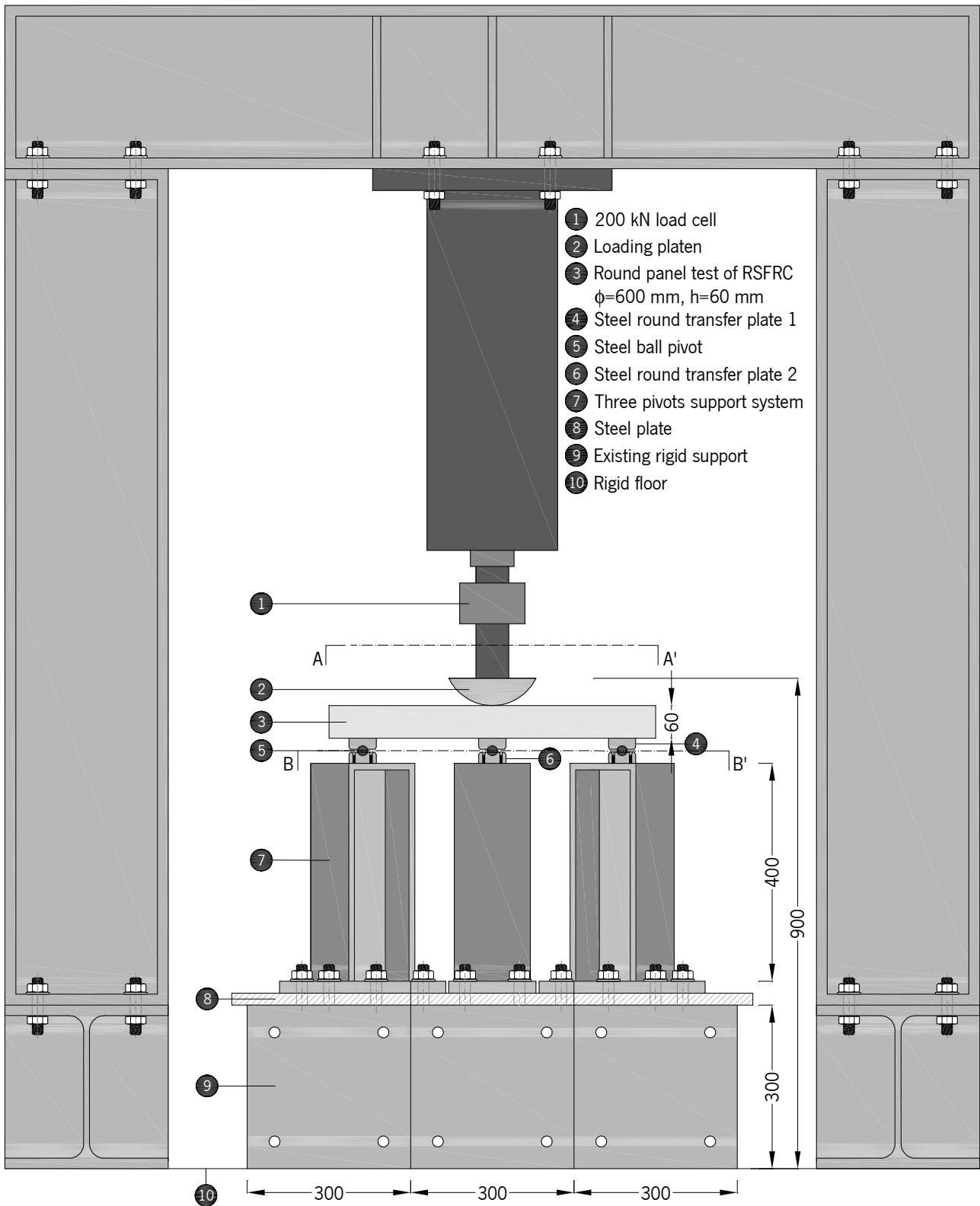


Figure C.1 – Drawing 1: Front view of the RPT-3ps test setup (units in mm)



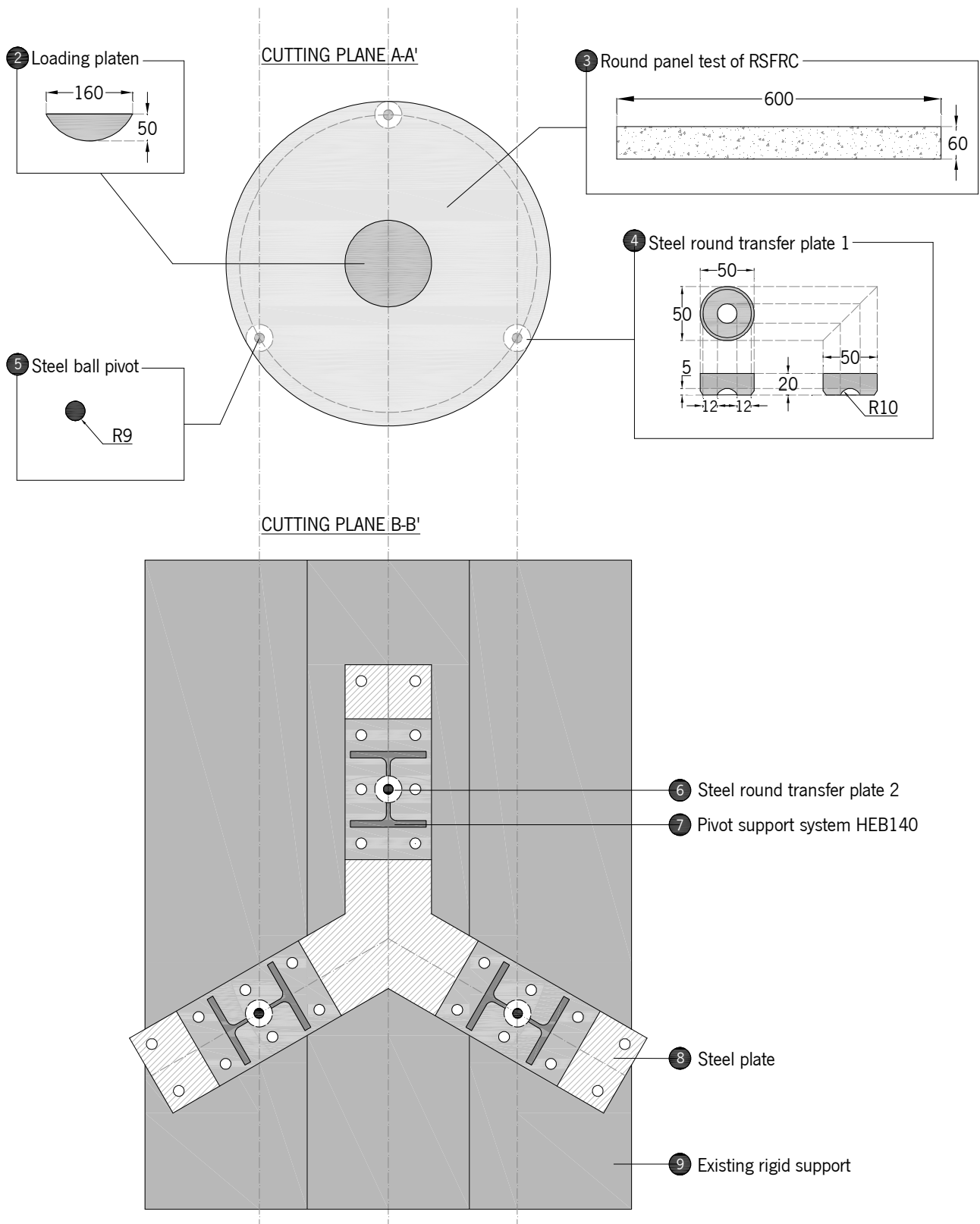


Figure C.2 – Drawing 2: Top views and details of the RPT-3ps test setup by the cutting planes A-A' and B-B' (units in mm)



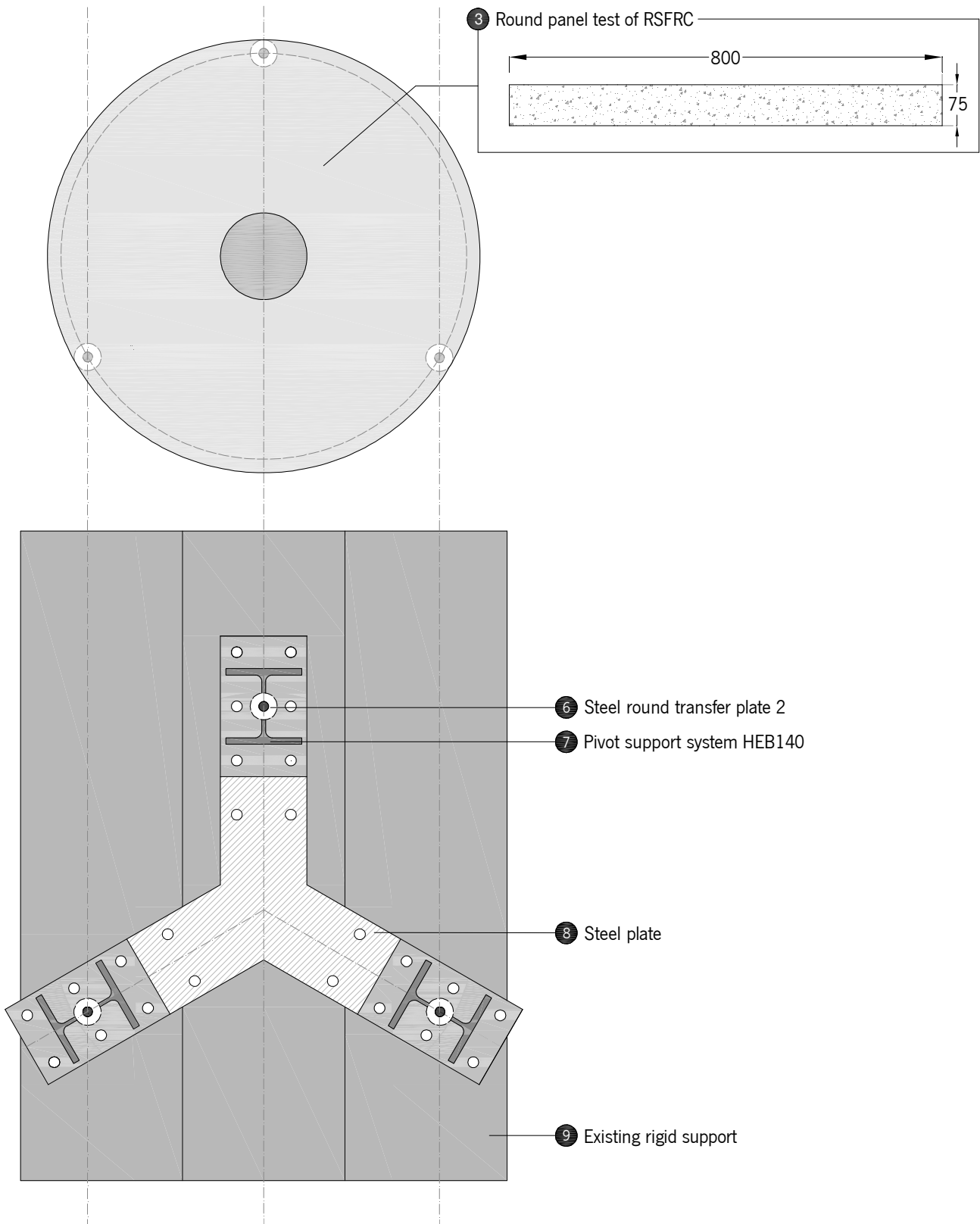


Figure C.4 – Drawing 4: RPT-3ps test setup for round panels with 800 mm diameter (units in mm)

---

# Appendix D

---

## **MODES OF FAILURE OF ROUND PANELS**

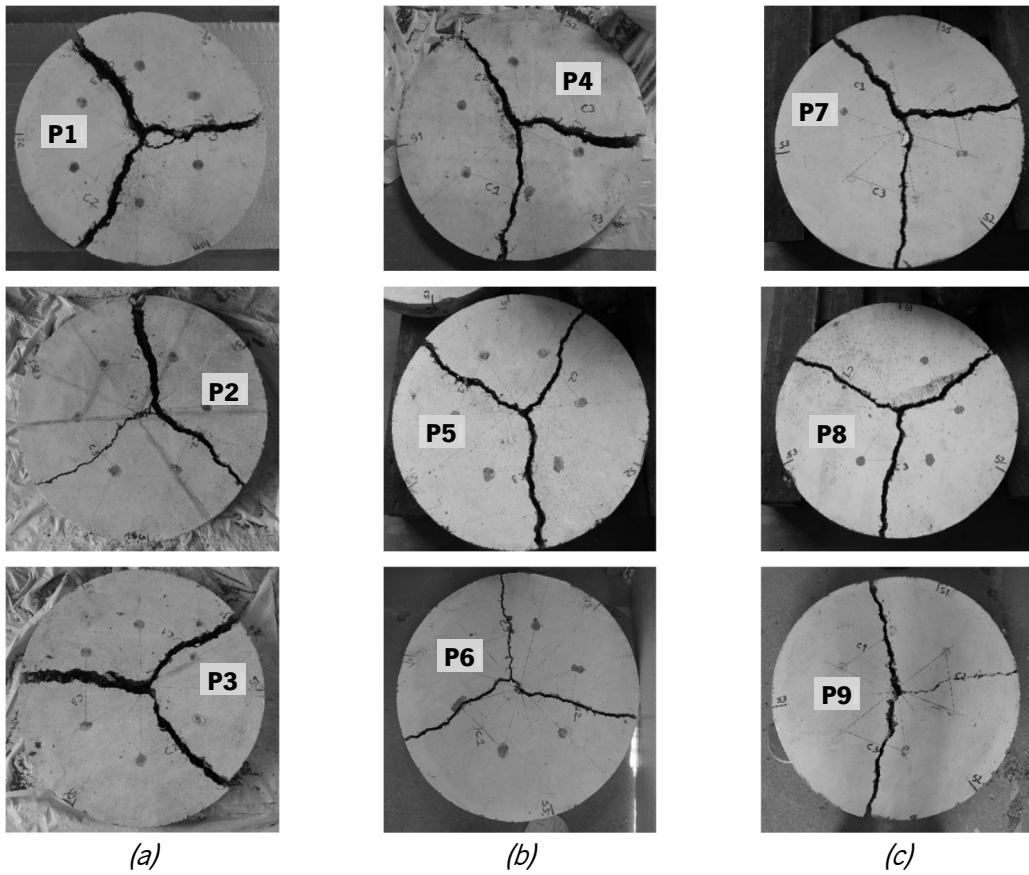


Figure D.1 – Crack patterns of the round panels of: (a) Series I\_CI; (b) Series II\_CI; (c) Series III\_CI

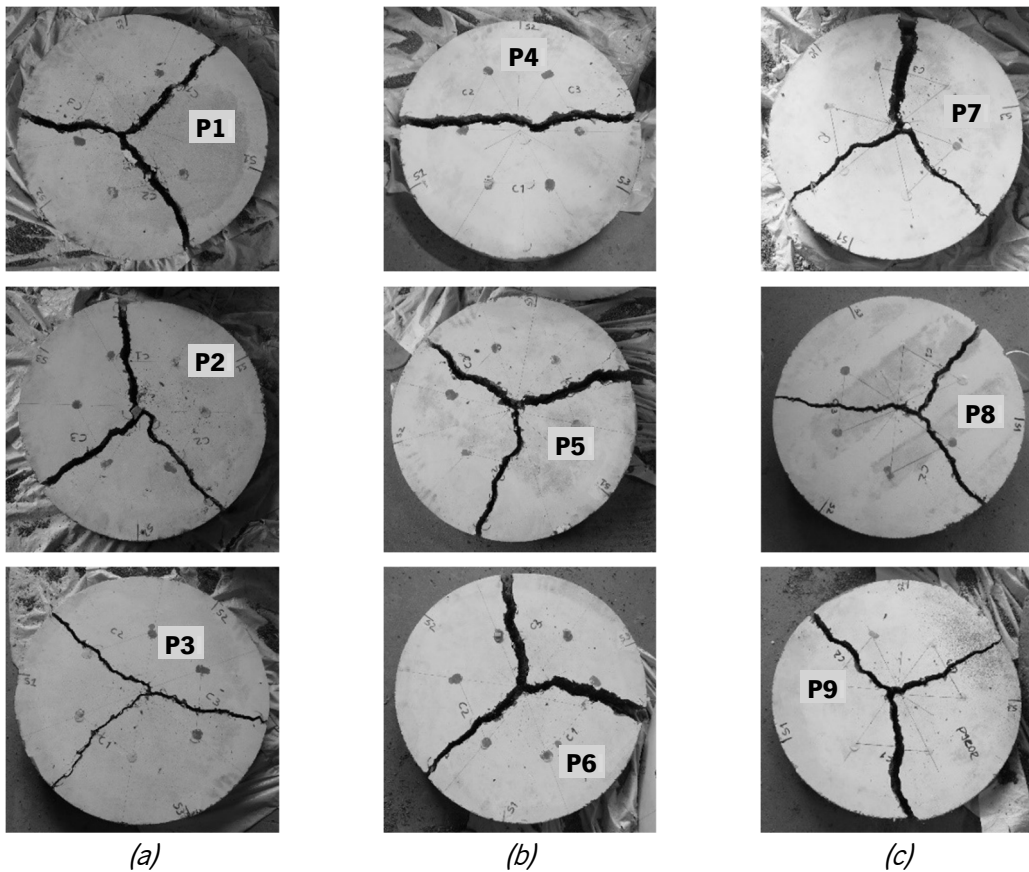


Figure D.2 – Crack patterns of the round panels of: (a) Series I\_REF; (b) Series II\_REF; (c) Series III\_REF

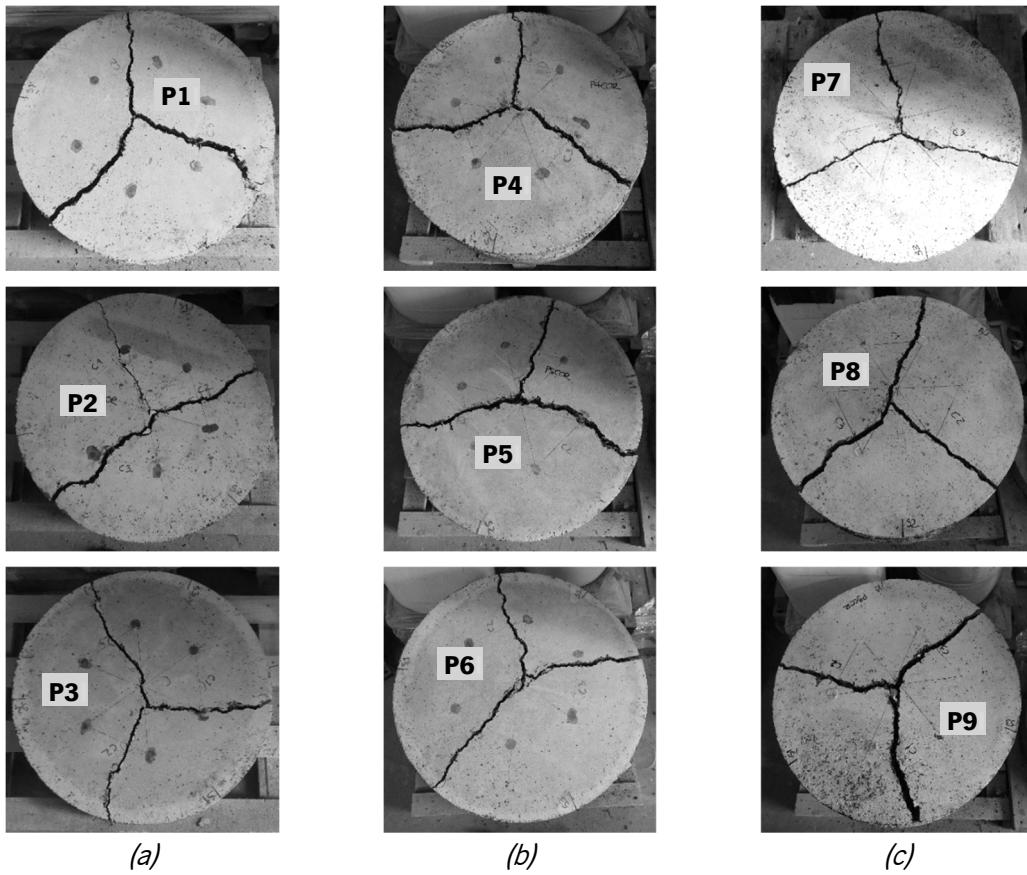


Figure D.3 – Crack patterns of the round panels of: (a) Series IV\_CI; (b) Series V\_CI; (c) Series VI\_CI

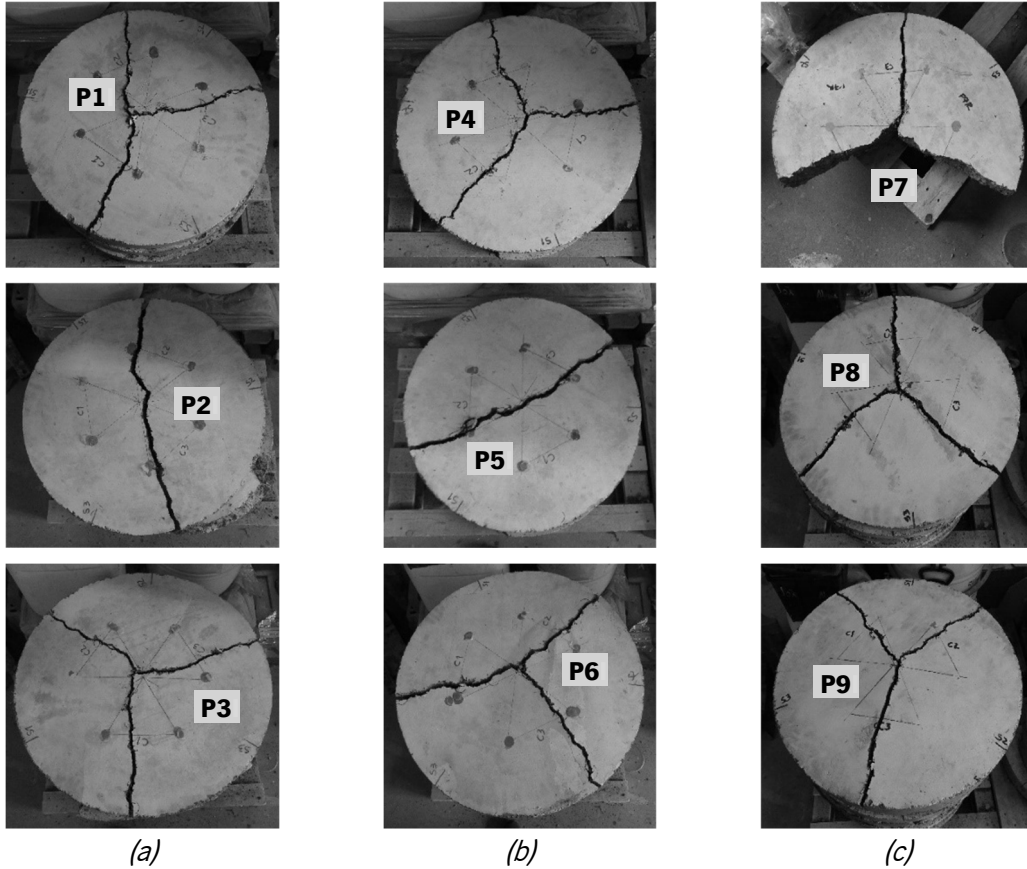


Figure D.4 – Crack patterns of the panels of: (a) Series IV\_REF; (b) Series V\_REF; (c) Series VI\_REF